



Delft University of Technology

Temperature-chemistry-microstructure correlations for alkali-activated binders

Miranda de Lima Junior, L.C.

Publication date
2025

Document Version
Final published version

Citation (APA)
Miranda de Lima Junior, L. C. (2025). *Temperature-chemistry-microstructure correlations for alkali-activated binders*. [Dissertation (TU Delft), Delft University of Technology].

Important note
To cite this publication, please use the final published version (if applicable).
Please check the document version above.

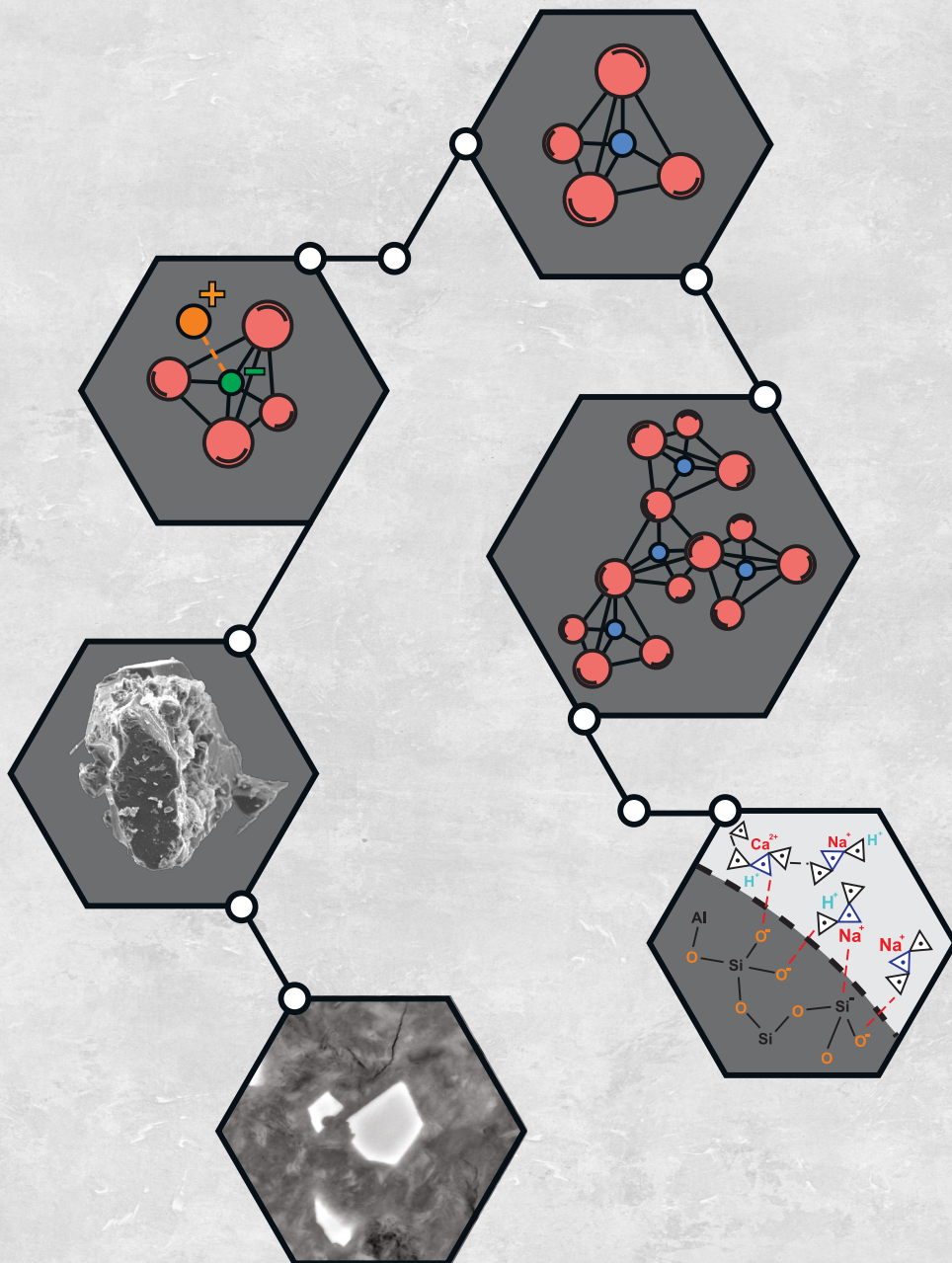
Copyright
Other than for strictly personal use, it is not permitted to download, forward or distribute the text or part of it, without the consent of the author(s) and/or copyright holder(s), unless the work is under an open content license such as Creative Commons.

Takedown policy
Please contact us and provide details if you believe this document breaches copyrights.
We will remove access to the work immediately and investigate your claim.

*This work is downloaded from Delft University of Technology.
For technical reasons the number of authors shown on this cover page is limited to a maximum of 10.*

TEMPERATURE-CHEMISTRY-MICROSTRUCTURE CORRELATIONS FOR ALKALI-ACTIVATED BINDERS

Luiz Miranda de Lima



Temperature-chemistry-microstructure correlations for alkali-activated binders

Dissertation

For the purpose of obtaining the degree of doctor

at Delft University of Technology

by the authority of the Rector Magnificus Prof.dr.ir. T.H.J.J. van der Hagen,

Chair of the Board for Doctorates

to be defended publicly on Monday, June 16th, 2025, at 17:30

by

Luiz Cezar MIRANDA DE LIMA JUNIOR

Master of Science in Materials Science and Engineering

Ponta Grossa State University, Brazil

Born in Guarapuava, Brazil

This dissertation has been approved by the promotor:

Promotor: Prof.dr.ir. G. Ye

Promotor: Prof.dr. J.L. Provis

Composition of the doctoral committee:

Rector Magnificus,
Prof.dr.ir. G. Ye,
Prof.dr. J.L. Provis,

Chairperson
Delft University of Technology, promotor
Paul Scherrer Institute, Switzerland, promotor

Independent members:
Prof.dr. B. Lothenbach

EMPA - Swiss Federal Laboratories for Materials
Science and Technology, Switzerland

Prof.dr.ir. S. Matthys
Prof.dr.ir. H.E.J.G. Schlangen
Dr. R. Snellings
Dr. O. Copuroglu
Prof.dr. H.M. Jonkers

Universiteit Gent, Belgium
Delft University of Technology
Katholieke Universiteit Leuven, Belgium
Delft University of Technology
Delft University of Technology reserve member

This research was carried out in the Microlab, Delft University of Technology, and was financially supported by the European Union's Horizon 2020 research and innovation program, under the Marie Skłodowska-Curie agreement No. 813596 (PhD Training Network on Durable, Reliable and Sustainable Structures with Alkali-Activated Materials - DuRSAAM).



Keywords:

Alkali-activated materials, infrared spectroscopy, dissolution kinetics, phase assemblage, microstructure characterization, isothermal calorimetry, thermodynamic modelling, dissolution kinetics, scanning electron microscopy

Printed by:

Gildeprint, the Netherlands

Thesis format by:

Luiz Miranda de Lima

Cover design by:

Luiz Miranda de Lima

ISBN:

978-94-6496-426-4

Copyright © 2025 by Luiz Miranda de Lima

An electronic version of this dissertation is available at:

<http://repository.tudelft.nl>

*“Se manter de pé contra o que vier.
Vencer os medos. Mostrar ao que veio.
Ter o foco ali e sempre seguir rumo à vitória.”*

Dead Fish - Vitória (2015)

To my parents, who taught me most of what I know,
and to my wife, who always gave me the energy
I needed to continue fighting.

Table of contents

List of symbols.....	vii
List of abbreviations	ix
Chapter 1. General introduction.....	1
1.1 Research background.....	3
1.2 Research aim and objectives.....	6
1.3 Research scope.....	7
1.4 Research methodology	7
1.5 Research outline.....	9
Chapter 2. Literature survey	13
2.1 Introduction	15
2.2 The concept of alkali-activated materials	15
2.2.1 Selection of raw materials	15
2.2.2 Challenges of conventional precursors	21
2.2.3 The introduction of chemistry-based approaches	23
2.3 Structural characterization of precursors	26
2.4 Kinetics of alkali-activating reactions.....	30
2.4.1 Dissolution	30
2.4.2 Precipitation of reaction products.....	33
2.4.3 Reaction mechanisms	36
2.4.4 Characterization of hardened binders	38
2.5 Modelling of alkali-activated materials.....	41
2.5.1 Thermodynamic modelling for phase assemblage	41
2.5.2 Microstructure modelling through combined kinetic and thermodynamic approaches.....	43
2.6 Identification of research gaps and the motivation of this research.....	46
Chapter 3. Synthesis and microstructural characterization of glasses resembling conventional precursors	49
3.1 Introduction	51
3.2 Materials and Methods.....	52
3.2.1 Synthesis of glasses resembling slags and fly ashes.....	52
3.2.2 Characterization of synthetic precursors.....	52
3.3 Results.....	53
3.3.1 Chemical composition of synthetic precursors	53
3.3.2 Structural analysis of synthetic precursors	55

3.4 Discussion.....	64
3.4.1 Glass phase segmentation with XRD.....	64
3.4.2 Interactions between SiO_4 and $\text{AlO}_4/\text{AlO}_6$ groups in fly ash-type glasses.....	65
3.4.3 Influence of CaO in the destabilization of glass network.....	67
3.5 Conclusions and outlook.....	70
Chapter 4. Dissolution kinetics of synthetic precursors	73
4.1 Introduction	75
4.2 Materials and methods	77
4.2.1 Preparation of synthetic glasses for dissolution experiments	77
4.2.2 Dissolution experiments	78
4.2.3 Thermodynamic calculations.....	79
4.2.4 Characterization of residual powder.....	80
4.3 Results.....	81
4.3.1 Dissolution mechanisms at room temperature	81
4.3.2 Characterization of residual framework after dissolution	87
4.3.3 Effect of temperature on dissolution of fly ash-type glasses.....	92
4.3.4 Determination of forward dissolution rate equations	95
4.4 Discussion.....	101
4.4.1 Selective dissolution of Ca- and Al-species.....	101
4.4.2 Validation of dissolution rate equations	103
4.5 Conclusions and outlook.....	106
Chapter 5. Early-stage reactions of alkali-activated synthetic precursors	109
5.1 Introduction	111
5.2 Materials and methods	114
5.2.1 Preparation of coarse synthetic precursors	114
5.2.2 Dissolution experiments and study of residual dissolution material	115
5.3 Results.....	117
5.3.1 Dissolution experiments in NaOH solutions at 20 °C	117
5.3.2 Dissolution experiments in waterglass solutions: characterization of residual material	129
5.3.3. Characterization of early reaction kinetics with in-situ isothermal calorimetry	134
5.4 Discussion.....	136
5.4.1 Effect of chemistry on initial degree of reaction	136
5.4.2 Precipitation mechanisms in low-Ca precursors	138
5.4.3 Mechanisms of N-A-S-H gel precipitation.....	140
5.5 Conclusions and outlook.....	143
Chapter 6. Phase assemblage of alkali-activated pastes with synthetic precursors	147
6.1 Introduction	149

6.2 Materials and methods	150
6.2.1 Preparation of synthetic precursors	150
6.2.2 Preparation of pastes	151
6.2.3 Characterization of hardened pastes	152
6.2.4 Isothermal calorimetry	154
6.2.5 Quantitative determination of reaction products	154
6.3 Results and discussions	156
6.3.1 Activation of individual precursors - 20 °C	156
6.3.2 Activation of individual precursors - 60 °C	167
6.3.3 Activation of blended precursors - 20 °C	175
6.4 Development of chemistry-temperature based correlations	182
6.4.1 Degree of reaction	182
6.4.2 Empirical definition of <i>phase assemblage indices</i>	184
6.5 Conclusions and outlook	188
Chapter 7. Numerical simulation of alkali-activated materials	191
7.1 Introduction	193
7.2 Methodology	194
7.2.1 Thermodynamic modelling	194
7.2.2 Numerical simulation - coupled kinetic and thermodynamic modelling	195
7.3 Results	199
7.3.1 Thermodynamic equilibrium of alkali-activated binders	199
7.3.2 Coupled thermodynamic and kinetic modelling	209
7.4 Validation of numerical simulation - comparison with experimental data	225
7.4.1 Evolution of degree of reaction	225
7.4.2 Phase assemblage	227
7.5 Conclusions and outlook	231
Chapter 8. Retrospection, contributions, and recommendations for future research	233
8.1 Retrospection	235
8.2 Conclusions and contributions of this research	238
8.3 Outlooks and recommendations for future research	246
References	249
Appendix A Database of precursors utilised across scientific literature	281
A.1 Chemical compositions of traditional and alternative precursors	281
A.2 Geographical distribution of primary sources of byproducts utilised as precursors	286
Appendix B Structural characterization of synthetic glasses	289
B.1 Chemical compositions through XRF	289
B.2 Structural characterization with ²⁹ Si NMR and Raman	290

B.3 Structural characterization of precursors described in literature.....	291
Appendix C Thermodynamic and kinetic properties of aqueous species and solid phases used for microstructure modelling.....	295
Appendix D Determination of forward dissolution rates	299
D.1 Methodology.....	299
D.2 Experimental results.....	299
D.2.1 Results generated in this work.....	299
D.2.2 Results obtained from literature	302
Appendix E Supplementary information utilised in Chapter 6	305
E.1 Isothermal calorimetry curves of alkali-activated synthetic glasses	305
E.2 SEM micrographs utilized for microanalysis with EDS.....	306
E.3 Detailed results from quantitative X-ray diffraction analysis.....	306
Summary.....	309
Samenvatting	311
Acknowledgements	315
CURRICULUM VITÆ.....	321

List of symbols

Roman lower case letters

a_i	Ion size	[Å]
b_y	A parameter for common short-range interactions of the charged species	
d_{eq}	Effective particle diameter	[µm]
d_{max}	Maximum particle size	[µm]
d_{min}	Minimum particle size	[µm]
i	Aqueous species	
m	Mass	[g]
n	Reaction order	
r	Overall dissolution rate	[mol/m ² /s]
r_+	Forward dissolution rate	[mol/m ² /s]
Δt	Variation in time	[s]
v_X	Molar fraction of element X in fly ash	
x	Element considered in dissolution rate equations	
z_i	Charge of species i	

Roman capital case letters

A	Pre-exponential parameter in dissolution rate equations	
A_n	Kinetic parameter of nucleation	[m ³ /s]
A_y	Pressure dependent parameter for calculation of activity of aqueous species	
B_n	Thermodynamic parameter of nucleation	
B_y	Temperature dependent parameter for calculation of activity of aqueous species	
C_P^0	Standard heat capacity	[J/mol/K]
E_a	Activation energy of the dissolving element	[J/mol]
$\Delta_f G^0$	Gibbs free energy of formation	[kJ/mol]
$\Delta_f H^0$	Enthalpy of formation	[kJ/mol]
IAP	Ion activity product	
J	Nucleation rate	[m ³ /s]
K_{sp}	Solubility product	
M_s	Activator modulus	
N	Number of species in reaction	
$\frac{NBO}{T}$	Ratio of the non-bridging oxygen atoms to oxygen atoms in tetragonal coordination	
$P(\Delta t)$	Nucleation probability at the time interval Δt	
R	Gas constant	[J/mol/K]
S	Supersaturation index of reaction products	
SSA	Specific surface area	[m ² /g]
S^0	Standard entropy	[J/mol/K]
T	Absolute temperature	[K]
T_{ref}	Reference temperature of 293.15 K	[K]
V	Volume of alkaline solution	[L]

V_0	Initial volume of glass in unreacted paste	[cm ³]
V_t	Residual volume of glass in paste at time t	[cm ³]
V^0	Standard molar volume	[cm ³ /mol]

Greek letters

$\alpha(t)$	Degree of reaction at time t	[%]
γ_i	Activity coefficient of species i	
ρ	Density of synthetic glass	[g/cm ³]

List of abbreviations

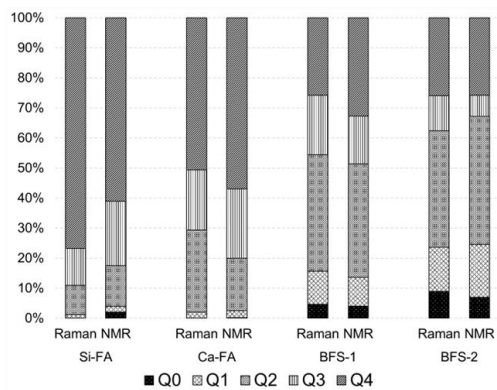
AAMs	Alkali-activated materials
ASTM	American Society for Testing and Materials
ATR-FTIR	Attenuated total reflection Fourier transform infrared spectroscopy
BF	Basalt fines
BFS	Blast furnace slag
BET	Brunauer-Emmett-Teller
BSE	Backscattered electron
BWA	Biomass wood ash
C-(N-A-)S-H	Variations of C-S-H gels, including C-A-S-H, C-N-S-H and C-N-A-S-H
C-A-S-H	Calcium aluminosilicate hydrate
C-N-A-S-H	Calcium sodium aluminosilicate hydrate
C-N-S-H	Calcium sodium silicate hydrate
C-S-H	Calcium silicate hydrate
Ca-FA	Calcareous fly ash
CAIs	Calcium-aluminum rich inclusions
CAS	CaO-Al ₂ O ₃ -SiO ₂ glass system
DTG	Differential thermogravimetric
EDS	Energy dispersive spectroscopy
ESI	Effective saturation index
FA	Fly ash
GEMs	Gibbs energy minimization software
GGBFS	Ground granulated blast furnace slag
ICP-OES	Inductively coupled plasma optical emission spectroscopy
IAP	Ion activity product
LDH	Layered double hydroxides
LS	Limestone
MAS NMR	Magic angle spinning nuclear magnetic resonance
MP-AES	Microwave plasma-atomic emission spectrometer
MSWI-BA	Municipal solid waste incineration bottom ash
N-A-S-H	Sodium aluminosilicate hydrate
N-C-A-S-H	Sodium calcium aluminosilicate hydrate
N-(C-)A-S-H	N-A-S-H and/or N-C-A-S-H
NBO	Non-bridging oxygen
NEN EN	Royal Netherlands Standardization Institute with European level standards
NWF	Network forming oxides
NWM	Network modifying oxides
PC	Portland cement
PDF	Powder diffraction file
POFA	Palm oil fuel ash
PSA	Paper sludge ash

Q	Quartz
QXRD	Quantitative X-ray diffraction
RHA	Rice husk ash
rpm	Revolutions per minute
SAM	Salicylic acid and methanol dissolution treatment
SEM	Scanning electron microscopy
SCBA	Sugar cane bagasse ash
SCM	Supplementary cementitious materials
SF	Silica fume
Si-FA	Siliceous fly ash
SL	Metallurgical slags
SSA	Sewage sludge ash
XRD	X-ray diffraction
XRF	X-ray fluorescence

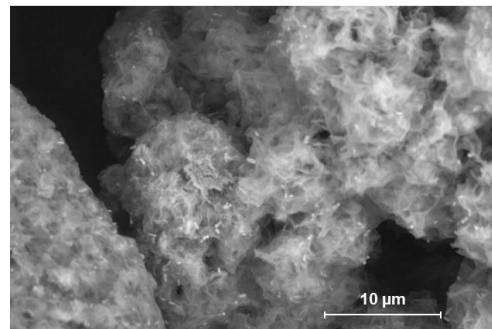
Chapter 1.

General introduction

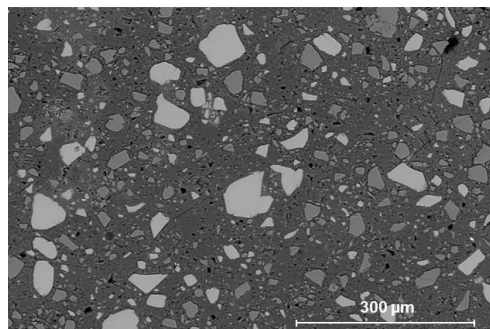
1. Dissolution kinetics of precursors: Correlation of structural characteristics of precursors with the evolution of pore solution



2. Early-stage reactions: Study of the reaction mechanisms involved in the precipitation of the first reaction products and their influencing factors



3. Evolution of phase assemblage: Assessment and prediction of the distribution of different reaction products through the stable microstructure



This chapter provides a general introduction of this research project. A short summary on the current status of technology and the main challenges of alkali-activated materials, as well as the existing research opportunities in this field, are highlighted. Finally, the objectives, the scope of the research, the methodology and an outline of the thesis is presented.

1.1 Research background

The development of modern societies requires the utilization of long-term, reliable, and cost-effective infrastructural materials. With the building industry acting as a pushing factor of economic growth [1,2], concrete arises as one of the main representatives of this scenario, especially in emerging countries [3-5]. Due to its substantial performance, longevity, and wide-spread availability, the world has heavily relied on its implementation in different applications, making it the most utilised man-made material around the globe [6]. However, such positive features are coupled with a few negative environmental aspects, mainly arising from its production chain. The production of Portland cement (PC), the main component of concrete mixtures, requires the extraction of non-renewable resources and makes use of a highly energetic process. It is estimated that the cement and concrete industries represent up to 9 % of all industrial water usage (2012) [7], as well as 7 % of the total global energy consumption (2018) [8]. Moreover, the massive decarbonisation of CaCO_3 during its production process - with an average CO_2 coefficient emission of $0.86 \text{ kg CO}_2/\text{kg}$ of clinker [9,10] - accounted for 5-7 % of the total global CO_2 emissions in the years 2020 and 2021 (2.6 Gton) [9,11,12].

The newest environmental policies concerning the reduction of CO_2 , such as the European Green Deal and the Inflation Reduction Act in the United States, demand the development of low CO_2 -emission solutions from players of the construction industry. The search for different building options, in vogue in the scientific community since the second half of the 20th century, brought several potential options for the field. The alternatives to lower the environmental impact of this industrial sector are based on extending the service life of concrete structures [13-18], on improving the circularity of old structures by implementation of recycled binder and recycled aggregates [19-23], and on the use of alternative binding materials using different sources of non-recyclable disposed byproducts [24-28]. Among the existing possibilities of the latter, alkali-activated materials (AAMs), or geopolymers¹, excel as one of the most mature options available in the market, given the extensive research performed over their performance and durability [29-35]. AAMs are composed of (calcium) aluminosilicate sources (so-called precursors), mainly regarded as byproducts from different industrial sectors, reacted with alkaline sources (so-called activator) to form a cementitious matrix physically similar to what is observed in hydration reactions of PC [36]. The precursors can be categorized as high- and low-Ca materials, and this classification represents major implications on their behaviour in forming a hardened binder. The majority of the raw materials implemented in AAMs are also widely implemented as supplementary cementitious materials (SCMs) in blends with PC, given the proximity in chemistry and performance of both systems - for instance, the Dutch standard NEN EN 197-1 allows a maximum content of 95 % of blast furnace slag in the composition of CEM III.

¹There exists a long debate over the terminology and definitions of alkali-activated materials and geopolymers, without a common agreement being reached. In this thesis, the term AAMs will be used and will cover both definitions.

Table 1.1: Summary of reported data on global production and expected demand of precursors for AAMs, and of Portland cement - values in million tonnes per annum.

	Slag	Fly ash	Portland cement
Production volume 2021	383 [37]	650-700* [38]	4200 [39]
Estimated production 2025	420 [37]	700*, **[40]	4700 [39]
Variation - 2018-2025	10 %	Up to 7 %	12 %

*The amount of produced fly ash was estimated from the conversion of coal consumption for energy generation (2.312×10^7 J/kg of coal - The American Physical Society), with a ash/coal ratio of 0. 10
(<https://www.jera.co.jp/en/sustainability/environment/waste/coal-ash>).

While the currently accessible literature allows satisfactory knowledge over the performance of hardened binders, issues concerning the marketability of conventional precursors, and consequently of AAMs, arise. In general, the availability of byproducts is not expected to follow the global demand of cement in the following years. As summarized in Table 1.1, the Portland cement demand is expected to reach a total of 4700 million tons by 2025 [39]. The increased demand from 2021 to 2025 is approximately 3 % and 6 % more than the expected availability of blast furnace slag² and coal fly ash³, the two most available and utilised commercial precursors. It is important to state that the availability of fly ash, in the second half of the decade, is projected to become stagnated or even to decrease [40], as the world is currently looking for alternative energy sources over coal. Additionally, the supplies of these alternative raw materials are geographically limited to regions in which they are produced. Finally, the variation in chemistry and mineralogy, influenced by their source materials and processing conditions of primary industrial processes, contributes to limiting a wider implementation of this technology.

The inconsistency in the chemistry of precursors imposes, what is potentially, the most difficult challenge to this class of materials. Conversely to their application as SCMs in blends with PC, which can rely on clinker as a standardized material to buffer their variations, changes in the chemical composition of precursors have an enormous impact in the performance and service-life of AAMs [29,41,42]. As observed in Figure 1.1, the CaO contents of fly ashes and slags reported in scientific literature presents variations up to 35 wt% and 25 wt%, respectively - the presence of CaO in the initial composition of precursors is an important parameter to be analyzed, since it can, among others, have a significant impact over the nature of the reactions taking place for each precursor, i.e. latent hydraulic or pozzolanic [43-46]. This issue is maximized in the cases of fly ashes (Figure 1.1a): in addition to the higher variability with respect to CaO content, they present wide fluctuations in the contents of SiO₂ and Al₂O₃. As a consequence, the changes in the Ca/(Si+Al) ratios are much more significant in fly ashes when compared to slags, and can represent extra complexity in understanding their reaction mechanisms.

Along with chemical composition, the reactivity and performance of AAMs can be influenced by an extensive range of variables. Consequently, it is not yet possible to derive an universal approach which predicts the performance and service-life of AAMs, despite the many efforts made by researchers throughout the world [47-49]. These multiple variables can be categorized in two main groups:

² The ground granulated blast furnace slag will be described throughout the thesis simply as “slag”.

³ The coal fly ashes will be described throughout the thesis simply as “fly ash”. Distinction will be made over the chemistry of the material, defining it as either calcareous fly ash or siliceous fly ash.

- Intrinsic factors inherent to the precursor: Chemical composition, mineral phases and quantity of amorphous material, all which have immediate impact on the microstructure and intrinsic reactivity of the precursor(s);
- Extrinsic factors: Processing and curing conditions of the AAM, such as nature and concentration of chosen activator, particle size distribution of precursor, mixing time and speed, use of admixtures, blending ratios (in case of a mixture of two or more precursors), temperature and time of curing, all which can be controlled by the operator.

The non-homogeneous availability of the main raw materials has driven the attention of researchers on the study of unconventional precursors [50-54], using alternative sources of wastes in different regions. Mostly, ashes from biomass and solid waste incineration present considerable potential to be used in blended systems with traditional precursors. And although this could partially solve the issue of global supply of raw materials, it would raise an extra concern within the intrinsic factors, widening of the range of chemistry and mineralogy of available binders.

The development of models able to estimate the performance and the service-life of AAMs could partially solve the issue of variation in chemistry and mineralogy. Based on chemical composition of reactive portions, thermodynamic modelling is a strong tool used to predict the equilibrium phase assemblage of cementitious systems [55-57]. However, a definitive implementation is currently limited to alkali-activated systems composed of high-Ca precursors [58], as literature is still missing reliable information over the thermodynamic data of reaction products observed in the alkali-activation of low-Ca materials.

Efforts on producing solid and extensive quantitative studies, evaluating the combined effect of both intrinsic and extrinsic factors on reactivity and performance of AAMs, would increase the public trust in this class of materials. Moreover, the improvement of modelling tools could facilitate the comprehension and the estimation of performance of such materials in long-term conditions. Consequently, extended implementation and increased marketability of the technology could be achieved. This research targeted a comprehensive understanding over the influence of these factors on different stages of alkali-activating reactions. From the early stages until the obtainment of hardened and mature microstructures, a coupled effect of binder chemistry with temperature and time was quantitatively measured. By the combination of experimental observations and simulation techniques, the addition of new features to GeoMicro3D [59], an in-house developed numerical modelling tool, was performed. This extension allowed the observation of the evolution of digitized microstructures of AAM-mixtures in different scenarios of precursors and curing conditions.

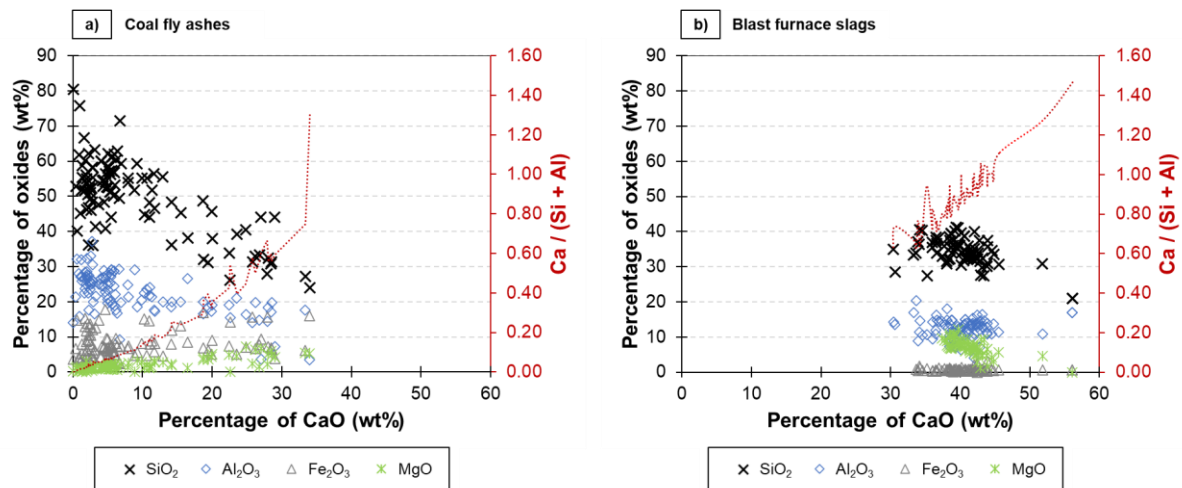


Figure 1.1: Distribution of chemical compositions of a) coal fly ashes and b) blast furnace slags reported in literature.

1.2 Research aim and objectives

This PhD project focuses on addressing the challenges of non-homogenous availability and variable chemistry of precursors. The primary aim of this project is to define correlations between the chemistry and curing conditions of alkali-activated binders with features of their microstructures. This study will involve the understanding of the different mechanisms involved in the individual stages of alkali-activated reactions, investigating the influence of multiple variables in each stage, leading to the development of reliable microstructure modelling tools which can estimate the performance and service life of these binders. To achieve this, the following objectives have been defined:

- To understand the effects of intrinsic and extrinsic factors on the kinetics of dissolution of different precursors,
- To clarify and correlate the different reaction mechanisms of AAMs according to characteristics of the mixture - nature and concentration of activators, type of precursor, and curing procedure,
- To characterize the evolution and maturation of (Ca-bound) sodium aluminosilicate hydrate (N-(C-)A-S-H) gels in both high- and low-Ca binders,
- To comprehend the effect of blending proportions of precursors in mature microstructures,
- To extend the possibilities of coupled kinetic-thermodynamic modelling tools, by simulating the microstructural evolution of alkali-activated materials made with low-Ca binders and blended precursors.

It is important to clarify that this research will not evaluate each precursor mentioned in Section 1.1 individually. Instead, it will focus on a range of compositions that encompasses most of them. This approach should provide sufficient coverage of the majority of options discussed in the literature and available for practical use.

1.3 Research scope

The approach selected in this research was on the utilization of synthetic glasses resembling slags, siliceous fly ash and calcareous fly ash, as precursors. This allowed the evaluation of completely amorphous structures, eliminating one intrinsic variable of the system (degree of crystallinity) and thus facilitating the interpretation of results. The synthetic precursors were subjected to study in early- and secondary-stages of alkali-activation. The results of the experimental observations were used for the extension of thermodynamic models and numerical simulation of alkali-activated materials. To maximize the comprehension of phenomena involved in such alkaline systems, the following restrictions were applied:

- The synthetic glasses were composed of only SiO_2 , Al_2O_3 and CaO . The Si/Ca atomic ratio of the glasses varied from 0.7 (representing blast furnace slag) to 4.1 (representing siliceous-fly ash).
- Highly-diluted conditions, with a 1:1000 ratio of glass against sodium hydroxide and sodium silicate solutions, were prepared to simulate the early-stage reactions of the synthetic glasses.
- The same activators were chosen for the study of alkali-activated pastes. Pastes were characterized after 1, 7 and 28 days.
- The kinetics of dissolution and hardened pastes of alkali-activated fly ash-like glasses were studied at 20 °C and 60 °C, while slag-like glasses were analyzed only at 20 °C.
- The water/precursor ratio of the analyzed pastes was 0.40 for slag-like glasses and 0.35 for fly ash-like glasses.
- No admixtures were used in the pastes
- Both thermodynamic modelling and numerical simulations were performed to evaluate the characteristics of the alkali-activated materials up to 7 days.
- Both thermodynamic modelling and numerical simulations were validated with simplified chemistry of precursors, following the strategy of the synthetic precursors.

1.4 Research methodology

The present research is intended to cover different phenomena involved in alkali-activated systems, following the sequence depicted in Figure 1.2: the first instants of the reactions will be investigated through the study of the dissolution kinetics of precursors in alkaline media; the early-stage reactions will cover the mechanisms of nucleation of reaction products and their influencing factors; and the later-stages will evaluate the evolution of these new phases into the obtainment of mature microstructures.

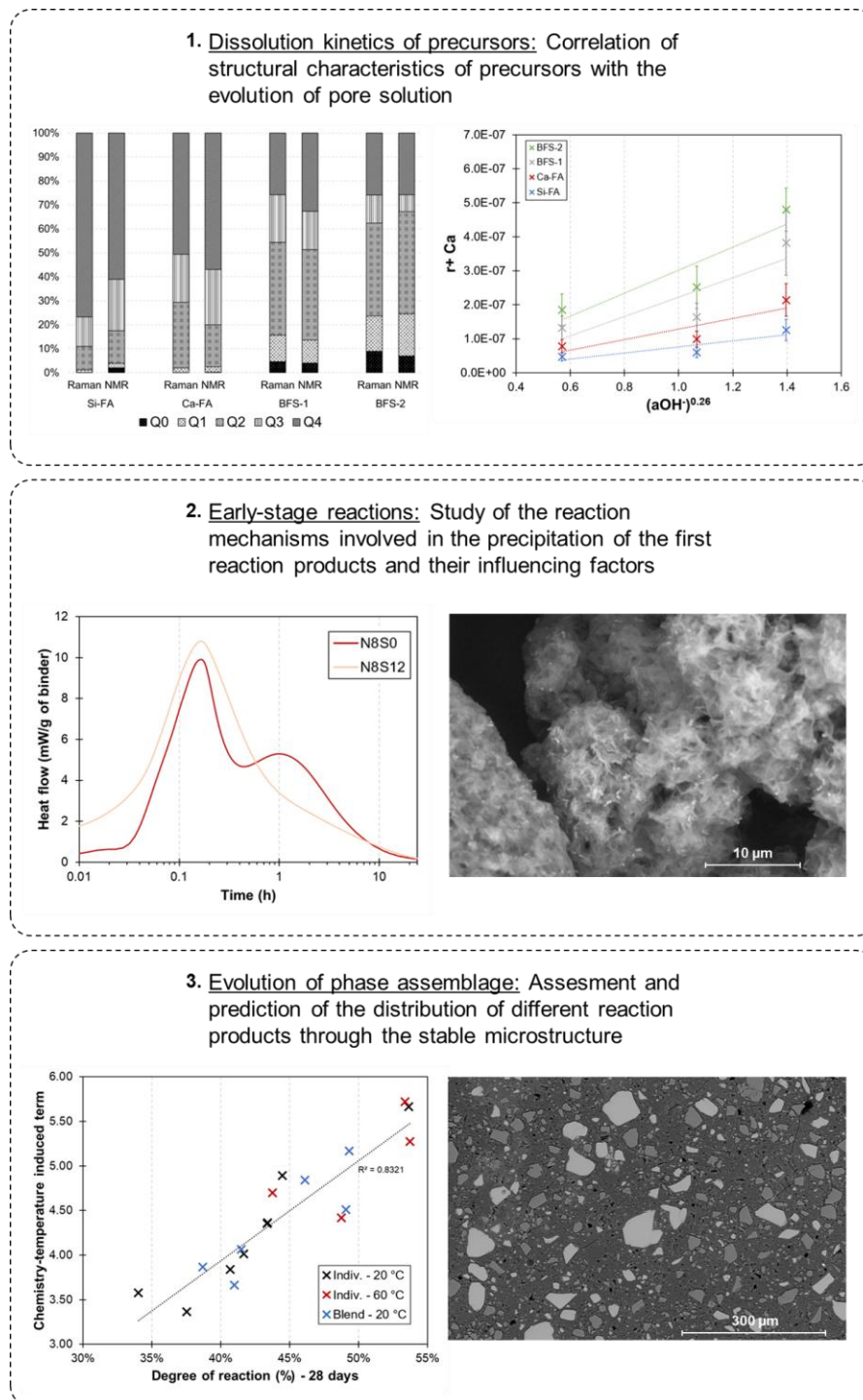


Figure 1.2: Distribution of the scope of this research in the different stages of alkali-activating reactions.

After the synthesis process, the initial mineralogy and chemistry of the synthetic glasses was characterized and compared to standard precursors, to assure the validity of the chosen approach. Detailed structural analysis was performed with Fourier transform infrared (FTIR) spectroscopy. The connectivity of the glass network and the availability of Si Qⁿ(mAl) and Al^{IV}-Al^V-Al^{VI} units was evaluated with Raman spectroscopy and solid state magnetic angle spinning ²⁹Si and ²⁷Al nuclear magnetic resonance (²⁹Si MAS NMR and ²⁷Al NMR), being quantitatively compared to the glass networks of naturally occurring slags and fly ashes according to their chemistry.

The early-stage of reaction was evaluated with dissolution experiments in highly diluted conditions. With a liquid/solid ratio of 1000, small quantities of powdered glasses were dissolved in 1:1000 sodium hydroxide and sodium silicate solutions up to 72 hours at 20 °C and 60 °C. This allowed the determination of a common empirical forward dissolution rate equation of the three main cations, based on chemical composition and environmental conditions - temperature and alkalinity. The characterization of residual material, after dissolution, was performed and used to assess which mechanisms take place in young and fresh mixtures. Differential thermogravimetry (DTG), FTIR, X-ray diffraction (XRD) and Raman spectroscopy were among the techniques used to evaluate the existence and the nature of reaction products formed in these initial stages.

The continuous evaluation of microstructure evolution, from fresh mixtures up to 28 days, was performed with pastes activated with the same activators as dissolution experiments. The differences in reaction mechanisms, according to the activator of choice, were observed via XRD, FTIR, and scanning electron microscopy (SEM) of polished surfaces of hardened pastes. With this experimental approach, it was possible to distinguish the phase assemblage of low- and high-Ca binders, and the influence of temperature on the final microstructure.

The implementation of selective dissolution of hardened pastes allowed the separation of the two main short-range ordered reaction products in alkali-activated materials: calcium (sodium alumino)silicate hydrate (C-(N-A)-S-H) gels and sodium (calcium) aluminosilicate (N-(C-)A-S-H) gels. The combination of this technique with SEM, and XRD coupled with Rietveld refinement, provided a precise study of the degree of reaction and phase formation. This allowed the quantitative correlation of the observed reaction products with the chemistry of the binder, leading to the determination of *reactivity indices* which could accurately predict the final phase assemblage based on characteristics of the mixture.

To extend the existing thermodynamic models of AAMs, N-A-S-H gels with Si/Al atomic ratios of 1, 2 and 3 were synthesized in inert atmosphere conditions. The determination of solubility products allowed the empirical derivation of other thermodynamic properties: standard Gibbs free energy of formation, standard enthalpy of formation, and standard entropy of formation. The combination of kinetic experimental observations with the improved thermodynamic database of low-Ca precursors were included in GeoMicro3D. The agreement between simulated and experimental results proved that the extended tool was able to cover a wide range of precursors - in individual or blended scenarios - and activators, accurately delivering a digital microstructure.

1.5 Research outline

This thesis is divided in five parts, as illustrated in Figure. 1.3. **PART I** covers the background and the motivation for this PhD project, with a summary of the most important information necessary to understand the findings presented. **PART II** focuses on the characterization of binders and on the effects of chemistry and processing conditions on initial stages of alkali-activation. The evolution of microstructure, from initial stages until a mature hardened matrix is obtained, is covered in **PART III**. **PART IV** contains the coupled thermodynamic and kinetic modelling of alkali-activated materials based on synthetic precursors, as well as the conclusions over the extended models developed during this project. Finally, **PART V** summarizes the main conclusions, contributions of this research, and offers

recommendations and suggestions for future work on this research topic. The content of each chapter is summarized as follows:

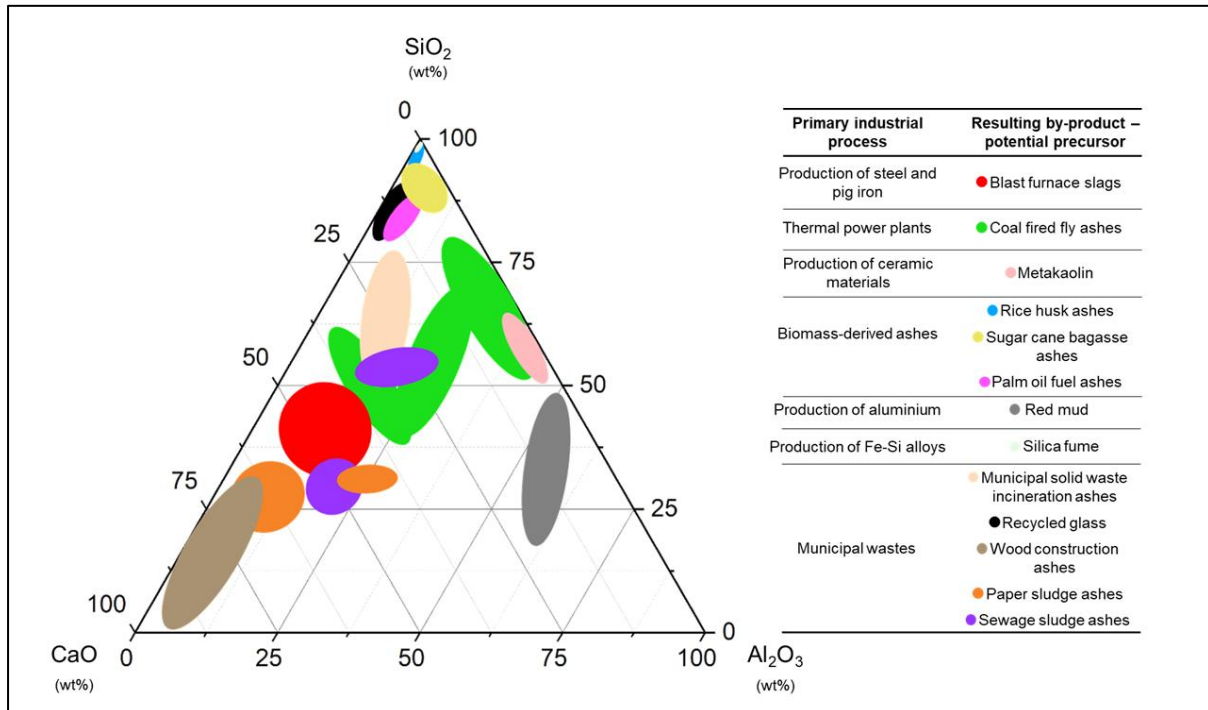
- **Chapter 2** contains a literature review about the main aspects of alkali-activated materials, the definition of different classes of binders and the stages of reaction. A summary of the effect of intrinsic and extrinsic factors on the evolution of reaction is given, and the current available modelling tools are discussed.
- **Chapter 3** explores and explains the differences in the network of reactive portions of high- and low-Ca precursors according to their initial chemical composition. The synthetic precursors obtained in this study were validated versus blast furnace slags and coal fly ashes described in literature as standard raw materials in alkali-activating systems.
- **Chapter 4** presents the evolution of the kinetics of dissolution, according to the alkalinity of the solution and the environmental temperature. The rates of dissolution, in far-from-equilibrium conditions, were obtained for Ca, Si and Al, and an empirical correlation of dissolution rates considering chemistry, temperature and alkalinity was determined.
- **Chapter 5** investigates the initial stages of phase precipitation reaction, characterizing which phenomena takes place in the nucleation processes of reaction products according to characteristics of mixture. The distinct conditions required to nucleate C-(N-A-)S-H and N-(C-)A-S-H gel-like phases were defined.
- **Chapter 6** follows the evolution of microstructure of individual and blended precursors. The definition of type and quantity of nucleated phases in hardened matrixes allowed the development of *phase assemblage indices*, which provided good agreement in the prediction of phase assemblage based on mix design and curing conditions.
- **Chapter 7** promotes the implementation of novel thermodynamic data of N-(C-)A-S-H gels in the modelling of alkali-activated binders. The accuracy of the extended model was evaluated versus the experimentally determined quantities of Ca-limited gels observed in fly ash-activated systems and blended systems with blast furnace slag. This chapter also covers the extension of the GeoMicro3D tool with the empirical and thermodynamic findings throughout the whole thesis. The newly derived dissolution rates and early-stage reactions were compared to the simulated conditions, and the digitized mature microstructure was compared to experimental findings and to the empirically derived reactivity indices.
- Finally, **Chapter 8** presents a summary of the scientific contributions of this research regarding reaction mechanisms of low-Ca, high-Ca and blended precursors in alkali-activated systems. Based on experimental evidence, fine tuning of binder chemistry can be performed and tailor-designed systems can be employed according to performance requirements, while reliable digitized microstructure can be used for further performance and durability simulation tools.

<u>PART I – Background and motivation</u>	
<u>Chapter 1:</u> General introduction	
<u>Chapter 2:</u> Literature survey	
<u>PART II – Structural characterization and initial instants of reaction</u>	
<u>Chapter 3:</u> Synthesis and microstructural characterization of synthetic precursors	<u>Chapter 4:</u> Dissolution kinetics of synthetic precursors
<u>PART III – Evolution of microstructure of alkali-activated binders</u>	
<u>Chapter 5:</u> Early-stage reactions of alkali-activated synthetic precursors	<u>Chapter 6:</u> Phase assemblage of alkali-activated pastes with synthetic precursors
<u>PART IV – Thermodynamic and numerical modelling of alkali-activated systems</u>	
<u>Chapter 7:</u> Numerical simulation of microstructure development of alkali-activated materials	
<u>PART V – Conclusions and outlook</u>	
<u>Chapter 8:</u> Retrospection, contributions and recommendations for future research	

Figure 1.3: Outline of this thesis.

Chapter 2.

Literature survey



The concept of alkali-activated materials has been cited in literature for more than 7 decades. Since then, the efforts of researchers have raised the fundamental understanding and the maturity of these binders, and several successful examples of applications in large-scale projects can be found throughout the world, proving their long-term performance and durability. The present Chapter provides a brief summary of the current state-of-the-art of this technology, displaying the main concepts of these systems, the in-depth investigation of the individual stages of reaction, and the characterization of the microstructural evolution through various experimental and modelling techniques. At the end, the existing possibilities for new research works will be addressed, opening the path for the developments to be explored in this thesis.

2.1 Introduction

This chapter presents a brief literature survey on the different stages involved in alkali-activating reactions, from the selection of raw materials until obtaining a hardened cementitious matrix and stable reaction products. A brief description of the requirements of appropriate precursors is given, and issues concerning inconsistency and availability of resources, which currently imposes a major limitation on the marketability of AAMs, are detailed. The available conceptual models of the kinetics of dissolution of precursors, as well as the mechanisms of nucleation of reaction products, will be described considering experimental observations. Finally, the chapter will include an overview of the thermodynamic and numerical modelling tools currently available for alkali-activated systems. Based on this literature survey, the gaps in scientific knowledge, the most relevant topics to be investigated, and the contributions of this dissertation to overcome these limitations are stated.

2.2 The concept of alkali-activated materials

Alkali-activated materials are obtained by the chemical reaction between an alkaline activator (a solution of hydroxide, silicate, or highly concentrated sulfates and carbonates of alkaline and alkaline-earth elements) and precursors comprising silicates with intermediate-to-low calcium content [46]. This reaction results in a hardened cementitious matrix, which is physically similar to hydrated Portland cement (PC), but presents mild differences in the final microstructure and chemical composition [46,60,61]. The term ‘intermediate-to-low-calcium’ distinguishes precursors from the minerals present in clinker: the former presents Ca/Si ratios up to 1.5, while the latter accounts for minerals in which CaO is by far the most representative portion, with Ca/Si ratios in the range of 2.0-3.0 [62,63].

2.2.1 Selection of raw materials

2.2.1.1 Precursors

The ideal structure of a precursor should be consisted of either amorphous portions in significant volumes, or crystals of ordered structures in the nanoscale range, and comprise the presence of reactive oxides, enabling the precipitation of reaction products similar to phases obtained via the hydration of PC [63,64]. The extent and the composition of the amorphous - also termed as glass⁴ or vitreous - region majorly influences the final features of the hardened binder, and the main expected components are SiO₂, Al₂O₃, CaO, with minor quantities of MgO and Fe₂O₃. The possibility of reusing byproducts from different industrial sectors represents an excellent environmental advantage of AAMs over other binders [65-72]. Considering chemistry requirements, a vast list of disposable materials presents potential to be used as a binding component, either alone or in combination with others in blended systems. Table 2.1 details several byproducts that are commonly mentioned in literature, along with the primary industrial process of each.

⁴It has been argued that glasses are not truly amorphous, as they still display atomic organization in short ranges, and can be considered as micro-crystals. In this thesis, the terms glass, amorphous and vitreous will be used as synonymous of amorphous materials.

Table 2.1: Industrial by-products reported in the literature as precursors for AAMs (add their main oxides).

Primary industrial process	Resulting by-product - potential precursor	Typical components (wt%)
Foundries and metal recovery plants	Blast furnace slag	$\text{SiO}_2 + \text{CaO} + \text{Al}_2\text{O}_3 > 75 \%$ *
	Basic oxygen furnace slag	$\text{CaO} + \text{SiO}_2$: 50-65 %; Fe_2O_3 : 10-30 % [73]
	Electric arc furnace slag	$\text{CaO} + \text{SiO}_2 + \text{Al}_2\text{O}_3$: 40-60 %; Fe_2O_3 : 30-45 % [74]
	Non-ferrous slags	-**
Thermal power plants	Coal fired fly ashes	$\text{SiO}_2 + \text{Al}_2\text{O}_3 + \text{Fe}_2\text{O}_3$: 40-90 %; $\text{CaO} + \text{MgO}$: 0-35 %*
	Coal fired bottom ashes	$\text{SiO}_2 + \text{Al}_2\text{O}_3 + \text{Fe}_2\text{O}_3$: 70-90 %; $\text{CaO} + \text{MgO}$: 0-10 % [75]
Production of aluminium	Red mud	Fe_2O_3 : 30-60 %; Al_2O_3 : 10-20 %; SiO_2 : 3-50 % [76]
Incineration of organic wastes	Rice husk ashes	$\text{SiO}_2 > 85 \%$ ***
	Sugar cane bagasse ashes	$\text{SiO}_2 > 70 \%$; CaO : 1-15 %***
	Palm oil fuel ashes	SiO_2 : 50-70 %; CaO : 3-10 %***
Municipal wastes	Municipal solid waste incineration ashes	SiO_2 : 17-75%; CaO : 15-70% [54]
	Recycled glass	SiO_2 : 55-75 %; $\text{CaO} < 20 \%$ [77]
	Wood construction ashes	CaO : 30-70 %; SiO_2 : 10-40 %***

*Source: this research.

**The typical components of non-ferrous slags are not listed due to their dependence on the ore, i.e. nature of the metal obtained in the primary industrial process.

***Source: Work developed in the same research group. Detailed compositions will be given in Appendix A.

Conventionally, precursors can be classified as high-Ca and low-Ca materials. This distinction promotes differences in their initial mineralogy and the involved reaction mechanisms, as schematically shown in Figure 2.1, and will be used through the whole thesis. Ca-rich materials usually display a higher amorphous degree and can be activated under moderate alkaline conditions, leading to the formation of variations of calcium silicate hydrate (C-S-H) gels, which can also be modified by the incorporation of Al (C-(A)-S-H). Additional variations occur by the uptake of alkaline elements forming the glass network - resulting in the formation of C-(N/K)-A-S-H and C-(N/K)-S-H gels (where N and K stand for Na_2O and K_2O , respectively), and their quantity and nature depends on the distribution of these secondary oxides [58,78-80]. The second group of precursors is comprised of Al- and Si-rich materials, such as fly and bottom ashes (coal fly ash, municipal solid waste incineration bottom ash, rice husk ash, biomass ashes) and metakaolin, and usually requires more aggressive conditions to initiate the activation process (high alkalinity and curing temperatures above ambient), resulting mainly in the formation of sodium-potassium aluminosilicate hydrate (N/K-A-S-H) gels [81-84].

Out of the many existing possibilities, blast furnace slags and coal fly ashes present the most relevant commercial potential, and have been extensively studied and implemented in large-scale projects for over 60 years [46]. As the two materials promote the reutilization of industrial residues, they require beneficiation steps prior to application as precursors, which can impact their characteristics and consequently their behaviour on alkali-activating reactions.

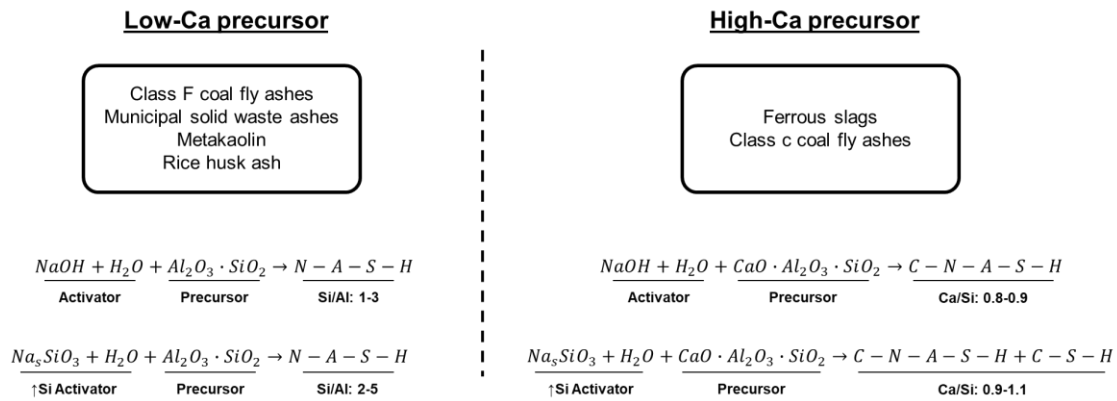


Figure 2.1: Conceptual chemicals reactions of alkali-activated materials, according to the Ca content of the precursor and activator - Elemental ratios obtained from [85-90]

Coal Fly Ashes

Coal fly ash is obtained as a valuable waste from thermo-electrical power plants, as illustrated in the scheme of Figure 2.2. When pulverized coal is inserted into furnaces for combustion and further energy generation, the non-combustible inorganic compounds melt and fuse in the form of droplets. These droplets are captured by exhaustion and separated from flue gases using electrostatic or mechanical precipitators, being cooled down to form spherical glassy particles ready for a secondary use [91]. Two main types of coal are used for energy obtainment: anthracite and bituminous coals are older and found in deeper layers of the soil, rich in carbon and silicon dioxide and being the optimum choice for power plants; sub-bituminous coals are found in shallower layers and contain lower levels of carbon [91,92]. These two classes present a well-defined division of the generated fly ash according to ASTM C-618. Siliceous fly ashes, or class F, obtained from the burning of high grade coals [93,94], contain low levels of calcium and a summed quantity of SiO_2 , Al_2O_3 and Fe_2O_3 higher than 70 %, while calcareous fly ashes, or class C, obtained from burning low grade coals, present high levels of calcium and a summed quantity of the other three main oxides between 70 % and 50 % [91,95].

Fly ashes present 40-90 % of vitreous material in its internal structure. This value can fluctuate according to the initial coal mineralogy, coal particle size distribution, and cooling conditions of the molten material. Particles of different sizes will quench at different rates: the smaller allow a more intense heat exchange with the environment, resulting in accelerated cooling a higher amorphous degree; large particles can allow internal recrystallization of the still-molten inner material by the slower cooling rate, increasing the residual crystalline volume [96,97]. The nature and quantity of the remaining crystalline phases are dependent on the overall mineralogy of the initial coal. Mostly, quartz is the main mineral found in fly ashes, since SiO_2 is the first or second main component of these materials. Minor quantities of mullite, hematite, tricalcium aluminate and lime can also be found according to the grade of the burnt coal [98-100].

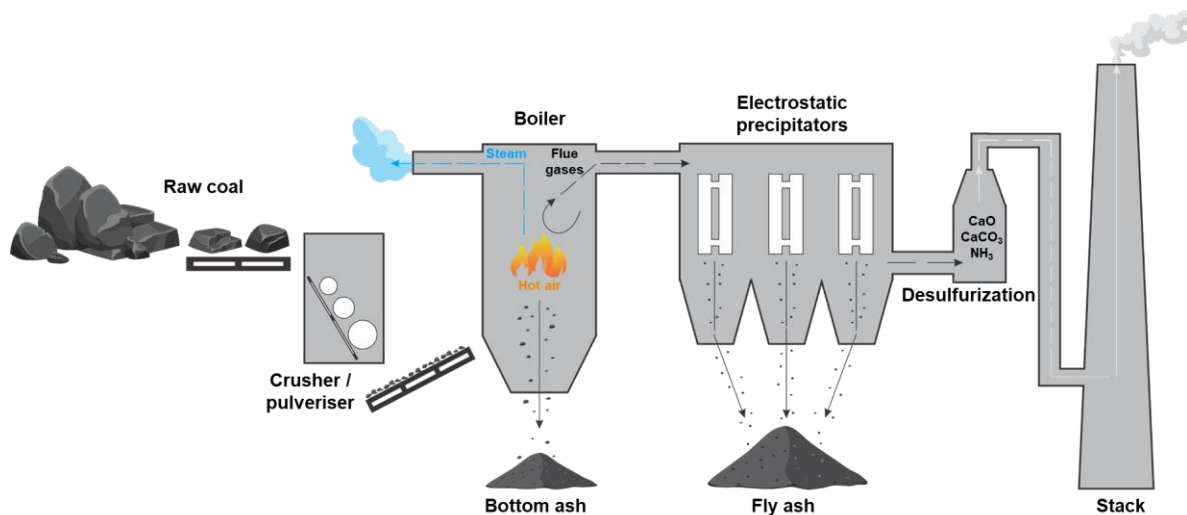


Figure 2.2: Schematic production processes of primary sources of coal fly ash. Source: author.

Blast furnace slag

Blast furnace slag is formed by the thermo-chemical reduction of iron ore inside blast furnaces for production of pig iron, the first component for steel manufacturing [46], which is schematically shown in Figure 2.3. The contaminants of the iron ore react with coke and the hot air inside the furnace to form a phase called *slag*, which is separated from the molten iron in the skimmer [83,101]. At the end of the melting process, the temperature of the slag is approximately 1500 °C, and the cooling method is essential to determine its properties and reactivity. Conventionally, water-cooling is used to enhance the heat exchange and accelerate the cooling rate, promoting a larger volume of amorphous material at the end of the process. Finally, the cooled slag is ground into a fine powder before being suitable to be used as a binder in cementitious systems - it is also commonly termed as ground granulated blast furnace slag (GGBFS). Slags commonly present CaO as its main component, followed by SiO₂, Al₂O₃ and variable quantities of MgO. The chemistry directly impacts the final reactivity, and can be measured by the basicity index (weight ratio of the sum of MgO and CaO related to the sum of ASiO₂ and Al₂O₃). This index determines the hydraulic level of the slag, which is directly related to its reaction mechanism as a cementitious binder - this will be further discussed in this thesis. Although not as remarkable as in fly ashes, variations in chemistry can still be expected in slags due to the source of the iron ore and the use of burning gases to enhance the burning capacity of the blast furnace [102].

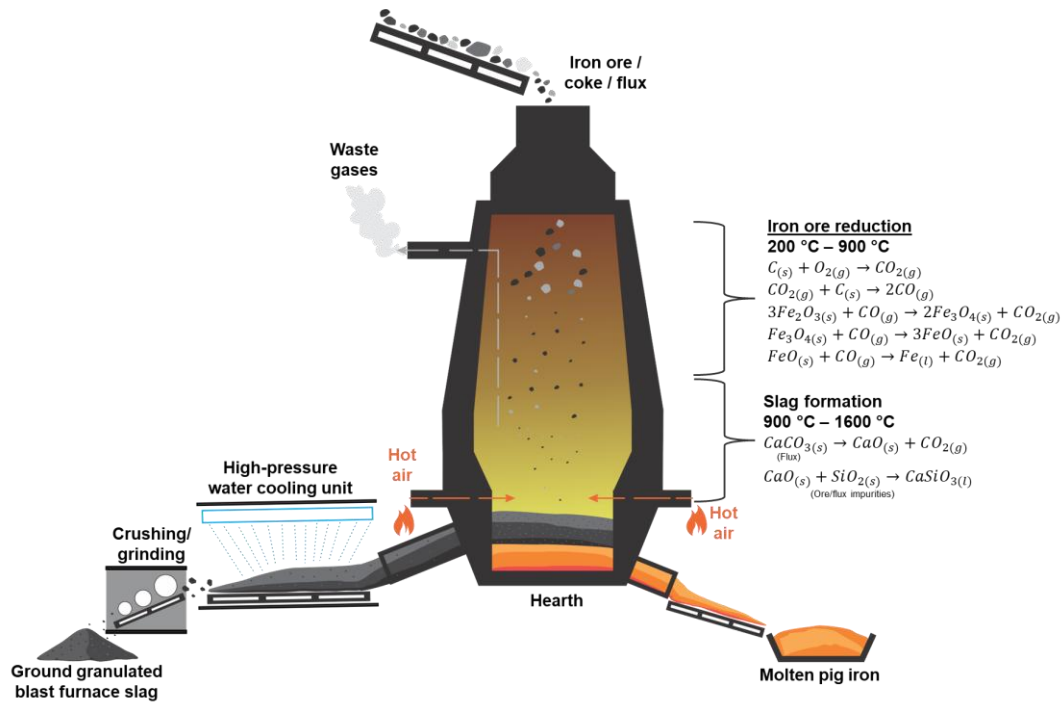


Figure 2.3: Schematic production processes of primary sources of blast furnace slag.

2.2.1.2 Activators

Activators display a combined role of catalyser and reaction media, facilitating the initial dissolution process of precursors and accelerating the stage of precipitation and stabilization of new solid reaction products [103]. In essence, these materials must present sufficient alkalinity to promote the breakage of the amorphous network of the precursors, and their concentrations should be optimized to avoid flash setting and to provide an adequate media for the precipitation and growth of stable reaction products [104]. In most applications, these components are prepared as liquid solutions in a separate step prior to the mixture with precursors, allowing sufficient time to promote a homogeneous distribution of reactive aqueous species.

The efficiency of an activator lies on the correct choices of types and concentrations of the alkalis, which can be correlated to the characteristics of the precursor. For instance, the differences in the dissolution behaviours of high- and low-Ca precursors demands specific characteristics from the activators:

- i. lower alkalinity levels are required to promote dissolution in high-Ca precursors requires due to their disordered network. Consequently, accelerated dissolution rates are obtained with the initial release of Ca and immediate formation of C-(N-A)-S-H gels, observed by higher calorimetric response in initial moments [105-107].
- ii. higher concentrations of the activator and higher temperatures are usually required in the activation of low-Ca precursors due to their highly-polymerized structure, targeting the achievement of a similar dissolution and accelerated formation of reaction products [46,108].

In general, an increased concentration of alkalis in aqueous media accelerates the reaction, favouring a stronger cohesion of the hardened matrix and, consequently, improving the mechanical performance of AAMs [62]. However, this enhancing effect is expected to occur until an upper threshold value, as the excess of alkaline ions can lead to additional issues in terms of workability, evolution of microstructure, and lifecycle assessment [109-111]. Flash setting and increased viscosity of the binder are among the main issues arising from extremely high pH levels of the activator [83], limiting to the continuity of the early-stage reactions and promoting the formation of a coarse microstructure. In addition, the excess of alkaline ions can favour the formation of expansive products via alkali-silica reactions or the occurrence of efflorescence at later stages [62,63], which compromises the long-term performance of concrete elements. Finally, high concentrations of activators can negatively influence the decarbonization potential of the binder, as activators present the highest global warming potential among the components of AAMs [112].

In practical terms, the majority of activators are composed of Na- or K-containing hydroxides, carbonates or silicates [46,113]. In the first two cases, the molarity of the alkaline solution and the ratios of $\text{Na}_2\text{O}/\text{K}_2\text{O}$ over precursor (n , or mass of alkaline oxide per 100 g of precursor) are the main governing parameters. With respect to sodium or potassium silicates, the silica modulus (M_s) of the solution calculated by Equation. 2.1:

$$M_s = \frac{[\text{SiO}_2]}{[M_2\text{O}]} \quad (2.1),$$

where SiO_2 represents the molar quantity of the oxide and $M_2\text{O}$ represents the molar quantity of either K_2O or Na_2O . When metallic silicate solutions (also termed *waterglass*) are used, the M_s of the activator is the main influencing factor in the overall reaction of the binder. For instance, the excess of the silicate modulus has been reported to cause a rapid workability loss of alkali-activated slag mixtures [114], causing a series of other issues to the mixture: limited setting time attributed to the accumulation of primary C-(N-A)-S-H-type gels [107,114,115], and uncontrolled stiffening process have been frequently reported in silicate-activated slag [116-118], leading to great challenges in practical aspects of the binders during mixing, delivery, pumping, casting, and consolidation of fresh mixtures.

Table 2.2 summarizes the main parameters of the alkaline solutions, i.e. the alkali concentration and the silicate modulus, and their optimal dosage for low- and high-Ca precursors. The alkali content and the silica modulus, in combination with the binder characteristics, govern the chemistry of the mix design formulation and thus the reaction mechanisms, directly affecting the mechanical properties of the material [110,119]. Due to the countless possible binders-activators combinations, it is difficult to generalise the effect of the system chemistry on the mechanical performance. For this reason, it is necessary to find and highlight recurring behaviours and correlations between chemistry and mechanical performance.

Table 2.2: Main characteristics of the alkaline solutions used for the production of AAMs [64].

	Alkaline potential of the solution	Dosage of $M_2O^*(n)$	$M_s = SiO_2/M_2O$
Low-calcium systems (CaO content < 10 wt%)	High	7.0 - 9.0 wt%	1.0 - 2.0
High-calcium systems (CaO content > 10 wt%)	Low	3.0 - 6.0 wt%	~ 0.75

*M stands for the specific cation, usually K or Na.

2.2.2 Challenges of conventional precursors

2.2.2.1 Geographical distribution and future availability

The practical implementation of slags and fly ashes is dependent on the existence of their primary industrial processes. In this context, the availability of these two precursors is strongly linked to the geographical distribution of raw materials for these two industries, illustrated in Figure 2.4. Coal was source for nearly 35 % of total global electricity in 2020 [120,121]. Approximately 85 % of global coal reserves are available in North America, Oceania, CIS⁵ countries and Asia, with the latter being responsible for approximately 80 % of total global coal consumption in 2020 [120]. However, coal-based energy is bound to massive CO₂ emissions [40], and the world is expected to gradually reduce and replace this type of energy by renewable sources. In this aspect, although global consumption of coal presents a discrete increasing trend [38], a few regions of the planet have already lowered its use. While Asia displays continues to raise its levels of coal consumption, with China operating over 3000 coal power plant stations in 2020 (Global Energy Monitor), Europe has nearly halved its coal consumption for energy production from 14.02 exaJoules (2010) to 7.70 exaJoules (2020) [38], a trend which has been followed by the majority of the continents. Up to 2040, the use of coal as an energy vector is expected to account for only 22 % of total global energy generation, and an expected limited availability of fly ashes is expected for the construction industry.

The availability of blast furnace slag is directly related to production levels of pig iron, as approximately 300 kg of slag are generated for each ton of pig iron produced in blast furnaces [122]. However, global production of pig iron displays a decelerated growth rate, with total production in the range of 1.3 billion tons in 2019 and 2020 [123] - with China being responsible for over 60 % of total amount. Production levels are expected to grow at low rates for the next 10 years, reaching 1.5 billion tons only in 2030 [124]. Recycling rates have distinct numbers in different locations for both precursors. In general, slag is a more mature product and presents higher reutilization rates in construction industry. Within the biggest consumers of this raw material, Europe immediately reuses approximately 82 % of its production according to 2018 (Euroslag), while the Nippon Slag Association reports that Japan has a recycling rate of 80 %. Reports from China present varying numbers with recycling rates reaching values as high as 95 %, while reports from the United States Geological Survey (USGS) have shown increasing slag import rates since 2017 to meet the demand of the domestic cementitious materials industry. These trends indicate that, similarly to fly ashes, the availability of slags is expected to be restricted in the coming years.

⁵The Commonwealth of Independent States (CIS) is a regional intergovernmental organization in Eurasia, and is composed of the following countries: Armenia, Azerbaijan, Belarus, Kazakhstan, Kyrgyzstan, Moldova, Russia, Tajikistan and Uzbekistan.

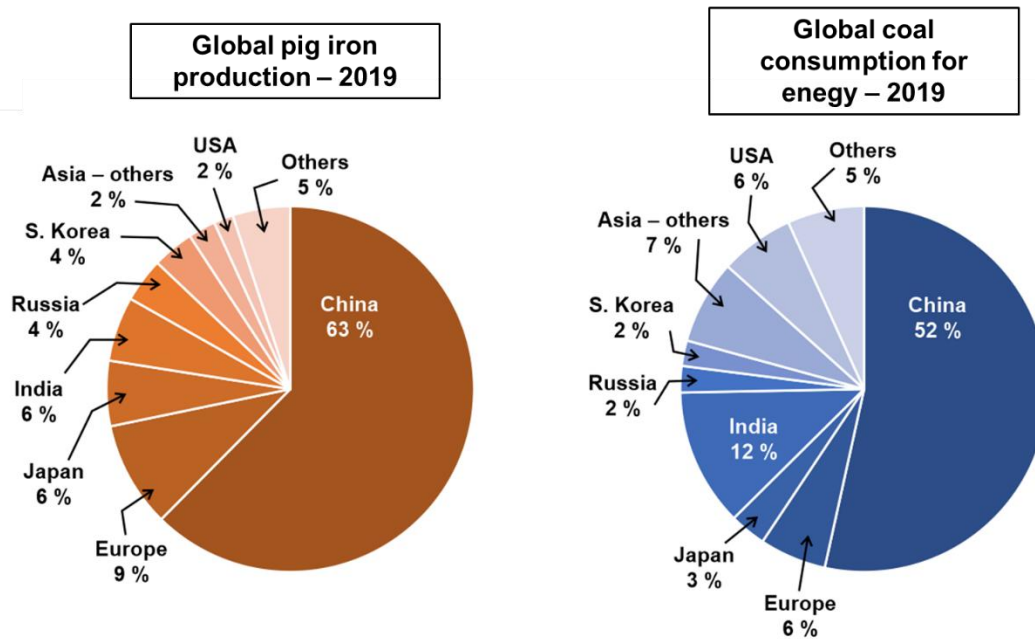


Figure 2.4: Distribution of the global production of raw materials used in the obtainment of blast furnace slag and coal fly ash [38,122].

2.2.2.2 Inconsistency of chemistry

Both fly ashes and slags present a wide variation of chemical compositions and mineralogy, which are dependent on different factors for each group of material. Coals contain a high quantity of organic components, and the coal grade of the local source combined with the secondary combustible materials have direct impact on the final chemical composition of fly ash [46]. It can also be expected that, within a same batch, fly ashes will present heterogeneities on its characteristics: different particle sizes go through different cooling rates, which consequently leads to a variation in levels of vitreous material and differences in reactivity according to fineness of the material [96]. Moreover, the implementation of coal in co-combustion powerplants - which is a common trend to reduce CO₂ emissions during the generation of energy - can lead to the contamination of the molten material, thus altering the final chemical composition. For instance, Sarabèr [125] and Wu et al. [126] demonstrated that the use of agricultural wastes, such as poultry dung, and of rejects from paper production, can increase the CaO content of the ashes, but the glass quantity is reduced in approximately 25 %. Similarly, Faleschini et al. [127] reported an increased content of unburned material when refuse-derived fuels (RDF) - mainly composed by papers and plastics - are burnt in combination with coal, which results in delayed setting and decreased strength of concrete when used as SCM.

With respect to slag, processes occurring inside blast furnaces are mainly controlled by temperature and mineralogy of the iron ore [128]. Coke, a coal-derived carbon-rich and high purity material, is used as fuelling agent, accounting for nearly 25 % of the total raw materials used in this process. The reduction of the ore and conversion into metallic iron is promoted by carbon monoxide obtained from the combustion of coke. The resulting slag is rich in residual SiO₂ and Al₂O₃ after the reduction and release of metallic Fe. The resulting molten material has a high viscosity and impedes the processing of the byproduct. For that reason, fluxes, such as limestone and dolomite, are added to the blast furnace to control

the viscosity of the slag, by inducing the inclusion of MgO and CaO into the molten material [129]. The amount of added fluxes should be optimized: sufficient material should be added to allow proper depolymerization of the liquid slag, but not in excess, as it could lead to the precipitation of solid calcium silicates, increasing the viscosity [130]. The composition of slags can be better controlled if proper care is taken on the choice and dosage of all raw materials, but mild variations are still expected according to the availability of resources.

Due to the larger number of variables on the primary production process, fly ashes tend to display a less homogeneous performance when used in AAMs in comparison to slag. Table 2.3 presents the changes in chemistry of the two precursors, considering a vast database of compositions and quantitative analysis reported in scientific papers from 2010 to 2020 for each material - see Appendix A for more details. In nearly all reported slags, CaO is the main component, and the high Ca/Si ratios facilitate the formation of Ca-containing hydrated gels from early moments over other phases. While the composition of siliceous fly ashes is dominated by SiO₂ and Al₂O₃, calcareous fly ashes represent an intermediate material in terms of chemistry, which is also reflected by the intermediate reactivity observed for this group of precursors. Additionally, the higher amorphous fraction of slags compared to fly ashes, which can be quite significant in some cases, adds an extra complicating factor on the activation of low-Ca precursors.

2.2.3 The introduction of chemistry-based approaches

The wide range of solid precursors and processing parameters introduces additional complexity to AAMs, significantly affecting the fresh and hardened binder properties. While this brings a certain versatility to this technology, allowing fit-for-purpose formulations, each mix design differs from the other in terms of reaction mechanisms. Currently, there are no standardized mixtures and only few regulations that promote a large-scale implementation of alkali-activated binders in individual countries - United Kingdom, Ukraine, Switzerland, and Australia [131]. A few authors have attempted to derive unified approaches, correlating factors such as activator proportions, precursor chemistry, water content, and the presence and content of admixtures to the performance of AAMs [47,48,132]. This could lead to the future design of performance-based approach standards and regulations, as AAMs were proved to display even superior performance and durability over PC-based materials in some aspects [29-33].

Table 2.3: Distribution of oxides, atomic ratios and amorphous degree of fly ashes and slags reported in scientific literature.

Precursor	CaO (wt%)	SiO ₂ (wt%)	Al ₂ O ₃ (wt%)	Ca/Si	Amorphous content
Granulated					
blast furnace slag	30-56	21-41	4-18	0.92-2.86	> 95%*
Fly ash - C**	20-28	21-41	2-14	0.53-1.43	53-89%
Fly ash - F**	1-14	36-67	16-39	0.01-0.43	44-86%

*The amorphous content of slag is assumed to be larger than 95%, as all data concerned water cooled slags.

**Classification of fly ash according to ASTM C618.

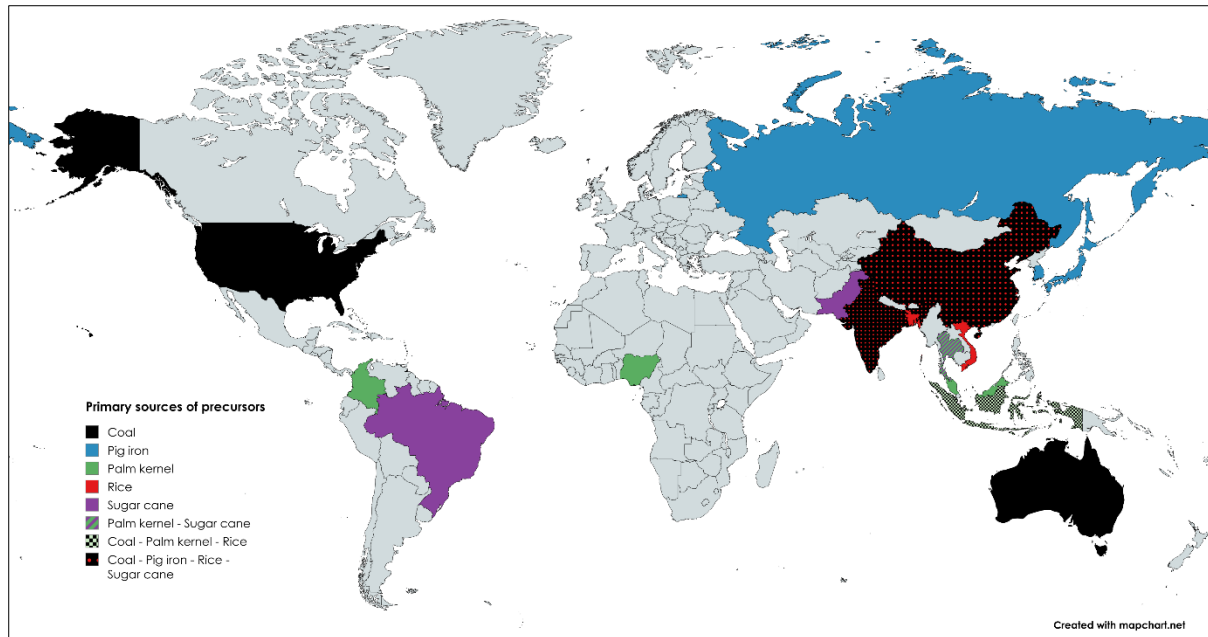


Figure 2.5: Countries with more significant production of primary processes of potential precursors of AAMs - Full data available in the Appendix A.

In addition to the inconsistent mix design, the future availabilities of both fly ash and slag do not follow the forecast of cement demand (see Table 1.1 in Chapter 1). One alternative approach to overcome the inconsistent supply and performance is the implementation of a *chemistry-based approach*, which considers the overall binder composition, accounting for both precursor and activator. This would widen the range of alternatives, as it could include conventional and non-conventional raw materials. If a combination of two or more precursors is allowed, the definition of an optimum mix design is facilitated by making use of locally available raw-materials, thus expanding the potential geographical range of application of this technology. For instance, ashes obtained from biomass wastes such as rice husk (RHA), palm oil fuel (POFA), and sugar cane bagasse ashes (SCBA), have been extensively studied in the past years as components in blended AAM mixes, reaching satisfactory performance when combined with slag and even with PC [65,133-137]. These byproducts are widely available in warmer climates, and noticeably tend to be distributed where conventional precursors are not available. The map shown in Figure 2.5 highlights the five main global producers of the source materials for slag and fly ash, and for the aforementioned biomass wastes. It is therefore clear that an expanded the list of precursors increases the capillarity of raw materials, and consequently can enhance the commercial and technical potential of AAMs.

Biomass ashes display, along with siliceous fly ashes, low overall-Ca content. Within this same group, other types of wastes easily found in all regions of the planet are on evidence in scientific literature [50] including municipal solid waste incineration ashes, recycled glasses, silica fume and red mud. There has been some recent focus of researchers on the use of other ashes which are produced in limited parts of the world but require specific processes, such as sewage sludge (SSA) [138], wood construction biomass waste ashes (BWA) [139,140] and paper sludge ashes (PSA) [141,142]. This last group of materials usually present a higher Ca content than the previous, but their applications as partial replacement for blast furnace slag or fly ash have been positively assessed in the technical literature in

some circumstances. Figure 2.6 presents an overall view of the chemical composition of several alternatives of precursors mentioned in literature, considering their contents of CaO , SiO_2 and Al_2O_3 . The chemistry of non-conventional materials fluctuates from Si-rich to Ca-rich compounds, while always maintaining Al_2O_3 values below 40 %. As the supply of these byproducts is limited compared to conventional ones, a chemistry-based approach could be a supporting factor on the development of blended mixtures for instance, by taking advantage of the main features of two or more materials, and will be the main point of investigation of this thesis. Consequently, mix design of AAMs could be tailor-designed according to the locally available raw-materials, expanding the potential geographical range of application of this technology.

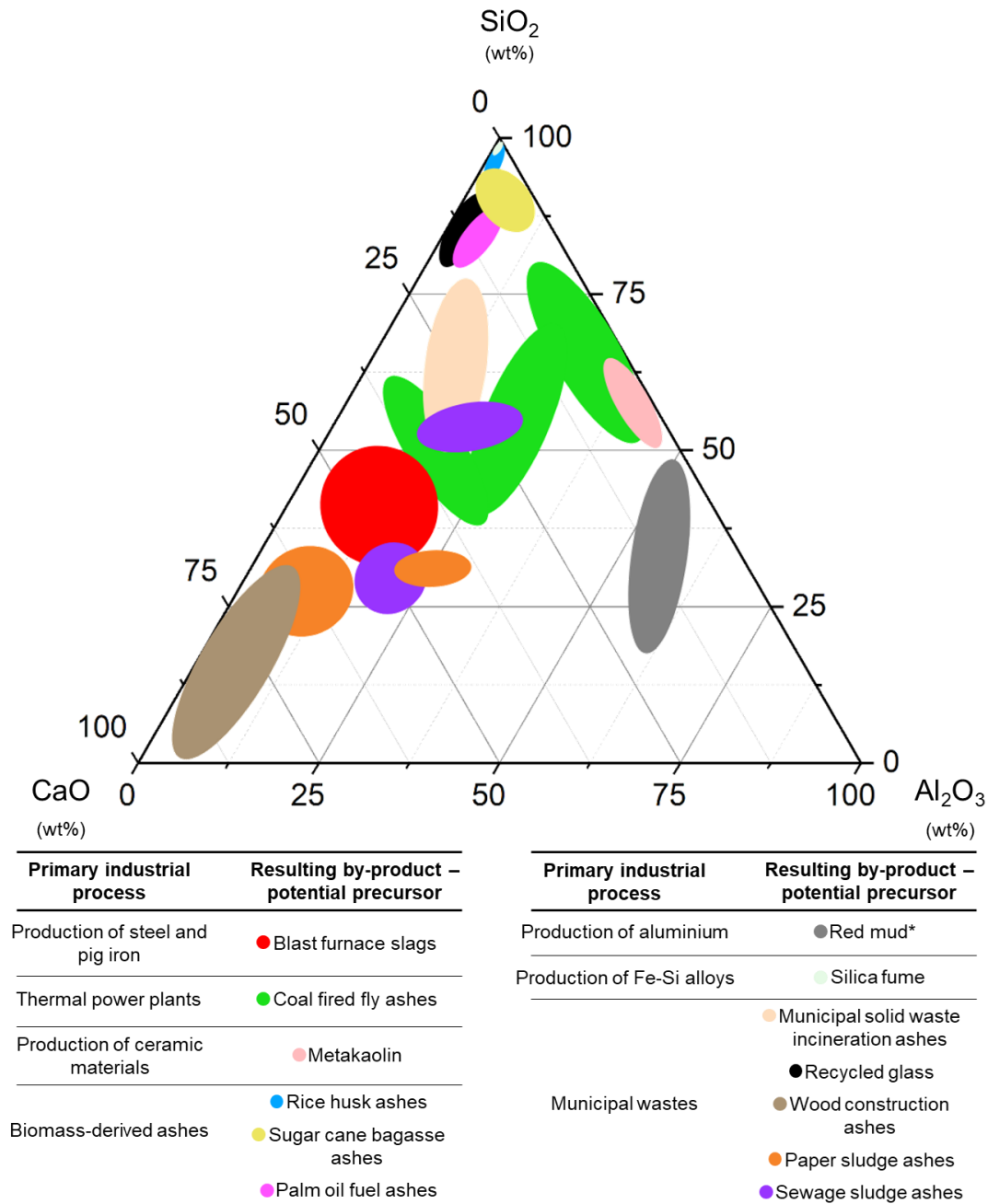


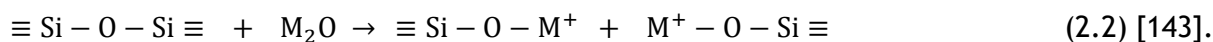
Figure 2.6: Variability of main oxides in the chemical composition of conventional and alternative precursors for AAM mixes. *Red mud presents significant amounts of Fe_2O_3 up to 50 wt%.

2.3 Structural characterization of precursors

The reaction potential of a precursor is linked to two main characteristics of the amorphous portion within its microstructure: total volume and connectivity, and chemical composition, two features which are strongly correlated. Additionally to the lack of long-range order, glass structures can be modified at the atomic short-range organization range by the presence of a few elements, and these alterations have a significant impact on the overall reaction process. A glass structure comprises, essentially, two types of components [143,144]:

- i. *network forming* (NWF) *oxides*, which present stronger M–O bonds and are more thermodynamically stable, forming strong and cohesive structures [143];
- ii. and *network modifying* (NWM) *oxides*, which disrupt M–O bonds and lower the overall ordering range of the local structure,

where M stands for metallic elements. The reactive portions of slags and fly ashes is composed by calcium aluminosilicate glasses, in which SiO₂ is the main NWF. Si presents a tetrahedral coordination (with SiO₄ as basic unit), and each oxide of the network can be shared with other tetrahedra in disordered forms, forming different structures as seen in Figure 2.7. Shared oxygen sites in between two tetrahedra are named *bridging* (T) O sites, and the connections made these elements in the silicate network can be disrupted by the presence of NWM oxides of alkaline and alkaline-earth elements. NWMs promote the breakage of Si–O bonds in bridging points and form separate Si–O–M⁺ bonds following the reaction displayed in Equation 2.2 [10]. The result is an even shorter range of atomic order due to the formation of *non-bridging oxygen* (NBO) sites - in AAM-precursors, CaO, MgO, Na₂O and K₂O are the most common NWMs [143]. By reducing the total amount of bridging oxygens, NWMs decrease the overall cohesion of the microstructure and reduce the energy barrier required to initiate dissolution and further stages of reaction [145,146].



Al₂O₃ presents a dual behaviour, as it can assume the role of both network former and modifier oxides [147,148]. The contribution of Al to the overall network is dependent on its availability compared to alkali and alkali-earth components. In general, Al is mainly expected to act as network former in tetrahedral coordination (Al^{IV}) when there is an excess of alkaline elements [143,149] - with Mⁿ⁺/Al ratio above 1, where M is the corresponding modifying element and *n* is the positive charge of the modifying cation. When acting as network form, Al usually substitutes Si in previously occupied sites, converting the basic unit into [AlO₄]⁻. As the natural coordination of aluminum is octahedral (Al^{VI}), the basic unit of Al-tetrahedra has a coordination number of 4, resulting in a negatively charged site. Hence, Al^{IV} requires the presence of a charge balancing cation to maintain the local electrical neutrality [143]. Oppositely, when Al³⁺/Mⁿ⁺ ratio is above 1, octahedrally coordinated (also termed sixfold) Al is the main observed nature [150]. It is assumed that, as long as the glass system is able to supply sufficient charge balancing elements, Al can completely assume the role of network former [96,151].

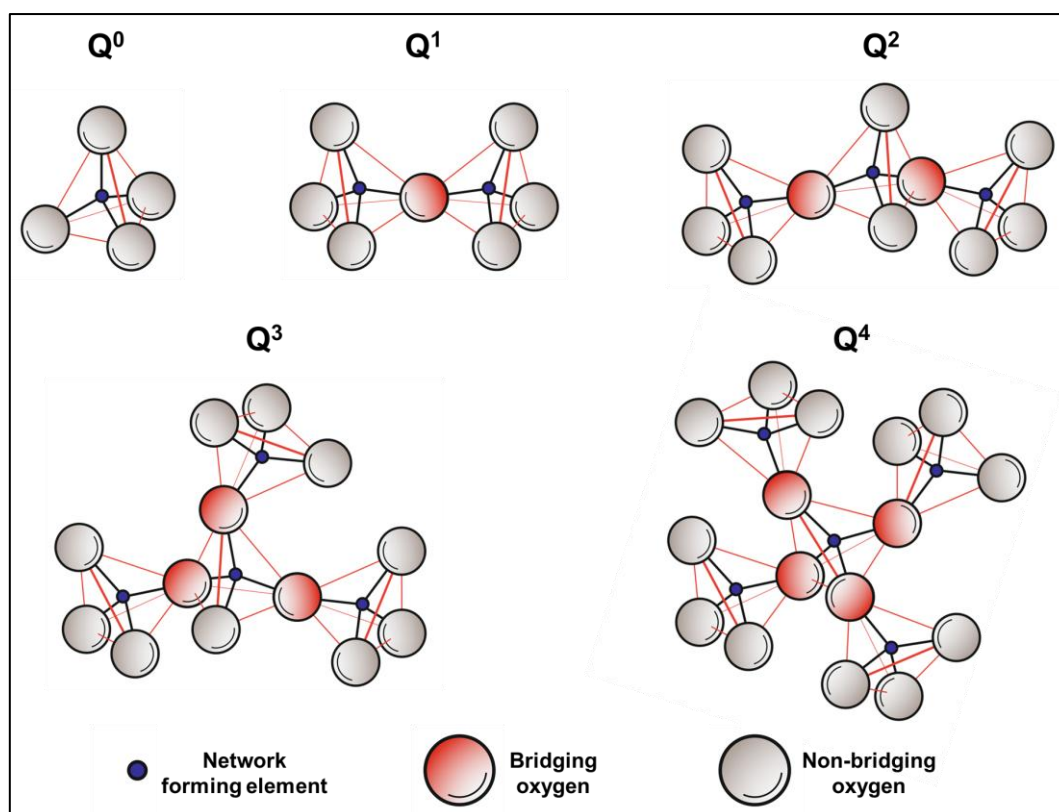


Figure 2.7: Silicate structures formed by sharing O in tetrahedral SiO_4 sites [144].

In glass structures, silicate sites are classified according to the amount of oxygen atoms shared between one or more tetrahedra. These units, or species, are identified with the $\text{Si Q}^n(m\text{Al})$ notation type. n refers to the quantity of connected units, and m indicates the number of Al atoms substituting Si in tetrahedral coordination. The value of n varies from 0, representing an individual SiO_4 unit, to 4, representing a fully connected network, and the value of m varies from 0 to 3 [152]. The identification and further quantification of each silicate unit can be achieved by solid state magic angle spinning nuclear magnetic resonance (MAS NMR) of different nuclei. MAS NMR allows an individual element investigation as it evaluates interactions of specific nuclei with close neighbours according to the initial magnetic field. The sketch in Figure 2.8 illustrate the differences in pure Si-species (Figure 2.8a) and Al-substituted Si-species (Figure 2.8b) as measured by ^{29}Si NMR spectroscopy, and how to identify each one according to their characteristic responses [143,152]. Additionally, ^{27}Al MAS NMR can be used to identify the three different Al-O units, as fourfold (Al^{IV}), fivefold (Al^{V}) and sixfold (Al^{VI}) coordination also have their own characteristic chemical shifts [152,153] - see Figure 2.8c.

In general, the inclusion of Ca in aluminosilicate glasses increases the frequency of Si species with low connectivity. The depolymerization effect of NWM elements has been described by many authors, and they induce a clear distinction between slags and fly ashes, for instance. Fly ashes can present up to 90 % of Si Q^4 species and nearly no remaining individual SiO_4 (Si Q^0) units, while slags display mainly networks with dimers and trimers (Si Q^1 and Q^2 , respectively) [152,154,155]. The response of ^{27}Al MAS NMR also changes according to the quantity of modifying cations. Kucharczyk [156] demonstrated that, in synthetic $\text{CaO-Al}_2\text{O}_3\text{-SiO}_2$ glasses, chemical shifts of Al^{IV} are more evident with increasing Ca/Al ratio, as Al^{V} and Al^{VI} related signal is no longer observed above a CaO/ Al_2O_3 ratio of 1.45. Additionally,

Neuville et al. [157] reported a structure fully composed by fourfold-Al in similar glasses at $\text{CaO}/\text{Al}_2\text{O}_3 = 1$, while traces of network modifying Al are still observed in percalcic glasses. This last observation is of great importance, as it can show the complexity of establishing absolute rules for vitreous materials due to the high level of structural disorder.

To some extent, the connectivity of the microstructure can be quantified and provide vital information over the reaction potential of a material. The calculation of the ratio of *non-bridging oxygens to bridging oxygens* (NBO/T) is often implemented in the literature [143,147,148], but requires sophisticated and complex techniques and modelling tools to be precisely determined. With respect AAMs, it can be summarized that increasing content of NWM compounds raise the structural disorder of amorphous regions, leading to an enhanced the reactivity of raw materials in alkali-activated systems.

The depolymerization effect of Ca can have significant influence in the short-range structures of the glass phases of precursors. In X-ray diffraction (XRD) patterns, relationships between the CaO content of the precursor with the maximum 2θ angle value of the diffuse scattering has been described by different authors. Diamond [158] and McCarthy et al. [159] were among the first authors to report such structural relationships, as they determined trends valid for low- and high-Ca fly ashes containing from 0.9 wt% to 20 wt% of CaO, by creating a database of 178 samples from different sources in USA. Goto et al. [160] extended this relationship by including the structural characterization of synthetic glasses mimicking the composition of slags. As shown in Figure 2.9, the results indicated a quasi-linear trend up to 50 wt% CaO content, which covers slags and siliceous fly ashes - the linear relationship is interrupted between a CaO wt% range of 20-30 wt%, as calcareous ashes display similar structures despite of their Ca content, with similar maximum 2θ diffraction angles between $30\text{-}32^\circ$.

The relationships described by the authors suggested differences in the short-range ordered structures for both high- and low-Ca precursors. The diffraction maxima of siliceous fly ashes are close to a few aluminosilicate dominated structures - mullite ($2\theta = 25.97^\circ$; PDF# 00-015-0776) and sillimanite ($2\theta = 26.19^\circ$; PDF# 00-001-0626) - and to pure SiO_2 phases like cristobalite ($2\theta = 21.95^\circ$; PDF# 00-011-0695), the latter being in agreement with structural characterization of metakaolin [161-166]. The diffraction patterns of slags often present maxima 2θ angles resembling Ca-Al-rich phases such as gehlenite ($2\theta = 31.36^\circ$; PDF# 00-020-0199) and åkermanite ($2\theta = 31.13^\circ$; PDF # 00-035-0592), and calcareous fly ashes are in the intermediate region between both areas. As conventional precursors display variable levels of residual crystalline phases, it is easily assumed that the glass structures resemble what would be stable crystalline arrangements formed by the locally available atoms [167]. This observation is in line with many results available in the literature [48,95,98,168,169], which cite fly ashes with residual mullite contents up to 22 % [100], and slags displaying well defined residual presence of gehlenite, åkermanite and different forms of calcium aluminates [170,171].

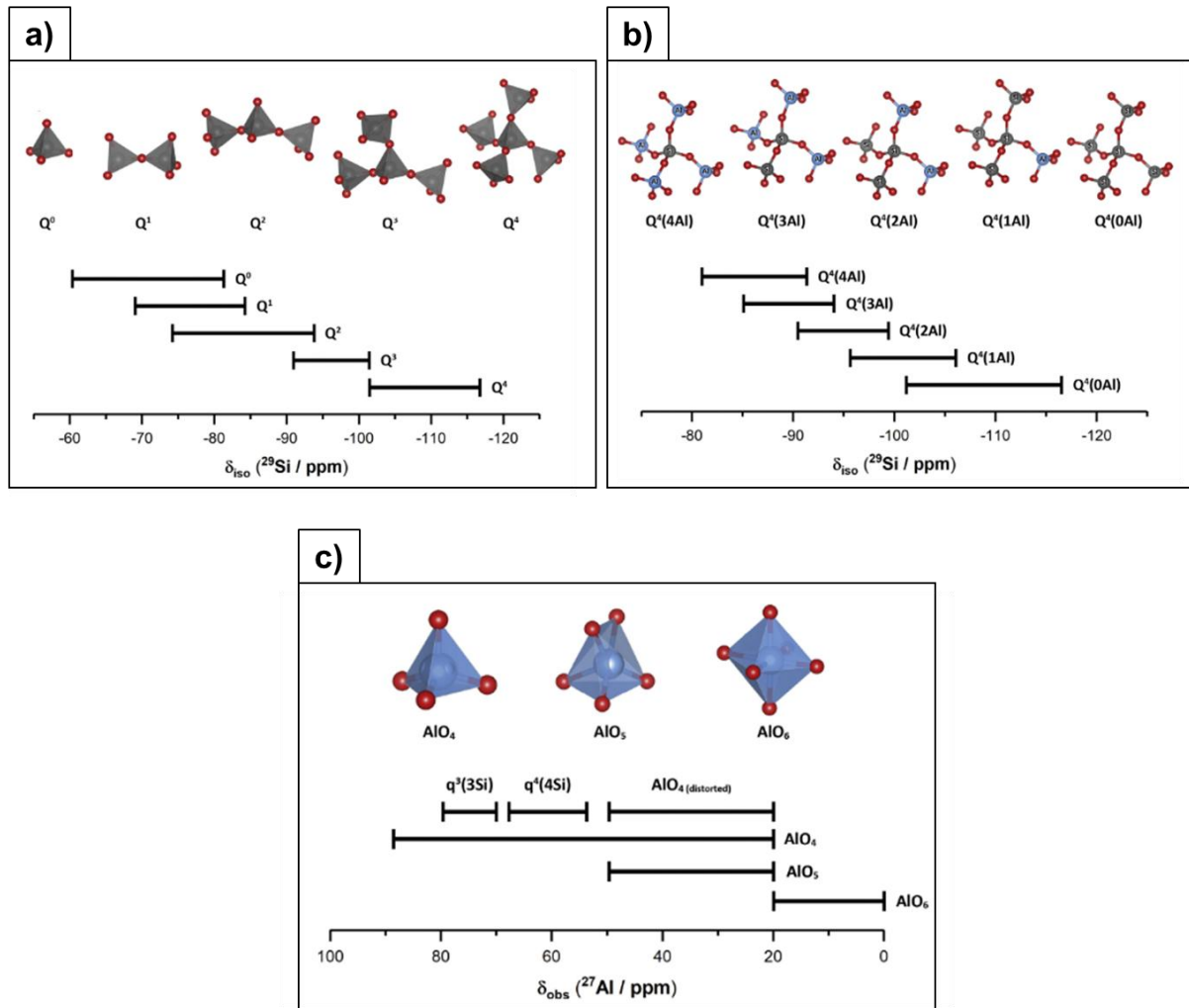


Figure 2.8: Typical ranges of chemical shifts for ^{29}Si and ^{27}Al MAS NMR of: a) SiO_4 tetrahedra; b) Al-substituted SiO_4 tetrahedra; and c) Al-O units (adopted from [152]).

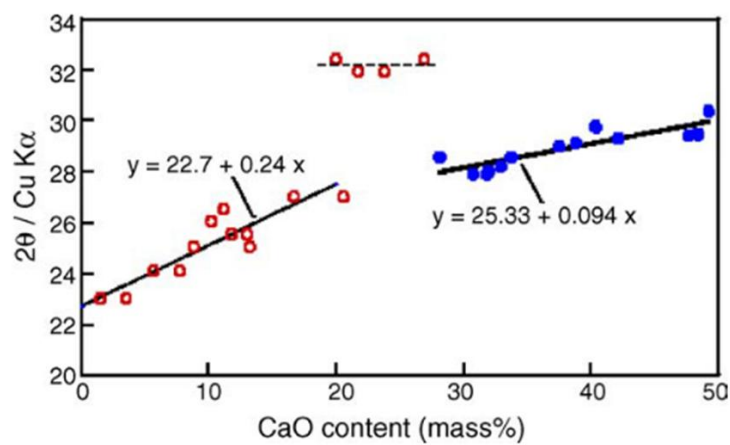


Figure 2.9: Correlation of the maximum 2θ position with the CaO content (wt%) of different precursors [160].

2.4 Kinetics of alkali-activating reactions

The reaction potential of an alkali-activated system, which comprises the early stages of reaction and the evolution and final features of its microstructure, are largely dependent on the mixture design and on processing conditions. In a simplified way, the reactivity of precursors can be directly linked to the initial content of CaO, especially in initial stages [172], and at room temperature, materials with low or no content of Ca will display a delayed reaction. Consequently, the reaction mechanisms involved in AAMs are mostly Ca-dependent: precursors can be classified as *latent hydraulic* (materials which require only water and react in a later stage of hydration process when the pH of the pore solution is high enough to trigger dissolution) and *pozzolanic* (material which required the presence of calcium hydroxide to trigger its dissolution) [44,45], and this classification can indicate the ideal conditions of the reaction media (type and concentration of activator and temperature) which are most appropriated for different precursors.

The evolution of the reaction can be followed using different techniques, and each stage of the overall reaction requires its specific techniques [173]. The dissolution of precursors and the evolution of pore solution can be observed in highly-diluted systems [174-176]. By implementation of a solution/precursor volume above 1000, the initial phase precipitation is significantly delayed, allowing the study of very-early moments of reaction. In this same scenario, the evolution of cation concentration with time, which is ideal for the obtainment of dissolution rates, is performed using inductively coupled-plasma optical emission spectroscopy (ICP-OES) or microwave plasma-atomic emission spectrometer (MP-AES). In the next stage, essential information over the evolution of the kinetic of reaction can be observed, among other techniques, by isothermal calorimetry and scanning electron microscopy [173,177]. The former quantifies the evolution of heat release, intimately correlated with enthalpy of formation of reaction products, while the latter provides a visualization of the microstructure in higher magnification. Moreover, spectroscopy techniques and X-ray diffraction provide information over the nature and quantity of phases in equilibrium at different times [99,178,179], proving to be powerful tools in the characterization of AAMs.

2.4.1 Dissolution

Alkali-activating reactions begin with the dissolution of the precursor as the first stage, which occurs immediately after contact with the alkaline activator [113]. Dissolution is a continuous process that promotes the breakage of covalent and ionic bonds from the glass network, releasing reactive aqueous species to the surrounding media. The phenomena of dissolution is triggered by the ionic strength of the liquid activating solution [63,180,181], and the rate of detachment of elements from the original framework is dependent on the polymerization degree of the aluminosilicate network of the precursor [143,148].

The scheme shown in Figure 2.10 illustrates the steps and provides the basic reactions involved in the dissolution of raw materials - Step A indicates the initial system. The process begins by a proton exchange mechanism between aqueous species and cations loosely bound to the glass network [113] - both network modifiers (light red) and charge compensators (orange). This triggers a significant release of Na^+ , Ca^{2+} , and other network modifying elements into the aqueous solution, as described in the Step B [113], and is often described

as a cationic leaching process. The H^+ proton adsorbed in this exchange mechanism has a smaller ionic radius than the alkaline cations, which induces extra disorder to the local structures and facilitates the sequential steps [182]. Further on, hydrolysis of primary and stronger covalent bonds of bridging oxygen atoms begins (Steps C, D and E), and the precursor is continuously consumed as the formation of *reactive layers* reduces the original particles. The intensity of this stage is directly equivalent to the alkalinity of the aqueous media, as higher pH leads to a higher concentration of OH^- species. The hydrolysis can happen due to breakage of aluminosilicate chains or opening of rings into smaller chains [183]. Although usually congruent dissolution is assumed [148,184], a few authors claim a faster dissolution of Al species, with Si dissolution occurring on a further step [180,181], as Al-O are normally weaker than Si-O bonds. Steps C and D describe the earlier hydrolysis of Al-O bonds in successive stages: first, $O-AlO_2^-OH$ and is formed in the reactive interface by the disruption in one bridging oxygen; sequential hydrolysis take place in Al-O bonds until individual Al sites reacts with additional H^+ protons from the solution to form $Al(OH)_4^-$, a reactive Al-aqueous species [180]. The hydrolysis of Si-O bonds follows a similar two-stage reaction (Steps E and F), with the formation of $Si(OH)_4$ aqueous species. The overall scheme describes the stage of the maximum dissolution rates of the precursor. The release of cations to the media occurs at independent rates, and is not influenced by the solution feedback solution [185]. This accelerated dissolution stage is termed forward dissolution, and will be decelerated once a supersaturation level of reaction products is achieved [186,187].

A few studies have focused on evaluating the influence of chemical composition on the initial stages of alkali-activating reactions, also termed *forward dissolution period*, which covers the stages prior to the stable precipitation of reaction products. Using a liquid to solid ratio of 1000, Snellings et al. [184] investigated the dissolution kinetics of synthetic glasses resembling blast furnace slag, siliceous, and calcareous fly ashes in sodium hydroxide (NaOH) solutions. The author reported forward dissolution rates of Si ($r_{+,Si}$) and Al ($r_{+,Al}$) up to one order of magnitude higher for percalcic glasses when compared to low-Ca, as shown in Figure 2.11. With a similar setup, Schöler et al. [148] obtained a reaction degree around 6 times higher for synthetic glasses resembling blast furnace slag in comparison to siliceous fly ash-like glasses as measured by the cation concentration present in the pore solution after 7 days of experiment.

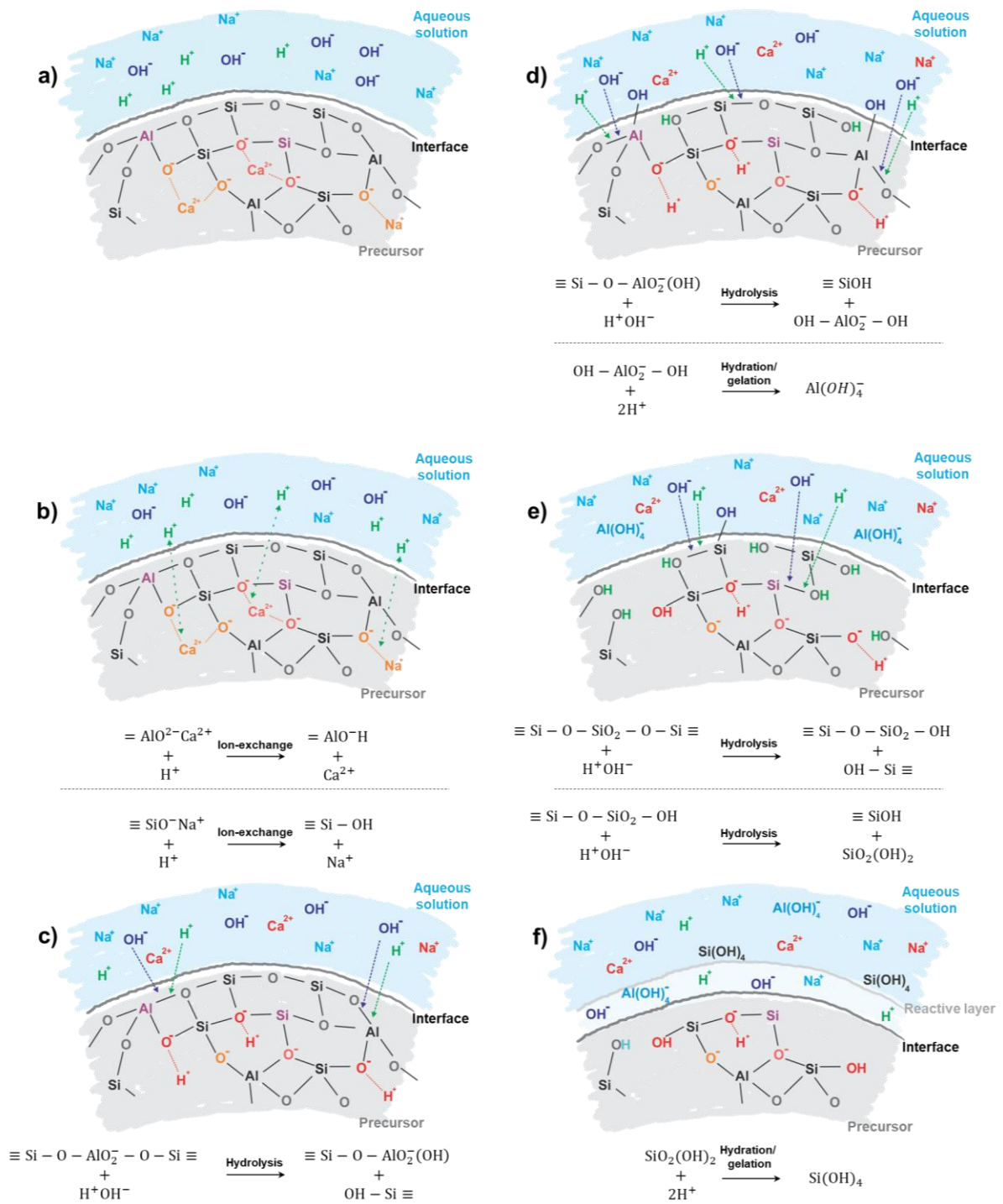


Figure 2.10: Illustrated scheme of the dissolution of precursors in alkaline solutions.

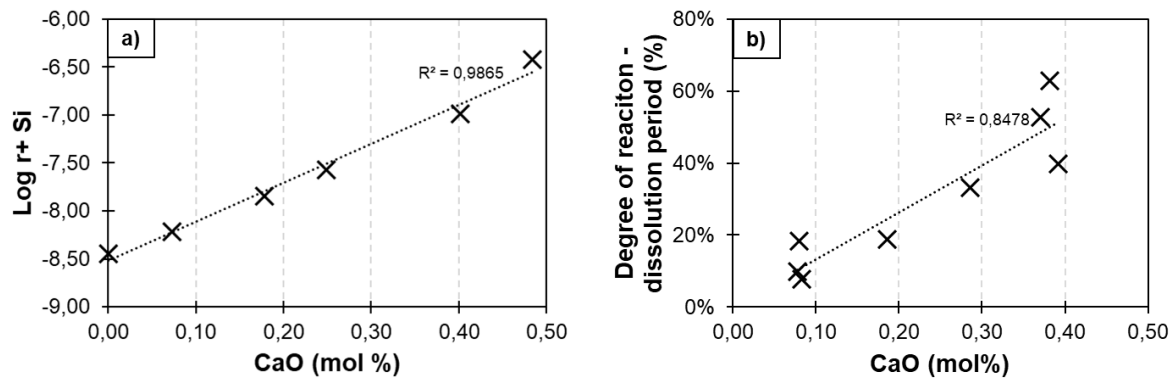


Figure 2.11: Influence of the content of CaO of synthetic glasses on different properties: a) forward dissolution rate of Si (chart adapted from data available in [184]); and b) degree of reaction (chart adapted from data available in [148]).

With the evaluation of slag dissolution in high-pH solutions, Zuo [175] combined with the data from Snellings and developed equations that predicts the forward dissolution rate of Si and Ca. Based on the structural parameters of precursor and alkalinity of the solution, a good agreement among the two set of data was found. The author based the study on the quantity of NBO of slag, which can represent an extra complexity when evaluating additional precursors. Aiming the understanding of the effect played by Mg, Hamdam et al. [172] compared the dissolution behaviour of synthetic slags obtained in the $\text{MgO-CaO-SiO}_2\text{-Al}_2\text{O}_3$ system. With fixed Si and Al contents, the authors did not observe significant changes in dissolution rates arising from a gradual substitution of CaO by MgO, in agreement with the non-observed changes in glass structure. With respect to fly ashes, Gangapatnam et al. [188] demonstrated that the quantity of the amorphous phase is crucial on determining the dissolution kinetics rate of these materials. By comparing two ashes with very similar chemistry, the authors reported that changes in concentrations of Si and Al are proportional to the reduction of the total amorphous volume of the ashes - a 30 % drop in total amorphous volume led to cation concentrations approximately 35 % lower when compared to ashes with larger amorphous portions.

2.4.2 Precipitation of reaction products

After the initial reaction stage, the release of elements begins to be decelerated and the precursor leaves the forward dissolution behaviour [113,189]. This occurs due to the supersaturation of reactive species in the reaction media, and the scenario becomes favorable for the initial nucleation of solid reaction products. Along with the initial dissolution, the visualization of these sequential stages can be performed with in-situ isothermal calorimetry, which measures the heat flow of the reaction with time as both network breakage and nucleation occur through exothermic reactions [173].

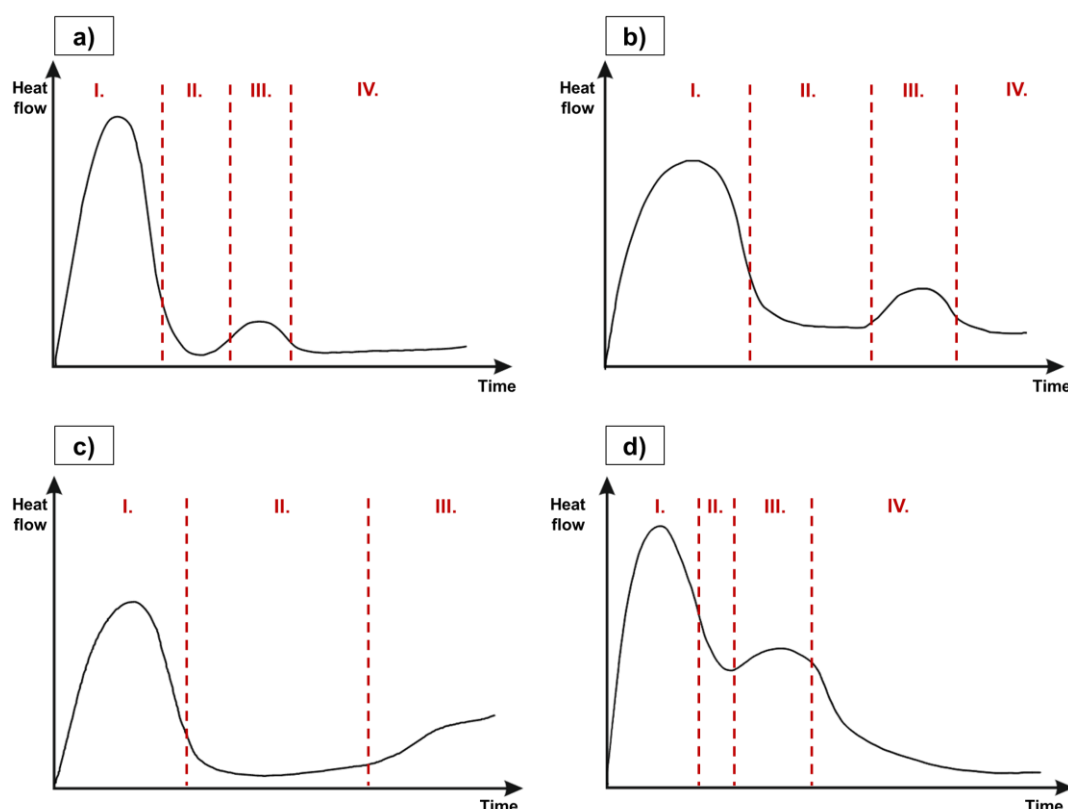


Figure 2.12: Example isothermal calorimetry curves of alkali-activated materials: a) high-Ca precursors activated with single components and b) silicate or carbonate solutions; c) low-Ca precursors cured at room temperature and d) temperatures above 50 °C.

In general, all precursors display an initial heat release peak, related to the initial dissolution process, but the sequence of calorimetric response is dependent on characteristics from both precursor and activator. Example curves are shown in Figure 2.12: a two-peak curve is expected for the alkali-activation of slag. In systems activated with hydroxide solutions (Figure 2.12a), the initial peak is correlated to the initial fast dissolution rate of the precursor (Stage I), followed by an induction period (Stage II), an acceleration period, characterized by a second wave of element release and the nucleation and growth of reaction products [44,106,108] (Stage III), and a final deceleration period of the reaction (Stage IV). This final stage represents a gradual densification of the microstructure, in processes controlled by diffusion of residual reactive species [190]. When a silicate solution or a carbonate solution is implemented (Figure 2.12b), the induction period is extended, due to the lower pH of the solution [191], and a broader and a less intense dissolution peak is obtained in Stage I. In low-Ca systems cured at room temperature (Figure 2.12c), especially when hydroxides are used as activators, not only a slower detachment of cations from the network is observed, but a less pronounced mechanism of nucleation and growth of new phases is expected, also resulting on less intense initial peak and an extended induction period [106,192]. If a higher temperature curing regimen is implemented, despite the activator, the expected calorimetric response is similar to the typical behaviour of silicate/carbonate-activated slags (Figure 2.12d), with increased heat flow in the dissolution period [175,192] and accelerated nucleation of reaction products [190].

The different calorimetric response arising from the activating solution, in alkali-activated slag, were illustrated by Ravikumar et al. [193] and Bilek Jr et al. [191], using different

silicate modulus and different molarities of sodium hydroxide, respectively. As seen in Figure 2.13a, a reduction in the alkalinity of the solution (denoted by larger silicate modulus or lower NaOH concentration) postponed and decreased the height of the peaks related to the acceleration period [193]. In the second case (Figure 2.13b), the authors suggest an optimized NaOH concentration of 7 M: increased reactivity is observed until this upper threshold value of NaOH, and above it, flash setting and hindered nucleation are expected [191]. With respect to low-Ca precursors, Chithiraputhiran et al. [106] studied the differences in responses of alkali-activated fly ash using NaOH solutions at 25 °C, 35 °C and 40 °C. In agreement with literature, only one calorimetry peak is observed for pastes cured at 25 °C. Increasing temperature, not only increases the height of the initial peak related to dissolution, but also leads to formation of a secondary peak related to a second wave of nucleation of new phases. Sun [194] evaluated the effect of temperature on heat release of alkali-activated pastes using individual fly ash and metakaolin as precursors and NaOH as activator. Figure 2.13c shows an evident improved reactivity when temperature is increased from 20 °C to 40 °C, with clear observation of acceleration periods for fly ash. It can be also noticed that the metakaolin-containing system displayed a smaller area under the calorimetry curve (Figure 2.13d). Although the height of the initial peak is higher for metakaolin than for fly ash (due to higher amorphous content), lack of Ca in the microstructure inhibits formation of further reaction products, and therefore the exothermal response of the paste is lower.

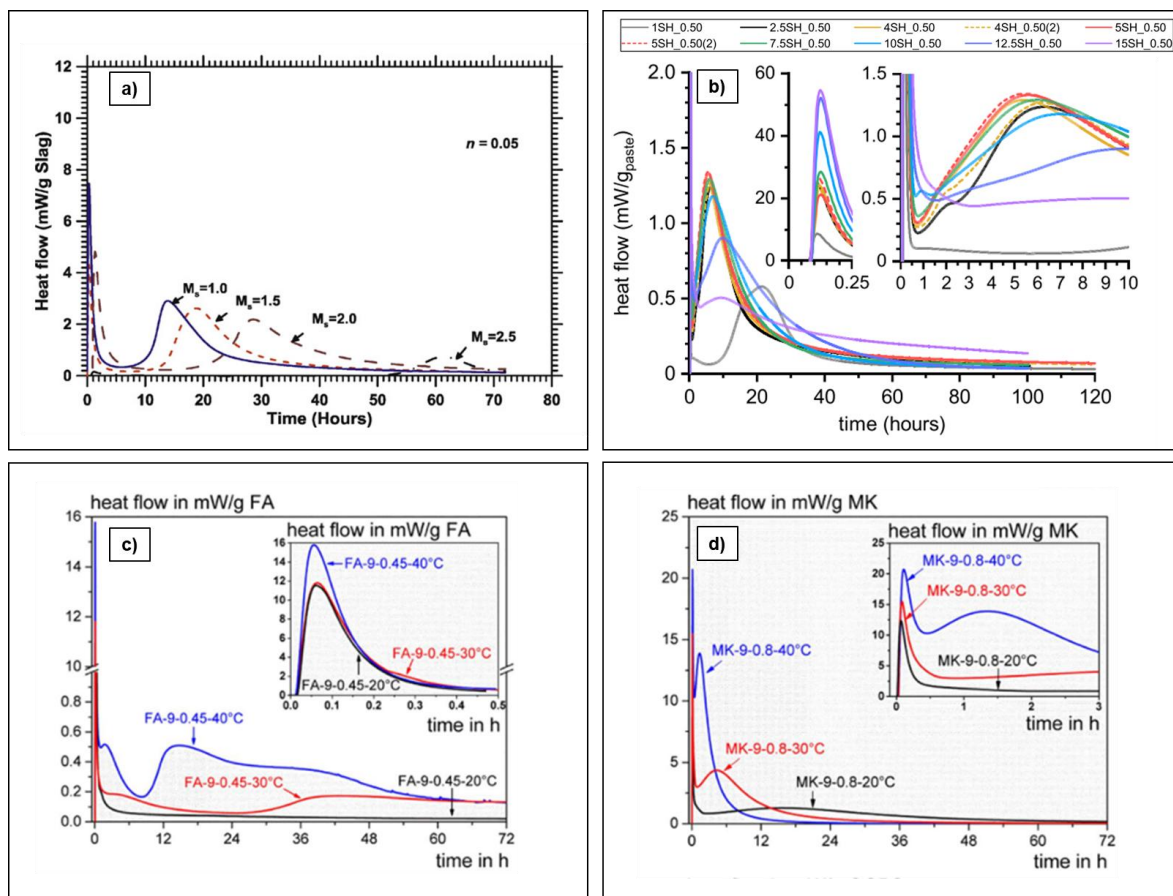


Figure 2.13: Examples of isothermal calorimetry investigation of alkali-activated materials: alkali-activated slags using a) silicate modulus [193]; and b) NaOH concentrations (concentration is indicated by the index followed by the SH - sodium hydroxide code) [191]; c) NaOH-activated fly ash and d) metakaolin cured at different temperatures (adopted from [194]).

2.4.3 Reaction mechanisms

The cementitious matrix formed in hardened alkali-activated systems consists of short-range ordered hydrated gels and secondary products, and the level of Ca supplied by the precursor controls both the sequence of reactions and the main characteristic of the main reaction products. With respect to mechanisms, Suraneni et al. and Ramanathan et al. [44,45] investigated the reactivity of 54 alternative binders divided in 12 groups, through thermogravimetric analysis and isothermal calorimetry experiments - although the authors labeled them as SCMs, these binders are also described in literature as precursors in alkali-activated systems. The authors reported that, although aspects such as amorphous content and particle fineness display influence in the final reactivity, Ca-rich binders can be classified as latent hydraulic materials, since it requires the consumption of lower amounts of alkaline species to display a relatively high heat of reaction. Figure 2.14 shows the different classifications, in which most of the tested metallurgical slags (SL) are in the field of latent hydraulic materials, while low-Ca materials, such as fly ashes (FA) and silica fume (SF), are located in the region of pozzolanic materials. Additionally, limestone (LS), quartz (Q) and basalt fines (BF), materials notoriously with high quantities of crystalline fractions, are considered inert.

Concerning reaction products, the hydrated gels to be formed can be categorized in two main groups according to the role of Ca, as schematically illustrated in Figure 2.15. In Ca-rich systems, it acts as both anchor for nucleation of CaO sheets surrounding silicate chains with variable level of Al^{IV} substitution, and as charge compensator of $[AlO_4]^-$ sites along with other alkaline species (C-(N-A-)S-H-type gels) [62,63]; in systems containing low-Ca precursors, it is either incorporated in N/K-(C-)A-S-H gels [83,103] as charge balancing species, or it is consumed to form secondary reaction products. C-(N-A-)S-H-type gel displays lower Ca content (showing usually a Ca/Si ratio approximate to 1.0) and higher Al content (with Al/Si ratio in the range of 0.1-0.2) than PC-formed C-S-H [58,195-197]. The C-(N-A-)S-H gel is described in the literature as a low order version of tobermorite, which is one of the crystalline analogous structures of C-S-H - it is common sense to define the structure of C-S-H as being a poorly ordered jennite-like or 1.4 nm tobermorite-like phase, with alternate layers of CaO and finite silicate chains [58,196]. N/K-(C-)A-S-H-type gels are often regarded as a precursor of zeolite structures or nanostructured zeolites. These gels present similarities in the chemical composition minerals and structural arrangement with this class of mineral, as reported for X-ray pair distribution functions [198,199], and with the course of reaction, the initially formed disordered species can go through rearrangements and display structural organization depending on the conditions of the reactive media.

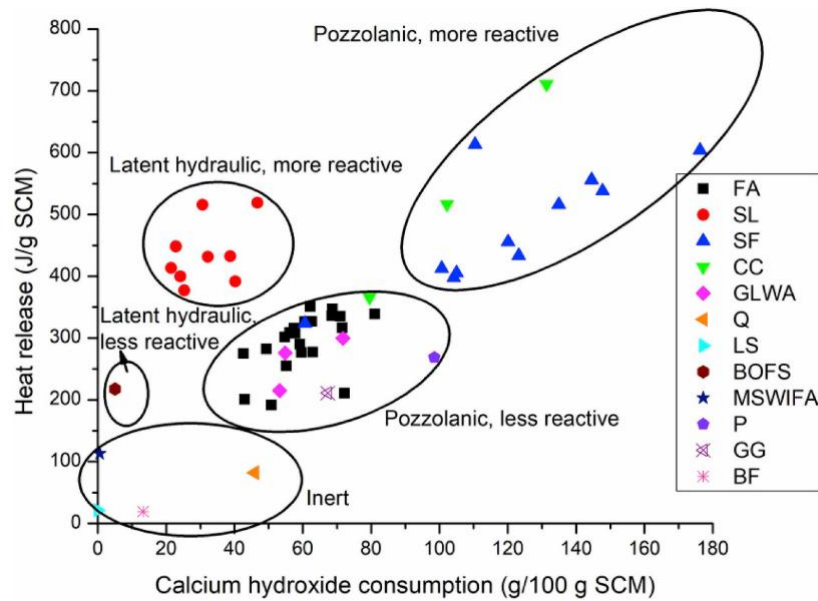


Figure 2.14: Definition of reactivity indexes of different SCMs/precursors based in heat release and calcium hydroxide consumption [44].

*Abbreviations: FA - Fly ash; SL - Slag; SF - Silica fume; CC - Calcined clay; GLWA - Ground lightweight aggregates; Q - Quartz; LS - Limestone; BOFS - Basic oxygen furnace slag; MSWIFA - Municipal solid waste incineration fly ash; P - Pumice; GG - Ground glass; BF - Basalt fines.

In both classes of precursors, secondary reaction products are commonly observed, contributing up to 15 % of the volume of the final microstructure of the hardened binder [89,108]. The type and amount of these phases is dependent on the presence of secondary oxides, on the curing conditions, and on the alkalinity of the solution [89,178,200], and their bulk compositions are usually out of the chemical composition stability range of the primary hydrated gels. The two main secondary products in high-Ca based systems are a Mg-Al layered double hydroxides (LDH) and AFm-type phases [58,201]. The first category comprises hydrotalcite-resembling phases, which are formed by alternate layers of brucite ($\text{Mg}(\text{OH})_2$) and gibbsite ($\text{Al}(\text{OH})_3$), is usually anchored at the surface of the particles of the precursor due to the low mobility of Mg, consuming the majority of Mg atoms supplied by the precursor [55,57,195,202], and is only observed with a MgO content above 5 wt% [58,203]. Authors have also reported that varying levels of MgO will not show effect on the chemical composition of C-(N-A)-S-H, and that the secondary oxide is only responsible for the formation of LDH or other additional reaction products [204,205]. AFm-type phases display a similar structural arrangement of LDHs, but the alternate layers are composed by gibbsite and portlandite ($\text{Ca}(\text{OH})_2$). In such structures, Ca^{2+} can be substituted by either Al^{3+} or Fe^{3+} , with anions providing charge-balancing conditions on the second layer [204].

In low-Ca systems, zeolites represent the most common secondary reaction products. As previously described, these phases comprise a group of crystalline materials with similar chemical composition to N/K-(C-)A-S-H gels but with a highly connected tetrahedral aluminosilicate network, displaying a channelized structure with high surface area [206,207]. Due to their similarity, N/K-(C-)A-S-H gels are considered nano-structured zeolite species which will not display a full crystallization behaviour due to insufficient curing conditions [99]. The type of zeolite to be nucleated is highly dependent on parameters of the reaction, such as $\text{H}_2\text{O}/\text{SiO}_2$ and OH^-/SiO_2 ratios, amount of cations, Si/Al ratio, and $\text{SiO}_2/\text{Na}_2\text{O}$ ratio [99].

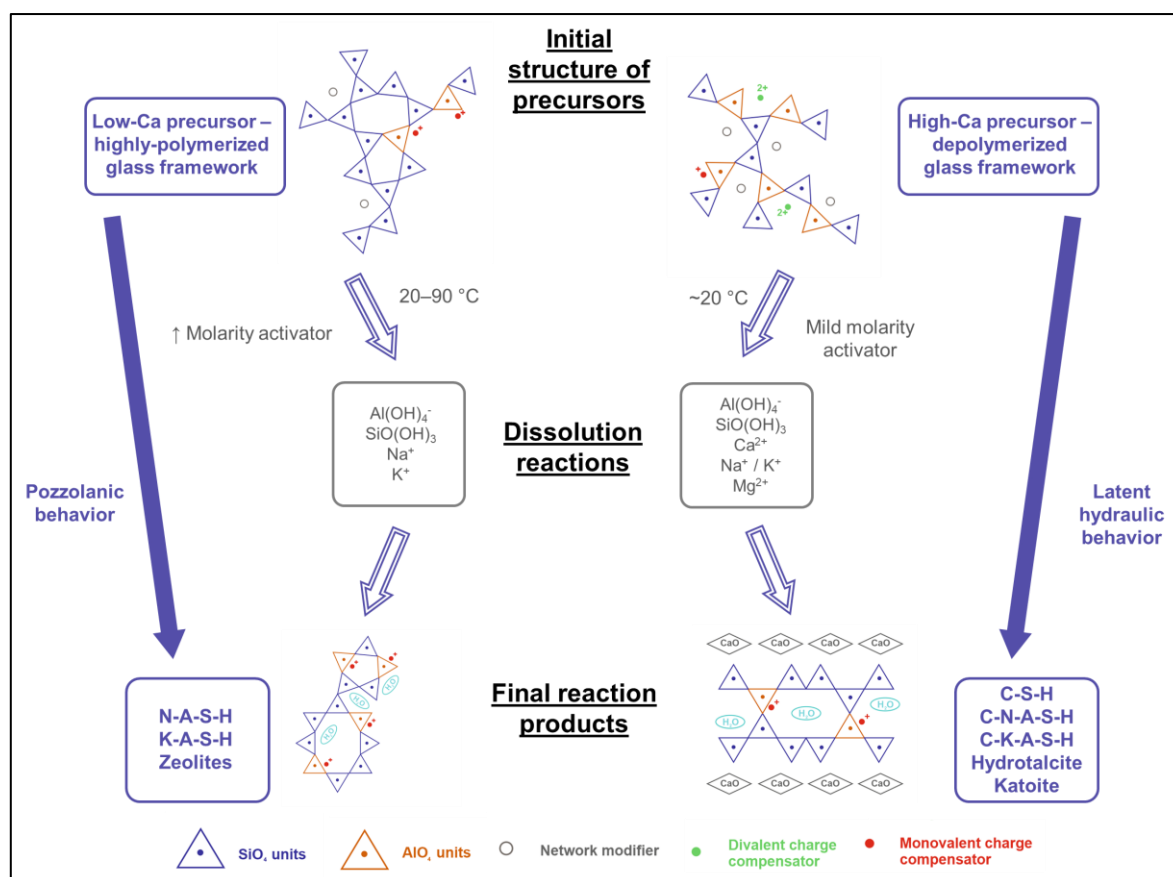


Figure 2.15: Conceptual model of alkali-activation of low- and high-Ca precursors (flowchart adapted from [83]).

2.4.4 Characterization of hardened binders

Given the low crystallization degree of hydrated gels, the distinction between the two main reaction products in alkali-activated binders is a complex process, being satisfactorily achieved only at qualitative level by use of spectroscopy techniques. Fourier transform infrared spectroscopy (FTIR) provides information over building units of different amorphous gels, distinguishing pure C-S-H gels and C-(N-A-)S-H gels from modified N-A-S-H through the shifting of vibration spectra, according to variable Si/Ca and Si/Al ratios [208–211]. As an example, Walkley et al. [212] investigated the evolution of microstructure of alkali-activated synthetic slag ($\text{CaO-Al}_2\text{O}_3\text{-SiO}_2$ system) and synthetic fly ash ($\text{Al}_2\text{O}_3\text{-SiO}_2$ system) powders using sodium silicate as activator (see Figure 2.16). The intense bands observed between $900\text{--}1000\text{ cm}^{-1}$, typical for the stretching vibrations of Si-O-T (with T representing both Si and Al) bonds, become sharper in slag-like glasses. In addition to the shoulder observed at 875 cm^{-1} , attributed to $[\text{AlO}_4]^-$ vibrations, a homogeneous presence of C-A-S-H phases, with low structural variation, is identified. Contrarily, the fly ash-system presents a broad band observed in the same spectral range. Silicate activated materials naturally increase the Si/Al ratio of the reaction products, decreasing the crosslinks of N-A-S-H chains, and thus hindering the growth of such gels in more ordered structures. The broad vibrations are an indication of 2-dimensional aluminosilicate chains, which can display different lengths and silicate coordination with variable Si/Al in each phase.

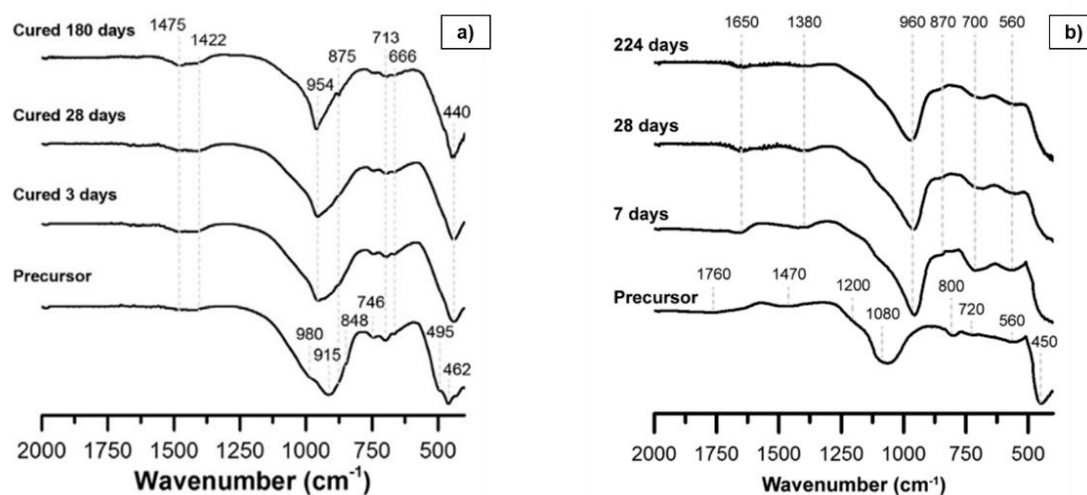


Figure 2.16: FTIR spectra of precursor and alkali-activated pastes of synthetic glasses: a) CaO-Al₂O₃-SiO₂ system; and b) Al₂O₃-SiO₂ system (adopted from [211,212]).

The use of ²⁹Si MAS-NMR (MAS NMR) complements the observations from FTIR spectroscopy, as the deconvolution of the spectra into individual curves allows a more detailed assessment of the microstructure of AAMs. Peng et al. [213] investigated the influence of the activator type and concentration on the final structure of N-A-S-H gel in alkali-activated fly ash. The ²⁹Si MAS NMR spectra of waterglass-activated systems presented a more Gaussian-like profile when compared to NaOH-activation - see Figure 2.17a. The deconvolution of the main curve indicated a wider presence of individual peaks 85-100 ppm range, typical of long and connected silicate chains (Si Q² and Q³), while increased concentration of hydroxide pushed the spectra towards more negative chemical shifts, assigned to crosslinked structures (Si Q⁴). In waterglass media, Bernal et al. [82] compared the ²⁹Si MAS NMR spectra of alkali-activated slag and fly ash. The shift of the curve to higher values in slag-systems, typical of a dimer- and trimer-dominated structures, indicates that C-(N-A)-S-H and C-S-H nuclei tend to be smaller, as the highly alkali content and Al-substitution hinders the formation of bigger chains.

Scanning electron microscopy (SEM) is an additional tool used to investigate the initial stages and the phase assemblage of hardened binders. The initial reactivity of fly ash particles, in NaOH solutions, was evaluated by Kuenzel and Ranjbar [214], who reported a strong influence played by temperature on this process. As demonstrated in Figure 2.18a, the dissolution process was progressively more significant from 25 °C to 145 °C, as nearly no alteration was observed initially, while only residual crystalline phases were detected at the highest temperature. The early-reactions and surface anchoring capacity of slag were evaluated by Bilek et al. [215] in waterglass and sodium hydroxide media. With isolated slag particles in suspensions with a liquid/solid ratio of 10, the authors verified that, in waterglass-based systems, a homogeneous and smooth surface was covering all particles, while NaOH promoted the nucleation of a porous network of reaction products - see Figure 2.18b. The envelopment of the surface of the precursor favours a homogeneous distribution of reaction products. In combination with reactive species provided by the activator, the initially precipitated phases will be able to grow in all directions, forming a densified hardened matrix combining with. Contrarily, the higher pH promoted by sodium hydroxide facilitates the localized dissolution of slag and the nucleation of outer products in specific directions, potentially resulting in a coarser microstructure.

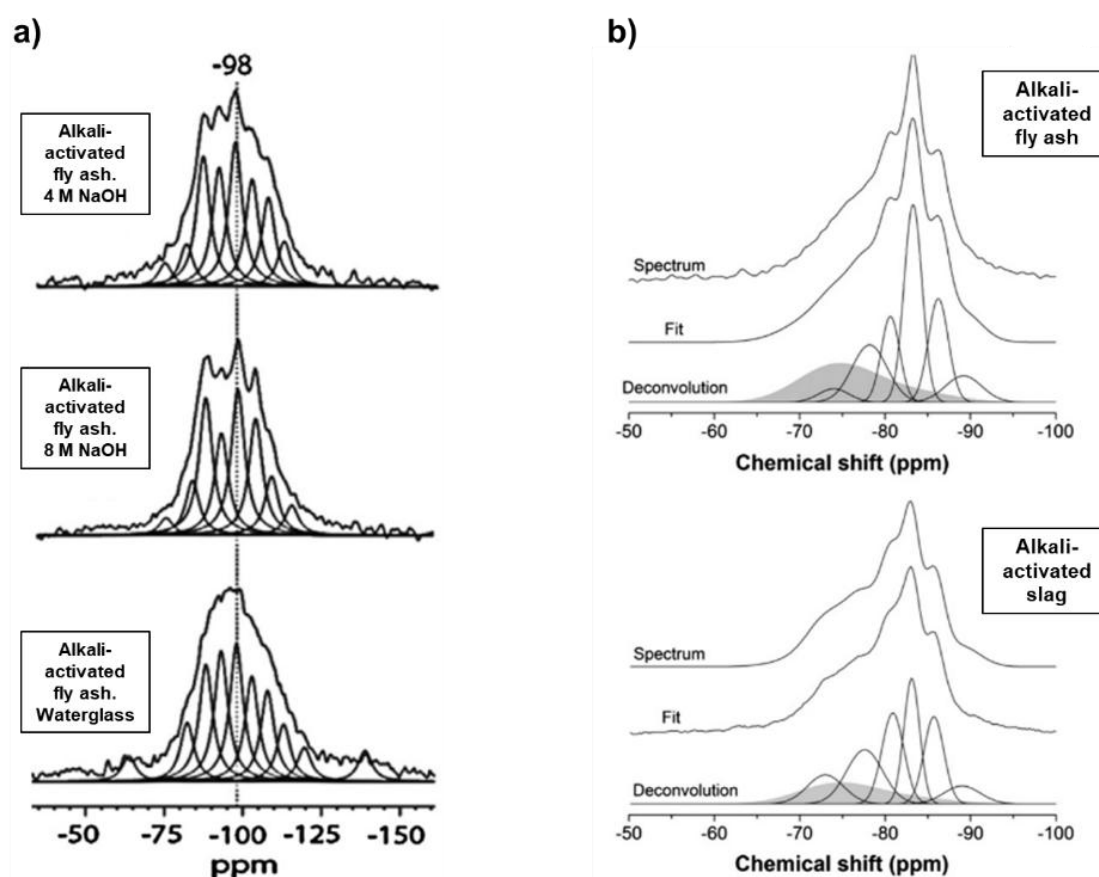


Figure 2.17: Deconvoluted ^{29}Si MAS NMR spectra for a) alkali-activated fly ash with different activators [213]; and b) alkali-activated slag and fly ash with waterglass [82].

The distribution of different phases within the microstructure can also be visualized, if chemical analysis are implemented with electron microscopy. Nedeljkovic [216] successfully performed phase segmentation on backscattered electron (BSE) images of polished surfaces, identifying distinct features in hardened binders comprised of individual slag and blended with fly ash (1:1). The author reported clear differences in the phase assemblage with respect to the interface between precursors and cementitious matrix, as shown in Figure 2.19. When slag is individually activated (S100), a large proportion of Mg-containing phases is visible, as expected for the formation of hydrotalcite in regions closer to slag particles. In blended systems (S50), formation of Mg-bearing rim phases is combined with C-A-S-H gel, which can be detected in interfacial zones between unreacted fly ash particles and the cementitious matrix. Moreover, both pastes presented an intimate mix of different hydrated gels, which, as discussed earlier, is a feature of alkali-activated binders.

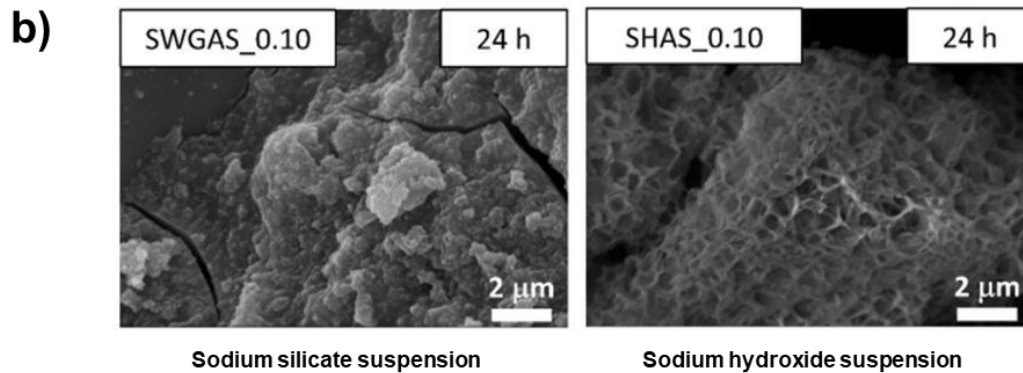
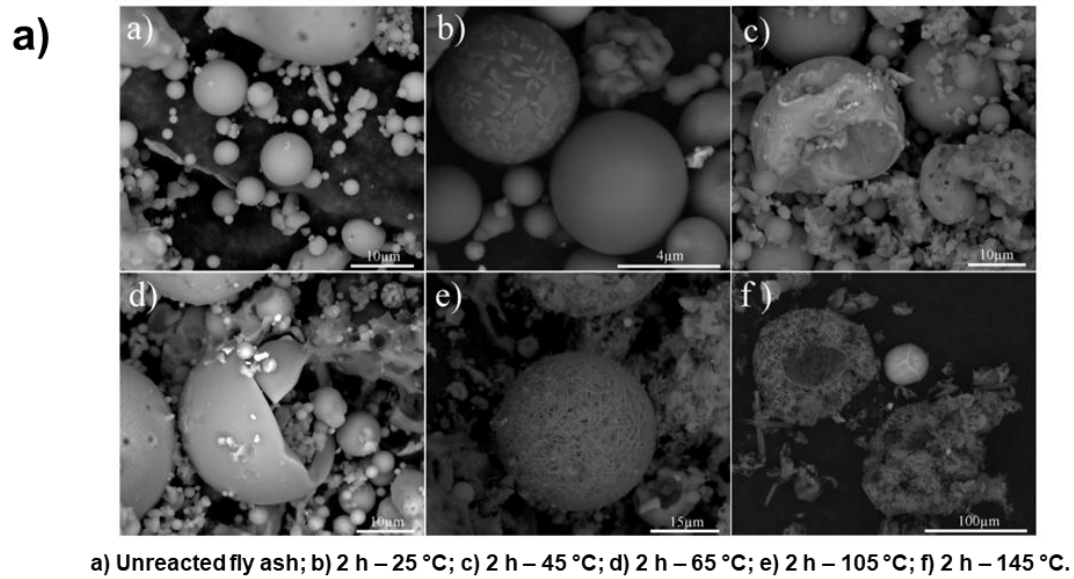


Figure 2.18: a) SEM micrographs of residual fly ash particles after 2 hours dissolution in 8 M NaOH solutions in different temperatures (adopted from [214]); b) slag surfaces after 24 hours of alkali-activation in suspensions with sodium silicate and sodium hydroxide (adopted from [215]).

2.5 Modelling of alkali-activated materials

2.5.1 Thermodynamic modelling for phase assemblage

The visualization of the evolution of hardening reactions, along with a quantification of final reaction products, represents a great interest for the applications of alkali-activated systems, as they can support predictive models of performance and service-life. In this scenario, thermodynamic modelling provides information about equilibrated systems at specific time periods, and can be a powerful tool not only to understand the influences of intrinsic and extrinsic factors on the distribution of reaction products and pore solution of mixtures, but also to predict degradation mechanisms arising from different causes, such as carbonation and chloride-penetration related issues.

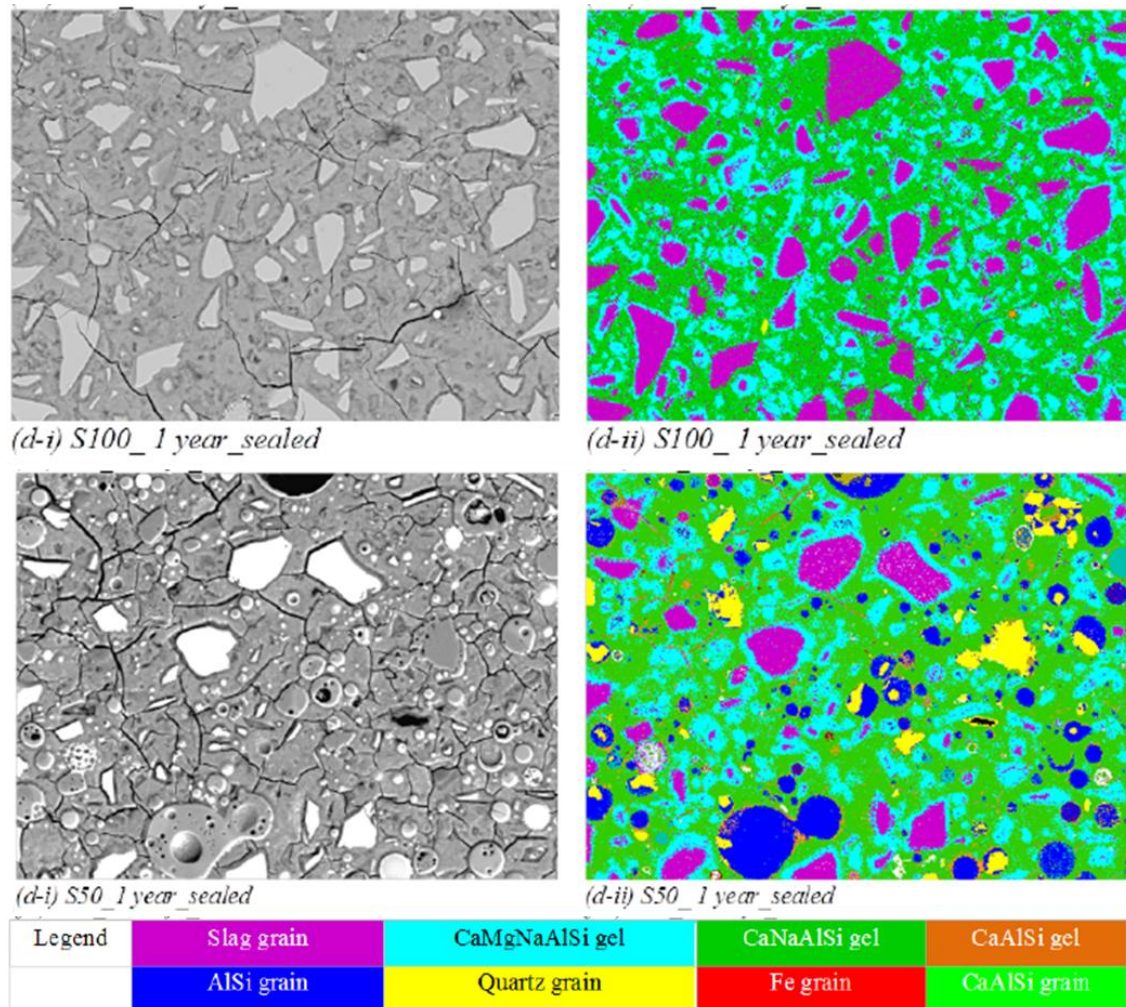


Figure 2.19: Phase assemblage of sodium silicate alkali-activated pastes of individual slag (S100) or combined with fly ash (S50), cured for 1 year (adopted from [216]).

Thermodynamic modelling of PC-based pastes [57,203,217], and the implementation of blast furnace slag [58,108,197,218], - as either SCM or precursor for AAMs - have been extensively investigated and validated with experimental findings. The level of accuracy of this type of models depends on the quality of the input thermodynamic data of raw-materials and potential phases to be formed. Myers et al. [58] worked on the development of C-(N-A)-S-H species and derived a model containing end-members of C-S-H, C-A-S-H, C-N-S-H and C-N-A-S-H groups with Ca/Si and Si/Al ratios in the range of 0.67-1.25 and 3.80-4.00 respectively. The Ca/Si used indicate that Ca^{2+} is the dominant cation in the gels, since they are above the ratio value of 0.72, which indicates individual growth of C-A-S-H-type species according to Fernández-Jiménez [219]. The model developed by Myers accounts for consistent thermodynamic data of C-(N-A)-S-H species, hydrotalcite-like phases, a few zeolite phases, and other crystalline phases commonly found in hydration/alkali-activation reactions [58,220,221].

The thermodynamic data of N-(C)-A-S-H gels is not fully developed up to now, which limits modelling of systems containing low-Ca precursors. The obtainment of solubility product and other relevant thermodynamic properties is a complex process, involving the synthesis of gels and long-lasting experiments, and several practical factors can influence the final results. A few authors experimentally determined the thermodynamic data of gels with Si/Al

ratios up to 3 [222-225], with satisfactory agreement among the reported results, while Zuo [175] used parameter fitting models to derive data for gels with ratios up to 4. More recently, Chen et al. [226] expanded the existing databases by determining the thermodynamic properties of Ca-bearing N-A-S-H gels with Ca/Si ratios up to 0.20. However, experimental observations demonstrated that N-A-S-H gels can reach Si/Al as high as 5, especially if waterglass is used as activator [88-90], while the roles of Ca in these species, and therefore their Ca/Si ratios, are not yet fully understood. The validation of experimentally derived data is not easy to be performed, as N-A-S-H gels are less stable than its crystalline zeolite counterparts. Recently, Ma and Lothenbach [207] developed an extensive database of zeolites, containing 36 different phases comprised of Al-, Na-, Si-, K-, and Ca- bearing phases, which can extend the modelling potential of alkali-activated materials.

Ke and Duan [227] investigated the influence of incremental amounts of slag on the modelled phase assemblage of waterglass-activated systems, simulating a blending of low- and high-Ca precursors. The increasing content of Ca, from the addition of slag, shifts the reaction products from a N-(C-)A-S-H-dominated structure, denoted by the formation of zeolites, to a C-(N-A-)S-H stable scenario, with secondary Mg-containing phases - see Figure 2.20a. The authors also developed a machine learning based tool able to predict the strength of the binder according to chemistry, reporting lower performance when CaO is in the range of 10-25 %. Such behaviour can be expected, as fly ash is known for having delayed reactions in blended systems, which require slag contents above 50 % to enhance the overall reactivity of the system [228,229]. Ke et al. [230] evaluated the degradation caused by CO₂, also in waterglass-activated slag systems (Figure 2.20b), demonstrating that at high carbonation levels, the formation of calcite and Na,Ca-aluminosilicate, arising from the commonly reported dissociation of C-N-A-S-H into CaCO₃ and disordered N-A-S-H gel, dominate the equilibrated structure. Moreover, Zuo [231] simulated the effect of chloride salts on the phase assemblage of alkali-activated slags using the same activator, predicting the formation of Friedel's salt ($[\text{Ca}_2\text{Al}(\text{OH})_6 \cdot 2\text{H}_2\text{O}]^+$) by the dissociation of katoite and hydrotalcite, and the binding of Ca and Al arising from the destabilization of C-(N-A-)S-H gels (Figure 2.20c).

2.5.2 Microstructure modelling through combined kinetic and thermodynamic approaches

Although thermodynamic modelling can predict an equilibrated phase assemblage, it requires the amount of reacted material - i.e. degree of reaction - as input. This parameter can be rather difficult to be obtained, requiring quantitative XRD analysis or grayscale threshold calculations obtained from SEM [173]. For that reason, there are only few available studies which can satisfactorily estimate the degree of reaction in alkali-activated systems, based on characteristics of the binder. Recently, Mills and Wagner [232] developed a kinetic model which correlates the evolution of shear modulus with the amount and the Si/Al ratio of precipitated N-A-S-H gel in fly ash activated mixtures. Caron et al. [233] proposed a model which predicts the evolution of reaction degree in waterglass-activated slags, with different silicate modulus. The authors considered the different mechanisms arising from differences in pH and Si-species concentrations, influenced by the silicate modulus of the activator, and successfully validated the proposed with data obtained in literature, obtaining a R² greater than 0.95. In addition, the same group combined this

model with prediction of phase assemblage, correlating the equilibrated structure with mechanical performance of alkali-activated binders [234]. Through experimental analysis made with nanoindentation, the authors were able to satisfactorily predict the Young's modulus of pastes and concretes, and the influence of parameters of the mixture in the mechanical properties.

With respect to the combination of kinetic models with mechanisms of phase precipitation, a few authors focused on the prediction of reaction products of alkali-activated fly ashes and metakaolin. Provis et al. [235] were among the first authors to propose models to characterize the structural arrangement of N-A-S-H-type gels, evaluating the influence of the Si/Al ratio of the precursor, the Na content of the precursor, and the reaction temperature in the formation of such species through mathematical correlations. In a sequential work, Monte Carlo simulations were implemented by White et al. [236] to observe the influence of activators in the nucleation and coalescence of disordered N-A-S-H species during the activation of metakaolin, distinguishing the formation of clustered species with NaOH and surface-anchored species in waterglass solutions. With a similar concept, the *HydratiCA* model [237], which was originally developed to simulate the hydration of cement, was expanded through the work of Valentini [238]. That author utilized the reaction-diffusion model based on stochastic algorithms and reaction kinetic equations to identify the delayed influence of waterglass in the nucleation of N-A-S-H gels, which then acted as seeds for the formation of zeolite-like structural arrangements.

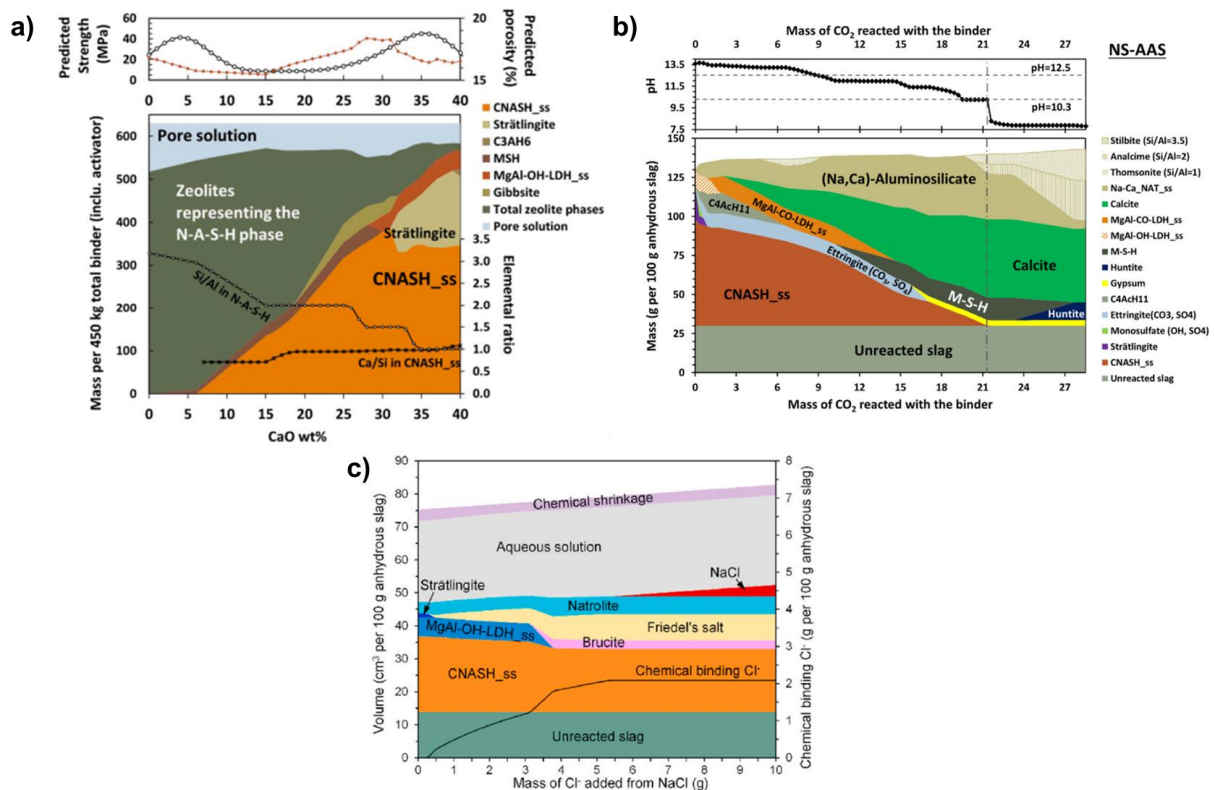


Figure 2.20: Thermodynamic modelling of waterglass-activated slags: a) effect of CaO wt%; b) effect of CO₂; and c) effect of Cl⁻ on phase assemblage (adopted from [227], [230], and [231], respectively).

More recently, the combination of kinetic with thermodynamic modelling of alkali-activated materials was proposed by Zuo [175], on an attempt to obtain a digital visualization of their reaction processes of these binders. The numerical simulation tool, called *GeoMicro3D*, combines aspects of precursor dissolution, reactive mass transport, probability of nucleation of reaction products, and thermodynamic equilibrium, allowing the observation of the evolution of the microstructure at different ages. The pioneer work of the author was validated with the obtainment of digital microstructures of alkali-activated slag systems, which are in accordance with individual thermodynamic modelling [218] and with experiments for NaOH and waterglass-activated binders [108]. The results reported by the author indicated agreement with the degree of reaction of the precursor, the pore solution, the overall porosity, and the distribution of reaction products throughout the cementitious matrix, as the model provided the observation of the spatial distribution of different phases in the microstructure - see Figure 2.21.

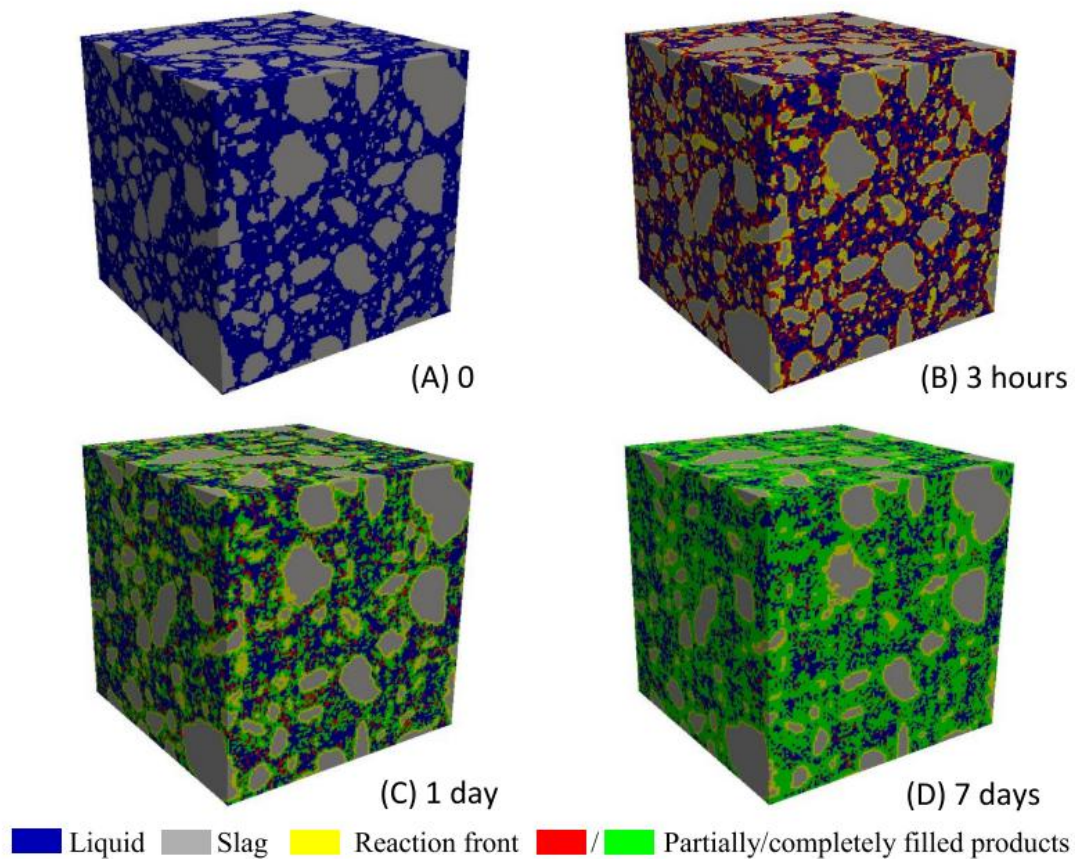


Figure 2.21: Simulated microstructure evolution of alkali-activated slag (adopted from [175]).

2.6 Identification of research gaps and the motivation of this research

The present Chapter provided a summary of the extensive research efforts made on the characterization of alkali-activated materials, specifically on characterizing and correlating their microstructural features with characteristics of the binder and the reactive media. The present state-of-the-art of the literature demonstrated a substantial knowledge on the different stages occurring in alkali-activating reactions, and special focus has been given to fly ashes and slags, as these represent the most mature available precursors. Despite the current understanding, the challenges presented in the beginning of the Chapter open new research possibilities, and an in-depth investigation of the influence of chemical compositions and curing methods could strengthen the acceptance and the applicability of these binders:

- **Dissolution kinetics of precursors:** Experimental evaluations of dissolution mechanisms have been satisfactorily performed, but they were limited to temperatures in the range of 20 °C and have been majorly performed for slag-based precursors. The current literature provides equations proposed to predict the dissolution rates of slag, according to the chemical composition of the precursor and to the alkalinity of the solution.

The existing structure-dissolution correlations rely on the quantitative knowledge of NBOs in the framework of the precursor, a parameter of complex and often inaccessible determination. Therefore, there is room for the extension and simplification of these models, including the effect of high-temperature processes and the validation of a wider range of chemical compositions, covering both high- and low-Ca precursors.

- **Reaction mechanisms:** The assessment of the kinetics of reaction of alkali-activated materials, and their correlations with the chemistry of the binder (considering both activator and precursor), have been mainly performed through qualitative approaches. These studies allow an estimation of the quantity and the distribution of reaction products in the microstructure of different systems. However, few studies cover the very early stages of reaction, limiting the knowledge on the precipitation of the first nuclei of reaction products which directly impact important practical parameters on the processing of these binders, such as fresh properties and setting time.

The possibility to combine observations of dissolution kinetics with the nucleation of the first nuclei of disordered gels, evaluating the influence of structure and on these mechanisms, opens a new window of investigation. Moreover, the development of a quantitative study, correlating intrinsic (chemical composition of the precursor) and extrinsic factors (curing regime and conditions of the activator) of the binders to the phase assemblage of reaction products, would result in service-life and performance prediction models with higher accuracy.

- **Modelling tools:** Current kinetic and thermodynamic models, individually, provide sufficiently reliable information about the extent of reaction and the phase assemblage of alkali-activated materials. The combination of the two approaches on microstructural modelling has been validated for individual slag-based systems, but have not been yet implemented for the equilibrium analysis of low-Ca precursors

under different activators and curing temperatures, or for the combination of two or more precursors.

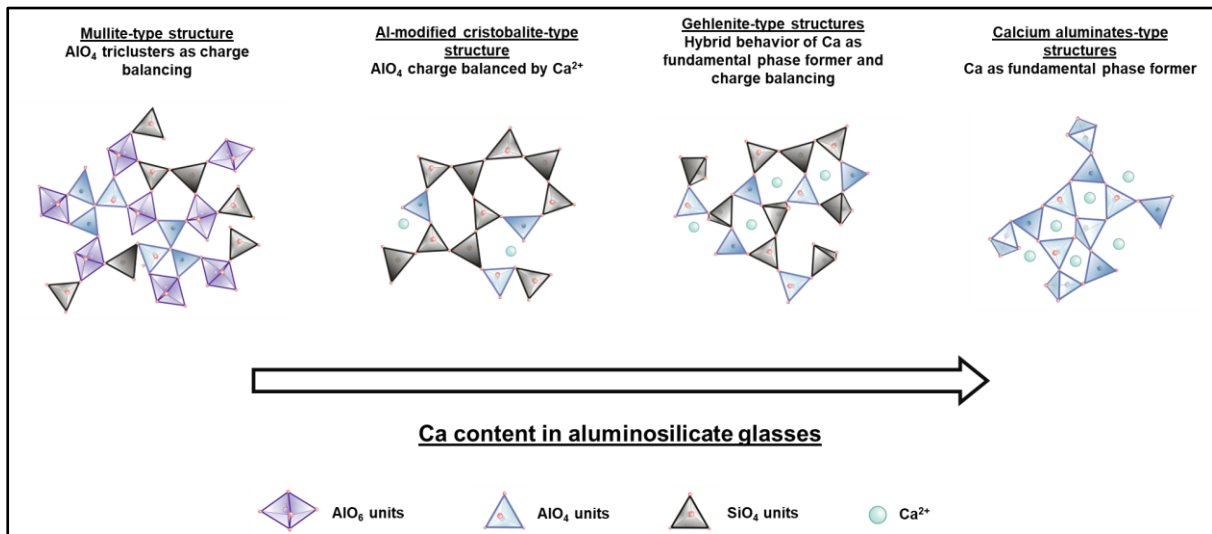
The validation of the thermodynamic data of N-(C-)A-S-H gels could enhance the modelling possibilities of alkali-activated materials, by extending the range of covered raw materials and processing parameters. Finally, the combination of correlations observed in kinetic phenomena-related experiments with quantitative prediction of phase assemblage, and their inclusions on tools such as GeoMicro3D, could deliver a powerful instrument on the accurate modelling of digital microstructures, essential for the expansion of the technology of AAMs.

- **Chemistry-temperature based approach:** The establishment of correlations between mechanical properties and chemical compositions of alkali-activated binders has been attempted by different authors, but the existing datasets are limited to few precursors and do not show a great agreement among them. In addition, the observed influences of temperature in the type and structural organization of reaction products raise additional challenges, making it more difficult to estimate the performance and service-life of alkali-activated binders. Especially in systems with low-Ca precursors, the choice of a curing regime can easily modify its behavior, and should always be accounted for during the definition of such correlations. The combination of the previous topics would promote the definition of multiple chemistry-temperature based relationships, which could facilitate the prediction of the behaviour of different alkali-activated binders in several environments. If performance-based standards are to be implemented in the near future, an in-depth understanding of the role of each element in the structural characteristics of precursors, and consequently in the development of the microstructure and performance of AAMs, would extend the range of potential precursors and activators whilst providing a greater level of confidence in the structural characteristics of these binders.

As alkali-activated materials demonstrate environmental advantages and a high potential to be regarded as a solution for the present and future of the building industry, there is a motivation for in-depth study of their reaction mechanisms, and how they are influenced by characteristics of the raw materials and external reaction parameters. Targeting aspects that directly influence the practical application of these binders, from fresh mixtures until mature systems, is the main objective of this research, and the development of binder/process-microstructure correlations will be discussed in the next chapters of this thesis.

Chapter 3.

Synthesis and microstructural characterization of glasses resembling conventional precursors



The mineralogy of the most common precursors utilised in alkali-activated materials can be considered of high complexity, due to the mixture of amorphous and highly disordered phases with residual crystalline structures. As discussed in Chapters 1 and 2, this brings additional challenges on the study of these binders and limits the applicability of these binders. Hence, a fundamental understanding of the various structures present in different precursors can facilitate the understanding of their reaction mechanisms, enhancing the reliability of alkali-activated materials. This Chapter presents the initial part of this thesis, comprising the preparation and characterization of synthetic glasses resembling commercial precursors. It was concluded that all precursors presented heterogeneity at sub-microscopic level, which is directly influenced by their respective chemical composition. Ca was shown to have multiple roles in glass structures according to its initial content, shifting from simple charge balancing cation to playing a pivotal role in the formation of certain phases. The conclusions over the influence of chemical composition in the disordered structures of precursors will be used as base for the remainder of this thesis.

3.1 Introduction

The chemical composition and the mineralogy of precursors have been shown to directly impact their reactivities and significantly influence the microstructure and the performance of alkali-activated binders [46]. Within the amorphous portion of a precursor, the connectivity of the glass network is largely ruled by the amount of network modifying oxides. While Si is the main contributor to the formation of rigid structures, alkali and alkali-earth elements play an important role in disrupting the connections between tetrahedra of Si- and Al-species, resulting in progressively depolymerized networks directly proportional to their content [143,150]. However, understanding the effect of each modifying element on the overall reaction mechanism is rather complex. With respect to network modifiers, this thesis focuses on the comprehension of the influence played by CaO in two aspects: the characteristics of amorphous structures; and the reactivity of low- and high-Ca precursors.

The approach of this research was on the synthesis of glasses with chemical compositions replicating the amorphous portion of commercial alkali-activation precursors. By doing so, a simplification of complex structures can be achieved, thus facilitating the observation of fundamental phenomena occurring at different stages of alkali-activating reactions.

This Chapter evaluates the influence of the main components (SiO_2 , Al_2O_3 and CaO) on the connectivity of the network of synthetic precursors, describing the role of each and their expected effects on the reaction potential of precursor materials. The different types of disordered structures formed in each glass were characterized using spectroscopic techniques and X-ray diffraction, and the heterogeneities in the structures were addressed. At the end of Chapter, a summary of the identified phases is provided, along with a schematic illustration explaining the role of Ca in the destabilization of aluminosilicate structures. The results and conclusions from this Chapter lay the groundwork for further research, as the microstructure of the synthetic glasses was observed to align with those of commercial slags and fly ashes. Figure 3.1 shows the position of this Chapter as the initial part of the structure of the thesis structure.

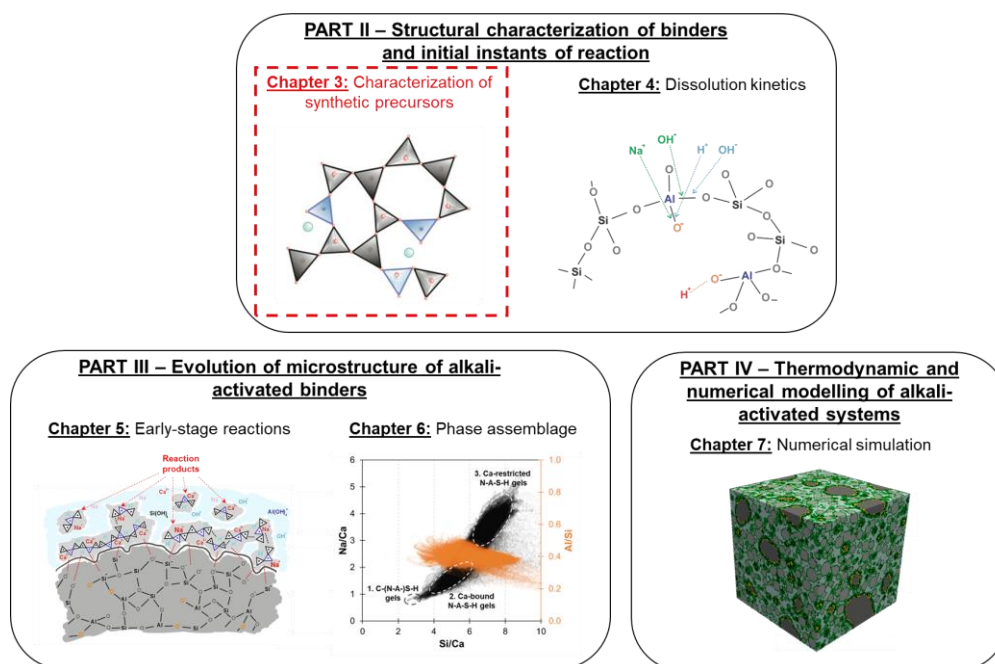


Figure 3.1: Schematic illustration of the structure of this thesis, highlighting the contributions of Chapter 3.

3.2 Materials and Methods

3.2.1 Synthesis of glasses resembling slags and fly ashes

Four different precursors, with simplified chemical compositions based on the CAS ($\text{CaO-Al}_2\text{O}_3\text{-SiO}_2$) system, were synthesized using a melting and quenching glass production method. Initially, stoichiometrically controlled quantities of reagent-grade SiO_2 (99.95 %), Al_2O_3 (98 %), and CaCO_3 (precipitated, 99 %, analytical grade) were mixed in a Retsch PM100 planetary ball mill for 2 hours at 200 rpm, in an 1:1 isopropanol (99.8 %) dispersion. The mixed dispersions were dried overnight at 105 °C, resulting in homogeneous powdered mixtures. The powders were then hand-pressed into alumina crucibles for melting in a Carbolite HTF1700 furnace. All glasses were exposed to a two-step melting route: firstly, from room temperature to 950 °C at a heating rate of 5 °C/min, with a 1 hour dwell time to ensure slow decarbonation of CaCO_3 ; and secondly, from 950 °C to a maximum temperature of 1600 °C at a heating rate of 10 °C/min, with a 2-hour dwell time. Shortly before the end of the second dwelling period, the molten material was immediately poured in a water bath to prevent crystallization of the glasses. After quenching, the obtained glasses were dried overnight at a conventional oven at 105 °C. Finally, the dried material was crushed, milled and sieved according to the desired particle size for each experiment. As each glass production process yielded 30-50 g of material, several batches were performed to accommodate all experiments. Among the synthetic precursors, the main distinguishing feature was the Ca/Si ratio, ranging from 0.25 to 1.40. The four glasses were designed to replicate siliceous fly ash (Si-FA), calcareous fly ash (Ca-FA), and blast furnace slags (BFS-1 and BFS-2), and the target chemical compositions are detailed in Table 3.1.

3.2.2 Characterization of synthetic precursors

The chemical compositions of the synthetic glasses were determined using a Panalytical Axios Max wavelength dispersive X-ray fluorescence instrument (XRF). The efficiency of the quenching process was assessed by X-ray diffraction (XRD) to evaluate whether the precursors presented residual crystalline structures. The XRD patterns were obtained using a Bruker D8 Advance diffractometer coupled with $\text{Cu-K}\alpha$ radiation ($\lambda = 1.54 \text{ \AA}$), with a scanning range of 8° -100° 2 θ , a step size of 0.020° 2 θ and a dwell time of 2 seconds per step.

Table 3.1: Range of chemical compositions of each group of synthetic glass.

Glass	Target normalized* oxide content (mol)			Target atomic ratios	
	SiO_2	Al_2O_3	CaO	Si/Al	Ca/Si
Si-FA	1.00	0.33	0.25	1.50	0.25
Ca-FA	1.00	0.33	0.50	1.50	0.50
BFS-1	1.00	0.33	1.00	1.50	1.00
BFS-2	1.00	0.33	1.40	1.50	1.40

*Normalized to the content of SiO_2 .

The internal structures were characterized using different spectroscopic techniques. Attenuated total reflection Fourier transform infrared (ATR-FTIR) spectroscopy was performed using a PerkinElmer Spectrum 100 FT-IR device with a universal ATR attachment, with a total of 32 scans and a resolution of 4 cm^{-1} . Raman spectroscopy was performed using a Renishaw inVia confocal Raman imaging microscope equipped with a 50x objective. A green laser with a wavelength of 532 nm was chosen as the excitation source. A total of 10 accumulations were obtained using 1 % laser power and an exposure time of 10 s. The total spectra were deconvoluted by 50 % Lorentzian/Gaussian functions, using a first guess for the centre and full width at half-maximum (FWHM) of each peak according to values described in literature. The deconvolution process followed two stages, as described in [239]. Initially, the vibration peaks attributed solely to Si-O bonds were identified, allowing a quantitative estimation of Si Q^n units through the implementation of Raman scattering coefficients. The summation of the individual vibrations of Si-O bonds was performed, enabling the obtainment of an envelope curve accounting for all Si-O interactions. As Al-O and Si-O contributions are partially overlapped in a Raman spectra [240], the subtraction of all Si-related vibrations allowed the observation of an Al-O dedicated spectra. Sequentially, a second deconvolution process was performed, enabling a qualitative analysis of the Al Q^n sites.

Solid state magnetic angle spinning nuclear magnetic resonance (MAS NMR) was implemented for comparison and validation of the Si Q^n observations made with Raman. MAS NMR measurements were performed using a Bruker Ascend 500 magnet (11.7 T) equipped with a NEO console operating at ^{27}Al and ^{29}Si resonance frequencies of 130.32 and 99.36 MHz respectively, using both 4 and 3.2 mm three channel MAS probe heads. The MAS rate was set between 10 and 15 for all measurements. Single pulse one-dimensional (1D) measurements were recorded for both ^{27}Al and ^{29}Si , with pulse lengths of 1.5 μs and 3.5 μs respectively. Recycle delays of 3 s for ^{27}Al and 5 to 60 s for ^{29}Si were set, allowing complete recovery of magnetization between scans. Deconvolution of the ^{29}Si spectra was achieved using a Gaussian function with a first guess for the centre and width of each peak. The resulting quantities were compared against Raman deconvoluted values, validating the use of the latter for further characterization in this research.

Among the three different spectroscopy-based techniques, FTIR provides the simplest qualitative overview of the presence and influence of CaO in Si- and Al-dominated compounds, facilitating the mapping of alkali-activating reactions in subsequent steps of the thesis. While both NMR and FTIR spectroscopy provide a quantitative approach to studying Si- and Al-dominated structures, NMR requires longer testing times. Comparing the spectra from these two techniques, using Raman scattering coefficients, confirmed the validity of Raman spectroscopy as a more efficient and straightforward method for further characterization in this project.

3.3 Results

3.3.1 Chemical composition of synthetic precursors

The chemical compositions of synthetic precursors, measured after all production batches, are exhibited in Figure 3.1 - see Appendix B for the detailed compositions of all batches. The four categories of glasses were distinguishable among them, as each group had its own

particular oxide content range. Significant variations in chemistry within each group were not observed, particularly for the synthetic fly ashes. However, a wider fluctuation in chemical composition was noted for the synthetic slags, with a total CaO content difference of 8.4 wt% between all members of BFS-2 category. These changes can be attributed to two factors: a potential contamination of Al from the crucible - the higher content of Ca leads to a lower melting point and consequently less viscous molten material, which can more easily detach Al from the crucible wall [143,241]; and the change in supplier of CaCO_3 . Figure 3.2 also compares the targeted and experimental Ca/Si elemental ratios, as it represents one of the main parameters used in this thesis to evaluate the behaviour of alkali-activating systems. It is worth noting that the higher melting point of fly ash-type glasses, due to the lower CaO content, reduced the final quantity of obtained material after the complete synthesis and grinding process. Therefore, it required extra production batches than synthetic high-Ca precursors. In the following Chapters, the specific chemistry of glasses used in each experiment will be given.

The chemical compositions of the synthetic precursors was also compared to nominal compositions of commercial materials. The ternary diagram shown in Figure 3.3 illustrates the $\text{CaO-Al}_2\text{O}_3\text{-SiO}_2$ distribution of synthesized glasses along with the vitreous portions of fly ashes and slags reported in the literature. In general, the synthesized glasses closely match the chemistries the groups they represent. The Ca-FA glasses are positioned in one of the extremities of the range of commercial calcareous fly ashes, representing an intermediate position between fly ashes and slags. However, such materials are known to display a considerably wide variation in chemistry, especially regarding CaO [29]. It is worth mentioning that commercial precursors usually present minor quantities of other cations working as network modifiers, which can induce small changes on the overall chemistry and structure of amorphous regions. With respect to siliceous fly-ashes, commercial compositions present lower contents of CaO than the synthetic ones. In the present research, a Si/Ca ratio higher than 4 was not possible to be obtained due to their extremely high melting temperatures - the maximum safe working temperature of the HTF furnace used was 1600 °C, which restricted the production of glasses with melting points above 1550 °C.

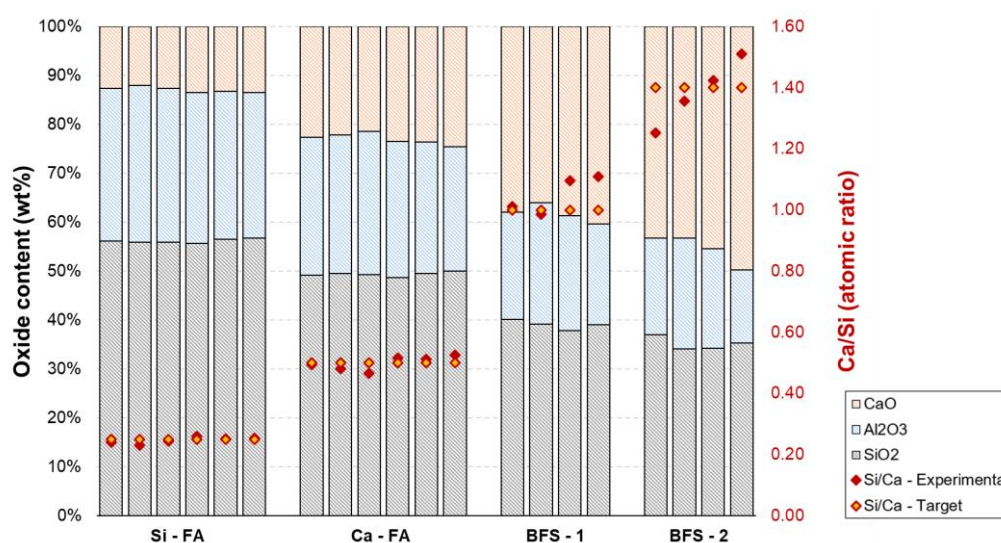


Figure 3.2: Chemical composition of several batches of synthetic glasses, according to their categories, obtained by X-ray fluorescence - secondary y-axis indicate the target and experimental Ca/Si ratios.

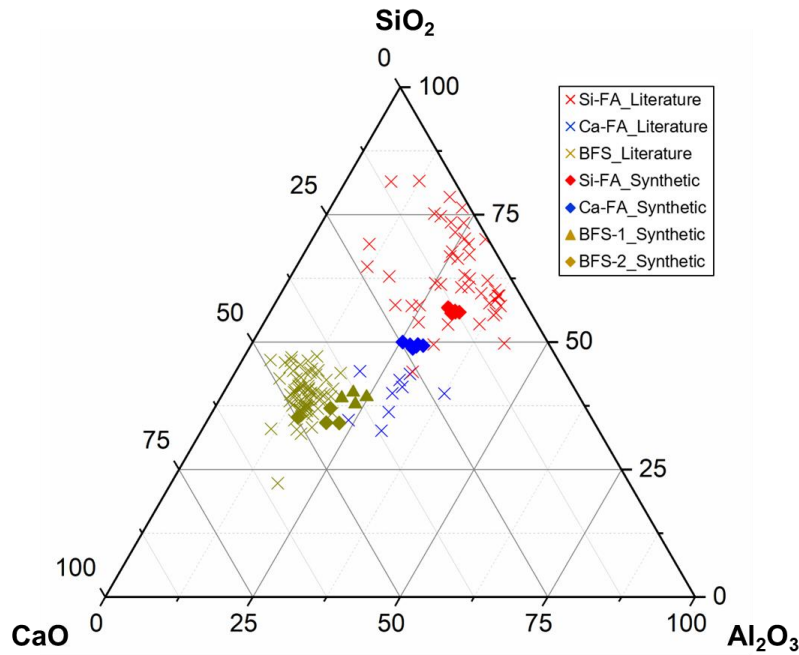


Figure 3.3: Ternary diagram representing the chemical composition of amorphous portions of commercial and synthetic fly ashes and slags - see Appendix B for detailed compositions.

3.3.2 Structural analysis of synthetic precursors

3.3.2.1 X-ray diffraction

The XRD patterns of two batches of each synthetic precursor are shown in Figure 3.4a. The patterns displayed correspond to the most extreme compositions within each precursor categories. All diffractograms demonstrated typical characteristics of amorphous materials, as a broad hump, with no additional peaks. It was not possible to spot differences between the two plots of a same category, while each group of precursors presented different characteristics among them. The centre of the hump shifts to higher 2θ angle values with increasing CaO content (average of 30.54° - BFS-2; 29.87° - BFS-1; 27.03° - Ca-FA; 26.51° - Si-FA), showing a strong influence of network modifying elements on the glass network. This characteristic follows the observations made by Diamond [158] and McCarthy [159], who observed a direct correlation between the maximum intensity of the 2θ value and the CaO content of different fly ashes. Moreover, the larger degree of polymerization of the network, in low-Ca materials, approximates the centre of the hump to the main diffraction peak of crystalline SiO_2 structures like quartz (PDF# 00-046-1045; $2\theta = 26.6^\circ$) and cristobalite (PDF# 00-011-0695; $2\theta = 21.9^\circ$), while the synthetic slags shift the centre of hump towards Ca-Al-rich phases such as tricalcium aluminate - C_3A ($3\text{CaO} \cdot \text{Al}_2\text{O}_3$, PDF# 00-038-1429, $2\theta = 33.2^\circ$) and mayenite - C_{12}A_7 ($12\text{CaO} \cdot 7\text{Al}_2\text{O}_3$, PDF# 00-006-0413, $2\theta = 33.4^\circ$).

Table 3.2: Chemical compositions and molar ratios of commercial precursors (amorphous portions) used for structural comparison with synthetic glasses.

Precursor	Oxide content (wt%)				Si/Ca	2 θ max
	SiO ₂	Al ₂ O ₃	CaO	MgO		
Commercial BFS	34.18%	9.05%	44.10%	7.40%	1.38	31.49
Synthetic BFS-2	36.76%	19.53%	42.97%	-	1.37	30.54
Commercial Si-FA	43.2%	18.78%	3.96%	2.11%	0.10	24.25
Synthetic Si-FA	56.23%	29.45%	13.35%	-	0.25	26.51

Figure 3.4b compares the XRD patterns of the two extreme cases of synthetic glasses, Si-FA and BFS-2, with commercial siliceous fly ash and commercial slag conventionally used in the same laboratory - see Table 3.2 for chemical compositions. The amorphous humps, centred at 24.25° (fly ash) and at 31.49° (slag) in the commercial materials, align closely with the values obtained for both synthetic glasses, evidencing that the simplified precursors can satisfactorily replicate natural structures. It must be stated that this similarity is observed despite some variations in the cation content of the amorphous composition. The content of Al₂O₃ in the amorphous portion of the commercial slag is approximately 10 wt % lower than in the synthetic one, while the commercial fly ash displays a similar difference in CaO content. These small fluctuations suggest mild internal differences in the vitreous regions when comparing both nominal and synthesized precursors, which however, are not sufficient to undermine their overall resemblance.

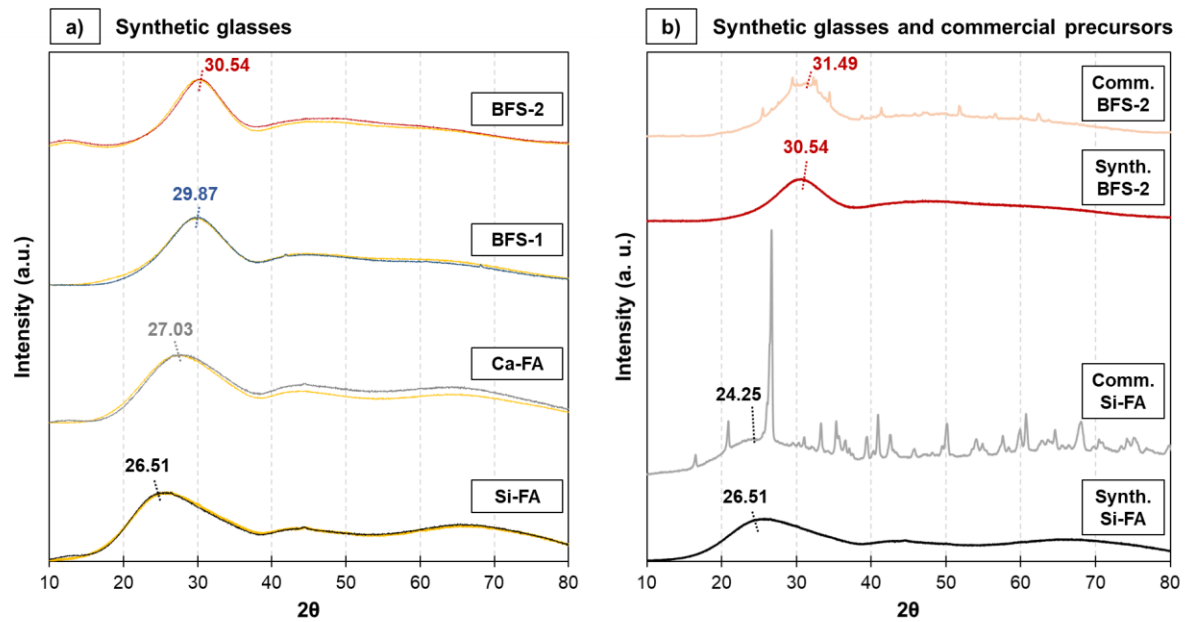


Figure 3.4: XRD patterns of synthetic precursors: a) four synthetic glasses obtained in this research; b) comparison of synthetic glasses and commercial (comm.) precursors.

Due to their condition of existence under metastability, glasses are usually heterogeneous at sub-microscopic level [96], and such differences are only perceived up to a scale of a few hundred angstroms. This can be, for instance, the result of a separation of the melt into two or more metastable vitreous phases during cooling [34]. The sequence of this chapter will attempt to evaluate these differences and to establish a relationship with the initial chemistry of the synthetic glasses.

3.3.3.2. *Fourier transform infrared spectroscopy*

Figure 3.5 shows the FTIR spectra of one batch of each of the four synthetic precursors. All glasses exhibit a broad band centred between $880\text{--}938\text{ cm}^{-1}$, attributed to the asymmetric stretching of bridging oxygens in Si–O–T units (T = tetrahedral Si or Al), a feature normally observed in the network of aluminosilicate precursors [172,211,242,243]. The shift of this band towards higher wavenumbers, proportional to the overall SiO_2 content, is expected due to fewer disruptions in the microstructure [210], similarly to the shift observed in the 2θ centre of XRD patterns - see Figure 3.3. As reported by Handke et al. [244], the breakage of Si–O–T bonds, which is directly correlated to the presence of network modifying oxides, promotes the formation of non-bridging Si–O $^-$ sites, decreasing the average coordination number of the aluminosilicate framework. Consequently, the higher concentration of non-bridging oxygens (NBOs) reduces the covalent nature of the network as a whole, and favors more ionic behaviour of the structure. This results in a weakening of molecular vibrations of Si–O–T bonds in shared units [245,246], as observed by the broadening of the main band in slag-glasses.

Glass Si-FA displays a shoulder at 1040 cm^{-1} , and the interpretation of which is debated in literature. Some authors claim it is specific to asymmetric vibration of Si–O–Si [181,210,243], indicating a densely packed silicate network. However, the infrared spectra of natural aluminosilicate minerals, such as sillimanite and andalusite, polymorphs of the Al_2SiO_5 mineral series, are also active at this frequency range [247]. These bands could therefore be assigned to the vibration of SiO_4 units connected to AlO_5 or AlO_6 species, which are present in these two minerals. Hence, it can be assumed that the low Ca content in Si-FA promotes isolated regions of pure Al-Si glasses, in which Ca has little influence over the disruption of the local networks.

Moreover, all glasses exhibit a small band centred at approximately 680 cm^{-1} , attributed to the asymmetrical stretching vibration of Al–O bonds present in AlO_4 groups [248,249]. This band becomes broader and less evident with decreasing Ca content. These interactions are in agreement with the presence of fourfold coordinated Al in the presence of an excess of charge balancing cations [143], becoming less evident in systems lacking Ca.

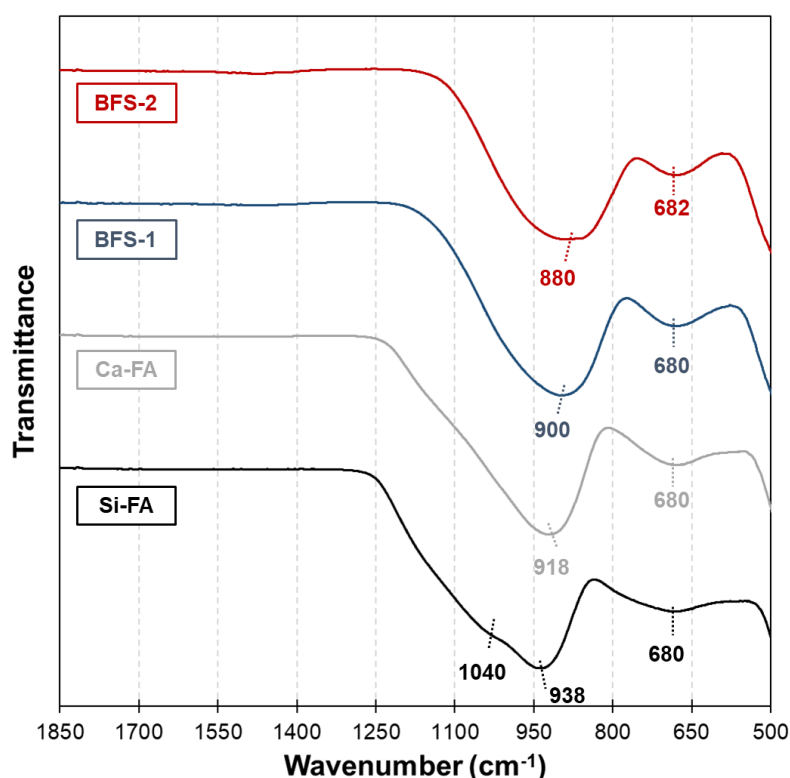


Figure 3.5: FTIR spectra of the four categories of synthetic precursors.

The comparison of FTIR spectra of the four groups of glasses does not show significant differences among them, as all precursors present a fully amorphous calcium aluminosilicate structure. However, with the course of this research, this technique will be helpful to elucidate the different behaviour of each material during dissolution experiments and for hardened pastes of blended glasses.

3.3.3.3 Solid state NMR and Raman spectroscopy

Investigation of Si-O-T bonds

The full Raman spectra of synthetic glasses, plotted in Figure 3.6a, corroborate the observations from FTIR analysis. Low-Ca glasses show stronger resonances in the 300-700 cm^{-1} range, as this region represents the continuous silicate and aluminosilicate chains [250]. Additionally, the region attributed to Si Qⁿ units shifts towards higher wavenumbers with decreasing Ca content, indicating a stronger presence of highly polymerized SiO₄ sites. The similar pattern observed in the full ²⁹Si MAS NMR spectra, shown in Figure 3.5b, emphasizes that individual and loosely connected tetrahedra units are more evident in slag-like glasses, potentially contributing to a more reactive network.

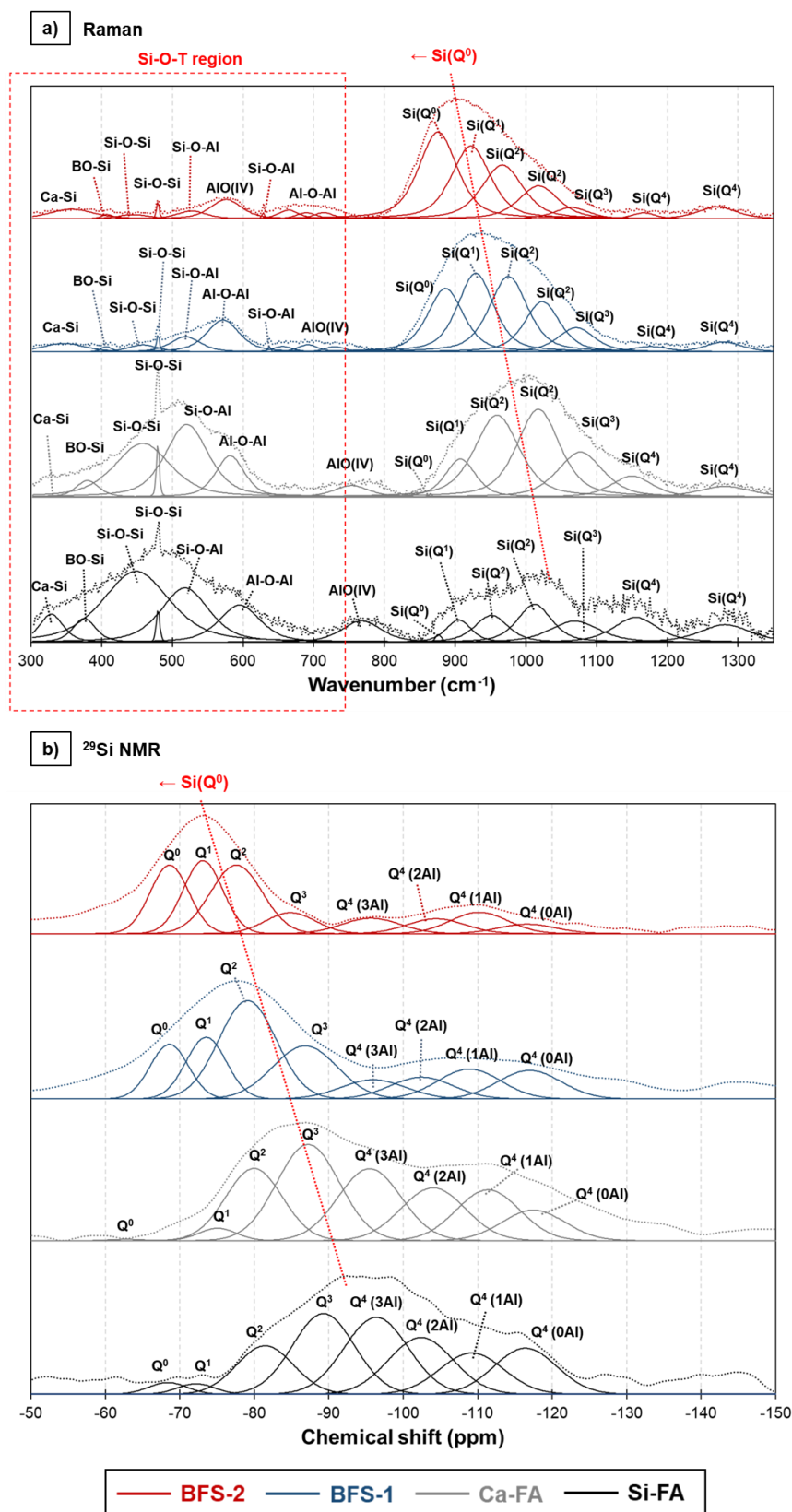


Figure 3.6: Spectra of synthetic glasses obtained with different spectroscopy techniques: a) Raman and b) ²⁹Si NMR. The dashed lines represent the full spectra, and the solid lines represent the deconvoluted spectra.

The deconvoluted curves of both Raman and ²⁹Si MAS NMR spectra, shown in Figures 3.6a and 3.6b, respectively, were used to quantitatively determine the Si Qⁿ units. By using

Raman scattering coefficients [239], it was possible to compare the results obtained in both techniques, which displayed similar results as indicated in Figure 3.7. The low- and high-Ca precursors displayed significantly different responses in the two spectroscopy measurements. The proportion of fully connected Si Q⁴ units decreased from 70.31 % in Si-FA, to 25.86 % in BFS-2 (Raman spectra), while individual tetrahedra (Si Q⁰) were virtually not present in fly ash-like glasses, indicating the strong effect played by CaO on destabilizing the network of the synthetic precursors.

The depolymerization effect of Ca is more clearly observed in the plots of Figures 3.8a and 3.8b, which shows a quasi-linear correlation between the Ca fraction in the precursors and the sum of Si Q⁰ and Q¹ units, and with the sum of Q³ and Q⁴ units ($R^2 = 0.99$ and 0.89 , respectively). The correlation was proposed using information obtained from the synthetic precursors described in this Chapter, and commercially available precursors analyzed in literature - Blotevogel et al. [251] studied slags which were rich in silicate sites with low coordination, given the high concentration of modifying cations in its composition; conversely, fly ashes were reported to contain a high number of chain-like (Si Q²) and connected chain (Si Q³) structures [208], similarly to the synthetic precursors. In summary, it is observed that the initial chemistry of the amorphous portion allows a direct indication of its structural order, and overall behaviour of one precursor, which is primarily influenced by the presence of Ca. This could offer a practical and simplified approach to study the polymerization degree of the network than the determination of NBO/T ratios, which requires complex techniques and data treatment for the obtainment of accurate results. It is worth mentioning that other modifying species, such as Mg or alkali-earth elements, can act along with Ca on the disruption of the aluminosilicate network - this can explain the mild differences observed in the slope of the trendlines calculated for synthetic glasses-only and for all precursors. The effect of these other modifying elements will not be covered in this work.

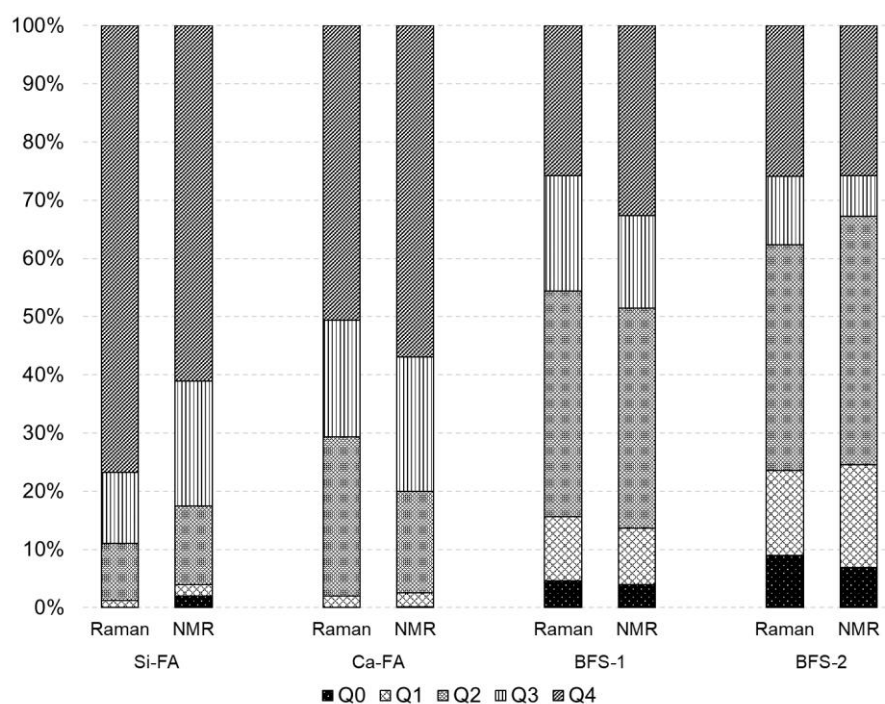


Figure 3.7: Quantitative determination of Qⁿ(Si) sites using Raman and ²⁹Si NMR techniques - see Appendix B for the full details of the experiment.

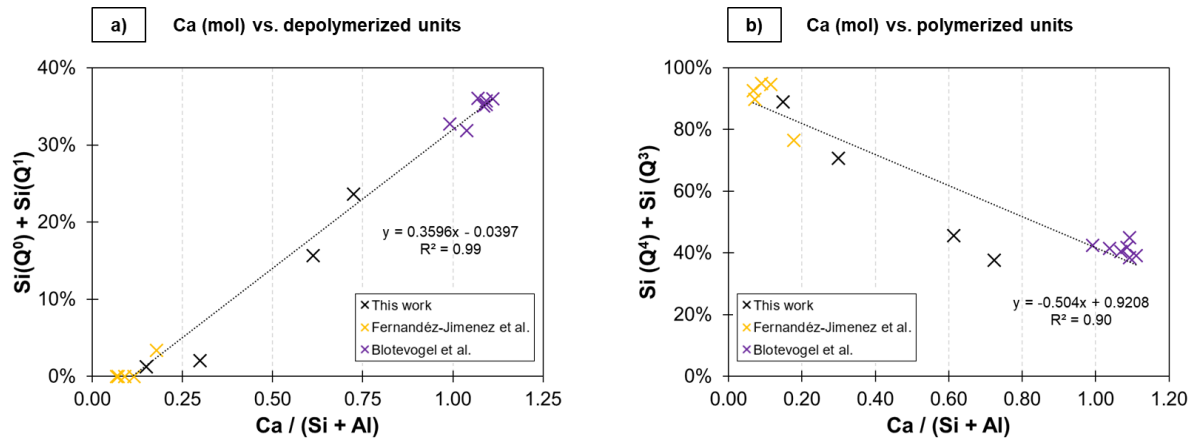


Figure 3.8: Correlation between the fraction of Ca and the quantitative distribution of $\text{Q}^n(\text{Si})$ sites in synthetic and commercial precursors [208,251]: a) depolymerized units; b) polymerized units - see Appendix B for detailed structural analysis.

The interpretation of ^{29}Si MAS NMR deconvolution, shown in Figure 3.7, provides further evidence of the role played by Ca in aluminosilicate frameworks. The plot shown in Figure 3.9, combining data from the present work and from literature [208], indicates a logarithmic relationship between Al-substituted Si Q^4 sites versus the Ca/Al ratio of each glass. The substitution and formation of AlO_4 sites within continuous silicate chains has long been known to occur preferentially in sites with higher polymerization [151], which explains the significant presence of $\text{Si Q}^4(3\text{Al})$ and $\text{Q}^4(2\text{Al})$ units. The plot also indicates that slag glasses, identified in the high Ca/Al region, present low substitution degrees. This might be considered an unexpected trend, since structures with large proportions of CaO are known to enhance the chemical shifts of Al^{IV} [252,253] - this feature was also observed in the FTIR spectra, as bands assigned to AlO_4 units were progressively stronger with higher Ca contents (Figure 3.5). It is suggested that Ca induces the stabilization of separate structures containing Al^{IV} , where Si-species are not the main network former, either by the combination of multiple AlO_4 units or the formation of isolated calcium-aluminate-like structures - this will be discussed in details in Section 3.4.2.

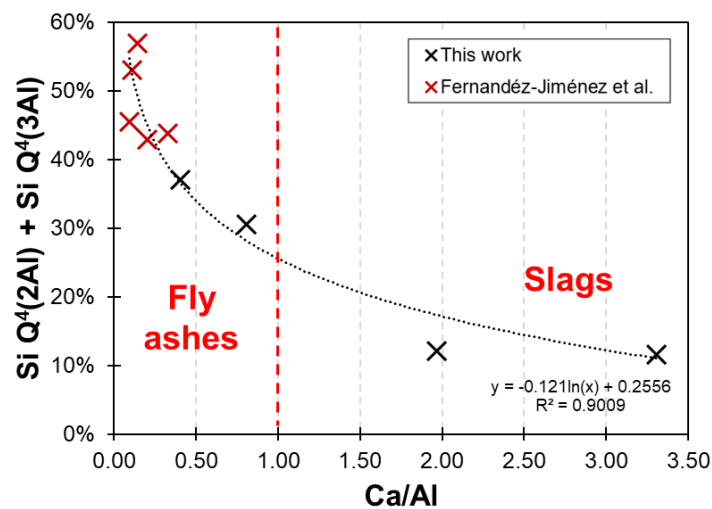


Figure 3.9: Correlation between Al^{IV} substitution in highly-polymerized sites and the Ca/Al molar ratio of commercial and synthetic precursors - including additional data adopted from [208] available in Appendix B.

Investigation of Al-related interactions

The contributions of the main Si–O interactions, in the Raman spectra of each synthetic glass (Figure 3.6a), were used to obtain the accumulated contribution of silicate structures to the overall spectra. By subtracting this Si-enveloped line, it was possible to visualize in more detail the contributions of Al–O to the overall Raman spectra with lower interference from Si. The deconvoluted Al-related spectra, plotted in Figure 3.10, indicate three major features of Al interactions to the amorphous network. All glasses displayed a strong band in the 575–595 cm^{-1} interval, attributed to Al–O–T interactions which can still be influenced by Si-containing sites [240]. These bands are assigned to the transverse motion of bridging oxygens within Al–O bonds in fourfold coordination, typical of a network forming site, and gradually decrease in intensity with Ca/Si ratio. This type of interaction arises from the influence of two types of structural units: six-membered rings of interconnected Al-substituted and Si-tetrahedra [254,255], indicated by enhanced signals in fly ash-type glasses; and triclusters of tetrahedral sites, which form smaller rings by the sharing of two bridging oxygen one with the other [151,255]. In addition, slag-like glasses display two distinct bands in the 650–700 cm^{-1} range, assigned exclusively to the bending of interconnected AlO_4 units [254,256].

The final region, above 700 cm^{-1} , is attributed to the interaction of bridging oxygens in SiO_4 units with octahedral units of Al. More specifically, this band is characteristic of vibrations occurring in dioctahedral minerals, where two of three available octahedral positions are occupied [257]. In phyllosilicate minerals [258,259] the intrinsic properties of an adjacent cation in octahedral coordination affects the Si–O–Si vibration in bridging positions, and the Raman position determines a few aspects of the structure. Hence, although bands in the Al spectra from 700–800 cm^{-1} are often attributed to Si–O interactions [149,260], the presence of Al^{VI} intensifies the spectra in this region. With a lower Ca/Si ratio, the band slightly shifts to higher wavenumbers upshifts and increases in intensity. This behaviour suggests the promotion of densely packed vitreous regions, as a less pronounced disruptive presence of Ca maintains more consistent bond lengths and, consequently, more consistent Si–O binding force constants [260].

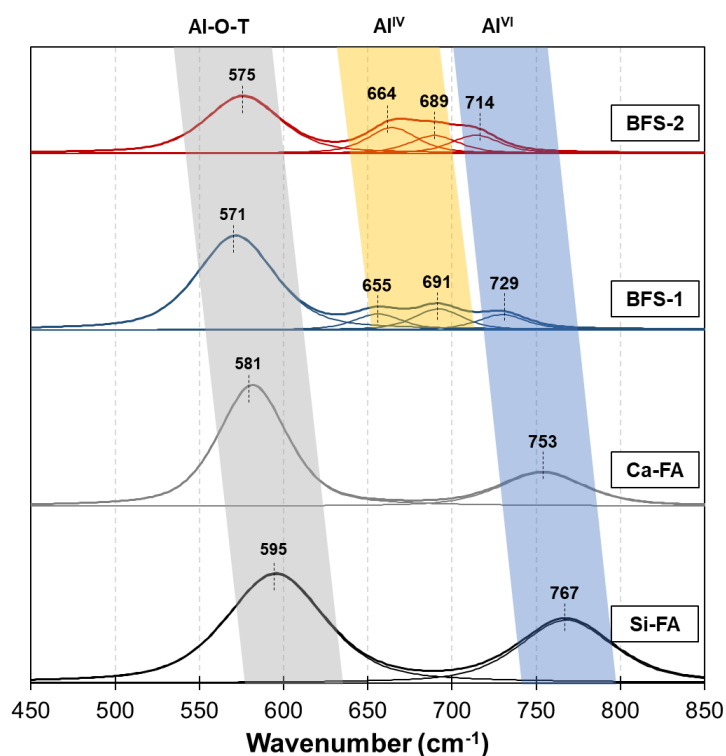


Figure 3.10: Deconvoluted Al-O Raman spectra of synthetic precursors - T = tetrahedral Si or Al.

The ^{27}Al MAS NMR spectra, displayed in Figure 3.11, present a broad hump spanning from approximately 75 to -50 ppm in all glasses. These broad bands covers the three main states of Al: Al^{IV} , Al^{V} and Al^{VI} . However, it is not possible to define specific positions on the curves, which prevents the quantitative determination of the Al units. It is interesting to mention that such a broad spectrum is not so commonly observed in commercial slags, which usually show stronger and defined peaks of Al^{IV} and mild presence of Al^{V} and Al^{VI} - it should be kept in mind that the current research had glasses produced only with Ca as NWM and a very fast cooling rate. Additionally, the ^{27}Al MAS NMR experiments here were performed with a magnetic field of 11.6 T. The use of higher magnetic fields is advised to avoid quadrupolar interactions which interfere in the final spectra [152,261].

In a system depleted in Ca, the higher ordering level of the network forces Al to play a crucial part in the network formation. The low level of alkaline oxides may also intensify the miscibility gap between Al and Si [262], leading to the formation of separate regions of Al-rich and Si-rich structures via a spinodal-like decomposition phenomena [96], as evidenced by the strong Al—O—Al bands centred at 575-595 cm^{-1} . The analysis of the synthetic glasses with energy dispersive X-ray, through scanning electron microscopy, did not identify heterogeneities in their chemistries. Therefore, it is suggested that the synthetic fly ash-type glasses do not present a fully homogeneous amorphous structure, but instead have isolated regions with distinct structural characteristics at sub-microscopic scales.

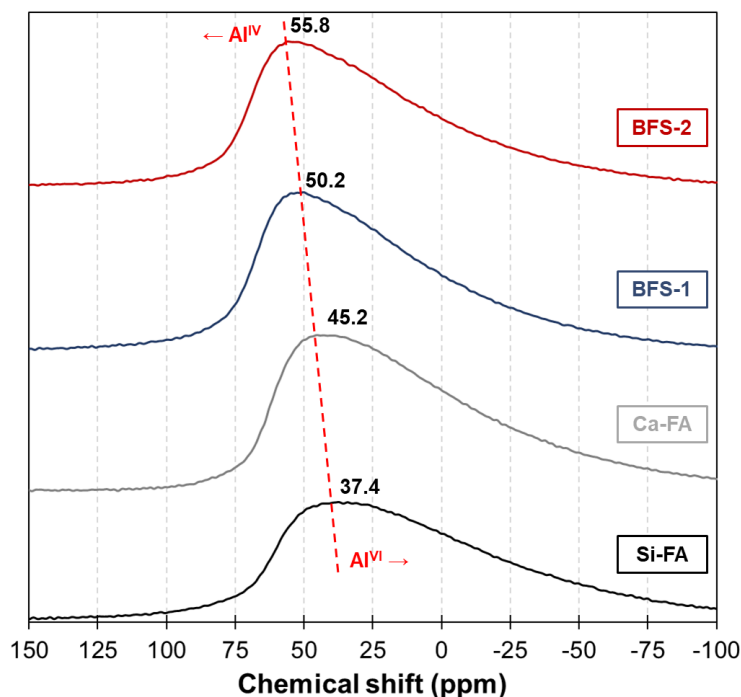


Figure 3.11: ^{27}Al MAS NMR spectra obtained for the four synthetic glasses.

3.4 Discussion

3.4.1 Glass phase segmentation with XRD

The 2θ angle of the maximum intensities in the amorphous hump of the synthetic glasses was shown to shift to higher values with increasing CaO content, as indicated in Figure 3.4. A similar correlation was first studied by Diamond [158], who reported a linear trend valid for low- and high-Ca fly ashes containing from 0.9 wt% to 20 wt% of CaO. McCarthy et al. [159] supported this correlation by creating a database of 178 samples from different sources in the USA, deriving a similar, although not identical, trend. However, the linear relationship was interrupted at an upper CaO wt% threshold of approximately 20 wt% in both cases, as all calcareous ashes appear to have a maximum 2θ diffraction angle between $30\text{--}32^\circ$.

It is well known that fly ashes are not fully amorphous products [96,98], with crystalline phases accounting for as much as 50 % of their overall structure [263]. Residual regions with ordered structures are mainly formed during the cooling stage of the coal residue after combustion, attributed to low heat exchange rates usually occurring in the inner core of the ash particle [96]. In both siliceous and calcareous fly ashes, quartz and other Si-dominated phases are among the main remaining structures after cooling [168,169,263,264], while Ca is usually kept in disordered regions due to its facilitated mobility in melt states [265] among other factors. It is then reasonable to assume that the correlations proposed by Diamond and McCarthy would show better agreement if only the amorphous composition of the fly ashes were considered.

The precursors synthesized in this Chapter were designed to simulate the compositions of both blast furnace slags and fly ashes. In this study, the highest CaO content reached 49.1 wt%, while the maximum XRD peak intensity remained at a 2θ value close to 30° . These

results are similar to the work of Goto et al. [160], who synthesized 13 different slags using a similar procedure. By combining both sets of data with the characterization of the commercial precursors described in Sections 3.3.1 and 3.3.2, it was possible to extend the observations made by Diamond and McCarthy. Figure 3.12 shows the logarithmic relationship that is proposed to correlate the chemical composition of amorphous portions with maximum 2θ angle, represented as $(\text{CaO}/\text{SiO}_2 \cdot \text{CaO}/\text{Al}_2\text{O}_3)$ vs. 2θ , in both low- and high-Ca compounds. The evolution of the correlation clearly presents separated regions in both ends. Additionally to the crystalline phases of SiO_2 quartz ($2\theta = 26.6^\circ$) and cristobalite ($2\theta = 21.9^\circ$), Si-FA glass displays a diffraction maximum close to those of aluminosilicate dominated structures - e.g. mullite ($\text{Al}_6\text{Si}_2\text{O}_{13}$; $2\theta = 25.9^\circ$; PDF# 00-015-0776) and sillimanite (Al_2SiO_5 ; $2\theta = 26.2^\circ$ PDF# 00-001-0626). Meanwhile, the maxima for synthetic slags resemble those observed in gehlenite ($\text{Ca}_2\text{Al}(\text{AlSi})\text{O}_7$; $2\theta = 31.4^\circ$; PDF# 00-020-0199).

As the plot in Figure 3.12 shows a two-region curve, it is plausible to assume that the shift of the maximum diffraction peak reflects a transition from Si-dominated phases to a high-Ca type of glass structures for precursors of alkali-activated systems. This observation is in agreement with several results available in the literature [48,95,98,168,169], with mullite representing up to 22 % [100] of the mineralogical composition of fly ashes, and slag displaying residual presence of structures in the melilite-group [170,171], with gehlenite representing the Mg-free phases and calcium aluminates - such as C_3A and mayenite - appearing in some steel slags [266,267].

3.4.2 Interactions between SiO_4 and $\text{AlO}_4/\text{AlO}_6$ groups in fly ash-type glasses

In aluminosilicate melts, some immiscibility between Al_2O_3 -rich and SiO_2 -rich components is usually observed within a specific Al_2O_3 content range of 30 to 50 wt% [262]. The immiscibility phenomenon occurs mainly due to the high energy barrier to accommodate AlO_6 octahedra in the corner-shared network of SiO_4 , or Al-substituted tetrahedra in existing silicate structures. This phenomenon extends the presence of pure SiO_2 phases up to Al_2O_3 contents around 30 at% [150,262]. Outside the miscibility gap, Al either incorporates in SiO_4 units in fourfold coordination in the lower end [153,268], or fully behaves as a fundamental component in mullite-like structures in octahedral coordination in the upper end. In the present research, all glasses had a $\text{SiO}_2/\text{Al}_2\text{O}_3$ ratio within the immiscibility range, with Al representing 29 to 37 wt% of the normalized composition, considering only the two oxides.

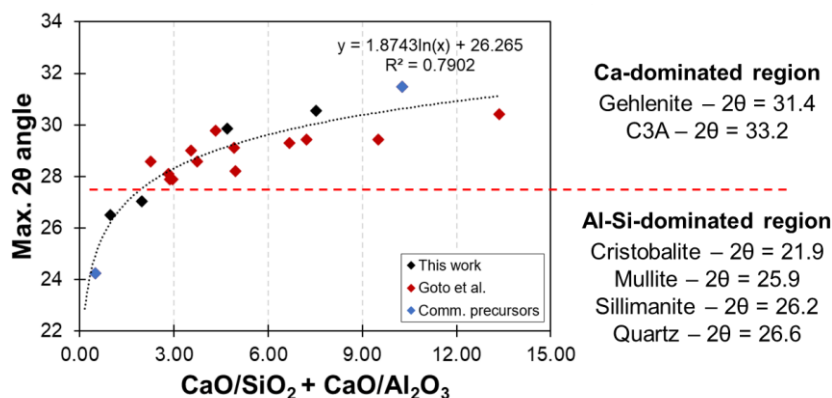


Figure 3.12: Correlation of the maximum 2θ position with chemistry of synthetic glasses - including additional data adopted from [160], with estimation of max 2θ angle values detailed in Appendix B.

In the presence of network modifying oxides, the miscibility gap has been demonstrated to be inhibited or hindered, as these cations reduce the energy required for the accommodation of AlO_4^- sites due to their charge-balancing role [262,269]. In the current work, even a minor presence of CaO in synthetic fly ash-glasses appears to limit the formation of pure silicate regions, due to the significant Al-O-T interactions identified with Raman spectroscopy (Figure 3.10). The signal responses in the ranges of 550-600 and 650-700 cm^{-1} are both assigned to AlO_4 contributions in the Al-O Raman curve, but only the first one is observed in fly ash-type glasses here. This region is assigned to the transverse motions of bridging oxygens in Al-O bonds, resulting from three dimensional frameworks of shared SiO_4 and AlO_4 sites [254,255]. As the ^{29}Si NMR spectroscopy indicated high levels of Al-substitution in tetrahedral sites (Figure 3.9), it is assumed that such structures are formed by the attachment of Ca^{2+} as charge compensator. After Ca is fully consumed, Al atoms in fourfold coordination are combined into tricluster tetrahedral regions, composed of three AlO_4 units sharing one common bridging oxygen [253,255,270]. These oxygens form a natural charge-balancing mechanism [150,271], with the presence of one tribridging oxygen for every Al-substitution, excluding the requirement for the presence of Ca^{2+} . Both Al-substitution and the formation of triclusters suggest that Al can be incorporated into separate glass phases within low-Ca glasses.

Additionally, fly ash glasses also displayed stronger reflections above 700 cm^{-1} , resulting mainly from SiO_4 - AlO_6 interactions. As this region is influenced by Si-related vibrations, it is difficult to attribute it to one specific type of structure. Literature suggests that it arises from the interaction between Si-tetrahedra sites with Al-octahedral sites, typically seen in orthosilicate minerals [257,272]. However, electron orbitals in AlO_5 and AlO_6 related bands might overlap with each other each other [273], creating issues with confident assignment. As reported by Zhai et al. [260] and Schneider et al. [273], Al in fivefold coordination is usually observed in the formation of sillimanite or mullite structures, as an unstable formation of AlO_6 units. The presence of five- and six-fold coordinated Al is in agreement with the observed ^{27}Al NMR bands (Figure 3.11), which become broader with decreasing Ca content. Moreover, the observation of sillimanite-typical bands in the FTIR spectra (1040 cm^{-1} - see Figure 3.5), especially in Si-FA glass, strengthens the hypothesis of AlO_6 -containing structures coexisting with SiO_4 - AlO_4 interactions.

The qualitatively determined structure of low-Ca precursors, summarized in Table 3.3, highlights several features, particularly regarding the combined roles of Si and Al. It is concluded that there exists an intimate mixture of regions of mullite- or sillimanite-like structures, which display interactions of SiO_4 with AlO_4 and SiO_4 with $\text{AlO}_5/\text{AlO}_6$ groups, but a clear distinction between the contributions of each phase was not possible. As the slow cooling of pure silicate melts generates cristobalite as a final phase [96], the formation of structures resembling Al-modified cristobalite is reasonable, since aluminosilicate glasses are known for displaying distinct silicate-rich structures with lower contents of Al_2O_3 [268,269]. In addition to the previous statement, a minor presence of triclusters of AlO_4 was inferred from Al-related Raman bands - see Figure 3.10. This is somehow expected since these structures have been reported as nucleation sites for mullite crystallization in aluminosilicate glasses [274].

Table 3.3: Summary of the findings of glass structures of the four synthetic glasses, with a qualitative definition of the presence of each resembled phase.

Phase resemblance	Ratios	Si-FA	Ca-FA	BFS-1	BFS-2
	Ca/Si	0.23	0.47	1.04	1.41
	Ca/Al	0.40	0.81	1.96	3.31
	Identification	↑↑↑	↑↑	↑	↑
		<u>XRD</u> : ($2\theta < 28^\circ$) <u>Raman</u> : (700-800 cm^{-1})	<u>XRD</u> : ($2\theta < 28^\circ$) <u>Raman</u> : (700-800 cm^{-1})	<u>Raman</u> : (700-800 cm^{-1})	<u>Raman</u> : (700-800 cm^{-1})
Mullite	Evidence	<u>FTIR</u> : (1040 cm^{-1}) <u>^{27}Al NMR^a</u> : (centre < 38 ppm)			
	Identification	↑↑	↑↑	↑	↑
		<u>XRD</u> : ($2\theta < 28^\circ$) <u>Raman</u> : (550-650 cm^{-1})	<u>XRD</u> : ($2\theta < 28^\circ$) <u>Raman</u> : (550-650 cm^{-1})	<u>Raman</u> : (550-650 cm^{-1})	<u>Raman</u> : (550-650 cm^{-1})
Al-modified cristobalite	Evidence	<u>FTIR</u> : (938 cm^{-1}) <u>^{29}Si NMR</u> : ($\text{Q}^4(2\text{Al})$ + $\text{Q}^4(3\text{Al}) > 35\%$)	<u>FTIR</u> : (938 cm^{-1}) <u>^{29}Si NMR</u> : ($\text{Q}^4(2\text{Al})$ + $\text{Q}^4(3\text{Al}) > 30\%$)		
	Identification	-	↑	↑↑	↑↑
			<u>^{29}Si NMR</u> : (Q^2 - 23%)	<u>XRD</u> : ($2\theta > 29.5^\circ$) <u>^{29}Si NMR</u> : (Q^2 - 38%)	<u>XRD</u> : ($2\theta > 29.5^\circ$) <u>^{29}Si NMR</u> : (Q^2 - 38%)
Gehlenite	Evidence	-			
	Identification	-	-	↑↑	↑↑
				<u>XRD</u> : ($2\theta > 29.5^\circ$) <u>Raman</u> : (650-700 cm^{-1})	<u>XRD</u> : ($2\theta > 29.5^\circ$) <u>Raman</u> : (650-700 cm^{-1})
Calcium aluminates	Evidence	-	-	<u>FTIR</u> : (680 cm^{-1}) <u>^{27}Al NMR</u> : (50.2 ppm)	<u>FTIR</u> : (680 cm^{-1}) <u>^{27}Al NMR</u> : (55.8 ppm)

↑↑↑ - Dominant phase supported by multiple techniques and literature.

↑↑ - Significant presence, confirmed by multiple techniques.

↑ - Minor presence, suggested by only one technique.

3.4.3 Influence of CaO in the destabilization of glass network

In general, the addition of alkaline and alkaline-earth elements has a dual effect on the glasses studied in this chapter: charge compensation of AlO_4^- sites and network depolymerization [143]. This depolymerization limits the ordering range of SiO_4 units, resulting in a less covalent network [96]. In this study, the broad signals observed in the ^{27}Al MAS NMR spectra - see Figure 3.11 - suggest structural disorder arising from the inclusion of CaO in the glass network. The centre of the chemical shift, stronger in the Al^{IV} -attributed region for all glasses, becomes more positive with increasing Ca/Al ratios, due to the change in the nature of the first neighbors [270]. The very broad nature of the spectra also indicates that there are contributions related to four-, five- and sixfold Al-coordination hidden under the broad spectra in all four synthetic glasses.

At first glance, one might consider the presence of multiple Al coordination to be contradictory, since the abundance of Ca^{2+} at $\text{CaO}/\text{Al}_2\text{O}_3$ ratios above 1 promotes the stabilization of AlO_4^- units [96]. Through both experimental analysis and molecular dynamics simulations, the average coordination number of Al has been extensively observed to be

lowered to values closer to four in the presence of excess Ca in CAS systems [151,153]. However, whether Al fully acts as a network former in percalcic glasses is still in debate. Through high-field ^{27}Al NMR, Neuville [270] identified a continuous presence of Al^{V} in different percalcic glasses in the $\text{CaO-Al}_2\text{O}_3\text{-SiO}_2$ system, with similar chemistries to glasses BFS-1 and BFS-2. Additionally, sixfold coordinated Al has been reported to be present in $\text{CaO-Al}_2\text{O}_3$ melts [153] and peralkaline aluminosilicate glasses modified with MgO and CaO [149], when only fourfold coordination would conventionally be expected.

In the four synthetic glasses discussed here, different coordination numbers of Al could not be fully resolved in a quantitative approach, and would require an approach such as complex multi-quantum NMR analysis coupled with molecular dynamics simulations for a precise determination. Nonetheless, the qualitative information obtained with both ^{27}Al MAS NMR (Figure 3.11) and Raman spectroscopy (Figure 3.10) delivers important structural information, as summarized in Table 3.3. In the former technique, Al^{IV} vibrations appeared to be stronger in Ca-rich glasses, and in the latter, the second AlO_4 related vibrations range ($650\text{-}700\text{ cm}^{-1}$), attributed to interactions of interconnected AlO_4 units, is observed only in high-Ca precursors. As initially summarized in early work by Englehardt [96], Al^{IV} is the dominant species when $\text{CaO} > \text{Al}_2\text{O}_3$, and the exact role of Al is dependent on the total CaO content. For instance, in gehlenite (with $\text{Ca}/\text{Al} = 1$), Al-substitution occurs mainly in chain-like linkages of SiO_4 (Si Q^2) [154]. The analysis made with ^{29}Si NMR for slag-glasses showed a significant presence of Si Q^2 species (Figure 3.7), potentially characterized as $\text{Si Q}^2(1\text{Al})$ and $\text{Q}^2(2\text{Al})$ units. This observation indicates the strong formation of structures resembling gehlenite in both BFS-2 and BFS-1, as this phase is composed of corner sharing tetrahedral dimers [275].

Moreover, it is suggested that the higher CaO content in the slag-type glasses, especially in glass BFS-2, promoted the formation of isolated calcium-aluminate structures depleted in Si, as evidenced by the shift of the maximum 2θ angle in the XRD patterns (Figure 3.3) in addition to spectroscopic analysis. In Ca-Al systems with high Ca content, Al^{IV} species can be combined to form either triclusters or 6-membered rings of AlO_4 units [253]. In both cases, Ca occupies the cavities of the rings in either 6- or 8-fold coordination, forming structures typically found in tricalcium aluminate (C_3A) and mayenite (C_{12}A_7) [253,276-278].

The formation of separate phases is supported by the presence of calcium-aluminum rich inclusions (CAIs) observed during cooling processes of Ca-Mg-Si-Al melts simulating chondrite meteorites. The crystallization sequence of such components converts a spinel-type (Al_2O_3 , $1550\text{ }^\circ\text{C}$) structure into gehlenite ($\text{Ca}_2\text{Al}_2\text{SiO}_7$, $1400\text{ }^\circ\text{C}$) and further into anorthite ($\text{CaAl}_2\text{Si}_2\text{O}_8$, $1260\text{ }^\circ\text{C}$) [279], promoting a reduction of the Al ratio of these structures influenced by lower maximum temperatures and slower cooling rates of the melt [280]. In the present work, the formation of pure Al_2O_3 phases is not expected for glasses BFS-2 and BFS-1 due to their low content of Al. Alternatively, it is here suggested that the formation of Al-Ca rich structures occurs in the first instants after quenching, while the inclusion of Si into new phases takes place in secondary stages. This assumption aligns with the configurational entropy of $\text{CaO-Al}_2\text{O}_3\text{-SiO}_2$ minerals [275], which identifies two different tetrahedral sites (T_1 and T_2) in Mg-free gehlenite: T_1 sites are occupied exclusively by Al, while T_2 sites display a mixture of AlO_4 and SiO_4 [281]. Additionally, gehlenite was also observed as an intermediate product in the synthesis of various calcium aluminate phases [282], which may help to explain the higher reactivity of high-Ca precursors.

With respect to the role of Ca, its coordination number has been shown to change according to its total content in CAS systems. Octahedral coordination is the natural form of this element in CaO, and this could be an initial guess of the predominant nature when acting either as a networking modifier or as a charge compensator [252,283]. However, a few observations show distinct roles for Ca. For instance, Petkov et al. [283] reported coordination numbers as low as 5.2 when $\text{CaO}/\text{Al}_2\text{O}_3$ is lower than 1, while Shimoda et al. [284] found values close to 8 in systems with $\text{Ca}/\text{Al} = 1.43$. Ca in higher coordination is typically observed in crystalline C_3A and C_{12}A_7 phases [253], which can support the observations made with spectroscopy techniques in this Chapter.

The schematic drawings in Figure 3.13 provide a better visualization of the roles of Ca in the formation of different amorphous structures in aluminosilicate glasses, based on its initial content. At the lower CaO levels, mullite-type structures or cristobalite-like regions are favored, with Al substitution in tetrahedral site. The former which combines SiO_4 units with Al in both octahedral and tetrahedral coordination, is favored in significantly limited presence of Ca, which instead utilised the AlO_4 triclusters to function as charge-balancers, while the latter already counts with the presence of Ca^{2+} for the same purpose. In the higher end, Ca is suggested to present a fundamental phase forming role, inducing the stabilization of gehlenite-type structures combining both SiO_4 and AlO_4 units or isolated calcium aluminate structures, which partially explain the higher reactivity of high-Ca components.

Thus, in addition to acting as a depolymerizing and charge balancing agents, Ca appears to promote the formation of calcium aluminate and high-Ca aluminosilicate structures, given the strong evidences that both gehlenite- and calcium aluminate-type structures like structures in glasses resembling slags.

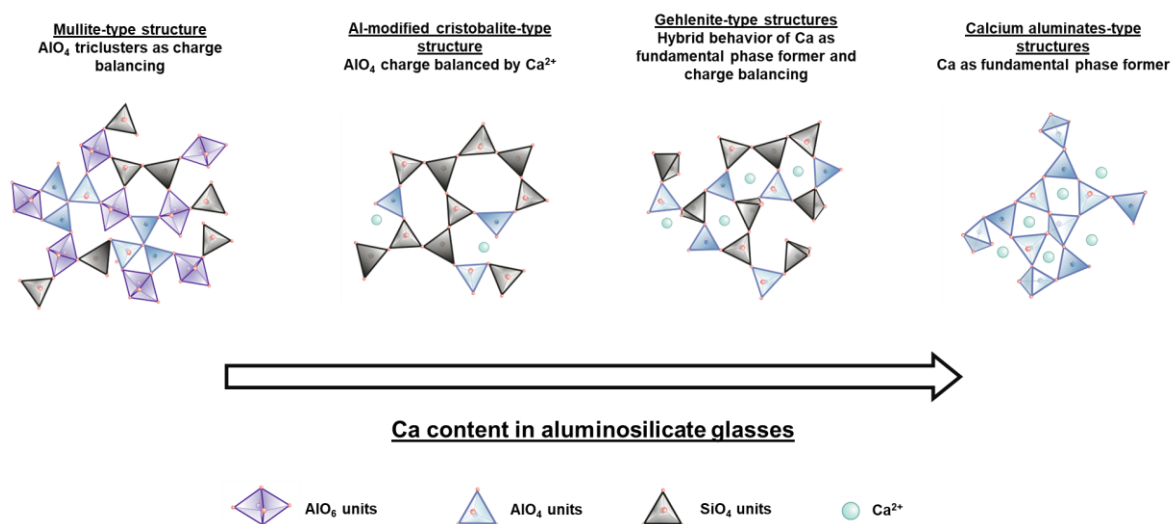


Figure 3.13: Schematic representation of the roles played by Ca in the structure of aluminosilicate glasses.

3.5 Conclusions and outlook

This chapter evaluated the strong influence of chemical composition on the framework structure of synthetic glasses resembling slags and fly ashes. The approach of this chapter is based on the use of four different techniques - XRD, FTIR, MAS NMR, and Raman spectroscopy - to study the internal structure of synthetic precursors, with each technique complementing the others. X-ray diffraction (XRD) provided a broad view of how the presence of Ca induced a major change in the framework, from an Al-Si-dominated to a Ca-Al-dominated structure. Infrared (FTIR) and Raman spectroscopy allowed for the characterization of short-range interactions, detailing Si-O and Al-O interactions within different structural units. Finally, nuclear magnetic resonance (NMR) offered a complementary assessment of the framework regarding nuclei interaction with close neighbours. By combining the three spectroscopic techniques, it was possible to define a preferential fourfold coordination of Al in slag-glasses, while fly ash glasses presented strong responses in the AlO_6 range, whilst still displaying Al-substitution in tetrahedral sites.

Based on the experimental results obtained, the following conclusions and observations are given:

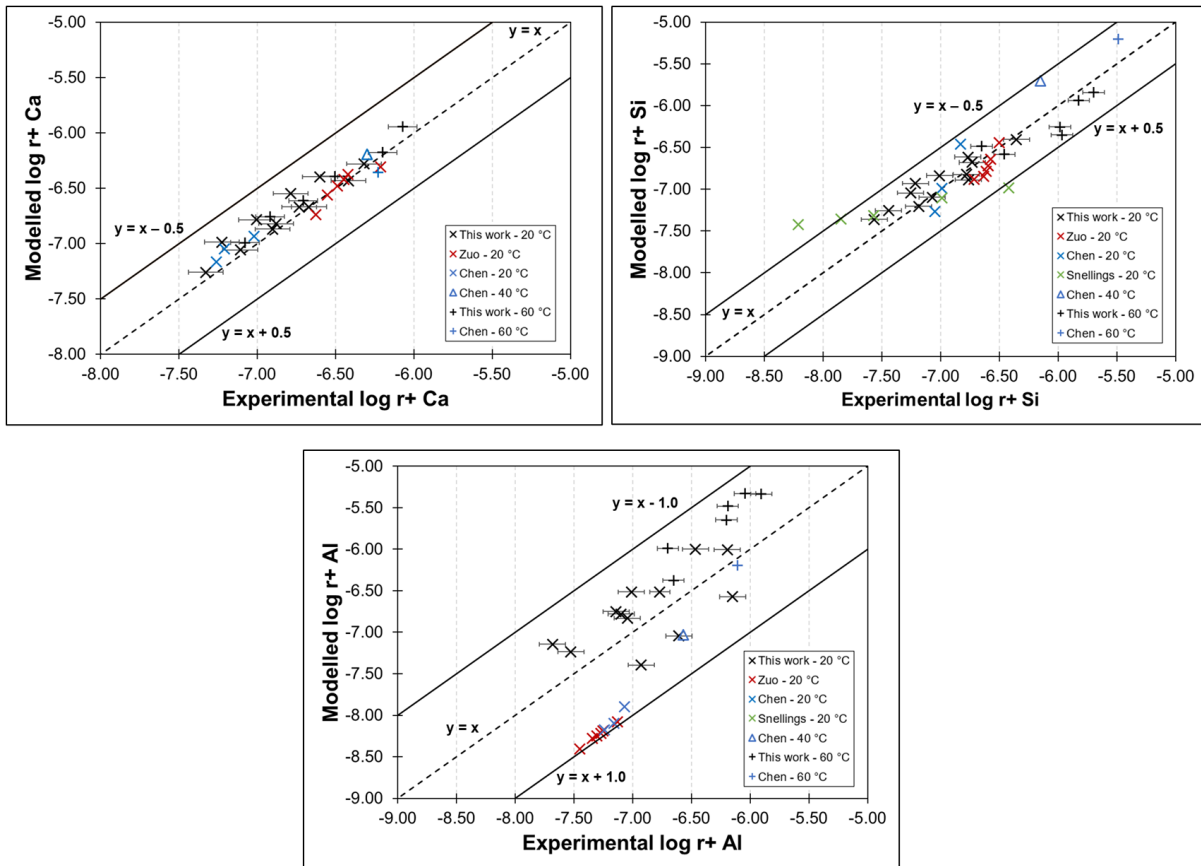
- The synthetic glasses successfully replicated the chemical composition and the structure of the amorphous portions of commercial precursors. Despite some minor differences in atomic ratios, particularly in the overestimation of Ca content, due to equipment limitations, the diffraction patterns showed clear similarities when comparing commercial and synthetic precursors.
- By combining the present results with data reported in literature, a correlation of the diffraction pattern was established with respect to the content of Ca of each glass. Fly ash-glasses displayed diffraction angle maxima in the same range as Al-Si- and Si-rich minerals, such as mullite and cristobalite. On the other hand, slag-glasses shifted the amorphous hump towards Ca-Al-rich phases, such as gehlenite and some calcium aluminates.
- Differences at sub-microscopic level were identified with spectroscopic techniques, as the glass structures were observed to be heterogeneous below this scale. Synthetic fly ashes displayed separate regions with mullite-like structures, characterized by strong interactions between SiO_4 and AlO_5 - AlO_6 regions, and Al-substituted cristobalite. The absence of extra network modifying oxides favored a residual presence of Al in fourfold coordination, which is not typically observed in CAS glasses. The formation of triclusters of Al- and Si-tetrahedra, observed in Raman spectra, assumed the role of charge compensation of $[\text{AlO}_4]^-$ units due to the low content of Ca.
- In slag-glasses, a strong presence of Al^{IV} was identified through Raman and infrared spectroscopy. In combination with the significant presence of Si Q^2 and Q^3 units and XRD patterns, the formation of gehlenite-like regions was assumed. Moreover, the observation of AlO_4 -exclusive clusters, typically seen in calcium aluminate minerals, suggests the formation of isolated regions in which Si is not present.
- Finally, it is possible to conclude that Ca has varying roles within the whole glass structure, shifting from charge balancer, mainly in low-Ca glasses, to network modifier and even as the nuclei of isolated Ca-Al structures, in high-Ca compounds.

It is suggested that Ca plays both roles in all glasses due to their highly disordered structure, but a quantitative analysis could not be resolved.

The heterogeneities in the glass structures evaluated in this chapter is extremely important for determining the reaction potential of each precursor in alkali-activation. Even with a qualitative phase determination, studying the initial stages of reactions can be more assertively correlated to the chemical composition of the precursor, allowing a precise prediction over reaction mechanisms in alkali-activated systems. The findings from Chapter 3 will be instrumental in establishing correlations between chemistry and dissolution kinetics in Chapter 4, and between chemistry and the degree of reaction/phase assemblage in Chapter 6.

Chapter 4.

Dissolution kinetics of synthetic precursors



When solid precursors are mixed with an alkaline activating solution, the process of dissolution and leaching of reactive species immediately starts, being the first step in the sequence of reactions of alkali-activated materials. The full understanding of the different phenomena occurring at this stage is rather complex, being highly influenced by intrinsic and extrinsic factors of each binder as described in Chapter 1. This Chapter investigates the true effect of precursor chemistry, concentration of the alkaline activator, and temperature, on the kinetics of dissolution, observing the evolution of element release with time for synthetic glasses. Ca was observed to be the triggering element in the dissolution of all synthetic glasses at 20 °C through ion-exchange processes, but different mechanisms were found to take place at higher temperatures. At the end, this Chapter provides an empirical estimation of the dissolution rates of Ca, Si, and Al at different temperature, and an excellent agreement was observed between the experimental rates and the values obtained by the derived equations.

4.1 Introduction

The kinetics of dissolution of precursors provide vital information over the initial stages of the reaction of alkali-activated systems. During this period, the solution becomes supersaturated with reactive species, eventually leading to the nucleation of the first reaction products. Dissolution and initial phase precipitation are the main processes that influence fresh properties and the initial heat release of the mixture, which directly impact practical procedures during the application of alkali-activated materials. These factors can dictate the optimum mixing, casting, and demolding methods and times according to the choice of raw materials. The extent and intensity of this first stage are influenced by both the initial features of the amorphous portion of the precursors and the aqueous media in which the reaction takes place. Therefore, a detailed study on the initial reaction, and an understanding of the factors that influences it, is crucial for comprehending the entire reaction process.

The processes and mechanisms of glass dissolution (or corrosion) have been widely studied in the field of nuclear waste management [182,285,286], where glass materials are considered efficient for waste immobilization. The progress of the dissolution process is measured by alteration on the surface of the reactive material, and is divided into three stages, as schematically shown in Figure 4.1:

- I. *Forward period*, characterized by the fast release of reactive mobile species (e.g., Na^+ , K^+) via ion-exchange or interdiffusion processes and hydrolysis of Si-O and Al-O bonds [287];
- II. *Residual period*, with the achievement of an equilibrated dissolution rate due to the formation of a passivating layer on the surface of glass particles;
- III. *Resumption period*, when a secondary acceleration of the dissolution rate is triggered by changes in saturation degree of the dissolving media [186,288].

Alkali-activated systems present a significantly more aggressive environment compared to the likely immersion environments of glasses used in nuclear waste immobilization applications, due to both alkalinity and possible high temperature. The resumption of an accelerated dissolution, seen in Stage III, can either continue as a steady corrosion process or take up to several years to occur for nuclear waste glasses [288,289], while the same phenomena may occur within hours in AAMs. The fast reactions involved in alkali-activated systems can sometimes cause overlap between two or more stages, which might lead to misinterpretations of the overall reaction process [189,290].

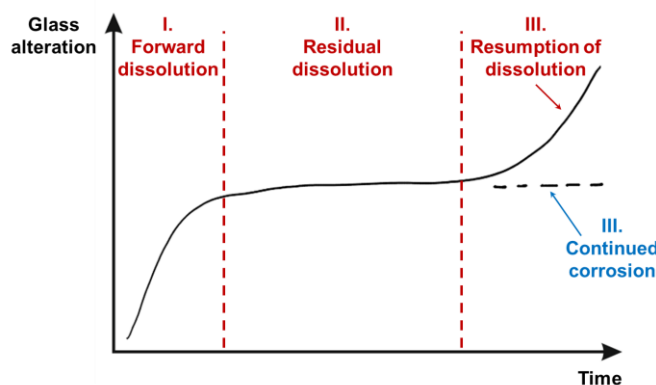


Figure 4.1: Schematic correlation of the evolution of glass alteration during dissolution processes.

Studies on the kinetics of dissolution are usually performed in *far-from-equilibrium* conditions, focusing mainly on the forward period, which describes the mechanisms occurring prior to the initial precipitation of reaction products. Such scenario is achieved with the implementation of highly diluted conditions, which prevent rapid supersaturation with respect to the most common reaction products, facilitating the study of early reactions in alkali-activated systems. By using a solution-to-glass ratio of 1000 and even 2000, some authors have analyzed the evolution in the concentration of the main elements and empirically derived forward dissolution rates. These rates can then be used to study initial phase precipitation and strength development [148,172,175,184,188,291].

High-Ca glasses are expected to display higher dissolution rates [81,291,292], and therefore greater reactivity. The quick release of network modifying agents initiates the dissolution of a precursor. This selective element detachment indicates an initial leaching of reactive species, which are then available to combine with others and form the first nuclei of reaction products [113]. For instance, Snellings [184], and Newlands and Macphee [291], evaluated the influence of chemistry on the forward dissolution rates of synthetic glasses composed only of Ca, Si and Al oxides. In both works, the authors reported dissolution rates one order of magnitude higher in percalcic glasses resembling blast furnace slags than for glasses resembling fly ashes, with Ca leading the dissolution process in such binders. Ca is also observed to rapidly react with secondary available species to form reactive surfaces in the particles of glasses, delaying a significant release of Si and Al into secondary dissolution stages [291]. Schöler et al. [148] used more complex systems with synthetic glasses containing other network modifying elements, and reported the additional influence of Al on dissolution and overall reactivity of the tested binders, as this element is known to be leached from the precursor particles prior to Si [293,294].

Ca is distinguished from other NWMs because it can more easily combine with OH or Si-species to precipitate phases in the initial moments, like portlandite ($\text{Ca}(\text{OH})_2$) or other Ca-based hydrates [79,295]. For these reasons, Ca-containing minerals can present hydraulic behaviour, which means that an alkaline environment is not strictly required to initiate the dissolution. In contrast, low-Ca precursors are considered pozzolanic, and thus require accelerating agents such as increased temperature or alkalinity, to enhance their dissolution and consequently their reactivity [45,168].

This Chapter aims to understand the true effect of precursor chemistry on the kinetics of dissolution by observing the evolution of element release with time for the four different synthetic glasses obtained in Chapter 3. Alkaline environments were used to evaluate the effect of pH, and different temperatures were tested to examine the dissolution characteristics of low-Ca precursors. The element leaching process was correlated to the structural characterization of the synthetic precursors, including the residual structure of the unreacted portion of each glass. In the end, a dissolution rate-based theory, considering chemical composition, temperature and alkalinity, was developed to determine the forward dissolution rate of the three elements in the synthetic glasses. Figure 4.2 shows the position of Chapter 4 as the final component in Part II of this thesis, providing data on how glass structures influence the initial stages of reaction of alkali-activated materials.

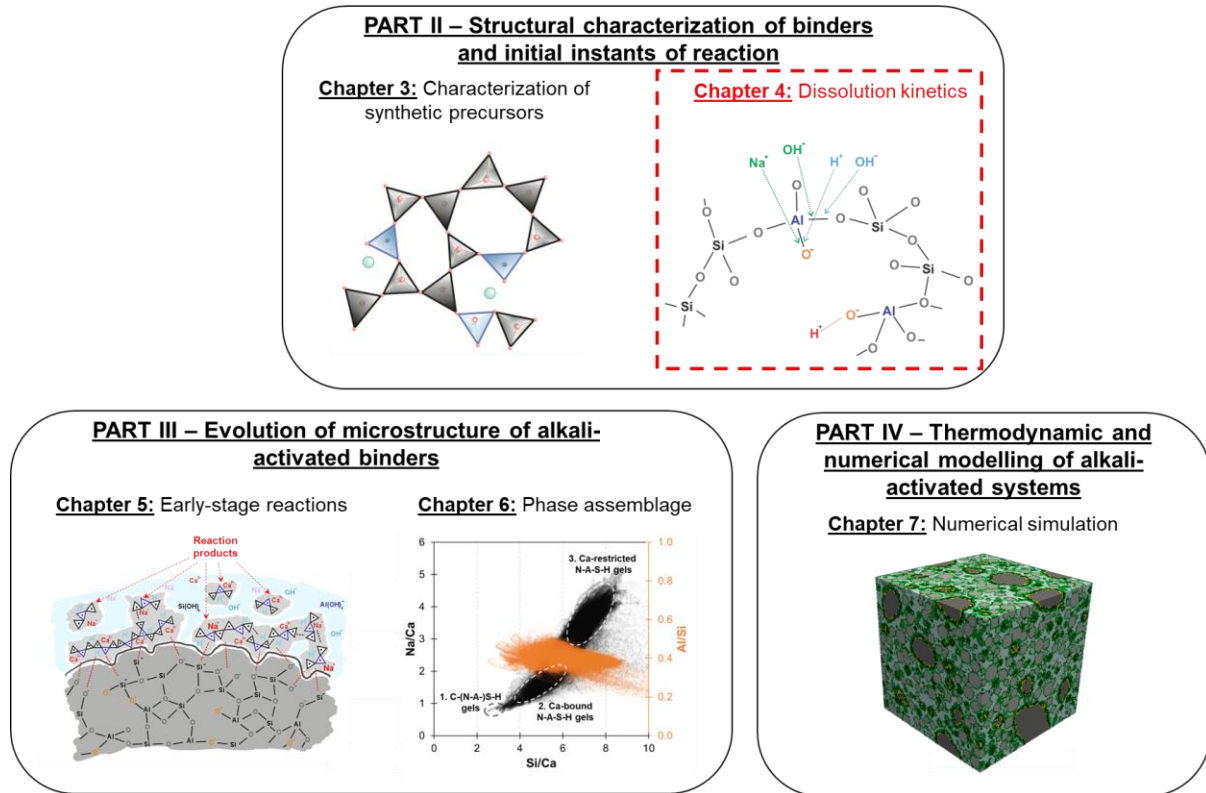


Figure 4.1: Schematic illustration of the structure of this thesis, highlighting the contributions of Chapter 4.

4.2 Materials and methods

4.2.1 Preparation of synthetic glasses for dissolution experiments

The synthetic precursors used in this chapter were obtained as part of the production batches described in Chapter 3. For this experimental campaign, glasses with relatively high particle sizes were used to slow the dissolution kinetics. This approach allowed for testing over longer periods of time to observe the evolution of cation concentration, preventing the precipitation of the first reaction products [296]. After the quenching step, the glasses were ground and milled to achieve a d_{10} size of approximately 60 μm . The particle size distribution was measured by laser diffraction, and the average density of each glass was measured using an Anton Paar Ultrapyc 5000 pycnometer through helium gas displacement. The specific surface area (SSA) of the initial glasses was estimated using the geometric method according to McGrail et al. Equation 4.1 [297]:

$$SSA = \frac{6}{\rho \cdot d_{eff}} \quad (4.1),$$

where m is the mass of the glass sample (g), ρ is the density of the particle (g/cm^3), and d_{eff} is the effective particle diameter obtained by Equation 4.2 which considers the maximum (d_{max}) and minimum (d_{min}) particle sizes:

$$d_{eff} = \frac{(d_{max} - d_{min})}{\ln(d_{max}/d_{min})} \quad (4.2).$$

The specific chemical composition and the physical characteristics of the utilised batches are given in Table 4.1, and the cumulative particle size distribution is shown in Figure 4.3.

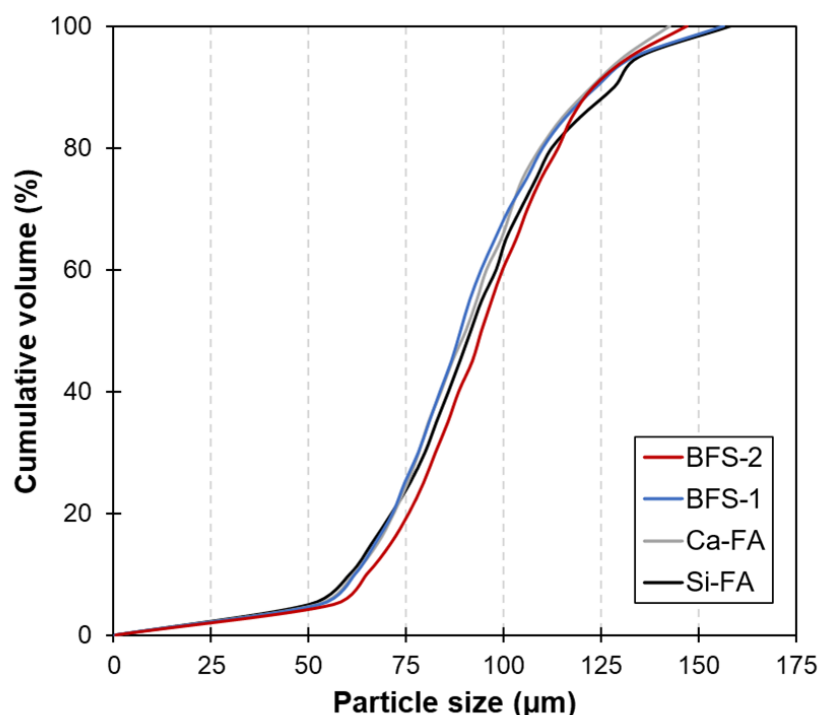


Figure 4.3: Cumulative particle size distribution of the studied glasses, obtained by laser diffraction

4.2.2 Dissolution experiments

Far-from-equilibrium conditions are usually achieved in highly diluted systems, preventing the precipitation of reaction products in the initial stages. Following similar approaches described in literature [148,176,184], the dissolution experiments were carried out with a solution/glass ratio of 1000. 1 L of sodium hydroxide (NaOH) solutions were used to dissolve 1 g of powdered glass in polyethylene vessels pre-cleaned with nitric acid and deionized water. The solutions were adjusted to three different molarities using a 50 % commercial liquid NaOH (Brenntag, Dordrecht, Netherlands) and deionized water. The four glasses were tested in 0.15 M, 1.5 M and 3 M media at room temperature ($20\text{ }^{\circ}\text{C} \pm 5\text{ }^{\circ}\text{C}$). After corrections made with activity coefficients, calculated through thermodynamic modelling (see section 4.2.3 for more details, these concentrations yielded pH values calculated to be equal to 13.04, 13.97 and 14.27, respectively, which are in the range of the pore solution observed in Portland cement systems, and activations performed in moderate and highly-alkaline environments [90,175,184]. Additionally, glasses Si-FA and Ca-FA were subject to the same solutions in a closed environment at $60\text{ }^{\circ}\text{C}$. The solutions were constantly stirred at a low rotational rate ($\sim 250\text{ rpm}$) for the whole period of the experiment. Samples were collected at 5 min, 10 min, 15 min, 30 min, 45 min, 1 hour, 2 hours, 4 hours, 6 hours and 24 hours for each system. Approximately 10 mL of solution was collected from the vessels with a syringe in every sampling, and immediately vacuum filtered using a Whatmann $2.5\text{ }\mu\text{m}$ filter paper. The filtered samples were stored in a cooled chamber at $4\text{ }^{\circ}\text{C}$ for further investigation. After each sampling, fresh NaOH solution of the original concentration was added to maintain a constant solution-to-initial surface area ratio.

Table 4.1: Chemical composition and physical characteristics of synthetic glasses used in dissolution experiments.

Glass	Normalized* content (mol)			d_{10} (μm)	d_{50} (μm)	d_{90} (μm)	S (m ² /g)	ρ (g/cm ³)
	SiO ₂	Al ₂ O ₃	CaO					
Si-FA	1.00	0.31	0.25	60.5	91.6	128.4	0.0110	2.60
Ca-FA	1.00	0.29	0.53	61.5	90.4	122.6	0.0113	2.71
BFS-1	1.00	0.31	1.21	61.8	88.9	123.7	0.0099	2.88
BFS-2	1.00	0.25	1.52	64.9	94.3	123.0	0.0098	2.96

*Normalized to the content of SiO₂.

The temporal evolution in concentrations of Si, Al and Ca, was measured by inductively coupled plasma-optical emission spectroscopy (ICP-OES). Prior to analysis, samples were diluted in 1:10, using a 0.2 vol% solution of nitric acid. Analysis was performed using a PerkinElmer Optima 5300DV ICP-OES spectrometer.

4.2.3 Thermodynamic calculations

Thermodynamic calculations were carried out to obtain effective saturation indices (ESI) of the most commonly observed solid phases in alkali-activated systems. This parameter supports the comprehension of the formation of reaction products during initial reaction stages, based on the presence and concentrations of aqueous species in the pore solution of cementitious systems. ESIs were individually calculated for each reaction product using Equation 4.3:

$$ESI = \frac{1}{N} \cdot \log \left(\frac{IAP}{k_{sp}} \right) \quad (4.3),$$

where N indicates the number of species participating in the reaction, IAP is the ion activity product which measures the effective activity of species at the moment of analysis, and k_{sp} is the solubility product of the phase under analysis. Positive values of ESI indicate supersaturation in the aqueous media and potential phase nucleation, while negative values indicate undersaturation and absence of phase precipitation [175]. In the present work, ESI is solely used to verify whether phase precipitation was avoided during dissolution experiments, as the goal of the experimental setup was to promote negative saturation indices for all phases - i.e. ensuring that far-from-equilibrium conditions were maintained.

The IAP is calculated by the ratio of the activities, or effective concentration, of products and reagents of a chemical reaction. The aqueous dissociation of SiO₂ Equation 4.4 is used as an example for the calculation of the IAP of this reaction, according to Equation 4.5:



$$IAP = \frac{\{H_2O\} \cdot \{SiO_3^-\}}{\{SiO_2\} \cdot \{OH^-\}^2} \quad (4.5).$$

The activity of each ionic species was determined using the Gibbs energy minimization software GEM-Selektor 3.4 (GEMs) [298,299]. The software activity calculations are performed using the built-in extended Debye-Hückel equation in Truesdell-Jones, shown in Equation 4.6:

$$\log \gamma_i = \frac{-A_y z_i^2 \sqrt{I}}{I + B_y a_i \sqrt{I}} + b_y I \quad (4.6),$$

where z_i is the charge of each species i , I is the ionic strength of the solution, a_i is a ion size parameter set at 3.31 for all charged ions, A_y and B_y are pressure and temperature dependent coefficients, and b_y is a semi-empirical parameter equal to 0.098 which uses NaOH solutions, at 25 °C, as base. The modelling tool considered the concentration of elements measured by ICP-OES and the Nagra-PSI thermodynamic database [221] for the calculation of activities of aqueous species, and the solubility products of the main reaction products observed in alkali-activated systems with available data in literature for calculation of effective saturation indices⁶. Table 4.2 details the chemical reactions and solubility products of the phases considered in this analysis, and Table C.1 in the Appendix C details the thermodynamic properties of the aqueous species. Solid phases containing Mg and Fe were not considered in this analysis of synthetic binders, although they are likely to precipitate in standard alkali-activated systems.

4.2.4 Characterization of residual powder

After the final sampling, the solution was vacuum filtered under the same conditions described in section 4.2.2, and the residual powders were collected to observe whether nucleation had occurred. The filtered material was washed with deionized water in two cycles until a pH of 7 was reached, then submerged in isopropanol for 48 hours to prevent any further dissolution or precipitation of reaction products. The samples were then filtered again, dried for 10 minutes at 40 °C in a closed oven, and vacuum stored.

Table 4.2: Dissolution reactions and equilibrium solubility products of reaction products in synthetic alkali-activated systems considered for thermodynamic calculation of effective saturation indices.

Solid phase	Dissolution reactions	log k_{sp}	Ref.
C-A-S-H (5CA)	$(CaO)_{1.25} \cdot (Al_2O_3)_{0.125} \cdot (SiO_2) \cdot (H_2O)_{1.625}$ $\leftrightarrow 1.25Ca^{2+} + SiO_3^{2-} + 0.25AlO_2^- + 0.25OH^- + 1.5H_2O$	-10.75	[30]
C-N-A-S-H (5CNA)	$(CaO)_{1.25} \cdot (Na_2O)_{0.25} \cdot (Al_2O_3)_{0.125} \cdot (SiO_2) \cdot (H_2O)_{1.25}$ $\leftrightarrow 1.25Ca^{2+} + SiO_3^{2-} + 0.25AlO_2^- + 0.5Na^+ + 0.25OH^- + 1.5H_2O$	-10.40	[30]
Na-C-S-H (INFCN)	$(CaO) \cdot (Na_2O)_{0.3125} \cdot (SiO_2)_{1.25} \cdot (H_2O)_{1.1875} + 0.375OH^-$ $\leftrightarrow Ca^{2+} + 1.5SiO_3^{2-} + 0.625Na^+ + 1.375H_2O$	-10.70	[30]
C-S-H (T2C)	$(CaO)_{1.5} \cdot (SiO_2) \cdot (H_2O)_{2.5}$ $\leftrightarrow 1.5Ca^{2+} + SiO_3^{2-} + OH^- + 2H_2O$	-11.60	[30]
Portlandite (CH)	$Ca(OH)_2 \leftrightarrow Ca^{2+} + 2OH^-$	-5.20	[31]
N-A-S-H (NASH_1)	$(Na_2O)_{0.5} \cdot (Al_2O_3)_{0.5} \cdot (SiO_2) \cdot (H_2O)$ $\leftrightarrow SiO_3^{2-} + AlO_2^- + Na^+ - 2OH^- + 2H_2O$	-6.51	[11]
Katoite (C ₃ AH ₆)	$Ca_3Al_2(OH)_{12} \leftrightarrow 3Ca^{2+} + 2Al(OH)_4^- + 4OH^-$	-20.50	[31]
Strätlingite (C ₂ ASH ₈)	$Ca_2Al_2SiO_2(OH)_{10} \cdot 3H_2O$ $\leftrightarrow 2Ca^{2+} + 2Al(OH)_4^- + SiO(OH)_3 + OH^- + 2H_2O$	-19.70	[31]
C ₄ AH ₁₃	$Ca_4Al_2(OH)_{14} \cdot 6H_2O \leftrightarrow 4Ca^{2+} + 2Al(OH)_4^- + 6OH^- + 6H_2O$	-25.25	[31]
Si-hydrogarnet (C ₃ AS _{0.84} H _{4.32})	$Ca_3Al_2(SiO_4)_{0.84}(OH)_{8.64}$ $\leftrightarrow 3Ca^{2+} + 2AlO_2^- + 0.84HSiO_3^- + 3.16OH^- + 2.32H_2O$	-26.70	[32]

⁶The activities of water and pure solids is equal to 1. Refer to [85,86] for more information on thermodynamics of cementitious materials.

Differential thermogravimetric analysis were performed on the glasses after dissolution using a Netzsch TG-449-F3-Jupiter thermoanalyzer, in a temperature range from 40 °C to 900 °C, a heating rate of 10 °C/min, and an argon purge atmosphere of 70 mL/min. Attenuated total reflection Fourier transform infrared (ATR-FTIR) spectroscopy and Raman spectroscopy analysis were performed on the residual glasses following the same specifications described in section 3.3.2. Deconvolution of the spectra was performed, aiming at the individual identification of Si- and Al-related interactions in the overall Raman response.

4.3 Results

4.3.1 Dissolution mechanisms at room temperature

4.3.1.1 Influence of solution pH in dissolution kinetics

0.15 M NaOH solutions

The measured concentrations of Ca, Al and Si, in 0.15 M NaOH solutions, are shown in Figure 4.4. It is possible to observe, in all glasses, a non-steady regime occurring up to 2 hours of sampling (region I), followed by a linear evolution in concentrations until the end of the experiment. This initial non-linear behaviour has been identified by other authors [184,300], and is characteristic of a complex process, involving the competition of several mechanisms [301,302]. Given the high pH of the solution, this can be understood as an *instantaneous disequilibrium shock*, where weakly-bound atoms are immediately released from the framework after contact with solution, through a combination of leaching, ion exchange and dissolution reactions [301]. As a result, Ca shows the highest concentration during this initial period in all experiments, especially in fly ash-type glasses. The maximum measured concentration was 1.63 times larger in Si-FA than BFS-2 (Si-FA = 0.077 mmol/L; BFS-2 = 0.047 mmol/L). This can be an indication of the presence of internal Ca-rich structures in slag glasses, which strongly binds Ca atoms into the amorphous portion, making them less susceptible to initial leaching in such structures. Such observation arises from the observed presence of gehlenite- and calcium aluminate structural units in the synthetic precursors, detailed in Chapter 3.

After 2 hours, a steady dissolution takes place for Si and Al until 24 hours (region II), with different slopes being observed depending on the precursor. The intense release of elements, driven by the hydrolysis of Si- and Al-O bonds, produces localized negatively charged surface sites, due to the presence of Si-O⁻ and Al-O⁻ bonds [176,303]. This second observed period corresponds to Stage I of the glass dissolution theory described in the Introduction section of this chapter - see Figure 4.1 and related discussion - as all elements are continuously detached from the framework at a rapid dissolution rate. This regime allows for the calculation of forward dissolution rates, which will be discussed in the next sections. In all glasses, Ca deviates from the linear trend after 6 hours. This behaviour was more prominent in fly ash-type glasses, where Ca concentrations decrease from 6 to 24 hours, resulting in a final Ca concentration that is three times lower (0.03 mmol/L) than the value observed for BFS-2 (0.10 mmol/L).

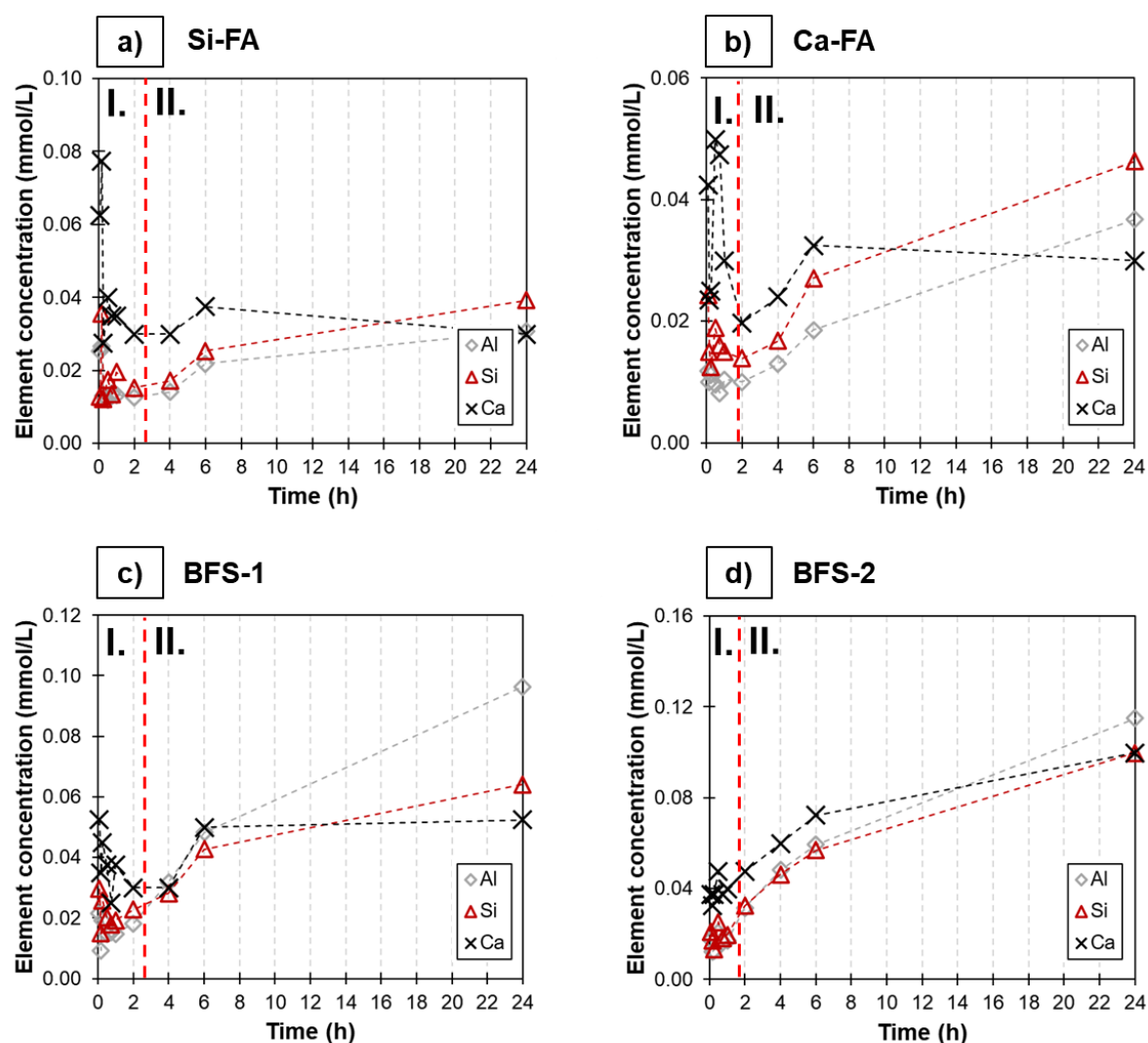


Figure 4.4: Temporal variation of concentrations of Ca, Al and Si, as measured by ICP-OES, in synthetic glasses dissolved in 0.15 M NaOH solutions: a) Si-FA; b) Ca-FA; c) BFS-1; and d) BFS-2.

In order to identify the consequences of the decelerated release of Ca, effective saturation indices (ESI) were calculated using the concentration values measured at different times. Especially in the absence of other ionic species, Ca is known to show high compatibility with OH^- , leading to the formation of portlandite [79,304], which could partially consume Ca from the solution. However, the plots displayed in Figure 4.5 do not show positive saturation indices for any phase, including portlandite, in the two most extreme glasses (Si-FA and BFS-2). One possible explanation is the adsorption of aqueous Ca^{2+} , and the formation of a porous Ca-rich layer in the reactive surfaces [305]. The exposed negative sites of the substrate can easily attach positively charged species, forming a non-continuous passivating layer and preventing the diffusion of OH^- into inner layers of the reacting glass [306,307]. This assumption could also partially explain the non-linearity of the evolution of Si concentrations after 6 hours, particularly in slag-type glasses.

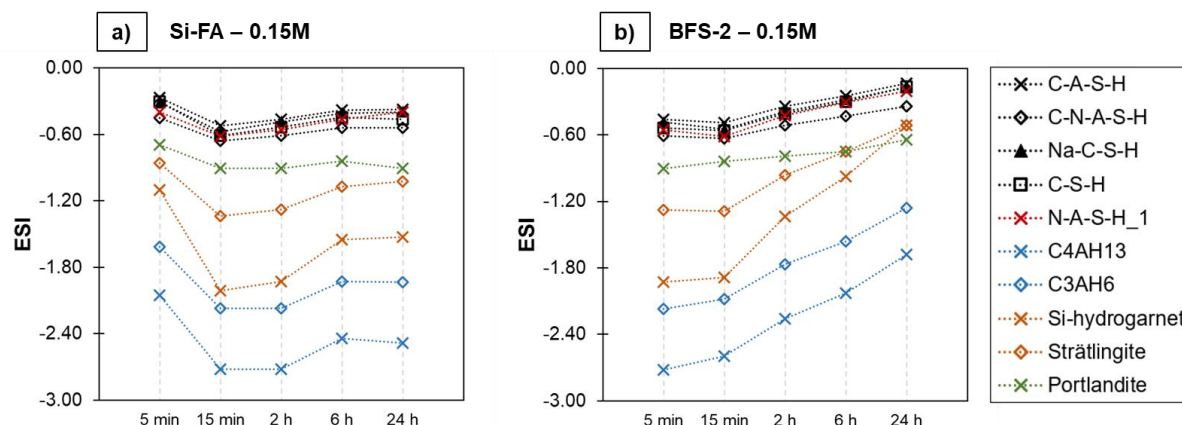


Figure 4.5: Effective saturation indices (ESIs) calculated for the potential precipitation of reaction products during the dissolution of synthetic glasses in 0.15 M NaOH solutions: a) glass Si-FA; b) glass BFS-2 - refer to Table 4.2 for the code of each phase.

Additional important information can be obtained from the results shown in Figure 4.4, distinguishing the first mechanism taking place during dissolution of precursors. A linear evolution in Ca concentration was observed up to 6 hours. Beyond this point, the Ca/(Si+Al) ratios of the measured concentrations, normalized to the same ratio in the original composition of each synthetic glass, were significantly higher in fly ash-type than in slag-type glasses, as summarized in Table 4.3. The previous chapter discussed the more polymerized structure formed in fly ash glasses, with both Si-FA and Ca-FA displaying Si Q³ and Q⁴ species occupying over 80 % of the SiO₄ units. The slower release of Si and Al from these two precursors demonstrates their enhanced preference for ion-exchange processes in the early stages of dissolution, following conventional dissolution mechanisms in alkaline media [189,308,309]. This behaviour is assumed to be directly correlated with the polymerization degree of the original glass framework. Consequently, the intense hydrolysis of aluminosilicate structures is delayed in these less reactive systems, occurring only at later stage due to the high energy barrier required to break the polymerized framework of fly ash-type glasses, even under far-from-equilibrium conditions.

1.5 M and 3 M NaOH solutions

The influence of pH on the release of Ca, measured for glasses Si-FA and BFS-2, is illustrated in Figure 4.6. In the plots, two distinct behaviours can be noticed between the two precursors. The non-steady period was observed to be more influenced by the NaOH molarity of the solution in Si-FA than in BFS-2, as the maximum Ca concentration shifted from 0.07 mmol/L (1.5 M NaOH - Figure 4.6a) to 0.21 mmol/L (3 M - Figure 4.6b) for the fly ash-type glass in the first samplings. However, different from the observations at 1.5 M NaOH, higher alkalinity hindered a continuous release of Ca in the second stage of dissolution, as the measured concentrations at 6 and 24 hours were similar (Figure 4.6 b). Similarly, BFS-2 presented a decelerated cation release after 6 hours in both solutions. The final measured concentrations, after 24 h, were similar for the two glasses regardless of the NaOH molarity - 0.08 and 0.11 mmol/L for Si-FA, and 0.26 and 0.24 mmol/L for BFS-2 at 1.5 M and 3 M NaOH, respectively. In such cases, other details should be evaluated. The length of the steady period was shortened for the fly ash-type glass in a higher pH environment, as the changes in measured Ca concentrations were negligible from 2 to 24 hours. For BFS-2, the net concentration change in the forward period must be taken into account. Increasing the

molarity of NaOH to 3 M (Figure 4.6d) represented a net change in Ca concentration of 0.14 mmol/L, approximately 70 % higher than the measured difference in 1.5 M NaOH solution (Figure 4.6c). These observations suggest the existence of a maximum concentration of Ca that is in equilibrium with the surrounding solution under far-from-equilibrium conditions, and that the local pH affects the time needed to achieve a threshold cation concentration, depending on the composition of each respective glass.

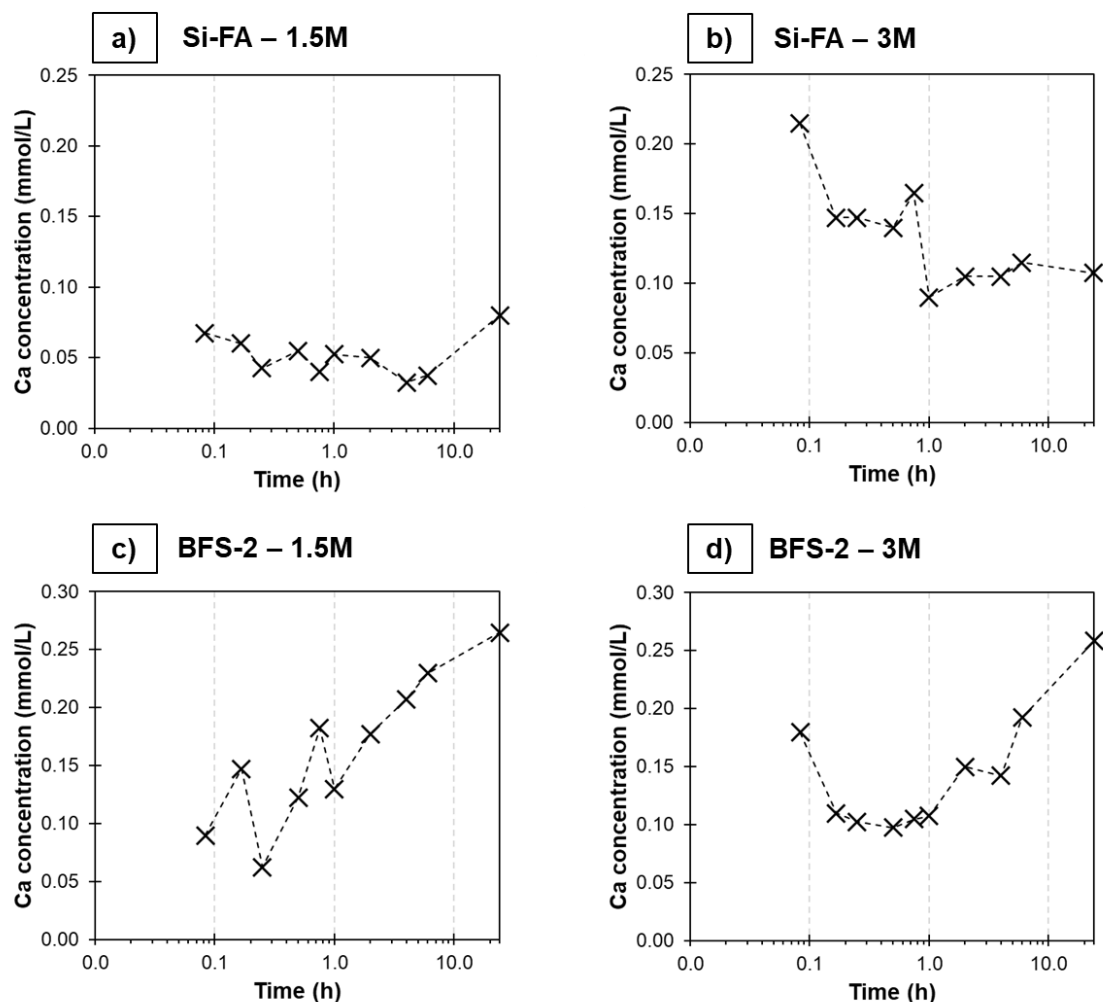


Figure 4.6: Evolution of concentrations of Ca observed for different alkali concentrations: Si-FA glass at a) 1.5 M and at b) 3 M; and BFS-2 glass at c) 1.5 M and d) 3 M NaOH solutions.

Table 4.3: Summary of Ca-related dissolution data measured in 0.15 M NaOH solutions.

Glass	Ca/(Si+Al) ratio in original glass	Normalized Ca/(Si+Al) in the solution at 6 h
Si-FA	0.16	2.42
Ca-FA	0.33	1.06
BFS-1	0.68	0.37
BFS2	1.00	0.27

Characterization of residual dissolution powder

The high concentrations measured during the initial stages, coupled with the hindered evolution of the steady period, suggests that Ca is being quickly consumed for the nucleation of solid products in 1.5 M and 3 M NaOH solutions, unlike what was observed in lower alkalinity conditions. In order to evaluate this assumption, differential thermogravimetry (DTG) tests were performed on the residual powders collected after the dissolution under these two conditions. The DTG curves, plotted in Figure 4.7, display mass loss peaks characteristic of the dehydroxylation of portlandite (centred at approximately 475 °C) for all glass systems. The formation and stabilization of $\text{Ca}(\text{OH})_2$ should not be a surprise, as the coupling of Ca and OH^- is favoured by the delayed release of Si-species in all conditions [79,205]. Interestingly, it was not possible to establish a correlation between the areas under the $\text{Ca}(\text{OH})_2$ related peaks and the chemical composition of the glasses, as no incremental increase or decrease of these signals was observed according to the Ca content in the original glass. In literature, portlandite is often described as an activated complex of the alkaline dissolution of Ca-containing minerals. In initial stages, it is formed as a metastable intermediate phase prior to the irreversible precipitation of stable new solid products [186,310]. It can be thus suggested that portlandite is being successively precipitated and dissolved in the aqueous media, due to the high solution/glass ratio and the constant stirring.

The formation of unstable compounds can also explain the differential water loss peak centred at approximately 570 °C, which is attributed to poorly-ordered calcium carbonate phases [311,312] due to the decomposition of metastable portlandite nuclei [79]. Under such high liquid/solid ratios, the reactive glasses are solids are extremely susceptible to carbonation, being prone to carbonation and formation of a vaterite-like compound. As indicated by Sauman [313], this phenomenon can occur even during the short exposure time during transport of the solid residue to the DTG device, and in the present work, carbonation might have resulted from the washing cycles of the glasses after dissolution was ceased. A mild precipitation of Ca-based hydrated gels is observed for slag glasses at 3 M solutions, arising from a more significant Si dissolution. Nonetheless, the total amount of precipitated gel during the experiments can be considered negligible, which confirms that the experimental setup was reliable in maintaining the forward dissolution period conditions.

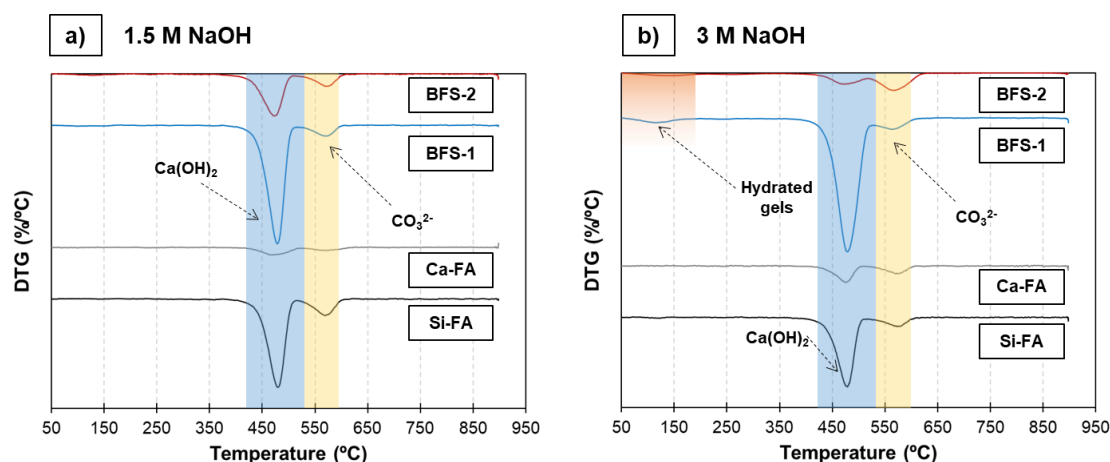


Figure 4.7: DTG curves of the four synthetic glasses measured after dissolution experiments performed with: a) 1.5 M; and b) 3 M NaOH solutions.

The evolution of Si/Al ratios with time, normalized to the initial glass chemistry, also distinguishes the dissolution mechanisms of the two groups of precursors. The plots in Figure 4.8 show that, after the non-steady period, Al is more easily detached from the network than Si regardless of the alkalinity and initial glass chemistry. This observation has been made before by a few authors [211,314], as Al-O bond energies are weaker than Si-O [315], facilitating their earlier hydrolysis. The atomic ratios, after quickly reaching their maximum values, tend to decrease following a logarithmic-like trend towards what appears to be a steady value after the 24 hours of the experiment. This can be an extra indication of the deceleration in dissolution rates, characteristic to the end of the first stage in the classic theory of glass dissolution. The final values at 24 hours, however, show significant differences between the two glasses. The high-Ca precursor displays a more significant release of Al in both solutions, resulting in a final Si/Al ratio (normalized to initial atomic ratio) approximately a factor of two lower than the values calculated for glass Si-FA - 0.42 versus 0.70 at 1.5 M, and 0.36 versus 0.57 at 3 M. A few assumptions can be made here:

- I. The release of one Ca atom can facilitate the hydrolysis of Al-O bonds in AlO_4^- sites that were being charge-balanced by it; as high-Ca precursors were shown in Chapter 3 to have a large concentration of Al^{IV} , accelerated leaching of Al is likely to occur.
- II. The coupled higher dissolution of Ca and Al can also indicate the combined dissolution of the isolated regions rich in calcium aluminate structures described in Chapter 3, as minerals like mayenite and C_3A are more prone to early dissolution than Si-rich phases [316]. On the other hand, Al has a strong presence in octahedral coordination in isolated structures of Si-FA that resemble mullite. AlO_6 is naturally more stable than AlO_4 , due to its lower Lewis acidity [50], which increases the energy barrier for bond breakage and hinders a pronounced release of Al in low-Ca glasses.

The validation of these assumptions is rather complex, and would require sophisticated analysis and possibly a broader range of investigated materials. Nonetheless, the next section attempts to provide answers to the different dissolution mechanisms observed at room temperature.

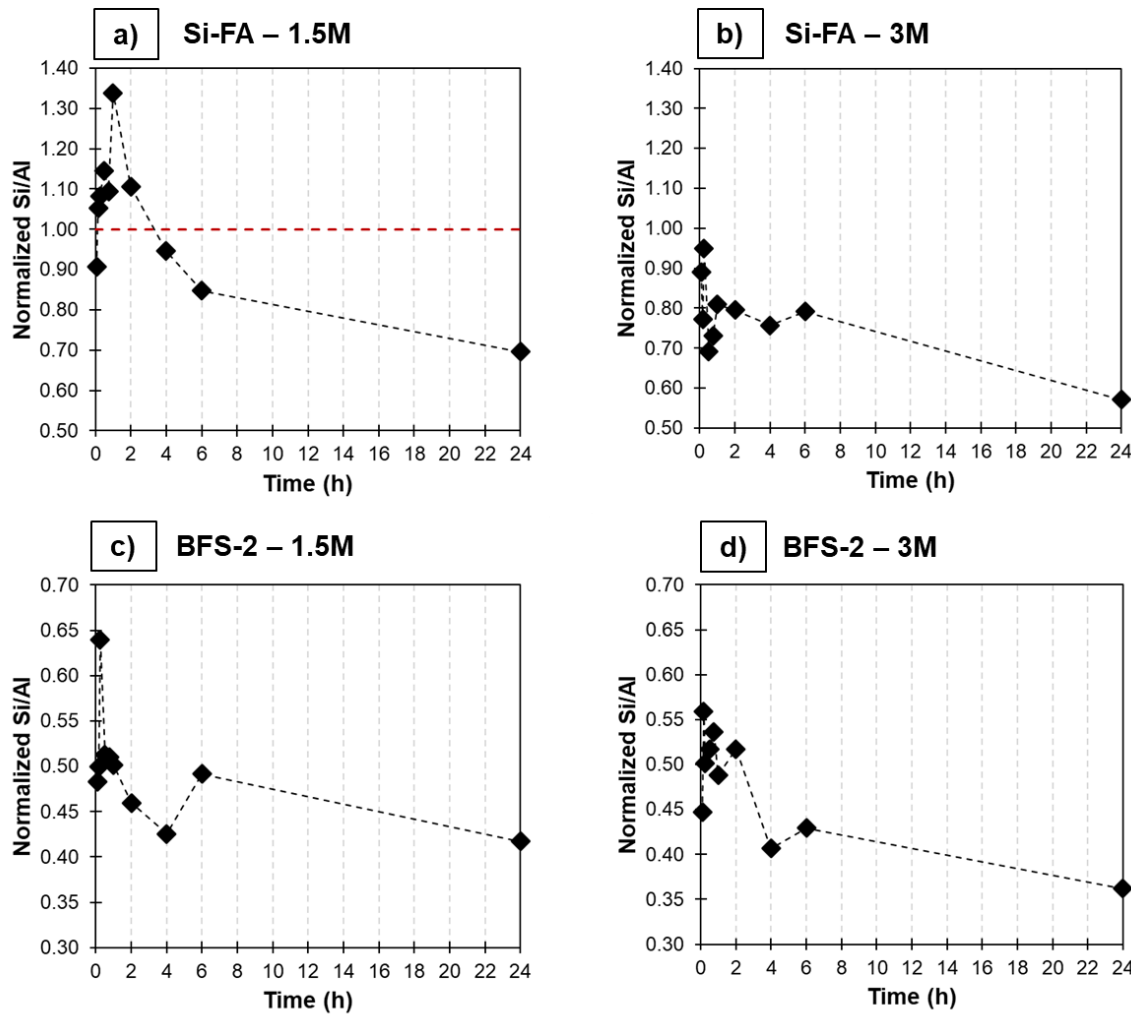


Figure 4.8: Normalized Si/Al ratios measured for the dissolution of synthetic precursors in different alkaline solutions: glass Si-FA in a) 1.5 M and b) 3 M; and glass BFS-2 in c) 1.5 M and b) 3 M NaOH solutions.

4.3.2 Characterization of residual framework after dissolution

4.3.2.1 Characterization through Raman spectroscopy

Quantitative analysis of Si Q^n sites

Figure 4.9 compares the Raman spectra of unreacted (original synthetic glasses) and dissolved glasses in 1.5 M NaOH solutions. The plot clearly illustrates distinct mechanisms, as the differences in the curves change gradually according to the CaO content of the glasses. In the spectral range attributed to Si Q^n sites (800 and 1200 cm^{-1}), slag-type glasses display a significantly decreased intensity relatively to the other regions after dissolution, as the intensity of the solid lines are significantly lower than the dashed lines. The lower signal indicates a strong hydrolysis wave, responsible for disrupting the original aluminosilicate framework. On the other hand, fly ash-type glasses presented the opposite trend. The 400-600 cm^{-1} range of the curve for residual glasses was shown to decrease in intensity compared to the Si Q^n -related spectral range. The low content of modifying elements favours a more covalent vitreous framework in low-Ca materials, which naturally shows a higher resistance to hydrolysis [310]. As this region of the spectra is mainly

attributed to vibrations in Si-O-T bonds, it can explain the lower reactivity commonly observed in fly ash-type glasses, which usually require longer periods to promote the depolymerization of the original network at room temperature [46,113].

The differences in how hydrolysis reactions take place are better explained by the values in Table 4.4. The large reduction in Si Q⁴ sites of Si-FA after dissolution, by approximately 25 %, indicates that the glass framework is being slowly depolymerized, with the conversion of three-dimensional into chain-like structures - considering that Q² species have doubled their quantity. It is noticeable that this trend is not followed in glass Ca-FA, as no significant variation in the quantity of silicate species was calculated among unreacted and residual glasses. It is here assumed that the stronger network connectivity of glass Si-FA acts as an extra obstacle for the disruption of the whole framework. This observation is in agreement with the work from Oey et al. [317], as the authors reported reductions in the range of 1.5 logarithmic units in the dissolution rates of commercial siliceous compared to commercial calcareous fly ashes, arising from the notoriously higher number of *dissolution constraints* generated by the higher structural rigidity of the former. For that reason, fully connected tetrahedral sites (Si Q⁴) must be the first ones to suffer hydrolysis after the initial etching of surface sites (Si Q³), as they are present in larger proportions in the unreacted structure of glass Si-FA.

The above assumption is in agreement with the discussions of Hamilton et al. [318], who stated that the hydrolysis between two Si Q⁴ bonds, which is slower than in less polymerized units, serves as a network-opening reaction, being the rate controller of the overall dissolution of feldspar minerals [319]. Additionally, a few authors have showed that Al^{IV} preferentially substitutes Si in the most polymerized sites of aluminosilicate glasses [320] to facilitate charge compensation [321], causing extra localized network distortions. In agreement with the previous section, the assumption of preferential hydrolysis of AlO₄ sites which were being charge balanced by Ca²⁺ is strengthened, being further supported by the fact that hydrolysis of AlQ⁴-SiQ⁴ are more favourable than SiQ⁴-SiQ⁴ [288]. This process leads to a sequential breakage of the SiO₄ sites that were originally connected to this Al atom, increasing the density of two-dimensional chain-like structures and decreasing the proportion of three-dimensional networks. The evaluation of this proposed sequence of reactions would require the characterization of residual dissolved glasses collected at earlier times, which will not be assessed in this research.

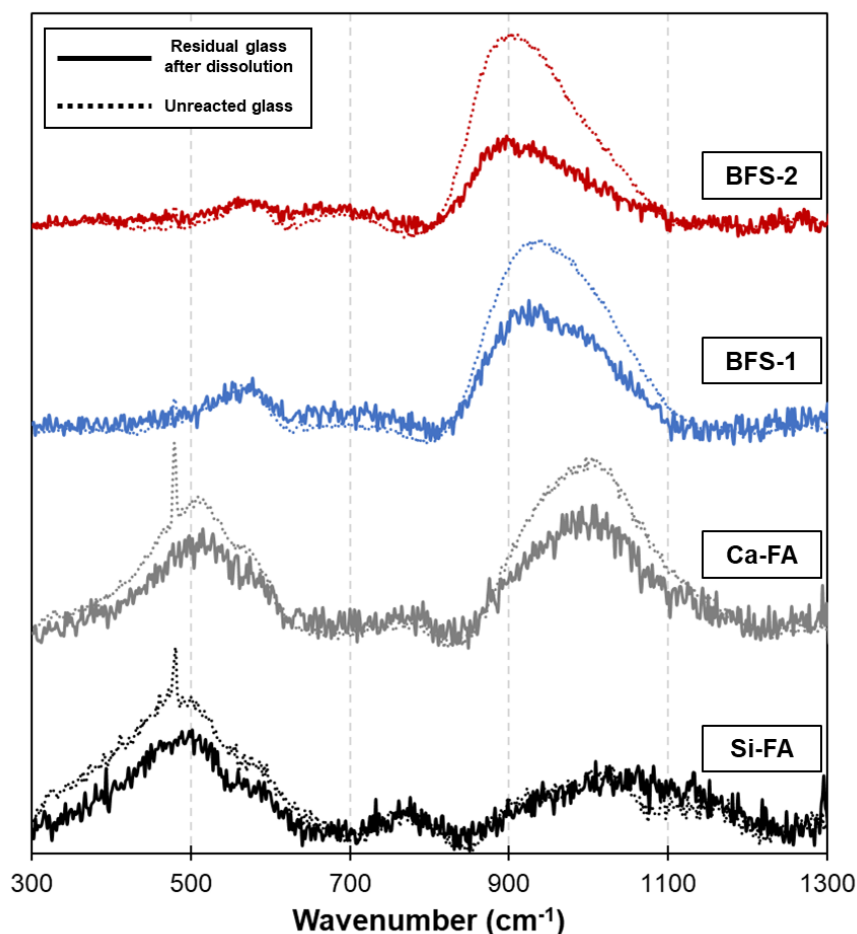


Figure 4.9: Raman spectra measured before and after dissolution experiments (1.5M NaOH) - dashed lines indicate unreacted and solid lines indicate residual glasses after 24 hours of dissolution.

Conversely, the deconvoluted quantity of Si Q⁴ species in residual powders increased gradually for glasses with higher initial Ca content, and can be directly related to the relationship of Si/Al ratios calculated after 24 hours - see Figure 4.6. If a favoured hydrolysis of Al-O bonds in sites previously charge compensated by Ca²⁺ takes place as previously suggested, one could raise a point of contradiction, as Al is usually stated to display preferential substitution in Si Q⁴ sites [151]. In this case, two explanations can be provided: Mysen [322], supported by Henderson et al [253], stated that the location of the incorporated Al³⁺ is influenced by the Al/Si ratio of the glass, with substitution in dimers increasing in glasses with lower contents of Al. As the structure of unreacted glasses shows traces of Ca-Al-phases - see Section 4.4 for more details - fewer Al atoms would be incorporated into the silicate framework, reducing localized Al/Si ratios and favouring Al incorporation in Q² sites. Otherwise, the more significant presence of Ca naturally increases the abundance of charge balancing elements, reducing the requirement of self-balancing by fully connected sites. In either case, it is a fact that Al displays higher dissolution rates in initial moments.

Table 4.4: Deconvoluted quantity of silicate species in the four synthetic glasses, before (unreacted) and after (residual) dissolution experiments, calculated with Raman spectroscopy.

Glass		Si Q ⁰	Si Q ¹	Si Q ²	Si Q ³	Si Q ⁴
Si-FA	Unreacted	0.02 %	0.62 %	11.63 %	17.42 %	70.31 %
	Residual	0.72 %	4.34 %	24.87 %	14.95 %	55.14 %
Ca-FA	Unreacted	0.01 %	1.59 %	22.97 %	21.50 %	53.92 %
	Residual	0.05 %	2.09 %	25.12 %	17.89 %	54.85 %
BFS-1	Unreacted	4.57 %	11.09 %	38.71 %	19.83 %	25.81 %
	Residual	4.31 %	11.56 %	21.91 %	20.74 %	30.47 %
BFS-2	Unreacted	8.93 %	14.67 %	38.78 %	11.76 %	25.86 %
	Residual	7.31 %	11.34 %	27.38 %	15.85 %	38.13 %

Qualitative determination of Al sites

Following the same procedure as in the previous chapter (see Section 3.2.2), the deconvolution of the overall Raman spectra resulted in an isolated curve for Al-O interactions. As shown in Figure 4.10, none of the Al contributions was ceased after dissolution, with selective release of Al being observed for all glasses. In general, when comparing the spectra of glasses dissolved for 24 hours with unreacted glasses, the intensity of the Al-O-T interactions in the 550-650 cm⁻¹ range was much closer to both regions attributed to AlO₄ and AlO₆ in the former than in the latter. This indicates that the dissolution had a significantly higher impact in Al with tetrahedral coordination rather than other species. The preferential breakage and release of Al^{IV} agrees with the previous assumption: hydrolysis takes place, initially, in AlO₄ units which were being charge compensated by Ca²⁺, decreasing interactions between Si- and Al-tetrahedra without necessarily depolymerizing the entire framework. This is also supported by the negligible changes observed in the 650-700 cm⁻¹ range, attributed to the formation of triclusters of AlO₄ groups - see Chapter 3 for more details. These Al-rich structures function as their own charge compensators [262], and the absence of Ca²⁺ eliminates a localized ion exchange, thus preventing a significant initial breakage of these units. Similarly, the interactions between Si-tetrahedra and Al-octahedra (700-800 cm⁻¹) remained nearly intact for all glasses, suggesting that these structures are more compact and present a higher energy barrier for their disruption.

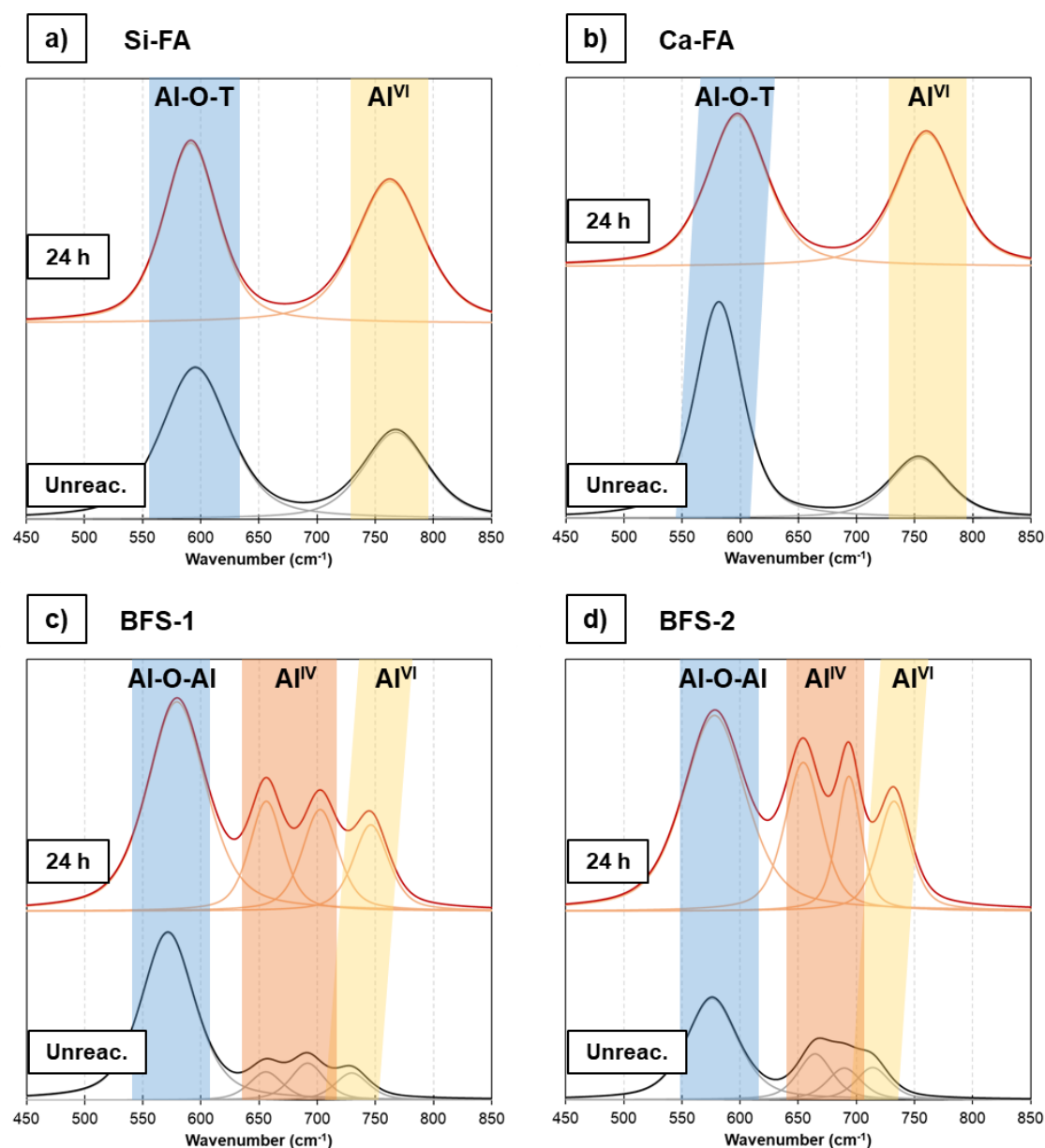


Figure 4.10: Al-O isolated Raman spectra before and after dissolution experiments of the synthetic glasses in 1.5 M NaOH solutions: a) Si-FA, b) Ca-FA, c) BFS-1 and d) BFS-2.

4.3.2.2 Characterization through Fourier transform infrared spectroscopy

The residual glass framework can be visualized in more details in the FTIR spectra of glasses Si-FA and BFS-2, shown in Figures 4.11a and 4.11b, respectively. Following observations made using Raman spectroscopy (Figure 4.9), glass BFS-2 displayed lower intensities in the Si-O-T attributed band after dissolution, which was centred at 880 cm^{-1} in both unreacted and residual glasses. In addition, this main band displayed a step and the formation of two distinct areas, generating a new minimum value centred at 845 cm^{-1} for the dissolved glass. The newly formed band is characteristic of AlO_4 species [85,211], equally to the bands centred at 680 cm^{-1} (attributed specifically to triclusters of tetrahedral-Al [320]), which were not influenced by dissolution.

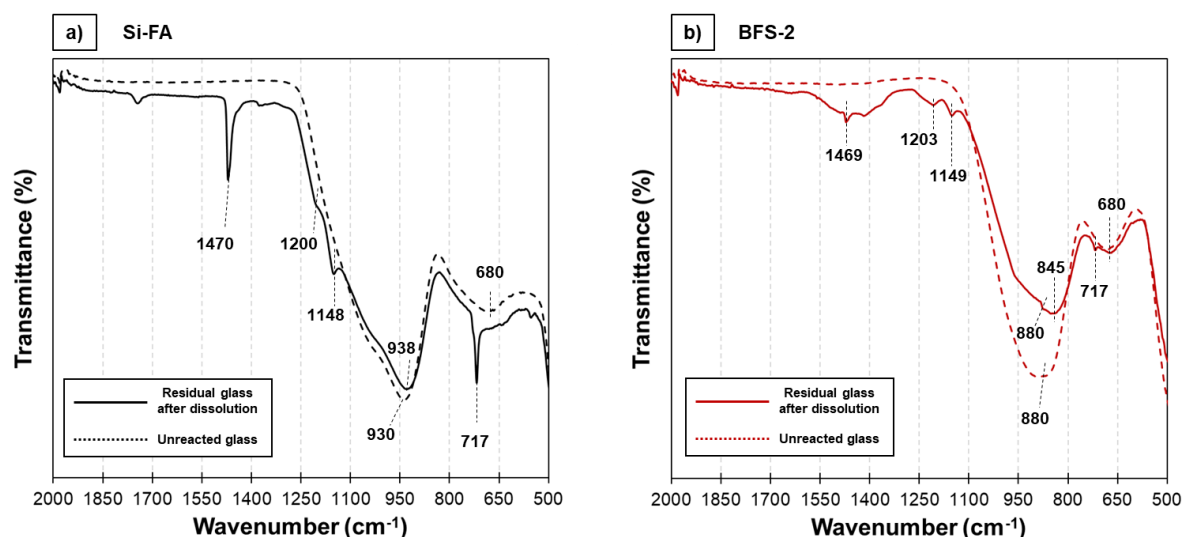


Figure 4.11: FTIR spectra of unreacted and residual glasses after dissolution in 1.5 M NaOH solutions: a) Si-FA, and b) BFS-2 - solid lines indicate residual glasses and dashed lines indicate unreacted glasses.

The remaining features of the spectra in Figure 4.11b indicate a few similarities in the dissolution of glasses Si-FA and BFS-2. The sharp band observed at 717 cm^{-1} for residual Si-FA (Figure 4.11a), which has a much smaller intensity in the slag-type glass, is attributed to bending vibrations of Si-O-Si in 6 membered rings [99,318] in the residual silicate structure. It is reasonable that these structures have a stronger reflection in fly ash-type glasses, which display a much denser initial framework due to the lower amount of modifying elements. The interesting point is that both glasses display small peaks centred at approximately 1200 and 1150 cm^{-1} : the first one is attributed to vibrations of AlO_6 units, typical of mullite [245,323], while the second is characteristic of silica-gel and end-chain SiO_4 structures [311]. The observation of the latter shoulder is in agreement with deconvolution of Raman spectra shown in Table 4.4, since the depolymerization of the network could lead to an increased amount of end-chain members. The presence of Al in sixfold coordination is also following the responses of Al-isolated Raman spectra, as all glasses displayed residual AlO_6 -related interactions. It is important to state that these mullite-like structures were present in all unreacted glasses in minor quantities, being observed more clearly only in the framework of Si-FA. Finally, both spectra show contributions from CO_3^{2-} compounds in the residual glasses ($\sim 1470\text{ cm}^{-1}$) [311,324], consistent with observations made using DTG (see Figure 4.7). These findings confirm the selective release of Al^{IV} from Al-O-Si-rich over Al-rich regions during the initial stage, as AlO_4 -rich phases appeared to remain intact.

4.3.3 Effect of temperature on dissolution of fly ash-type glasses

The increase in temperature, from $20\text{ }^{\circ}\text{C}$ to $60\text{ }^{\circ}\text{C}$, showed a major influence on the release of Ca in the Si-FA glass, according to the plots shown in Figure 4.12. This effect is amplified by the pH of the solution, with the differences in the final concentrations between the two temperatures progressively increasing with the molarity of NaOH molarity - measured concentrations were 2.33, 3.25 and 3.63 times higher at $60\text{ }^{\circ}\text{C}$ compared to $20\text{ }^{\circ}\text{C}$ for 0.15 M, 1.5 M and 3 M solutions respectively. Moreover, the evolution of Ca release presented a linear trend throughout the whole experiment at $60\text{ }^{\circ}\text{C}$, even for the lowest molarity, contrarily to observations made at $20\text{ }^{\circ}\text{C}$. As demonstrated by Mercado-Depierre et al. [307],

the implementation of higher temperature increases the release rate of Si along with Ca, and induces the precipitation of C-S-H nuclei. However, the ion activity product of C-S-H has been demonstrated to be lowered at temperatures above 20 °C [325], especially at early hydration times. In the present setup, the resulting higher solubility caused by the increased temperature imposed a barrier over the formation of stable gels due to the effect of temperature in the solubility product of hydrated gels [326,327]. Nonetheless, the eventual precipitation of Ca-Si containing phases occurring in the bulk solution could prevent the formation of passivating layers in the reacting substrate [309], allowing a continuous release of Si and Al and extending the forward dissolution period.

Following the behaviour of Ca, the combined influence of pH and temperature on the release of Si is displayed in Figure 4.13. The concentration of Si, measured at 24 h, versus the product of the initial OH⁻ concentration with the SiO₂ fraction in the original glass, showed two separate linear trendlines. The intensified effect of temperature is noticed by the change in the slope of the trendlines, which showed a higher angle for the 60 °C data. It is important to state that glass Si-FA displayed one point out of the trend at room temperature, which can be correlated to the potential entrapment of Si in passivating layers on the surface of the reacting particles, as this phenomenon is more favoured at lower temperatures [328,329], or to the combination of Si⁻ with Ca-species for the formation of unstable nuclei. The measured Ca content at 6 hours was three times higher in 3 M than in 1.5 M for Si-FA (0.11 versus 0.04 mmol/L). Such enhanced Ca concentration in the surrounding solution could favour the attachment of the element to form Ca-rich phases directly on or close to the surface, similarly to what is observed in slag-glasses at lower molarities.

The higher slope observed in Figure 4.13 demonstrates that the combination of temperature and alkalinity forms a more energetic environment. It is thus interesting to observe the interaction between network forming agents in the overall dissolution. In the previous section, Al has been shown to be detached from the framework at higher rates at room temperature. However, implementation of higher temperature leads to final normalized Si/Al ratios close 1 in the two fly ash-type glasses, as summarized in Table 4.5. A very similar ratio was also observed at 2 h, which marks approximately the beginning of the steady dissolution period. The comparison of ratios calculated at different temperatures suggests that the occurrence of congruent dissolution of Si and Al requires higher temperatures. Gin et al. [308] demonstrated that, at lower pH within the alkaline range, the rate of hydrolysis of Si-O bonds is slower than the passivation of the reactive surface by the just-released cations. This agrees with the suggestion that Ca-rich altered layers are formed in lower alkalinities, while at higher pH, hydrolysis is more significant, thus increasing the release rate of Si into a congruent regimen with Al - note that, at 2 h, Si/Al increases with molarity of solution.

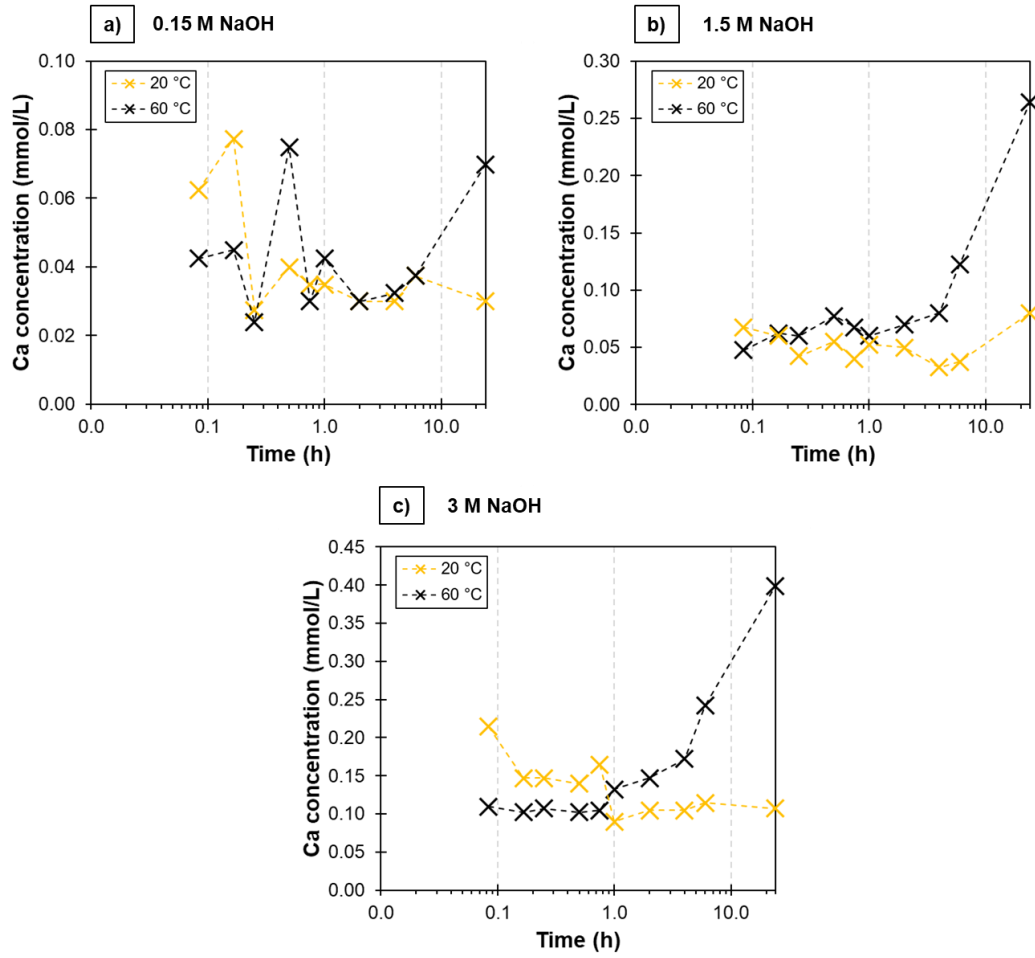


Figure 4.12: Temporal evolution of Ca concentration, measured in dissolution experiments of glass Si-FA (20 °C and 60 °C) at different concentrations of NaOH: a) 0.15 M; b) 1.5 M; and c) 3 M.

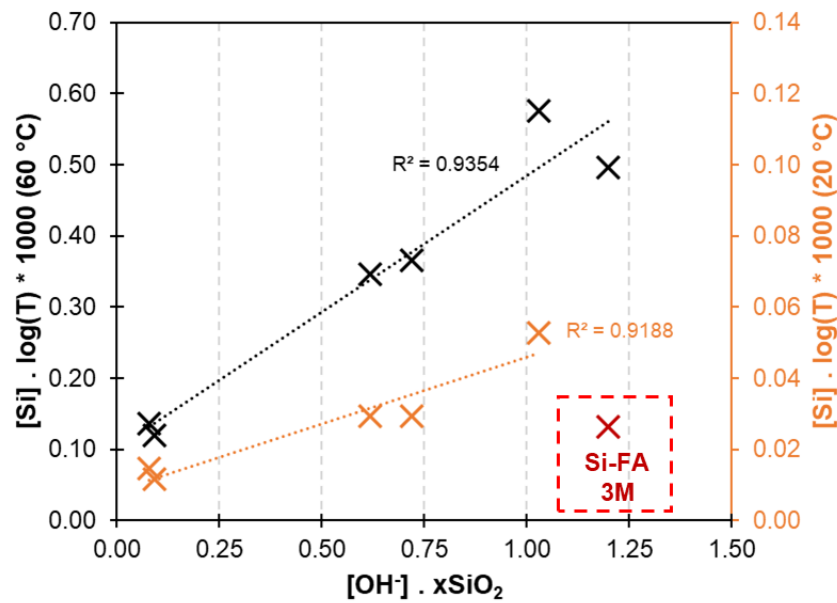


Figure 4.13: Coupled influence of pH (denoted by the calculated OH^- concentration with GEMs) and temperature (K) on the dissolution of Si measured at 24 hours, normalized to its original fraction - $[\text{Si}]$ is the measured concentration of Si, $[\text{OH}^-]$ represents the calculated concentration of OH^- according to the molarity of the solution, and $x\text{SiO}_2$ represents the molar fraction of SiO_2 in the original glass composition.

Table 4.5: Normalized Si/Al ratios in fly ash-glasses measured at 2 and 24 hours of dissolution experiments.

Molarity	Glass	Normalized Si/Al ratio - 2 h		Normalized Si/Al ratio - 24 h	
		20 °C	60 °C	20 °C	60 °C
0.15 M	Si-FA	0.75	0.93	0.79	1.06
	Ca-FA	0.83	0.89	0.76	1.02
1.5 M	Si-FA	1.11	1.05	0.70	1.04
	Ca-FA	0.79	0.91	0.60	0.99
3 M	Si-FA	0.80	1.03	0.57	1.03
	Ca-FA	0.83	1.00	0.58	0.99

4.3.4 Determination of forward dissolution rate equations

The results reported in this section were used for the empirical determination of equations that predict the forward dissolution rates of Si, Ca and Al, accounting for chemical compositions, temperature and characteristics of the solution. These derivations also considered experimental data reported in literature by different authors in similar conditions. The forward dissolution rate (r_+ [$\text{mol}/\text{m}^2 \cdot \text{s}$]) of one individual component within the overall glass structure is defined by equation 4.7 [330,331]:

$$r_{+,x} = \frac{d(x)}{\Delta t} \cdot \frac{V}{m \cdot SSA} \quad (4.7),$$

accounting for the linear change in concentration of x with time ($d(x)/\Delta t$, [$\text{mol}/\text{L} \cdot \text{s}$]), the initial mass of the whole compound (m [g]), the volume of the solution (V [L]), and the initial specific surface area of the compound (SSA [m^2/g]). This rate represents the amount of leached material - in the present case, the amount of each component oxide that was released from the framework - relative to time, normalized by the surface area of the reacting glass, during the steady dissolution period. The calculated dissolution rates include a propagated experimental error of $\pm 25\%$, as discussed by Snellings and Schöler [148,184], accounting for approximated variations of $\pm 20\%$ in the specific surface area of the glasses and $\pm 10\%$ in the measured element concentration in the leachate solutions.

4.3.4.1 Forward dissolution rate of Ca

In the previous sections, the forward dissolution rate of Ca was observed to be influenced by three factors:

- The fraction of Ca in the original raw material,
- The pH of the solution, indicated by the NaOH molarity, and
- The temperature of the experimental setup.

The influences of pH and temperature have been explored in the dissolution of both crystalline minerals [332-334] and glasses [186,301,310,314,331,335] utilizing different forms of Arrhenius-type relationships. This approach suggests that the dissolution rates show a linear correlation with pH and an exponential correlation with the temperature of the reactive media, as shown in Equation 4.8:

$$r_+ = A \cdot a_{H^+}^n \cdot \exp\left(\frac{-Ea}{R \cdot T}\right) \quad (4.8),$$

where r_+ designates the forward dissolution rate, A stands for a pre-exponential non-temperature dependent parameter, a_{H^+} describes the influence of the pH of the media measured by the activity of hydrogen (H^+), n is the order of the reaction, Ea is the activation energy of the dissolution reaction, R is the universal gas constant, and T designates the absolute temperature. Unlike Equation 4.7, the present work considered the activity of OH^- (a_{OH^-}) to evaluate the influence of solution pH in dissolution phenomenon, as the used concentrations of NaOH were higher than usually found in literature for this topic - a_{OH^-} was determined through thermodynamic modelling (GEMS) simulating the initial conditions of each solution.

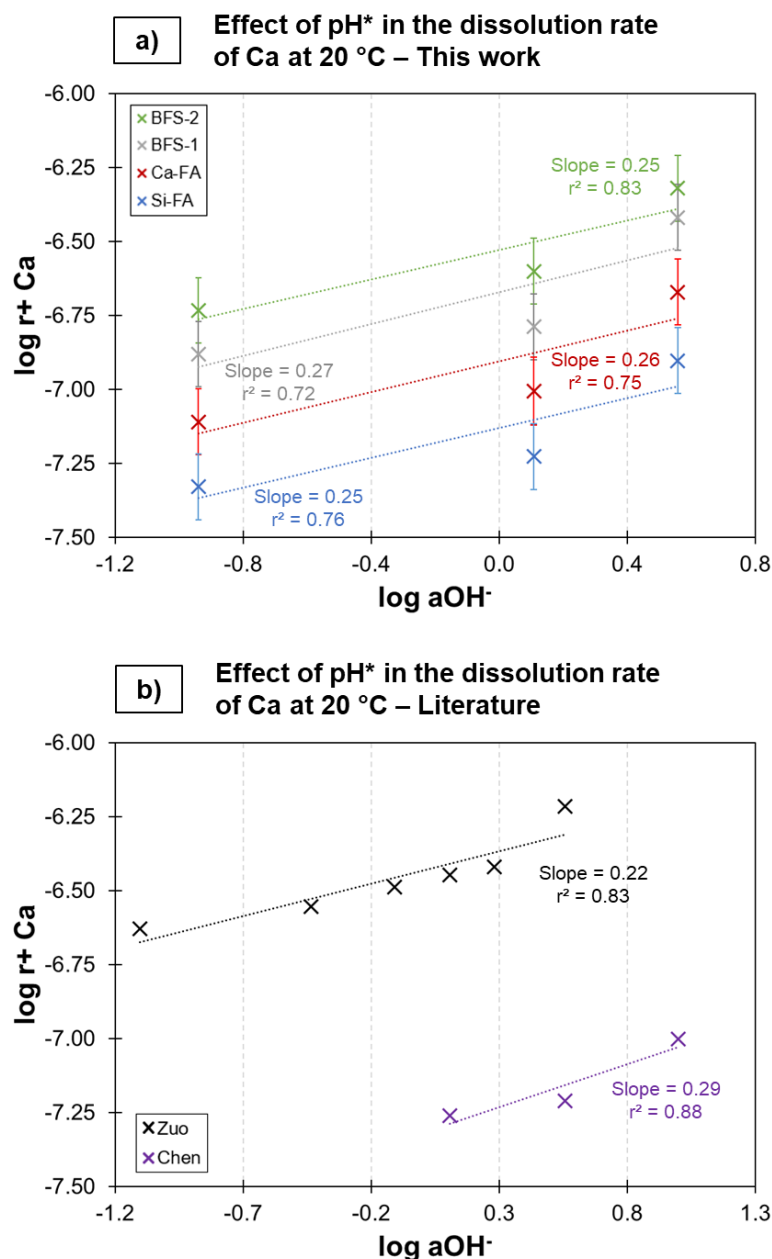


Figure 4.14: Correlation of the logarithm of forward dissolution rates of Ca with the logarithm of the activity of aqueous OH^- , at 20 °C, for a) synthetic glasses; b) commercial precursors from literature.

The chart in Figure 4.14 illustrates the impact of the OH^- activity in the leaching of Ca, which includes both the synthetic glasses produced in this work and additional data sets from literature: Zuo [175], who obtained dissolution rates of one commercial slag at different NaOH concentrations (0.1 - 3 M) at 20 °C; and Chen (data to be published, obtained in the same laboratory), who performed dissolution experiments with commercial fly ash in different NaOH concentrations (1.5 M - 5 M) at different temperatures - see Appendix D for more details. For all the evaluated samples, the plots indicate a positive linear correlation of the logarithm of the dissolution rate with the logarithm of a_{OH^-} . Figure 4.14a shows the behaviour of the synthetic glasses produced in this work, and Figure 4.14b shows the correlations observed for the results reported in literature. In the two charts, the six calculated trendlines presented approximately the same slope, with a mean average of 0.26 ± 0.02 .

The strong agreement observed among the experimental setups, including this work and those of other authors, suggests that the slope can empirically define the order of the reaction influencing the activity of OH^- . By implementing this correction factor in the pH of the solution, it was possible to verify the effect of the initial chemistry of each raw material in their respective Ca dissolution rates. The plots in Figures 4.15a (this work) and 4.15b (Zuo and Chen) illustrate the correlation of the forward dissolution rates with the corrected values of a_{OH^-} . While the two parameters presented a positive linear correlation among them, the trendlines of the six datasets showed differences in their respective slopes. It was observed that the trendlines belonging to slag-type glasses and the commercial slag had larger angles, strengthening the significant impact of the content of Ca in its initial release. This observation allowed the derivation of a linear relationship between the slope of each trendline and the fraction of Ca of the reactive materials, illustrated in Figure 4.15c - the Ca fraction of the commercial precursors considered their amorphous compositions.

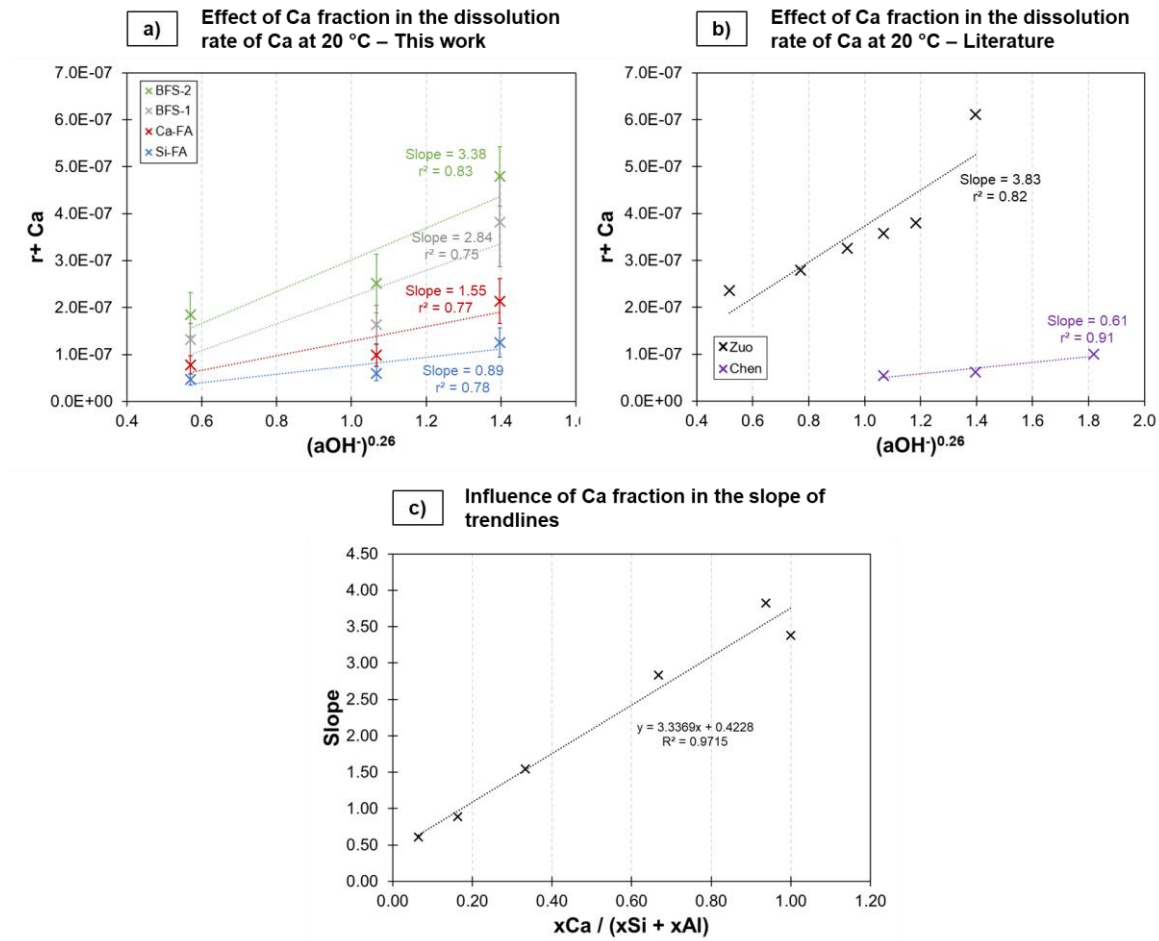


Figure 4.15: Correlation of the forward dissolution rates of Ca with the reaction order corrected activity of aqueous OH^- , at 20 °C, for a) synthetic glasses; b) commercial precursors from literature; c) influence of fraction of Ca in the slope of the individual trendlines shown in the previous plots.

It is understood that the linear equation of the trendline shown in Figure 4.15c represents the pre-exponential factor of an Arrhenius-type relationship, indicating that the chemistry of the raw material has an additional influence on the activity of OH^- in dissolution reactions. Based in the present observations, Equation 4.9 was empirically derived to estimate the forward dissolution rates of Ca at 20 °C considering the influence of the pH of the reactive media (indicated by a_{OH^-}), the reaction order (0.26), and the Ca fraction of the precursor under reaction, where x_{Ca} , x_{Si} and x_{Al} indicate the fractions of Ca, Si and Al in the composition of the glasses, respectively.

$$\log r_{+,Ca} = 0.26 \cdot \log(a_{OH^-}) + \log\left(3.3369 \cdot \frac{x_{Ca}}{(x_{Si} + x_{Al})} + 0.4428\right) \quad (4.9),$$

The influence of temperature in the early release of Ca in fly ash-type glasses is illustrated in Figures 4.16a (Si-FA) and 4.16b (Ca-FA). These plots show the correlations between the logarithm of forward dissolution rates with the alkalinity of the solution, with the latter considering the activity of OH^- corrected by both the empirical reaction orders and the influence of the pre-exponential factor (Ca-fraction based) previously determined. Similarly to the effect on the leaching of Si, shown in Figure 4.13, linear trendlines with higher slopes were obtained for the experiments carried out at 60 °C. Nearly-identical patterns were observed for the two glasses, as the slopes of the trendlines were significantly similar for both Si- and Ca-FA glasses at each respective temperature.

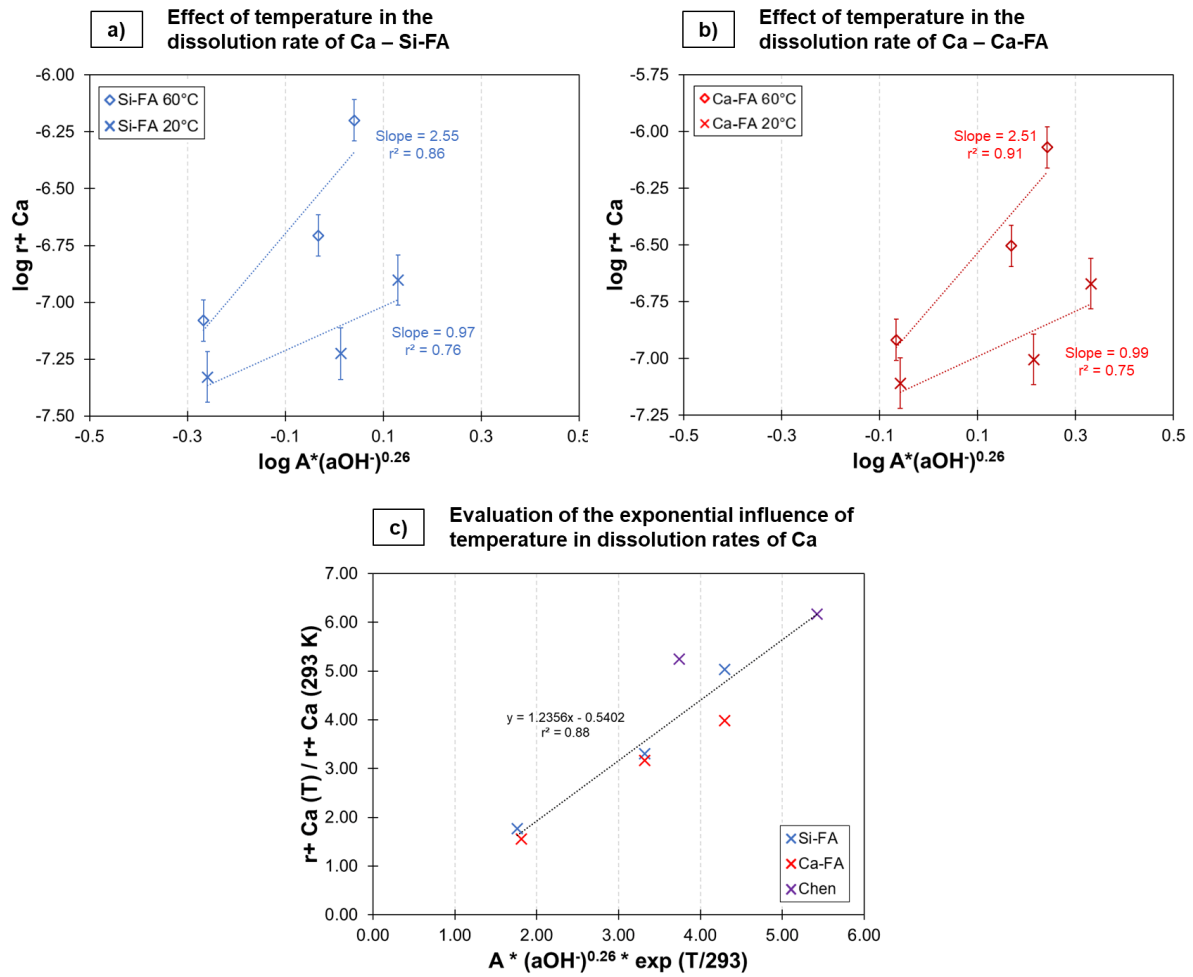


Figure 4.16: Influence of temperature in the forward dissolution rates of Ca in fly ash-type glasses: a) glass Si-FA; and b) glass Ca-FA; c) influence over the reference temperature of 293.15 K.

In an Arrhenius-type relationship, the exponential influence of temperature requires the determination of the activation energy of the reaction. Typically, the empirical definition of the activation energy of a system utilises datapoints obtained at multiple temperatures for an accurate estimation. However, for a same material, this parameter has been previously demonstrated to display variations according to the pH of the reactive media [333,336,337], inducing an additional challenge on empirically-defined correlations. In the present work, the determination of the activation energies of the dissolution reactions was not performed due to a combined limitation of tested temperatures with the use of more than one solution alkalinity. Conversely, the influence of temperature in the dissolution rates of Ca was performed through a direct correlation of the experimental results obtained at 60 °C - $r_{+,Ca}$ (333.15 K) - versus results obtained at 20 °C - $r_{+,Ca}$ (293.15 K). By considering the former as variable and the latter as reference temperatures, the plot in Figure 4.15c presents the relationship between dissolution rates and the product of $A \cdot (a_{OH^-})^{0.26}$, corrected by an exponential term correlating a ratio of the two temperatures, considering the experimental data obtained in this work and the data from Chen obtained at 40 °C and 60 °C.

The high coefficient of determination ($r^2 = 0.88$) observed in the trendline in Figure 4.15c suggests that the proposed temperature correction term can be implemented for the

empirical definition of forward dissolution rates of Ca. By combining this observation with the previously defined parameters, Equation 4.9 was modified to consider, in addition to solution alkalinity and precursor chemistry, the influence of temperature in the empirically defined Equation 4.10:

$$\log r_{+,Ca}(T) = \log \left(3.3369 \cdot \frac{x_{Ca}}{(x_{Si} + x_{Al})} + 0.4428 \right) + 0.26 \cdot \log(a_{OH^-}) + \log r_{+,Ca}(293.15 \text{ K}) + \frac{T}{674.78} + 0.092 \quad (4.10),$$

where T indicates the absolute temperature of the system (K), and T_{ref} indicates the reference temperature (293.15 K).

4.3.4.2 Forward dissolution rates of Si and Al

The data obtained in this work allowed for establishing a correlation between the dissolution rates of all the analysed elements from the original precursors. As the overall dissolution begins with ion exchange reactions of modifying oxides, the calculated forward dissolution rates of Si were observed to be linearly correlated with values obtained for Ca, corrected by the influence of temperature. It is worth noting that direct correlations between the dissolution of Si with glass chemistry and temperature, following a similar pattern as described in the previous section, were not achieved. The relationship displayed in Figure 4.17a included the same reported data set from Zuo and Chen, confirming the accuracy of these empirical observations in different scenarios.

Finally, a correlation between dissolution rates of Si and Al was established based on their initial fraction of each element on the reacting precursor. It should be emphasized that, following the discussion on selective Al dissolution from the Section 4.3.2, the plot in Figure 4.17b demonstrates that Al tends to leach at higher rates than Si, with all values clustering in the upper half of the chart. By the combination all the declared correlations, equations 4.11 and 4.12 were empirically defined for the forward dissolution rates of Si and Al, respectively:

$$\log r_{+,Si} = 0.9373 \cdot \log r_{+,Ca} \cdot \left(\frac{293.15}{T} \right) - 0.5673 \quad (4.11),$$

$$\log r_{+,Al} = \frac{0.6516 \cdot \log r_{+,Si} \cdot x_{Si} + 0.2523}{x_{Al}} \quad (4.12).$$

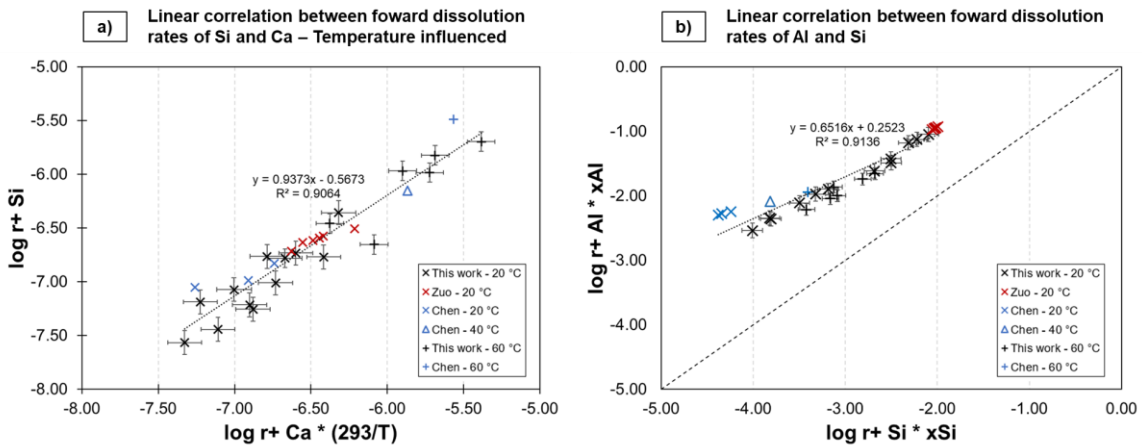


Figure 4.17: Correlations established during dissolution experiments: a) forward dissolution rates of Ca versus Si; and b) forward dissolution rates of Si versus Al.

4.4 Discussion

4.4.1 Selective dissolution of Ca- and Al-species

In literature, the dissolution of glasses and minerals is often reported as a unique rate, which indirectly implies the assumption of stoichiometric release for all components [332,334]. However, this research demonstrated that this is not always the case, as elements were detached from the framework at different rates, influenced by the initial glass chemistry and conditions of the reactive solution. In multi-oxide minerals, the overall dissolution process should be a combination of individual relative dissolution rates credited to each component [338,339], and the same analogy can be implemented to multi-component glasses. Since there is more than one pathway of network breakage that can take place [340,341], the dissolution of multi-component glasses is favoured in comparison with single oxide compounds.

In alkaline environments, congruent dissolution of cations from multiple-oxide precursors has been reported by a few authors [59,176,292], but inter-elemental relationships change according to the composition of the amorphous portions. Using synthetic glasses, Snellings [184] demonstrated that the release of Si was congruent with Al in compositions resembling slags and fly ashes, but Ca leaching was accelerated in fly ash-like samples. Incongruent dissolution of highly polymerized glasses is somehow expected. As stated previously, dissolution starts with ionic exchanges, usually between hydrogen protons and metallic cations [113,189]. In fly ash glasses, the low initial CaO content results in a limited presence of Ca^{2+} as charge compensator, allowing a significant portion of Ca atoms to behave as a disruptive agent in the initial structure [151]. When assuming the role of network modifier, Ca^{2+} is mainly coordinated by NBOs, while bridging oxygens and charge compensation in AlO_4^- sites promote a stronger ionic behaviour of Ca-O bonds [342]. Therefore, modifying cations are more weakly bound to the overall framework than charge compensating cations, facilitating the exchange with H^+ , and leading to higher immediate leaching.

When plotting the concentrations of Ca versus Si measured at 6 hours, normalized to their initial contents, differences in reaction mechanisms are more clearly observed - the choice for a period of 6 hours is to maintain all data points still within the steady dissolution period. As shown in Figure 4.18, fly ash-related data points are found in the lower right side of the chart, which denote the more significant release of Ca over Si, while slag-glasses data points are closer to the line that determines congruent dissolution - i.e. $[\text{Ca}]/\text{Ca} = [\text{Si}]/\text{Si}$. It can also be noticed that an increased pH favours a larger deviation from stoichiometric release, as datapoints referring to fly ash glasses dissolved with a 3 M NaOH solution are the most outliers in the plot. Following the assumption previously made, the excess Na^+ cations in higher alkalinity solutions accelerates Ca leaching in fly ash glasses, as a significant portion of Ca atoms are bound to NBO rather than forming strong ionic Ca-O bonds and are therefore available for ion exchange.

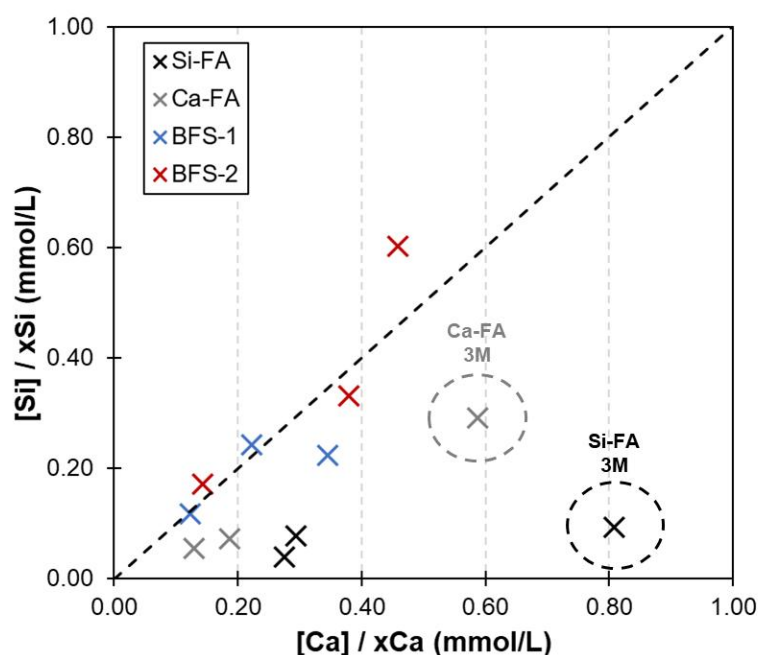


Figure 4.18: Dissolution rates of Ca and Si measured at 20 °C, relative to their initial fractions (xSi and xCa) in synthetic glasses.

The conclusions from Chapter 3 stated that, at sub-microscopic levels, the structure of the synthetic glasses can be heterogeneous. The presence of isolated regions of the framework with distinct structures can therefore explain the non-congruent dissolution of Al compared to Si, which is not commonly reported in literature. Based on the dissolution experiments, the scheme shown in Figure 4.19 proposes the sequence of reactions leading to a favoured dissolution of Al:

- in AlO_4 sites which require charge compensation, ion-exchange occurs between one Ca^{2+} (or one Na^+ in Na-containing glasses) and one H^+ (step I), leaving a localized negative charge (step II);
- the presence of one non-neutral site attracts water and NaOH molecules more easily, favouring alkaline hydrolysis of AlO_4 on that region, but still leaving a localized negative charge (step III). Both H^+ and Na^+ are shown in the sketch as the two species are expected to favour bond breakage in alkaline solutions;
- a second alkaline hydrolysis reaction takes place in the same region, due to the unbalanced oxygen atom,
- releasing $\text{AlO}_2^-(\text{OH})_2$ to the media (step IV). This aqueous Al species can either
- dissociate into AlO_2^- , or consume more H^+ to form aluminium hydroxide, two highly reactive species which will further coalesce with other cations and precipitate new phases [113,339]. This preferential Al release was progressively more intense with increasing alkalinity, probably due to the excess of OH^- species in the solution.

This observation provides a clear explanation for the differences in the stoichiometry of the release of Al and Si observed in current study, as well as reported in literature, as the majority of authors performed experiments at limited alkalinity.

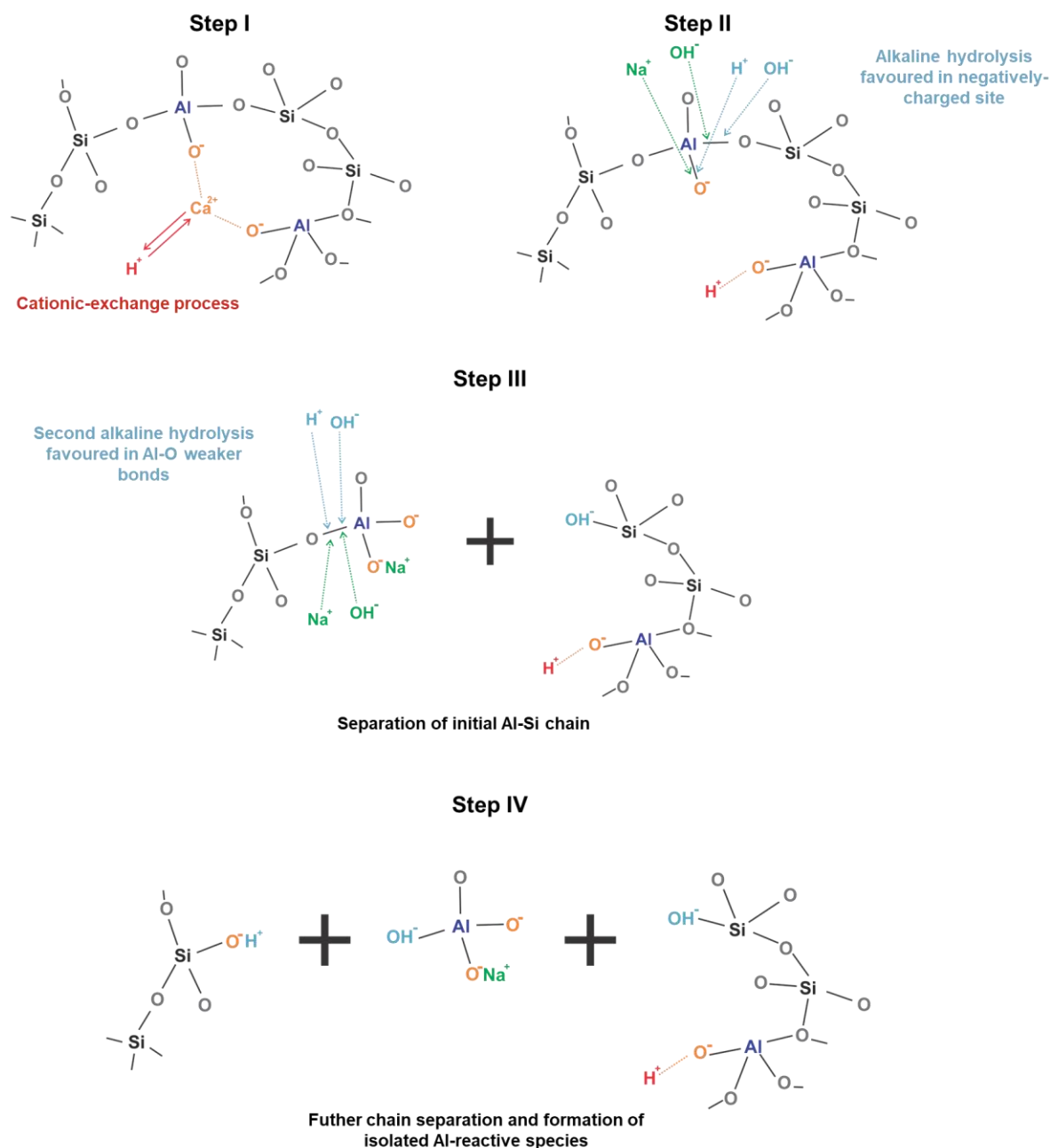


Figure 4.19: Schematic preferential dissolution of Al in CAS glasses.

4.4.2 Validation of dissolution rate equations

The forward dissolution rates defined in Section 4.3.4 were compared against the experimental values determined both in this research and by other authors [175,184]. Figure 4.20 shows the plot of the modelled dissolution rates of Ca, calculated using Equations 4.9 (20 °C) and 4.10 (40 °C and 60 °C), versus the experimentally determined values. An excellent match between modelled and experimental values was observed, with all points falling within a margin of ± 0.5 log units. Unlike what was reported by Zuo [175], the empirical equations proposed in this Chapter do not consider the ratio of NBO/T in the original glass network. As summarized in Chapter 2, the precise determination of this parameter can be complex and requires sophisticated techniques. Contrarily, the equation

defined in this Chapter indirectly considered this feature via the fraction of Ca in the unreacted precursor, which was shown to be the main influencing factor on the depolymerization of the network. This is visualized by the incremental increase of Si Q^0 and Q^1 units with increasing Ca content - see Figure 3.7 - and the presence of isolated Ca-Al glass structures of higher reactivity - see Section 3.4 for more details.

The modelled forward dissolution rates of Si and Al were also compared with experimental values from various authors. As illustrated in Figure 4.21a, a good agreement was maintained with respect to Si, as the majority of the data points fall within the stipulated ± 0.5 log units range. However, the results reported by Snellings [184] deviated more than the others, especially in the most extreme compositions, with modelled values overestimating the dissolution rates of Si in fly ash-type glasses. That author performed all dissolution experiments in an environment with a pH of 13, which can decelerate the release rate of Si. The empirical equation defined in this Chapter considered the present experiments, along with data from Zuo and Chen, which relied on solutions with higher alkalinity. The increased pH enhanced the potential of ion-exchange reactions, and consequently facilitated the detachment of Si from the framework in sequential stages. Therefore, it could be expected that these equations estimate a higher release of some species in milder alkaline conditions. As the initial pH in the pore solution of alkali-activated materials is usually maintained between 13.5 - 14.5 [175,343-345], it is reasonable to accept the predictions given by the defined equations, especially in the mentioned range. However, extending the upper and lower limits of investigated alkalinities could improve the accuracy of the proposed model in milder environments.

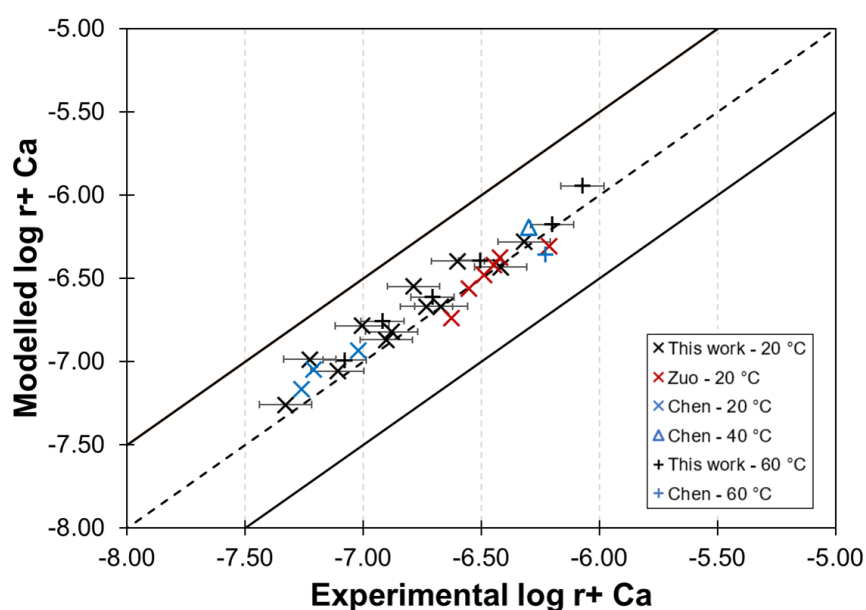


Figure 4.20: Comparison of experimental and calculated forward dissolution rates of Ca via the empirical equations defined in this work.

The relationship between modelled and experimental values of the forward dissolution rate of Al, seen in Figure 4.21b, showed the largest discrepancies among the three evaluated elements. The range of agreement was expanded to ± 1.0 log units, and larger variations were observed with the underestimation of predicted values. This was especially observed for the comparison of modelled vs. experimental data points obtained from the work of Zuo [175], who reported stoichiometric release of Al with respect to Si for commercial slag, and for the results from Chen obtained at 20 °C. With respect to the former, the slower predicted release of Al can be somehow expected if the dissolution rates of Si are considered. While that author reported congruent dissolution of Si and Al, the present results indicated that the dissolution of synthetic slags disfavoured immediate Si leaching, and the normalized release of Al was nearly two times faster - see Figure 4.8. Therefore, as the dissolution of Al is estimated based on Si-related rates, it is plausible that the modelled dissolution rates would slightly underestimate values given the slag composition in the work of Zuo.

Additionally, despite being slightly underestimated at room temperature, the experimental data from Chen displayed a similar behaviour to synthetic fly ashes. The data points for rates predicted at 60 °C are positioned in the upper part of the chart, highlighting the significant influence played by temperature in the dissolution of low-Ca precursors. In Section 4.3.3, it was demonstrated that, despite the NaOH molarity, the final normalized Si/Al ratios increased when comparing dissolution data obtained at 20 °C and 60 °C (Table 4.5), reaching values very close to 1.00. This leads to the conclusion that, at higher temperature, a congruent relationship between Si and Al is achieved, improving the accuracy of the modelled dissolution of Al at 60 °C.

Dissolution experiments are challenging to replicate in the exact manner across different setups. As comprehensively summarized by Thorpe et al. [287], the attempt to establish a common test to understand the degradation and dissolution mechanism of glasses, mainly driven by the field of nuclear waste disposal glasses, has led to the development of over 20 different methods through a continuous optimization, among standardized and non-standardized ones. However, an agreement towards one common setup that could cover all aspects of glass dissolution has not been yet achieved due to the many variables observed in these systems. Along with requiring great planning and assertive sampling time/treatment/storage, they rely on different steps that individually present experimental errors related to the operator and the equipment. The estimated error from 10 - 25 % in the measured elemental concentration of the leachate can lead to variabilities in the range of 0.15 - 0.20 log units in the calculated dissolution rates, as commonly used in literature and implement in this work. Additionally, a precise determination of specific surface areas is difficult to achieve. Different techniques used to determine the initial surface area, and the changes in the reactive surface are occurring during the experiment [287] can induce extra error factors into the determination and interpretation of dissolution rates. The normalization of the measured cation concentrations with respect to Brunauer-Emmett-Teller (BET) determined surface areas can lower the obtained rates by a factor of 2-3, as determined by Icenhower et al. [310,331]. The datasets presented in Figures 4.18 and 4.19 considered surface areas obtained using both techniques, which may explain some of the fluctuations observed in the trend behaviours.

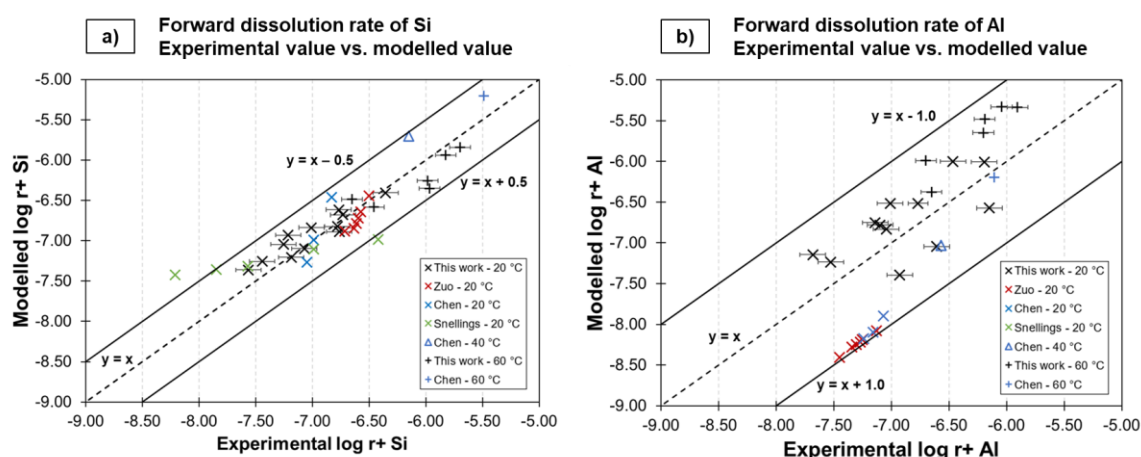


Figure 4.21: Comparison of experimental and modelled forward dissolution rates of: a) Si and b) Al.

4.5 Conclusions and outlook

The understanding of the dissolution period of precursors provides crucial information for optimizing processing conditions, allowing for the enhancement or delay of the initial reaction. This chapter focused on studying the factors influencing the release of elements from the network of synthetic precursors, evaluating how chemistry, alkalinity and temperature affect forward dissolution rates of Si, Ca and Al. From the obtained results, the following conclusions can be drawn:

- Leaching was observed immediately after contact of synthetic precursors with alkaline solutions, with Ca displaying the highest leaching rate during this non-steady period. Fly ash-type glasses showed enhanced Ca release within the first 2 hours of the experiment, suggesting that the element is more loosely bound to the glass framework when assuming the role of network modifier.
- The pH of the solution affected the dissolution rates in all glasses, with shorter steady dissolution periods observed at higher alkalinities. At room temperature, Ca displayed the same saturation level at 1.5 and 3 M NaOH solutions, as the final measured concentrations were the same in both conditions for glasses Si-FA and BFS-2. Ca was also observed to favour the formation of amorphous portlandite and carbonated phases, as ion-exchange processes favored the initial leaching of Ca before the release of Si and Al.
- Different dissolution mechanisms were observed depending on the chemistry of the precursor. In slag-type glasses, the enhanced dissolution of Si and Al was attributed to a less depolymerized structure. Raman spectroscopy revealed that hydrolysis reactions took place simultaneously at SiO_4 sites of all coordination levels, significantly impacting the continuity of aluminosilicate structures. Fly ash-type glasses displayed favoured initial disruption of ring structures, as the concentration of Si Q^4 was significantly reduced after dissolution, especially for glass Si-FA. The high packing density of the framework suggests that the depolymerization of highly-coordinated silicate sites is necessary prior to a significant hydrolysis of Si- and Al-O bonds.
- Raman spectroscopy suggested that Al exhibited selective dissolution in tetrahedral coordination. This occurs by the favoured breakage of Al-O bonds in AlO_4^- sites that

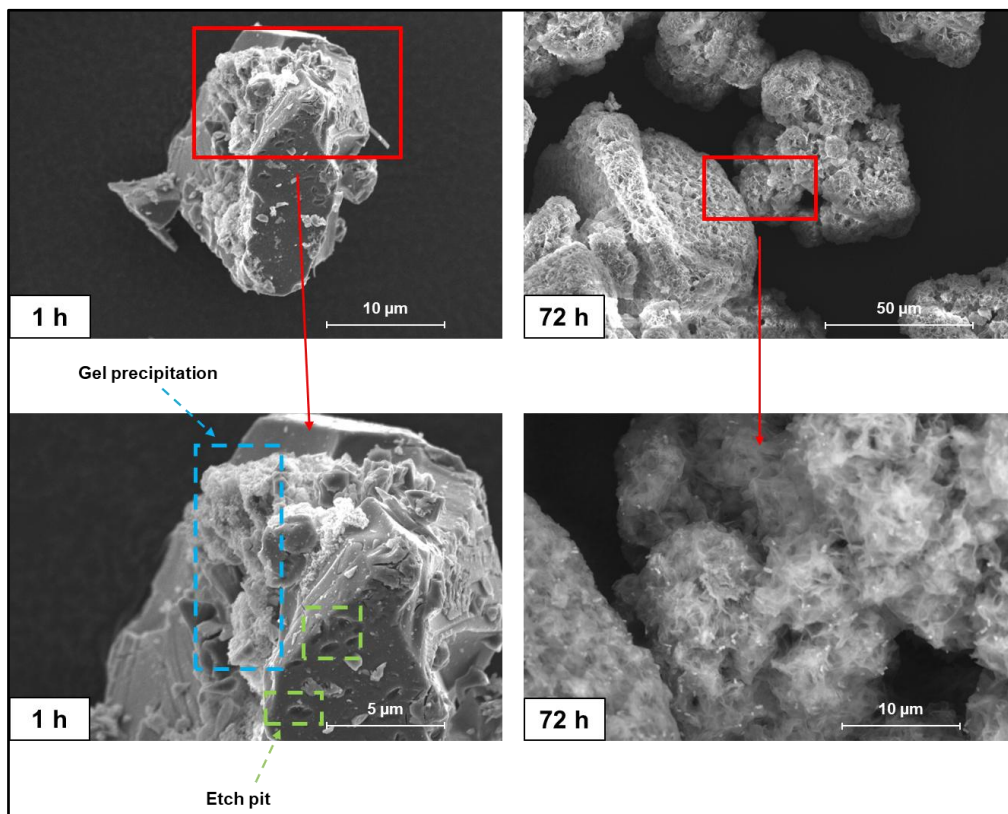
were charge balanced by Ca^{2+} cations, which appear to be weakened after the leaching of the latter in the ion-exchange stage. Additionally, clustered regions of Al-tetrahedra and $\text{SiO}_4\text{-AlO}_6$ were observed to suffer only minor modifications, showing that the Al-substituted tetrahedra sites (Al-modified cristobalite regions) are more likely to be disrupted in this period.

- Infrared spectra of residual glasses displayed signals of mullite-like structures in both BFS-2 and Si-FA glasses after dissolution. Moreover, the main Si-O-T band of glass BFS-2 was split in two distinct regions (Si-O-Al interactions and AlO_4 -rich residual structures), suggesting that phase separation plays an important role in the dissolution process.
- A congruent dissolution behaviour of Si with respect to Al was observed in fly ash-glasses at 60 °C, caused by accelerated dissolution rates due to the combined effect of alkalinity with temperature. The release of Ca was also enhanced, as higher temperatures promoted the dissolution of unstable nuclei of Ca-containing phases.
- Finally, the empirical determination of forward dissolution rates proved successful, showing satisfactory agreement when experimental data from four different authors. Mild differences were observed in the predicted behaviour of Si, with the equations slightly overestimating dissolution rates at lower alkalinity. In fly ash- glasses, the lack of observed congruent dissolution regimen may underestimate the dissolution of Al at 20 °C, but predictions at increased temperature validated the defined equations.

The results shown in this Chapter provide valuable insights into the kinetics and the residual structure of precursors after dissolution. The unexpected findings concerning the latter (portlandite precipitation and phase separation during dissolution) provide insights into mechanisms taking place in sequential stages, which will be explored in Chapter 5 of this thesis. The empirically defined equations showed to be suitable in considering the suggested selective dissolution processes, while displaying good agreement with other experimentally reported values in alkaline environments. Finally, it should be kept in mind that the formation of altered layers or activated complexes could have impacted the dissolution rates to some extent, which was not possible to be quantified. This subject will be considered in Chapter 8, during the modelling of dissolution rates according to numerical simulations.

Chapter 5.

Early-stage reactions of alkali-activated synthetic precursors



The early stages of reaction of alkali-activated materials is directly correlated to the microstructure development of each formulation, having direct impact in their behaviour as fresh mixtures and in the evolution of properties during the stages of hardening. The combined choices of activator and precursor with curing procedures dictate the mechanisms of phase precipitation, affecting among others, the pore solution, strength development, porosity distribution and overall stability of the systems under reaction. This Chapter aims to correlate the dissolution kinetics of synthetic precursors with the first moments of microstructure development, correlating the elemental leaching at initial stages with the saturation and development of the initial reaction products. At the end, the influences of temperature and activator in slag-type and fly ash-type glasses is given, and a distinction between homogeneous and heterogeneous precipitation is concluded through a combination of different experimental techniques aided by visualizations made through scanning electron microscopy.

5.1 Introduction

As discussed in Chapter 4, the dissolution process of precursors in alkaline media is either coupled with, or immediately followed by the precipitation of new solid phases. Understanding the nucleation mechanisms and the nature of these initial solid products is essential, as these phases provide insight into the ongoing reaction stages (both continuous dissolution and growth of reaction products) and strength development. In that sense, the study of early-stage properties is as important as the evaluation of long-term performance and durability of AAMs, given the strong impact they play on the fabrication routes and on the nature of the application of these materials [177,346]. For instance, the precipitation and distribution of reaction products have a great impact on the rheology and the development of yield stress in fresh mixtures [104,114,115,347]. A proper understanding of these phenomena could support the tailored design of mixtures and fabrication processes.

The illustration in Figure 5.1 schematically shows a general correlation between the evolution in heat release and the mechanisms of dissolution phase precipitation in alkali-activated systems. After the first contact of the precursor with the alkaline solution, the initial system transits through the wetting and dissolution period (I.), a physical phenomenon involving the coupled cation leaching and initial complexation of reactive species into nuclei of new solid phases [205,348] during the forward dissolution regimen [189] - see Chapter 4 for more details. This accelerated dissolution is then slowed (I. - II.), as surrounding media becomes supersaturated with certain species, lowering the chemical affinity for the continuity of dissolution. This moment, characterized by the *induction period* (II.), can be strengthened by the formation of passivating layers on the surface of precursors - whether this layer is formed or not is dependent on the chemistry of the raw material and alkalinity of the solution [328,349]. The following stages involve different chemical phenomena and occur due to the precipitation of new reaction products (III.) and the growth of initially nucleated phases (IV.), representing the *acceleration peak* in calorimetry tests. The reaction then shifts into diffusion-controlled processes, similar to the fourth period observed in calorimetric curves (see Figure 2.10), which will lead to the growth and stabilization of solid products [189,350]. Moreover, the formation of new phases represents the consumption of aqueous species, bringing them again into undersaturated conditions. The chemical affinity for dissolution of the precursor is again increased, which can lead to a second, but slower, element release [288,351].

Early-stage properties, whether related to consistency or strength development, can be influenced by both external factors and intrinsic characteristics of the raw materials. Among the external factors, high pH environments and implementation of temperature favour the initial dissolution of glasses and accelerate the precipitation of new solid phases. By studying the evolution of rheology in fresh alkali-activated fly ash pastes, Kashani et al. [352] found that, at room temperature, the use of alkali hydroxides accelerated the strength development of slag-based pastes compared to sodium silicate due to the higher alkalinity, while Sun et al. [353] reported an increase in viscosity and yield stress correlated with higher the silicate modulus of waterglass solutions. Similarly, Rifaai et al. [354] reported a progressively faster development of yield stress with higher molarity of NaOH solution. This, however, occurred up to a maximum concentration of 8 M, as higher molarities resulted in hindered polymerization despite the enhanced dissolution rate due to the supersaturation of reactive species, and stronger repulsive forces between particles. Additionally, the

authors stated that temperature has been concluded to impact the mechanical behaviour more significantly than the molarity of the solution. Palacios et al. [355], stated that a mild increase in silicate modulus, from 0 to 0.25, at 65 °C, was shown to increase the yield stress in 44 % whilst maintaining a similar activation energy of reaction, indicating that temperature enhances the reaction potential of waterglass without necessarily changing the reaction mechanism.

Among the intrinsic properties, the presence of alkali and alkali-earth elements is essential to disrupt the polymerized networks formed by Si-O bonds [113,143,158,356], and to accelerate the evolution of the microstructure. As an extrinsic factor, the increase in alkalinity of the activator has a similar influence, and both conditions play crucial additional roles in the chemistry of reaction products. For instance, Deir et al. [357] found that slag-based pastes, activated with waterglass and cured for 1 day at 50 °C, achieved approximately 2.5 and 2.8 times higher compressive strength values than pastes made with calcareous and siliceous fly ashes, respectively, with the same activator and curing conditions. Moreover, the authors reported that, with the same silicate modulus, increasing Na₂O content led to the formation of C-(A-)S-H gels with higher Ca/Si ratios in slag-based pastes. In a similar trend, Le Saout et al. [88], verified a change of Ca/Si from 0.89 to 0.82 in 1 day old alkali-activated slag pastes, when activated with NaOH and waterglass respectively, while the degree of hydration decreased from 47 % to 41 %. Al has also been shown to directly influence the phase assemblage of mortars and pastes made with synthetic glasses in the first three days of reaction, particularly increasing the formation of AFm phases [156,211]. In Ca-free systems, the Si/Al ratio of N-A-S-H gel has been found to follow the initial elemental ratios in a quasi-linear trend, as the NaOH-activation of sodium aluminosilicate synthetic glasses reached final ratios of 1.7 and 5.3 after 20 hours of curing at 80 °C (initial element ratios of 2.0 and 6.3, respectively).

With respect to the nature of initial reaction products, the distinction between the Ca-rich and other gels is hard to achieve, as hardened cementitious matrices are composed of a continuous mixture of different reaction products. A few authors have implemented phase segmentation through chemical analysis [108,177,210,214,358-361], which has showed to be helpful in the observation of secondary reaction products within the hardened matrix. With respect to hydrated gels, their nanoscale structural arrangements imposes extra challenges, as they are usually intermixed forming agglomerated regions composed of several gels with different chemical compositions. The implementation of selective dissolution based on a combination of salicylic acid and methanol (SAM), suggested initially by Takashima [362], can be used on an attempt to quantify the amount of each gel. This treatment is considered suitable for the dissolution of Ca-containing amorphous and short-range ordered structures, such as C-S-H, C-A-S-H and C-N-A-S-H. In longer curing periods, SAM dissolution has been successfully used for the qualitative study and quantification of N-A-S-H gel in alkali-activated blends of slag and fly ash [210,363]. In a system composed of only SiO₂, CaO, and Al₂O₃, selective dissolution becomes an important tool to distinguish nucleation paths of each phase, as the amount of secondary products becomes limited. However, it should be noticed that this environment can produce an aggressive media, which can also partially dissolve small agglomerates of aluminosilicate structures which do not contain Ca as charge balancing cation [364].

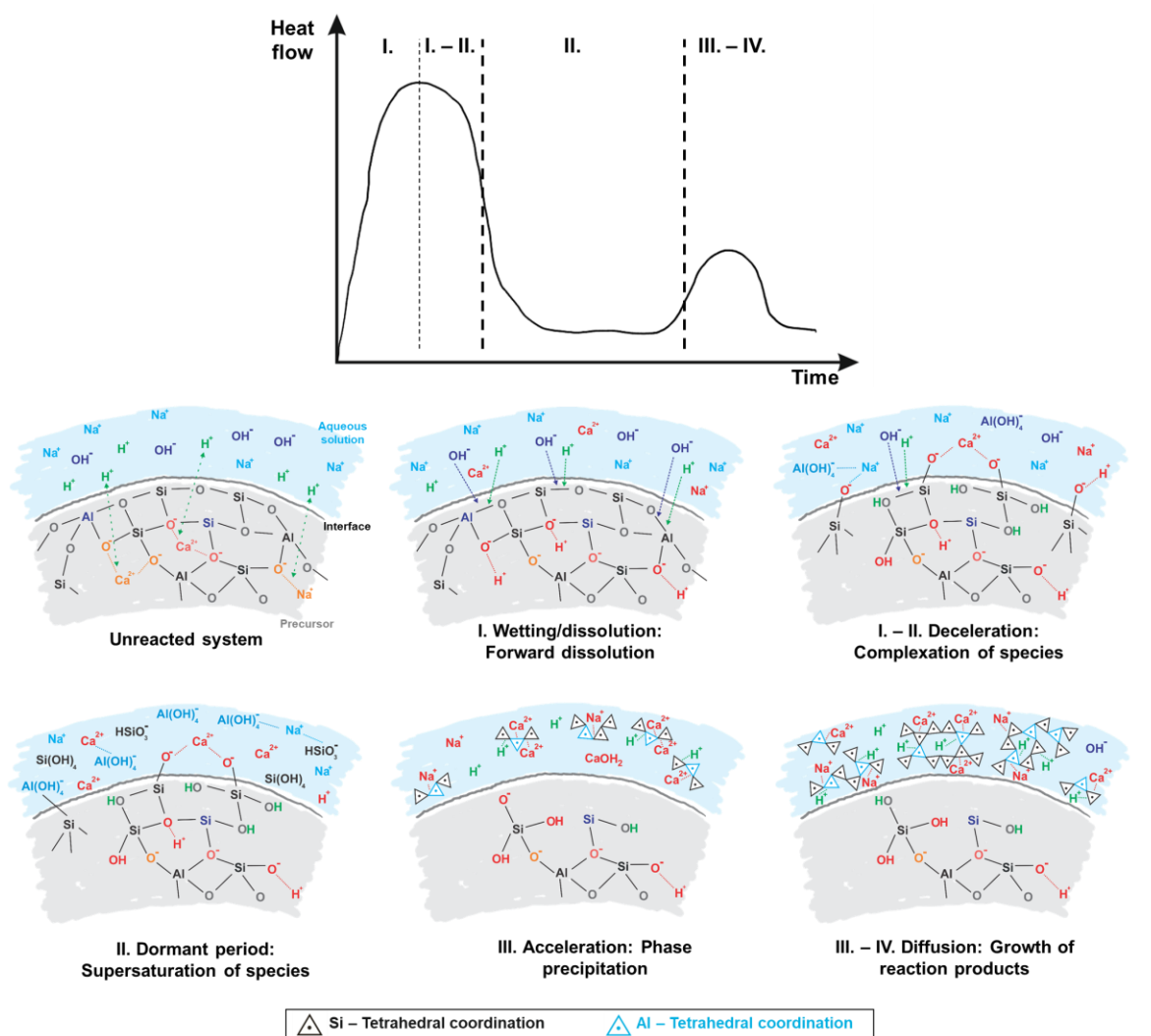


Figure 5.1: Schematic correlation between precursor mechanisms of dissolution and phase precipitation and isothermal calorimetry curves in alkali-activated systems.

The available literature highlights the influence of chemical composition on the overall reactivity of alkali-activated binders. It is still not clear how composition affects the kinetics of phase nucleation and growth after initial element release in the first steps of dissolution. In order to understand the mechanisms involved in the early stages of alkali-activation, this Chapter investigates the effect of chemistry on the precipitation of phases in the initial stages of alkali-activation reactions. The realization of dissolution experiments in alkaline solutions of synthetic glasses with simplified composition, similar to siliceous and calcareous fly ashes and blast furnace slags, and the study of residual solid material, provided a detailed assessment of the influence of each element on initial reaction mechanisms of AAMs. The study demonstrated distinct paths on the formation of reaction products according to the initial characteristics of the precursor, indicating that small changes in chemistry can have large impacts on the development of properties of alkali-activated binders. The results obtained in this Chapter will be used as basis for understanding the reaction path of different mixtures and their influences at later stages of the microstructure, and will support the validation of the microstructure modelling tool, which will be described in Chapter 7. Figure 5.2 shows the position of Chapter 5 within the study of microstructure evolution in this thesis.

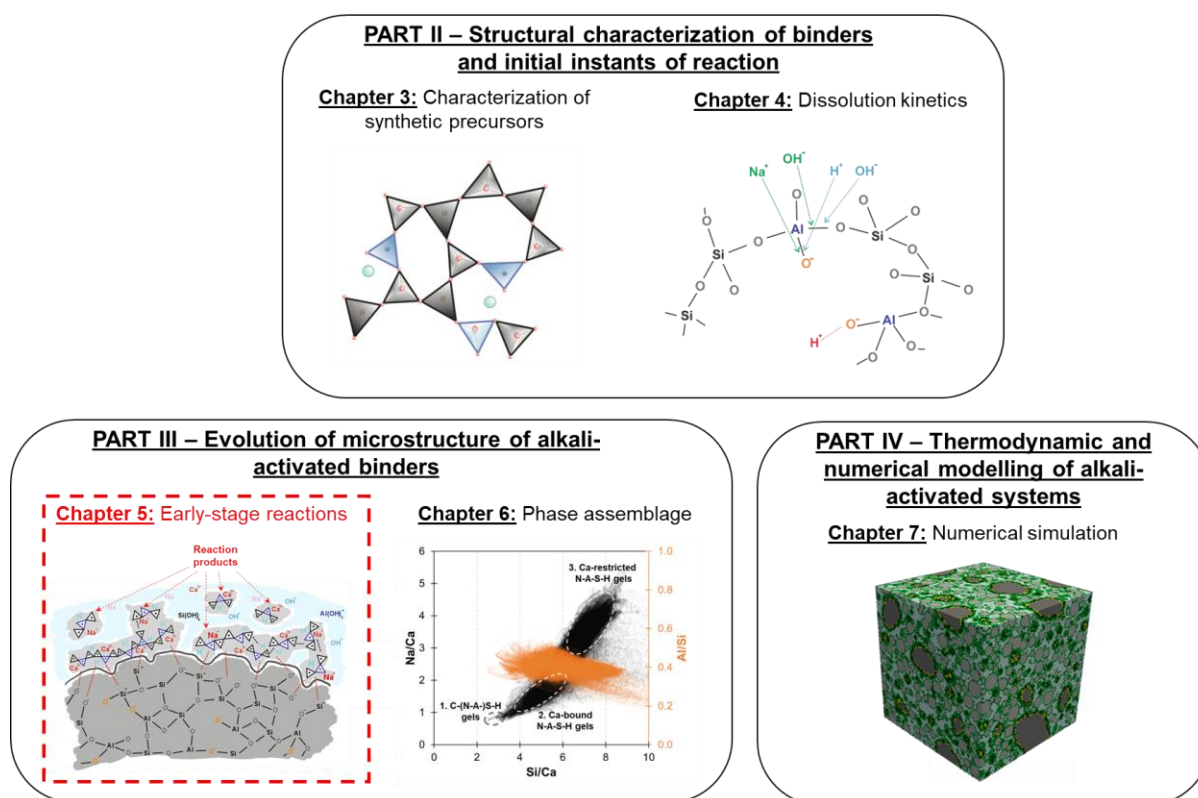


Figure 5.2: Schematic illustration of the structure of this thesis, highlighting the contributions of Chapter 5.

5.2 Materials and methods

5.2.1 Preparation of coarse synthetic precursors

The synthetic glasses used in this chapter were obtained as part of the melting/quenching procedures described in Chapter 3. As the goal of this experimental campaign was to observe the initial precipitation of reaction products, fine glasses were used to accelerate the dissolution and promote the nucleation of new phases. The synthetic glasses were prepared following the procedure described in Section 3.2.1 in Chapter 3. After quenching and drying, glasses were ground and milled until the obtainment of a d_{50} size of approximately 25 μm . Similar to the description in 4.2.1, the particle size distribution was measured by laser diffraction. Two different batches of glasses were used in this chapter: the first batch, consisting of all four synthetic glasses, was used for dissolution experiments of fine particles; the second batch was used for the preparation of pastes, by alkali-activating the glasses Si-FA and BFS-2. The compositions of each batch along with physical particle characteristics are detailed in Table 5.1, and the particle size distributions are shown in Figure 5.3. These compositions comprise the several batches of synthetic glasses prepared throughout this thesis, as described in Section 3.3.

Table 5.1: Chemical composition, measured by X-ray fluorescence, and physical characteristics of the synthetic glasses used for dissolution experiments and for casting pastes.

	Glass	Normalized* content (mol)			d_{10}	d_{50}	d_{90}
		SiO ₂	Al ₂ O ₃	CaO	(μm)	(μm)	(μm)
Dissolution	Si-FA	1.00	0.32	0.23	4.81	27.54	61.63
	Ca-FA	1.00	0.33	0.49	5.10	28.70	58.72
	BFS-1	1.00	0.33	1.00	3.93	23.46	58.86
	BFS-2	1.00	0.39	1.39	3.94	22.01	52.16
1-day paste	Si-FA	1.00	0.31	0.25	4.23	26.08	58.42
	BFS-2	1.00	0.25	1.53	5.10	22.15	57.99

*Normalized to the content of SiO₂.

5.2.2 Dissolution experiments and study of residual dissolution material

The study of dissolution kinetics performed in this chapter followed a similar procedure to the experiments described in Section 4.2.2 in Chapter 4. The main difference between the two experimental campaigns was in the particle sizes of synthetic glasses. While glass particles of d_{50} between 89 and 94 μm were implemented in previous Chapter, the present experiments evaluated the dissolution kinetics of finer particles, with a d_{50} of approximately 25 μm . The choice of lower particle sizes was made to promote the precipitation of reaction products in different conditions, as this Chapter aims to understand the effect of glass chemistry and activating solution into the phenomena of precipitation of reaction products.

Highly-diluted systems, with a liquid/glass ratio of 1000, were prepared in two different scenarios. A 1.5 M sodium hydroxide solution was prepared by the dilution of a 50 % commercial liquid NaOH (Brenntag, Dordrecht, Netherlands) in deionized water. A sodium silicate (waterglass) solution, maintaining the same Na₂O concentration and a silicate modulus of 1.5, was prepared by the mixture of NaOH with a commercial waterglass solution (PQ Corporation, Eijsden, Netherlands. SiO₂ = 30.5 %; Na₂O = 15.0 %; H₂O = 54.5 %) and deionized water. Using NaOH, the four glasses were submitted to test at room temperature (20 \pm 5 °C), while Si-FA and Ca-FA were dissolved at 60 °C, in a closed shaking incubator with controlled temperature. With waterglass, Si-FA was tested at room (20 °C) and high temperature (60 °C), and glass BFS-2 was tested only at 20 °C. In each system (glass + solution), samplings were collected after 1, 24 and 72 hours of experiment, and separate setups were prepared for each sampling time. The temporal evolution in concentrations of Si, Al and Ca, and the calculations of effective saturation indices of the main reaction products were performed using the same procedures described in Sections 4.2.2 and 4.2.3, respectively.

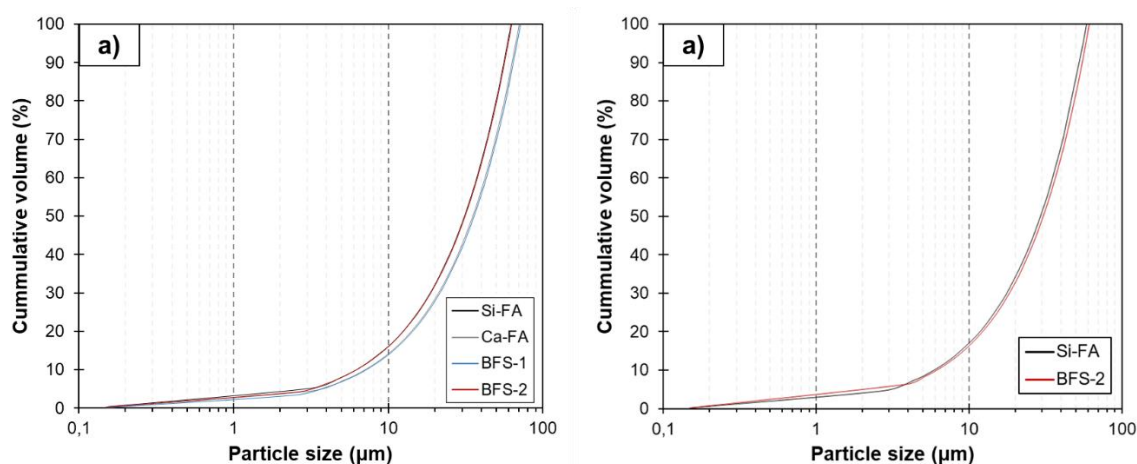


Figure 5.3: Particle size distribution of glasses used for: a) dissolution experiments; and b) preparation of pastes.

After sampling the liquid phase from each dissolution setup, residual solid material was collected by vacuum filtration of the entire solution. The remaining material was washed with deionized water for two times, immersed in isopropanol for 24 hours, filtrated again, and stored in a vacuum desiccator prior to analysis.

5.2.2.1 *In-situ isothermal calorimetry of alkali-activated pastes*

A total of 6 pastes were prepared by the alkali-activation of glasses Si-FA and BFS-2. In order to simulate the environment promoted by dissolution experiments, two activating solutions were formulated: system N8S0 consists of NaOH solution with 8 wt% Na₂O with respect to the mass of synthetic glass, and system N8S12 consists of a waterglass solution with the same amount of Na₂O and a silicate modulus of 1.5. In-situ calorimetry tests were performed using a TAM Air calorimeter (TA Instruments), and data referring to heat release of each paste was collected for 24 hours. Glass BFS-2 was subject to activation in both N8S0 and N8S12 systems at 20 °C, while pastes with glass Si-FA were mixed with each activating solution and cured at 20 °C and 60 °C. For the preparation of in-situ conditions, the glass powders were kept in a glass ampoule inside the equipment at the desired temperature for 24 hours prior to mixing, and the activator was kept in a syringe. After this period, the activator was injected into the glass ampoule, and the pastes were mixed for three minutes with an external stirrer, allowing the recording of the calorimetric response from the onset of reaction.

After each calorimetry test, the pastes were removed from the sample holders, crushed, and immersed in isopropanol for one week to stop the hydration. The crushed pastes were utilised for further characterization of microstructure.

5.2.2.2 *Characterization of residual materials from dissolution and calorimetry tests*

Following the methods described in Sections 3.2.2 and 4.2.2, the microstructure of the residual dissolution materials and the crushed pastes were analyzed using X-ray diffraction (XRD) (Bruker D8 Advance), differential thermogravimetric (DTG) analysis (Netzsch TG-449-F3-Jupiter), and attenuated total reflection Fourier transform infrared (ATR-FTIR)

spectroscopy (PerkinElmer Spectrum 100 FT-IR). Additionally, scanning electron microscopy (SEM) was performed to evaluate the surface conditions during early stage reactions of dissolution and the interface between unreacted particles and the cementitious matrix of pastes. Backscattered and secondary electron images were obtained with a FEI Quanta FEG 650 instrument with acceleration voltages between 5 - 15 kV. Both dissolution residue and crushed pastes were carbon coated prior to microscopic analysis.

5.2.2.3 *Selective dissolution treatment*

A selective dissolution treatment with salicylic acid and methanol (SAM) was performed to evaluate the mechanism of precipitation of N-A-S-H gel in the 1 day cured pastes. Following the procedures described by different authors [108,210,363,365], 1 g of crushed paste was dissolved for 2 hours in a solution containing 60 g of methanol and 4 g of salicylic acid. After the treatment, the solution was filtrated and the residual material was washed with methanol and dried at 105 °C for 2 h. The resulting powder was characterized using DTG and FTIR measurements, providing important structural information about the obtained N-A-S-H gel.

5.3 Results

5.3.1 Dissolution experiments in NaOH solutions at 20 °C

5.3.1.1 *Influence of glass chemistry in dissolution kinetics*

The evolution of elemental concentrations up to 72 hours of dissolution of fine glasses in NaOH solutions, measured at room temperature, is presented in Figure 5.4. It is possible to distinguish two different behaviours when comparing high- and low-Ca precursors. For the low-Ca precursors, (i.e., fly ash-type glasses), presented a continuous evolution of all elements through the experiment, with a more pronounced increase in Ca concentration seen from 24 to 72 hours - particularly in glass Ca-FA. Due to the higher initial fractions of Al and Si, these two elements had a stronger presence in the solution of the Si-FA sample at 24 h. After 72 hours, both elements presented virtually the same concentrations in the two fly ash-type glasses, indicating a similar reaction pattern in both precursors.

Conversely, the concentrations of Si and Al leached from high-Ca precursors (i.e., slag-type glasses) presented a steep increase, from 1 to 24 hours, and a deceleration (BFS-1) or a mild drop (BFS-2), from 24 to 72 hours. This behaviour indicates the consumption and coupling of the two cations with each other and with other species, suggesting that nuclei of new solid phases are formed within the first 24 hours of dissolution. In glass BFS-1, the concentration of Ca reached the maximum value after 1 day, while a continuous but slight depletion was measured for BFS-2 since the first sampling. It is well known that, with higher fractions of network modifying oxides, ion-exchange processes are enhanced, which leads to an acceleration of the initial leaching of these elements [182,297,349]. In this context, the higher fraction of CaO in BFS-2 favours a faster supersaturation of Ca^{2+} , and consequently accelerates its coupling with other aqueous species.

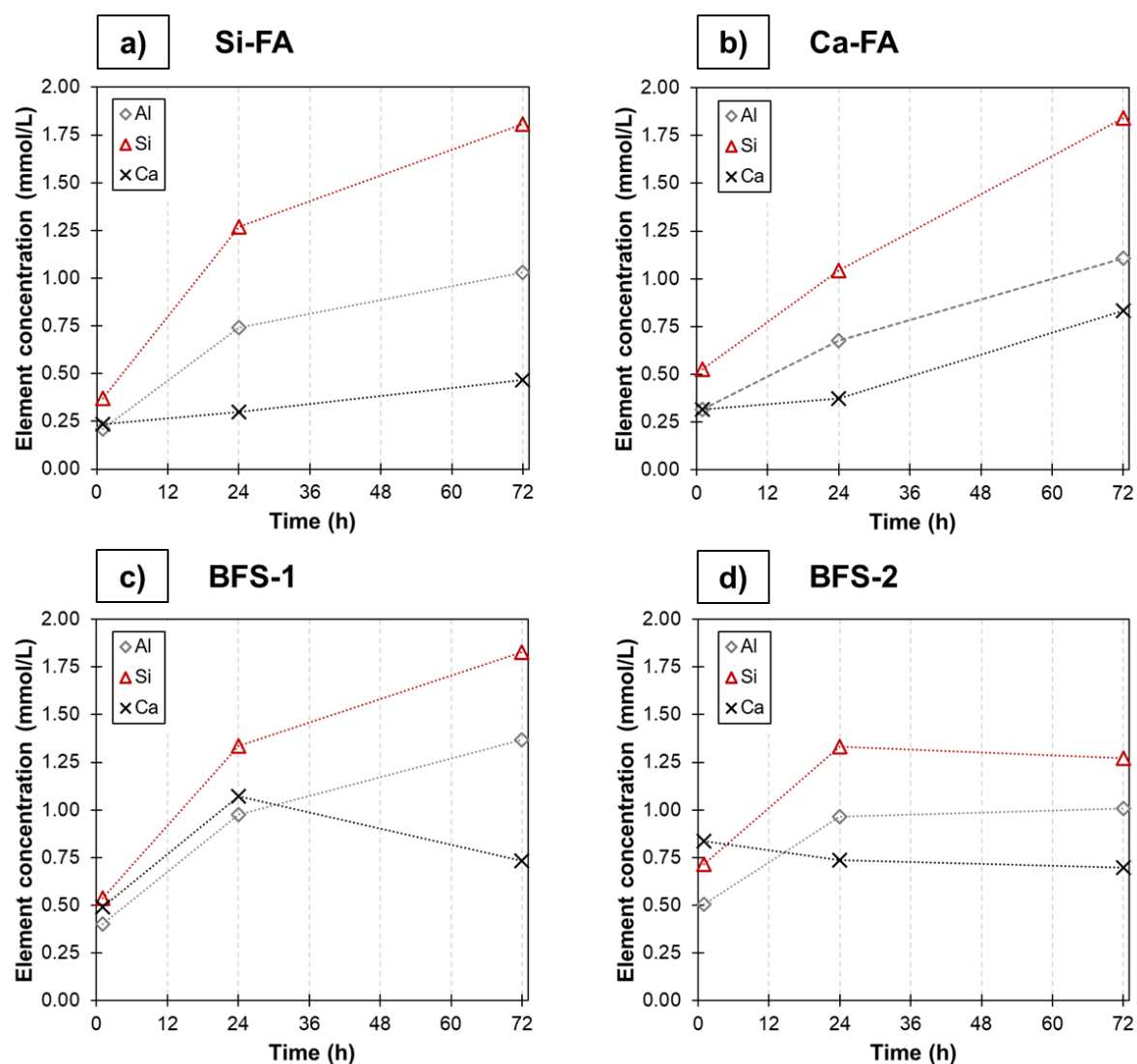


Figure 5.4: Temporal element evolution measured from NaOH solutions at 20 °C.

At 24 hours, the measured values of all elements were lower in the two fly ash-type glasses. The limited leaching of Ca slows the dissolution and reaction processes as a whole, extending the duration of the forward dissolution period of low-Ca precursors (see Chapter 4 for more details). Consequently, the measured concentrations of Al and Si were up to 30 % higher for slag-type glasses at this period, with the latter dropping from 1.33 (BFS-2) and 1.34 (BFS-1) mmol/L to 1.26 (Si-FA) and 1.04 (Ca-FA) mmol/L, respectively. Such observations are in agreement with the findings in the literature for different groups of precursors. Schöler et al. [148] reported forward dissolution rates of Al 19 times higher in synthetic slags ($x_{\text{CaO}} = 0.37$) compared to synthetic siliceous fly ash ($x_{\text{Ca}} = 0.08$). Similarly, Singh et al. [188] evaluated the influence of Ca content in the dissolution of Si and Al in siliceous fly ashes, reporting concentrations of the two elements up to 1.5 times higher in the leachate in the same period for materials with higher initial CaO content, by comparing fly ashes with 2.46 wt% CaO versus 1.65 wt% CaO.

5.3.1.2 *Characterization of residual dissolution materials with thermogravimetric analysis*

Differently from the regime observed in Chapter 4, the use of finer glass particles and the longer experimental period in this study are expected to drive the dissolution towards Stage II, when the solution becomes supersaturated and promotes the formation of different reaction products - see Section 4.3.1. The evidence of this phenomenon is seen in different levels in the DTG curves plotted in Figure 5.5. The delayed nucleation process in low-Ca binders resulted in small or non-existent peaks in the 50 - 150 °C region in Figures 5.5a and 5.5b, which correspond to the evaporation and dehydroxylation of hydrated gel phases [173,219]. In Figure 5.5a, a small peak can be observed in this region after 24 hours of dissolution, which disappears in the last measurement of glass Si-FA. The limited dissolution of Si and Al favours the speciation of Ca^{2+} and OH^- . This phenomenon is better observed by the significant response in the regions centred at approximately 475 °C and 570 °C, attributed to portlandite [156,366] and poorly-ordered calcium carbonate phases, such as aragonite [324], as the latter is usually observed due to carbonation of amorphous $\text{Ca}(\text{OH})_2$ [311]. Conversely, Figure 5.5b shows a small peak in the gel phases region after 72 hours, with decreased signals arising from the presence of portlandite and amorphous carbonate-related phases for the calcareous fly ash-type glass. These observations arise from the stronger evolution of all elements in the 24 - 72 hours period for Ca-FA - the increases in concentrations of Al, Si and Ca in this period were 0.43, 0.80 and 0.46 mmol/L, respectively, for Ca-FA, compared to 0.28, 0.54 and 0.16 mmol/L for Si-FA, as illustrated in Figure 5.4.

In alkali-activated systems, the formation of hydrated gels occurs by a polymerisation-like phenomenon of several aqueous species, leading to the precipitation of small solid nuclei (or simply units) in the bulk solution [367], or by reactions anchored at the surface of precursor and filler particles [368,369]. In both cases, the time required for the coalescence and conversion of these small agglomerates into stable nanostructured C-S-H- and N-A-S-H-like phases is dependent on the chemical degradation of the precursor and supersaturation levels [367,370]. In the present fly ash-type glasses, it is more likely that small agglomerates of ionic species are formed at the surface of reactive particles than in the solution, as the lower dissolution rates calculated in Chapter 4 favour undersaturation levels in the whole solution - see section 5.3.1.1 for more detailed discussions. As described in the literature [307,371], Ca-species can be easily attached to the negatively charged surfaces of reactive particles in glass-solution interfaces, forming units of altered layers with C-S-H-like compositions that are easily dissolved at high pH [349] and in constant stirring conditions [372]. Therefore, the limited initial content of CaO suggests that, in both Si-FA and Ca-FA, the initially detected gels are still unstable and could not bind other positively-charged species, facilitating the dissociation of unstable surface units.

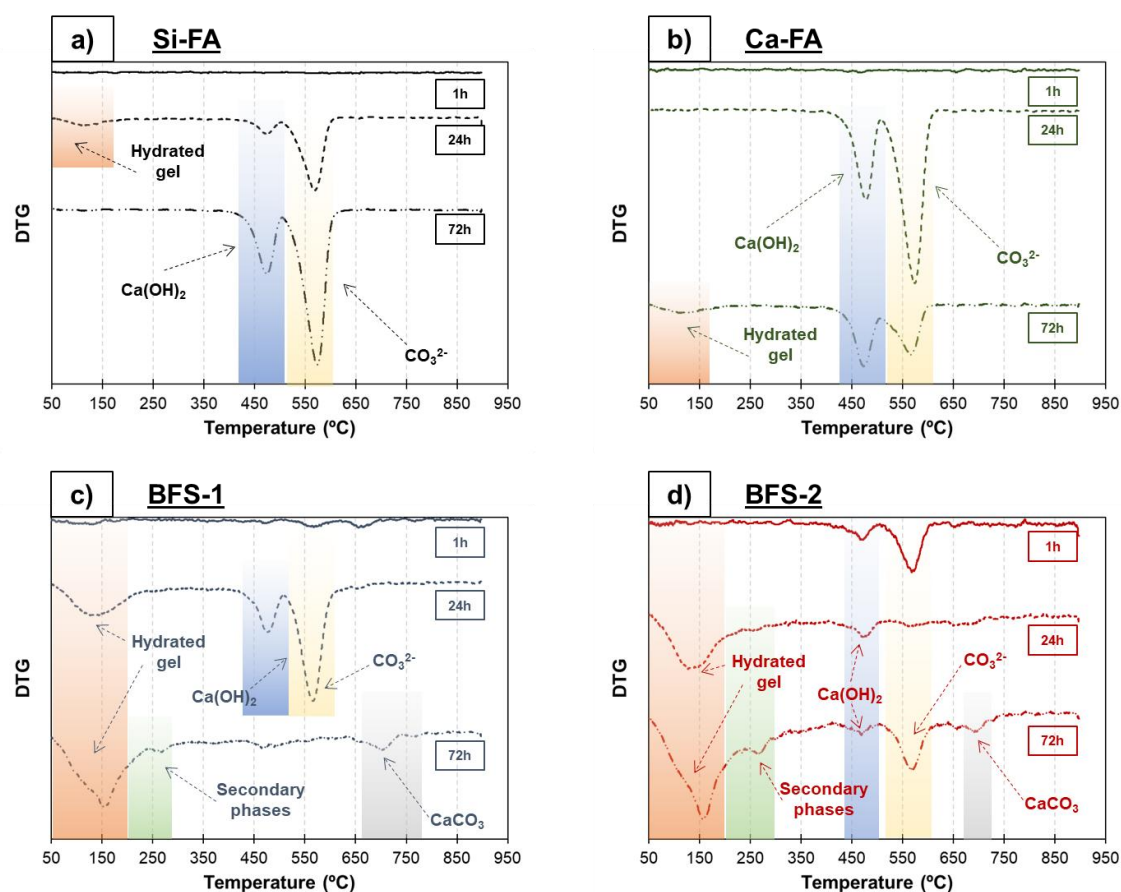


Figure 5.5: DTG curves of residual powders collected after room temperature NaOH-dissolution at different periods: a) glass Si-FA; b) glass Ca-FA; c) glass BFS-1; and d) glass BFS-2.

Slag-type glasses displayed potential for immediate phase precipitation due to their naturally higher CaO fractions, and consequently, higher reactivity. The curves shown in Figures 5.5c and 5.4d indicated the formation and carbonation of portlandite after the first sampling, as the initially measured concentrations of Ca in BFS-1 and BFS-2 were significantly higher than in fly ash-type glasses. At 24 h, Ca was still more noticeable in high-Ca precursors, although the concentrations of Si and Al did not show great variation among all glasses in the 24-72 hours period. The increased water loss arising from C-S-H-like phases indicates the coalescence of small units into stable gel particles. This phenomenon is followed by the presence of mass loss peaks centred at approximately 700 °C, attributed to the decarbonation of stable CaCO_3 [156,324] after 3 days of dissolution. It is here suggested that the growth of initially formed gel nuclei occurs at the expense of the destabilization of portlandite, dissociating it and allowing complexation of Ca^{2+} with Si- and Al-species. This reaction prevented the CO_2 uptake by Ca(OH)_2 , favouring the decalcification of C-(N-A-)S-H gels into calcite following conventional carbonation processes. Finally, the remaining presence of portlandite and aragonite after 72 h, in glass BFS-2, arises from an excess of Ca^{2+} in solution over other species after gel stabilization, as dissolution experiments indicated that the pore solution was depleted in Si and Al at this time.

In addition to the primary reaction products, the DTG curves illustrate a mild formation of secondary phases in high-Ca glasses. The weight loss detected between 200 and 300 °C can be attributed to the formation of different Ca-Al-containing phases, such as hydroxy-AFm (C_4AH_{13}) and katoite (C_3AH_6), with both phases displaying loss of water from octahedral

layers within this temperature range [173]. These layered double hydroxide (LDH) and hydrogarnet phases are some of the most common secondary reaction products in alkali-activated cements - especially those derived from high-Ca precursors [373], and are formed by the coupling of octahedral sites of Ca and Al, charge balanced by OH^- , which is favoured in systems with low Si in pore solutions [374].

5.3.1.3 Calculation of effective saturation indices

Formation of primary phases:

Following the previous experimental observations, the formation of hydrated gel-phases was observed in all four glasses at some point. A quick precipitation of C-(N-A)-S-H and N-A-S-H structures is expected in alkaline environments [114,375,376], but the exact nature of the formed gels is difficult to determine. With respect to gel distinction, the calculation of effective saturation indices (ESIs) of the most common gels provides extra information about preferential phase formation [56,377]. The results detailed in Table 5.2 show that, interestingly, the highest final ESIs of gel phases are calculated for the glass Ca-FA, which showed only minor signs of C-(N-A)-S-H/N-A-S-H formation in the DTG curves. In slag-type glasses, the saturation indices of all gels were nearly unchanged from 24 to 72 hours, while fly ash-type glasses presented a significant increase in the same period. The combination of positive calculated indices with negligible gel formation for Si- and Ca-FA demonstrates how unstable this initial phase formation stage can be. It is noticed that, besides being positive, a minimum ESI value must be achieved to allow the growth of stable reaction products. As nuclei of solid compounds require time to coalesce and become energetically favourable, a thermodynamic stability threshold must be met to overcome kinetic constraints and allow the setting of new phases [378,379], but the precise determination of this threshold ESI was not performed. Initial units, spontaneously formed by speciation of Ca^{2+} with silicate species or with OH^- in supersaturated conditions [369,380], are thermodynamically stable [381]. Although their precipitation and coalescence are linearly correlated with the saturation index [382], the true value of the growth rate depends on several parameters, such as temperature, quantity of crystallites and presence of secondary phases [367,370]. Therefore, the absence of phases detected by DTG does not reflect the supersaturation level of the solutions, which probably display the presence of several nuclei which were not anchored in reactive surfaces - it is worth mentioning that the resolution of DTG is not sufficiently high to identify the presence of unstable solid nuclei at nanoscale ranges.

The formation of Ca-containing gels is observed to be more dependent on absolute concentrations than on ratios of aqueous species. In all cases, C-S-H (T2C), followed by Na-bound C-S-H and C-A-S-H, was the most thermodynamically stable phase independent of the measured Ca fraction among the three elements, which fluctuated from 14 % (Si-FA - 24 h) to 32 % (BFS-1 - 72h). Contrarily to C-S-H, supersaturation of N-A-S-H gel was only calculated in only two samplings under specific conditions of the pore solution. The Ca fraction in the pore solution had a major influence on gel stability, as positive indices for the N-A-S-H phase were obtained with Ca/(Si+Al) ratios below 0.30. It is here suggested that, above this threshold, Ca binding with Si- and Al- species is more energetically favourable than Si-Al interactions. This is somehow expected from electrostatic considerations, as negative aluminate and silicate ions - e.g. $\text{SiO}(\text{OH})^{3-}$ and $\text{Al}(\text{OH})^{4-}$ - are supposed to be repelled from each other, while Ca^{2+} can be attracted to either negative units. Similar trends have been

observed by other authors in blended mixtures of slags and fly ashes, with C-A-S-H being proposed to be the main reaction products in mixtures containing up to 70 % of slag [219,228,383], and the formation of porous surface-anchored C-S-H gels being favoured in portlandite rich solutions in fly ash systems [306]. However, there must be also sufficient Al in the pore solution to allow its incorporation into tetrahedral sites and favour the stabilization of N-A-S-H-like units, since Si/Al ratios above 1.70 resulted in negative saturation indices for glass Si-FA. As determined by Fernández-Jiménez et al [293], Al-rich gels are more likely to be formed in initial stages, due to the higher normalized dissolution of Al [180] and the preferential breakage of Al-O over Si-O bonds in initial stages. The Si/Al ratios of initial N-A-S-H nuclei have been experimentally demonstrated to be between 1 [384] and 1.4 [293] up to 8 hours of reaction, following the element ratios observed in the present pore solutions.

Formation of secondary reaction products:

The plots in Figure 5.6 showed that the ESIs of Ca-Al-rich phases and portlandite are higher than calculated values for hydrated gels in the two most extreme glasses (Si-FA and BFS-2). Hydroxy-AFm (C_4AH_{13}) was the most supersaturated compound, with a saturation index after 72 hours of 0.50 and 0.67 for Si-FA and BFS-2, respectively. For glass BFS-2, the accelerated release of Si and Al, favoured by its intrinsically higher reactivity, induced an immediate supersaturation of all phases, which was maintained relatively constant throughout the whole experiment. Due to the favourable binding of Ca with Al-species, BFS-2 showed signals related to katoite (C_3AH_6) and hydroxy-AFm (C_4AH_{13}) in the DTG curves already after 24 h. Despite the lower calculated indices, the formation of strätlingite (C_2ASH_8) should also be considered, as this phase can combine all elements in solution and accommodates Al in both octahedral and tetrahedral coordination [385,386]. In thermogravimetric experiments, strätlingite reflections can be hidden under other LDH phases as it presents loss of interlayer water between 200 and 300 °C [173]. It is, however, unlikely that it would remain stable at later stages despite displaying supersaturation indices, as it has been observed to be stable only at very limited fractions of Al in pore solution [114,387]

Table 5.2: Summary of elemental ratios and ESIs calculated for the primary reaction products phases from experimental findings in NaOH-dissolution at 20 °C.

Glass	Dissolution period	Element ratio		ESI				
		Si/Al	Ca/(Si+Al)	C-S-H (T2C)	Na-C-S-H (INFCN)	C-(A-)S-H (5CA)	C-(N-A-)S-H (5CNA)	N-A-S-H (NASH_1)
Si-FA	24 h	1.71	0.15	0.32	0.14	0.15	0.05	- 0.07
	72 h	1.76	0.16	0.43	0.23	0.24	0.13	- 0.01
Ca-FA	24 h	1.54	0.22	0.33	0.14	0.15	0.06	- 0.09
	72 h	1.66	0.28	0.53	0.28	0.30	0.18	0.01
BFS-1	24 h	1.37	0.46	0.53	0.26	0.30	0.18	- 0.04
	72 h	1.33	0.23	0.51	0.27	0.29	0.17	0.02
BFS-2	24 h	1.37	0.32	0.47	0.23	0.26	0.14	- 0.04
	72 h	1.26	0.31	0.46	0.22	0.25	0.14	- 0.04

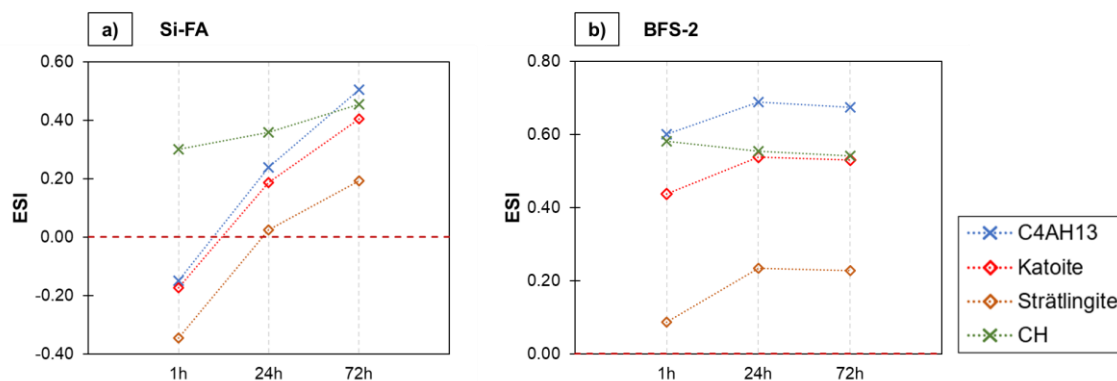


Figure 5.6: Effective saturation indices (ESIs) calculated for secondary reaction products during the 1.5 NaOH-dissolution of glasses: a) Si-FA and b) BFS-2.

Similarly to hydrated gels, it can be noticed that positive saturation indices are not sufficient to indicate the nucleation (formation) of secondary phases, and that there exists an ESI threshold which regulates the stable formation of reaction products. This is especially observed in the siliceous fly ash-type glass, which showed positive indices for all phases after 24 hours, and supersaturation with respect to portlandite at all periods. The constant presence of portlandite, also detected in the dissolution of coarse glasses in Chapter 4, suggests that it is formed as an activated intermediate complex by the speciation of Ca with OH^- anions formed, consuming aqueous Ca while Si- and Al-species are not yet available [381]. This is supported by the DTG curves of glasses Ca-FA and BFS-1, as the formation and growth of C-S-H-like gels decreases the peaks of portlandite and amorphous carbonated phases in both cases.

5.3.1.4 Characterization of initially precipitated phases

X-ray diffraction analysis:

The residual powders collected after 3 days of dissolution were characterized using X-ray diffraction, supporting the identification of the early-precipitated phases. As seen in Figure 5.7, the broad amorphous hump was still present in all residual glasses without major modifications. In all cases, the centre of the hump did not show major shifts compared to the original glasses, which demonstrates that the highly-diluted conditions only promoted the breakage of the most superficial regions of glass particles, maintaining the bulk structure still intact. Minor peaks of new phases were identified in all samples after 72 hours of dissolution. The formation of gel phases in the four glasses, except Si-FA, is evidenced by the presence of peaks characteristic of tobermorite (PDF # 00-029-0331) [89,388], being more strongly observed in Figure 5.7b for slag glasses-based systems. These reflections are also similar to Al-modified tobermorite, but the determination of the exact type of gel formed at such stages is not feasible from XRD reflections alone. Following the thermogravimetric analysis, both slag-type glasses displayed the presence of hydroxy-AFm (C_4AH_{13} - PDF # 00-002-0077), which had the highest supersaturation degree calculated among all phases. The exposure of the residual material to the atmosphere led to the formation of carbonated phases, which were observed to be different according to the reactivity of each glass. Monocarboaluminate ($\text{Ca}_4\text{Al}_2(\text{CO}_3)(\text{OH})_{12} \cdot 5\text{H}_2\text{O}$ - PDF # 00-036-0377) and calcite (CaCO_3 - PDF # 00-005-0586) were detected in both BFS-2 and BFS-1, arising from the carbonation of hydroxy-AFm and C-S-H phases, respectively. Minor reflections of

strätlingite (C_2ASH_8 - PDF # 00-029-0285) were also observed for high-Ca precursors. Strätlingite can be formed alternatively to C-A-S-H gel in high-Al environments, as it combines Si, Al and Ca in more ordered structures [55,374]. Finally, the peaks attributed to all secondary phases were higher in BFS-2, following the more significant water release measured between 200 and 300 °C from thermogravimetric analysis.

In fly ash-type glasses, reflections attributed to portlandite (PDF # 00-044-1481), aragonite (PDF # 00-033-0268), and hemicarboaluminate ($Ca_4Al_2(CO_3)_{0.5}(OH)_{13} \cdot 5.5(H_2O)$ - PDF # 00-036-0129), were detected. The nature of the detected CO_2 -bound phases is influenced by the type of precipitated primary and secondary products. The carbonation of C-(N-A)-S-H produces both hemicarboaluminate and monocarboaluminate, according to the level of CO_2 contamination, as increasing carbonation degree induces the formation of the latter [389]. With the current results, it is suggested that hemicarboaluminate is formed not necessarily by lower contamination level, but instead by the insufficient presence of Ca-containing units, while stable gels would be prone to full carbonation, converting into monocarboaluminate.

Scanning electron microscopy:

The visualization of residual particles after dissolution test via SEM, shown in Figure 5.78 supported the suggested distinct paths of phase precipitation, according to the class of each precursor. Low-Ca glasses displayed an agglomeration of particles and only minor surface alteration after 3 days - see Figures 5.8a and 5.8b. The limited reactivity of Si-FA, which displayed the lowest concentrations of Ca during dissolution experiments, completely hindered the formation of visible altered layers, as there were not sufficient Ca^{2+} to be attached and form surface ionic complexes. In Ca-FA, the surface of reactive particles was partially covered by agglomerated species, as observed in the enlarged images. The conversion of leached layers into a passivating film should not be favourable, given the high alkalinity of the solution [176,349]. Instead, it is assumed that leached layers are the first step in the precipitation process, providing anchoring and growth points for initially formed nuclei following a heterogeneous nucleation path [368,369]. These surface reactions are also observed to occur concurrently with formation of surface etching pits (highlighted by the yellow dashed frames), promoted by localized chemical attack typically formed in highly unsaturated conditions during dissolution of glasses and minerals [288,390].

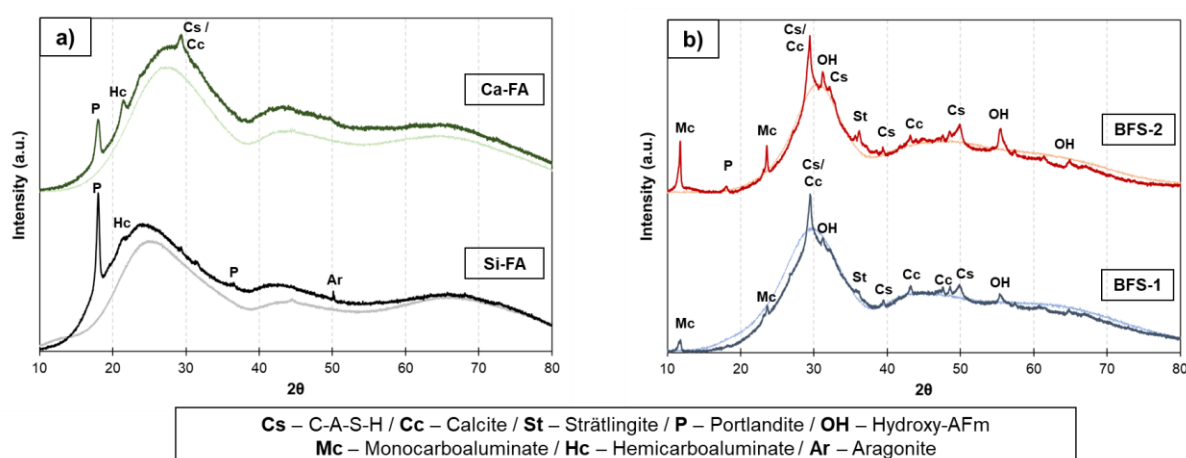


Figure 5.7: X-ray diffraction patterns of residual powders collected after 72 hours of NaOH-dissolution: a) fly ash glasses; b) slag glasses - bright background lines represent the unreacted glasses in all plots.

Conversely, the surfaces of glass particles were completely modified by the precipitation of reaction products in both high-Ca glasses. The enlarged areas suggest the formation of thicker and continuous layers, arising from the attachment of aqueous species in larger proportions. As described by Dove et al. [391], dissolution requires less energy to occur in naturally rough sites in mineral surfaces. It can be assumed that the depolymerized structure of slag-glasses promotes the formation of regions of higher stress, generating sites which resemble dislocation cores in crystalline minerals [392], creating natural steps and increasing the total roughness of the surface. As dissolution rates and heterogeneous nucleation are directly proportional to specific surface area [310,338,382], these natural surface defects can favour an accelerated alteration of glass particle, thus enhancing the overall reactivity.

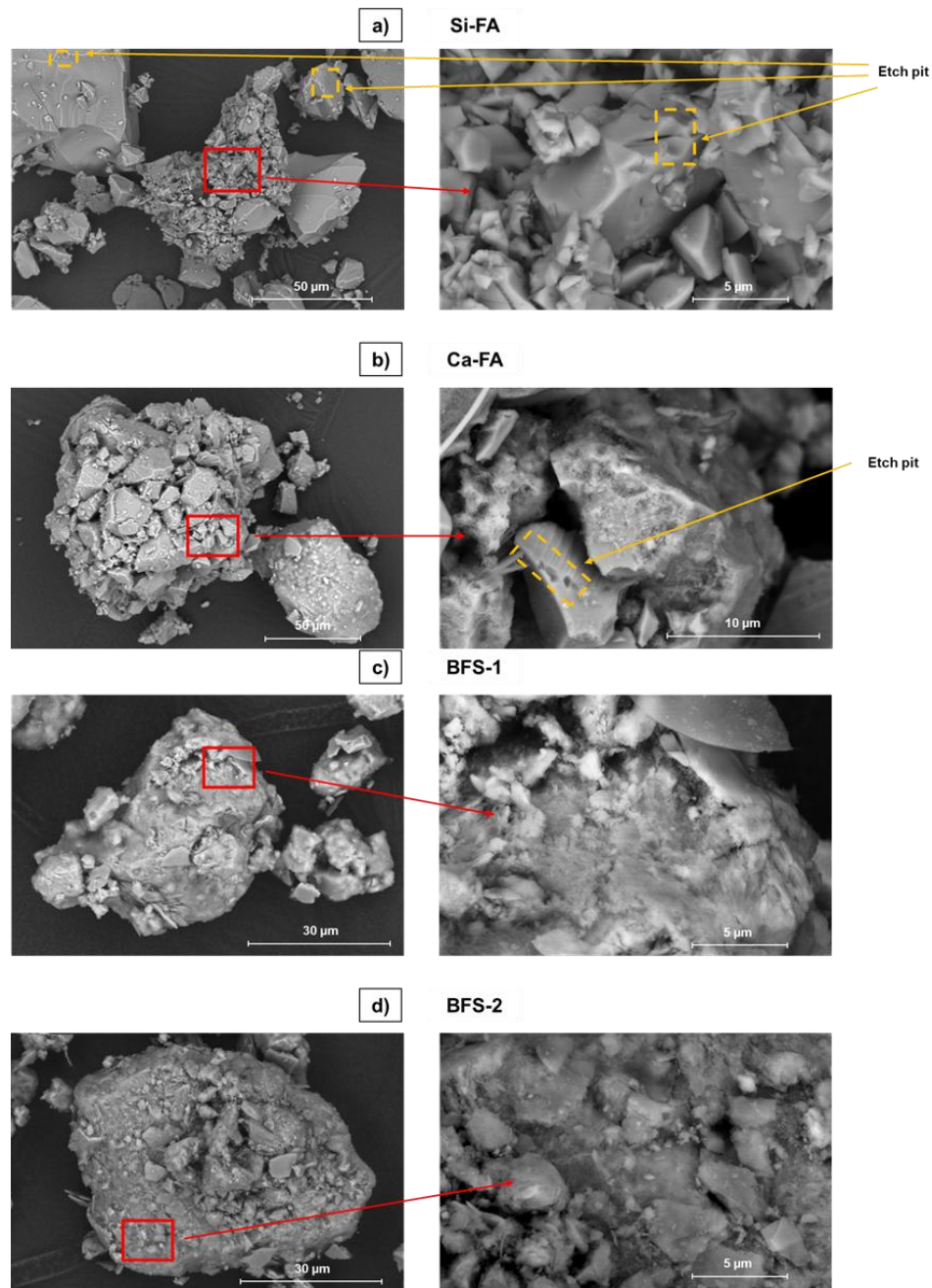


Figure 5.8: Observation, with SEM, of residual surfaces of glasses dissolved for 72 hours in 1.5 M NaOH solutions at 20 °C: a) glass Si-FA; b) glass Ca-FA; c) glass BFS-1; d) glass BFS-2.

5.3.1.5 Influence of temperature on early-stage reactions

Influence of NaOH as activator:

The application of temperature is often used to enhance the reaction potential of precursors with natural lower reactivity [54,393,394]. The concentrations of Si, Al and Ca, measured during the dissolution of fly ash glasses in 1.5 M NaOH solutions, at room temperature (20 °C) and 60 °C, are given in Table 5.3. It is noticed that both Si and Al are present in significantly higher concentrations in the high-temperature scenario. This observation is in agreement with the calculated forward dissolution rates at 60 °C, which were 20-36 times higher for Si, and approximately 10 times higher for Al, when comparing with values obtained at 20 °C - see Chapter 4 and Appendix C for more details. On the other hand, Ca release did not present the same behaviour, as concentration values were maintained in the same range throughout the whole experiment despite being initially higher at 60 °C when comparing concentrations measured at 1 h.

The limited release of Ca compared to Si and Al, throughout the whole experiment, indicates that ion-exchange processes are suppressed by chemical attack through hydrolysis. This could be favoured by a deeper penetration of the alkaline solution triggered by the high-temperature, which increases the potential of disruption of Si-O and Al-O bonds from the original glass framework. This assumption is supported by simulated dissolution scenarios described in literature. Kalahe et al. [395] observed that the dissolution of Na⁺ doubled from 25 °C to 90 °C, but cation binding in the reactive surface decreased, while Deng et al. [396] reported a continuous increase in the accumulated number of reactions per unit volume (nm³) with temperature in modelled sodium silicate glasses, which were a factor of 1.6 higher at 77 °C compared with 27 °C. With the current results, it is thus suggested that the prompt leaching of Ca occurs in similar way as observed at 20 °C, and the accelerated and continuous release of Si and Al, driven by favoured Si-O and Al-O hydrolysis, promotes an immediate binding between Ca and the two elements to form the initial solid nuclei. To support this assumption, it is stated that the low initial CaO contents of the fly ash-type glasses ease the chemical affinity for Ca dissolution, and as the just-leached species are readily bound to other Al- and Si-ions, Ca concentrations in solution are maintained in a *pseudo-steady-state* behaviour.

Table 5.3: Evolution of element concentration in the dissolution of fly ash-type glasses at room temperature and at 60 °C, in 1.5 M NaOH solutions.

Glass	Element concentration (mmol/L)								
	1 h			24 h			72 h		
	Al	Si	Ca	Al	Si	Ca	Al	Si	Ca
Si-FA (60 °C)	0.79	1.29	0.34	3.68	5.20	0.18	4.30	5.98	0.31
Si-FA (20 °C)	0.21	0.37	0.23	0.74	1.26	0.30	1.03	1.81	0.47
Ca-FA (60 °C)	0.76	1.26	0.55	2.69	2.96	0.29	3.81	4.00	0.22
Ca-FA (20 °C)	0.31	0.52	0.32	0.68	1.04	0.37	1.11	1.84	0.83

Characterization of residual materials with DTG analysis:

The precipitation of reaction products after dissolution experiments is better visualized in the DTG curves, plotted in Figure 5.9. Differently from room temperature experiments (Figure 5.4), strong signals between 50 - 200 °C, attributed to the formation of hydrated gels, are already seen in both glasses at 24 h. The increased peaks in this region indicates that the coalescence of stable solid nuclei is achieved in earlier periods at 60 °C, as the thermogravimetric responses were intensified up to 72 hours of dissolution. The reduced presence of portlandite-related peaks (470 °C), combined with the formation of stable calcium carbonate (650 - 750 °C) support the stabilization of hydrated gels. Combined with a larger peak area for nanostructured gels, glass Ca-FA displayed residual evidence of disordered carbonates and a mild portlandite response after 72 h. Despite showing lower Ca concentration than glass Si-FA in the last dissolution sampling, the Ca/(Si+Al) ratio (0.04) of Ca-FA was slightly higher than the calculated value for Si-FA (0.03), indicating Ca binding with OH⁻ due to insufficient amounts of Si and Al in the solution.

At 60 °C, Ca-containing phases still display a remarkable influence on early precipitation mechanisms, as shown in Figure 5.10. The calculation of effective saturation indices for both glasses indicated that N-A-S-H gels are not favored until the end of the experiment. Similarly to room temperature dissolution, a threshold Ca concentration seemed to control the preferential gel formation. N-A-S-H is thermodynamically favoured at Ca/(Si+Al) ratios above 0.03, which is 10 times lower than the threshold ratio observed at 20 °C. Although there is limited available data evaluating the effect of temperature on solubilities of both C-(N-A-)S-H and N-A-S-H, they have been observed to increase with temperature [326,327], but at a higher rate for the latter. Regarding Ca-containing phases, Lothenbach et al. [203] reported changes in solubility product less than 0.5 log units for the crystalline phases of tobermorite ($-8.0 < k_{sp} < -7.5$) and jennite ($-6.5 < k_{sp} < -6.0$) from 25 °C to 75 °C, while Myers estimated differences in the same range for C-A-S-H gels with variable Al content, with k_{sp} values between -9.5 and -8.5 among four different gel end members. On the other hand, Ma and Lothenbach [207] evaluated the changes in solubility for zeolites faujasite-X (Si/Al = 2) and faujasite-Y (Si/Al = 1.25), which are considered crystalline counterparts of amorphous N-A-S-H gels with low Si/Al ratio. Those authors estimated variations of k_{sp} up to 1.2 log units for the two phases, ranging from -8.9 to -6.5 (normalized to Si ratio). These results can support the influence of temperature on the extended undersaturation levels of N-A-S-H observed at 60 °C, despite the enhanced dissolution of Si and Al.

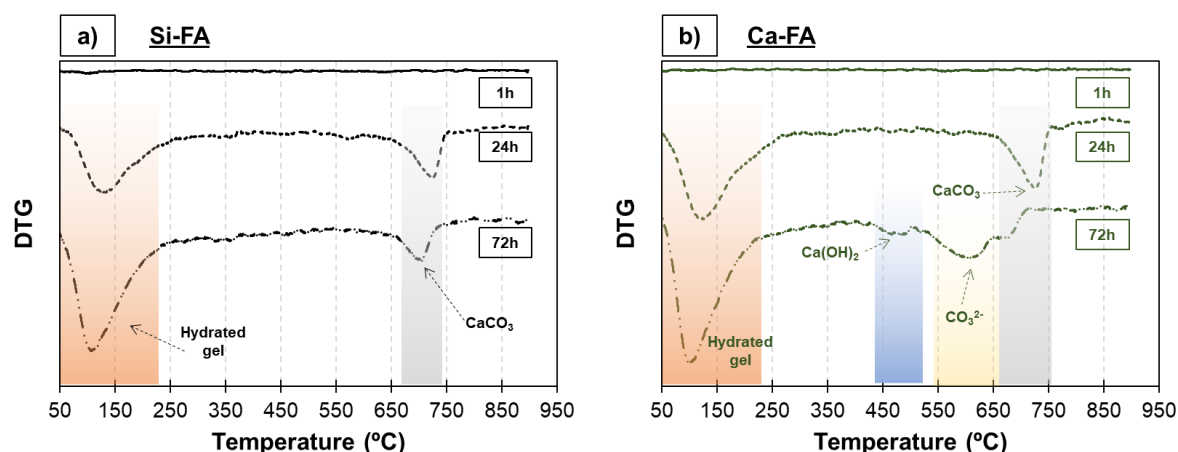


Figure 5.9: DTG curves of residual material collected after dissolution at 60 °C: a) Si-FA; b) Ca-FA.

Calculation of effective saturation indices (ESI):

ESI calculations demonstrated that C-S-H is the most likely phase to be formed (T2C), followed by Na-bound C-S-H (INFCN), C-A-S-H (5CA) and C-N-A-S-H (5CNA) gels. This is strengthened by the XRD patterns of both glasses after 72 hours of dissolution, also shown in Figure 5.11. Reflections of Al-substituted tobermorite 1.4 nm (PDF # 00-026-0331) were observed in both patterns, showing that Ca-based gels are still strongly formed despite the low Ca content in fly ash-glasses. In Ca-FA, strong evidence of vaterite (PDF # 00-033-0268) was also detected. This polymorph of calcium carbonate is usually formed during initial carbonation stages in low relative humidity environments [82], and is expected to convert to the most stable calcite form with time. Along with Ca-rich products, the diffractograms display reflections of zeolite-like phases, such as faujasite-X (PDF # 00-039-1380), hydroxysodalite (PDF # 01-072-2329), and chabazite-Na (PDF # 00-031-1271), due to the arrangement of Si-O-Al in small ordered units. It should be also stated that additional gel-related reflections are still expected, as both C-(N-A)-S-H and N-A-S-H gels present additional amorphous structures hidden in the overall XRD curve. Therefore, a quantitative determination of each formed gel and the validation of the calculated saturation indices is not feasible through XRD analysis and would require additional experiments.

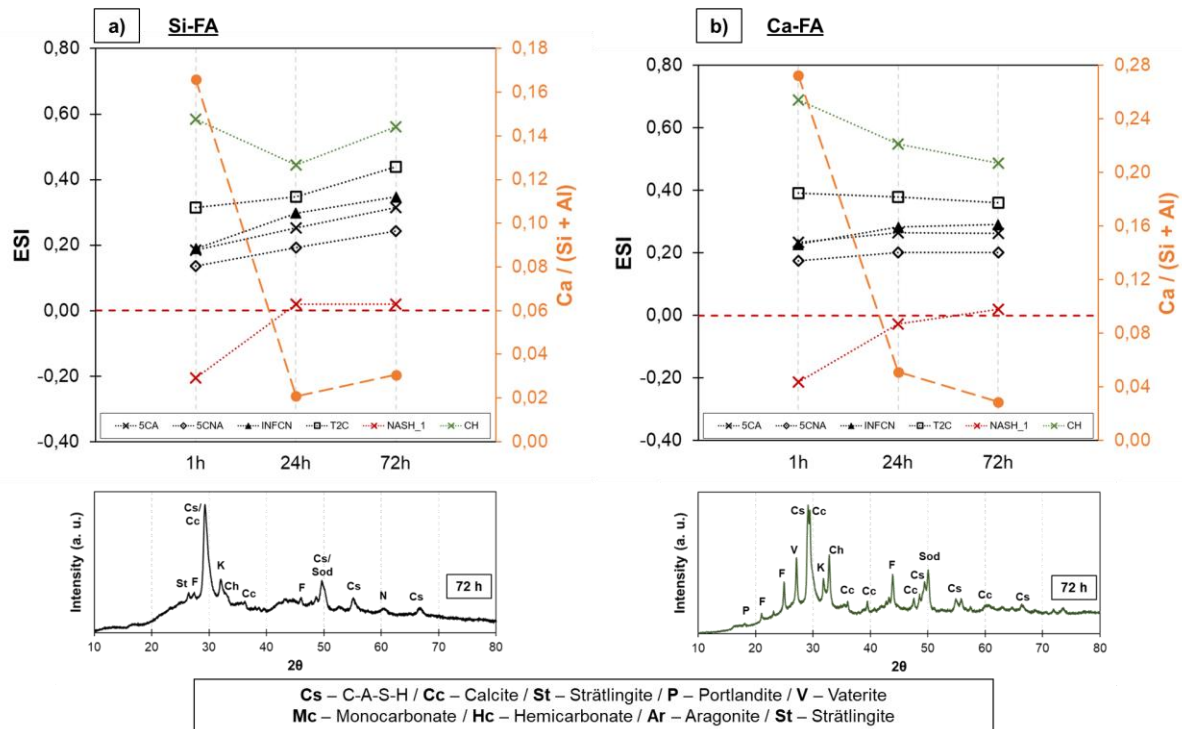


Figure 5.10: Calculated ESI's at different periods, and XRD patterns of residual powders after 72 hours of dissolution at 60 °C: a) Si-FA; and b) Ca-FA.

5.3.2 Dissolution experiments in waterglass solutions: characterization of residual material

Differential thermogravimetric analysis:

The DTG curves of residual Si-FA glass collected after dissolution in waterglass solutions, at room temperature, are plotted in Figure 5.11. The positive influence in phase precipitation promoted by the liquid sodium silicate is observed by the earlier reflections related to portlandite and aragonite - peaks centred at approximately 470 and 560 °C respectively - which are already detected after 1 hour of dissolution. A mild reflection related to hydrated gels, between 100 and 150 °C, is also observed at 1 hour and 24 h, but the reflection is absent after 3 days. Moreover, the evidence of carbonated portlandite is kept constant throughout the whole experiment. It can be inferred that waterglass bursts an immediate reaction, due to the quicker coupling of Ca^{2+} with Si-species into small crystallites [397]. However, the stabilization of these phases is only achieved in later stages not covered in this experimental setup.

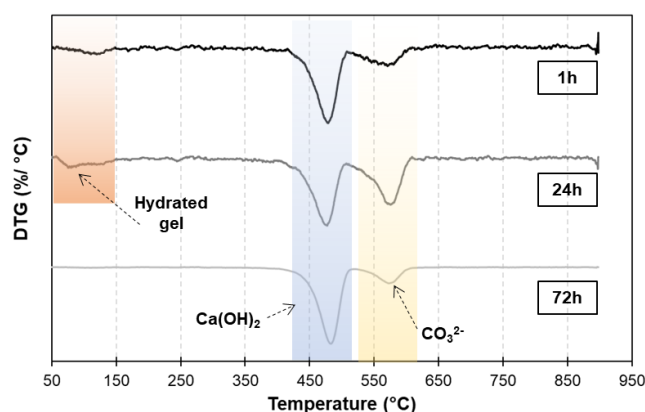


Figure 5.11: Differential thermogravimetric curve of residual Si-FA glass after dissolution in waterglass solutions, at 20 °C.

Fourier transform infrared spectroscopy analysis:

The effect of solution type on dissolution and gel formation can be evaluated using FTIR analysis, comparing the residual materials (solid line) with the original glasses (dashed line). The differences for glass Si-FA in various setups are shown in Figure 5.12. At room temperature (Figure 5.12a), the residual materials did not show significant differences from one solution to the other. In both spectra, remanent Al-Si rich structures are observed with bands centred at approximately 1200 and 1150 cm^{-1} , assigned to vibrations of AlO_6 in mullite-like structures [245,323] and vibrations of Q^4SiO_4 units in silica gel and quartz [248,361]. Moreover, the shoulders located at 1040 cm^{-1} were still present after dissolution, which is attributed to a densely packed Si-O-Si network by asymmetric vibration of silicate units [181,210,243]. The reflections observed at 717 , 636 and 553 cm^{-1} are attributed to different vibrations of Si-O-Si and Si-O-Al bonds, which form secondary building units occurring in single and double structures of different zeolite phases [206,210]. Double rings (636 cm^{-1}) have stronger signals in NaOH-exposed samples than single rings (717 and 553 cm^{-1}), since the lower content of aqueous Si favours interlocking of aluminosilicate units in three dimensional structures [206,304,398]. The main and broadest band in the spectra, located between $1100 - 850\text{ cm}^{-1}$, is assigned to Si-O-T interactions [172,211,242,243]. Compared to unreacted glass, the shift of this region displayed moderate differences according to the solution. In NaOH solutions, the Si-O-T band did not present changes with respect to unreacted glasses. In less alkaline solutions, promoted by waterglass, the centre of the band moved towards lower wavenumbers, which is an opposite trend to what is commonly observed in systems with an overall higher Si content. In the latter system, it could be assumed that the lower alkalinity promotes a continuous leached layer with a greater binding of Ca and silicate species in the reactive surface. As the carbonation related bands detected at 1470 cm^{-1} [212,399] are more intense, this supports the facilitated carbonation of unstable Ca- and Si- containing species formed close to the surface of glass particles.

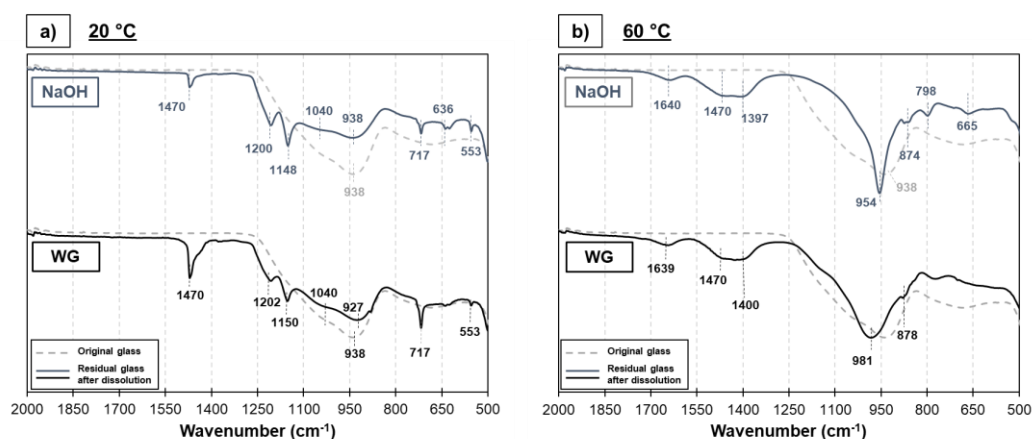


Figure 5.12: FTIR spectra of the residual material collected after dissolution of Si-FA in NaOH and waterglass solutions at: a) 20 °C and b) 60 °C - dashed lines indicate spectra of the original glass, and solid lines indicate spectra of the residual glasses.

Figure 5.12b indicates that the influences of the alkaline solution are more clear at 60 °C. Initially, the bands at approximately 1600 cm⁻¹ are attributed to chemically bound water [193,228,400]. In agreement with DTG curves (Figure 5.11), this evidences the presence of stable reacted phases in both glasses, which was not significantly observed in the spectra of samples dissolved at 20 °C. The centre of the Si-O-T band also showed major differences according to each solution. In waterglass systems, the availability of aqueous Si-species facilitated the stabilization of aluminosilicate chains with higher Si/Al ratios [87,206], thus shifting the band towards higher wavenumbers. Contrarily, sodium hydroxide promoted the formation of fewer variations of structural units in terms of both chain length and Si/Al ratios, resulting in the narrowing of the band centred at 954 cm⁻¹. In both scenarios, incorporation of AlO₄ is observed in the 874 cm⁻¹ region, assigned to the asymmetrical stretching of tetrahedrally-coordinated Al in Si-O-Al bonds within both N-A-S-H and C-(N-A)-S-H gel [205,211]. In NaOH systems, small peaks centred at 798 and 665 cm⁻¹ are observed, which are typical of symmetric stretching of Si-O-Si in quartz [87,245,401]. These reflections suggest that 3-dimensional Si-rich small structures are formed already in the initial stages of reaction, which facilitate the growth of zeolite phases at longer stages of the reaction. Conversely, in waterglass systems, a minor band at 774 cm⁻¹ indicates the formation of Na-chabazite (Na₂Al₂Si₄O₁₂·6H₂O) [207], suggesting a moderate formation of organized units with a Si/Al ratio of 2.

Scanning electron microscopy:

The study of residual glass surfaces, shown in Figure 5.13, allows an easier comprehension over the different paths taking place at each solution. When exposed to liquid sodium silicate, the glass particles suffer less localized attacks and, instead, have a more homogeneous dissolution, as a reduced quantity of etching pits was observed at 20 °C (Figure 5.13a). The formation of ‘steps’ in the surface of glasses, highlighted by the yellow dashed frames, appears to be a delamination process by the release of continuous flakes, which has been previously observed in pharmaceutical glasses [402,403]. It is proposed that after initial leaching process, the quick complexation of leached Ca²⁺ with OH⁻ and hydrated SiO₃²⁻, intensified by the significant initial concentration of the latter two species in the alkaline solution, facilitates the adsorption of positive species in the negatively-charged reactive surfaces, facilitating the formation of longer chain-like precipitates. In a combined

scenario of alkalinity with constant stirring, the detachment of these precipitates results in the breakage of neighbouring Si-O and Al-O bonds, releasing larger glass flakes to the aqueous media following a fibrous-like fracture pattern. This type of surface alteration, strongly observed after 24 h, converts into the presence of platelet-like agglomerates after 72 hours (highlighted by the yellow dashed circles), due to the association of Ca^{2+} mainly with Al-species. Early precipitation of layered double hydroxides and portlandite, with similar morphologies, have been identified before in the dissolution of glass fibres in NaOH [189], as well as during the use of calcium sulfoaluminate cements for waste contention [404]. In both cases, the formation of such precipitates can occur due to the attachment of Al in reactive surfaces, which is energetically more favourable than the initial incorporation in existing C-S-H structures in high liquid/solid ratios [189], and to the formation of portlandite, as supported by the DTG curves in this period - see Figure 5.5.

At higher temperature (Figure 5.13b), the mechanisms of dissolution are slightly different. A combination of delamination with etching pits is observed at 24 hours (green dashed frames), with the observation of minor gel formations in localized regions of reactive surfaces (blue dashed frames). The high temperature regime facilitates hydrolysis processes [405], leading to a more aggressive attack reaching deeper portions of the glass framework. At longer periods, the precipitation of LDHs is suppressed by the formation of larger disordered hydrated gel regions, which cover a large portion but not the whole reactive surfaces. These gel structures are probably formed in regions which were previously altered in initial stages, covering delaminated and etched areas of the original glass (green dashed frame at 72h).

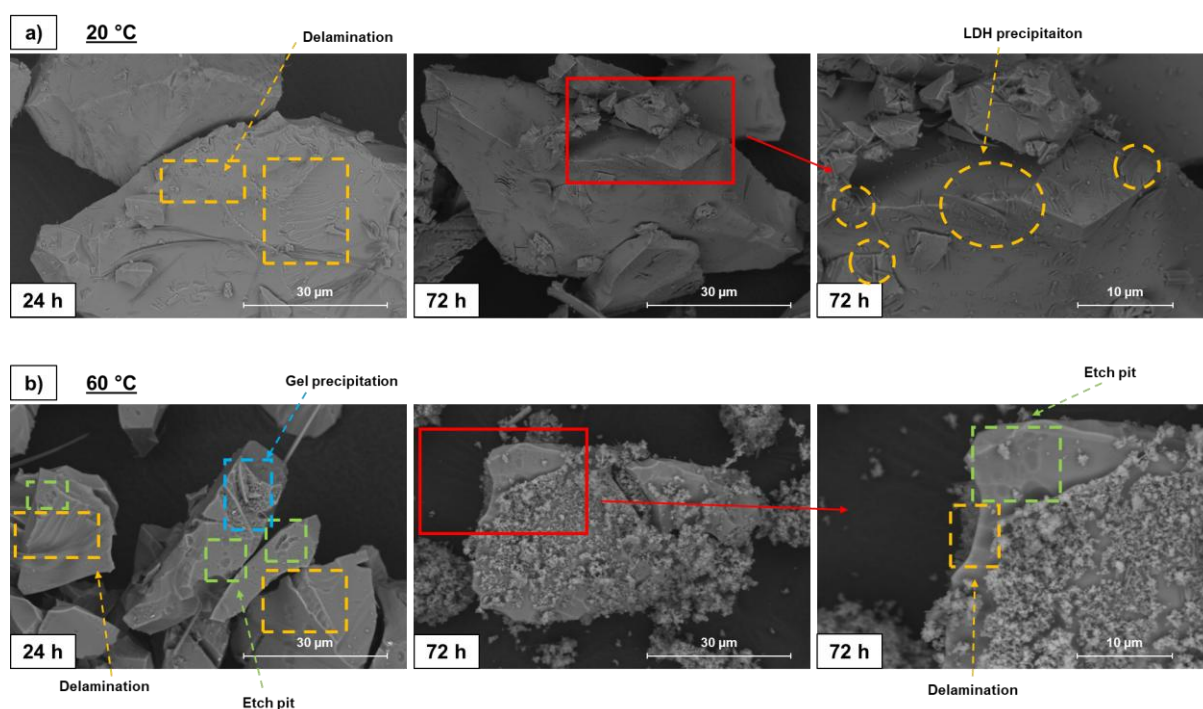


Figure 5.13: SEM micrographs of residual Si-FA glass particles after dissolution in waterglass solutions at: a) 20 °C, and b) 60 °C.

In NaOH solutions, the combination of alkalinity and temperature results in a significantly more aggressive environment, as observed in the SEM micrographs in Figure 5.14. Several etching pits are observed after only 1 hours of dissolution, better visualized in the enlarged images (green dashed frames). This surface attack occurs concurrently with the mild formation of altered layers in isolated regions, considering significantly higher dissolution rates at 60 °C compared to 20 °C. After 72 h, the particles are completely covered, and it is not possible to observe residual signs of unreacted surfaces. The reaction products form a thicker and porous layer - compared to waterglass-activated systems - with disordered morphology, as it is not possible to visualize structural ordering in one preferential direction.

The differences in the SEM micrographs suggest the promotion of two distinct reaction mechanisms, according to the conditions of the aqueous media. In both cases, at 60 °C, a significant amount of hydrated gels have been identified by DTG analysis. In waterglass systems, the observation of residual intact regions of glass surfaces indicates that a nucleation processes far from reactive surfaces dominates the reaction. The use of sodium silicate favours a naturally high initial concentration of silicate species in solution, which promotes the *homogeneous precipitation* of small crystallites in different locations of the solution. As the collection and characterization of residual material considers only the residual solid portion of the solution, the majority of nuclei that were eventually formed in the bulk solution will be eliminated during filtration, especially if the critical nuclei size to overcome kinetic constraints has not been achieved yet - the pore size of the utilised filter paper was 2.5 µm. Conversely, sodium hydroxide favours a *heterogeneous nucleation* regime, with gel precipitation being mainly anchored by glass surfaces since the first instants of the reaction.

The DTG curves demonstrated that stable nanostructured gels were formed earlier in NaOH than in waterglass systems, as the former had peaks in the 50 - 150 °C region already after 24 h. Homogeneous nucleation seems to be a slower process, arising from a potential slower dissolution rate in such conditions. The silicate-rich environment limits the coalescence and growth of small crystallites, as it promotes the adsorption of Si-species in their surface [406,407]. Moreover it also reduces the chemical affinity for SiO₂ dissolution, limiting the dissolution reaction as a whole [351]. On the other hand, NaOH induces a higher reactivity in initial moments with the earlier formation of altered layers, which convert into hydrated gels in sequential steps. In the ongoing reaction, this favours an outward growth of surface products, which will eventually bind with surface anchored gel in adjacent particles. The connection between coarse gel structures between two particles creates both a diffusion barrier for the continuity of dissolution, and entrapped irregular porosity [190,202]. This is commonly reported during alkali-activation of both high- and low-Ca precursors, as NaOH promotes a higher reactivity in initial moments [115,352], but an overall similar-to-lower degree of reaction when compared with sodium silicate solutions [111,175,408].

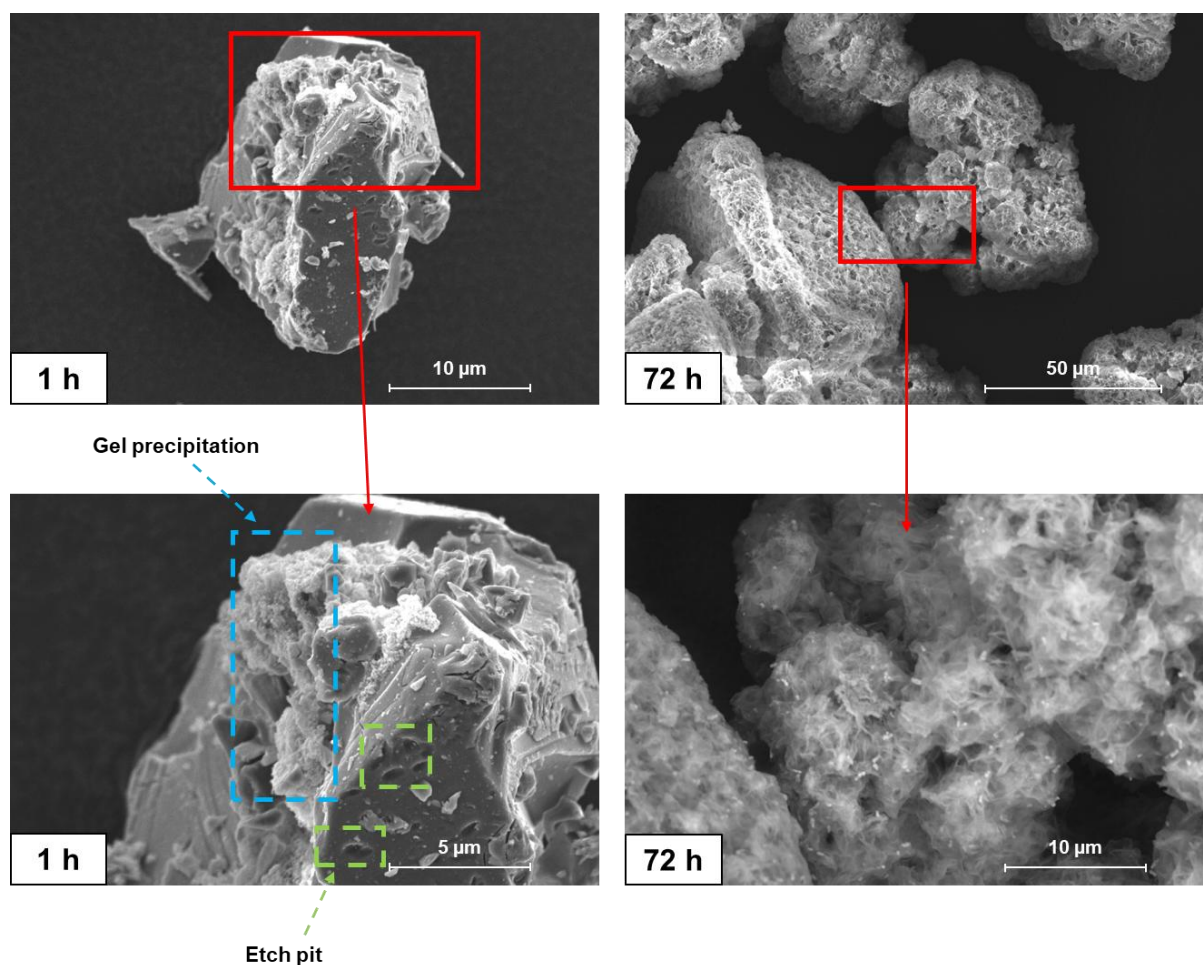


Figure 5.14: SEM micrographs of residual glass particles after dissolution in NaOH solutions at 60 °C.

5.3.3. Characterization of early reaction kinetics with in-situ isothermal calorimetry

Pastes of glasses Si-FA and BFS-2, activated with sodium hydroxide and waterglass, were monitored for the first 24 hours of reactions with in-situ calorimetry. The evolution of heat flow, shown in Figure 5.15, showed clear differences between the two glasses at 20 °C. The variations in dissolution peaks, according to the activator, were more pronounced in the activation of Si-FA (Figure 5.15a). The use of waterglass significantly influenced the duration and intensity of the peak, reaching 8.27 mW/g compared to 3.95 mW/g for NaOH-activation. As the dissolution rate of low-Ca precursors is significantly hindered at room temperature, the absence of aqueous silicate species in NaOH-systems limits the nucleation of crystallites in the bulk solution, and probably reduces the amount of reactions occurring on top of glass surfaces. Implementation of waterglass favours a homogeneous-like precipitation of reaction products and mildly enhances the reaction potential of the system, as it maintained a calorimetric sign higher in all moments. However, this precipitation still occurs at a low rate, resulting on an overall limited reaction in the first 24 hours, which has been reported many times for low-Ca precursors [83,156,177].

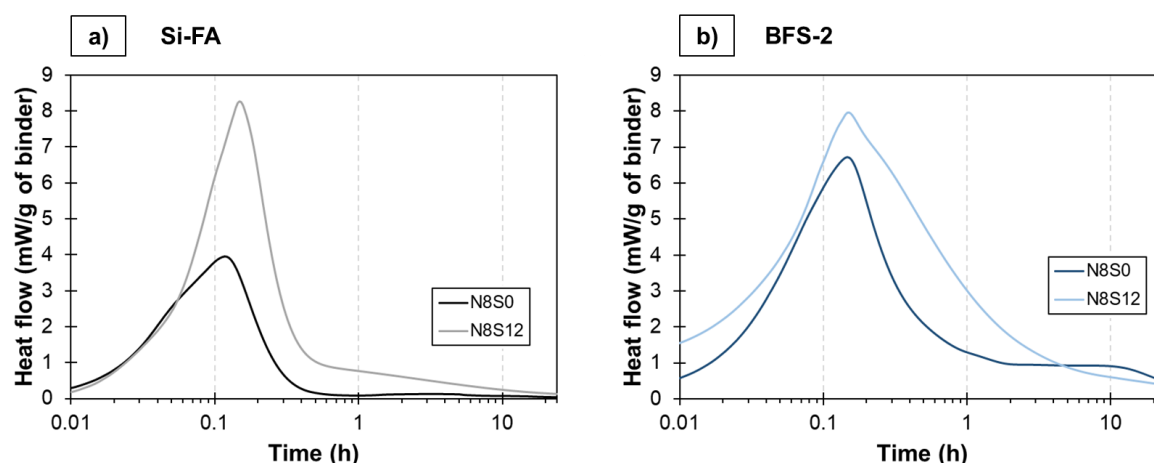


Figure 5.15: Isothermal calorimetry curves for glasses activated at at 20 °C in NaOH and waterglass solutions: a) glass Si-FA; and b) glass BFS-2.

The effect of waterglass on widening and increasing the height of dissolution peak was also detected in the alkali-activation of BFS-2 (Figure 5.15b). In the NaOH-activated system, an earlier deceleration of the curve followed the initial dissolution wetting and dissolution period. Although the formation of a subsequent acceleration peak was not clear, the heat flow was kept nearly constant for approximately 8 hours before dropping to the lowest values, which were higher than the signal from waterglass-activated glass at 24 h. In system N8S12, the first peak indicates that reactions follow a similar reaction path as observed for Si-FA, due to the availability of aqueous species from the activator. The influence of activator on the early-reaction has also been reported by a few authors. Sun et al [104] found similar initial patterns in alkali-activated slags, as a progressively increasing silicate modulus widened the first dissolution peak and further delayed the acceleration period, until eventually it was not observed with an M_s equal to 2. Bilek et al. [215] reported an extended induction period of 24 hours in pastes activated with sodium silicate, while NaOH promoted an acceleration period after 3 hours of reaction.

At 60 °C, the reactions are significantly accelerated for glass Si-FA in both activating scenarios, as observed in Figure 5.16. Following the observations made at room temperature for both Si-FA and BFS-2, the use of waterglass widens the dissolution peak, but the difference in intensity is not as remarkable as seen at 20 °C. The SEM micrographs (Figure 5.14) demonstrated that both dissolution and gel formation appeared to be enhanced in NaOH solutions, in agreement with the increased calorimetric response in initial moments of reaction. Despite the limited hydrolysis and etching pits occurring due to the lower pH of the pore solution in a waterglass-based system (Figure 5.13b), the aqueous silicate species create a more homogeneous distribution of solid nuclei in the bulk solution. As stated by Aretxabaleta and Manzano [397], the speciation between Ca^{2+} and H_3SiO_4^- , bound to 5 water molecules and a hydroxyl group to complete the coordination of Ca, is a highly exothermic process, which results in a rise in the early calorimetric response. Therefore, the first peak in waterglass-systems represents both dissolution and initial phase nucleation, as the two phenomena are occurring concurrently with each other, promoting a higher heat flow in the first hours of reaction. Furthermore, it hinders the formation of an induction period [177,409], as the solution is expected to remain in supersaturated conditions since earlier moments due to the presence of liquid silicate species, hindering the intensity but extending the forward dissolution period.

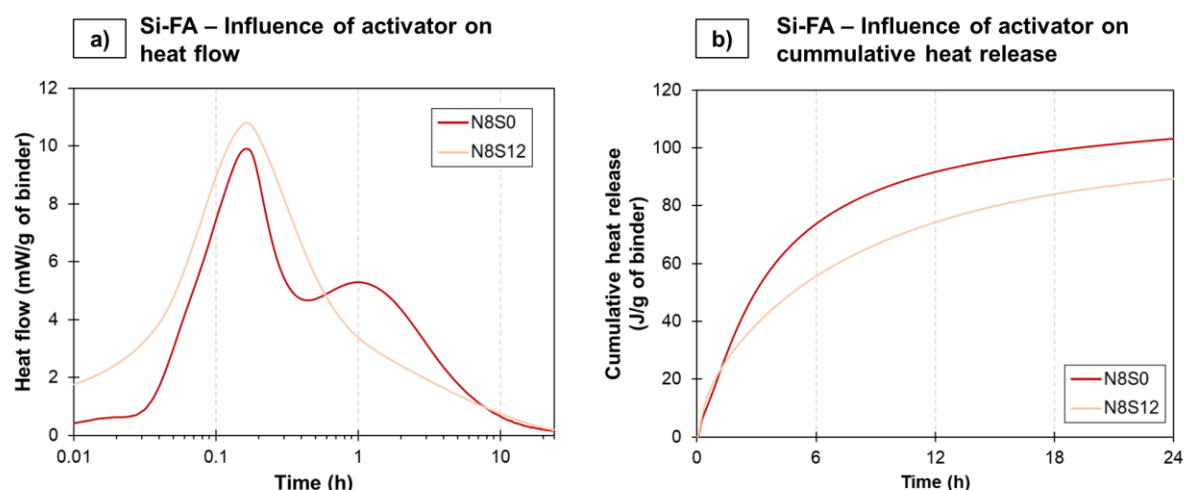


Figure 5.16: Isothermal calorimetry curves of the first 24 hours of glass Si-FA activated with NaOH and waterglass at 60 °C: a) heat flow evolution and b) cumulative heat release versus time.

Finally, the acceleration period promoted by NaOH boosts both the precipitation and the polymerization of solid phases, evidenced by the signals of chemical attack and surface anchored reaction products earlier than in waterglass systems through SEM imaging (Figure 5.14). The lower Si/Al ratio of the binder resulting from the use of sodium hydroxide is expected to facilitate the connection of Al-O-Si nuclei, favoured by the preferential dissolution of Al from the precursor [179,212]. The resulting phenomenon is a more rapid crosslinking of Al-rich species, leading to the formation of nuclei of nanocrystalline sites, thus generating additional acceleration peaks in alkali-activated low-Ca precursors. Conversely, waterglass systems favour the formation of amorphous gels of higher Si/Al ratio, which requires more time for a structural rearrangement into more ordered phases [25,79]. As a consequence, the accumulated heat release is larger at 24 hours in the N8S0 system, which is explained due to the exothermic nature of crosslinking processes [179].

5.4 Discussion

5.4.1 Effect of chemistry on initial degree of reaction

In alkali-activated systems, the differences in reaction mechanisms are influenced by both binder chemistry - considering precursor and activator - and curing temperature. Correlations between degree of reaction and chemistry have been observed by several authors, mainly concerning long stages of alkali-activation [47,48,410-413]. At early ages, the establishment of parameters based on intrinsic and extrinsic variables is not so simple, and requires the early characterization of such materials.

With the present results obtained by in-situ isothermal calorimetry, it was possible to associate the reactivity of the system with the binder chemistry of each paste made with glasses Si-FA and BFS-2, as shown in Figure 5.17. The combination between the fractions of Ca and Na, and the ratio of total Si with Si fraction only from the precursor, resulted in a nearly-linear correlation ($R^2 = 0.962$) with the accumulated heat release of pastes cured for 24 hours at room temperature. The reactivity of a system is known to be directly influenced by the presence of network modifying oxides in the glass composition [45,156] and the concentration of the alkaline solution [88,193,360]. In this context, Ca presence favours the

depolymerization of the glass frameworks, and the presence of Na indicates a higher alkalinity, with the latter indirectly facilitating the hydrolysis processes and the acceleration of the forward dissolution period. The proposed correlation is in agreement with the results reported by Kucharczyk et al. [156], as the authors stated a reduction in the degree of reaction of CAS glasses from approximately 30 % to 6 % after the first 24 h, as the Ca content was reduced from 50 mol% to 5 mol%, respectively.

With respect to waterglass solutions, the aqueous silicate species had an additional positive effect in the overall reaction, whilst maintaining the linear correlation in Figure 5.17 for pastes cured at 20 °C. However, when compared to NaOH-activated glasses, SEM micrographs demonstrated a less significant formation of reaction products covering glass surfaces during early stages - see Figures 5.8 and 5.13. As observed by Sun et al. via cryo-SEM [104], sodium silicate solutions promote less flocculated systems in the surroundings of particles of precursors, and smaller nuclei of reaction products are homogeneously distributed in the bulk matrix, while NaOH favours a quick precipitation of hydrated gels and secondary phases anchored in the precursor surface. Consequently, despite generating higher heat release for the activation of both Si-FA and BFS-2, waterglass-based systems can still present lower degrees of reaction. Reductions in the degree of reaction of slags activated with waterglass, compared to sodium hydroxide, have already been reported by Ben Haha et al. [408] and Le Saout et al. [88] in different magnitudes, after 24 hours of curing. Therefore, in combination with the present results, it can be concluded that phase precipitation dominates over the heat release of dissolution of precursors in the first day of reaction of alkali-activated binders.

The implementation of higher curing temperatures changed the reaction mechanisms, and it was not possible to extend the relationship proposed for systems cured at 20 °C in Figure 5.17 to the data for 60 °C. The results reported in Section 5.3.1.4 demonstrated that the leaching of Ca through ion-exchange processes, responsible for triggering the forward dissolution of Si and Al at room temperature, is limited at 60 °C. This occurs due to the higher ionic strength of the solution, which favours the strong occurrence of hydrolysis of Si-O and Al-O bonds regardless of Ca release [405]. It is thus suggested that the forward period changes its behaviour in higher temperatures, occurring simultaneously with a significant formation of primary nuclei of reaction products. However, this feature is limited only to Si and Al, since a continuous increase in concentrations of the two elements, combined with a nearly-constant concentration of Ca, was measured up to 72 hours of dissolution experiments, despite the observation of DTG peaks of nanostructured gels. Singh et al. [188] observed similar behaviour in the dissolution of fly ashes at 20 °C and 60 °C. Those authors found that, at similar alkalinity, the release of Ca was only 3-8 % higher, while Si concentration increased almost 80 % at higher temperature. These observations are corroborated by the work from Kuenzel and Ranjbar [214], who reported that the dissolution of fly ash is more dependent on temperature than on alkalinity. It is therefore proposed here that Ca is no longer the driving mechanism of reactivity of precursors at high temperature, with Si and Al being the main drivers for alkali-activation along with the activator.

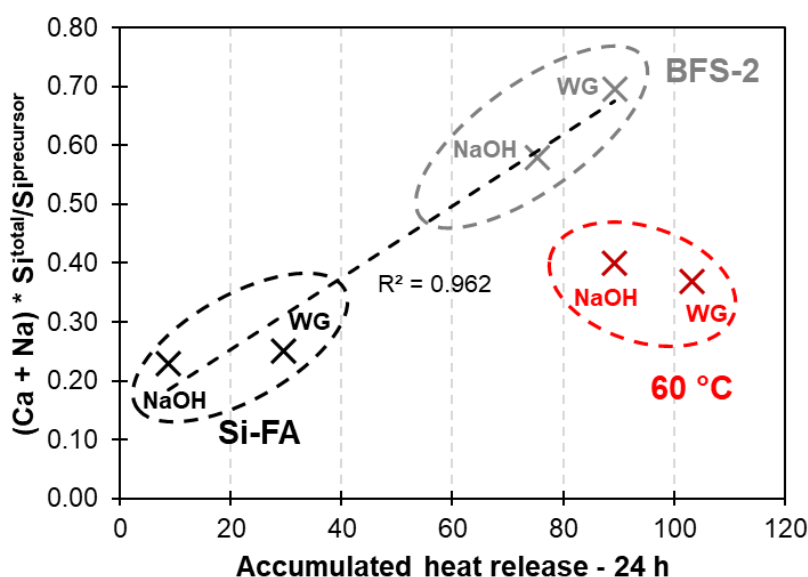


Figure 5.17: Correlation of binder chemistry with accumulated heat release, after 24 hours of curing, of Si-FA and BFS-2 pastes activated with both waterglass and NaOH.

5.4.2 Precipitation mechanisms in low-Ca precursors

Figure 5.18 shows secondary electron SEM micrographs of crushed paste particles used in the isothermal calorimetry tests performed at 60 °C. The crushing of the pastes provide an interesting visualization of the interactions between glass particles and the alkaline solutions, providing information on the mechanism of phase precipitation and the interface between cementitious matrix and precursor. It can be easily noticed that there are clear differences in the surface of glass particles according to the activating solution. Figure 5.18a depicts a very intense presence of etching pits of different sizes, distributed through all the unreacted particles. These affected areas arise from the strong chemical attack fostered by the combination of temperature with alkalinity, resulting in larger areas than what is observed in waterglass systems. It is possible to observe the formation of crystallites of different sizes inside and in the vicinity of these areas (highlighted in the yellow dashed frames). It is thus assumed that localized attacks, via hydrolysis, are essential to promote these areas as the initial nucleation sites in sodium hydroxide-rich media. Conversely, the N8S12 system depicted in Figure 5.18b presented a cleaner homogeneous surface, with a less pronounced amount of etching pits (green dashed frames) and the presence of long and continuous steps (blue dashed frames). The few visible etching pits demonstrate that homogeneous nucleation is less dependent on chemical attack and alkalinity as heterogeneous reactions, while the steps indicate that products with longer and continuous chains are favored in such solutions.

In NaOH-systems (Figure 5.18a), the formation of a surface-anchored percolated network of different zeolite-like materials has been reported in literature before for low-Ca precursors. In such media, the reactive surfaces in early stages are comprised of a porous layer formed by small crystals of aluminosilicate structures, following the same pattern seen in Figure 5.14. The composition of these products is dependent mainly on the chemistry of the binder, and the use of additional techniques is necessary to accurately define the nature of such

zeolites. For instance, Álvarez-Ayuso et al. [414] used XRD to identify the presence of chabazite, zeolite 4A and zeolite NaP1 in fly ash pastes activated with 12 M NaOH, while Ferrand et al. [415] and Ribet and Gin [351] reported the formation of analcime and Na-phillipsite in glasses dissolved with NaOH for long periods. On the other hand, the more homogeneous distribution of nucleation sites in waterglass systems creates a continuous but amorphous gel without a strong preferential orientation [48,398]. As a consequence, a stronger interface bonding is created between the hardened matrix and the residual unreacted particles.

Among the two solutions, the main differences are observed in the images with the highest magnification in Figure 5.18, more precisely in the surface conditions arising from each activator. The use of waterglass (Figure 5.18b) promoted a rougher surface, which arises probably due to the pronounced binding of Ca^{2+} and other positive species in the top layers of the glass particles. This leached layer induces the formation of small and homogeneously distributed granules, which can easily attach crystallites formed in the bulk solution. The smoother glass surfaces, observed in NaOH-systems (Figure 5.18a), indicate that granules of nucleation sites are not so well distributed, reducing the adhesion of glass particles with reaction products. Although this was not the object of study of this research, such differences in the nucleation path and matrix-precursor interface are expected to have a significant impact in the strength development in the fresh state of pastes with low-Ca materials. These initial observations indicate that an optimum balance between dissolution and nucleation rates can be achieved via an appropriate dosage of activator, considering alkalinity and availability of reactive liquid sites.

The sketch in Figure 5.19 presents an illustration of the different reaction paths arising from the use of different activating solutions in low-Ca precursors. In a system based on sodium hydroxide (Figure 5.19a), the formation of crystallites in the bulk solution is limited in the first moments of reaction, and the initial reaction products are majorly anchored in surface spots which were heavily attacked by hydrolysis (5.19b). In a second step, this results in the formation of a porous network of reaction products strongly attached to etching spots in the reactive surface (5.19c). On the other hand, the use of sodium silicate (5.19d) promotes a more homogeneous distribution of etching pits with smaller areas (5.19e). This leads to a stronger attachment of reaction products to the reactive surface, whilst nucleation is still observed in regions more far from the reactive surfaces (5.19f), leading to refined microstructure of the hardened binder. The sketch is also in agreement with the discussion made in the previous section: while the glass displays a higher dissolution degree in NaOH-based systems, the amount of reaction products in waterglass-solutions is higher in the first day of reaction.

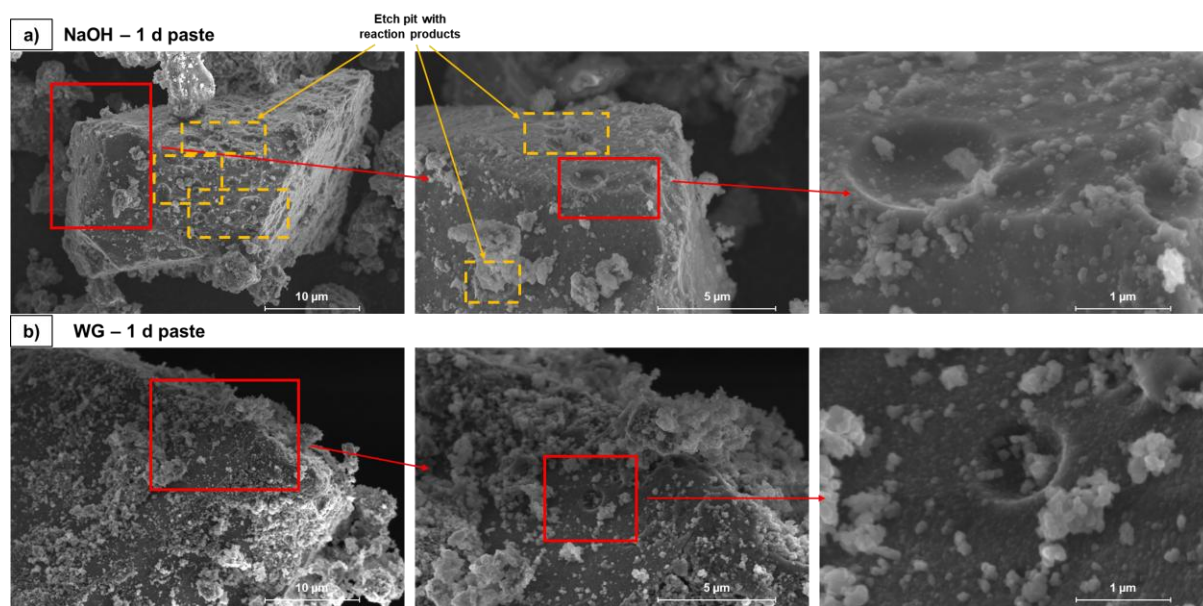


Figure 5.18: Secondary electron SEM micrographs of crushed paste particles of glass Si-FA activated with a) NaOH and b) waterglass solutions at 60 °C, cured for 24 h.

It is here concluded that, for low-Ca precursors, the type of nucleation strongly affects the structure of the N-A-S-H gel to be formed. Homogeneous-like precipitation of reaction products favours a more cohesive gel, as small nuclei easily coalesce with each other into a continuous layer of reaction products. The result is a strong adhesion of the matrix to unreacted particles with reduced porosity. The implementation of hydroxide-based activators gives a noticeable attack into the precursor top layers, accelerating the dissolution rate but not necessarily the overall reaction process by the formation of stable reaction products. As a consequence, reaction products are poorly distributed throughout the microstructure, and the resulting matrix has a percolated porous network of nanosized disordered zeolite structures.

5.4.3 Mechanisms of N-A-S-H gel precipitation

During the early stages of the activation reactions of low-Ca glasses, the nucleation and stabilization of nanostructured hydrated gels was only favoured at 60 °C, as demonstrated in section 5.3.1.4. As Ca no longer presents the role of main reaction driver in this curing regime, it could be assumed that N-A-S-H has preferential formation over other Ca-containing gels. However, the calculation of effective saturation indices displayed the opposite trend, as C-S-H was demonstrated to be the most thermodynamically likely phase to be precipitated, while the formation of N-A-S-H gel was favoured only in secondary steps.

The implementation of the selective dissolution treatment with salicylic acid and methanol (SAM), which is able to dissolve amorphous and short-range ordered Ca-based reaction products [363] and allow a dedicated study of other gels, provided interesting observations concerning the kinetics of precipitation of N-A-S-H-like phases at 60 °C in Si-FA-containing pastes. As seen in Figures 5.20a and 5.20b, a slightly higher weight loss was measured up to 300 °C for the SAM-residue material collected from NaOH-activated pastes, typically attributed to the loss of bound water in hydrated gels [173,416]. This follows the higher weight loss measured for pastes before selective dissolution, and the difference among the

two activators is the same before and after SAM treatment. Although the measurement of water loss is not necessarily linearly correlated with degree of reaction, as it is not possible to determine the exact amount of structural water bound to each gel phase, the higher loss follows the more intense calorimetric response measured for the system N8S0 in the same period. Additionally, in NaOH-activated paste, the release of water was slightly shifted towards higher temperatures, which can be an indication of the entrapment of water in the porous network of reaction products observed in Figure 5.14, formed by nanostructured gels resembling zeolite.

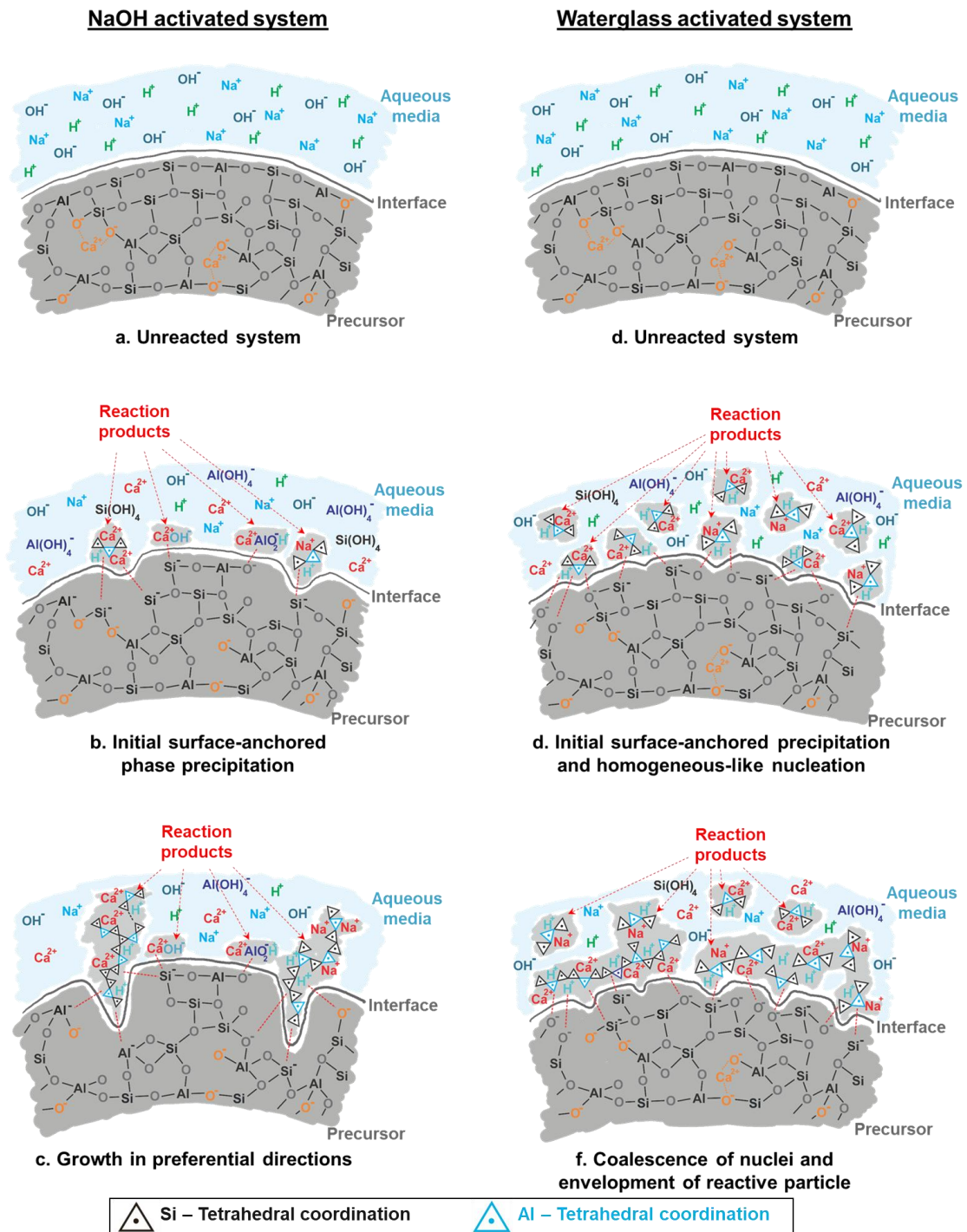


Figure 5.19: Schematic illustration of the different precipitation mechanisms in NaOH- and waterglass-activated systems.

Differences in N-A-S-H precipitation on each solution are better visualized with FTIR analysis in Figures 5.20c and 5.20d. The Si-O-T-related band, centred between $950\text{--}1000\text{ cm}^{-1}$ [172,211,242,243], moves to higher wavenumbers in both pastes after the SAM treatment. This shift is somehow expected, as the removal of Ca increases the Si fraction in the reaction products. Still in this region, system N8S12 presented a higher Si/Al ratio in its aluminosilicate chains, displaying the highest value for the centre of the Si-O-T band. An interesting feature of the curves is the shoulder observed at 903 cm^{-1} in both systems, attributed to Si Q² bonds [361]. The stronger reflection observed in waterglass-activated paste suggests a more pronounced chain-like formation of N-A-S-H gel with sodium silicate. Conversely, the presence of zeolite-like reflections [87,190,207,318,417,418], stronger in N8S0, confirms the structural differences in the residual gels according to the activator, supporting the water loss observed at higher temperature being caused by the porosity of the matrix containing short-range ordered zeolite structures.

As a conclusion, it was demonstrated that very similar quantities of N-A-S-H gel are formed regardless of the activating solution after 24 hours of curing at $60\text{ }^{\circ}\text{C}$. The nature of the activator has a major influence on the structure of the gels, which were observed to be more ordered in NaOH-based systems. A quantitative determination of these phases could not be resolved, as it is not possible to determine the formula of each gel, especially with respect to water content. Lastly, the combination of thermodynamic calculations with experimental observations implies that the precipitation of N-A-S-H-like phases occurs simultaneously with Ca-containing gels. These latter phases represent a significant portion of the reaction products, forming a hardened matrix which presents an intimate interconnection between different nanostructured gels.

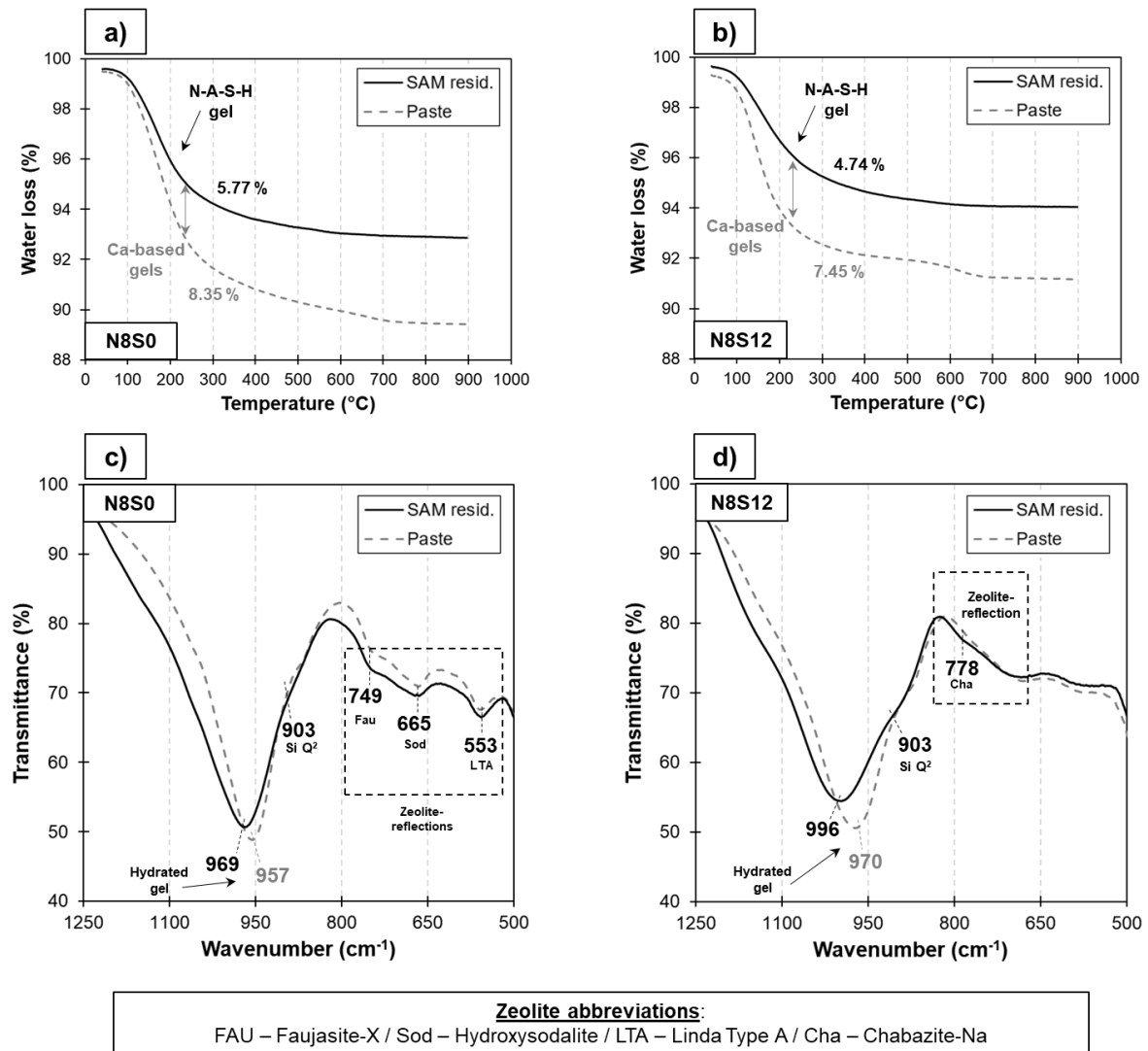


Figure 5.20: Characterization of Si-FA-containing pastes cured for 1 day at 60 °C, before and after SAM treatment: DTG measurements of systems a) N8S0 and b) N8S12, and FTIR of systems c) N8S0 and d) N8S12.

5.5 Conclusions and outlook

The visualization and analysis of early stages of reactions provide important information on the structure and distribution of the primary reaction products, as these features have direct impact on the fresh properties and strength development of cementitious binders. The study of the dissolution kinetics of fine powders intentionally drove the reaction into the next stage, favouring the initial formation of solid phases. By analyzing the residual powder collected after dissolution, it was possible to qualitatively determine the nature and the volume of the primary reaction products, strongly linked to the reaction potential of each system. Further on, the calorimetric and image evaluation of pastes cured for 24 hours allowed the establishment of a connection between nucleation processes and stabilization of solid phases.

This chapter targeted the comprehension of the effect of chemistry and temperature on the distinct precipitation mechanisms in the alkali-activation of synthetic glasses, evaluating also the influence of time in the precipitation of the first solid nuclei and mechanisms

involved on their growth and stabilization. Based on the results presented, the following conclusions and observations were defined:

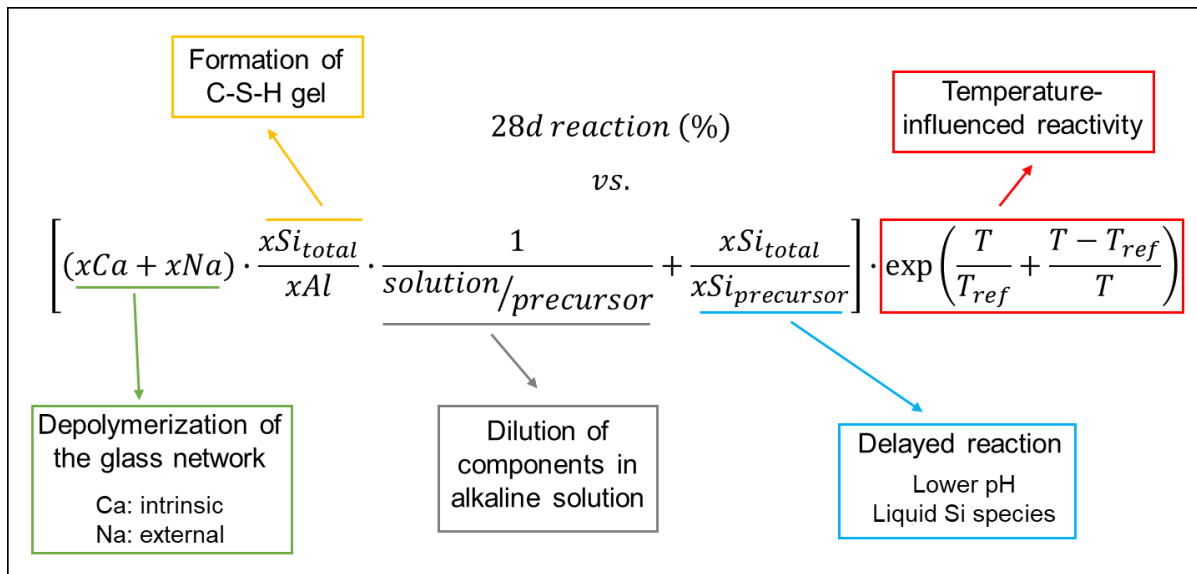
- The calculation of effective saturation indices indicated that there is a minimum supersaturation degree required to allow the stability of a phase. This effect arises from the size of the crystallites that are precipitated in initial stages, as they require time to coalesce and form nuclei above a critical volume to become thermodynamically stable.
- The reactivity of a system can be evidenced by the nature of the carbonated phases that were identified. In slag-type systems, formation of calcite and monocarboaluminate indicated the carbonation of C-S-H-like phases. In fly ash-type systems, the formation of hemicarboaluminate indicated insufficient gel precipitation, as the formation of hydrated gels was hindered at 20 °C for fly ash glasses.
- Ca was the main driver for the reactivity of synthetic glasses at room temperature. At 60 °C, the mechanisms were changed, and hydrolysis reactions were favoured on top of ion-exchange reactions in initial moments.
- Si-FA and BFS-2 presented similar differences regarding nucleation mechanisms according to the activator of choice. In both cases, the formation of leached layers was only evidenced in waterglass-based systems.
- Differences in activating solutions promoted different nucleation mechanisms. NaOH provided a significant anchoring effect on the reactive surfaces, triggered by the strong hydrolysis promoted by the highly alkaline environment. The lower alkalinity of sodium silicate reduced the chemical attack on the glass surfaces, promoting a more homogeneous distribution of reactive spots. Combined with the nucleation of small solid nuclei far from the reactive surfaces, due to the presence of aqueous silicate species, such systems promote a stronger envelopment of the reactive surfaces, resulting in a higher cohesion between the matrix and the unreacted precursor.
- The use of a curing temperature of 60 °C was vital to comprehend the effect of the activating solution on the early reaction kinetics. In glass Si-FA, NaOH promoted a faster dissolution of the precursor up to 24 h, accelerating the precipitation of reaction products at the surface of the precursor. Sodium silicate accelerated the initial formation of small crystallites but hindered their further growth, resulting in a reduced overall reaction degree.
- In low-Ca precursors, the precipitation of N-A-S-H-like gels is significantly limited at room temperature, and occurs concurrently with Ca-based gels at 60 °C. With either activator, the final matrix is composed of an intimate mixture of both types of gels. The use of NaOH facilitates the formation of nanosized ordered structures, resulting in a porous network with stronger zeolite-like preferential orientations.

The characterizations of reaction mechanisms performed in this Chapter, at such early ages, can be used for optimization of mixtures based on microstructure and strength development. Combined with the identification of the reactivity of a system, the determination of the structure of the primary reaction products is vital on the comprehension of the development of features still in fresh states, and on the setting of the system. The presented findings will be explored and extended in Chapter 6, which will evaluate the evolution of microstructure with time. The obtainment of mature and stable

microstructures will be correlated to the initial mechanism of reaction, and the influence of temperature and chemistry on the sequential stages of reaction will be addressed.

Chapter 6.

Phase assemblage of alkali-activated pastes with synthetic precursors



In alkali-activated materials, the composition and the behaviour of a stable microstructure are dependent on the degree of reaction of the precursor(s) and in the distribution of reaction products in the bulk activated matrix. Similarly to the descriptions made in the previous chapters, these characteristics are highly influenced by both intrinsic and extrinsic factors of the mixture, and the large amount of existing variables in these binders creates challenges on the development of application-driven formulations. This Chapter aims to establish correlations between binder formulation and curing parameters to the evolution of hardened microstructures, identifying how each parameter influences the reaction potential of a system and the distribution of reaction products. At the end, the work proposes empirically-defined correlations which quantifies the degree of reaction and distinguishes the contributions of the main categories of reaction products to the overall phase assemblage within the hardened microstructure of alkali-activated binders.

6.1 Introduction

Differences in the reaction kinetics of alkali-activating systems have been identified, multiple times, to be influenced by the nature of the components of the mixtures [193,204,348,357,419,420]. From changing the overall porosity [110,344,412] to favouring specific reaction products [89,200,365], mild fluctuations in the proportions or chemical compositions of raw materials can promote significant impacts in the sequence of reactions, affecting the development of properties in fresh state and hardened conditions.

Independent of the specific activators and precursors, the main reaction products are generally categorized within Ca-dominated or Al-Si-rich phases. The first group comprises the commonly observed variations of calcium silicate hydrate (C-S-H) gels, accounting for the presence of Al as replacement in tetrahedral sites in SiO_4 chain structures, and a mild uptake of Na (or K, although the analysis here will refer solely to Na) as an additional charge-balancing cation - forming the category of C-(N-A-)S-H gels. The second is formed by sodium aluminosilicate hydrate (N-A-S-H) gels and zeolites, composed of frameworks of SiO_4 and AlO_4 tetrahedra, mainly charge-balanced by Na but which can also display a minor uptake of Ca as charge balancing cation - forming the category of N-(C-)A-S-H gels.

Since the two main reaction products will mainly display short-range ordering of their structures, they are usually found intimately mixed with each other in a hardened cementitious matrix. A few authors have attempted to distinguish the formation of the two categories, establishing threshold chemical compositions based on atomic Ca/Si, Na/Ca and Si/Al ratios [89,219,421,422] via energy dispersive spectroscopy (EDS) analysis. However, these results are restricted to a post-reaction assessment, and a quantitative estimation based on inputs of the mixtures have only been recently assessed using thermodynamic modelling [227]. Despite being a promising alternative, the lack of consistent databases for amorphous N-(C-)A-S-H gels represents a challenge in the thermodynamic modelling of alkali-activated binders. The prediction of the formation of Al-Si-rich reaction products through zeolite-phases is often performed in literature, but the naturally more stable configurations of these crystalline products over amorphous gels results in a kinetic limitation of thermodynamic models, preventing the observation of the crystallization phenomena of disordered N-(C-)A-S-H species and consequently overestimating the final amounts of zeolites in stable systems.

This chapter aims to establish a three-way correlation in alkali-activated binders, connecting the mixture design (chemistry) to the degree of reaction and the phase assemblage of reaction products. Based on experimental observations, the influence of chemistry, temperature and age on kinetics of reaction were evaluated in 18 different mixtures. The methodology developed in this experimental campaign targets the distinction of the main reaction products in the amorphous and semi-crystalline portions of hardened binders, working as an additional tool to the post-reaction investigations described in literature. Finally, empirically-defined indices are proposed to estimate the quantitative formation of each category of reaction products, based on the chemistry of the raw materials and the curing temperature. Figure 6.1 illustrates the position of Chapter 6 as the final part of the study of microstructure evolution in the present thesis, which will provide the final inputs and validation criteria for the modelling tools to be developed in Chapter 7.

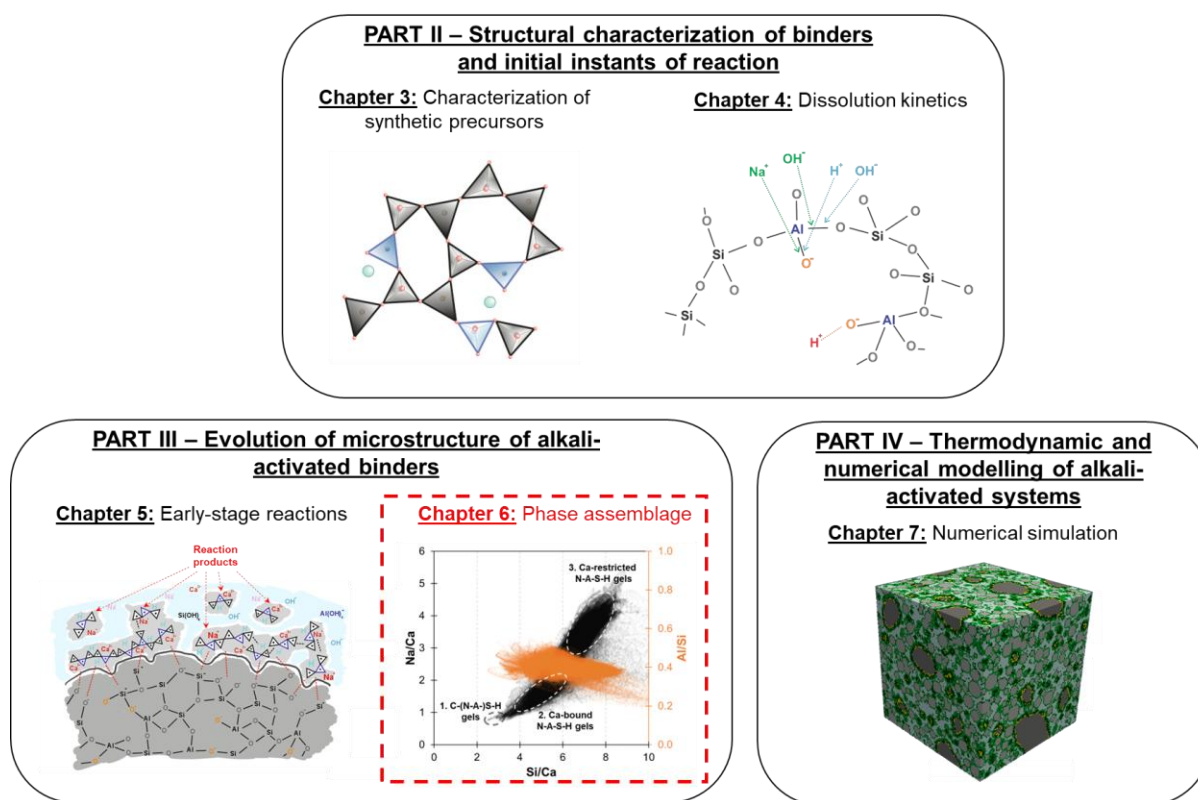


Figure 6.1: Schematic illustration of the structure of this thesis, highlighting the contributions of Chapter 6.

6.2 Materials and methods

6.2.1 Preparation of synthetic precursors

The synthetic glasses used in this chapter were obtained via the melting/quenching procedures described in Chapter 3 - see Section 3.1. The glasses were activated to obtain of pastes, which were subjected to different curing regimes (time and temperature) and further characterized by different techniques. After quenching and drying, the synthetic precursors were ground and milled, targeting a d_{50} of approximately 25 μm . Three different batches of glasses were used in this chapter: two groups, comprised of the four categories of precursors, were used for the preparation of pastes cured for 7 and 28 days at 20 °C - one group per curing age; one group, comprised of synthetic fly ash-type glasses, was used for pastes cured at 60 °C - the same group was used for both curing ages. The use of different batches for each group of samples was required because a limited amount of material (approx. 50 g) was obtained from each batch in the glass synthesis process - see Chapter 3 for more details. The compositions of each batch are detailed in Table 6.1, and the particle size distributions are shown in Figure 6.2.

Table 6.1: Chemical composition of synthetic glasses used to produce pastes, according to the curing method of each batch - compositions normalized to the molar content of SiO_2 , as measured by X-ray fluorescence.

	Glass	Type	Chemical composition (normalized molar ratios)		
			SiO_2	Al_2O_3	CaO
7-days paste	Si-FA	Siliceous fly ash	1.00	0.34	0.23
	Ca-FA	Calcareous fly ash	1.00	0.34	0.48
	BFS-1	Blast furnace slag	1.00	0.37	0.99
	BFS-2	Blast furnace slag	1.00	0.31	1.25
28-days paste	Si-FA	Siliceous fly ash	1.00	0.33	0.24
	Ca-FA	Calcareous fly ash	1.00	0.34	0.52
	BFS-1	Blast furnace slag	1.00	0.35	1.10
	BFS-2	Blast furnace slag	1.00	0.35	1.42
60 °C - cured pastes	Si-FA	Siliceous fly ash	1.00	0.31	0.25
	Ca-FA	Calcareous fly ash	1.00	0.32	0.51

6.2.2 Preparation of pastes

Pastes were prepared by the activation of synthetic glasses with four defined activating solutions: systems N4S0, N8S0 and N12S0 were NaOH solutions with 4 wt%, 8 wt% and 12 wt% of Na_2O per mass of glass, and system N8S12 was a waterglass solution, with 8 wt% of Na_2O per mass of glass, and a silicate modulus of 1.5. The activators were prepared following the description in Section 5.2.2, aiming for a water/precursor ratio of 0.40 for the slag-type glass based mixtures, and 0.35 for fly ash-type glass based mixtures - changes followed suggestions made by [175] due to the lower water demand of fly ashes. Additionally, pastes with blended precursors were prepared using mixtures of the two most extreme glasses, BFS-2 and Si-FA, with mass ratios of 70:30, 50:50, and 30:70, respectively named B70, B50 and B30 according their content of BFS-2.

The activating solutions N8S0 and N8S12 were used to activate each of the synthetic precursors, cured at 20 °C for 7 and 28 days in sealed conditions. Fly ash-type glass based pastes (glasses Si-FA and Ca-FA) were also cured following a two-step procedure: 7 days at 60 °C, and then at 20 °C up to a total of 28 days of curing, under sealed conditions - these pastes will be referred as 60 °C-cured for the remainder of the Chapter. The hardened pastes were characterized after 1, 7, and 28 days of curing. Activators N4S0 and N12S20 were used for limited experiments with glasses BFS-2 and Si-FA, cured only for 7 days at 20 °C (both glasses) and at 60 °C (Si-FA only). Table 6.2 details the mixtures used for this Chapter.

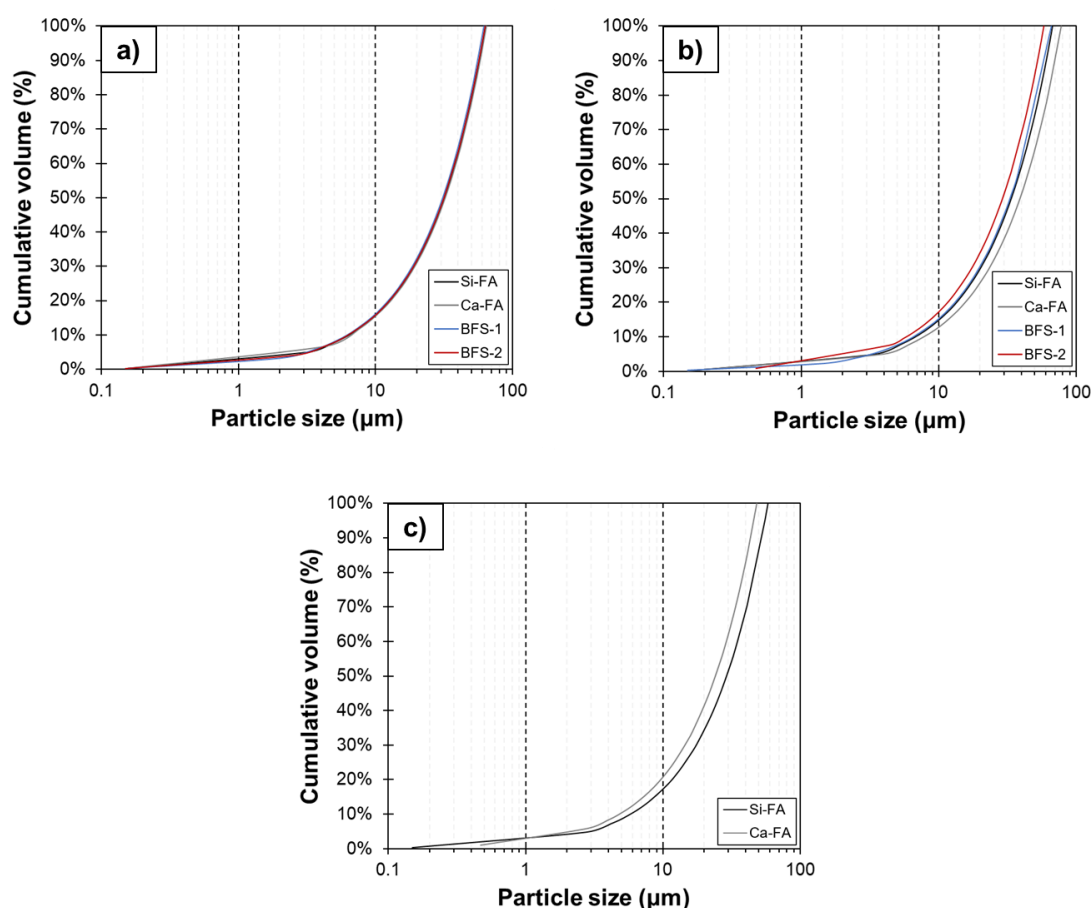


Figure 6.2: Particle size distribution of glasses used for: a) pastes cured for 7 days at 20 °C; b) pastes cured for 28 days at 20 °C; c) pastes cured at 60 °C.

6.2.3 Characterization of hardened pastes

After each specific curing regimen, part of the pastes were crushed and immersed in isopropanol solution for one week to allow solvent exchange and stop their hydration. Afterwards, the crushed materials were characterized using X-ray diffraction (XRD) and Fourier transform infrared (FTIR) spectroscopy. The analysis followed the descriptions detailed in Section 3.2.2, for the former, and 4.2.2, for the latter.

The remaining portions of the pastes were impregnated in epoxy after solvent exchange treatment, ground with SiC sandpaper and polished with diamond pastes down to a particle size of 0.25 μm . The polished samples were characterized with scanning electron microscopy (SEM) coupled with energy dispersive spectroscopy (EDS) in order to evaluate the distribution and composition of reaction products, and to characterize the residual particles of unreacted precursors and their interface with the hardened cementitious matrix. 20-25 backscattered electron (BSE) images were obtained for each mixture at 7 and 28 days, using the same specifications detailed in Section 5.2.4. The ilastik machine learning software [17] was implemented to perform phase segmentation of the microstructure, distinguishing unreacted particles from pores and hardened matrix. The ilastik software is a versatile trainable tool, being able to distinguish different image features in cement microstructures via pixel classification [423,424]. The segmentation was performed according to the grey level of each pixel and characteristics of the neighbouring units, classifying them within one

of the three categories. An example of this procedure is shown in Figure 6.3 for a 28-days cured B50 specimen (N8S12 system) activated with waterglass.

If a statistically sufficient quantity of images is used, the area of unreacted particles in a two-dimensional image can be assumed to be equal to their volume fraction in a three-dimensional analysis [173]. This approach allowed the estimation of the degree of reaction of each paste. As the initial volume fraction of the synthetic precursors in each paste is easily calculated via the mixture design details, a relative change in the amount of unreacted material allows the determination of the reaction degree, at a specific age, according to Equation 6.1:

$$\alpha(t) = \left(1 - \frac{V_t}{V_0}\right) \cdot 100\% \quad (6.1),$$

where $\alpha(t)$ is the degree of reaction at time t , V_t is the volume fraction of the precursor at time t , and V_0 is the initial volume fraction of the precursor.

Table 6.2: Details of pastes prepared for alkali-activation and further characterization.

System	Precursor	Na ₂ O ^a	SiO ₂ ^b	Water/precursor	Curing temperature
N8S0	BFS-1	8.0 %	-	0.40	20 °C
	BFS-2	8.0 %	-	0.40	20 °C
	Ca-FA	8.0 %	-	0.35	20 °C / 60 °C
	Si-FA	8.0 %	-	0.35	20 °C / 60 °C
	B70 ^c	8.0 %	-	0.40	20 °C
	B50 ^d	8.0 %	-	0.40	20 °C
	B30 ^e	8.0 %	-	0.40	20 °C
N8S12	BFS-1	8.0 %	11.6 %	0.40	20 °C
	BFS-2	8.0 %	11.6 %	0.40	20 °C
	Ca-FA	8.0 %	11.6 %	0.35	20 °C / 60 °C
	Si-FA	8.0 %	11.6 %	0.35	20 °C / 60 °C
	B70 ^c	8.0 %	11.6 %	0.40	20 °C
	B50 ^d	8.0 %	11.6 %	0.40	20 °C
	B30 ^e	8.0 %	11.6 %	0.40	20 °C
N4S0 ^f	BFS-2	4.0 %	-	0.40	20 °C
	Si-FA	4.0 %	-	0.35	20 °C / 60 °C
N12S0 ^f	BFS-2	12.0 %	-	0.40	20 °C
	Si-FA	12.0 %	-	0.35	20 °C / 60 °C

^aWeight percentage of Na₂O with respect to the mass of precursor.

^bWeight quantity of SiO₂ with respect to the mass of precursor, aiming a silicate modulus of 1.5

^cObtained by a mixture of 70 wt% of glass BFS-2 and 30 wt% of glass Si-FA.

^dObtained by a mixture of 50 wt% of glass BFS-2 and 50 wt% of glass Si-FA.

^eObtained by a mixture of 30 wt% of glass BFS-2 and 70 wt% of glass Si-FA.

^fPastes prepared exclusively for characterization with isothermal calorimetry and X-ray diffraction.

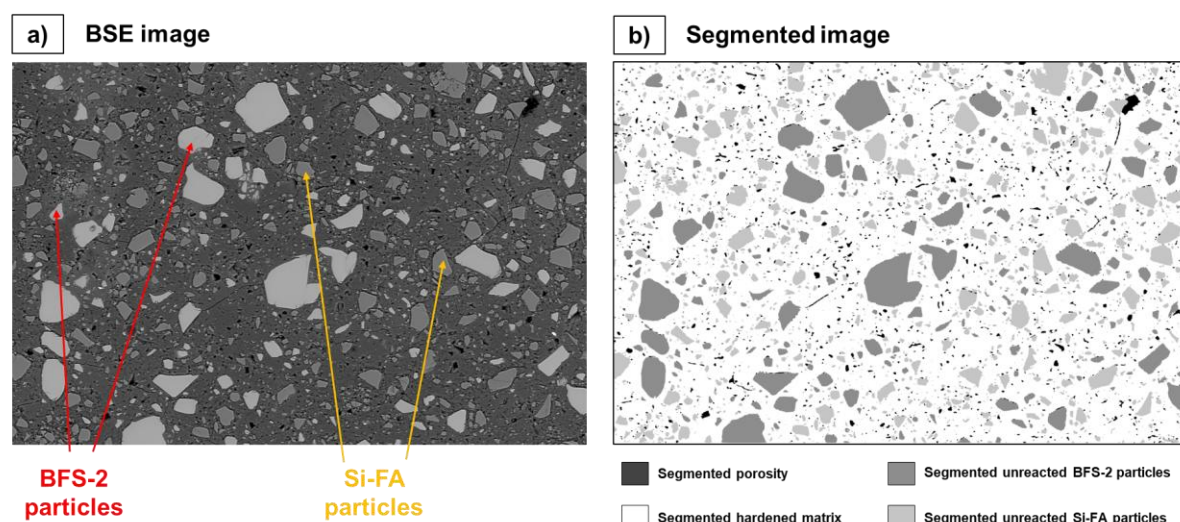


Figure 6.3: Application of phase segmentation on a BSE image of a B50 specimen obtained in the present work, activated with waterglass (system N8S12) and cured for 28 days: a) original image obtained via SEM; b) segmented image.

With respect to EDS analysis, element mapping was performed using a ThermoScientific Magnaraw detector in Si-FA-containing pastes cured at 60 °C. The edxia method [425] was implemented for the distinction of the hardened matrix and unreacted particles. This approach generated a hypermap with over 500,000 data points, allowing a detailed characterization of the chemical composition of the hardened matrices.

Additionally, hardened pastes were subjected to a selective dissolution treatment using a solution of salicylic acid and methanol (SAM), which promotes the dissolution and elimination of amorphous and short-range ordered C-(N-A-)S-H gels from the microstructure of the hardened pastes - see section 5.2.5 for more details. This procedure promoted the isolation of N-(C-)A-S-H and other secondary phases, allowing a dedicated characterization of their structures, and a quantitative determination of each category of reaction products in the hardened binder.

6.2.4 Isothermal calorimetry

The evolution of kinetics of reaction for all mixtures was monitored using isothermal calorimetry, via the preparation of additional paste samples. Following the details given in Table 6.2, a total of 5 g of binder was prepared for each mixture. The synthetic glasses were added to the designed solutions and the mixtures were stirred for three minutes prior to being added to the calorimeter. The calorimetric response was recorded during first seven days of reaction, at 20 °C for all glasses, and also at 60 °C for fly ash-activated glasses. For blended precursors, the heat release was measured for 14 days, allowing the monitoring of any delayed reactivity of one of the components. The specifications of the device are given in section 5.2.3.

6.2.5 Quantitative determination of reaction products

Quantitative X-ray diffraction (QXRD) analysis was performed for all pastes after 28 days of curing, aiming at the determination of the amount of each reaction product formed within

the hardened cementitious matrixes. Following the solvent exchange process, the crushed materials were mixed with 10 wt% ZnO (PDF # 00-036-1451) as internal standard. The XRD scans were performed using the procedures described in Section 3.2.2. The quantitative calculations were performed using the Rietveld refinement method via the Profex-BGMN [426] software, considering crystalline anisotropic and texture refinement corrections, following suggestions made in [173]. The structures considered for the calculation are shown in Table 6.3, which considers all reaction products identified in the assessment of pastes without ZnO throughout this research. Figure 6.4 displays an example of the output results, obtained via the refinement of pastes made with glass BFS-2, activated with waterglass (system N8S12).

This research proposes a methodology to estimate the fractions of reaction products separated in three categories: C-(N-A)-S-H gels as amorphous structures dominated by Ca; N-(C-)A-S-H gels as amorphous gels with low or no Ca-content, and zeolite-like compounds; and other secondary Ca- and Al-favoured crystalline phases, such as strätlingite, katoite and AFm phases. By using an internal standard of known weight, it is possible to distinguish the weight fraction of each phase and calculate the proportion of amorphous material with any software dedicated to QXRD analysis. In hardened pastes, the amorphous portion is comprised of unreacted precursors, disordered C-(N-A-)S-H and disordered N-(C-)A-S-H gels. The determination of the degree of reaction of each paste, using phase segmentation of SEM micrographs, allowed the subtraction of the contents of unreacted glasses from the amorphous fraction determined by the Rietveld refinement. Additionally, the weight loss measured during the SAM extraction method was used to subtract the contributions of Ca-dominated phases to the same region. By combining these techniques, it was possible to quantitatively distinguish the proportions of unreacted material and each gel type to the overall amorphous region, along with the quantification of secondary reaction products. These values were used to propose a *Phase assemblage index* of formation of each category of reaction products, and will be detailed in Section 6.4.2 and in Appendix E.

Table 6.3: Phases considered for the quantitative determination of reaction products via QXRD analysis - when structural files were not available within the ICDD PDF 4+ database, the closest structures from the Crystal Open Database (COD) were used.

Category of reaction products	Phase	Structure ID
Crystalline counterparts of C-(N-A-)S-H gels	14 Å tobermorite	PDF # 00-026-0331
	Al-substituted tobermorite	COD 1527001
	9 Å tobermorite	COD 9013974
Crystalline counterparts of N-(C-)A-S-H gels	Chabazite-Na	COD 9014093
	Faujasite-Y	COD 1538323
	Hydroxysodalite	PDF # 01-072-2329
	Natrolite	PDF # 00-045-1413
	Gismondine	PDF # 00-020-0452
Other crystalline Ca-rich phases	Katoite	PDF # 00-024-0217
	Strätlingite	COD 9005059
	Monocarboaluminate	COD 1000459
	Calcite	PDF # 00-005-0586

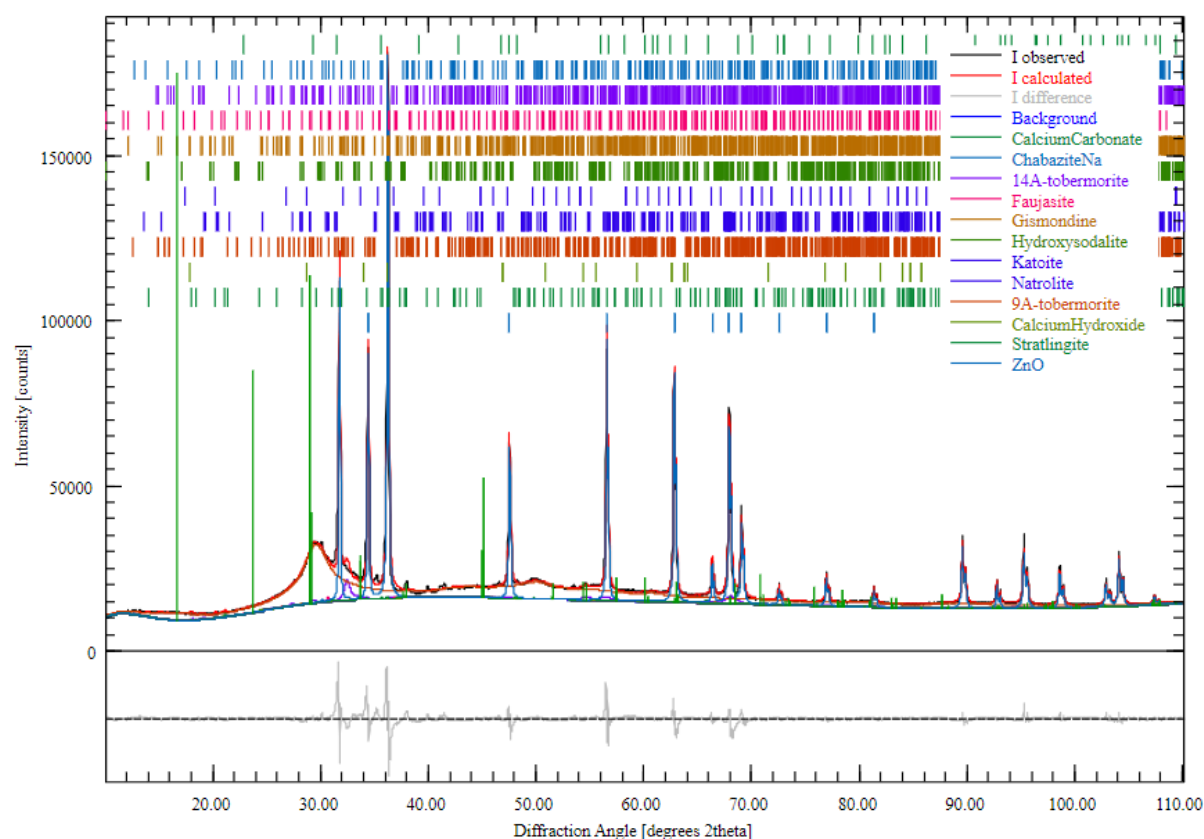


Figure 6.4: Example output of QXRD performed for paste made with glass BFS-2, activated with waterglass (system N8S12), using Rietveld refinement method via Profex-BGMN [20] software - individual characterization of reaction products detailed in Table 6.3.

6.3 Results and discussions

6.3.1 Activation of individual precursors - 20 °C

6.3.1.1 Reaction kinetics and microstructure

Assessment of the evolution of heat release:

The isothermal calorimetric characterization of pastes cured for 7 days, at 20 °C, is shown in Figure 6.5a and 6.5b, for systems N8S0 and N8S12, respectively. In general, the highest calorimetric responses were measured with pastes made with slag-like glasses, independent of the activator. Moderate differences in the reaction kinetics are identified according to the precursor.

In Figure 6.5a, four distinct stages are highlighted for NaOH-based systems. After the wetting and dissolution peak (I), a short deceleration period was observed (II) with different durations according to each precursor, characterized by a mild change in the slope of the descending initial peak. Slag-type glasses displayed wider and longer dissolution periods lasting up to 50 min, while the same stage was ceased after approximately 30 min for fly ash-type glasses. The intensity of the measured heat flow during the second stage was directly proportional to the Ca content of the precursor. As both precursor dissolution and formation of Ca-containing nuclei are exothermic processes [194,397,427], the initial periods of reaction are expected to be more significant in slag-type glasses due to the

quicker supersaturation of the solution with reactive species, arising from higher CaO contents. In a similar way, the same chemistry-heat release correlation was observed in the subsequent acceleration stage (III). However, a significant increase in the calorimetric response was measured only for pastes made with glass BFS-2, indicating that structural changes might have occurred in this period - this will be further discussed in the next Section. Sequentially, the same precursor displayed a quick drop in the measured heat flow entering the last stage of reaction (IV), while glass BFS-1 presented a slower and continuous deceleration, prolonging the length of the third period. In fly ash-type glasses, a nearly-steady signal was measured during the third stage, which was extended with similar intensity into the fourth stage. It is still possible to observe small variations in the last period, leading to short periods of increased heat release credited to a delayed reaction characteristic - highlighted in the red circles.

The calorimetric signal measured in pastes activated with waterglass (Figure 6.5b) showed distinct reaction features. For both high- and low-Ca glasses, the first period (I) was extended to approximately 3 - 5 hours and 1 hour, respectively, suggesting that the precipitation of the first reaction products takes place concurrently with glass dissolution via a homogeneous-like mechanism, following observations made in Section 5.3.3. Similar conclusions have already been obtained in Chapter 5, as the presence of liquid silicate species, supplied by the waterglass solution, facilitates the formation of crystallites of Ca-Si and Ca-Al species in the initial moments of reaction, enhancing the initial heat release of the system. Sequentially, all pastes presented a deceleration stage with changes in the slope of the curves (II). However, it was not possible to distinguish clear subsequent acceleration periods, conversely to observations made for system N8S0. Similar exothermic responses have been addressed during the activation of metakaolin [428] and slag [107], as an increasing silicate modulus promoted a continuously reduced intensity of the acceleration stage until it became unnoticed above $M_s = 1.5$. In the present work, all samples displayed a final constant drop in the heat flow rate, reaching the final stage of reaction (III). The second period occurred at earlier age and was longer in fly ash-type glasses, and the final deceleration of the curves was initiated after 10 hours of reaction. Slag-type glasses had an extended deceleration-like period, which lasted up to 24 hours of reaction before a continuous drop in heat release was measured.

Considering a broader range of activators, the non-linear effect of Na_2O concentration on the reaction of pastes containing glasses Si-FA and BFS-2 can be observed from the chart in Figure 6.6. The obtained results indicated that, depending on the precursor, the influence of the activating solution on the evolution and total heat release has different trends. For both fly ash- and slag-like glasses, the total heat released during 7 days of curing increased from systems N4S0 (83.1 and 172.5 J/g, respectively) to N8S0 (112.9 and 193.0 J/g), and dropped for system N12S0 (88.7 and 190.1 J/g).

In general, it is expected that an increased alkalinity - denoted by the higher concentration of Na - accelerates the dissolution kinetics and increases the exothermic response of a system up to a threshold value [46,357,429]. The plot in Figure 6.6 indicated that this threshold changes according to the nature of the precursor positively impacting the degree of reaction. Glass Si-FA presented a more significant drop in cumulative heat release when the Na_2O concentration increased from 8 wt% to 12 wt%. In system N4S0, the alkalinity is probably insufficient to pronouncedly promote the breakage of Si-O and Al-O bonds, limiting the initial reaction of the low-Ca precursor. Conversely, at 12 wt%, Na_2O was shown to be in

excess. As the dissolution rate of a precursor is directly controlled by the alkalinity of the system (indicated by the pH of the solution), an enhanced initial release of Si- and Al-species took place in system N12S0, promoting a quick supersaturation of the aqueous phase and increasing the initial calorimetric response of the reaction.

Figure 6.6 also provided the ratio of heat release measured at 7 days to 1 day, providing insights into the development of a reaction. For glass Si-FA, a mild increase in Na₂O was effective in improving the initial and secondary stages of alkali-activation, with system N8S0 displaying the highest final (7 days) and highest ratio (7 days / 1 day) of cumulative heat release. Among all Si-FA based pastes activated with NaOH, the calculated ratio of heat release was the lowest in system N12S0, as the reaction was significantly limited after an initial burst of dissolution. In this scenario, two potential explanations can be given: the solubility of N-A-S-H gel is known to be higher with increasing pH [219], reducing the polymerization phenomena between Al- and Si-species [179,194,430,431] - this can influence the phase precipitation stage, lowering the exothermic response after the first day of reaction; additionally, the high supersaturation indices in initial moments trigger a premature coagulation of small solid nuclei and the formation of a thick layer of reaction products surrounding the reactive glass particles [307] - this would lead to a limitation in the diffusion of reactive species from the inner parts of the precursor particles, limiting the continued dissolution of the precursor.

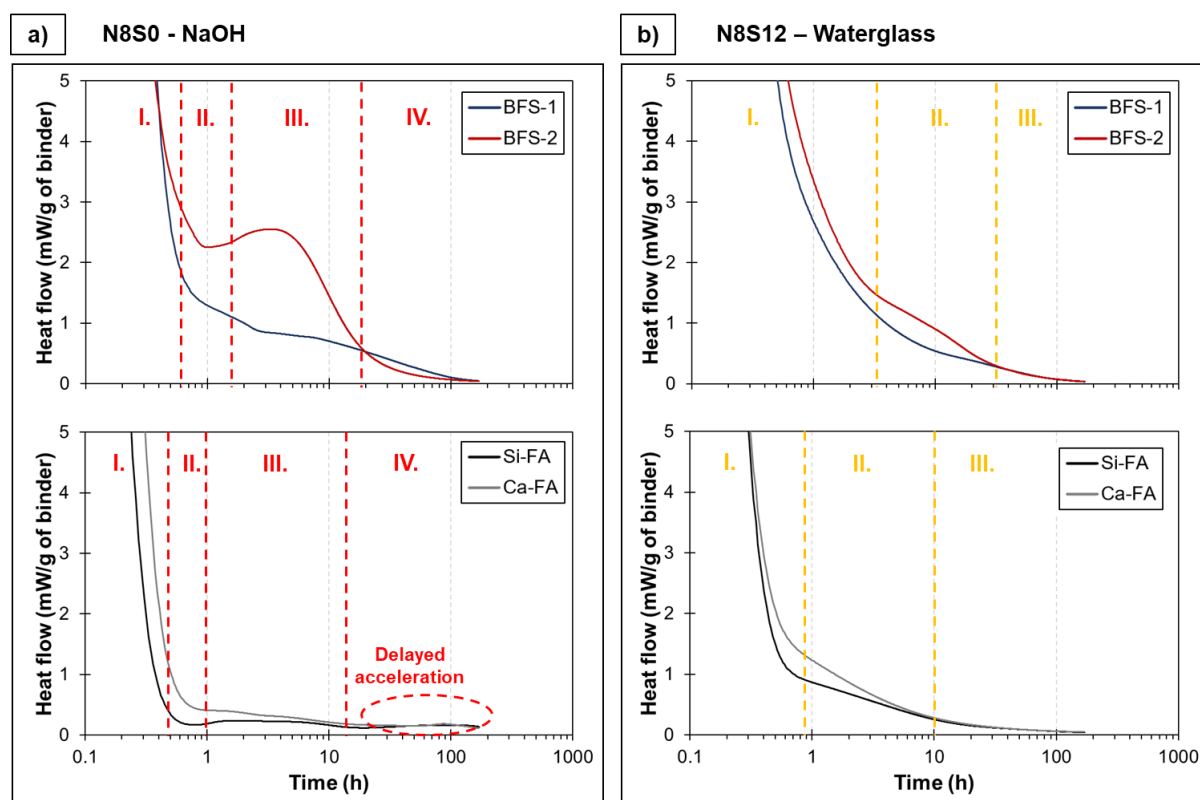


Figure 6.5: Heat flow evolution of pastes made with synthetic glasses and activated with a) sodium hydroxide (N8S0); and b) waterglass (N8S12) - all samples were cured at 20 °C for 7 days.

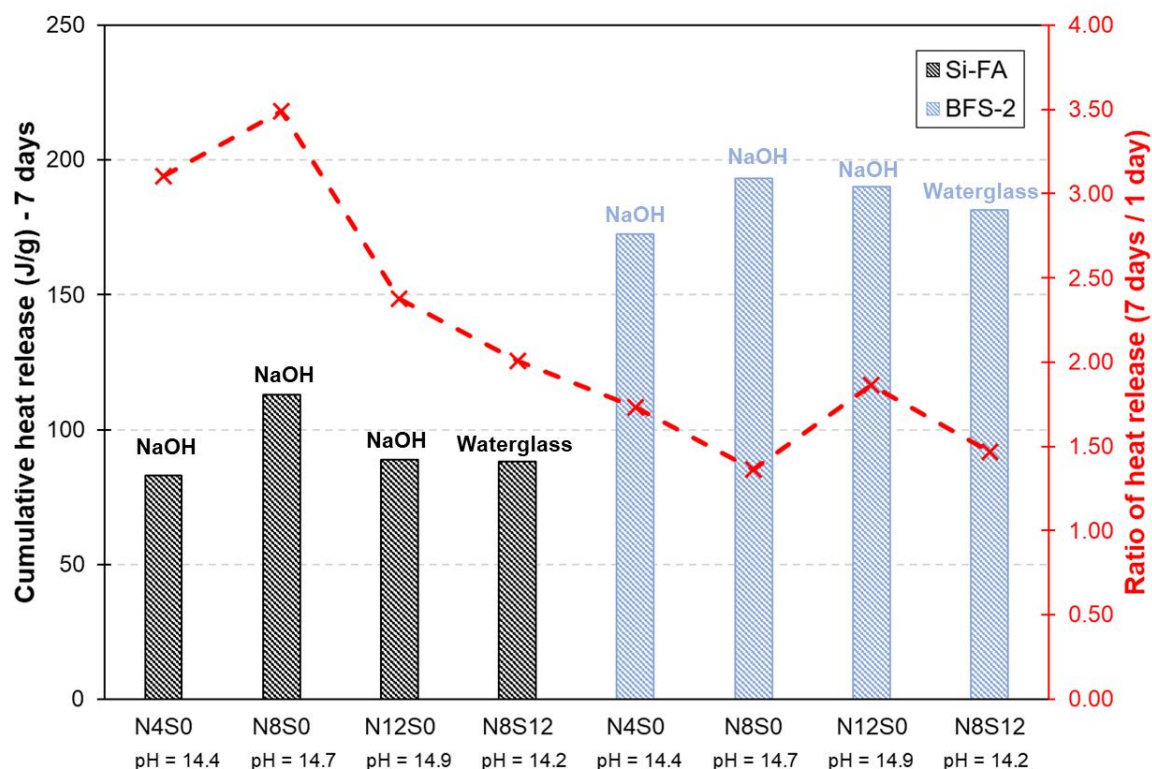


Figure 6.6: Relationship of the evolution of cumulative heat release with final values measured in the 20 °C isothermal calorimetry test of alkali-activated pastes using glasses Si-FA and BFS-2. The pH values were calculated via thermodynamic equilibrium using GEMs - see Appendix E for more details of the individual calorimetry curves.

With respect to waterglass, the addition of aqueous silicate further reduces the pH of the reactive media and hinders the dissolution of Si-FA. As a consequence, the overall reaction and final cumulative exothermic response is limited (88.2 J/g). However, the aqueous silicate species supplied by the activator can work as seeding agents in the early stages of reaction [181]. Their presence is expected to accelerate the nucleation of reaction products and to induce a higher initial calorimetric response. This enhanced nucleation step densifies the reactive matrix, and limits the reaction to more diffusion-controlled processes in sequential stages. Consequently, system N8S12 had the lowest heat release ratio of 7 days/1 day among all pastes made with glass Si-FA. Finally, it is worth mentioning that no significant acceleration periods were observed in the alkali-activation of Si-FA in the four mixtures - see Appendix E for more details on the individual isothermal calorimetry experiments - which is credited to the low reactivity of fly ash-type glasses at room temperature.

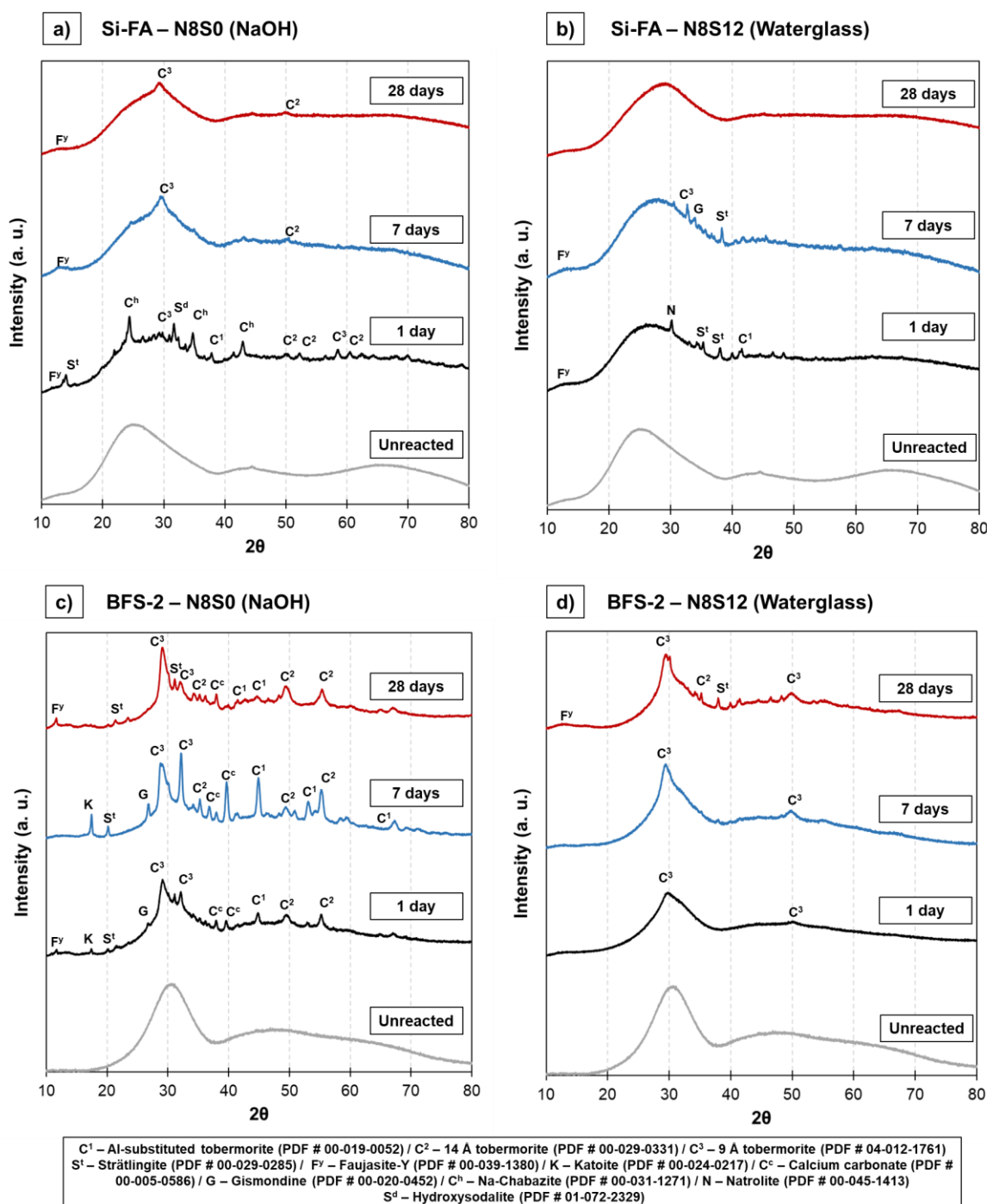
The influence of Na₂O concentration was slightly different in pastes containing glass BFS-2. In general, the 7 days cumulative heat did not show great variations among the four activating solutions, but a few observations are interesting to be addressed. In system N4S0, the mild alkalinity was sufficient to promote an overall significant reaction considering the cumulated calorimetric response after 7 days. At 8 wt%, Na₂O could be considered to be already in excess, with system N8S0 displaying the lowest calculated values of heat release ratio (1.36, vs. 1.73 in system N4S0). However, the cumulative measured values at 7 days, in both N8S0 and N12S0 systems, indicated that the excess of alkalis did not limit the reaction as a whole. In very alkaline systems, the acceleration stage is usually retarded [191,194], and the same trend was observed in the present work.

In system N12S0, the deceleration period was extended for nearly 9 extra hours when compared to the other NaOH solutions - see Figure E.2 in Appendix E. A less intense acceleration peak was identified after 10 hours of reaction. This promoted a limited cumulative heat release in the first 24 h, but intensified the reaction at later stages, as the highest heat release ratio 7 days/1 day was calculated in system N12S0. Conversely to what was observed for glass Si-FA, the continuation of the reaction at such high alkalinity for glass BFS-2 could have occurred due to a few reasons related to the more reactive nature of the precursor: the residual glass framework after the initial dissolution period still had a relatively high Ca concentration, which kept the reaction at higher rates in secondary stages; higher initial dissolution promoted less glass surface alteration and more intense phase precipitation in the bulk matrix, hindering the effect of surface passivation - these will be addressed in the next sections. Finally, the prolonged dissolution period in waterglass-activated systems, which also accounts for the early homogeneous-like nucleation mechanism - see Chapter 5 for more details - promotes an intense heat release in the first day of reaction and a low heat release ratio 7 days/1 day, similarly to Si-FA-containing pastes. As BFS-2 is naturally more reactive, the overall reaction is more intense, resulting in a final exothermic response (181.4 J/g) of the same magnitude as in NaOH-activated pastes.

X-ray diffraction (XRD) study of microstructure:

The evolution of microstructure of the two most extreme glasses, from 1 day to 28 days, is illustrated in the XRD patterns plotted in Figure 6.7. In general, the intensity and quantity of solid phase-related peaks decreased with time independent of the precursor and the activator, resulting in an unexpected trend compared to the literature. Several authors have found that, with time, nuclei of ordered structures grow in preferential directions, forming crystalline phases of low-range order [211,212,228,409]. Moreover, pastes activated with waterglass displayed more amorphous characteristics with both precursors, with the absence of intense peaks at all ages.

In pastes made with glass Si-FA, the early observation of zeolite-like reflections is stronger than for BFS-2, although the latter displays an overall more intense presence of peaks. When Si-FA is activated with NaOH (Figure 6.7a), it is possible to distinguish, at 1 day, small peaks related to faujasite-Y (F^y), Na-chabazite (C^h) and hydroxysodalite (S^d). The introduction of waterglass as activator significantly reduced the early formation of zeolitic compounds (Figure 6.7b), as only faujasite-Y and natrolite (N) were detected. The presence of different Ca-containing phases, with the identification of strätlingite (S^l) and variations of tobermorite-related phases (C^1 , C^2 and C^3 - see the legend in Figure 6.7 for structural details of each phase), was observed at early stages in both solutions, but system N8S12 promoted stronger presence of these phases. Potentially, the quick complexation between the initially released Ca-species with the readily available aqueous silicates not only facilitates the formation of variations of Ca-Si-phases, but also delays the precipitation of units with high Al-Si-purity, following observations made in [104,178].



At 28 days, the binders displayed an amorphous characteristic in the two Si-FA-based systems. As the reaction has been shown to be delayed in low-Ca precursors via isothermal calorimetry (see Figure 6.6), it is here expected that the late precipitation and limited growth of reaction products is responsible for this amorphization process. The attachment of new nuclei with various structural arrangements into existing ones, during the diffusion-controlled stage of reaction, creates continuous reaction products without preferential ordering directions, reducing the overall structural arrangement. As the coalescence and transformation into crystalline phases is a very slow process [432], the hardened alkali-

activated matrix is expected to display amorphous-like characteristics at 28 days, with a similar diffraction response as the unreacted precursor - although it should be stated that structural rearrangement into more ordered products could still take place at long periods [192,409].

Similar observations are found for pastes containing glass BFS-2, as system N8S0 (Figure 6.7c) resulted in a higher density of identifiable peaks compared to system N8S12 (Figure 6.7d). At 1 and 7 days, a minor presence of secondary reaction products like katoite (K) and strätlingite is observed along with disordered tobermorite variations. Katoite-related signals are absent at 28 days, while strätlingite is reduced in intensity, indicating that they have either been intermixed with other gel phases or simply converted into different structures. A significant presence of gel-related phases was observed at 28 days. It is also possible to distinguish the formation of gismondine (G) and faujasite-Y in both scenarios, which can occur due to the binding or the ionic-exchange of Ca with existing Si-Al structures [433,434], or directly as a secondary reaction product. However, only the latter is still observed at 28 days, showing sharper peaks in NaOH-activated pastes. In system N8S12, the older samples appear to initiate the process of growth of specific phases, as the intensities of Ca-dominated phases and faujasite-Y are slightly higher.

Microstructure visualization with scanning electron microscopy (SEM):

As previously mentioned, the growth of the matrix into a more amorphous nature occurs in the opposite direction of trends usually reported in literature. In the present pastes, the use of scanning electron microscopy supports the findings from XRD and provides better conclusions regarding the unexpected behaviour of the studied mixtures.

Figure 6.8 displays a comparison of BFS-2 pastes, in both N8S0 and N8S12 systems, cured for 7 and 28 days. It is possible to see that, independent of the activator, the cementitious matrix becomes more dense with the course of time, as a decreased open porosity is visualized. The observation of the formation of denser matrices at 28 days suggests that phases which were formed in the initial moments are slowly embedded into the cementitious matrix during secondary reaction stages, when the reaction becomes diffusion-controlled as described in the discussion over the evolution of heat release earlier in this Section. Since the present research made use of glasses of high purity, it is suggested that the limited formation of secondary phases, a phenomenon commonly observed in systems based on synthetic precursors [156,211,435], enhances the growth potential of disordered hydrated gels as the main reaction products. Thus, the reduction in intensity of ordered phases observed in the XRD patterns, such as strätlingite, katoite, or even zeolite-like reflections, occurs due to the amorphization of the hardened matrix. However, it is important to state that this process could be only temporary, as slow diffusion-controlled processes could lead to the conversion of disordered phases into crystalline structures at later age [373,436].

With respect to the distribution of reaction products, differences among the activators are very clear. At 7 days, two distinct morphologies are observed in the hardened matrix in system N8S0 (Figure 6.8a). Platelet- or needle-like phases are formed in the porous regions, and their edges are connected to thick layers of reaction products surrounding unreacted glass particles. While these inner rim products are commonly observed in NaOH (or KOH) activated pastes, due to the early precipitation of hydrates anchored at the surface of dissolving slag particles [178,204], it is suggested that the phases connecting these regions

represent a mixture of Si-incorporated calcium aluminates - i.e. strätlingite - and C-(A-)S-H phases, as they have been observed to promote bridges between slag grains [437,438]. The growth into a needle- or plate-like morphology could have occurred due to the porous microstructure, which allowed their grow in a preferential direction similarly to the sheet-growth phenomena of C-S-H [439,440]. At 28 days, the hardened binder showed a more dense characteristic. The presence of the needle-like phases is still visible but less evident, and they appear to be incorporated into the bulk matrix. Following the densification of the matrix compared to 7-day cured pastes, it can be concluded that a delayed formation of outer products fills the initial porosity, preventing the ordered growth of existing structures whilst attaching them to the continuous matrix.

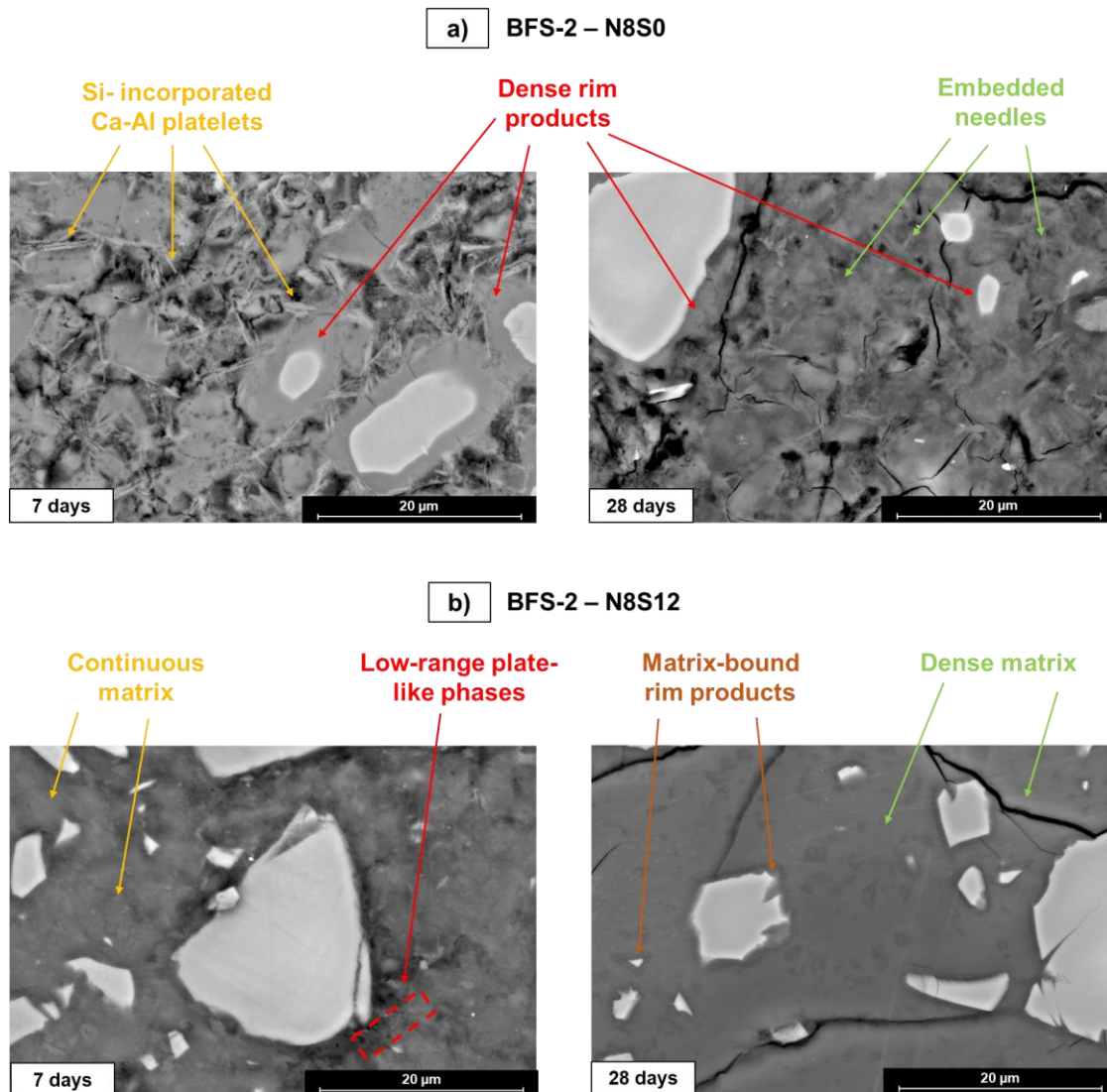


Figure 6.8: BSE images of the evolution of microstructure of BFS-2-based pastes, from 7 to 28 days, according to the activating solution: a) NaOH (N8S0) and b) waterglass (N8S12).

In system N8S12 (Figure 6.8b), the microstructure is more dense in general. The higher precipitation rates in initial moments, arising from the high concentration of aqueous silicates, facilitate the formation of a continuous and amorphous matrix instead of a larger variety of nanosized structures [175,441]. Therefore, changes in the morphology of reaction products are less clear. At both ages, the cementitious matrix appears to be more continuous than in NaOH-activated pastes, and older samples displayed a very dense and amorphous characteristic as expected from the XRD patterns - see Figure 6.7. At 7 days, the interface between the matrix and a few glass particles is slightly porous, with the precipitation of short-ordered plate-like phases - most likely strätlingite, according to XRD reflections. These phases are completely incorporated into the matrix at 28 days, which displays a strong adhesion with rim products surrounding BFS-2 particles. Moreover, the formation of layers of inner phases appears to be thinner than in system N8S0, providing an extra indication of the intense phase precipitation occurring distantly from the precursor in waterglass solutions.

The effect of the chemistry of the precursor on the morphology of the hardened matrix, for the other three synthetic glasses, is observed in Figure 6.9 for 28-day cured N8S0 systems. The lower intrinsic reactivity of precursors with decreasing CaO contents leads to an increased visual porosity in the cementitious matrix. In Si-FA-based pastes, it is possible to observe the chemical attack on the surface of glass particles and the poor bonding between their surfaces with the hardened matrix, as they appear isolated within the bulk microstructure. It should be stated that, in these images, the porosity might be overestimated due to cracking occurring during sample preparation. Nonetheless, this phenomenon emphasizes the weakly formed alkali-activated matrix in a low-reactivity environment with low Ca and high Na contents (8 wt% Na₂O) [46,442,443]. In pastes produced from glass Ca-FA, the observation of chemical attack on the glass surfaces is still visible but less prominent, since it is possible to visualize an adhesion between rim products and the bulk matrix.

In general, glass BFS-1 promoted a significantly more continuous matrix than fly ash-type glasses. The favored formation of C-S-H-like phases, due to the higher content of CaO in slag-type glasses, promotes a space-filling effect of the porous matrix in Al-Si-rich environments, reducing the overall porosity of the microstructure [444]. It is possible to visualize, similarly to observations made for BFS-2-based pastes, short plate or needle-like products embedded within the matrix, most likely due to a mild formation of strätlingite. Moreover, the matrix appeared to have a strong adhesion with inner products, whilst visualization of chemical attack via etching pits was still possible.

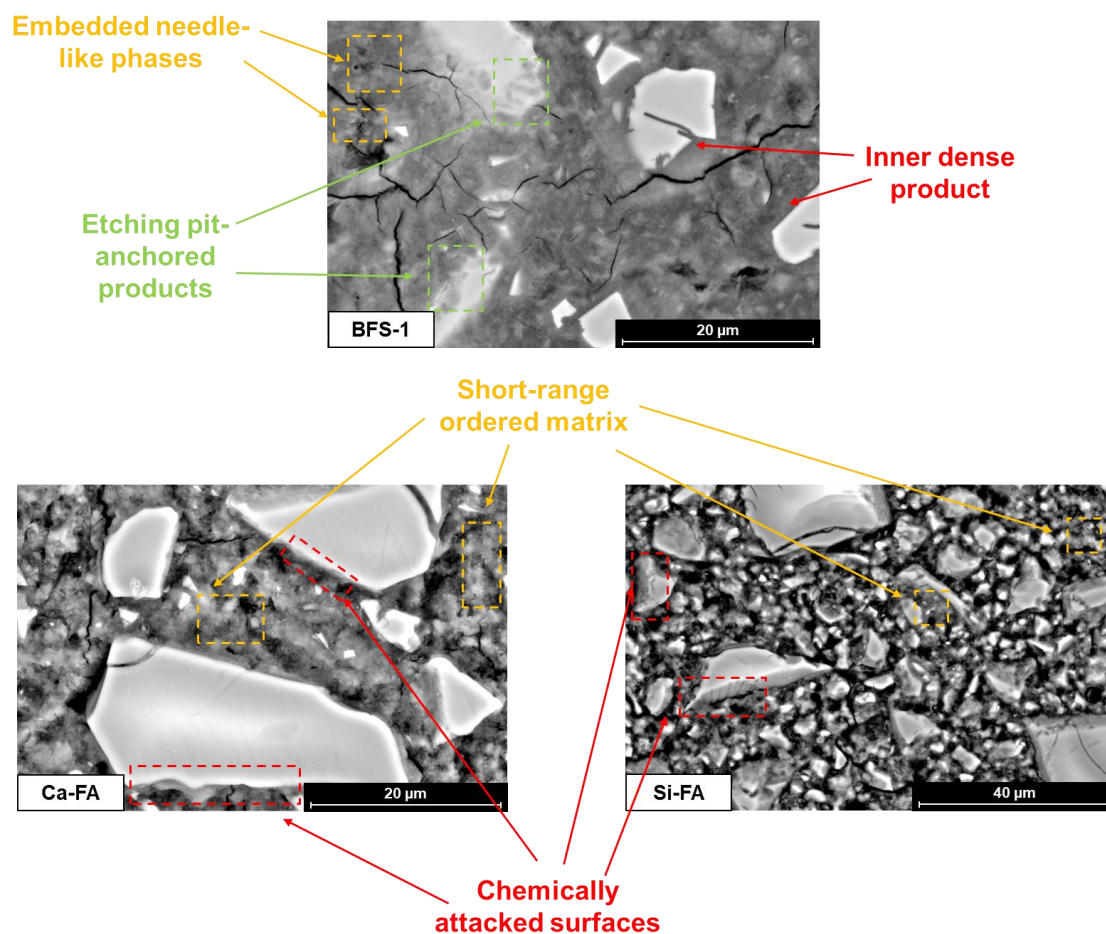


Figure 6.9: Backscattered SEM visualization of the morphology of the hardened pastes of NaOH-activated BFS-1, Si-FA and Ca-FA glasses, cured for 28 days - representation of system N8S0.

In waterglass-activated systems, it is not possible to visualize clear differences among pastes based on the same three glasses, via the images in Figure 6.10. Following the trends observed in NaOH-activated pastes, the decreasing CaO content leads to the formation of a progressively less dense matrix. However, even in the activation of glass Si-FA, the matrix appeared to be dense and a good cohesion between rim products and bulk matrix was obtained, following the amorphous characteristics of the XRD patterns - see Figures 6.7 and 6.8.

6.3.1.2 Determination of degree of reaction

The degree of reaction, determined by phase segmentation of SEM micrographs, can be correlated with the chemistry of the whole binder, accounting for both precursor and activator. The values detailed in Table 6.4 show the progressive increase in reactivity of systems according to the Ca content of the precursor, at both 7 and 28 days. Similar influences of chemistry have been addressed before by Ke and Duan [227] and Winnefeld et al. [412], who reported a combined effect of CaO and MgO on the evolution in strength and degree of reaction of alkali-activated fly ashes and metakaolin, and slags, respectively. It is interesting to emphasize that, in the present work, the calculated reaction degrees can be considered overall low, as values up to 70 % have been reported under similar conditions

[175,360,420,445,446]. It is assumed that, since the synthetic glasses represent pure and quite rapidly reactive environments, a content of 8 wt% of Na_2O is sufficiently high to boost the reaction in initial moments, creating thick layers of surface anchored-reaction products that prevent a significant diffusion of species from the inner cores of the precursor, thus hindering the continued dissolution of the glass at later stages.

Although an evolution in the calculated reaction degrees was observed as a function of time, different characteristics were observed according to the activating solution. Waterglass provided an additional effect on the reaction kinetics, providing an enhanced reactivity to the pastes from 7 to 28 days at a higher rate than sodium hydroxide for all precursors. As indicated in the SEM micrographs (Figures 6.8, 6.9 and 6.10), two aspects contributed to this effect: the rim products were thinner, and the cementitious matrices were significantly more dense in the outer product regions of N8S12 systems compared to N8S0. The first effect facilitates the continuous breakage of the glass network, as the diffusion barrier for dissolved species is lower in later stages. The second phenomenon indicates the contribution of homogeneous-like nucleation, which has a delayed effect on the reaction kinetics but results in a more cohesive and stronger matrix. The characteristics of waterglass have a great impact on the overall porosity of the system [447-449]. The correlation between silicate modulus, matrix density and evolution of reaction degree of precursors is not covered in this work but deserves more attention, as there is currently no consensus regarding the influence of silicate modulus above 1.5 on the porosity of alkali-activated binders in general [450,451].

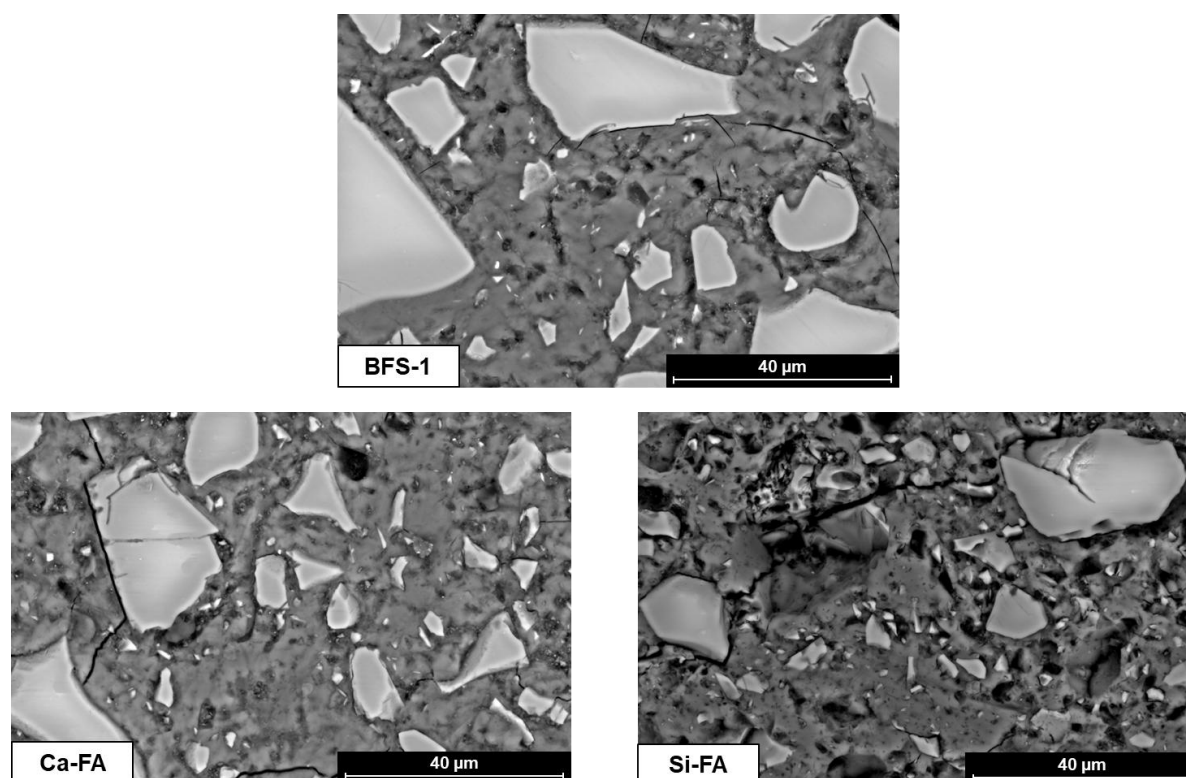


Figure 6.10: Scanning electron microscopy images of hardened pastes, cured for 28 days at room temperature, activated with waterglass - representation of system N8S12.

6.3.2 Activation of individual precursors - 60 °C

6.3.2.1 Reaction kinetics and microstructure

Isothermal calorimetry and XRD: influence of activator reaction mechanisms:

The evolution of the activation of glass Si-FA at 60 °C was monitored using isothermal calorimetry through the first 7 days of reaction. As shown in Figures 6.11a and 6.11b, the calorimetric response of the pastes presented different characteristics compared to the 20 °C cured ones - see Figure 6.5. In systems N8S0 and N12S0 (Figure 6.11a), after the dissolution period (I), a very short deceleration takes place for a few tens of minutes (II) before a new acceleration period occurs (III). A short-term increased response has been measured before in systems containing 8 wt% Na₂O [106,194], with temperature being observed to move the occurrence of this phenomena to earlier time. Differently from those previous works, the third stage of the pastes here is followed by another attenuation and further intensification of the calorimetric curve (IV), which precedes the diffusion controlled stage of the reaction (V). Additionally, the second acceleration peak was earliest in the highest alkalinity environment: in system N12S0, it was measured after only 5 hours of reaction, while the same response took place only on the second day of curing for system N8S0.

In the lowest alkalinity environments (Figure 6.11b), the reaction was observed to have only three stages. After the initial wetting/dissolution peak (I), the calorimetric signal displayed a continuous deceleration (stage II) before the reaction entered its final stage (III). In the paste activated with N8S12, the overall behaviour showed a similar trend to what was observed with N4S0, as a continuous deceleration was measured after the initial dissolution period. However, the dissolution peak with N8S12 showed a maximum heat release approximately 2.5 times higher, indicating that the reactivity was significantly enhanced, especially in the first hour.

When sodium hydroxide was the activator, the exothermic response changed according to the alkali dosage. In these situations, the reaction potential of low-Ca precursors was shown to be directly controlled by the NaOH concentration of the solution. Although this is not necessarily different from the influence of the activator at room temperature, the synergistic influence of temperature and alkalinity appeared to avoid a limitation of the reaction, from 1 to 7 days, in system N12S0.

Table 6.4: Evolution of the degree of reaction of alkali-activated pastes calculated at 7 and 28 days of curing - calculation via phase segmentation of SEM micrographs.

Activator	Glass	Ca fraction (mol%)	Degree of reaction (7 days)	Degree of reaction (28 days)	Ratio of degree of reaction (28 days / 7 days)
NaOH (N8S0)	Si-FA	0.15	34 ± 2 %	38 ± 4 %	1.10
	Ca-FA	0.27	33 ± 5%	34 ± 3 %	1.03
	BFS-1	0.42	36 ± 4%	41 ± 3 %	1.11
	BFS-2	0.51	39 ± 3%	43 ± 2 %	1.12
Waterglass (N8S12)	Si-FA	0.13	32 ± 4%	42 ± 3 %	1.32
	Ca-FA	0.24	37 ± 3%	43 ± 2 %	1.17
	BFS-1	0.38	38 ± 3%	44 ± 3 %	1.17
	BFS-2	0.46	40 ± 4%	54 ± 2 %	1.33

The mineralogical features resulting from these different reaction processes (as measured by their calorimetric responses) are observed in Figure 6.10c, as shown by the XRD patterns of pastes after 7 days. The high alkali dosage in systems N8S0 and N12S0 resulted in the detection of several peaks related to zeolite phases, consistent with the high exothermic response of both. Similarly to pastes cured at room temperature (Figure 6.7), the mineralogical structure of the hardened pastes resembled units of faujasite-Y (F^y), gismondine (G), natrolite (N), Na-chabazite (C^h) and hydroxysodalite (S^d). The presence of variations of C-(N-A-)S-H phases (C^1 , C^2 and C^3) indicate that N-(C-)A-S-H-like structures are not the sole phase even in low-Ca systems, as Ca-containing phases co-exist in the hardened matrix. Interestingly, these phases were stable in the most mature systems, conversely to what was observed at room temperature. At 20 °C, acceleration periods were not measured in low-Ca containing pastes (Figure 6.5), and the initially formed short-range ordered structures were embedded in the amorphous matrix with the course of reaction. These short-term bursts of heat release observed in the calorimetric response of pastes N8S0 and N12S0 indicate a strong conversion of gel units into ordered structures. Conversely, systems N4S0 and N8S12 presented similar features to those induced by the room temperature curing regime, as the microstructures were nearly completely amorphous, corresponding to the lack of measured acceleration peaks. The main difference among the two systems is the detection of gismondine-like reflections in N8S12, which indicates Ca-binding to structures in which Al and Si are the main components, while N4S0 displayed exclusively the formation of Ca-dominant phases (C^1 and C^3) - as N-A-S-H has already been demonstrated to be formed at secondary stages, in Chapter 5.

Study of morphology of hardened pastes by SEM:

Figure 6.12 shows SEM micrographs of the pastes made with glass Si-FA, cured at 60 °C for 28 days. In general, the bulk matrix was significantly more cohesive and continuous than what was observed with room temperature curing - see Figures 6.9 and 6.10. The influence of the activator nature is seen in two different aspects. In the more alkaline system (N8S0 - Figure 6.12a), it is possible to visualize a more aggressive attack on the reactive surfaces (yellow dashed frames), with multiple etching pits present in the edges of the unreacted particles - see also the enlarged images. These reactive spots are linked to the surrounding cementitious matrix, which appears to have a good adhesion with unreacted particles. System N8S12 (Figure 6.12b) shows a milder attack on glass surfaces, with less frequent etching pits better distributed through the reactive surfaces (blue dashed frames) - from the images with lower magnification, it is not possible to distinguish whether one system or the other had better adhesion between particles and matrix, as extra porosity occurred during sample preparation.

The second point of distinction arising from the choice of activator is better visualized in the enlarged images. Clearly, a more continuous matrix is observed in waterglass-activated pastes, due to the homogeneous precipitation mechanism of reaction products occurring in these solutions - see Section 5.3.2 for more details. With NaOH as activator (Figure 6.12a), the observation of a discontinuous network suggests that the different structural units initially formed have unrestricted preferential growth directions. It is here assumed that, conversely to system N8S12, the lacking homogeneous precipitation mechanism reduces the density of solid nuclei in the bulk solution and allows a higher degree of growth freedom for the reaction products, resulting in the formation of a caged-like porous microstructure instead of a continuous matrix, as shown in the enlarged section of Figure 6.12b. These

observations are consistent with results from X-ray diffraction (Figure 6.11c) which showed the presence of several zeolite-like reflections in NaOH-activated pastes and a fully amorphous characteristic of the pattern for the waterglass-activated paste.

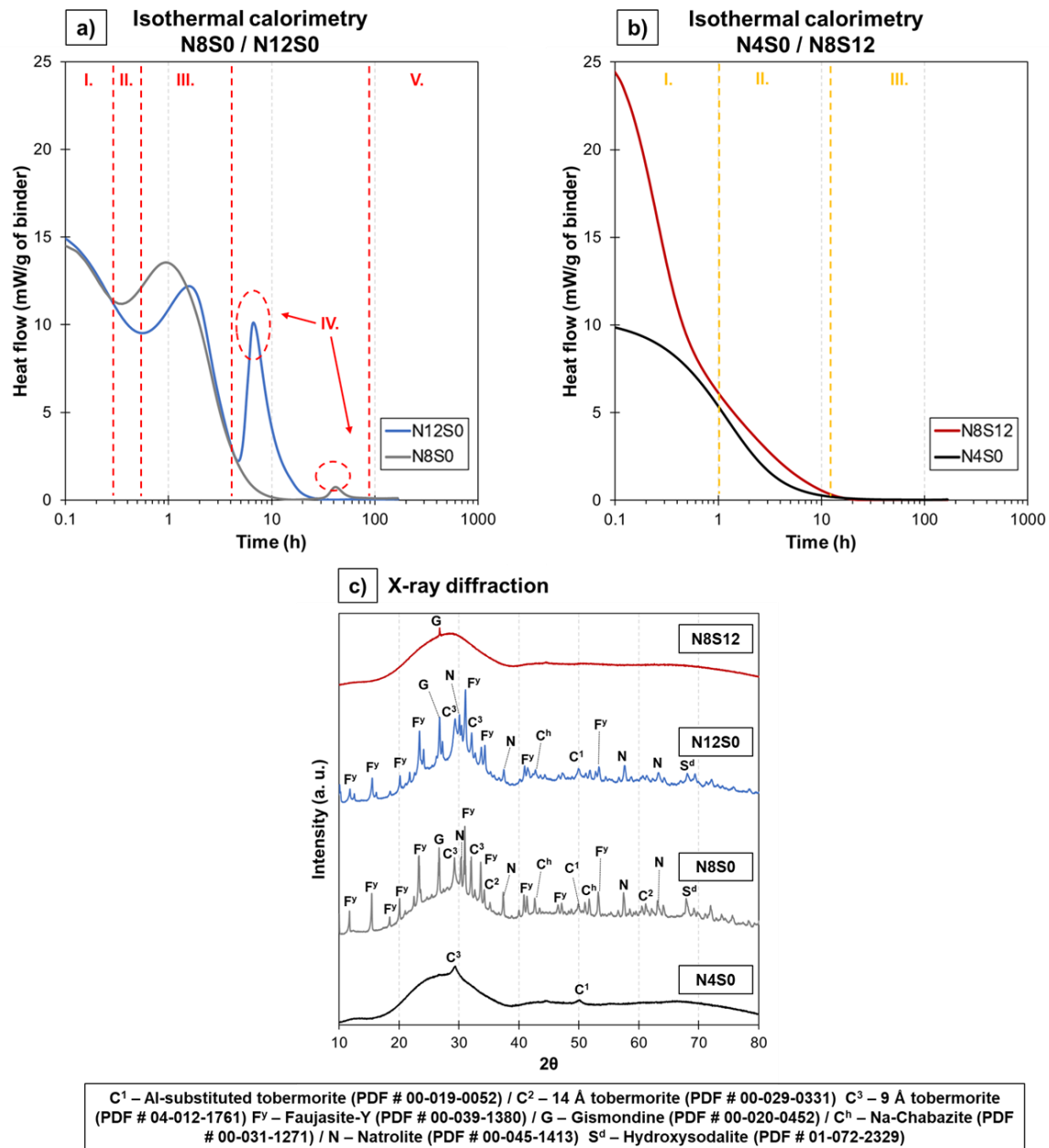


Figure 6.11: Study of the influence of the activator dosage in the reaction kinetics and microstructure of Si-FA-containing pastes, cured for 7 days, at 60 °C: isothermal calorimetry in systems a) N8S0, N12S0 and b) N4S0 and N8S0, and c) XRD patterns for the four systems.

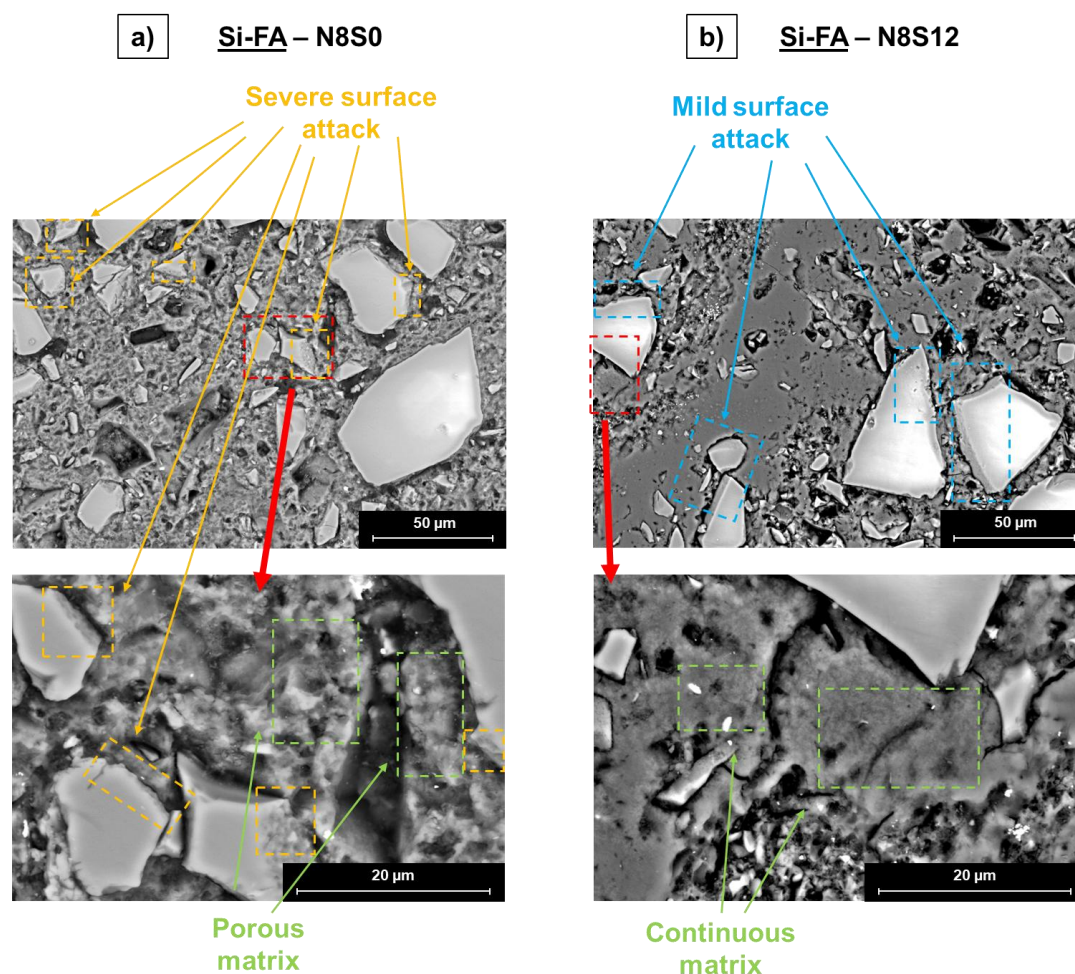


Figure 6.12: BSE images of pastes made with glass Si-FA, cured for 28 days at 60 °C, activated with: a) NaOH (N8S0); and b) waterglass (N8S12). Images with lower magnification indicate the alkaline surface attack into glass particles, and the enlarged images indicate the continuity of the hardened matrix.

6.3.2.2 Determination of degree of reaction

SEM micrographs were used to calculate the reaction degree of pastes activated with glasses Si-FA and Ca-FA in systems N8S0 and N8S12, via phase segmentation. The evolution in the reaction from 7 days to 28 days, and the comparison between curing regimen at 20 °C and 60 °C, are shown in Figure 6.13. In general, temperature had a similar effect in the two glasses on enhancing their reaction potential. At 60 °C, glass Si-FA presented slightly higher reactivity than Ca-FA after 28 days, especially in system N8S0, with a calculated degree of reaction approximately 5 % higher in the NaOH-activated system. On the other hand, the calcareous fly ash glass displayed a quicker response in the early kinetics: the evolution in the reaction degree values between the two periods was lower with both activators - 7 % and 2 % in systems N8S0 and N8S12, respectively, compared to 11.46 % and 10.62 % for glass Si-FA.

It is interestingly observed that, at 20 °C, the use of waterglass promoted a slower overall reaction evolution, with significant changes in the reaction degree taking place from 7 to 28 days. However, this pattern was not observed at 60 °C, especially for glass Ca-FA which showed minor changes in the degree of reaction (approx. 1 %). Instead, NaOH-activated

pastes presented more significant changes in the reaction between the two testing ages at higher curing temperatures - 10 % for glass Si-FA, and 6 % for glass Ca-FA. It is here suggested that the aqueous silicates, supplied by the waterglass solution, act analogously to nano-seeds in the precipitation of zeolites. At 20 °C, nucleation rates of these crystals are considerably slow in seed-aided synthesis [452,453]. In the same way, the precipitation of crystallites of zeolitic structures in the present mixtures, anchored in the aqueous silicate species, is prolonged further than 7 days due to the lower reaction rate of the system at 20 °C [192]. The rise in curing temperature is known to significantly increase the nucleation rates in the first moments and to enhance their growth potential [452]. With this in mind, it is possible to establish a direct connection between the evolution of the exothermic response and the evolution of the reaction degree of these pastes: as the condensation and coalescence of individual units is less exothermic than their own nucleation [162,180,454], the initial enhanced precipitation rate - aided by an accelerated dissolution rate in this curing regime - promotes both higher calorimetric response and higher reaction degree at 7 days, and a lower evolution in the rate of the reaction at further stages. This observation is consistent with isothermal calorimetry observations made at 20 °C (Figure 6.5) and 60 °C (Figure 6.11), as the higher curing temperature extended the initial stage of reaction from 1 to 10 hours, whilst showing negligible changes in the sequence of the reaction.

6.3.2.3 N-(C-)A-S-H gel: influence of activator on composition and structure

Selective dissolution treatment:

Following observations made in Chapter 5, the implementation of a higher temperature curing regime facilitated the precipitation and stabilization of N-A-S-H gels variations in low-Ca precursors. This is also consistent with XRD patterns interpretation, which showed the dominance of zeolite-related reflections in system N8S0 for glass Si-FA - see Figure 6.11c. With 28-day cured pastes, the implementation of selective dissolution treatment (SAM) allowed the isolation of aluminosilicate gels in the mature microstructure of fly ash-type glasses, and a comparison of the XRD patterns before and after SAM is given in Figure 6.14.

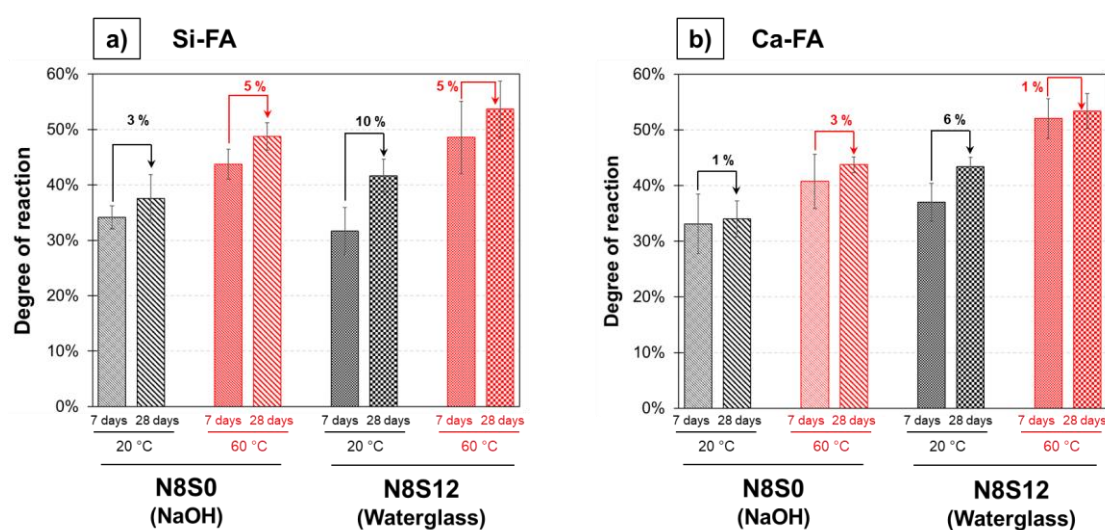


Figure 6.13: Influence of temperature on the evolution of degree of reaction, in both NaOH- (N8S0) and waterglass-based (N8S12) systems, from 7 to 28 days: a) pastes made with glass Si-FA; and b) pastes made with glass Ca-FA.

As determined by the procedure detailed in Section 6.2.5, N-(C-)A-S-H-like phases were calculated to contribute to 88 wt% and 96 wt% of the phase assemblage in systems N8S0 and N8S12, respectively. Despite having a similar quantity of sodium aluminosilicate structures, the characterization of the residual material after dissolution displayed significant differences according to the activating solution. In NaOH-based systems (Figure 6.14a), it is possible to visualize the reduction in C-(N-A-)S-H-like reflections from the hardened paste (dashed grey line) to the treated material (solid black line), with the limitation of the intensity of peaks assigned to phases C^3 and C^1 . In the spectra of the residual samples, the different zeolite-related contributions were maintained with high intensity, showing the efficiency of the method in mainly dissolving amorphous Ca-hydrated gels. It is still possible to observe the presence of Ca-containing phases, such as gismondine, after the selective dissolution. Overall, the amorphous portions of the pattern were reduced, especially above a diffraction angle of 40° . In different studies, this region has been shown to display several minor reflections in synthetic C-(N-A-)S-H gels [219,222,455]. Therefore, it is concluded that the removal of Ca-dominated phases by SAM treatment reduces the amorphization of the hardened matrix, as Ca is known for reducing the overall structural order of the reaction products in NaOH-based systems [456,457].

In system N8S12 (Figure 6.14b), it is not possible to distinguish peaks neither before or after the selective dissolution of pastes. However, it is clear that the diffraction maximum of the powders shifted towards lower angles after the SAM treatment. As indicated in Chapter 3, the location of the diffraction maximum is directly correlated with the Ca content of the material. Although subtle, the observed shift indicates the removal of Ca-containing phases from the structure of the paste, whilst the strong and cohesive amorphous matrix of the paste was kept after treatment, following observations from SEM micrographs shown in Figure 6.12. Moreover, the intensity of the amorphous regions of the diffractogram was reduced after the selective dissolution. Following the trend observed for system N8S0, this additional observation indicates the removal of amorphous Ca-based phases from the microstructure.

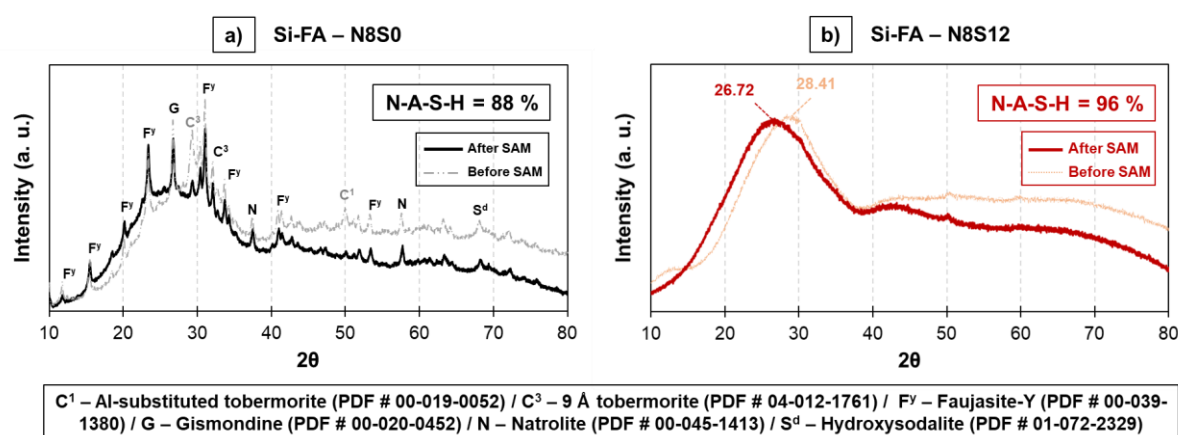


Figure 6.14: Comparison of phase assemblage of 60°C -cured Si-FA containing pastes before (dashed lines) and after (solid line) SAM selective dissolution treatment, using X-ray diffraction: a) pastes activated with NaOH (N8S0) b) and with waterglass (N8S12).

Evaluation of gel chemistry via element mapping:

The XRD patterns indicated clear differences in N-A-S-H-like structures according to the activating solution. The use of EDS for element mapping, through the application of the edxia method in SEM micrographs [425], provided important details of the composition and arrangement of these phases, as shown in the plots in Figure 6.15. As expected, waterglass-activated pastes presented an overall higher Si content, indicated by the changes in the Si/Ca and Al/Si quantities. With over 500,000 data points in the hypermaps of each sample, the ranges of Si/Ca and Al/Si ratios shifted from 3.19-3.79 (N8S0) to 5.53-7.50 (N8S12), and from 0.53-0.65 (N8S0) to 0.36-0.41 (N8S12), respectively - these values represent 80 % of the total datapoints collected during processing of the EDS mapping data.

The most interesting feature is the influence of the activator on the calculated Na/Ca ratios. In both plots from Figures 6.15a and 6.15b, it is possible to distinguish three areas: a high-Ca region (1), with atomic ratios lower than 1.0-1.2; an intermediate-Ca region (2), with ratios in the range of 1.0-2.5; and a low-Ca region (3), with atomic ratios higher than 3.0. It is here proposed that the high-Ca region (1), which is more strongly observed in system N8S0, accounts for different C-(N-A-)S-H gels, while regions (2) and (3) represent the formation of Ca-bound (N-(C-)A-S-H) and Ca-restricted N-A-S-H phases, respectively. The use of the term *restricted* in the third group is suggested due to the unlikely formation of completely Ca-free structures in any system containing a minimum amount of Ca [228,357,458], especially due to the lack of secondary oxides in the current precursors which could lead to the binding of Ca in secondary reaction products, such as Mg- and Fe-LDHs. These propositions are partially consistent with the work of Zhao et al. [422], who determined the formation of separate Ca-based and N-A-S-H gels with Na/Ca ratio lower than 0.72 via EDS point analysis and FTIR spectra.

In the histogram shown in Figure 6.15c, the characteristic Na/Ca ratios measured in each paste are more clear. System N8S0 presented a narrower distribution, with one main peak in the Ca-bound gel range (region 2) centred in the 2.0-2.1 interval (region 2), and a smaller area observed in the lowest Na-content (region 1), centred in the 0.9-1.0 interval. Conversely, the use of waterglass resulted in a wider distribution of atomic ratios. Along with a small shoulder also observed in the Ca-dominated area, the second region presented three distinct peaks (Na/Ca of 1.7, 2.4 and 3.0) within a linear-like increase in frequency, while the main peak was observed in the Ca-restricted region (region 3), centred in the 3.5-3.6 interval - NaOH-activated paste also displayed a small shoulder within the same region (Na/Ca of 3.3).

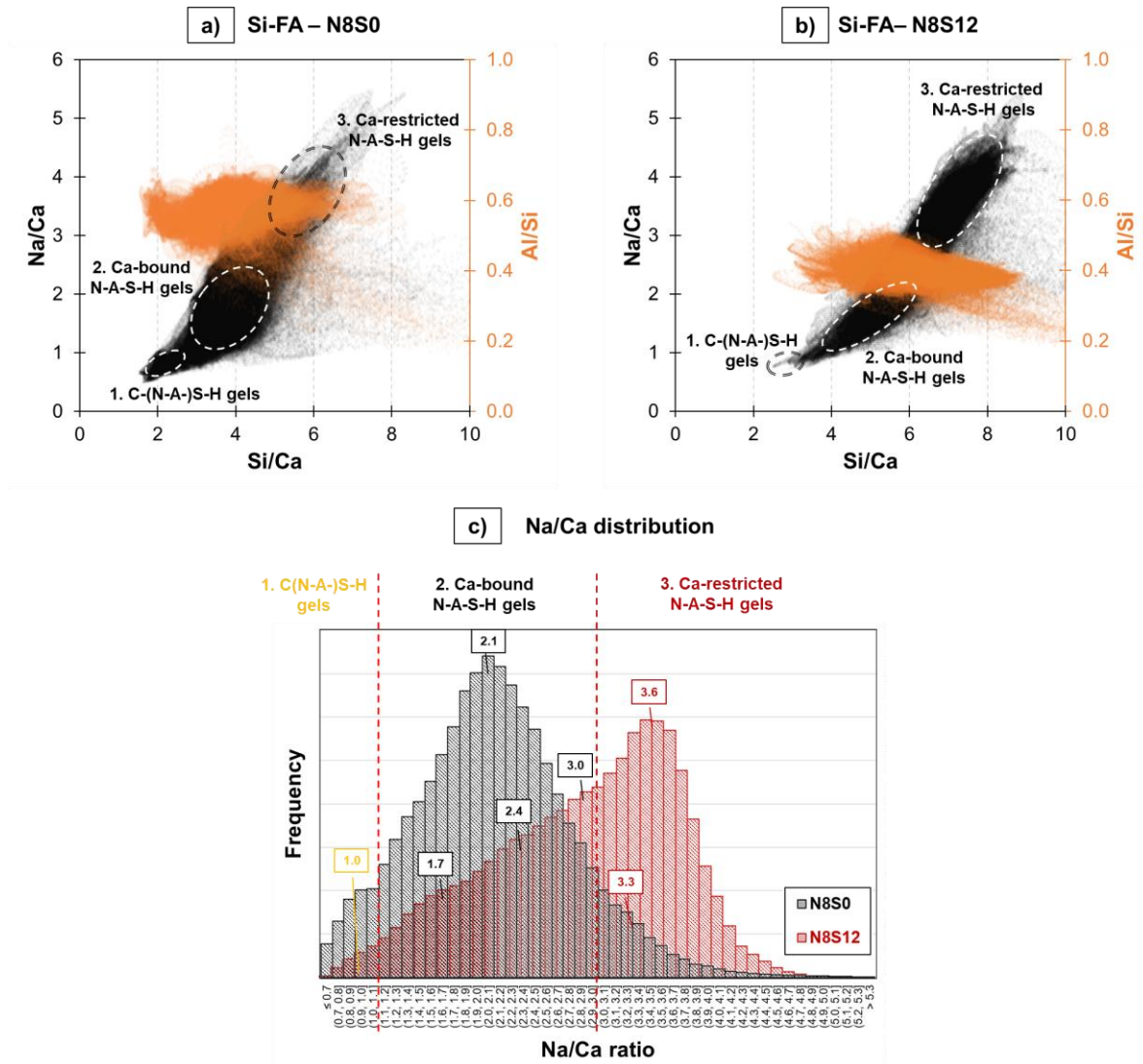


Figure 6.15: Relationship of different atomic ratios in the cementitious matrix of Si-FA-activated pastes cured at 60 °C: a) Pastes activated with NaOH (N8S0); b) Pastes activated with waterglass (N8S12); and c) histogram distribution of Na/Ca ratios in both systems.

Table 6-5: Distinction of different compositions of hydrated gels according to experimental observations, in 60 °C cured Si-FA pastes.

Gel type	Si/Ca	Na/Ca	Ref.
Separate C-(N-A)-S-H and N-A-S-H gels	0.52 - 1.39	— ^a	[13] ^b
	< 2.94	0.68 - 1.37	[15] ^c
	< 2.70	> 1.10	This work ^d
Ca-bound N-A-S-H gels	> 3.33	— ^a	[13] ^b
	> 3.45	> 2.17	[15] ^c
	2.80 - 6.00	1.20 - 3.00	This work ^d
Ca-restricted N-A-S-H gels	> 6.00	> 3.00	This work ^d

^a Not officially reported by the authors.

^b Values obtained from a mixture of synthetic N-A-S-H and C-(A)-S-H gels performed at 25 °C.

^c Values obtained from the alkali-activation of fly ash with variable Ca(OH)₂ contents, cured at 85 °C and 95 °C.

^d Values obtained by the alkali-activation of synthetic fly ash-type glass cured at 60 °C.

Despite the formation of a continuous cementitious matrix, the histogram suggests a separate growth of Ca-bound gels and gels with restricted incorporation of Ca in system N8S12, while an intermixed gel characteristic is favoured in NaOH-activated pastes. The stronger presence of the third region, in system N8S12, can be explained from different points of view. The use of waterglass naturally increases the Si content and reduces the Ca and Al fractions of the binder. In such media, the aqueous silicates are known to promote the formation of longer chains [180,213], favouring a more disordered microstructure. In 2-dimensional silicate chains, Al substitution in SiO_4 tetrahedral sites is hindered [360,459], which consequently reduces the need for divalent charge-balancing Ca^{2+} cations. Moreover, shorter chain lengths are observed in environments with high alkalinity and high Ca contents [460], favouring the promotion of more Ca-bound gels in system N8S0.

Following the results of elemental mapping, the present research proposes a three-gel regions model. The comparison provided in Table 6.5 shows that, according to the chemistry of the binder, the current results presented a similar trend with other findings with respect to the distinction between the formation of individual units of Ca-based gels and Ca-bound N-A-S-H gels. However, other authors have not described the formation of Ca-restricted gels [219,422], including higher Na/Ca ratios into the second group of phases. It is here proposed that these phases comprise amorphous units in which Ca has lower interference over the structure, and potentially in the performance of the reaction products. This is consistent with both XRD patterns and SEM micrographs, supporting the formation of less ordered structures in which Ca does not play a significant structural role.

6.3.3 Activation of blended precursors - 20 °C

6.3.3.1 Reaction mechanisms and microstructure

Isothermal calorimetry: effect of blending proportions on reaction kinetics:

The reaction kinetics of blended pastes B70, B50 and B30, using Si-FA and BFS-2, were evaluated using isothermal calorimetry for 14 days at 20 °C - see Table 6.2 for details on compositions. The choice of a longer period of analysis, compared to the activation of individual precursors, covers a potentially delayed effect of reaction of fly ash glass, following findings from Zuo [175] and Gao et al [348]. As shown in the plots in Figure 6.16, the calorimetric response did not show major differences with pastes made of individual precursors - see Figure 6.5. In NaOH-based systems (Figure 6.15a), the same four stage reaction was measured. After the wetting and dissolution period (I), the deceleration (II) and subsequent increased heat release (III) were proportional to the content of glass BFS-2, as blend B70 presented higher exothermic responses in both situations. In the diffusion-controlled process (IV), the inset of the chart shows that blend B30 appears to have a mildly higher heat release than the other systems, which could identify a delayed reaction of one of the two components of the blend.

In waterglass activated samples (Figure 6.15b), less prominent changes were observed in the calorimetric response of the three pastes. Activator N8S12 promoted a widened peak during the first hours of reaction (I), which covers the concurrent glass dissolution and initial phase precipitation phenomena. However, the observation of an acceleration stage, via the change in the slope of the deceleration curve, is not as clear as what was obtained in the individual activation of BFS-2. Instead, a smooth change in the slope of the curve was

observed exclusively in blend B70 during the second stage (II), which is initiated by a change in the slope of the decelerating curves. In sequence, the missing clear acceleration period, observed in Figure 6.16a, denotes the lack of stage III. Finally, stage (IV.) did not show any differences among the three blends, and the final measured heat flow was virtually the same in all systems. Other authors have reported similar reaction kinetics in blended systems, with secondary acceleration periods being delayed with increasing silicate modulus until they become absent above a threshold modulus value of approximately 2.0 [106,193,348,461].

Contrarily to observations made by Zuo [175], it was not possible to distinguish peaks credited to individual acceleration periods of fly ash- and slag-glasses in any of the evaluated pastes. The absence of a clear acceleration peak assigned to the low-Ca component could be potentially explained by the CaO content of the precursor. As discussed in Chapter 3, the Ca fraction of glass Si-FA (> 12 wt%) is higher than typical values obtained for commercial siliceous fly ashes, which is usually in the range of 1 - 10 wt% - see Table 2.3. It is here suggested that the Ca fraction of Si-FA is sufficiently high to enhance its initial potential, with a significant release of Ca-species from the precursor, leaving behind a Ca-depleted and aluminosilicate-rich glass framework. Similarly to what was observed in the individual activation of fly ash-like glasses (Figure 6.5), the lack of structural disorder caused by Ca removal reduces the reaction potential at secondary stages, promoting an overall retardation of the reaction kinetics.

SEM: visualization of the morphology of hardened pastes and determination of reaction degree:

The influence of blending proportion, on the final characteristics of the microstructure, was observed with scanning electron microscopy. The effect played by the activating solution is similar to what occurred for pastes cast with individual precursors. In system N8S12 (Figure 6.17a), the cementitious matrix is more dense and compact than in pastes activated with NaOH (Figure 6.17b). Despite of the presence of a few cracks caused by sample preparation, unreacted particles of both Si-FA (darker particles, identified with green arrows) and BFS-2 (brighter particles, identified with yellow arrows) were more strongly embedded in it - especially considering small particles up to 5 μm (blue dashed frames).

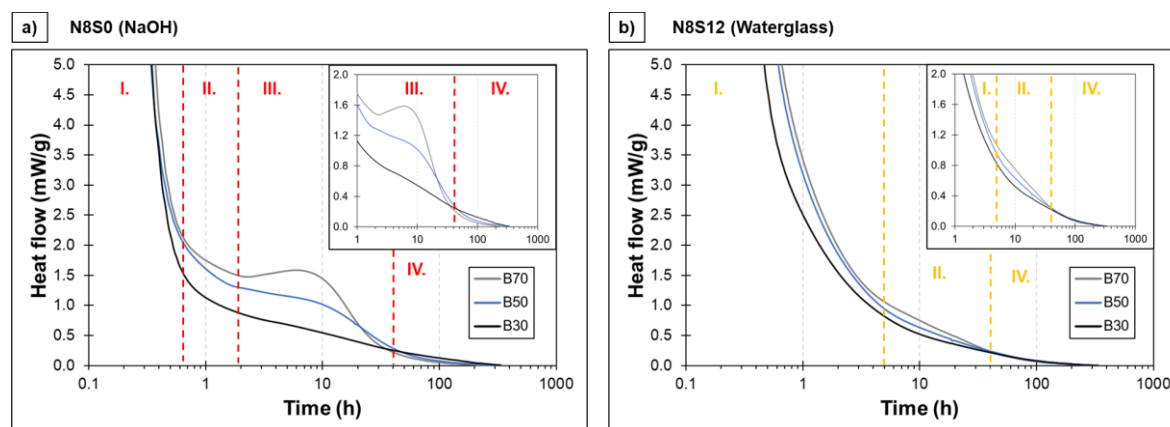


Figure 6.16: Evolution of reaction kinetics, through isothermal calorimetry, of blended systems comprised of glasses BFS-2 and Si-FA, activated with: a) NaOH (N8S0) and b) waterglass (N8S12) solutions.

In N8S0 systems (Figure 6.17b), the cementitious matrixes displayed a less dense characteristic, especially in blend B30 which had the largest content of Si-FA. It was possible to identify chemical attack at the surface of precursors (red dashed frames) in all mixtures, as both Si-FA and BFS-2 exhibited etching pits in all images. The adhesion of unreacted particles with the bulk matrix was not optimum, and the interfaces were more porous than in N8S12 systems. Similarly to individually-activated precursors, reaction products appeared to have preferential growth directions in all pastes. This created a porous network in the matrix, typically observed in NaOH-activated systems [215,462], but it was not possible to distinguish specific morphological characteristics - i.e. platelet-like phases - of different reaction products as observed in pastes made with individual precursors - see Figure 6.8.

In agreement with observations from Ismail et al. [228], the continuity of the matrix increased with larger proportions of glass BFS-2 in both N8S0 and N8S12 systems, as the increasing presence of a high-Ca precursor provides a more reactive nature for the whole system. This was not necessarily reflected in the overall degree of reaction indicated at the bottom of each SEM micrograph, which was relatively similar for all blended pastes considering the experimental error - experimental error is larger in pastes prepared with blended than individual precursors, due to the larger complexity of phase segmentation with one additional compound. Moreover, the isothermal calorimetry was not conclusive in distinguishing the contributions of each component to the overall reactivity of the pastes, and clear conclusions regarding the effect of the blending proportions on the final microstructure could not be achieved with these two techniques.

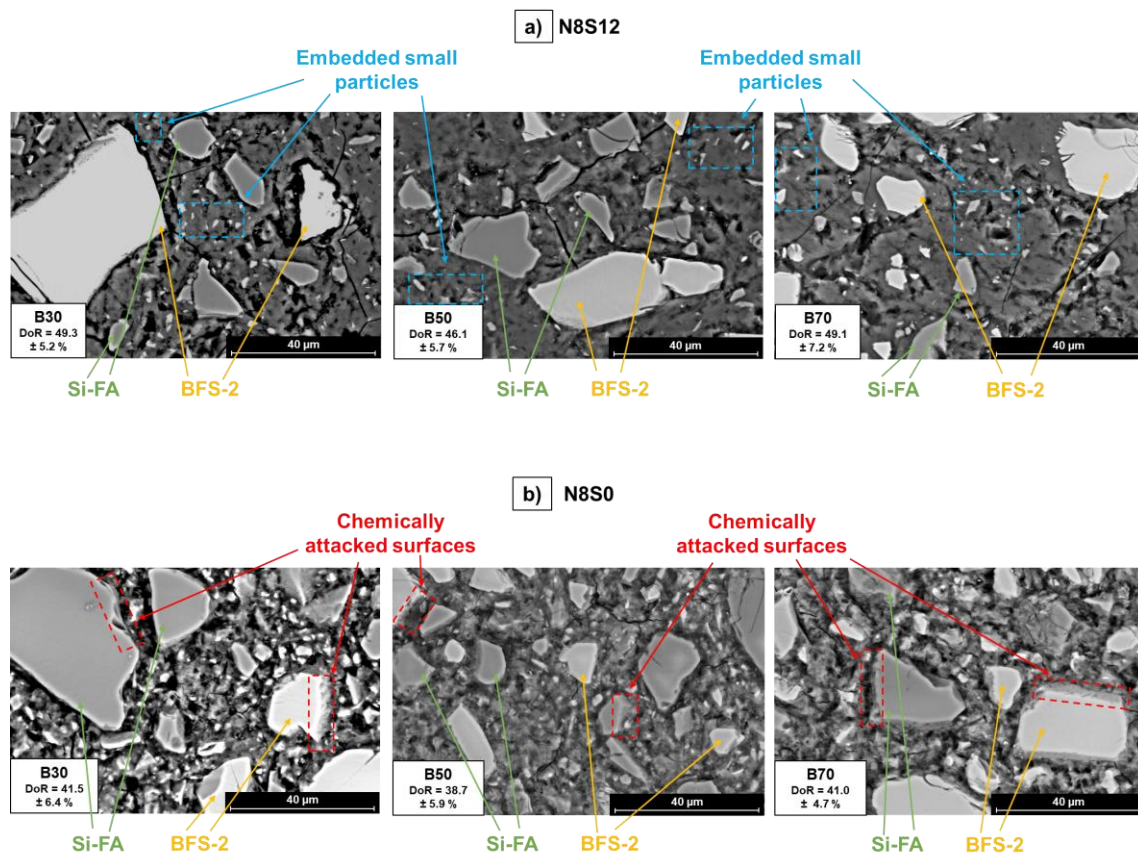


Figure 6.17: BSE images of the microstructure of blended pastes, cured for 28 days at 20 °C, along with the identification of their respective degree of reaction. Pastes activated with a) waterglass (N8S12) and b) NaOH (N8S0).

However, the assessment of the reactivity of individual components, via phase segmentation of SEM micrographs, provided interesting observations. The plots in Figure 6.18 show the degree of reaction, at 7 and 28 days, for glasses Si-FA and BFS-2 in the three blends. In both activating scenarios, the major component of the blend presented higher degree of reaction in blends B30 and B70. At 7 days, Si-FA represented 29.5 % (N8S0) and 32.2 % (N8S12) of the overall reaction degree in blend B30, while BFS-2 accounted for 24.4 % (N8S0) and 31.6 % (N8S12) in the latter - at 28 days, the main component still represented the most reactive portion of the blend. The continuity of the reaction, after 7 days, increased the contribution of the precursor of lower fraction in blends B30 and B70 to the overall reaction at different rates. For instance, glass BFS-2 displayed a significant evolution in blend B30 from 7 to 28 days, as its individual degree of reaction was 2.5 (N8S0) and 3 (N8S12) times higher at the end of the reaction. Conversely, glass Si-FA showed a lesser evolution in reaction, increasing only 2.7 % (N8S0) and 2.1 % (N8S0).

In blend B50, glass BFS-2 displayed a moderately larger influence in the overall reaction kinetics, as the calculated reaction degrees of the high-Ca precursor were higher in both solutions at both ages. This preferential reaction resulted in a delayed contribution from glass Si-FA, which showed a mild increase in reaction degree at 7 and 28 days, whilst negligible changes were observed in the reaction degree of BFS-2. The dominance of high-Ca-precursors has been addressed before [348,419,444,463], as typical features of slag were observed to dominate the microstructure of blended systems up to 0.75 slag:fly ash ratios.

Additionally, it is suggested that the slag-like component played a major role on enhancing the reactivity of glass Si-FA in the blended pastes. The overall degrees of reaction of the three blends were higher than the calculated values in individually-activated fly ash glasses in both activating solutions - see Table 6.4. In this scenario, the presence of Ca-species in the solution is essential to trigger the dissolution of fly ashes. The quick binding of the released species from fly ash with aqueous Ca, available from the initial cationic process of dissolution of BFS-2, intensifies the hydrolysis phenomena of Si-FA. For instance, C-S-H-like crystallites or portlandite sites have been observed to act as heterogeneous nucleation sites of N-A-S-H gel [456,464,465]. This can increase the rate of phase precipitation and intensify the dissolution of the fly ash-component, reducing the setting time [106] and accelerating the strength development of the mixture [398].

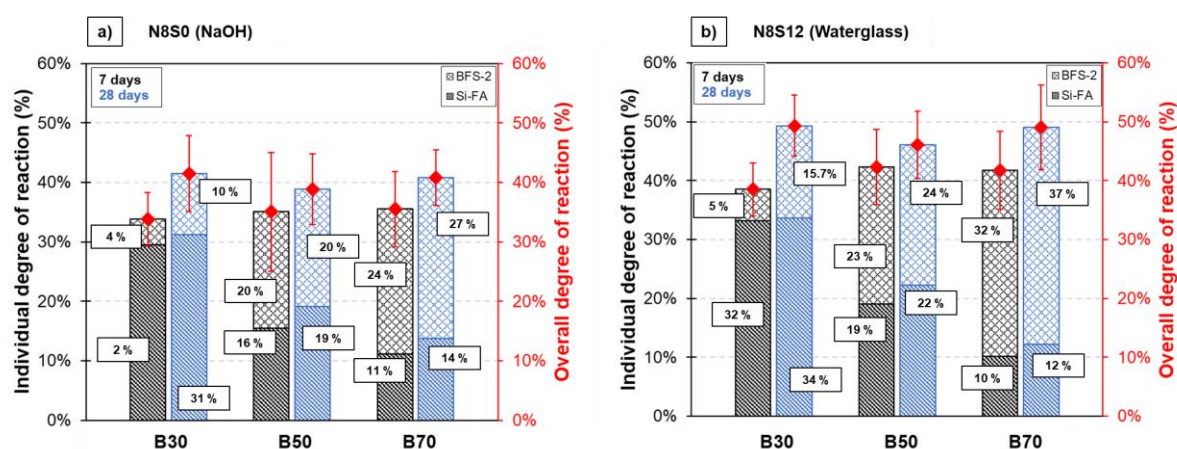


Figure 6.18: Evolution of the degree of reaction of blended pastes, in overall, and of the individual components of mixtures activated with: a) NaOH (N8S0) and b) waterglass (N8S12) - the error bar is attributed to the values of overall degree of reaction.

6.3.3.2 Study of reaction mechanism with Fourier transform infrared spectroscopy (FTIR)

The dominance of high-Ca precursors in blended systems is better visualized with FTIR analysis. The left hand of Figure 6.19a shows the spectra of pastes cured for 28 days with sodium hydroxide solutions (N8S0), showing mild but conclusive differences among the three blended systems. All pastes displayed reflections assigned to chemically bound water centred at $1641\text{--}1644\text{ cm}^{-1}$ and $1391\text{--}1393\text{ cm}^{-1}$ [228,400,466], and carbonation products between 1465 and 1471 cm^{-1} [311,324]. An increasing content of BFS-2 in the blending ratio had two effects on the spectra: i) increased the intensity of the small band centred at $892\text{--}893\text{ cm}^{-1}$, converting it from a shoulder-like nature to a small peak; and ii) reduced the intensity of the shoulder located at 865 cm^{-1} . Although none of them have strong intensities, the first one is usually attributed to C-S-H like structures. Yu et al [467] have assigned this band to Si-O stretching vibrations, which has been identified as being from Si Q^2 species in linear silicate chains [219]. The second is attributed to the vibration of terminal Si-O bonds [210,363].

In N8S0 systems, the combination of an absence of terminal unit-related responses in B70 (865 cm^{-1}), with increased signal of linear chain vibrations ($892\text{--}893\text{ cm}^{-1}$), suggests that a more amorphous matrix is present when BFS-2 is the main component of the system, due to the stronger formation of 2-dimensional silicate structures. On the other hand, as B30 presents higher intensity for terminal bridges, the presence of a larger quantity of small structural units is assumed, which would allow them to grow into preferential directions. This observation is consistent with SEM micrographs shown in Figure 6.17, with B30 displaying a porous caged-like and less dense cementitious matrix.

The implementation of waterglass (N8S12) provided similar trends to the blended systems, as shown in Figure 6.19b. All pastes presented reflections related to bound water and carbonation. The bands assigned to terminal Si-O bridges, located at $862\text{--}865\text{ cm}^{-1}$, was more intense for blend B30, and the intensity was continuously reduced as the proportion of BFS-2 was increased. This strengthens the argument that, in a fly ash dominated environment, the final reaction products tend to be more ordered at a smaller scale.

The effect of blending ratio on the nature of aluminosilicate chains is better seen in the enlarged spectral areas plotted in Figure 6.19 (right hand side). In both N8S0 (6.18a) and N8S12 (6.18b) systems, the centre of the Si-O-T band was shifted to higher wavenumber values with increasing Si-FA glass in the blended pastes. The stronger influence of glass BFS-2 in the reaction mechanisms is observed for the three blending ratios. Apart from blend B30 activated with waterglass, the centre of the main bands at 28 days of curing were closer to the measured values during the individual activation of BFS-2. This indicates that, although Si-FA had a major contribution in the reaction degree of B30 with both activators, the reaction products and the hardened matrix are still closer to what is usually obtained with high-Ca precursors.

In NaOH-activated pastes, the Si-O-T band has changed the centre position in blends B50 and B70 from 7 to 28 days. As fly ash components are expected to have overall slower reaction kinetics [176,184], this behaviour is somehow expected. The late release of Si- and Al-species from glass Si-FA promotes a change in the pore solution, and in the average chemical composition of the reaction products. A shift of the bands towards higher wavenumbers indicate a higher content of Si, and consequently, higher Si/Ca ratios in the

microstructure [211,399]. However, this trend was not observed in blend B30, and the significant evolution in degree of reaction of glass BFS-2 between the two periods did not promote changes in the Si-O-T band.

In waterglass-activated systems, the main band was also moved upwards according to the blending proportion of Si-FA. Curiously, B70 presented a shift in the opposite direction at the end of the curing regimen. One potential explanation is the lower release of Al in this system due to the lower overall content of the element - glass BFS-2 has the lowest fraction of Al among all synthetic glasses. This favours the formation of linear Si-Ca-chains in C-S-H-like phases in initial instants, and the delayed incorporation of Al increases the variation in solid species in the matrix, reducing the Si content of the hardened chains.

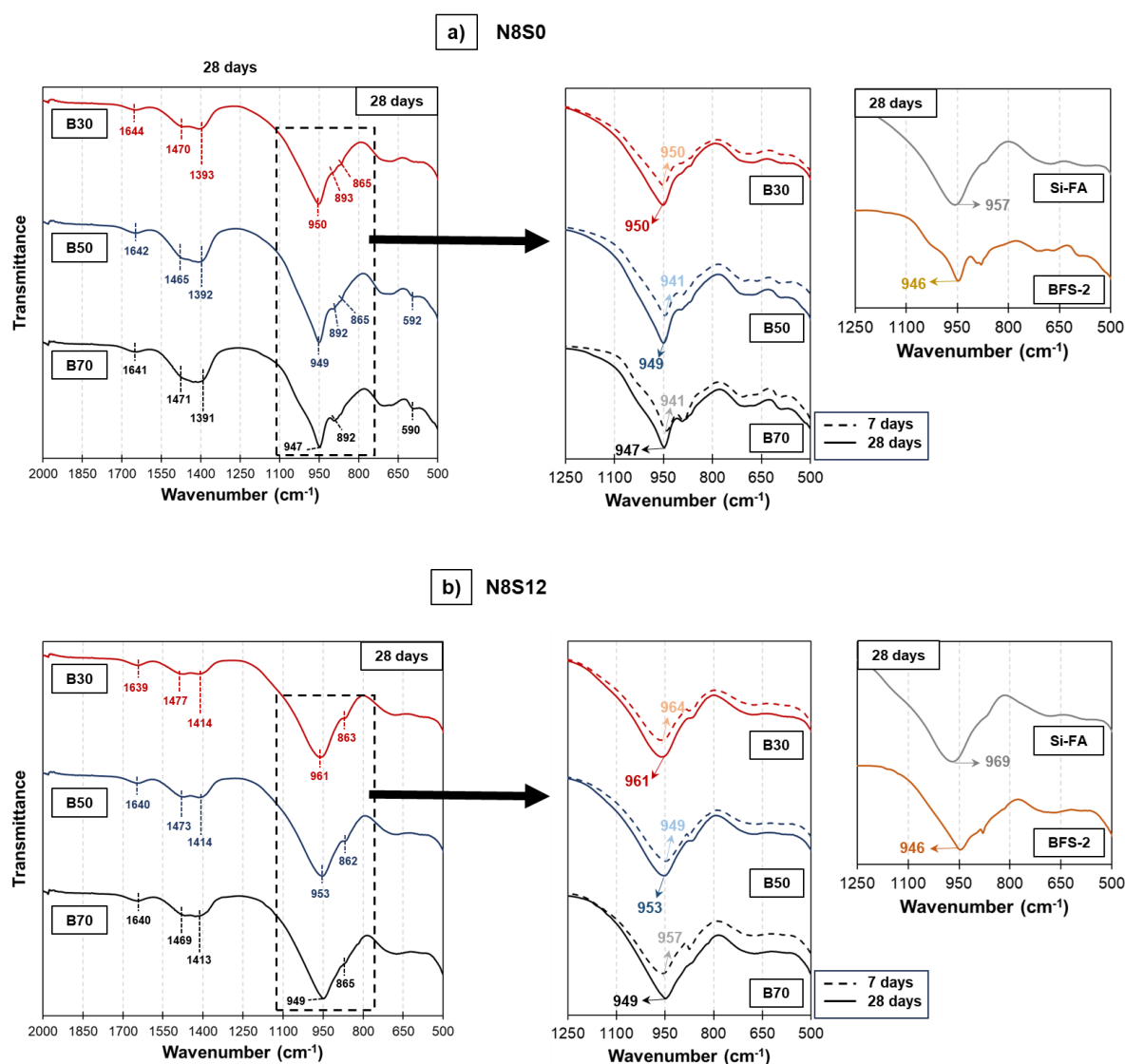
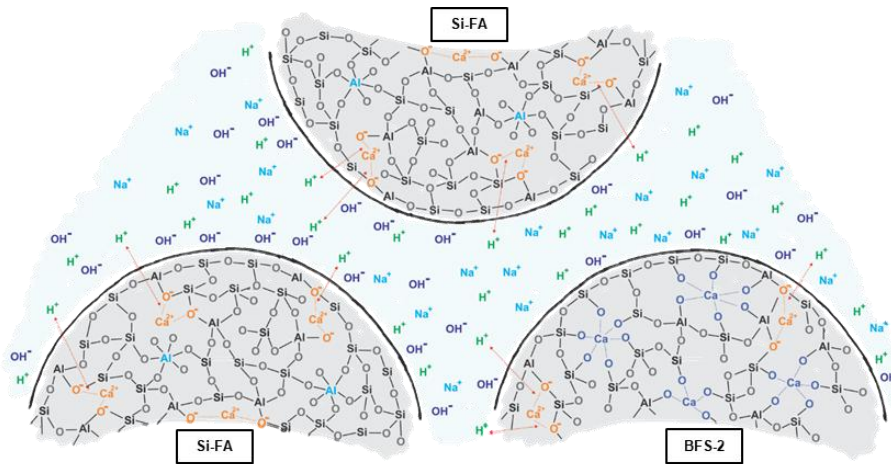
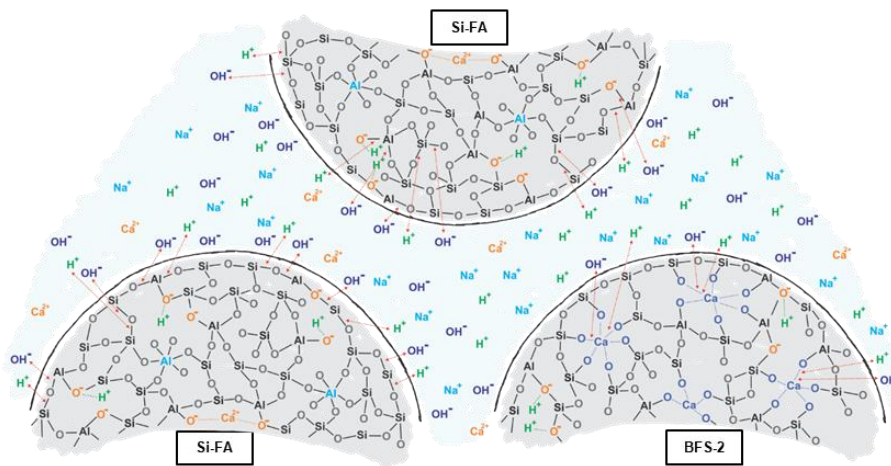


Figure 6.19: Visualization of the evolution in microstructure, through FTIR analysis, of blended pastes activated with a) NaOH (N8S0) and b) waterglass (N8S12). The enlarged areas present a comparison between 7-days (dashed lines) and 28-days (solid lines) of curing, with the 28-days cured individual pastes made with Si-FA and BFS-2 glasses.



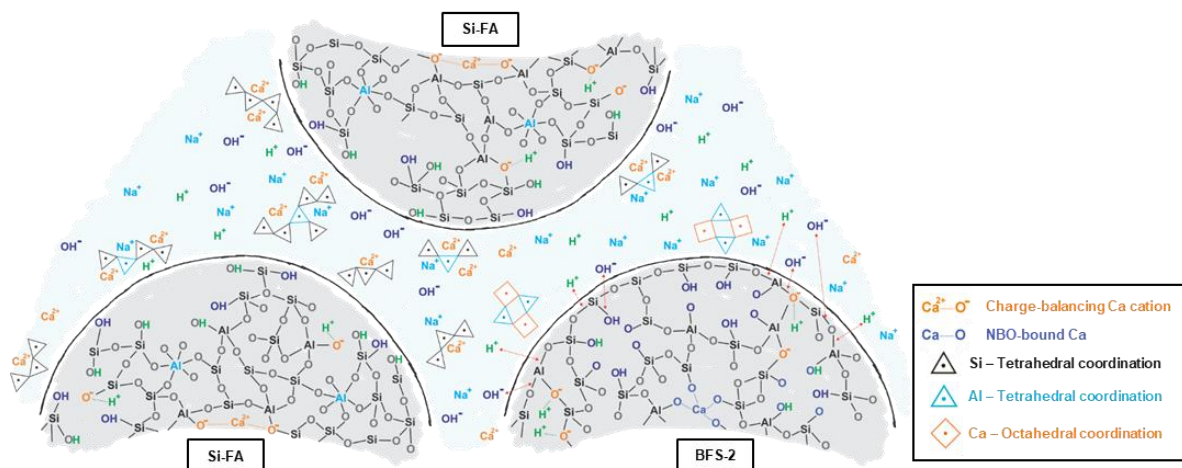
1. Cationic Exchange in high pH

Release of Ca²⁺ species – Si-FA and BFS-2



2. Hydrolysis of Si-O and Al-O bonds in high pH

Significant consumption of OH⁻ – Si-FA
Breakage of Ca-NBO bonds – BFS-2



3. Precipitation of Ca-based phases

Consumption of reactive species – Si-FA and BFS-2
Delayed Si-O and Al-O hydrolysis in mild pH – BFS-2

Figure 6.20: Schematic illustration of the reaction kinetics in blended systems, with larger proportions of fly ash glasses (Si-FA) than slag glasses (BFS-2).

Following the changes in the Si-O-T bands in the FTIR spectra, the sketch shown in Figure 6.20 illustrates the mechanism proposed to explain the unusual behaviour of glass BFS-2, with respect to the evolution of reaction degree in blend B30. It is suggested that, when added in minor proportions, the initial reaction of the slag-type glass is restricted to a significant release of Ca-species. After the cationic exchange process (step I), a higher consumption of alkaline ions occurs near the particles of Si-FA, since low-Ca materials require high pH to trigger their dissolution. This promotes a more significant hydrolysis phenomena of Si-O and Al-O bonds in the fly ash component (Si-FA), while the lower concentrations of OH⁻ near BFS-2 limit the hydrolysis to the breakage of Ca bound to non-bridging oxygens (step II). Sequentially, the just-released Ca cations from the high-Ca precursor (BFS-2) immediately combine with the dissolved species from the fly ash-type glass, forming the initial nuclei of reaction products and maintaining a high chemical affinity for the dissolution of Si-FA (step III). This step is consistent with the observations made by Puligilla and Mondal [468], who evidenced the positive effect of Ca in enhancing the dissolution of fly ash and precipitation of hydrated gels in blends with 15 wt% of slag. With the course of reaction, the alkalinity of the pore solution is expected to decrease - for instance, the pH of fly ash-based AAMs has been observed to drop by up to 0.5 units from 1 to 28 days in similar conditions [175,469,470]. Finally, the disordered structure of slag-type components is subject to a delayed chemical attack, as it requires milder alkaline conditions to promote its dissolution, resulting in a late burst of dissolution of glass BFS-2. It is thus expected that the immediate release of Ca, from the framework of slag-like glasses, accelerates the initial dissolution of low-Ca precursors, and that the intensity of this phenomenon is inversely proportional to the content of slag-type components in the blended system.

6.4 Development of chemistry-temperature based correlations

6.4.1 Degree of reaction

The analysis of reaction kinetics and microstructure of pastes with individual and blended precursors, at 28 days, allowed the establishment of a direct correlation between the degree of reaction and parameters of the reactive system - it is here assumed that, at 28 days, the system is sufficiently mature to allow the obtainment of such correlations without major changes due to curing age. The plot shown in Figure 6.21a displays the trend calculated for this empirically-defined *chemistry-temperature* relationship, which covers intrinsic (chemistry of the activator and precursor) and extrinsic (curing temperature) factors of the pastes.

As shown in the equation in Figure 6.21b, the proposed correlation is obtained from four individual factors, with three of them referring to atomic fractions of the different elements composing the mixtures and one referring to curing temperature, resulting in a dimensionless value:

- The first factor considers the atomic fractions of elements which enhance the depolymerization potential of the glass network, both internally and externally. This parameter is calculated from the presence of CaO (as a network modifier), in the former, and from the alkalinity of the activator (indirectly measured by the fraction of Na), in the latter.

- The second term considers the influence of the overall Si content and the Si/Al ratio of the system on the formation of C-S-H gels: the incorporation of Al in C-S-H gels has been reported to occur at secondary stages [417], at the same time that it might induce passivation of the reactive surface of precursors [175,471]; therefore, a higher Si/Al atomic ratio enhances the early reactivity of a system, which, in general, induces higher overall degree of reaction of a mixture.
- The third term represents the influence of the solution/precursor ratio, which considers that a higher dilution factor of the components, in systems with higher solution content, can result in a mild reduction of the reaction potential.
- The fourth term considers the presence of aqueous silicates, by proposing a ratio between the sole contributions of the precursor ($Si_{precursor}$), and the summed contributions from the activator and precursor (Si_{total}) to the overall Si content of the system. The present work has shown that the addition of waterglass promotes a slower evolution in the kinetics of reaction, but potentially enhances the total degree of reaction at later stages.
- Finally, the last term considers the influence of temperature, which has also been proved to significantly affect the evolution of the reaction in fly ash-based systems - see Section 6.3.2. The definition of an exponential influence of temperature follows the observations made in Chapter 4, as a similar approach was utilised on the empirical derivation of dissolution rates through an Arrhenius-type relationship.

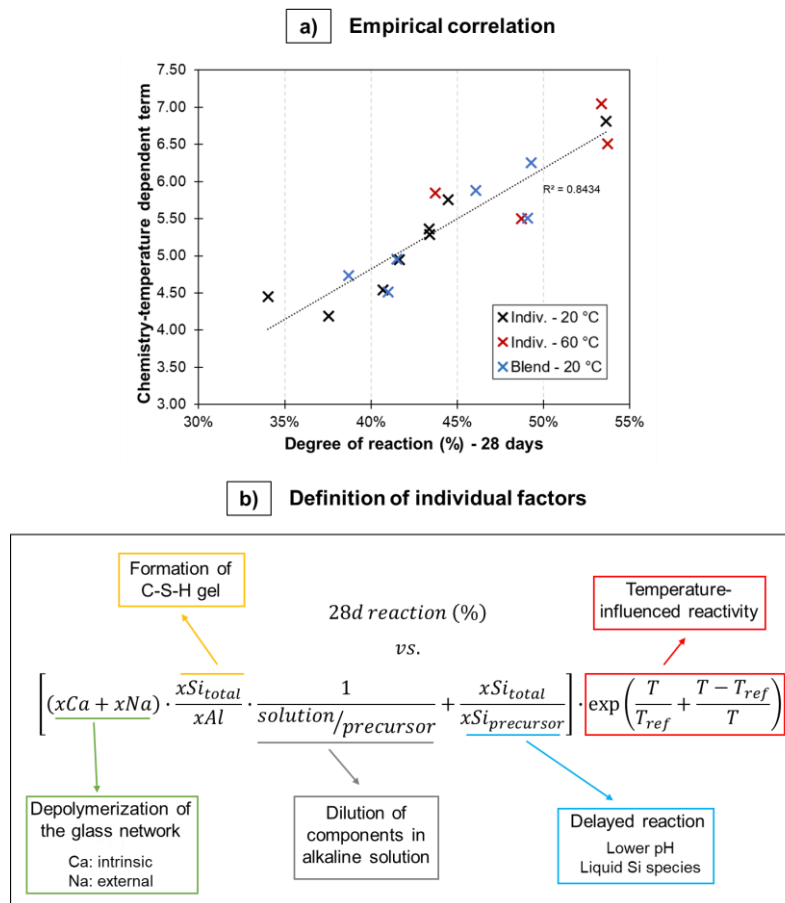


Figure 6.21: a) Empirical correlation established between the degree of reaction and chemistry-temperature of pastes obtained by the alkali-activation of individual and blended synthetic glasses; b) Explanation of each component of the empirical correlation.

The empirical correlation converged into a linear trend, showing a goodness of fit of 75 %. It is believed that the proposed equation provides a reliable estimation of the degree of reaction, as it utilises a large variety of mixtures in different scenarios and summarizes the main findings of the thesis.

6.4.2 Empirical definition of *phase assemblage indices*

The experimental procedure detailed in Section 6.2.5, by the combination of different characterization techniques (QXRD, SEM micrographs phase segmentation, and SAM treatment), was implemented in order to determine the amount of different reaction products in each of the pastes studied. The observed phases were classified in three categories: C-(N-A-)S-H gels, comprising variations of modifications of tobermorite; N-(C-)A-S-H gels, which include the variations of N-A-S-H- and zeolite-type structures identified with XRD; and secondary reaction products, composed of other crystalline phases in which Ca and Al play a crucial role in their formation, such as strätlingite, katoite and carbonated phases. With respect to the first two groups, the combination of selective dissolution methods with the degree of reaction of each paste allowed the distinction of the contribution of each category in the amorphous humps of the XRD patterns.

Moreover, it is important to state that the proposed experimental method did not allow the distinction between N-A-S-H gels with and without bound Ca in the second category, while EDS chemical analysis indicated a separate formation of such phases - see section 6.3.2.3. Nonetheless, the division between high- and low-Ca products is already interesting: characteristics such as elastic modulus [197,472,473] and chloride binding [474,475] are relatively similar in all sub-products of N-(C-)A-S-H gels, while the structural dominance of Ca significantly changes these properties in Ca-rich phases, due to its high polarizing effect which hinders the influence of Na in the gel structure [476].

Following a similar procedure from the previous section, empirically-defined *phase assemblage indices* are proposed to correlate the contribution of each category of reaction products to the overall alkali-activated matrix after 28 days of curing, assuming a mature microstructure at this age. The determination of each index, obtained via Equations 6.2, 6.3 and 6.4, considers the atomic fraction of components of the mixtures (precursor and activator) and curing temperature, resulting in unitless values.

$$C - (N - A -)S - H \text{ index} = \frac{Ca+Si}{Ca+Si+Al+Na} \cdot \frac{Ca}{Na} \cdot \frac{Ca+Si+Al}{Ca+Si+Al+Na} \quad (6.2),$$

$$(C -)N - A - S - H \text{ index} = \frac{Si_{precursor}+Al}{Ca+Si_{precursor}+Al+Na} \cdot \frac{Na}{Ca} \cdot \frac{Si_{all}}{Ca} \cdot \frac{Si_{all}}{Si_{precursor}} \cdot \frac{T}{T_{ref}} \quad (6.3),$$

$$\text{Crystalline Ca} - \text{Al rich phases index} = \frac{Al}{Ca+Si+Al+Na} \cdot \frac{Ca}{Si} \quad (6.4).$$

Each term of the three proposed expressions have individual contributions to the each individual index:

1. C-(N-A-)S-H index: the first term refers to the probability of precipitation of C-S-H gels, which is favoured in Ca-Si-rich environments - see Section 5.3.1; the second term considers the fraction of Ca with respect to the alkaline cations of the mixture, considering the structural role of Ca in the formation of reaction

- products when it is in excess [219,227], and the uptake of Na in C-S-H-like gels; and the third term considers the uptake of Al in C-S-H.
2. N-(C-)A-S-H index: the first term comprises the contributions exclusively from the precursor to the formation of Al-substituted silicate structures, favouring the formation of N-A-S-H gels; the second term is the opposite of the ratio of alkaline cations in the first index, as Na acts as a key element in the formation of N-A-S-H instead of C-S-H-like phases [213,477,478]; the third term considers the ratio of nucleating species of different categories of gels, since Si-rich environments enhance the potential of nucleation of N-A-S-H-like structures - see Section 5.3.2; the fourth term evaluates the influence of waterglass, which prompts homogeneous-like nucleation mechanisms and increases the potential nucleation of Si-dominated phases; and the fifth term considers the influence of temperature, which has been shown to enhance the early nucleation potential of N-A-S-H gels - see section 5.3.1.
 3. Crystalline Ca-Al-rich phases index: the first term comprises the fraction of Al in the binder, since strätlingite and katoite are preferentially formed in Al-rich environments [55,374]; and the second term considers the ratio of Ca over Si, which prompts the formation of AFm phases with Ca-Al binding [82].

For all pastes cured for 28 days, the resulting individual indices were summed and an overall value was obtained. The ratios of each category to the overall index, for each paste, are shown in a graded color-scale in Table 6.6 and compared to the experimental values obtained via the combination of QXRD and selective dissolution treatment - see Section 6.2.5. With respect to the primary reaction products, the indices of Ca-dominated gels and N-A-S-H-like phases followed an overall good agreement with the calculated fractions of each category. Pastes made with glass Ca-FA displayed a relatively high content of C-S-H-like phases when activated with NaOH, showing up to 54 wt% of C-(N-A-)S-H gels. This reflects the delayed precipitation of N-A-S-H gels, which have been shown in Chapter 5 to be thermodynamically stable only in environments with $\text{Ca}/(\text{Si}+\text{Al})$ below 0.23 at 20 °C. Consequently, the reduced ratio of Ca in the waterglass-activated Ca-FA system reduced the presence of amorphous Ca-based gels, contributing only up to 22 wt% of the hardened matrix. Additionally, the calculated amounts of N-(C-)A-S-H phases increased up to 12 wt% in the two fly ash glasses when comparing curing regimes at 20 °C and 60 °C. This last feature is consistent with the reaction mechanisms discussed in Chapter 5, as Ca is no longer the main reaction driver at higher temperatures.

The index related to secondary phases does not follow the same trend as the other two categories, but it was possible to observe higher index and quantities in NaOH-activated pastes with slag-glasses. As described previously, the formation of strätlingite, and the association of Ca with Al, occur in environments which are rich in these two elements. On the other hand, the precipitation of such phases is limited in the presence of liquid silicates (system N8S12), as the supersaturation of C-S-H-like phases is more easily achieved than other compounds. Additionally, these secondary reaction products are not strongly observed in fly ash-type systems, and both the index and calculated amounts of Al-rich phases are nearly zero for low-Ca glasses.

Table 6.6: Comparison of the proposed *Phase Assemblage Indices* with the quantitative determination of each category of reaction products. The graded color-scale scheme indicates the highest (darker tone) and lowest (lighter tone) for both index and calculated quantity of each category.

Glass	Activator	Curing temperature	C-(N-A)-S-H gels		N-(C-)A-S-H gels		Crystalline Ca-Al-rich phases	
			Index	Quantity	Index	Quantity	Index	Quantity
BFS-2	NaOH	20 °C	0.83	69%	0.08	24%	0.09	9%
BFS-2	WG	20 °C	0.81	87%	0.13	13%	0.06	0%
BFS-1	NaOH	20 °C	0.78	81%	0.11	14%	0.11	6%
BFS-1	WG	20 °C	0.76	82%	0.17	18%	0.07	0%
B70	NaOH	20 °C	0.72	77%	0.19	21%	0.09	4%
B70	WG	20 °C	0.67	66%	0.28	34%	0.06	1%
B50	NaOH	20 °C	0.58	64%	0.34	33%	0.08	3%
B50	WG	20 °C	0.51	50%	0.44	50%	0.05	1%
Ca-FA	NaOH	20 °C	0.44	54%	0.48	45%	0.07	3%
Ca-FA	NaOH	60 °C	0.42	43%	0.51	56%	0.07	0%
B30	NaOH	20 °C	0.39	59%	0.55	40%	0.06	3%
Ca-FA	WG	20 °C	0.37	22%	0.59	77%	0.04	1%
Ca-FA	WG	60 °C	0.34	13%	0.62	86%	0.04	2%
B30	WG	20 °C	0.32	30%	0.65	70%	0.03	0%
Si-FA	NaOH	20 °C	0.10	25%	0.88	75%	0.02	0%
Si-FA	NaOH	60 °C	0.09	12%	0.89	88%	0.02	2%
Si-FA	WG	20 °C	0.08	16%	0.91	84%	0.01	0%
Si-FA	WG	60 °C	0.07	4%	0.92	96%	0.01	2%

The reliability of the proposed indices is better visualized in the plots shown in Figure 6.22. The contribution of each index to the sum of the three categories - calculated as percentage - and the correlation of such values with the amount of each category of reaction products, reached a goodness of fit higher than 86 % for the two main gels, and the vast majority of the data points are found within a ± 10 % tolerance of the $y = x$ line. The interpretation of the main outliers on each chart, highlighted in Figures 6.22a and 6.22b, requires different explanations. In waterglass-activated Ca-FA, the phase assemblage index of C-(N-A)-S-H gels was overestimated, especially under the 60 °C curing regime, and the mixtures displayed larger quantities of N-(C-)A-S-H-like phases than expected. Although it was slightly distant from the tolerance, it still follows the expected trend, due to the combined contributions of temperature and aqueous silicates on the reaction mechanisms in fly ash glasses. Conversely, NaOH maximized the precipitation potential of Ca-dominated phases, resulting in an underestimation of N-A-S-H-like gels in 20 °C-cured Si-FA containing pastes and in blend B30.

Interestingly, glass BFS-2 promoted an unexpectedly high formation of the N-(C-)A-S-H category in system N850. Ca has been demonstrated to be incorporated into N-A-S-H structures in later stages of reaction of blends of fly ash and slag [363,468], altering the gel composition and leading to crosslinking of existing structures [211]. These late changes in the microstructure, favored by the coarse porosity in systems activated by N850, can both reduce the quantity of Ca-dominated structures and stiffen the microstructure, creating a barrier for the chelation of Ca ions and thus reducing the amount of dissolved material via SAM extraction. Nevertheless, the obtained results are following the proposed trend, and

these effects are not believed to highly influence the robustness of the proposed correlations.

Finally, it is important to state that the current systems do not have additional secondary oxides in their compositions, such as MgO , Fe_2O_3 , or even sulfate-components, preventing the formation of other secondary phases. The correlation shown in Figure 6.22c is the lowest among the three indices, despite all data points being located within the $\pm 10\%$ established tolerance.

It is concluded here that the proposed indices represent a reliable estimation of what may be expected in the activation of commercial precursors. However, it is still suggested to verify the need for refinement of the indices of secondary phases, especially for high-Ca precursors. In fly ash-rich systems, the formation of products different than amorphous gels and zeolites is rather limited [175,205,479], while the formation of hydrotalcite, strätlingite and other AFm phases can be significantly enhanced in high-MgO environments [89,227], typically observed in alkali-activated slags.

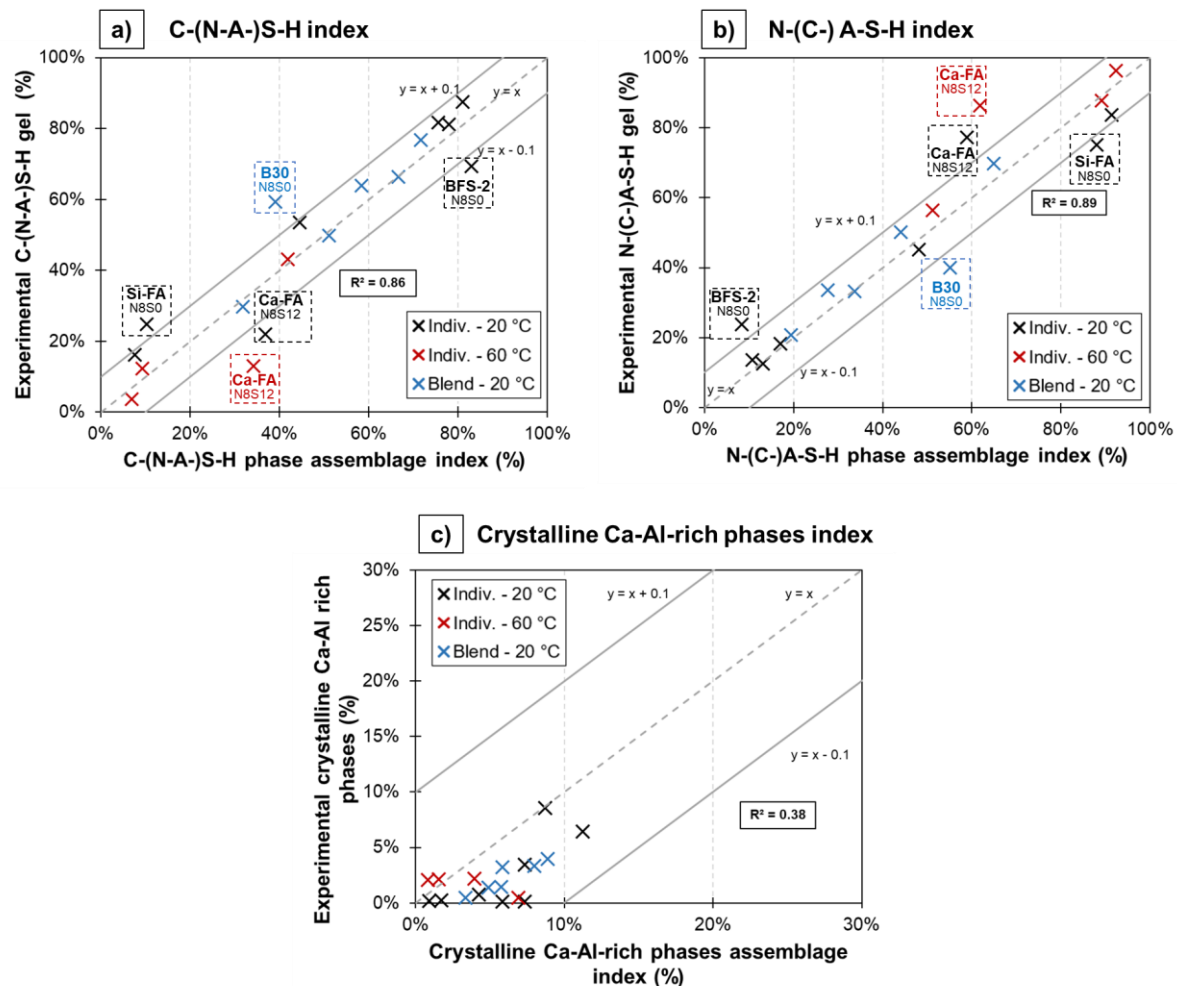


Figure 6.22: Correlation of the proposed Phase Assemblage Indices with the experimentally determined quantity of each category of reaction products: a) C-(N-A)-S-H gels; b) N-(C-)A-S-H gels; and c) Crystalline Ca-Al-rich crystalline phases. The dashed frames represent the main outliers on each plot.

6.5 Conclusions and outlook

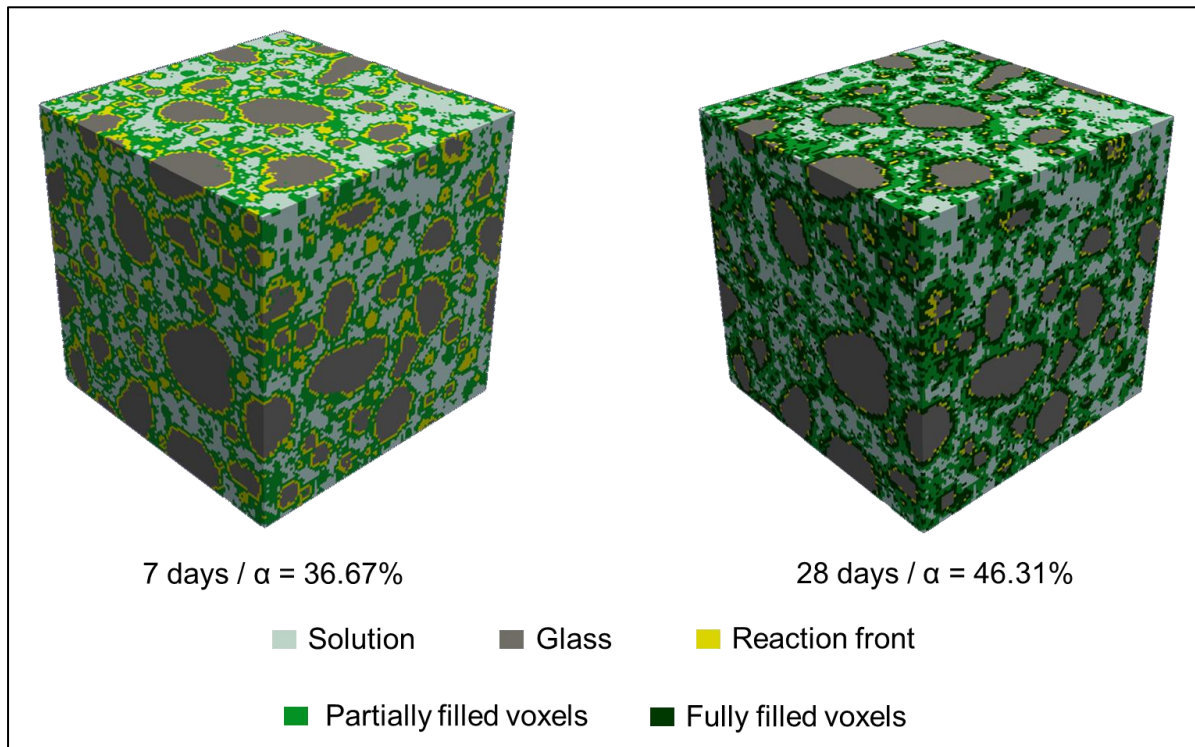
The study of the reaction kinetics of alkali-activated pastes, under different conditions, provides meaningful insights into the different stages and influencing factors of these binders. The present chapter focused on the assessment of curing temperature and binder chemistry on the evolution of reaction, and on the final characteristics of the hardened cementitious matrix. Based on the results obtained in this Chapter, the following conclusions and observations were made:

- At 20 °C, the reaction potential of a mixture, measured by isothermal calorimetry, is mainly governed by the Ca content of the precursor. Glass BFS-2 presented the highest values of degree of reaction after 7 and 28 days as measured by phase segmentation of SEM micrographs, while glass Si-FA presented delayed reactivity in the same ages. With respect to the alkaline solution, waterglass favored higher precipitation rates in initial stages but slower evolution of reaction. Nonetheless, it promotes a more cohesive characteristic of the cementitious matrix, and the porosity is significantly reduced when compared to NaOH-activated mixtures.
- A content of 12 Na₂O wt% was observed to be excessive for the NaOH-activation of glass Si-FA at 20 °C. The high alkalinity favored an immediate response of the system, enhancing the exothermic response in the first hour. However, the reaction appeared to be hindered in secondary stages, as the formation of a thick layer of reaction products surrounding the reactive glass particles limited the dissolution of the precursor. Under the same solution, a second acceleration peak was observed in isothermal calorimetry tests at 60 °C, which is connected to the transformation of initial units into zeolite-like ordered phases.
- Temperature and alkalinity displayed a synergistic combination to enhance the reaction potential of fly ash-type glasses. The degree of reaction, in systems N8S0 and N8S12, increased up to 30 % compared to 20 °C cured pastes.
- In general, gel phases are intimately mixed in hardened cementitious matrices. Despite of binder chemistry and curing conditions, it is nearly impossible to observe the precipitation of exclusively one type of gel structure (either Ca-dominated or Ca-restricted). In fly ash-type glass based systems, the use of waterglass solutions promotes a more clear phase separation, and the formation of three types of gels could be obtained.
- In blended mixtures, high-Ca precursors have a more significant impact in the overall reaction kinetics. In all three blends, glass BFS-2 enhanced the reaction potential of glass Si-FA, increasing its degree of reaction when compared to individually activated precursors. When BFS-2 was present with a lower content, its reaction was limited. It is suggested that its dissolution starts with a quick detachment of Ca in the initial moments, with a delayed release of Si- and Al-species in later stages.
- The empirical correlations proposed in this Chapter were successful to estimate the degree of reaction, and the quantities of each category of reaction products at 28 days. As the correlations were established using chemical compositions of the initial components, and curing conditions, it is believed that they may provide reliable tools on the estimation of characteristics of hardened binders, which is essential for future modelling conditions.

The empirical correlations defined for the degree of reaction, based on initial characteristics of the mixture, provided an interesting visualization of mature systems. This allows the implementation of different sources of raw materials, expanding the range of potential precursors and activators to be implemented in alkali-activated systems. It should be noted that an excess of alkalinity was not covered in this work, and this topic surely deserves more attention in future research. Additionally, the proposal of phase assemblage indices represents a powerful tool for modelling purposes of alkali-activated systems, as they facilitate the estimation of mechanical performance and durability, which are vital for the design and study of service life of concrete structures. A refinement of the indices might be necessary to include other minor components from the compositions of precursors, which might affect the precipitation and stabilization of secondary reaction products.

Chapter 7.

Numerical simulation of alkali-activated materials



In alkali-activated materials, the existence of reliable models which assess their performance and durability can facilitate their wider implementation. Due to the large amount of variables involved in these binders, simulation tools come as an easy and cost-efficient solution to reduce the experimental cost involved with validating their behaviour, providing a vital role on increasing the general trust in this class of materials. This Chapter concludes this thesis, describing the development of a numerical modelling tool which simulates the evolution of the microstructure of alkali-activated pastes in different conditions. The main results obtained in previous Chapters related to reaction kinetics and phase assemblage will be implemented for the development of additional modules in GeoMicro3D, enabling the simulation of binders obtained by low-Ca precursors and blended systems. The outcomes of the simulations will be compared with experimental results with respect to degree of reaction and quantitative analysis of reaction products, ensuring that the contributions of this work were crucial for the development of reliable microstructural modelling of alkali-activated binders.

7.1 Introduction

Modelling of traditional and alternative binders are an inexpensive and quick way to study the behaviour of cement-based products, providing relevant information regarding reaction kinetics, performance and service-life. These tools are utilised for a wide range of purposes (e.g. the observation of interactions between paste and admixtures, verification of leaching characteristics of hardened elements, estimate mechanical properties, among others), and can be implemented to understand the influence of multiple variables, such as raw materials and processing conditions, over the final characteristics of the binders. With respect to kinetics and phase assemblage, the extent of the reaction - or the degree of reaction - of a system and the volume of reaction products can be estimated by simply taking into account the initial content of water in the mixture [480], or by other more complex methods which consider physical, chemical and mineralogical aspects of the reactive particles [238,382,481-485]. Sequentially, the estimation of these characteristics facilitates the investigation of the structural build-up of a reactive system, as it is intimately linked with the formation of reaction products. The knowledge on the nature and the quantity of newly formed phases determines the structural conditions of the binder, from nano [486-489] to macroscales [490-492], and ultimately allows the prediction of the performance of these materials in fresh and hardened states.

Among different available tools capable of estimating microstructural and pore solution characteristics, thermodynamic modelling excels as one of the most reliable ones. While it has been widely used for Portland cement-based systems [57,203,217,493,494], its implementation in the field of alkali-activated materials (AAMs) has only recently been in focus, as detailed in Section 2.5.1. The extension of databases for the modelling of alkali-activated systems is an emerging field of research. With respect to N-(C-)A-S-H products, a few authors have attempted to experimentally define their thermodynamic properties [222,224,326]. However, the difficulty in synthesizing such species, especially those with high Si/Al ratios, and the complexity of the experimental setup necessary for such studies, limits the amount and applicability of available data in literature. Recently, in collaborations with Chen et al. as part of this thesis, several N-A-S-H [225] and N-(C-)A-S-H [226] gels were successfully synthesized with different atomic ratios, and their solubility products, among other thermodynamic properties, were determined. These works went beyond the existing data for this class of gels, and will allow a more reliable estimation of the microstructure of alkali-activated materials containing fly ashes, metakaolin, and other Si- and Al-rich precursors. With respect to reaction kinetics, a few authors attempted to model the precipitation and growth of reaction products in different alkali-activated binders. Among the different models described in Section 2.5.2, GeoMicro3D [59] excels as the most complete one, as it combines a kinetic approach of dissolution of precursors, and a thermodynamic model to predict an equilibrated phase assemblage of slag-based binders at different ages.

Following the functional structure of this thesis, illustrated in Figure 7.1, Chapter 7 investigates the evolution of digital microstructures of alkali-activated materials in different conditions. The physical characteristics of precursors defined in Chapter 3, and the chemistry-temperature influenced dissolution rates derived in Chapter 4, will be combined with the thermodynamic data of N-(C-)A-S-H species determined in collaboration with Chen et al. [225,226]. The integration of these datasets will be implemented in GeoMicro3D,

resulting in additional functionalities of the simulation tool which will include the activation of low-Ca precursors and mixed systems. The extended model will replicate the microstructure evolution of four different systems, including the individual and blended activations of the synthetic glasses Si-FA and Ca-FA (see Chapter 3 for more details on composition and mineralogy), and the influence of temperature in the reaction mechanisms of fly ash-type glasses. A detailed comparison between the simulated and experimental data obtained in this thesis was used to evaluate the performance of the new features of GeoMicro3D. The following characteristics were considered: the evolution of reaction degree (Chapters 4 and 6), the pore solution (Chapters 4 and 5) and evolution of phase assemblage (Chapters 5 and 6). The outcomes of Chapter 7 are expected to have major contributions to the technology of alkali-activated materials: by providing reliable microstructures obtained with different starting materials and reaction conditions, short- and long-term properties of these binders can be estimated, which are essential tools to validate their behaviour and increase the applicability of AAMs.

7.2 Methodology

7.2.1 Thermodynamic modelling

Thermodynamic modelling was performed to evaluate the influences of chemistry (precursor and activator) and temperature in the phase assemblage of different alkali-activated systems. The simulations were carried out using the Gibbs energy minimization software GEM-Selektor 3.4 (GEMs) [299] under a N_2 atmosphere and a pressure of 1 bar. The same procedure described in Section 4.2.3 was implemented for the calculation of the activity of each ionic species, which is essential for the determination of the equilibrium of the system. The PSI-Nagra [221] database was chosen as a source of thermodynamic data of aqueous species.

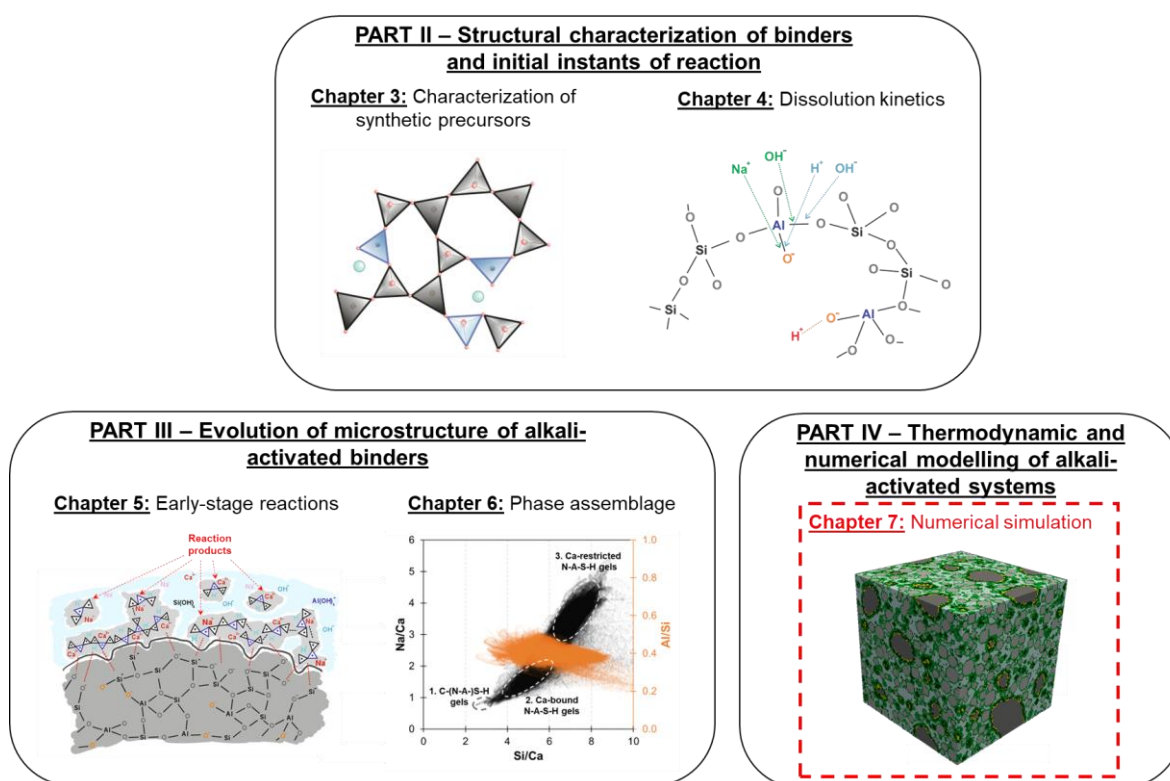


Figure 7.1: Schematic illustration of the structure of this thesis, highlighting the contributions of Chapter 7.

The implemented thermodynamic database of solid phases was Cemdata18 [220], which is widely used in the topic of simulations of cementitious binders. The solid phases considered in the present models followed the most common phases experimentally described in literature. As primary reaction products, the database included the CNASH-ss model developed by Myers et al. [58], comprised of pure calcium silicate hydrates (C-S-H), and other Al- and Na-bound calcium silicate species (C-A-S-H and C-N-S-H gels). These eight individual phases are categorized in the high-Ca group of solid phases, which will be generically identified as C-(N-A-)S-H. Low-Ca phases accounted for the thermodynamic database recently developed in collaboration with Chen et al. [225] in two sequential works: the first one accounts for three sodium aluminosilicate hydrate (N-A-S-H) species, with fixed Na/Al ratios of approximately 1 and variable Si/Al ratios of 1.1, 2.0 and 2.8; and the second comprises four different Ca-bound N-A-S-H gels, with Si/Al ratios of approximately 2.0 and 3.0 and Ca/Si ratios of approximately 5.0 and 10.0 [226]. These seven different phases are categorized in the low-Ca group of reaction products, which will be referred to as N-(C-)A-S-H. Additionally, a few selected zeolites were chosen from the database developed by Ma and Lothenbach [207], following the main experimental findings described in Chapters 5 and 6 of this work. Secondary Ca-containing reaction products accounted for calcium aluminate phases, such as C_3AH_6 (katoite), portlandite, and strätlingite, also described in Cemdata18. Tables C.1 and C.2, in Appendix C, detail the thermodynamic data of the aqueous species and solid products considered during simulations, respectively.

In thermodynamic simulations, the amount of reactive material must be defined as an input of the model. In the present work, the degree of reaction (α) of each precursor considered for the simulations was determined via Equation 7.1, which follows the empirical correlations derived in Chapter 6 and considers:

- i. the molar content of each element in the precursor (x_{Ca} , x_{Al} and $x_{Si_{precursor}}$) and in the activator (x_{Na} and $x_{Si_{activator}}$),
- ii. the curing temperature (T (K)) versus a reference temperature of 20 °C ($T_{ref} = 293.15$ K).

$$\alpha = \left[(x_{Ca} + x_{Na}) \cdot \frac{x_{Si_{precursor}} + x_{Si_{activator}}}{x_{Al}} \cdot \frac{1}{\text{solution/precursor}} + \frac{x_{Si_{precursor}} + x_{Si_{activator}}}{x_{Si_{precursor}}} \right] \cdot \exp\left(\frac{T}{T_{ref}} + \frac{T - T_{ref}}{T}\right) \quad (7.1).$$

The simulation assumed congruent dissolution of CaO, Al_2O_3 and SiO_2 , according to the overall reaction degree, and a fixed *solution/precursor* ratio of 0.4. The modelling was performed considering two alkaline solutions, replicating the experimental conditions from Chapter 6: system N8S0 consisted of a solution of sodium hydroxide (NaOH) with 8 wt% of Na_2O per mass of precursor, and system N8S12 consisted of a sodium silicate (waterglass) solution with the same Na_2O concentration and a silicate modulus of 1.5. Individual systems were modelled for each activating solution, and the influence of CaO content of the precursor in the final phase assemblage was evaluated. The influence of temperature, shifting from 20 °C to 60 °C, was evaluated in the simulation of reaction of glass Si-FA, individually activated both with NaOH and waterglass solutions.

7.2.2 Numerical simulation - coupled kinetic and thermodynamic modelling

The evolution of the microstructure of alkali-activated systems, through 28 days of reaction, was numerically simulated in different conditions of precursors and temperature. The

simulations were performed using *GeoMicro3D*, which describes digitally the evolution of the microstructure of alkali-activated materials at a paste level. In the present work, the tool was extended to include the kinetic observations of the dissolution of precursors obtained in Chapter 4 in this thesis, and the thermodynamic data of N-(C-)A-S-H gels as described in the previous Section.

The functionality of the tool, divided in five modules, is illustrated in Figure 7.2 through a simplified scheme - see [59] for more details:

- i. Firstly, the particles are distributed inside the simulation box using the extended Anm model [495], with a pre-defined box size and pre-defined characteristics of particle morphology. The solid component completely fills the nodes in which it is placed, and the chemical composition of each node is a homogeneous distribution of the initial chemistry of the precursor, while the solution voxels are uniformly distributed with aqueous species of the activating solution;
- ii. The simulation starts with an initial dissolution step, considering the dissolution rate equations obtained and described in Chapter 4 - see section 4.3.4 for more details - which are dependent on binder chemistry, temperature of the reaction and alkalinity of the activator;
- iii. A collision step is called, promoting the diffusion of aqueous species based on the Lattice Boltzman method, using a 7 cube velocity directions approach for 3D mass transport, in which aqueous species are regarded as source terms;
- iv. The thermodynamic module is initiated through GEMs, calculating the saturation indices of all reaction products in the nodes which are not completely filled with the precursor. If one or more phases are observed to be supersaturated, a nucleation probability is calculated for each respective component, based on nucleation rate and homogeneous and heterogeneous kinetic parameters;
- v. Finally, the appropriate phases are precipitated, and the digital microstructure is updated with the presence of reaction products.

The dissolution of the precursor enables the presence of nodes which are partially filled with the solid precursor and with aqueous species. If these nodes, or if nodes fully occupied by solution, indicate the supersaturation of one or more reaction products during the time interval of two simulation steps (Δt), the probability that these phases form nuclei larger than a critical thermodynamically stable size is calculated by Equation 7.2 [368]:

$$P(\Delta t) = 1 - \exp(-J \cdot V \cdot \Delta t) \quad (7.2),$$

where V stands for the volume of the solution portion in which the initial precipitates are formed, and J is the nucleation rate of each respective reaction product. If at least one critical nucleus is calculated to exist in the reactive node, the respective reaction product is allowed to precipitate in a stable way. The determination of nucleation rate of one phase, detailed in Equation 7.3, is dependent on its supersaturation index (S), and in two intrinsic parameters: the kinetic parameter (A) and the thermodynamic parameter (B) for heterogeneous nucleation, which are correlated to the molar volume and to the effective interfacial energy of each - see [175] for more details.

$$J(S) = A_n \cdot S \cdot \exp\left(-\frac{B_n}{\ln^2 S}\right) \quad (7.3).$$

1. Generation of simulation box



■ Solution ■ Glass

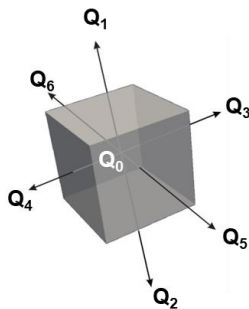
2. Dissolution step

$$\log r_{+,Ca}(T) = \log \left(3.3369 \cdot \frac{x_{Ca}}{(x_{Si} + x_{Al})} + 0.4428 \right) + 0.26 \cdot \log(a_{OH^-}) + \log r_{+,Ca}(293\text{ K}) + \frac{T}{674.78} + 0.092$$

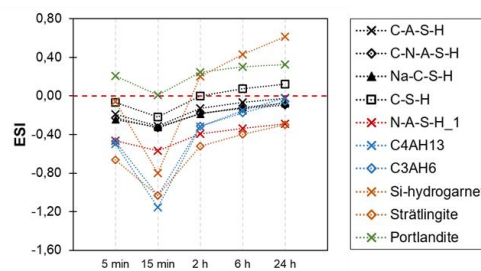
$$\log r_{+,Si} = 0.9373 \cdot \log r_{+,Ca} \cdot \left(\frac{293}{T} \right) - 0.5673$$

$$\log r_{+,Al} = \frac{0.6516 \cdot \log r_{+,Si} \cdot x_{Si} + 0.2523}{x_{Al}}$$

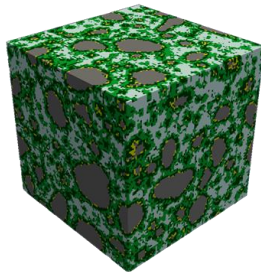
3. Collision step



4. Evaluation of saturation indices and nucleation probabilities



5. Precipitation and stabilization of reaction products



Voxel identification:

- Solution → > 95 vol% occupied by solution
- Glass → fully occupied by precursor
- Reaction front → partially occupied by dissolved precursor with solution
- Partially filled voxels → partially occupied by reaction products with solution
- Fully filled voxels → > 99 vol% occupied by reaction products

Figure 7.2: Simplified description of the functionality of *GeoMicro3D*.

After the positive formation of one or more reaction products, the nodes are updated with the partial or full presence of new phases. Once a reaction product is successfully precipitated, it is not affected by the surrounding solution nodes. In other words, the nucleation probability and thermodynamic equilibrium of one phase will only consider the concentration aqueous species in one specific time interval, aiming at a higher computational efficiency of the simulation tool. The digital microstructure distinguishes between five different types of nodes:

- unreacted nodes fully occupied by the precursor;
- solution nodes which are occupied by more than 95 vol% of solution;
- reaction front nodes which contain partially dissolved precursors;
- partially filled nodes containing a combination of solution and reaction products; and
- fully filled nodes which are occupied by more than 99 vol% of reaction products.

The thermodynamic data used in the numerical simulation followed the values utilised for the individual thermodynamic modelling - see Section 7.2.1. The kinetic parameter of nucleation of C-(N-A)-S-H gels and secondary reaction products were determined by Zuo through a parameteric study, while the thermodynamic parameter is individually calculated during simulations considering the thermodynamic data of each reaction product and other constants - see [175] for more details. The same parameters were considered for the nucleation of N-(C-)A-S-H gels and zeolites. Table C.3 in the Appendix C displays the complete list of parameters.

In the present work, the development of an updated version of GeoMicro3D (which includes the kinetic and thermodynamic findings of this work) was performed to simulate different experimental conditions of alkali-activated binders. The modifications to the original tool allowed the observation of digital microstructures of systems obtained by the activation of low-Ca precursors, in individual or blended conditions with high-Ca precursors, at temperatures ranging from 20 °C to 60 °C. These modifications targeted the extension of the accepted scenarios within GeoMicro3D with respect to the accurate replication of microstructures of alkali-activated binders. the experimental alkali-activation of the synthetic glasses described throughout this thesis. Four different systems were simulated using the updated tool. The modelled reactions of glasses with compositions similar to BFS-2 and Si-FA were simulated for a digital period of 28 days at a constant temperature of 20 °C, and the latter was also evaluated in a two-step curing regime: at 60 °C for the first 7 days, and at 20 °C for the remainder 21 days. Additionally, the alkali-activation of a blended system consisting of a 1:1 ratio of glasses BFS-2 and Si-FA was simulated for 28 days at 20 °C, following the composition of blend B50. In all cases, the activating solution consisted of NaOH, with a Na₂O concentration of 8 wt% per mass of precursor. The solution/precursor ratios were 0.40, for the activation of glass BFS-2 and blend B50, and 0.35 for the activation of glass Si-FA. These conditions replicate the pastes utilised to study the microstructural evolution of alkali-activated synthetic glasses described in Chapter 6, aiming for a more reliable comparison between simulated and experimental outcomes. Activators based on waterglass solutions were not utilised, as they would require more detailed information about the dissolution kinetics under a Si-rich aqueous environment. Table 7.1 summarizes the conditions tested with the updated version of GeoMicro3D.

Table 7.1: Summary of the systems simulated, utilizing the updated version of GeoMicro3D.

Precursor	Chemical composition (wt%)	Activator	Curing conditions	Water/precursor ratio
Glass BFS-2	CaO: 48.0 % SiO ₂ : 35.0 % Al ₂ O ₃ : 17.0 %	NaOH - N8S0 (Na ₂ O/glass = 8 wt%)	28 days - 20 °C	0.40
Glass Si-FA	CaO: 55.0 % SiO ₂ : 12.0 % Al ₂ O ₃ : 33.0 %	NaOH - N8S0 (Na ₂ O/glass = 8 wt%)	28 days - 20 °C	0.35
Glass Si-FA	CaO: 55.0 % SiO ₂ : 12.0 % Al ₂ O ₃ : 33.0 %	NaOH - N8S0 (Na ₂ O/glass = 8 wt%)	7 days - 60 °C; 21 days - 20 °C	0.35
Blend B50	1:1 ratio of glasses BFS-2 and Si-FA	NaOH - N8S0 (Na ₂ O/glass = 8 wt%)	28 days - 20 °C	0.40

7.3 Results

7.3.1 Thermodynamic equilibrium of alkali-activated binders

7.3.1.1 Effect of binder chemistry - precursor and activator

In the present work, the first step in the modelling process of reactions involving synthetic glasses consists in the observation of the thermodynamic equilibrium of these binders. As Ca has been observed to be strongly correlated to reaction mechanisms throughout this thesis, Figure 7.3 illustrates the influence of the element in the phase assemblage and pore solution of hardened binders simulating 28 days of curing at 20 °C - the simulation considered a fixed Si/Al molar ratio of 1.5 with variable CaO contents, which closely describe the compositions of the synthetic glasses used in this thesis. The plots show the changes in reaction products in NaOH (N8S0 - Figure 7.3a) and waterglass (N8S12 - Figure 7.3b) solutions - the degree of reaction was calculated by Eq. 7.1. Regardless of the activator, it is easily noticed that phases in which Ca is the main element, such as C-(N-A-)S-H gels, portlandite (CH) and katoite (C_3AH_6), become the main portion of the binder at CaO contents above 35-40 wt% - this behaviour will be discussed in details in the following Sections. Within this group, the contribution of portlandite to the overall phase assemblage presented an unusual feature in the higher-Ca portion of the plots, which is dependent on the activating solution: in system N8S0 (Figure 7.3a), it represented 42.2 wt% of the reaction products at the maximum CaO content, while in waterglass solutions (Figure 7.3b), it represented only 5.2 wt%. In both cases, the formation of portlandite was only observed when the Ca/Si ratio of the pore solution reached its lowest value (approx. 0.02), which was kept constant until the maximum Ca content of the systems.

Conversely, the contribution of Ca-dominated disordered gels (C-(N-A-)S-H) at the maximum CaO content increased from 26.6 wt% to 73.5 wt% when comparing NaOH to waterglass solutions, while the amount of katoite rose from 6.4 wt% to 14.4 wt%. This last feature suggests that the presence of soluble silicates in the pore solution favours stronger interactions of Ca with Si and Al, and thus facilitates the formation primarily of Ca-based disordered gels and secondly of calcium aluminates over portlandite. Typically, in waterglass-activated systems, the dominant mechanism of phase precipitation follows a homogeneous-type behaviour and promotes an intimately-bound growth of reaction products [199,202]. This leads to the stabilization of more homogenous microstructures than what is observed in NaOH-activated pastes, resulting in the intermixing between two or more types of amorphous gels as indicated in the experimental findings in Chapter 6 - see Section 6.4.2, and showing that thermodynamic equilibrium calculations can moderately replicate the kinetic behaviour of the binders.

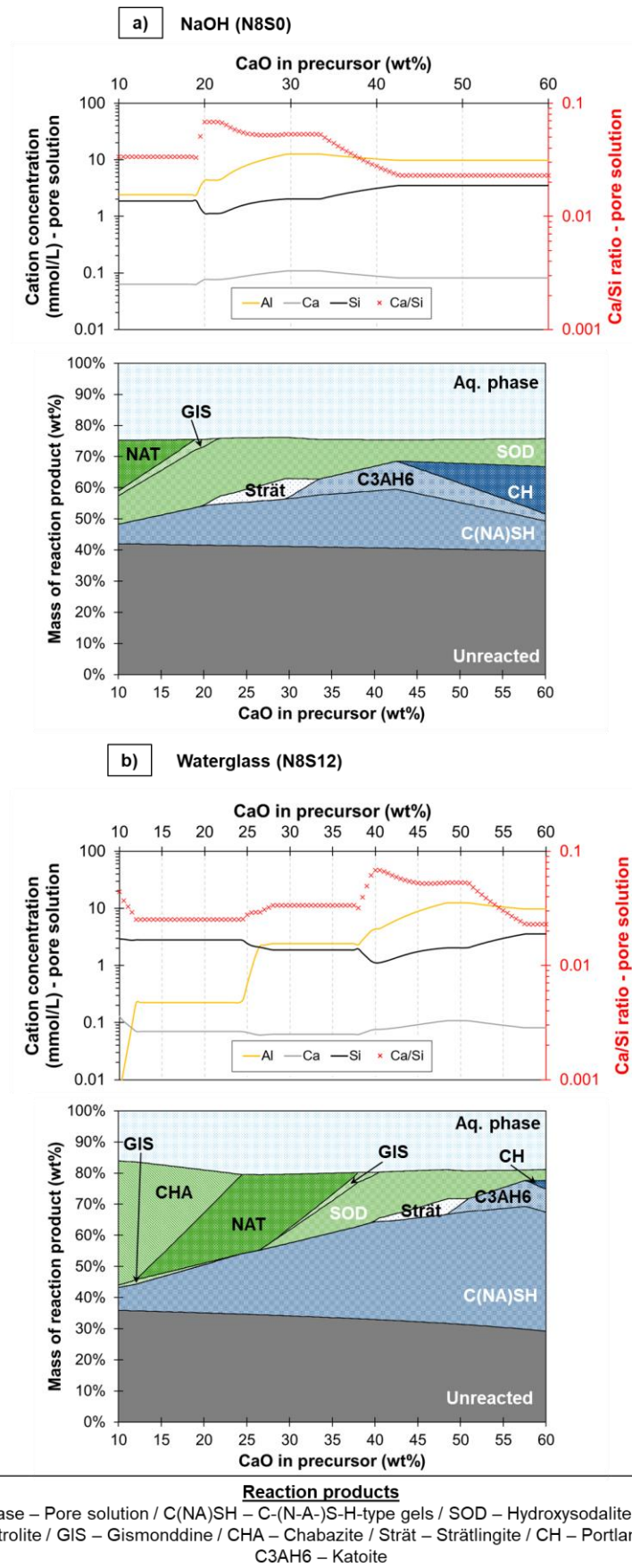


Figure 7.3: Influence of Ca content in simulated phase assemblage of glasses activated with: a) NaOH; and b) waterglass solutions.

With respect to reaction products that are Si-dominated, Figure 7.3 also shows that the presence of disordered N-A-S-H-type gels was limited by the formation of other more stable phases. Throughout the whole plot, five different zeolite phases were observed to be in equilibrium, which were also identified in the experiments described in Chapters 5 and 6 at early and later stages of reactions: natrolite (NAT), gismondine (GIS), hydroxysodalite (SOD) and chabazite (CHA). The plots indicate that, with both activators, an increasing CaO content significantly lowered the presence of zeolites in the final phase assemblage, but SOD was observed through the whole compositional range. This observation follows the results reported in Chapter 6, as pastes of alkali-activated slag-type glasses presented significantly higher amounts of Ca-based phases, whilst always displaying minor contents of N-(C-)A-S-H gels and zeolites as secondary reaction products.

The changes in the types of zeolites in equilibrium in the plots of Figure 7.3 followed a similar pattern in the two activating solutions. Natrolite ($\text{Na}_2\text{Al}_2\text{Si}_3\text{O}_{10} \cdot 2\text{H}_2\text{O}$) and hydroxysodalite ($\text{Na}_8\text{Al}_6\text{Si}_6\text{O}_{24}(\text{OH})_2 \cdot 2\text{H}_2\text{O}$), phases with Si/Al ratios of 1.5 and 1.0, respectively, were the main components in the lower CaO end of the charts in system N8S0 (Figure 7.3a). In system N8S12 (Figure 7.3b), a strong presence of chabazite ($\text{Na}_2\text{Al}_2\text{Si}_4\text{O}_{12} \cdot 6\text{H}_2\text{O}$ - Si/Al = 2.0) was higher in the lower CaO portion of the plot. These features are in line with experimental findings from Oh et al [496]: those authors have reported the co-existence of multiple zeolites from the ABC-6 family (which include both sodalites and chabazites) in the NaOH/waterglass activation of fly ashes, whilst the use of slags as precursors did not promote the formation of such structures. In any case, it is thus clear that the thermodynamic stability of zeolites is highly dependent on the Si content in solution. A moderate uptake of Ca in zeolite structures resembling N-A-S-H-type gels was observed by the formation of gismondine ($\text{Ca}_1\text{Al}_2\text{Si}_2\text{O}_8 \cdot 4.5\text{H}_2\text{O}$), which was present in the lower CaO portion of the plots. Lastly, the formation of Ca-Al phases is observed to become stable in a combined scenario of high-Ca and low-Si environments, as the formation of katoite has been delayed to CaO contents above 45 wt% in system N8S12.

Based on this discussion, the present thermodynamic models demonstrate that the type of activator has a great influence over the phase assemblage of hardened binders:

- In waterglass-activated systems, the excess of aqueous Si facilitates the binding of Ca with other elements, as indicated by the reduced presence of portlandite through the whole compositional range of the plots in Figure 7.3b. This favoured a stronger equilibrium of C-(N-A-)S-H gels at the expense of a reduction in the thermodynamic stability of zeolite phases, with the latter group displaying its minimum content at the maximum CaO content of the simulation;
- In NaOH-activated systems (Figure 7.3a), the lower overall concentrations of Si promoted the separate formation of C-S-H-type products, portlandite, and zeolites, which is observed by the absence of any unique highly-dominating phase in the whole CaO content range. This suggests the possibility for the formation of a less homogeneous microstructure, in agreement with the images obtained from scanning electron microscopy presented in Chapter 6 - see Section 6.3.1.

7.3.1.2 Thermodynamic stability of amorphous N-(C-)A-S-H gels and zeolites

In the simulated phase assemblage of alkali-activated low-Ca precursors, the results discussed in Section 7.3.1.1 demonstrated that zeolites display higher stability than disordered N-A-S-H-type gels. While this can be expected due to the structurally ordered characteristics of the former group, experimental observations often show a combined presence of the two groups in mature microstructures [398,409,497,498]. In order to compare the thermodynamic stabilities of the zeolites observed in Figure 7.3 versus N-A-S-H-type gels, effective saturation indices (ESI) of the two categories of reaction products were calculated for two scenarios: the waterglass-activation of synthetic glass Si-FA, which simulates a condition with high overall SiO_2 content from the binder (considering precursor and activator); and the NaOH-activation of synthetic glass BFS-2, simulating a condition with low overall SiO_2 content. With respect to the thermodynamic data of disordered N-(C-)A-S-H species, three gels with Si/Al ratios of 1.1 (NASH-1), 2.0 (NASH-2) and 2.8 (NASH-3) and two gels with Si/Al ratios of approx. 2.0 and Ca/Al ratios of 9.1 (NCASH-1) and 5.0 (NCASH-2) were considered - see Table C.2 in Appendix C for more details on thermodynamic data.

The plots shown in Figures 7.4a (waterglass - Si-FA) and 7.4b (NaOH - BFS-2) show similar patterns: zeolites and tectosilicates, with hydroxysodalite (SOD) as the main representative, were significantly more saturated in both scenarios (red lines). Moreover, it is easily noticed that the indices were higher in the simulated scenario of glass Si-FA (Figure 7.4a), reaching nearly 22.5, while they remained low at 6.6 for BFS-2 (Figure 7.4b). In addition to SOD, chabazite (CHA) and natrolite (NAT) presented similar values among them for the simulation of glass Si-FA, in agreement with the observations made in Figure 7.3. As the three phases have higher Si/Al within their compositions (2.0, 1.5 and 2.0, respectively), they are expected to be the main components in the lower CaO end of the simulation in a Si-rich environment with waterglass solutions.

Also in Figures 7.4a and 7.4b, the normalization of the calculated ESIs (black lines) to the molar content of SiO_2 of each phase, identified in the upper horizontal axis of the plots, provides interesting observations. Regarding N-A-S-H-type phases, the normalized saturation index of the gel with Si/Al ratio of 1.1 (NASH-1) remains in the same range as zeolites SOD and NAT, while an increasing Si/Al of the gels (NASH-2 and NASH-3) reduces their indices in the two studied systems. A similar behaviour is illustrated in Figure 7.4c for Ca-bound zeolites: despite showing a higher absolute saturation index, the normalized ESI of gismondine (GIS) is slightly lower than NCASH-1, a Ca-containing N-A-S-H-type gel. In this case, the normalization was made by considering the amount of Ca bound to 1 mol of SiO_2 in the structure of each phase. Additionally, the stability of Ca-containing zeolites and N-A-S-H-type gels is significantly reduced in the alkali-activation of glass BFS-2 (Figure 7.4d), as none of these two phases were visible at the high-Ca end of the plots from Figure 7.3.

A higher stability of zeolites, denoted by higher absolute ESIs, is somehow expected, as their crystalline structures tends to be more thermodynamically stable than amorphous arrangements [222,498,499], and many authors have used zeolite databases to represent the formation of N-A-S-H-type phases in low-Ca precursors [108,218,230]. However, despite the previous statement, the current results indicate that the accuracy of the database for disordered N-(C-)A-S-H gels developed in collaboration with Chen et al. [225,226] are in great agreement with the thermodynamic simulation for the precipitation of zeolites, as the

normalized ESIs of a few gel types were calculated to be close to or even more stable than most zeolite phases.

Following the previous observations, the alkali-activating reactions were simulated once more having hydroxysodalite (SOD) as the only allowed zeolite phase, along with N-(C-)A-S-H gels. Hydroxysodalite was maintained since it displays a higher Na-bound level in its structure than N-(C-)A-S-H-type species - $\text{Na}/\text{Al} = 1.33$ vs. $\text{Na}/\text{Al} \approx 1.0$, respectively. Figure 7.5 shows the evolution of phase assemblage according to the CaO content, in NaOH (7.5a) and waterglass (7.5b) solutions. In the two solutions, the formation of both N-A-S-H and N-(C-)A-S-H-type gels is more significant at lower CaO contents, representing a large portion of the phase assemblage in the composition range of glass Si-FA - highlighted by yellow dashed lines. In waterglass medium, the stability of the two groups is observed in higher CaO contents, up to approximately 35 wt%. Additionally, a reduction in the stability of the amorphous gels is compensated by the formation of SOD with both activators.

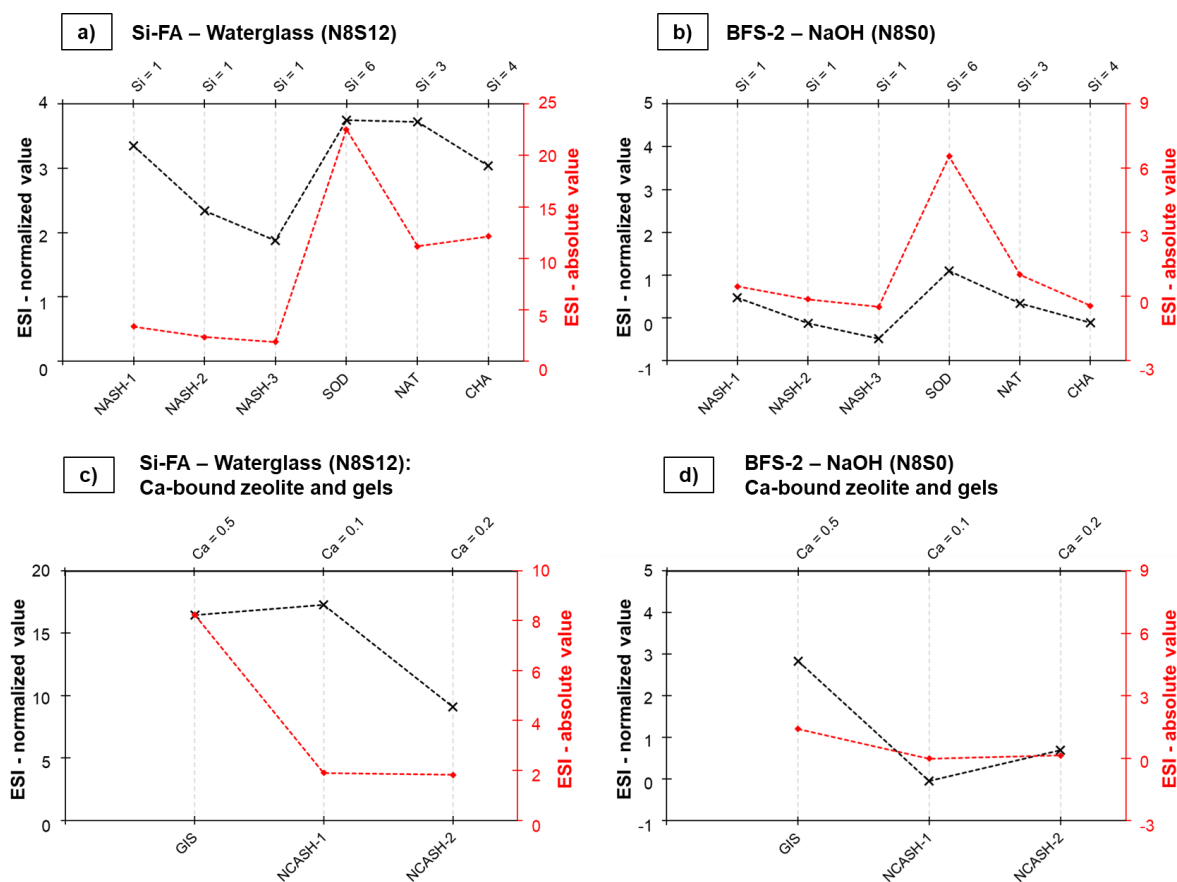


Figure 7.4: Absolute (red lines) and normalized (black lines) effective saturation indices of N-(C-)A-S-H gels and zeolite components in different systems considering: non-Ca bound zeolites for a) glass Si-FA activated with waterglass; and b) glass BFS-2 activated with NaOH; Ca-bound zeolites for c) Si-FA (waterglass); and d) BFS-2 (NaOH). ESI values were normalized with respect to the stoichiometry of Si (7.4a and 7.4b) or amount of bound Ca per mol of SiO_2 (7.4c and 7.4d) in each respective phase.

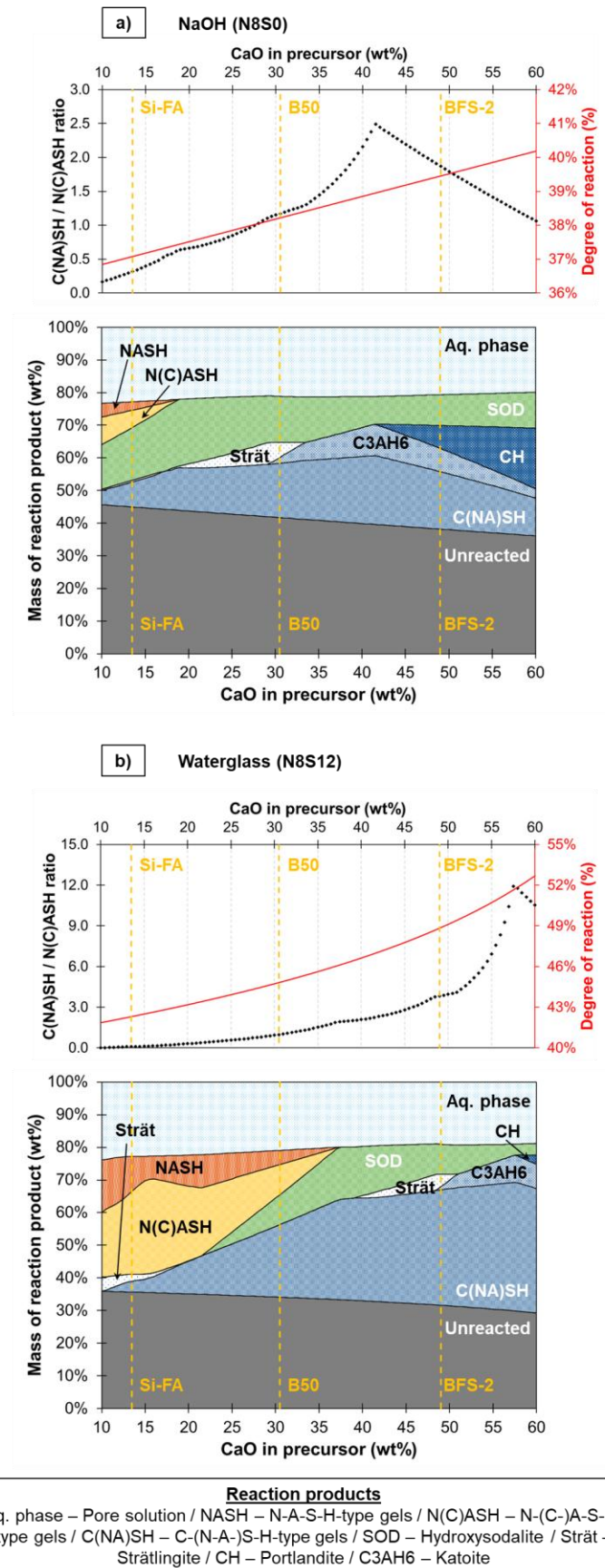


Figure 7.5: Influence of CaO in the phase assemblage of simulated systems, considering hydroxysodalite as the sole zeolite phase along with nanostructured hydrated gels: a) system activated with NaOH; b) system activated with waterglass.

Similarly to what is illustrated in Figure 7.3, at higher CaO dosages, the excess of Ca promotes the formation of crystalline secondary phases. The presence of strätlingite ($\text{Strät} = \text{Ca}_2\text{Al}_2\text{SiO}_7 \cdot 8\text{H}_2\text{O}$) and katoite (C_3AH_6) were observed up to a threshold content of CaO, suggesting an optimum window of precursor chemistry favouring the formation of secondary phases. Strätlingite has been reported to be more stable in low Si environments [500], which is in line with its presence within a narrower compositional range in the plots of system N8S12. Furthermore, Figure 7.5b indicated a transformation of strätlingite into katoite and sequentially to portlandite with increasing Ca content, in agreement with experimental findings that determined its incompatibility with the latter in high pH environments [387,501]. Above this threshold CaO content, which varied according to the activator, portlandite became the stable secondary phase due to the insufficient presence of Al and Si, in line with findings from Myers et al. [218]. For that reason, the calculated C(NA)SH/N(C)ASH ratios (which considers C-(N-A-)S-H phases in the upper term and both N-(C-)A-S-H and zeolites in the lower term) decreases after the same threshold.

While hydroxysodalite is the main stable Si-dominated component in high-Ca compositions, the two categories of reaction products were observed to co-exist in a few compositional scenarios. In the CaO content range of glass Si-FA, N-(C-)A-S-H gels represented a total of 34.1 wt% of all reaction products versus a total of 41.9 wt% for the zeolite phase. These values value represent the obtainment of a stable phase assemblage with equilibrated molar quantities of 0.02 M and 0.14 M for SOD and N-(C-)A-S-H gels, respectively, suggesting that an upper limit of formation of each phases can be considered to allow the concurrent formation of both products.

With respect to stability of different N-A-S-H type phases in the compositional range of glass Si-FA, the effect of aqueous silicate species arising from the activator promoted a shift in the most stable phases when compared to NaOH. As detailed in Table 7.2, N-A-S-H gels with Si/Al ratios of 1 and 2 were the main representative species in system N8S0, contributing to 7.0 and 3.6 wt% of all reaction products respectively, while the amount of the higher Si/Al gel NASH-3 significantly increased to become the most prominent phase in system N8S12. These results follow the observations of the higher stability of SOD observed in Figure 7.3: the zeolite phase represented a larger fraction of the phase assemblage at higher CaO contents in NaOH than in waterglass solutions, due to its low Si/Al ratio ($\text{Si}/\text{Al} = 1$).

Table 7.2: Contribution of each component of N-A-S-H and N-(C-)A-S-H gel groups in the simulated phase assemblage during the activation of glass Si-FA using different activators.

Phase	Si/Al	Ca/Si	NaOH (N8S0)	Waterglass (N8S12)
			wt% in phase assemblage	wt% in phase assemblage
NASH-1	1.00	-	7.0 %	0.1 %
NASH-2	2.00	-	3.6 %	6.9 %
NASH-3	2.78	-	0.8 %	18.7 %
N(C)ASH-1	2.00	0.11	5.2 %	24.1 %
N(C)ASH-2	2.17	0.20	8.6 %	23.1 %
N(C)ASH-3	3.12	0.08	0.3 %	1.3 %
N(C)ASH-4	2.78	0.15	8.9 %	12.9 %

Table 7.2 also indicates that, for both activators, the formation of gels with bound Ca was higher for Si/Al ratios close to 2.0 rather than 3.0, and this preference was enhanced in waterglass based systems - the summed contributions of N(C)ASH-1 and -2 to all reaction products was equal to 13.8 (NaOH) and 47.2 wt% (waterglass), while N(C)ASH-3 and -4 represented 8.9 (NaOH) and 14.2 wt% (waterglass). García-Lodeiro et al. [502] identified that, in synthetic N-A-S-H gels, Ca was observed to be incorporated into the disordered phases through an ion-exchange process with Na, whilst preserving the three-dimensional structure of the gels. Following the current results, it is proposed that Ca displays a preferential bonding in units with high Al content, as the amount of Al in tetrahedral coordination is directly correlated to the amount of bound Na ions for charge balancing of the structure. Moreover, gels with Ca/Si ratio equal or higher than 0.15 (N(C)ASH-2 and -4) represented 17.5 wt% (NaOH) and 36 wt% (waterglass) of the phase assemblages, addressing the facilitated uptake of Ca in aluminosilicate structures. These findings correspond with results presented in Chapter 5, as Ca-dominated and Ca-bound phases were observed to be formed earlier than N-A-S-H gels at 20 °C.

The plots shown in Figure 7.6 present a comparison between experimental (Exp.) and modelled (GEMs) amounts of each category of gel phases, considering their contributions to the total reaction products formed after 28 days of reaction - the modelled values consider binder compositions which are equivalent to the mixtures investigated in Chapter 6. In general, the simulated quantitative determination of C-(N-A-)S-H and N-(C-)A-S-H gels - displayed in red and black lines, respectively - presented a similar trend to the observations made with experimental values - see section 6.4.2 for more details. In both solutions, N-(C-)A-S-H gels, which comprise N-A-S-H, Ca-bound N-A-S-H, and zeolite phases, displayed a better agreement between the two sets of data. Modelled values tended to overestimate the formation of this category of phases, and the maximum difference between the simulated and experimental values was of 10.9 % (NaOH-activated BFS-1).

A larger variation was observed for the category of C-S-H-type gels, as thermodynamic modelling underestimated their precipitation. The major differences correspond to the larger contribution of Ca-bound secondary phases in NaOH-activated systems. As observed in Figure 7.5a, katoite, strätlingite and portlandite were constantly present in the phase assemblage of simulated systems, reaching a contribution as high as 48.6 wt% of the reaction products. This tendency, however, was reduced in system N8S12, suggesting that aqueous Si stabilizes the reactive system as a whole, reducing the formation of secondary crystalline phases.

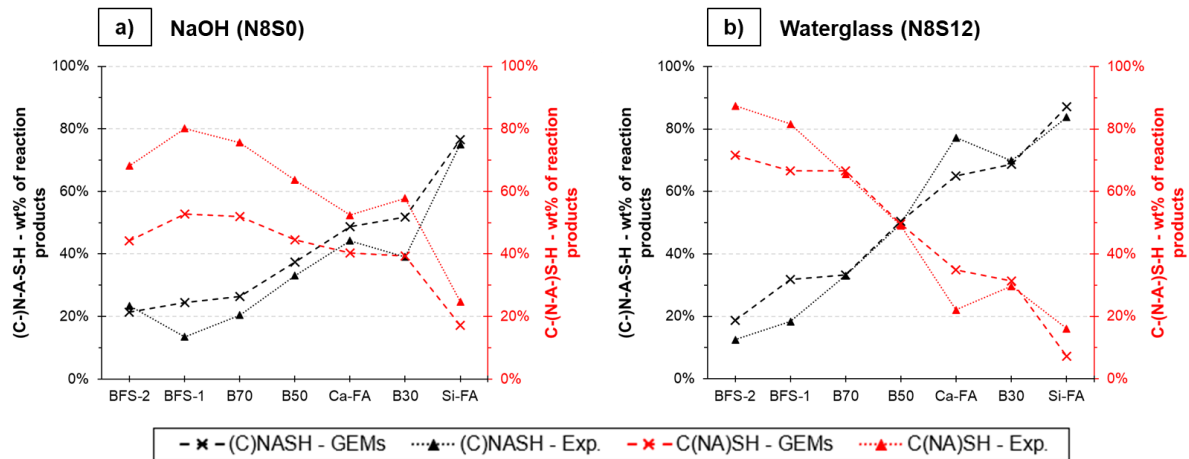


Figure 7.6: Modelled and experimental quantitative contribution of each group of reaction products to the overall phase assemblage: a) Systems activated with NaOH; b) systems activated with waterglass. The lines joining the data points are shown only as a guide to the eye.

7.3.1.3 Effect of curing temperature in thermodynamic equilibrium of alkali-activated binders

The effect of temperature was also evaluated in the simulated activation of glass Si-FA cured for 28 days. Figure 7.7 shows the evolution, in terms of the calculated phase assemblage, of the thermodynamic modelling of glass Si-FA activated with NaOH (Figure 7.7a) and waterglass (Figure 7.7b) solutions, cured at temperatures from 20 to 60 °C. In general, the simulated results displayed a similar trend to the experimental findings described in Chapter 6, with C-(N-A-)S-H gels becoming less stable at higher temperatures in both solutions, as Ca was shown not to be the main reaction-driver of fly ash-type systems at 60 °C - see section 4.3.3 for more details. This phenomenon facilitates the formation of crystalline structures with Ca uptake, observed by the enhanced stability of strätlingite at the expense of reduced C-(N-A-)S-H presence.

With respect to the formation of zeolites, simulations considering waterglass as activator (Figure 7.7b) did not show any stable formation of hydroxysodalite (SOD) at all temperatures, following the results obtained in the previous section which did not show any stable zeolite in the compositional range of glass Si-FA at 20 °C. However, in system N8S0, an interesting trend was observed. The simulated presence of N-(C-)A-S-H gels was increased following the rising temperatures, at the expense of a reduced formation of hydroxysodalite (SOD), while N-A-S-H gels did not demonstrate major differences at any simulated temperature. Two assumptions can explain this observation:

- the increased temperature induced a slightly higher degree of reaction, which shifted from 37.8 % (20 °C) to 42.0 % (60 °C). Consequently, a higher amount of Ca from the original precursor is released and available for the formation of reaction products. Similarly to the formation of crystalline secondary phases, Ca coupling to N-A-S-H structures was demonstrated to be thermodynamically favoured at higher temperatures;
- the reduction of the solubility product of hydroxysodalite, from 20 °C to 60 °C, was nearly two times greater than the reductions assumed for amorphous gels

(especially for gel N-C-A-S-H-2), the two main representatives of the non-crystalline products - see Table 7.2.

It is thus suggested that a rise in curing temperature represents an increasing stability of the nanostructure phases over the crystalline structure of SOD, reducing the contribution of the latter to the phase assemblage.

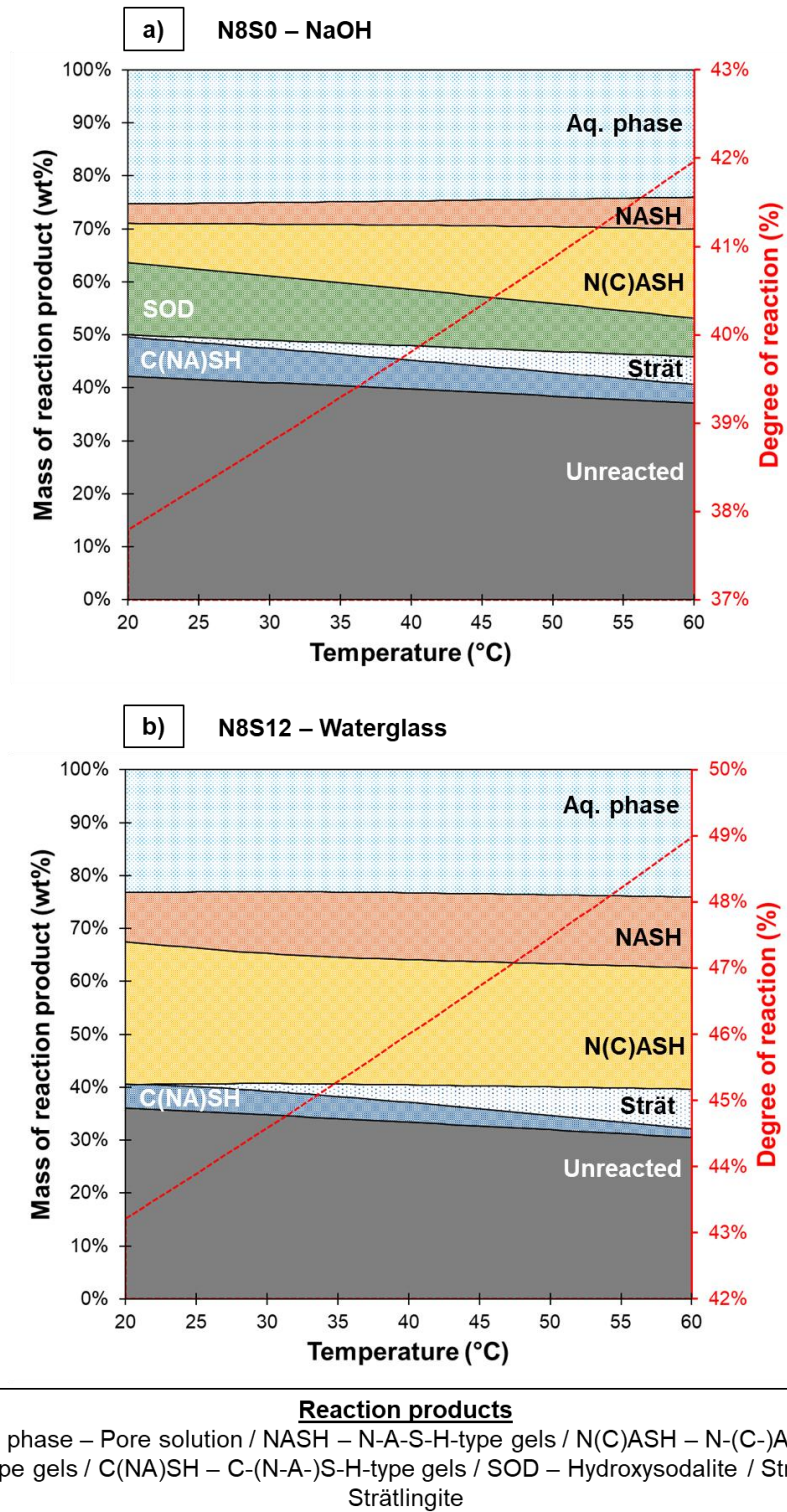


Figure 7.7: Influence of temperature on the modelled phase assemblage of glass Si-FA activated with: NaOH; and b) waterglass solutions.

7.3.2 Coupled thermodynamic and kinetic modelling

7.3.2.1 Numerical modelling of alkali-activated synthetic slag

As described in Section 7.2, the experimental findings of this thesis were implemented in the GeoMicro3D numerical modelling tool to extend its features. After the validation of the thermodynamic databases of zeolites and N-(C-)A-S-H-type gels, the alkali-activation of precursors resembling slag-type and fly ash-type glasses were simulated, aiming the evaluation of the accuracy of the updated tool.

The numerical modelling of the activation of glass BFS-2, in an NaOH medium, was simulated for a digital period of 28 days, and the outcomes of the first 24 h of reaction are observed in Figure 7.8. The plots and the visualization of the microstructure indicate a correlation between the pore solution and initial phase precipitation (Figure 7.8a). Ca is the first element to be detached from the framework of the precursor shortly followed by Si, while Al displays a slower release rate in initial stages - it is worth noting that the initial Al_2O_3 content of glass BFS-2 is relatively low, with Si/Al and Ca/Al molar ratios of 1.75 and 2.57, respectively. The evolution in the concentrations of Ca and Si presents a small step after approximately 10 minutes, indicating the beginning of the precipitation of C-(N-A-)S-H gels. Sequentially, the formation of portlandite (CH) during the first hour of reaction reduces the rate of release of Ca compared to Si. Finally, a significant drop in the presence of the three elements in the pore solution is observed at approx. 6 hours, which promotes a significant secondary precipitation of both portlandite and Ca-based gels and the beginning of the formation of hydroxysodalite (SOD). This last observation suggests that the reaction has entered its acceleration stage after the initial wetting and dissolution period, promoting a rapid increase in the amount of different reaction products.

The formation of portlandite, which was also observed in early stages in experimental conditions - see Chapters 4 and 5 - is expected in these periods in such alkaline environments while the system has insufficient amounts of other elements in solution [79,205,228]. Figure 7.8b provides a visual and clear evidence of the precipitation of portlandite in early stages. The digital microstructure illustrates the distribution of portlandite at the surface of the precursor particles since the first hour of reaction, indicating its potential role of an intermediate activated complex in alkali-activated systems - see section 4.3.1 for more details. The initially surface-anchored portlandite nuclei were observed to grow and form coarser reaction rims surrounding the precursor particles, and the total volume occupancy of the phase achieved 2.3 % after 24 hours of reaction.

Table 7.2: Solubility products of hydroxysodalite and nanostructured gels, according to temperature, normalized to the molar content of SiO_2 .

Component	$\log K_{sp}$ (20 °C)	$\log K_{sp}$ (60 °C)	Difference (20 °C - 60 °C)	Ref.
N-A-S-H 1 $(Na_2O)_{0.49} \cdot (Al_2O_3)_{0.46} \cdot (SiO_2)_1 \cdot (H_2O)_{0.48}$	-8.93	-7.86	1.07	[225]
N-C-A-S-H-2 $(Na_2O)_{0.23} \cdot (CaO)_{0.2} \cdot (Al_2O_3)_{0.23} \cdot (SiO_2)_1 \cdot (H_2O)_{0.4}$	-8.61	-7.88	0.73	Yun et al.
Hydroxysodalite (SOD) $(Na_2O)_4 \cdot (Al_2O_3)_3 \cdot (SiO_2)_6 \cdot (H_2O)_3$	-11.22	-9.83	1.39	[207]

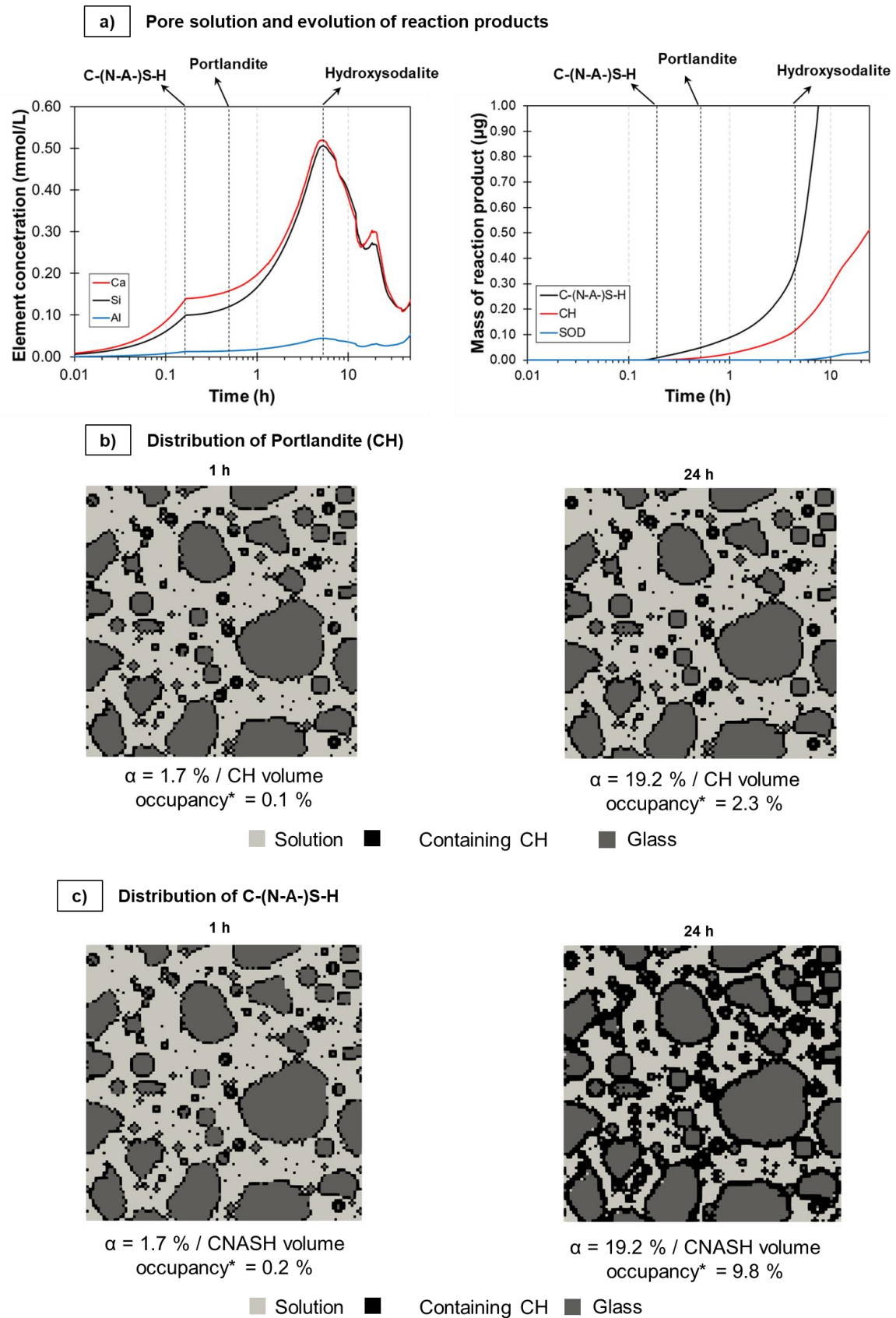


Figure 7.8: Simulation of the first 24 hours of reaction of alkali-activated glass BFS-2: a) correlation between pore solution and phase precipitation; b) distribution of portlandite after 1 and 24 hours; c) distribution of C-(N-A)-S-H gels after 1h and 24 h. *Volume occupancy indicates the contribution of each product to the total volume of the simulation box.

In combination with portlandite, the precipitation of C-(N-A)-S-H gels was also observed at very early stages of the reaction, while as significant presence of hydroxysodalite (SOD) was observed only after approx. 8 hours. As observed in the digital microstructures displayed in Figure 7.8c, Ca-rich gels were present in the same voxels as portlandite at 1 hour with slightly higher volume occupancy, consolidating the concurrent formation of both phases. With the course of reaction, the disordered gels quickly became the dominant phase of the microstructure, occupying a total volume of 9.8 % of the whole simulation box after 24 h. Consequently, it is possible to observe a significant change in voxels containing disordered gels, which were observed to connect two or more particles of precursor after the first day of simulated reaction.

The evolution of the reaction of the simulated system is shown in Figure 7.9a. As the simulation tool calculates the thermodynamic equilibrium of reaction products considering only unreacted species, the portlandite nuclei formed in the first moments of reaction (see Figure 7.8b) occupies a major volume of the final microstructure, in agreement with the simulations performed by Zuo and Ye [59]. However, it is observed that its quantity becomes quickly stable after the first two days of reaction, indicating that other phases are more thermodynamically favourable to be precipitated at later stages. In combination with Ca-based gels, the formation of hydroxysodalite was observed to occur since the first day but at a slower rate, representing approximately 12.1 % of the total volume after 28 days. Additionally, a small quantity of katoite as a secondary phase was formed after approx. 3 days of reaction. At later stages, these two components can be expected to become stable by the exhaustion of Si in the pore solution, consumed for the precipitation of zeolite phases.

Additional conclusions can be drawn from the digital microstructures shown in Figure 7.9b. While the quantity of solution voxels does not present major changes from 7 to 28 days, most of nodes filled with reaction products change from reaction front to partially filled voxels, and from partially filled voxels to fully filled voxels, indicating the continuous evolution of the reaction kinetics. In combination with the evolution of the degree of reaction of approx. 10 % between the two ages, the nucleation and growth of reaction products promoted a reduction in the overall porosity of the simulation box from 33.0 % to 29.3 %.

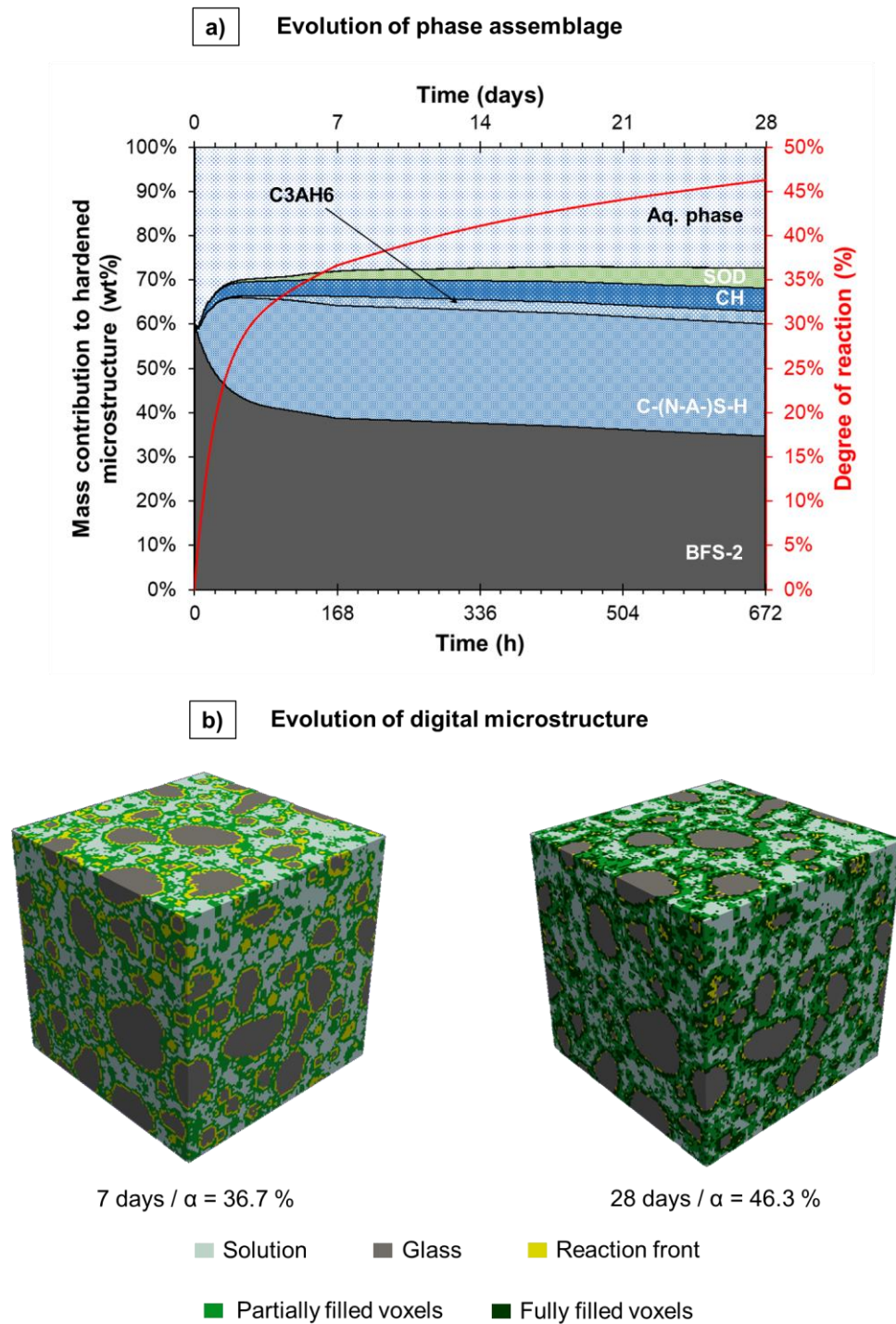


Figure 7.9: Evolution of the simulated alkali-activation of glass BFS-2 up to 28 days: a) phase assemblage; and b) digital microstructure.

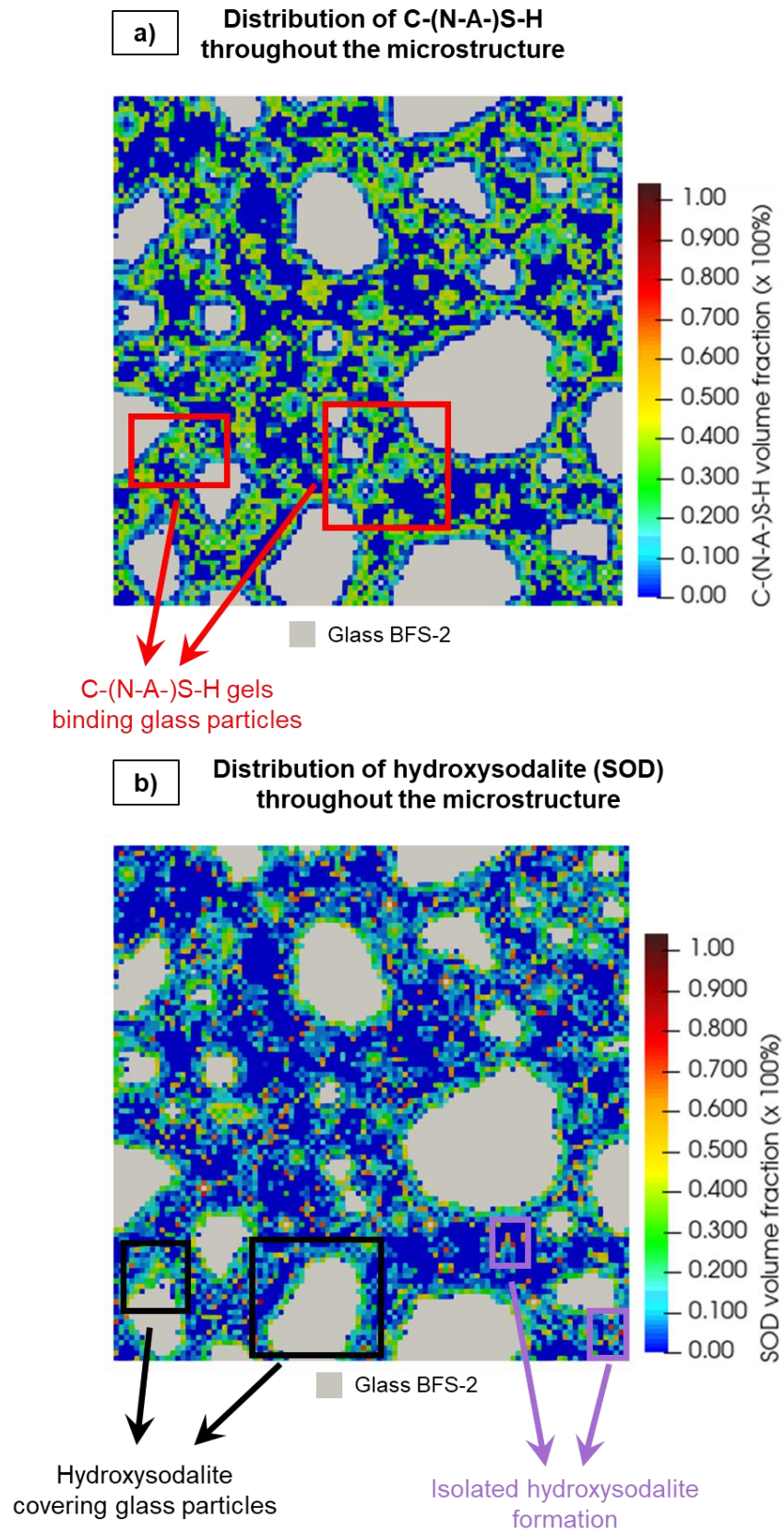


Figure 7.10: Distribution of reaction products within the simulated microstructure of alkali-activated BFS-2: a) C-(N-A-)S-H gels; and b) hydroxysodalite.

The distribution of C-(N-A)-S-H gels and hydroxysodalite throughout the digital microstructure is illustrated in Figure 7.10. The Ca-based gels (Figure 7.10a) are homogeneously distributed throughout the matrix and show large volume occupancy, as most of the voxels containing the category of reaction products present a volume fraction in the range of 0.3-0.5 - green and yellow colors. A strong presence of these gels is observed both at the surface of glass particles and in the bulk microstructure, as they appeared to create bridges between two or more particles of the precursor - highlighted in red frames. On the other hand, hydroxysodalite presents a less evenly distribution within the matrix (Figure 7.10b). In agreement with the findings from White et al. [199] for NaOH-activated slag, the presence of the zeolite phase is strongly observed as a thin rim-type phase covering the glass particles - see black frames in Figure 7.10b. Nonetheless, it is possible to observe a few isolated red-like spots throughout the bulk microstructure, indicating the presence of a few voxels nearly fully filled with the zeolite - highlighted in purple frames. This suggests a more significant formation of zeolites (or N-A-S-H gels) at later stages, acting as pore filling agents and reducing the overall porosity of the system, following experimental observations [106,503].

7.3.2.2 Numerical modelling of alkali-activated synthetic fly ash

Curing regimen - 20 °C:

The evaluation of the extended GeoMicro3D tool continued with the numerical modelling of the alkali-activation of glass Si-FA in NaOH, simulating the microstructural evolution for 28 days at 20 °C. In comparison with the activation of glass BFS-2 described in the previous section, one constraint was included into the Si-FA system: the simulation considered an upper thermodynamic stability limit of formation of hydroxysodalite, following the results shown in Section 7.3.2.1. The previously determined value of 0.36 mmol/cm³ was implemented considering the total volume of the simulation box in GeoMicro3D, which allows a concurrent formation of the zeolite phase and disordered N-(C-)A-S-H-type gels.

As shown in the plots in Figure 7.11, the obtained results indicated slower reaction kinetics when compared to the reaction of glass BFS-2 - see Figure 7.8. Following the findings from Chapter 4, a slow dissolution rate in fly ash-like glasses was expected, which is confirmed by the low concentrations of elements in pore solution obtained in the first 48 h of simulation (Figure 7.11a) - the maximum concentration of Si achieved in the first moments of reaction was 2.2 times higher in the pore solution of the alkali-activation of glass BFS-2. The initial phase precipitation occurred after approximately 2 h of reaction by the formation of portlandite, following a mild drop in Ca concentration.

The plots in Figure 7.11a show similarities with experimental observations: portlandite (CH) is the first product to be stabilized in the system after 1 h of reaction, and primary reaction products only became the dominant phases in the microstructure after 20 h, with the concurrent formation and growth of hydroxysodalite, at first, and C-(N-A)-S-H-type gels, sequentially. Despite being quickly precipitated, Figure 7.11b shows that portlandite does not present a significant evolution in the microstructure. Following a similar pattern to the observations made in the simulation of slag-type glass (Figure 7.7b), the presence of CH was limited to a surface-anchored product, as its contribution to the total amount of reaction products reduced by half from 10 to 48 hours.

With respect to primary reaction products, C-(N-A-)S-H-type gels are expected to be more stable in early reaction stages of low-Ca precursors, precipitating mostly at the expense of portlandite consumption once Si and Al ions are sufficiently available. However, as the thermodynamic equilibrium module of GeoMicro3D considers only non-reacted ions in solution for phase precipitation (due to optimization of computation efficiency) and disregards re-dissolution of solid components, it was observed that the formation of the zeolite phase was accelerated due to the lack of Ca ions in the pore solution - which were previously consumed for the formation of CH. Hydroxysodalite and C-(N-A-)S-H gels were initially precipitated as small nuclei anchored at the surface of glass particles. Figure 7.11c indicates that, despite representing 41.8 vol% of the reaction products at 10 hours, the number of voxels containing hydroxysodalite is more limited when compared to the distribution of CH. This observation is in agreement with other results reported in literature [202], as N-A-S-H-type gels are mostly concentrated at the edges of the particles of the precursor in early-stages of NaOH-activated fly ashes. In the same period, the contribution of Ca-based gels to the phase assemblage was significantly limited, as shown in Figure 7.11d.

While both hydroxysodalite and C-(N-A-)S-H gels had limited formation up to 10 hours, they represented approx. 60 vol% of all reaction products at 48 hours. This resulted in the formation of a thicker layer surrounding glass particles compared to the distribution of portlandite, indicating the connection between the two or more particles of precursors. However, a few voxels are observed to be empty in Figures 7.11c and 7.11d with respect to the presence of the two phases - see red dashed frames. As Figure 7.11b shows the presence of portlandite in these same voxels, this observation is an indication of the obtainment of a porous microstructure in the fly ash-type glass, following the results shown in Chapter 6 for the NaOH activation of glasses Si-FA and Ca-FA - see Figure 6.8.

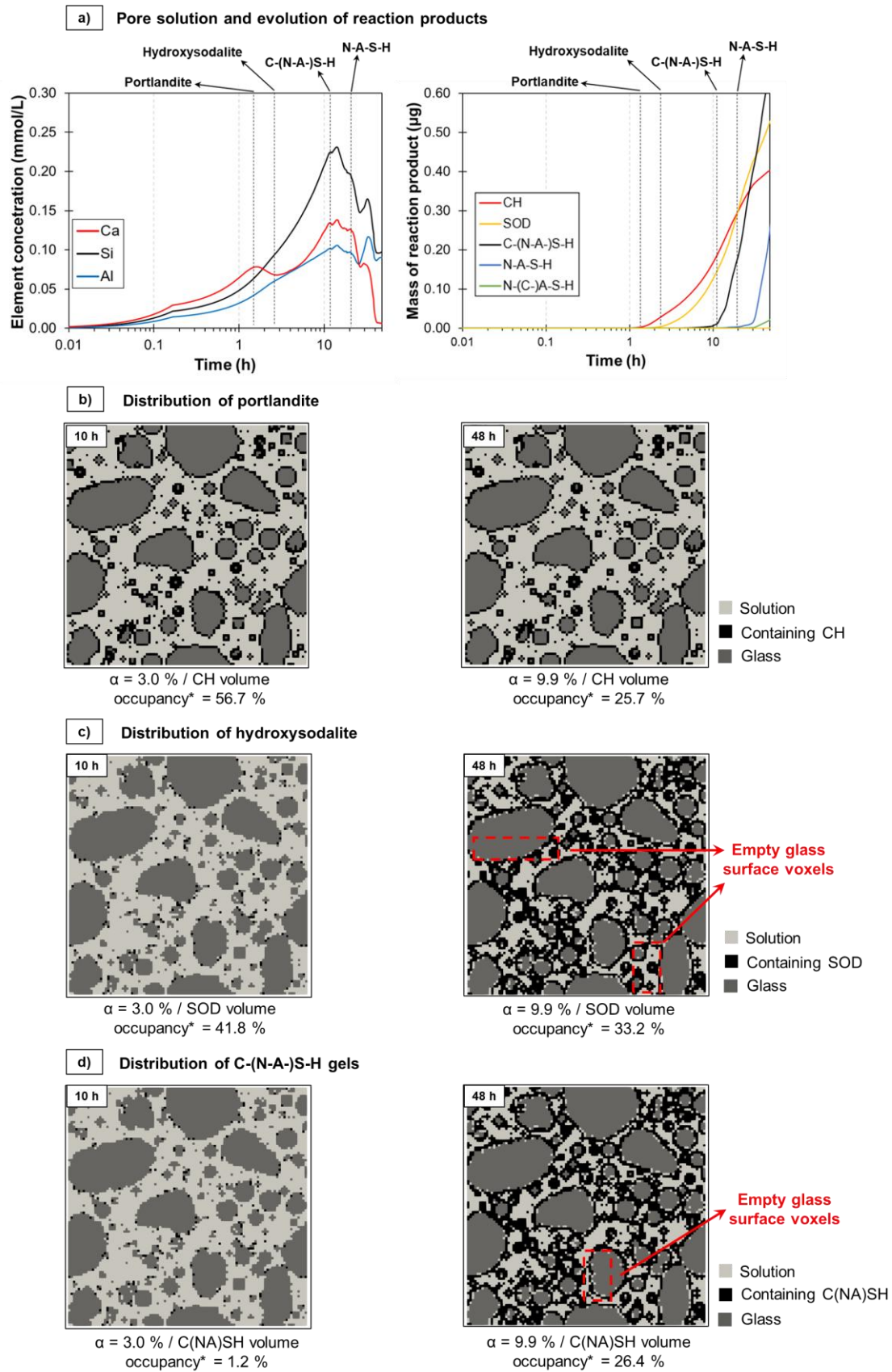


Figure 7.11: Characteristics of the first 48 hours of simulated alkali-activated of glass Si-FA: a) correlation between pore solution and precipitation of reaction products; b) evolution of the distribution of portlandite; and c) evolution of the distribution of N-A-S-H gels. *Volume occupancy indicates the contribution of each product to the total volume of reaction products.

An additional interesting feature of the simulation is observed by the distribution of hydroxysodalite and N-A-S-H-type gels throughout the microstructure. The slices of the microstructures show in Figure 7.12 show the evolution in the occupancy of the two phases from 7 to 28 days in the simulation box. Hydroxysodalite is observed to remain as a surface anchored product (Figure 7.12a), with negligible evolution until the end of the simulation. On the other hand, the presence of N-A-S-H-type gels displayed a significant evolution in the evaluated period (Figure 7.12b). The gel species were homogeneously distributed throughout the simulation box, occupying nearly all voxels in the bulk matrix (Figure 7.12b). This observation emphasizes the slow kinetics of reaction of low-Ca precursors, and is in agreement with literature findings: Walkley et al. [212] reported that, during the alkali activation of synthetic fly ashes, the formation of a mature microstructure can take more than 7 days in NaOH-activated systems. It is important to state that this observation can be, to some extent, a consequence of the establishment of an upper thermodynamic limit of formation of the zeolite phase - additional research would be required to provide extra insights into the combined thermodynamic-kinetics of evolution of disordered gels and crystalline structures.

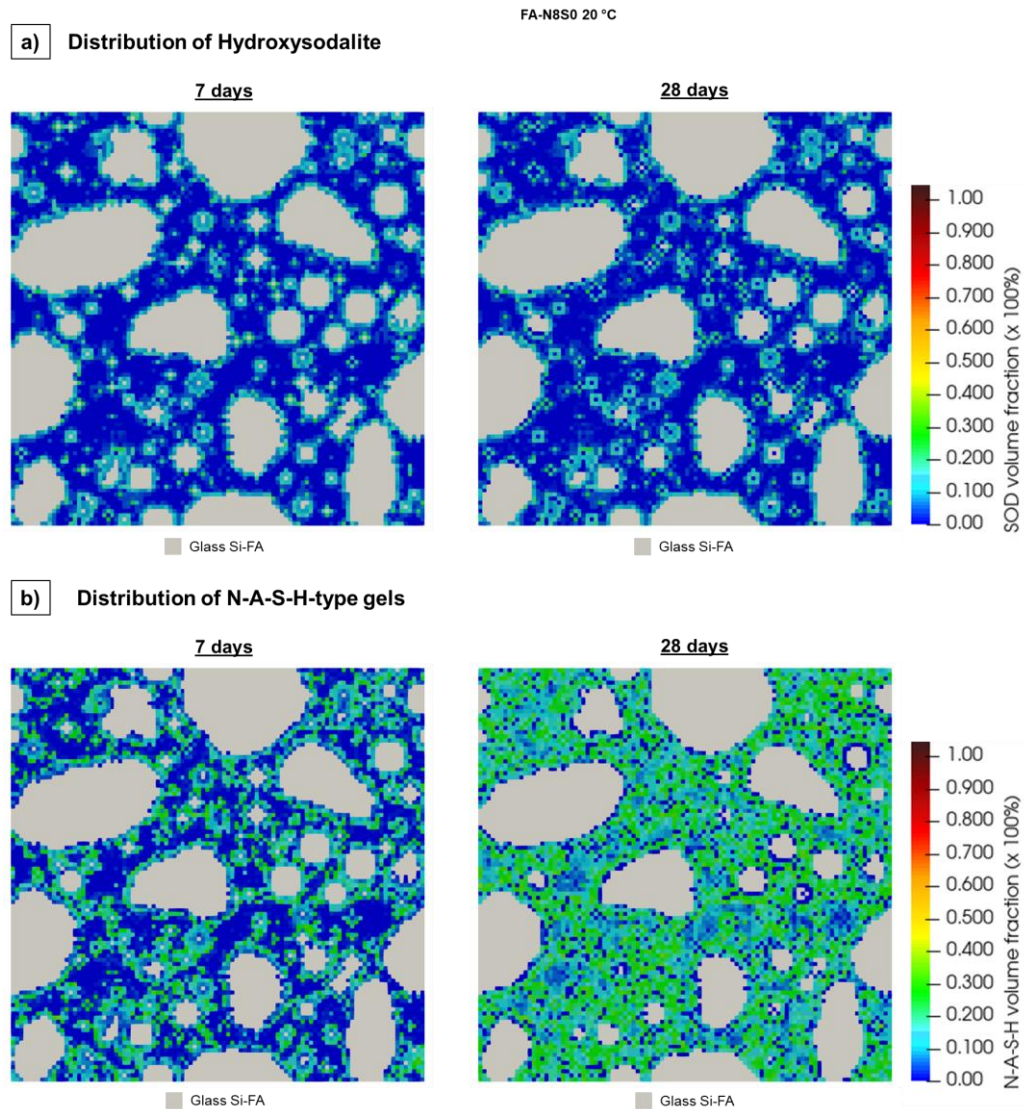


Figure 7.12: Evolution of the distribution of reaction products in the simulated alkali-activation of glass Si-FA at 7 and 28 days: a) hydroxysodalite (SOD); and b) N-A-S-H-type gels.

Curing regimen - 60 °C and 20 °C:

The implementation of a curing temperature regime of 60 °C for the first 7 days of reaction, and at 20 °C for the remainder of the simulation, promoted a significant acceleration of the kinetics of reaction, as seen in Figure 7.13. The precipitation of primary reaction products initiates in the first minutes of reaction, with the precipitation of N-A-S-H gels shortly followed by the initial formations of hydroxysodalite and N-(C-)A-S-H gels (Figures 7.13a and 7.13b), promoting a mild reduction in the concentrations of Si and Al. The release of Si from the precursor to the pore solution continues to evolve until approx. 1 hour, while Al remains at a more constant concentration during the first 24 hours of reaction. The observed drops in concentration of the two elements coincided with the more significant formation of C-(N-A-)S-H species at first, and sequentially with the precipitation of strätlingite.

With respect to the early evolution of the reaction, the simulated system accurately replicated the trends in the reaction kinetics of experimentally observed in Chapter 6. The in-situ calorimetry curve of NaOH-activated glass Si-FA, shown in Figure 7.13c, shows two individual peaks: the first, assigned to the precursor wetting and dissolution, occurs due to accelerated Si and Al releases, leading to immediate formation of N-(C-)A-S-H-type gels and hydroxysodalite which contribute to the intensity of the exothermic response. The second peak, assigned to an acceleration period, is promoted by an additional release of Si and Al coupled with Ca dissolution, leading to a significant formation of other Ca-bound phases.

An additional observation can be addressed with respect to the behaviour of Ca. Following the experimental observations made in Chapters 4 and 5, the release of Ca is known to be limited at 60 °C due to changes in the dissolution mechanisms - hydrolysis of Si-O and Al-O bonds have a more significant impact in the dissolution than the release of Ca^{2+} through cation exchange, as detailed in Section 5.4.1. The plot in Figure 7.13a indicates that the concentration of Ca in the pore solution was maintained at levels approximately 10x lower than Si and Al. This is suggested to occur through a combination of two factors: the delayed release of Ca with the local temperature, and the quick consumption of Si and Al for precipitation of reaction products. Due to the quick evolution in the reaction degree at 60 °C (reaching 16.8 % at 1 hour), the latter effect lowers the saturation indices of N-(C-A-)S-H gels and hydroxysodalite, promoting a continuous formation of these phases at very early stages, as shown through the evolution of reaction products displayed in Figure 7.13b. The microstructure slice in Figure 7.13d shows all particles of the precursor surrounded with partially filled voxels creating thick rims, which act as a diffusion barrier for the release of Ca to the solution. As a result, the formation of both primary and secondary Ca-dominated phases was delayed to later stages in the current simulation.

Influence of temperature in phase assemblage and microstructure:

The effect of the curing regimes on the phase assemblage are clearly observed in Figure 7.14, and the plots in logarithmic time scales facilitate this observation. When the system is cured at 20 °C for the whole period (Figure 7.14a), modifications are only visible after 10 hours of reaction. Portlandite, C-(N-A-)S-H gels and hydroxysodalite are observed to be part of the phase assemblage in earlier periods, while N-A-S-H gels become the main reaction product after approx. 72 hours. The implementation of higher temperature curing (Figure 7.14b) significantly accelerated this effect, with hydroxysodalite and N-A-S-H gels quickly representing the main portion of reaction products after less than 1 h of reaction.

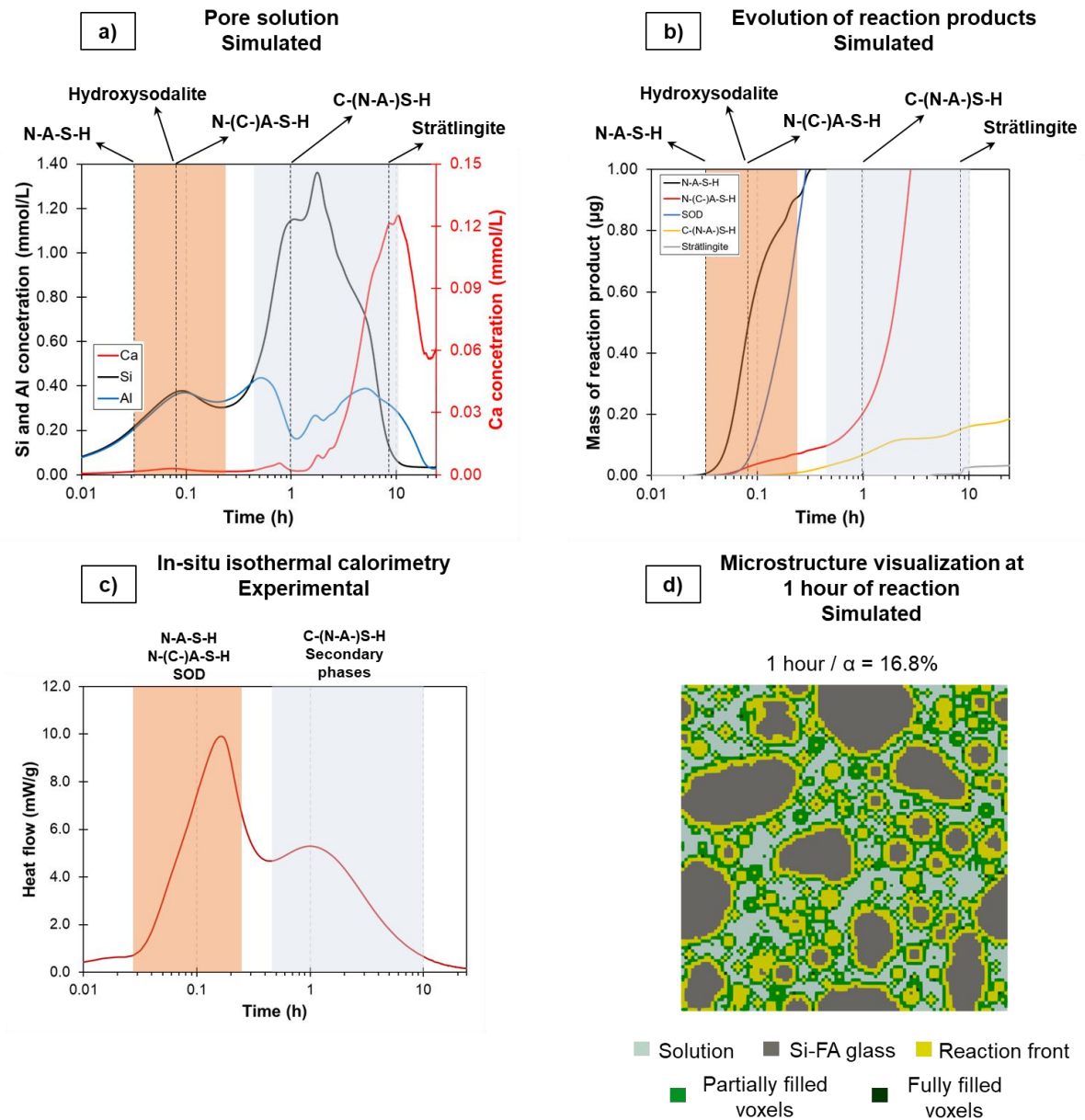


Figure 7.13: Characteristics of the first 24 hours of simulated alkali-activation of glass Si-FA, cured at 60 °C: a) correlation between pore solution and phase precipitation; b) comparison with experimental isothermal calorimetry; and c) visualization of the simulated microstructure.

Interestingly, it is noticed that the degree of reaction evolves in three steps at 60 °C: in the first hour of reaction, both hydroxysodalite and N-A-S-H-type gels are stabilized and account for the vast majority of the phase assemblage; the second stage is represented by the growth and the stabilization of N-A-S-H and N-(C-)A-S-H gels, respectively, from 1 to 10 hours, indicating that the zeolite phase has reached its upper thermodynamic stability limit of formation; finally, the third period comprises the formation of Ca-dominated phases, such as C-(N-A-)S-H gels and secondary crystalline phases - strätlingite, katoite, and portlandite, until a stagnation of the reaction kinetics is reached after approx. 100 hours. This observation follows the findings from [228], who used Fourier transform infrared spectroscopy to conclude that C-S-H-type gels could be formed as a secondary reaction product during the activation of low-Ca fly ashes. The late formation of Ca-dominated phases occurs after the exhaustion of aqueous Si and Al species, following the evolution of

the pore solution shown in Figure 7.13a. In the extended version of GeoMicro3D, this feature is enhanced at higher curing temperatures due to the differences in the mechanism of Ca release from the precursor at 60 °C [405], which ultimately hinder the early formation of C-S-H-type gels and other Ca-bearing crystalline phases.

In the two curing regimes, the formation of N-(C-)A-S-H over N-A-S-H gels and hydroxysodalite is limited, following a different pattern observed in thermodynamic modelling - see Section 7.3.2.1 for more details. In the system cured at 20 °C, this was caused by the previous consumption of Ca for the formation of secondary phases and C-(N-A-)S-H gels. The depleted presence of Ca in the pore solution lowers the saturation indices of Ca-bound N-A-S-H species, favouring the formation of zeolite-type phases and pure N-A-S-H gels. Conversely, the lower incorporation of Ca in N-A-S-H gels at 60 °C cannot be explained by the formation of other Ca-bearing phases, which had a significant precipitation only in the third acceleration stage of the reaction. In general, the concentration of Ca in the pore solution was maintained low in the initial moments and increased after approx. 10 hours of reaction. At that point, N-A-S-H and SOD had already been stabilized and represented the majority of the microstructure, consuming a large amount of aqueous Si and Al species previously available. Moreover, the precipitation of N-(C-)A-S-H gels competed with other crystalline secondary phases, which could represent a further limitation in the precipitation of the disordered species. It is thus concluded that the influence of the kinetic and thermodynamic parameters of nucleation of all N-(C-)A-S-H-type gels deserve more attention, and future works could cover this gap in the modelling of alkali-activated materials.

The influence of temperature is also observed in the slices taken from the simulated microstructure shown in Figure 7.15, after 28 days of reaction. Since the two modelled situations used the same input box, the comparison between the two curing regimes is facilitated. In Figure 7.15b, the presence of solution nodes and nodes fully filled with reaction products is noticeably lower. In Figure 7.15b, the particles located inside the red dashed frame present a larger area of nodes belonging to the category of the dissolution front, which represents a combination of dissolving precursor with rim reaction products. This reflects a combination of the second acceleration period and a higher overall degree of reaction promoted by temperature, which is nearly 7 % for the model initially cured at 60 °C. Consequently, the porosities of the boxes decrease from 30.2 %, for the reaction taking place at 20 °C, to 14.1 %, for the second curing regime, in consistency with experimental findings [175,398,409,504].

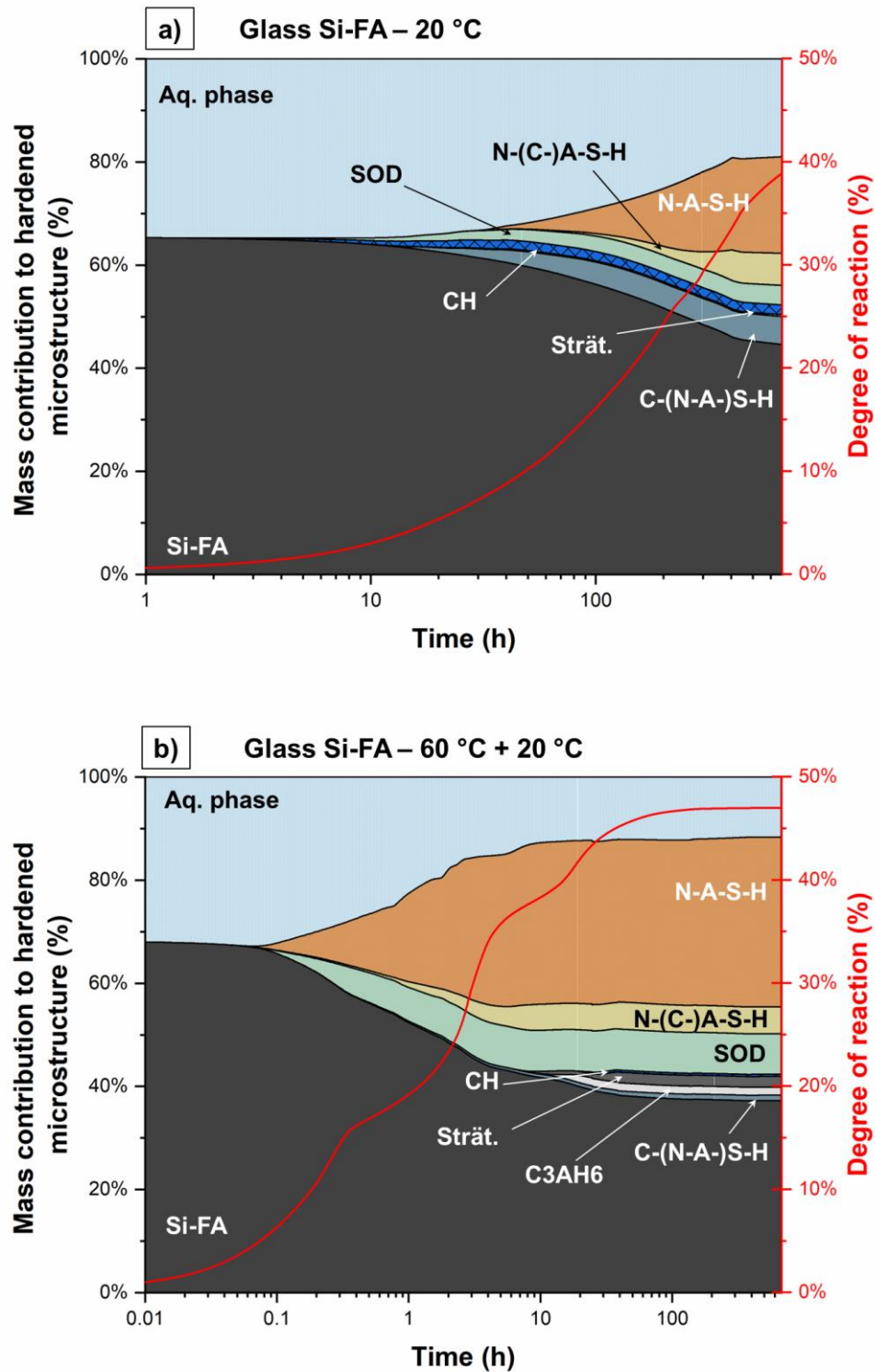


Figure 7.14: Evolution of phase assemblage of the simulated alkali-activation of glass Si-FA: a) curing at 20 °C for 28 days; b) curing at 60 °C for 7 days, and 20 °C for the remaining 21 days.

7.3.2.3 Simulated alkali-activated blended systems

In sequence, the simulated alkali-activation of system B50, which consists of a mixture of glasses Si-FA and BFS-2 in a 1:1 proportion, was performed in NaOH media at 20 °C for 28 days. Figure 7.16 shows the evolution of the phase assemblage and reaction degree up to 28 days for the two individual components in the blend. Following the previous simulations made with individual precursors, portlandite was the first phase to be formed, achieving stability after approximately 2 days of reaction since minor changes were observed in its amounts after this period. After 28 days, the phase assemblage presented a balanced proportion of C-(N-A)-S-H gels and hydroxysodalite. The former category represented the main contribution to the microstructure among all formed phases, accounting for 51.6 % of all reaction products, while the latter, which mimics the precipitation of N-A-S-H gels, contributed to 30.2 %.

The formation of hydroxysodalite was observed to occur at a slower rate. In general, at 20 °C, the precipitation of phases which do not contain Ca is delayed to secondary stages, as observed in previous models and experiments - see Section 5.4.2 for more details. In the present simulation, this feature is enhanced by the slower reaction kinetics of glass Si-FA, which dissolves at a slower rate and reaches a plateau of the reaction degree earlier than glass BFS-2. The delayed formation of the zeolite phase is in line with literature, as different authors reported a dominance of C-S-H-type gels in the microstructure of slag:fly ash blends at different slag proportions [228,348,419,444,463] - for instance, Ismail et al. [228] reported that N-A-S-H-type gels became the main reaction product only when the amount of fly ash was higher than 75 % in blends with slag. Consequently, the reaction degree of the high-Ca component BFS-2 is nearly 20 % higher than low-Ca component Si-FA after 28 days.

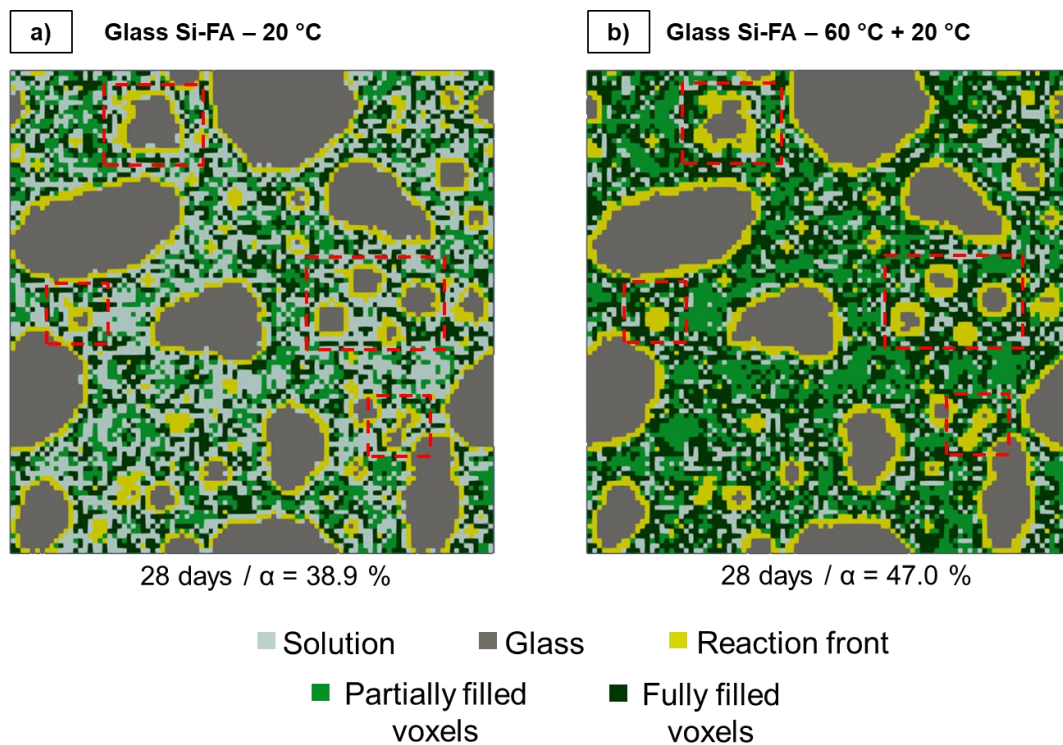


Figure 7.15: Final simulated microstructure obtained from the simulation box of the simulated alkali-activation of glass Si-FA: a) curing at 60 °C for 7 days and 20 °C for the remaining 21 days; b) curing at 20 °C for 28 days.

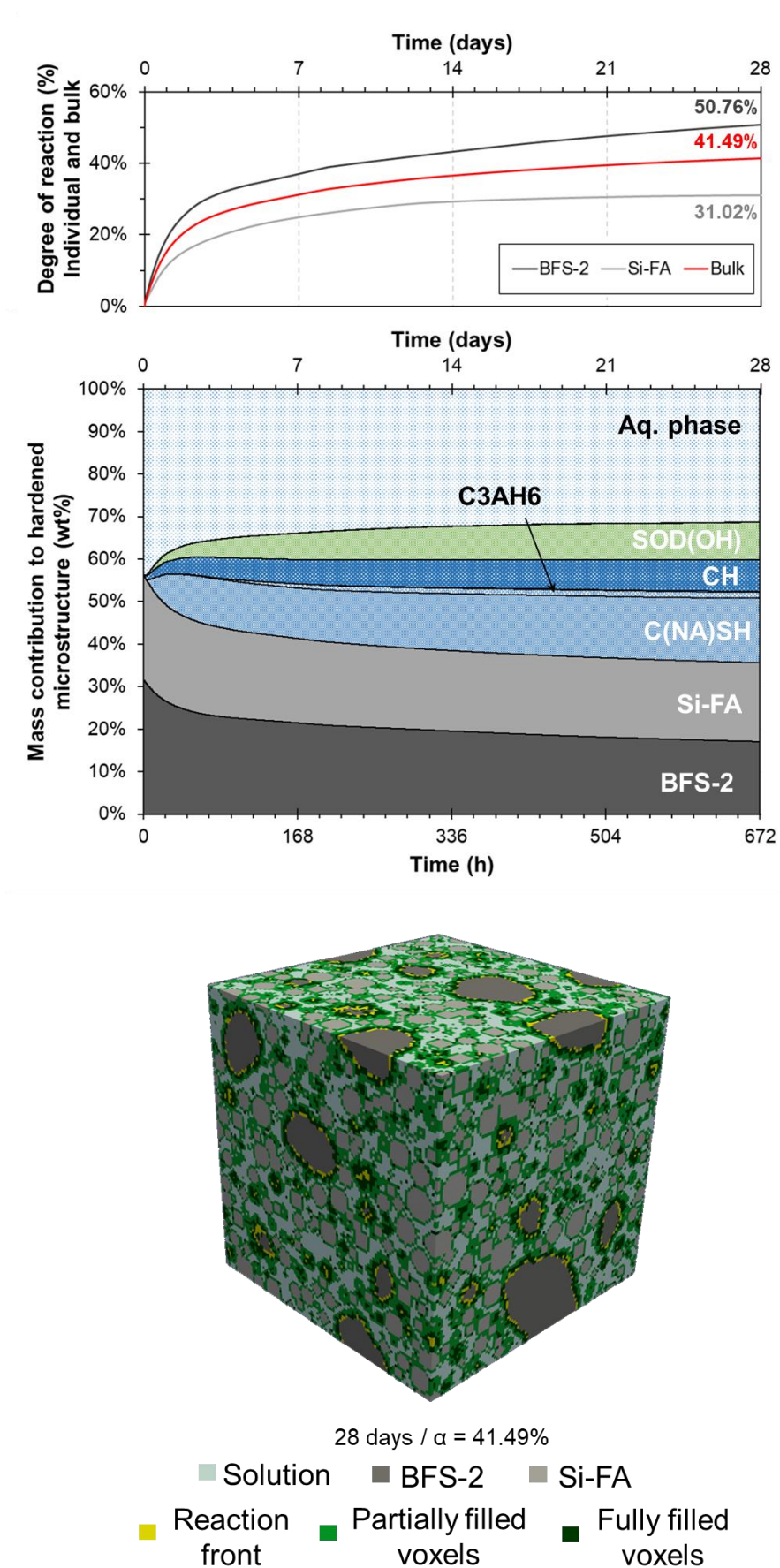


Figure 7.16: Evolution of the simulated alkali-activation of blend B50, through 28 days.

Along with differences in the reaction degree, the interfaces of the particles of precursors with the bulk microstructure were moderately different for each component. As illustrated in Figures 7.17a and 7.17b, the distribution of the two main reaction products, i.e., C-(N-A-)S-H and hydroxysodalite was less significant in the regions surrounding particles of glass Si-FA. The thicker rim products observed around glass BFS-2 indicate the preference for initial reaction of slag components in blended systems, promoting higher cohesion with the particles since early stages. These observations are in agreement with experimental findings through SEM micrographs, which described a stronger binding of particles of glass BFS-2 to the activated matrix compared to glass Si-FA in NaOH-activated B50 blends - see Figure 6.16.

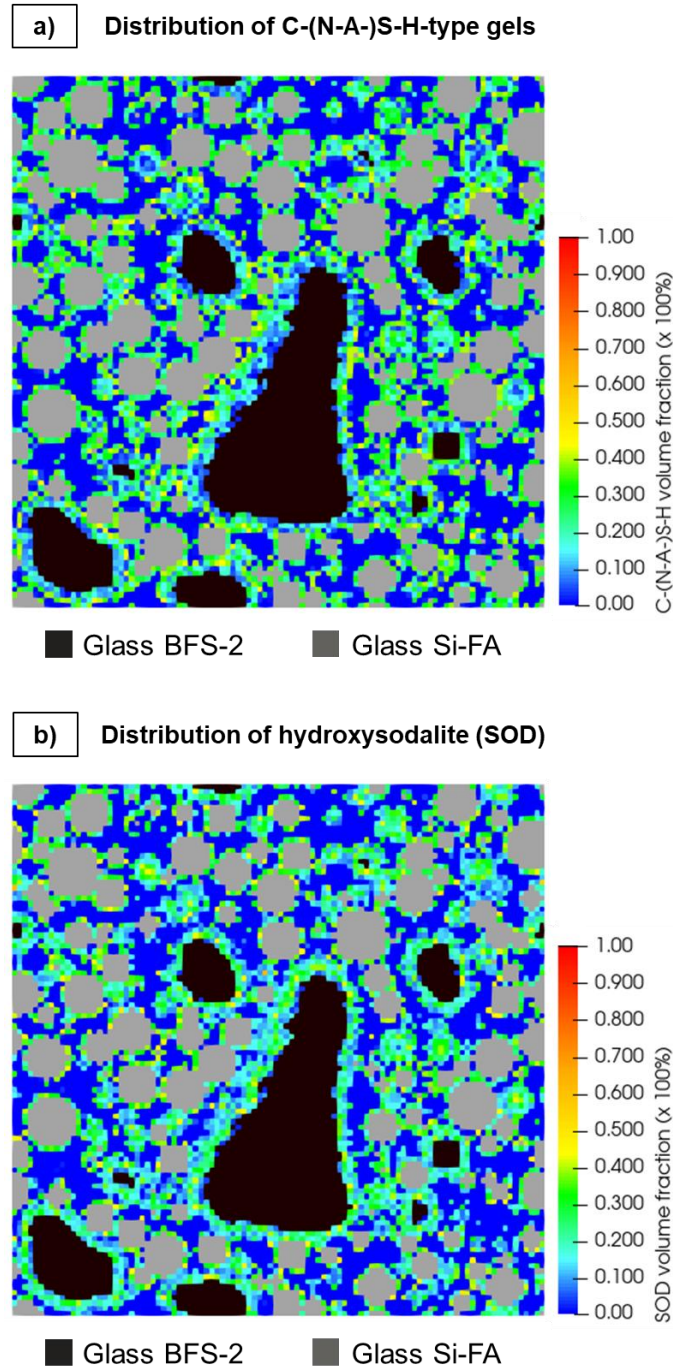


Figure 7.17: Distribution of the main reaction products, after 28 days, within the microstructure of the simulated alkali-activated B50 blend: a) C-(N-A-)S-H gels; and b) hydroxysodalite (SOD).

7.4 Validation of numerical simulation - comparison with experimental data

7.4.1 Evolution of degree of reaction

The comparison of the degree of reaction obtained by simulation with the values determined experimentally in Chapter 6 is given in Figure 7.18 for individual precursors. The simulated degree of reaction of glass BFS-2 (Figure 7.18a), at both 7 and 28 days, presented very good agreement with experimental values, as the curve obtained with the GeoMicro3D model is nearly within the experimental error calculated in section 6.3.1.2. At 7 days, the reaction degree was equal to 36.7 % and 38.7 % for modelled and experimental scenarios respectively, evolving to 46.3 % and 43.3 % after 28 days. The chart also suggests that the reaction is not fully ceased after the end of the simulation, as the graph indicates an evolution in the reaction degree beyond 28 days at a low rate. Exponential fitting of the curve, following the procedure available in [505,506], indicates a final degree of reaction of approx. 57 % under the simulated conditions, which is within the expected range for this type of reactions [88,204,507].

With respect to glass Si-FA, the simulated reaction was initially significantly slower at 20 °C, but achieved very good agreement with experimental data after 28 days (Figure 7.18b) - 37.6 % versus 38.9 % for the experimental and simulated conditions, respectively. The evolution of the numerically simulated reaction, from 7 to 28 days, indicates a similar trend of moderate kinetics compared to experiments, but the rate of evolution of reaction occurred at a slower pace than in the experimental conditions. Exponential fitting of the simulated curve indicates that the reaction is not expected to continually evolve, and final expected reaction degree is approx. 40 %.

Conversely, the implementation of a curing regime at 60 °C for the first 7 days of reaction significantly accelerated the simulated reaction (Figure 7.18c). Few changes were observed in the degree of reaction after the first 7 days, resulting in a quick stabilization of the microstructure and few changes in the assemblage of reaction products, observed in Figure 7.18c. After 28 days, the obtained values were 48.7 % and 45.3 %, for the experimental and simulated scenarios, respectively. Additionally, the plot indicates that the reaction has reached its final stages, as the curve assumed a plateau-like behaviour at the end of the simulation.

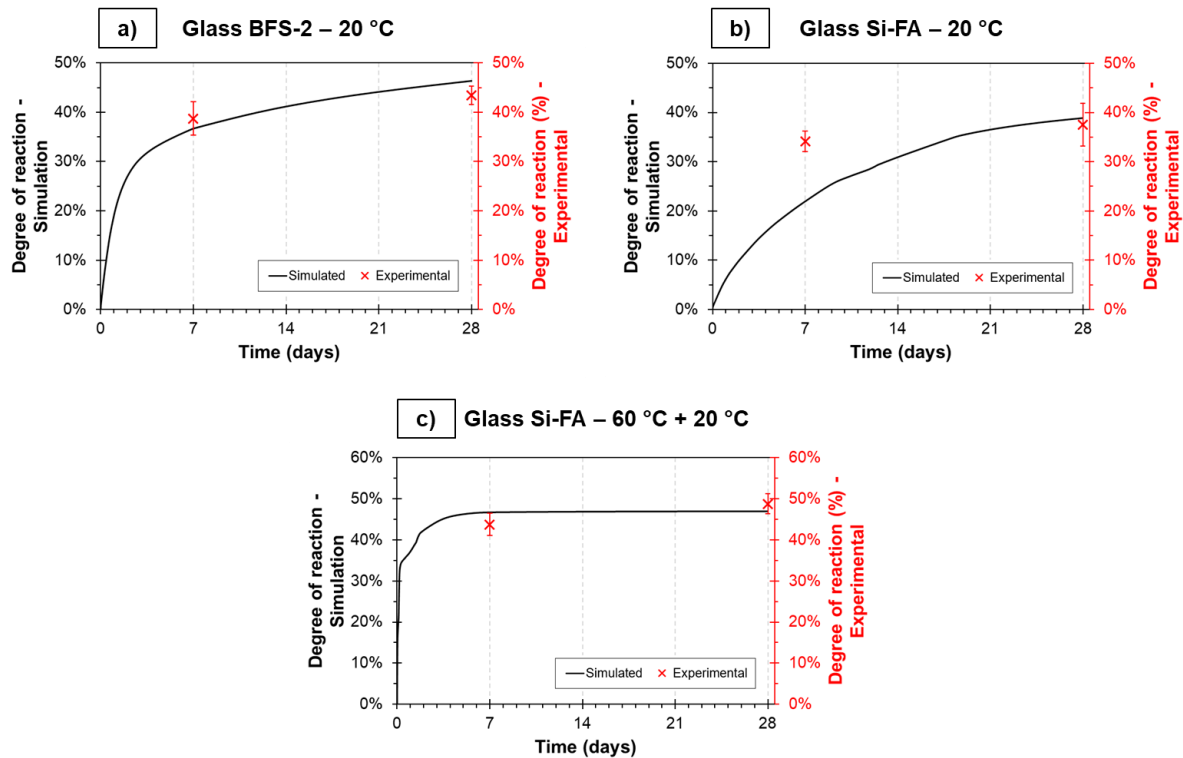


Figure 7.18: Comparison of the evolution, in degree of reaction, of simulated and experimental NaOH alkali-activation of the following systems: a) glass BFS-2, cured at 20 °C; b) glass Si-FA, cured at 20 °C; and c) glass Si-FA, cured at 60 °C for 7 days and then at 20 °C.

The slower evolution of the reaction kinetics of the fly ash-type glass, and the continued evolution in the reaction of the slag-type glass, are also observed in the blend B50. As shown in the plot in Figure 7.19, the simulated overall degree of reaction reached very good agreement with experimental data: at 28 days, results obtained with GeoMicro3D indicated a total reaction degree of 40.9 % versus a calculated value of 39.3 % for the experimental conditions. With respect to individual components, the glass Si-FA presented a similar evolution in its individual reaction degree from 7 to 28 days, increasing 3.1 % in the simulated and 4.1 % in the experimental system. Conversely to the fly ash component, the contribution of BFS-2 to the overall reaction continued to evolve until the end of the simulation, increasing 6.9 % versus only 0.6 % for the experimental value. This latter observation is in line with the individually simulated activation of BFS-2, indicating that the simulation tool can moderately overestimate the duration of the reaction when high-Ca precursors are utilised.

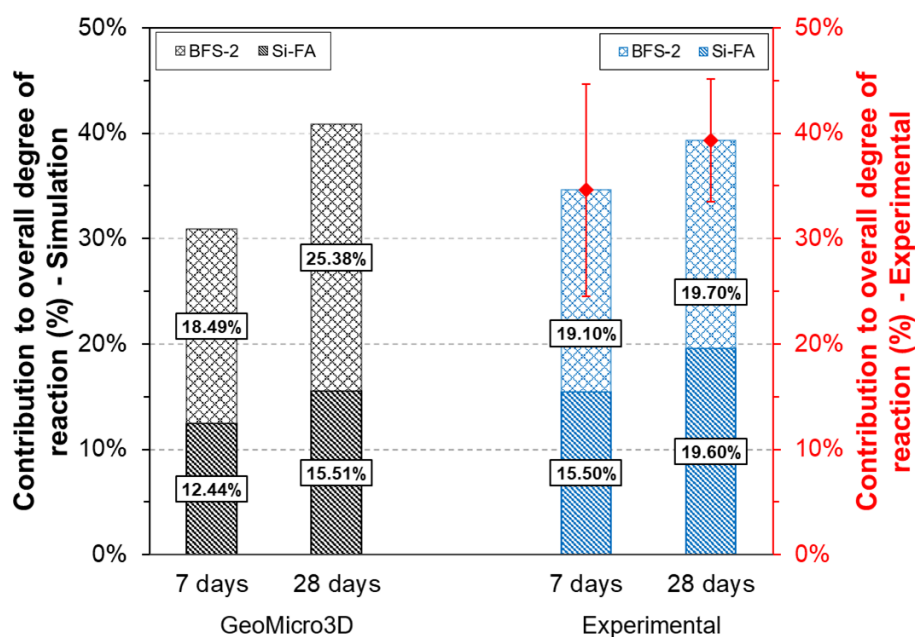


Figure 7.19: Evolution of the degree of reaction of blend B50, in simulated and experimental conditions, considering the individual precursors and the overall system.

7.4.2 Phase assemblage

After the simulation reactions reached 28 days, the phase assemblage of the reaction products were quantitatively evaluated for each system. Following the approach described in Chapter 6, the newly formed phases were categorized in three groups:

- i. C-(N-A)-S-H gels, comprising amorphous Ca-dominated phases;
- ii. N-(C-)A-S-H phases, comprising N-A-S-H gels, hydroxysodalite and Ca-bound N-A-S-H gels; and
- iii. Secondary crystalline phases, comprising katoite, strätlingite and portlandite.

The contributions of each category to the total amount of reaction products were compared between experimental (obtained in Chapter 6) and numerically simulated values (obtained with GeoMicro3D).

Within the N-(C-)A-S-H category, the plots in Figure 7.20 indicate very good agreement for the reactions made with glass Si-FA, while high-Ca systems containing glass BFS-2 presented larger differences between experimental and simulated values. As observed in Figures 7.20a and 7.19b, this category accounted for the majority of the reaction products in both curing regimen of glass Si-FA: N-(C-)A-S-H phases represented more than 75 wt% of reaction products in all experimental and modelled scenarios, and the difference between experimental and simulated values was lower than 5 wt% in the two curing conditions. With respect to high-Ca precursors, the individual (Figure 7.20c) and blended (Figure 7.20d) activation of glass BFS-2 reduced the contributions of this category to the overall microstructure. In general, the numerical modelling underestimated the amount of N-(C-)A-S-H-type phases, resulting in a difference of 11-12 wt% in their final quantities. A slightly larger variation was obtained with B50, mostly due to the larger extent of reaction of glass BFS-2 in the blend.

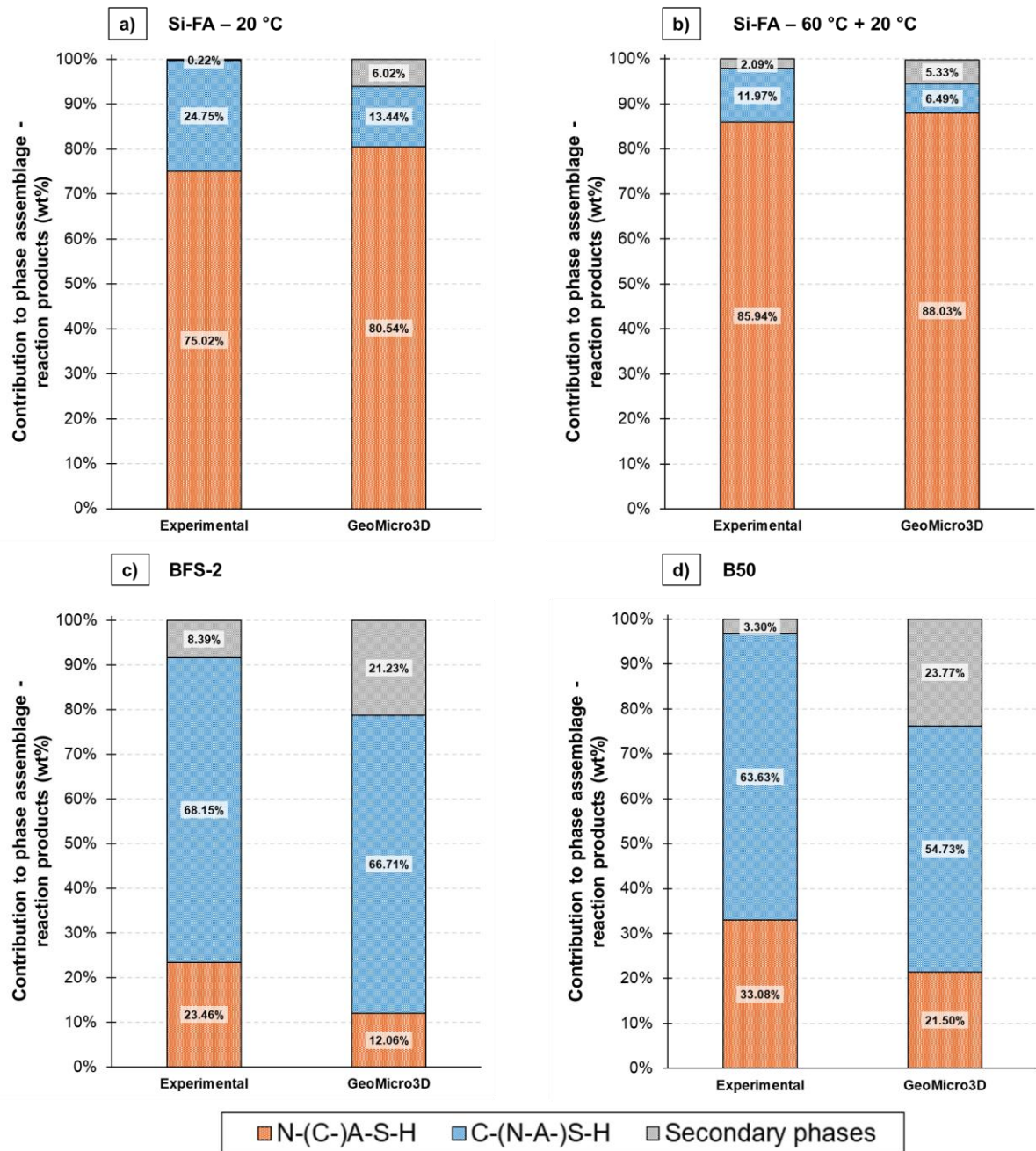


Figure 7.20: Contributions of different categories of reaction products to the final phase assemblage of glasses activated with NaOH, calculated for experimental and modelled conditions: a) glass Si-FA, cured at 20 °C; b) glass Si-FA, cured at 60 °C for 7 days and then 20 °C for 21 days; c) glass BFS-2 cured at 20 °C; and d) blend B50 cured at 20 °C.

The contributions of C-(N-A-)S-H gels and secondary crystalline phases presented an inverse trend among them. In the four systems evaluated, an underestimation of C-S-H-type gels in the numerical simulations was followed by an overestimation of secondary phases at different levels. This discrepancy arises from the existing limitations in thermodynamic databases and models, which consequently influence the simulations performed with GeoMicro3D:

- GEMs, as a thermodynamic modelling tool, does not include kinetic effects in its equilibrium calculations. Therefore, the model utilises the total amount of reactive Ca, Si and Al as inputs to determine the most stable reaction products.

- GeoMicro3D incorporates the core code of GEMs to promote an approach which combines kinetic considerations and thermodynamic equilibrium modelling. However, it considers only unreacted species in the pore solution as inputs to determine the formation of new reaction products, while phases previously predicted to be precipitated are kept unmodified until the end of the simulation. Therefore, it does not cover phase transformations or any other processes requiring redissolution of newly formed phases, thus preventing the shift of initially formed reaction products to different ones.

Within the four tested systems, the variations of the two categories remained in the range of 5-11 wt% for C-(N-A)-S-H gels, and 6-20 wt% for secondary phases. The main differences for the latter category were observed for the alkali-activation of glass BFS-2 (Figure 7.20c) and blend B50 (Figure 7.20d), two systems with high initial Ca content from the chemistry of the precursors. The kinetic module included in GeoMicro3D had a direct impact on the differences observed in Figure 7.20. The ability to replicate the faster release of Ca over other species during early stages of dissolution - which is a positive feature of the tool with respect to an accurate replication of dissolution kinetics - is maximized in systems containing slag-type glasses, facilitating the formation of portlandite within the highly alkaline environment of the digital pore solution. However, the significant consumption of this element in the initial moments of reaction reduces its availability for sequential phase precipitations, and then the initially formed nuclei remain stable throughout the whole simulation. This means that portlandite is unable to participate in any pozzolanic-type reactions at later age in this simulation methodology. With respect to secondary phases, it is well known that crystalline products are more thermodynamically stable than amorphous compounds, and therefore the binding of Ca with other elements is expected to more favorably promote the formation of katoite and strätlingite over disordered gels.

During the simulated alkali-activation of high-Ca glasses, the excessive formation of portlandite in the initial stages promotes an interface between the particles of high-Ca glasses and the matrix which is surrounded by portlandite nuclei, as shown in the microstructure slice in Figure 7.8b. A schematic illustration of the differences between the expected distribution of reaction products in experimental and modelled conditions is shown in Figure 7.21: while a stronger adhesion of reaction products to the glass surface is observed in experiments, which was confirmed by SEM micrographs throughout Chapters 5 and 6, the phase assemblage of the simulated conditions suggest the formation of a thin portlandite-rich layer around the reactive particles.

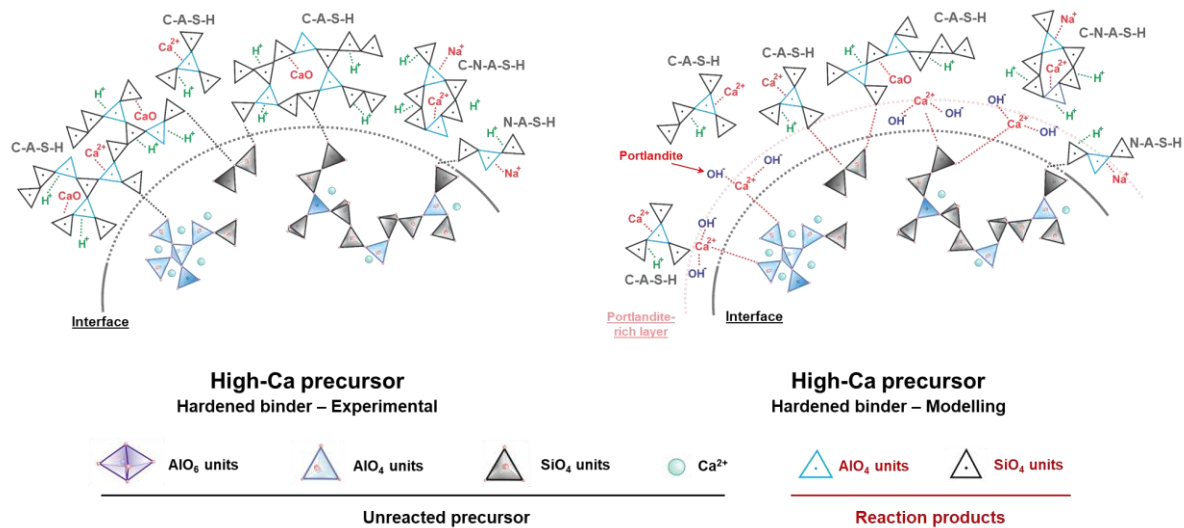


Figure 7.21: Schematic illustration of the expected differences between experimental and modelling scenarios in glass-matrix interfaces in high-Ca activated systems, highlighting the significant formation of portlandite in simulated conditions.

Table 7.3 provides a detailed comparison between experimental and modelled data for C-(N-A)-S-H gels, strätlingite, katoite, and portlandite for reactions comprising high-Ca precursors. The amount of portlandite formed in the two systems is significantly higher than what was experimentally observed, and this observation has different impacts in each reaction. In the simulated activation of glass BFS-2, the consumption of Ca in early stages did not promote major changes in the formation of katoite, strätlingite, and C-S-H-type gels. Instead, it was the responsible for reducing the amount of products within the N-(C-)A-S-H category – see Figure 7.20, as the formation of Ca-bound N-A-S-H gels was observed to be limited in comparison with pure N-A-S-H and hydroxysodalite phases. On the other hand, the excessive formation of portlandite in the activation of blend B50 impacted the formation of the remaining phases, as this system presented the largest differences between experimental and simulated values for C-(N-A)-S-H and N-(C-)A-S-H gels. This is suggested to occur due to two reasons: the intrinsic lower Al content in glass BFS-2, and the slower reaction kinetics of glass Si-FA in the blended paste, with both conditions resulting in a delayed release of Al to the pore solution. Since the phase assemblage was composed of C-(N-A)-S-H, minor quantities of hydroxysodalite and excess of portlandite, the late presence of Al favoured the precipitation of katoite over other products through binding with Ca, as this phase displayed significant formation after approx. 72 hours of reaction – see Figure 7.16. At the same time, strätlingite displayed negligible amounts in the microstructure after 28 days, and the growth of zeolites and N-(C-)A-S-H gels was restricted, emphasizing the late role displayed by Al in the development of the microstructure in this system.

Table 7.3: Contributions of Ca-dominated phases to the phase assemblage of alkali-activated reactions comprising glass BFS-2 and blend B50.

Category of phases	BFS-2		B50	
	Experimental	GeoMicro3D	Experimental	GeoMicro3D
C-(N-A)-S-H	68.1 %	66.7 %	63.6 %	54.7 %
Katoite + strätlingite	8.1 %	7.4 %	3.3 %	8.2 %
Portlandite (CH)	0.0 %	13.8 %	0.3 %	15.6 %

As a conclusion, it was demonstrated that the implementation of numerical modelling tools can accurately replicate the reaction kinetics of alkali-activated systems. However, limitations in the thermodynamic equilibrium considerations induce errors of up to 12 % in the estimation of C-S-H-type gels. The metastable nature of the majority of some reaction products imposes challenges when comparing their equilibrium versus other crystalline phases. For that reason, a detailed study about the combined precipitation of C-(N-A-)S-H gels with other secondary phases is here suggested, aiming the determination of thermodynamic constraints that precipitation the formation of the former category in a realistic way, following the approach considered in this work for the formation of N-(C-)A-S-H gels versus zeolites.

7.5 Conclusions and outlook

The use of numerical modelling tools to study the evolution of the microstructure of alkali-activated binders, either in fresh or hardened states, is a quick and flexible way to observe the influence of multiple variables in their behaviour and performance. Moreover, the development of a reliable tool which accommodates a wide range of precursors, activators and curing conditions, would come as a powerful resource that can increase the outreach and applicability of these materials. The present Chapter targeted the development and implementation of new features into GeoMicro3D, aiming at the characterization of digital microstructures of alkali-activated systems in different scenarios of precursors and temperature. Through the inclusion of experimentally derived kinetic considerations and recently developed thermodynamic databases, the workflow presented in this work focused on the validation of the extended GeoMicro3D modelling tool to accurately simulate the reaction kinetics and phase assemblages of alkali-activated pastes versus experimental findings. Based on the results presented in this Chapter, the following conclusions can be drawn:

- Following experimental observations, Ca was observed to be the main influencing factor in the predicted phase assemblage of systems through thermodynamic modelling. When evaluating the influence of the chemistry of the precursor, a shift in the phase assemblage from a domain rich in zeolites and disordered N-A-S-H-type gels, to one having Ca-dominated phases as the main products, is observed at CaO contents above 35 wt% in the precursor. This effect is enhanced in simulated conditions utilizing waterglass as activator versus NaOH, due to the facilitated binding of Ca with Si and Al in the presence of soluble silicates.
- The thermodynamic database of N-(C-)A-S-H gels provided a reliable estimation of the phase assemblage of low-Ca precursors in the evaluated alkali-activated systems. The implementation of thermodynamic constraints to a few zeolites, considering the Si/Al and Na/Al ratios of the compounds, resulted in co-existence of crystalline phases and amorphous gels, which has been observed in previous experiments for the alkali-activation of synthetic fly ashes.
- Simulations performed with the extended GeoMicro3D modelling tool provided a reliable evolution of the degree of reaction versus experimental results. The inclusion of dissolution rates derived earlier in this work enabled the observation of early formation of portlandite in all systems, because of the faster release of Ca from the precursors as observed during dissolution experiments. The continuity of

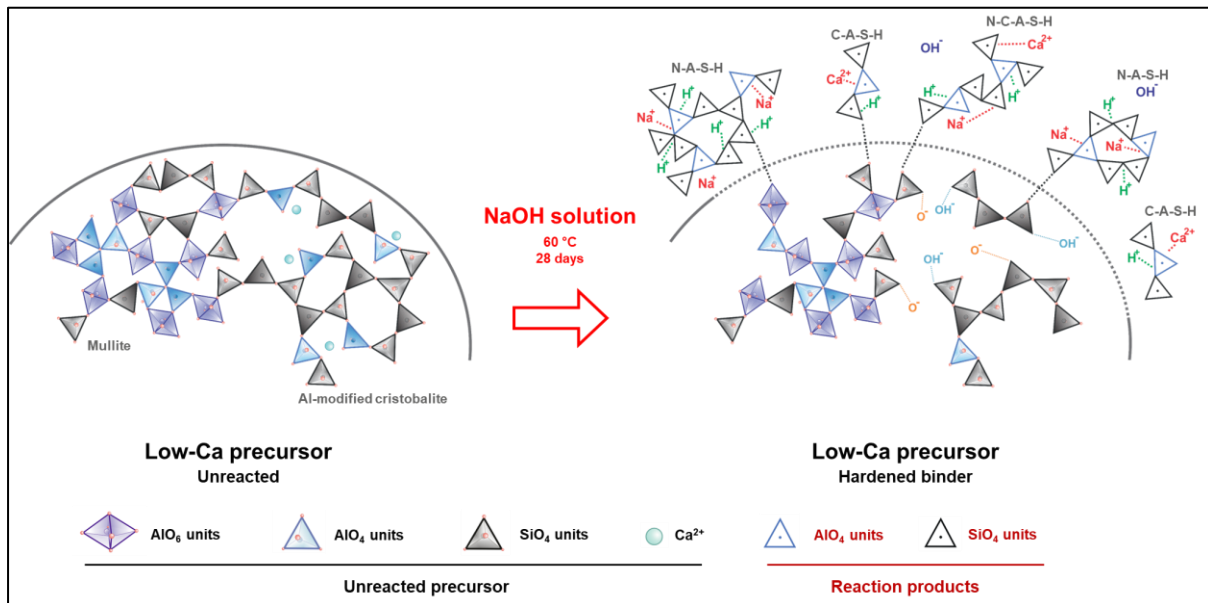
the reactions, throughout the whole simulated period of 28 days, resulted in reduction of overall porosity of simulated pastes.

- The precipitation of primary reaction products replicated the expected outcomes observed in alkali-activated pastes: C-(N-A-)S-H dominated the kinetics of phase precipitation in the activation of glass BFS-2 and blend B50, with a concurrent formation of hydroxysodalite occurring at lower rates; conversely, glass Si-FA displayed a more clear stage separation, with N-(C-)A-S-H gels clearly precipitating in the first moments of reaction, followed by a delayed formation of Ca-dominated phases.
- The digital microstructures produced with the numerical simulation were consistent with experimental findings. In blend B50, glass Si-FA was observed to have a weaker adhesion to the matrix compared to glass BFS-2. Additionally, temperature was observed to be directly linked to the reduction of the final porosity of the reactive system of glass Si-FA, in line with scanning electron microscopy images obtained for alkali-activated pastes.
- Finally, the formation of N-(C-)A-S-H gels and zeolites had very good agreement between simulated and experimental conditions for low-Ca precursors. An overestimation of crystalline Ca-based phases was observed in both thermodynamic and numerical modelling, especially for the high-Ca precursor, which consequently limited the formation of the other categories of reaction products. The largest differences in quantities of each category between experimental and simulated conditions were for N-(C-)A-S-H, although the agreement among all scenarios was still very good.

The implementation of new features into GeoMicro3D resulted in positive agreements between digital and experimental findings, highlighting the contributions of this Chapter to the obtainment of digital microstructures of systems based on both high- and low-Ca precursors, under different curing regimen. The inclusion of dissolution rates as a first step of the simulations, and thermodynamic equilibrium calculations as a second step, allowed the understanding and the replication of both early and later stages of the reaction. These observations indicated that the chemistry-temperature relationships developed earlier in this Thesis can be combined with GeoMicro3D, potentially enabling the future utilization of the extended modelling tool to estimate both fresh (rheology and early strength development) and hardened (durability and long term behaviour) properties for different binder compositions. It is important to state that, despite the positive outcomes, a refinement of thermodynamic constraints concerning Ca-dominated products and the inclusion of re-dissolution of solid phases might be necessary to further increase the accuracy of the model, and is suggested for future investigations.

Chapter 8.

Retrospection, contributions, and recommendations for future research



The sequential stages of alkali-activation reactions have been extensively investigated in this work, from the initial instants of contact between solid precursors with alkaline solutions, to the formation of hardened and stable microstructures. Through the fundamental investigation of the reaction kinetics and the identification of influencing parameters on each stage, this study evaluated the behaviour of low- and high-Ca precursors activated with distinct alkaline solutions, proposing empirically-based correlations and modelling tools to predict the evolution of their characteristics with the course of the reaction. This Chapter provides a summary of the main findings of this thesis, correlating the experimental findings with the gaps in literature identified at the beginning of this study. The Chapter finishes with suggestions for future work, targeting the continuous development and improved applicability of the technology of alkali-activated materials.

8.1 Retrospection

In the pathway towards the decarbonization of the construction industry, alkali-activated materials are considered one of the most viable options of sustainable building materials, as they combine the avoidance of the utilization of Portland cement with the repurposing of industrial byproducts. However, from an industrial perspective, a few challenges limit their acceptance and a wider application of this technology, as discussed in Chapter 1:

- i. The limitation on geographical availability of the main raw materials, combined with the variability in chemistry and mineralogy of precursors, generates uncertainties over the replication of the behaviour of AAMs in different locations;
- ii. The utilization of novel materials as precursors - which can increase the number of potential raw materials, especially in regions with limited supply of blast furnace slags and coal fly ashes - is not yet a mature alternative. These alternative components do not present a well-established production process in most cases, and their production volumes are usually low, raising questions over their contributions to a reliable supply-chain for industrial applications.

The present PhD thesis aimed at uncovering a few of the challenges with the implementation of these binders. In summary, this research proposed to correlate binder chemistry and curing conditions to microstructural characteristics, aiming at the estimation of the behaviour of alkali-activated materials at different stages of reaction, according to the study route illustrated in Figure 8.1.

This PhD thesis presented a systematic investigation of the kinetics of reactions of alkali-activated materials in experimental and simulated conditions, from the initial stages of dissolution of precursors in alkaline solutions, to the development of mature microstructures. The experimental approach of this study consisted in the use of synthetic precursors obtained with variable amounts of SiO_2 , Al_2O_3 and CaO , which replicated the structure of blast furnace slags and coal fly ashes, the two most utilised precursors in industry and in research. The main experimental findings were utilised as base for the development of the main deliverable of this thesis: a numerical simulation tool which provides a digital observation of the evolution of microstructures, at paste level, with multiple conditions of precursors, activators, and curing regimes. The structure of this study, illustrated in Figure 8.1, was divided into five sections: one section which provides the problem statement and the motivation behind this work, three technical sections which describe the workflow of this thesis, and one final section with the general conclusions and contributions of this work.

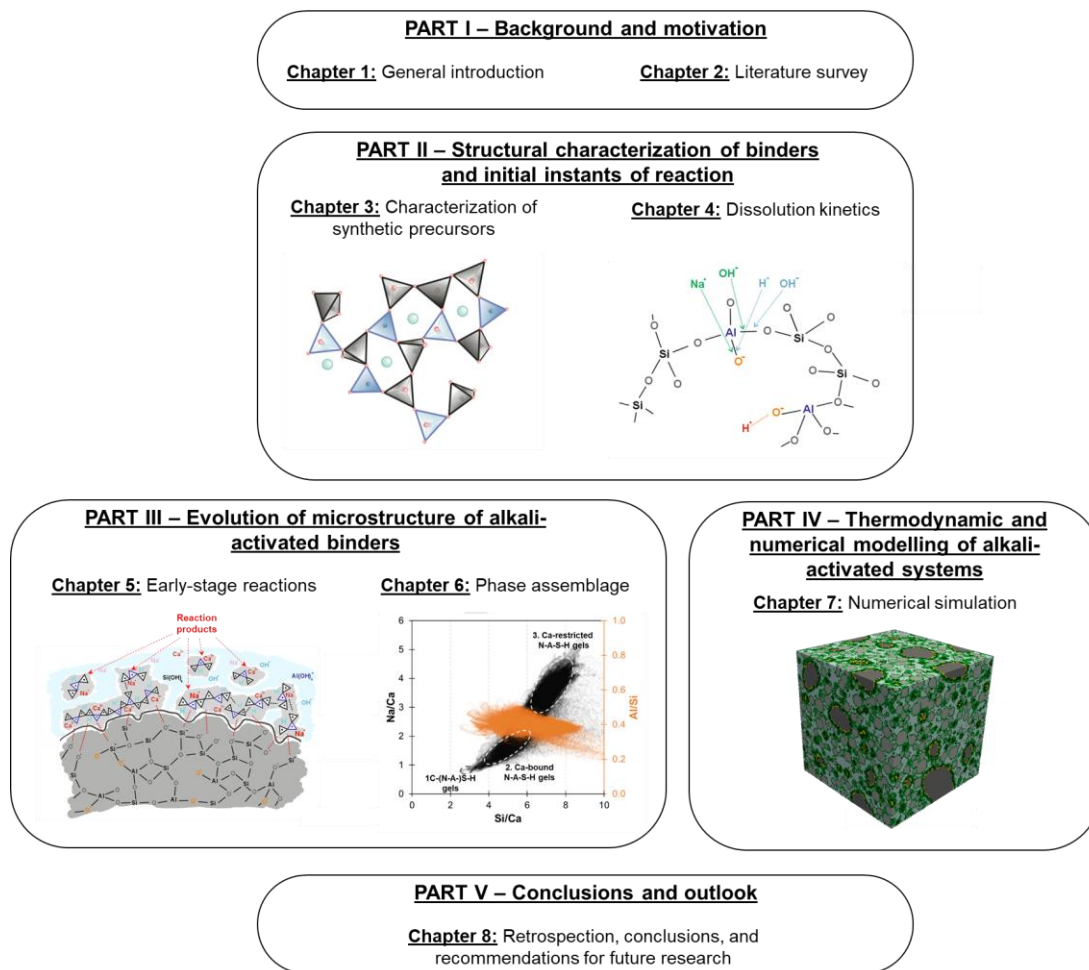


Figure 8.1: Schematic illustration of the structure of this thesis.

Summary of research

With respect to the Chapters comprising the technical sections of this thesis, a summary of each is provided:

Part II: Structural characterization of precursors and initial instants of reaction

Chapter 3 presented the synthesis route and the characterization of the synthetic precursors utilised in all of the Chapters of this thesis. The precursors were obtained through a melting-quenching route, and four glasses of different chemical compositions were produced. The composition of each glass was simplified to account for SiO_2 , Al_2O_3 and CaO as the main constituents of the precursors. The amounts of each oxide were stoichiometrically controlled to replicate the structural characteristics of two types of blast furnace slags, one type of calcareous fly ash, and one type of siliceous fly ash. A combined quantitative and qualitative study was performed to investigate the influence of CaO , as network modifying oxide, on the distortion of the framework of each glass. The structures of the synthetic precursors were characterized with Fourier transform infrared (FTIR) and Raman spectroscopy, solid state nuclear magnetic resonance (SS-NMR), and with X-ray diffraction (XRD). The connectivity of the framework of the precursors was determined and correlated to the overall chemistry of each, through the quantification of Si Q^n units, and the

qualitative determination of Al Qⁿ units. XRD diffractograms and FTIR spectra were utilised to identify the formation of heterogeneities at sub-micro levels, providing an additional correlation between chemical composition and glass structure.

Chapter 4 covered the study of the dissolution kinetics of the synthetic precursors. Relatively dilute solutions of NaOH, in different molarities, were prepared to assess the evolution in dissolution of all glasses, and different environmental temperatures were implemented in studies involving fly ash-type glasses. The temporal evolution in concentrations of Ca, Si and Al was studied with inductively coupled plasma optical emission spectroscopy (ICP-OES), and the residual structure of the glasses was characterized with Raman and FTIR spectroscopy. Aiming for a facilitated assessment of reaction kinetics, the chapter proposed empirically derived equations of the forward dissolution of each element, proposing a correlation which estimates the behaviour of any glassy precursor within the studied compositional and temperature ranges.

Part III: Evolution of microstructure of alkali-activated binders

Chapter 5 focused on the study of the initial moments of alkali-activating reactions. The mechanisms of precipitation of reaction products were investigated in NaOH and waterglass solutions. FTIR spectroscopy, differential thermogravimetric (DTG) analysis and XRD were among the techniques utilised to identify the formation of intermediate metastable phases and primary reaction products, correlating the findings with chemistry of the precursor and of the activating solution. Scanning electron microscopy (SEM) images allowed a direct visualization and association of alkaline activators to two precipitation mechanism of reaction products - either through heterogeneous nucleation as surface-anchored products, or through homogeneous nucleation in the bulk solution, with additional observations of the evolution of the structural build-up of such phases. In-situ isothermal calorimetry of the first 24 hours of reaction provided additional insights into the structural transformation of disordered gels. In addition, the use of selective dissolution through salicylic acid/methanol (SAM) treatment was implemented to distinguish the contributions of gels of different chemistry to the early phase assemblage of alkali-activated pastes.

Chapter 6 proposed multiple correlations between chemistry, reaction kinetics and microstructure of alkali-activated binders through empirical observations. Pastes prepared with the four individual precursors activated with waterglass and NaOH solutions, and with blends of high- and low-Ca glasses, were cured up to 28 days at 20 °C and 60 °C. A combination of XRD, selective dissolution through the SAM treatment, and SEM micrographs allowed the estimation of the degree of reaction of each paste and the distinction and quantification of all reaction products contributing to the phase assemblage.

Part IV: Thermodynamic and numerical modelling of alkali-activated systems

Chapter 7 covered the implementation of new features and the development of an extended microstructure modelling tool. The findings of this thesis related to dissolution kinetics and from external data related to the thermodynamic properties of N-(C-)A-S-H gels were included in GeoMicro3D, enabling the simulation of the alkali-activating reactions of low-Ca precursors and blended systems. The evolution in the degree of reaction and phase assemblage of digital microstructure were validated against experimental findings, ensuring the ability of the developed tool to accurately simulate alkali-activation reactions in multiple combinations of precursors and curing conditions.

8.2 Conclusions and contributions of this research

Throughout the five main Chapters of investigation, this thesis focused on providing relevant inputs to the scientific and engineering communities in the field of alkali-activated materials. With the knowledge obtained in the path towards microstructural modelling of these binders, the main findings and contributions of this work are described below:

1. Precursors have heterogeneities, at sub-microscopic level, in unreacted conditions, and during the early stages of dissolution

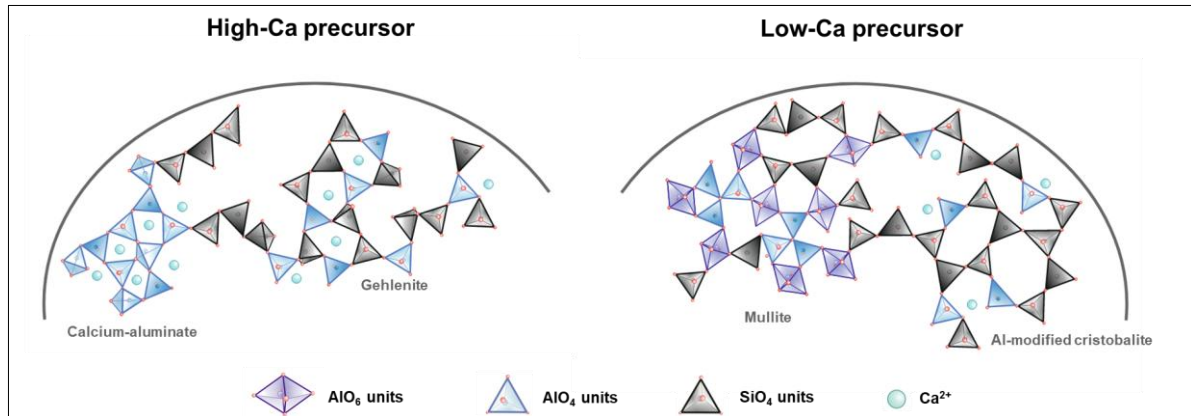


Figure 8.2: Schematic illustration of the heterogeneities in the glass structures of high- and low-Ca synthetic precursors.

It is a known fact that the amorphous portion of precursors is the predominant reactive phase in alkaline solutions. The findings from Chapter 3 identified that, within an amorphous framework, different short-range ordered arrangements resembling crystalline components can co-exist, and these isolated structures are directly influenced by the bulk chemical composition of the precursor, as schematically shown in Figure 8.2.

Linear correlations between $\text{Ca}/(\text{Si}+\text{Al})$ ratios and Si Q^n units of the synthetic precursors were obtained, and the nature of the qualitatively identified structures were observed to shift according to an increasing amount of CaO , as illustrated in Figure 8.3.

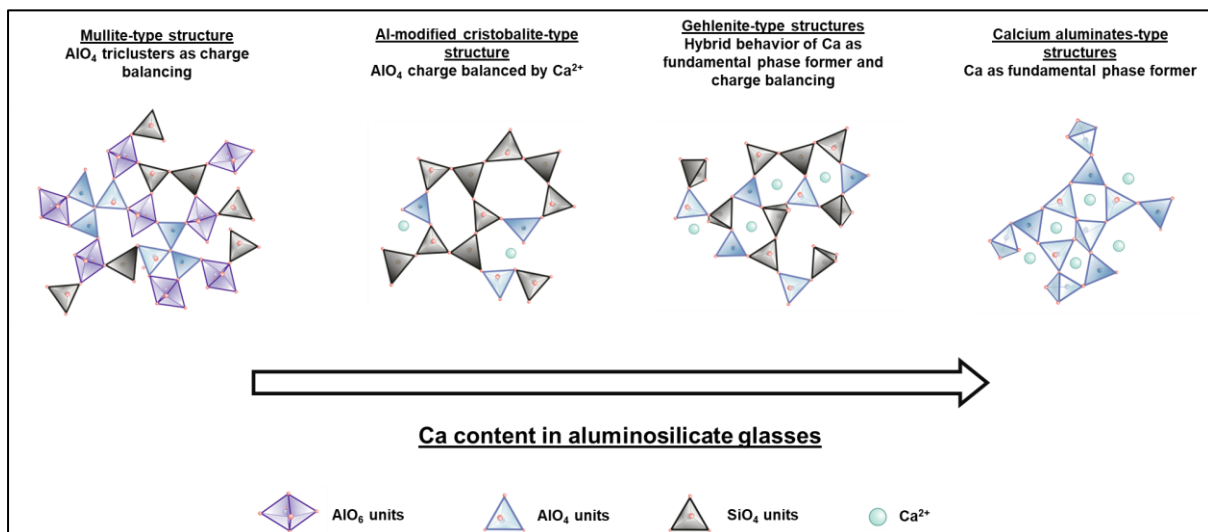


Figure 8.3: Schematic representation of the influence of Ca in the structure of aluminosilicate glasses.

These heterogeneities displayed a direct impact in the dissolution characteristics of each glass. Through the characterization of residual glasses after dissolution experiments, Chapter 4 provided evidence of localized disruption of the framework in isolated regions of the precursors:

- i. Al showed selective dissolution in tetrahedral coordination in gehlenite-type and Al-modified cristobalite-type structures, as sites charge balanced by Ca^{2+} were weakened after the release of the cation during the initial stages of dissolution.
- ii. Si showed preferential disruption of Q^3 and Q^4 sites in the highly polymerized structures of fly ash-type glasses, as the breakage of ring and three dimensional structures was necessary prior to a significant hydrolysis step in two-dimensional sites (Si Q^2 and Q^1). On the other hand, the less polymerized structure of high-Ca glasses promoted the preferential release of Si Q^1 and Q^2 units during the investigated period.

Finally, Chapter 4 identified the presence of mullite-type structures in residual glasses after the first stages of dissolution, with the four synthetic glasses displaying clear Si-O-T and AlO_4 -rich reflections in infrared spectroscopy. These findings supported the occurrence of heterogeneities in the framework of the precursors and the preferential dissolution of certain structures, promoting the formation of intermediate disordered structures during the early stages of alkali-activating reactions.

2. Mechanisms of glass dissolution and phase precipitation are influenced by chemistry and temperature

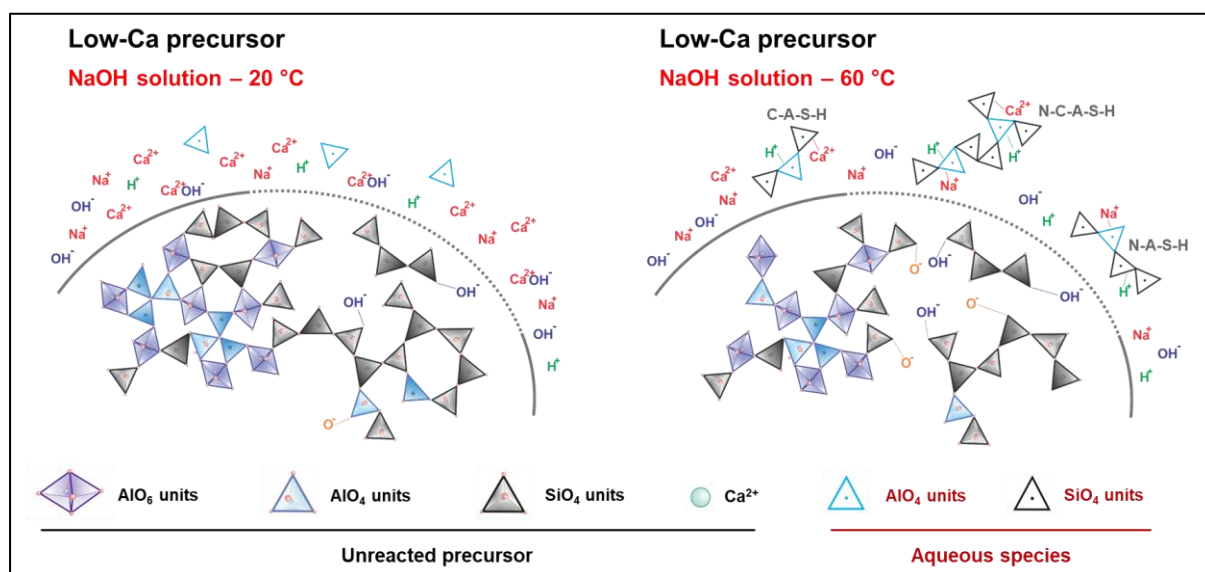


Figure 8.4: Schematic illustration of the influence of temperature on the dissolution and phase precipitation kinetics of low-Ca precursors.

As demonstrated in multiple research works available in the literature, the dissolution of amorphous components in alkaline solutions starts with a cation exchange process, leaching alkali and alkali-earth elements to the surrounding solution. In the glasses investigated in this thesis, this phenomenon was observed through an initial higher dissolution rate of Ca for all precursors, at 20 °C, in Chapter 4. Specifically in fly ash-type glasses, the early release of Ca was nearly two times more significant than in slag-type glasses, as observed by the concentrations measured in the pore solution. This observation suggests that this

element is more loosely bound to the glass framework if it acts solely as a network modifier, compared to its behaviour when incorporated in gehlenite-type or isolated Ca-Al based structures in slag-type structures.

Additionally, at 20 °C, the initial release of Ca favoured the dissolution of Al over Si, especially in slag-type glasses, as Al-O regions were weakened by the leaching of the network modifying element. At 60 °C, however, Ca displayed a less impactful role in the dissolution of fly ash-type glasses: although high concentrations were still measured in the first minutes of the experiments, the period of steady-dissolution of Ca was shorter than what was observed at 20 °C. Hydrolysis of Si-O and Al-O bonds became the dominant phenomenon over ionic exchanges, and a stoichiometric release of Si and Al was obtained - the influence of temperature is schematically shown in Figure 8.4, which emphasizes the combined release of the two elements at 60 °C.

Despite these observations, the empirically defined forward dissolution rates of Si and Al were demonstrated in Chapter 4 to be dependent on the precursor's Ca content. In addition, the initial stages of phase precipitation, detailed in Chapter 5, clearly demonstrated the influence of Ca in the nature of newly formed reaction products, either as intermediate activated complexes or as stable phases. Table 8.1 provides the evidence found in this thesis for the mechanisms of dissolution of each precursor, and the influence in the subsequent precipitation of first reaction products.

Table 8.1: Evidence of the dissolution mechanisms of each class of synthetic precursor, and their consequences into the precipitation of reaction products at early stages of reaction.

Glass type	Dissolution mechanism	Initial phase precipitation
Slag - 20 °C	Leaching of Ca quickly followed by Al, resulting a Si-rich residual structure	Portlandite and amorphous carbonates quickly converting to calcium-aluminates and C-S-H-type gels
Fly ash - 20 °C	Longer period of Ca leaching followed by non-stoichiometric release of Al (first) and Si (secondly)	Portlandite and amorphous carbonates for a longer period, slowly converting to C-S-H
Fly ash - 60 °C	Immediate ceasing of Ca leaching followed by a strong stoichiometric release of Si and Al - see Figure 8.3	Ca-bound N-A-S-H gels with short-range ordered zeolite characteristics

3. Disordered gels co-exist in hardened matrices, and their distinction can be achieved with a combination of multiple analytical techniques

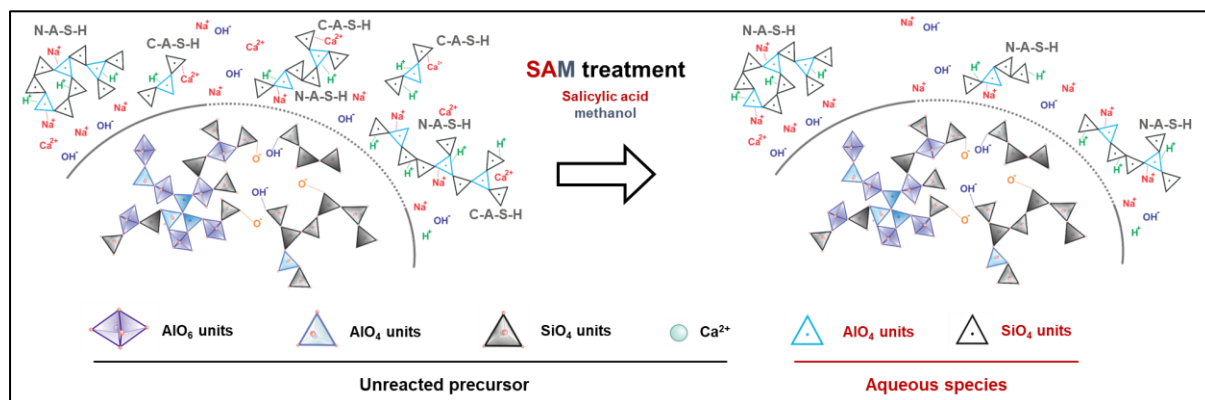


Figure 8.5: Schematic illustration of the dissolution of C-(N-A-)S-H-type gels via SAM treatment.

In mature microstructures, both C-(N-A-)S-H and N-(C-)A-S-H gels are usually intermixed within the bulk matrix, and the distinction between the two phases is not always feasible. In all of the mixtures analyzed in this thesis, the results from Chapters 5 and 6 demonstrated that the two phases are always present in the characterized systems at 7 and 28 days, in variable quantities according to the composition of the precursors and activators. In the early stages of reaction, C-S-H-type species were shown to be the first type of gel to be precipitated in systems cured at 20 °C irrespective of the structure of the glass, while Ca-containing N-A-S-H gels were the primary reaction products in the early stages of reactions occurring at 60 °C.

For all precursors, the use of waterglass solutions as activators promoted more homogeneous microstructures compared to NaOH-activated systems, lowering the overall porosity and reducing the growth of ordered structures, as evidenced with XRD analysis in Chapter 6. Through energy dispersive spectroscopy (EDS) mapping, this homogeneity was proven for the activation of glass Si-FA cured at 60 °C: NaOH cured paste had a clearer separation of phases, with a high presence of Ca-bound N-A-S-H gels and limited amount of pure N-A-S-H gels. Conversely, waterglass promoted a wider distribution of Ca content in the activated matrix, with more equal identified quantities of C-(N-A-)S-H, N-A-S-H and N-(C-)A-S-H gels.

In an attempt to separate and quantify the two categories of gels, Chapter 6 proposed an approach based on three different experimental techniques:

- i. SEM: quantification of the degree of reaction of each mixture through image segmentation;
- ii. QXRD: subtraction of the degree of reaction from the total amorphous content of each mixture;
- iii. Selective dissolution through SAM treatment: subtraction of the contribution of C-(N-A-)S-H gels to the amorphous content of each mixture by weight loss.

Within the above list, the SAM treatment was utilised as a tool to dissolve C-(N-A-)S-H gels from the hardened binders, facilitating the characterization of the microstructure and additional reaction products - Figure 8.5 provides a schematic illustration of the effect of SAM solutions in hardened binders. In Chapters 5 and 6, the use of DTG, XRD and FTIR before and after the selective dissolution, among other techniques, proved the ability of the technique in separating the two categories of gels at both early- (24 hours) and later stages (28 days). The points of evidence utilised for the individual study of each category of gel are detailed in Table 8.2:

Table 8.2: Evidence of the dissolution of C-(N-A-)S-H species from the hardened binder after SAM treatment.

Technique	Evidence	Thesis allocation
Differential thermogravimetric analysis DTG	i. Reductions in the weight loss percentage in the 40 °C - 200 °C temperature range after SAM treatment	Chapter 5 Section 5.4.3
Fourier transform infrared spectroscopy FTIR	i. Shift of the centre of Si-O-T band, in the 1000-900 cm ⁻¹ towards higher wavenumbers	Chapter 5 Section 5.4.3
X-ray diffraction XRD	i. Removal of peaks assigned to variations of C-S-H-type structures ii. Shift of centre of amorphous band in the 25-35° range towards lower 2θ values	Chapter 6 Section 6.3.2.

4. The blending proportion of two precursors influences the kinetics of reaction

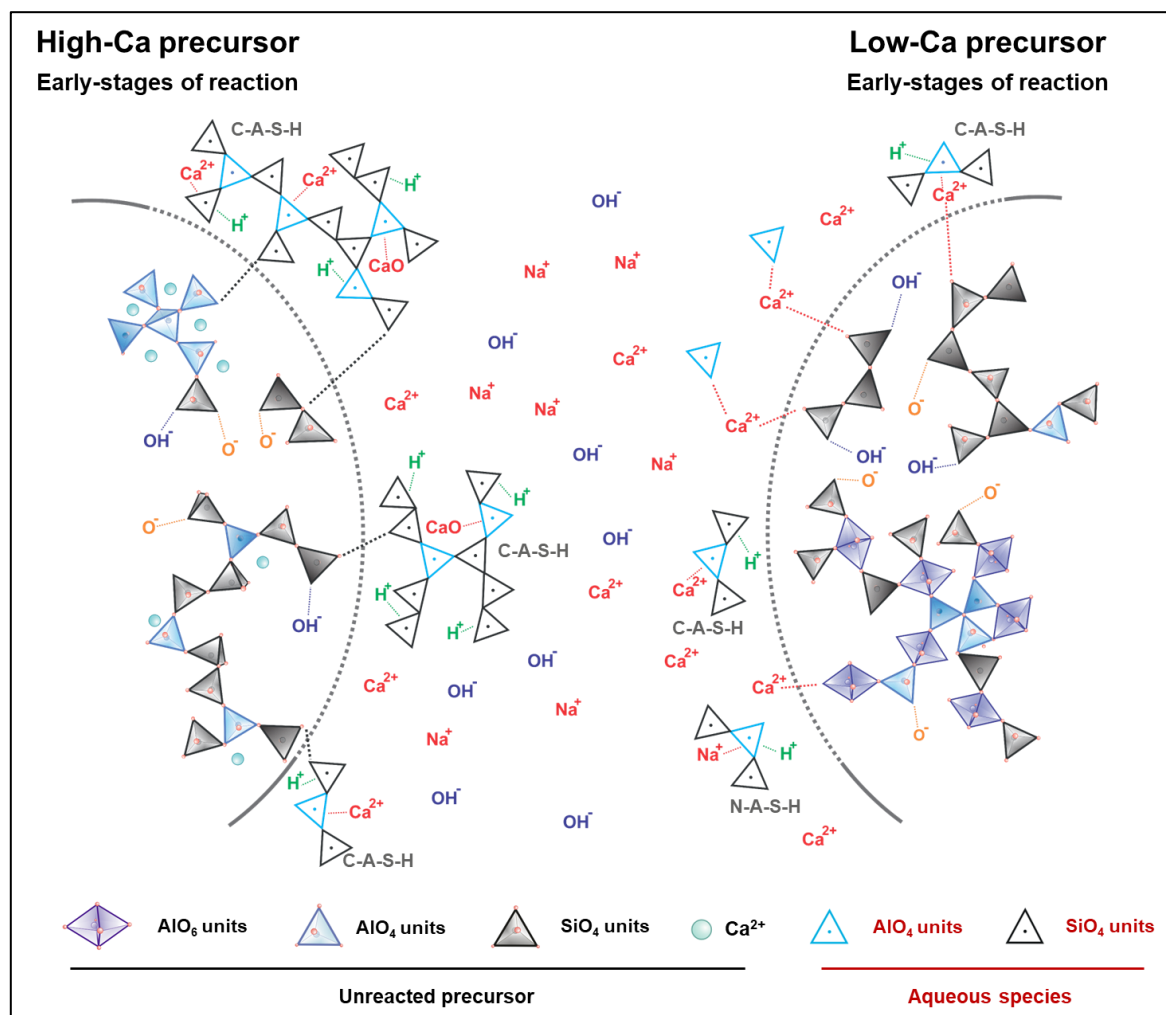


Figure 8.6: Schematic illustration of the influence of high-Ca precursors in the reaction kinetics of low-Ca precursors, in the early-stages of reaction.

In binder formulations containing blends of two or more precursors, the reaction kinetics of the individual components rarely follow a congruent pattern among them, as one material tends to display larger contributions to the overall reaction in the alkali-activated system. Chapter 6 demonstrated that, when slag-type and fly ash-type glasses were mixed in a 1:1 proportion, the former dominated the reaction in the first days, and the influences of the latter were more visible after 7 days of reaction, as seen through the evolution in degree of reaction and phase assemblage. This was supported by SEM micrographs, which demonstrated differences in the interface of glass particles with the hardened matrix: glass BFS-2 presented stronger adhesion to the hardened matrix, while stronger signals of chemical etching were observed at the edges of glass Si-FA particles, a feature additionally enhanced in NaOH- over waterglass-activated samples.

In general, blending with glass BFS-2 was observed to increase the reaction potential of the fly ash-type component in all tested proportions. As schematically shown in Figure 8.6, the findings of Chapter 6 suggested two slightly different kinetic pathways for this influence:

- i. When in larger or similar content (B70 and B50), glass BFS-2 had the main contributions to the initial stages of reaction of the blend due to its intrinsic higher reactivity. With the course of time, the degree of reaction of the slag-type

component decelerated, but the pore solution remained rich with the aqueous species released from it. These ions behaved as a binding site for Si and Al species released from the network of glass Si-FA, promoting an immediate oligomerization of the two species and continuously lowering their saturation indices. Consequently, the hydrolysis phenomena of Si-O and Al-O bonds of the fly ash-component are intensified, thus enhancing its reaction potential in secondary stages of reaction.

- ii. When in lower content (B30), the dissolution of BFS-2 was limited to a more significant leaching of Ca and delayed release of Si and Al. As the initial content of glass Si-FA was larger in blend B30, the fly ash-type component concentrated the alkalis in solution to promote its dissolution. The Ca that was made available by the slag-type component acted as a nucleation site for the species dissolved from glass Si-FA in a similar way as in the other blends, and accelerated the dissolution of glass Si-FA at the initial stage of reaction. As a consequence, glass BFS-2 presented a Ca-depleted framework in the first days of reaction, and its main contributions to the overall blend reaction was only observed after 7 days of curing.

5. Chemistry- and temperature-based correlations can be implemented in the prediction of different characteristics of alkali-activated materials

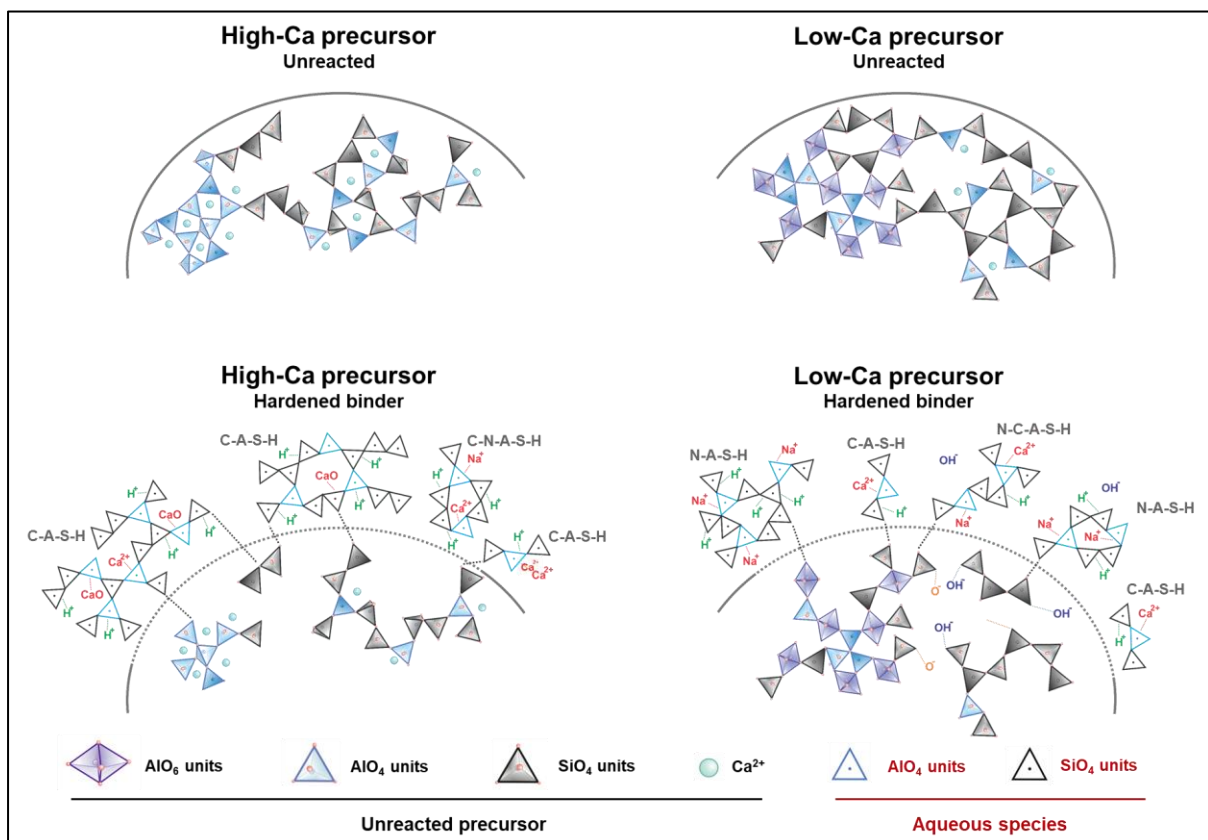


Figure 8.7: Schematic illustration of the differences in reaction products formed during the activation of high- and low-Ca precursors.

As mentioned in Chapter 1, one of the main challenges of alkali-activated materials lies in the variations of the chemical compositions and mineralogy of precursors, whether they are obtained as industrial byproducts or as natural materials. Still in Chapter 1, the use of chemistry-based approaches was suggested as a method to increase the relevance and applicability of these binders, and in different sections of this thesis, correlations were found for different properties of the investigated systems with both intrinsic and extrinsic characteristics of the mixtures.

The reaction potential of one precursor was shown to be influenced by three parameters, which have been extensively used as the main drivers for the estimated characteristics:

- i. Ca, as a network modifying component in glass structures, was demonstrated in Chapter 3 to facilitate the breakage of atomic bonds of network formers (i.e. Si-O and Al-O) and disrupt the overall framework. Consequently, the element acts as an intrinsic agent for the reactivity enhancement of precursors, as observed by dissolution kinetics, in Chapter 4, and degree of reaction, in Chapter 6.
- ii. The alkalinity of the solution is directly correlated with the reaction potential of a system as an external factor, since it provides OH⁻ units which facilitate the hydrolysis of Si-O and Al-O bonds. Increasing the alkalinity of the activator is an extrinsic reactivity enhancement action, but the concentration of the activator should be carefully chosen: when in excess, activators can limit the long term reactivity as shown in Chapter 6.
- iii. The implementation of different curing regimes has additional positive impacts in dissolution and reactivity. The curing regime of 60 °C provides more opportunity to overcome the energy barrier for breakage of bonds, enhancing the dissolution potential of fly ash-type glasses in Chapter 4, reducing the solubility of most reaction products, and accelerating the evolution of reaction degree in Chapter 6.

The nature of the activating solution was also shown to influence the characteristics of the investigated systems, influencing the early (dissolution kinetics and mechanisms of phase precipitation) and later stages (porosity of the microstructure, homogeneity of the matrix, adhesion of particles to the matrix) of reaction, as schematically shown in Figure 8.7. Waterglass solutions provide an additional presence of aqueous silicate species homogeneously distributed in the pore solution, which promote the formation of Si-bearing phases throughout the whole matrix and provide an additional contribution to the reaction extent. In summary, 6 different chemistry-temperature-solution approaches were proposed, as detailed in Table 8.3.

Table 8.3: Summary of the chemistry-based correlations defined in this thesis.

Chemistry-based approach considerations	Proposed correlation	Thesis allocation
Ca/(Si+Al) and Ca/Al atomic ratios	Amount of Si Q ⁿ (mAl) units in the mineralogy of precursors	Chapter 3 Section 3.3.3
Fraction of Ca in the precursor, with temperature and solution alkalinity using an Arrhenius-type relationship	Forward dissolution rates of Ca, Si and Al	Chapter 4 Section 4.3.4
Chemistry of the precursor, activator, solution/binder ratio and exponential influence of curing temperature	Degree of reaction of pastes prepared with different activators and cured up to 60 °C	Chapter 6 Section 6.4.1
Chemistry of the precursor and activator	Amount of C-(N-A)-S-H gels and secondary crystalline reaction products in the microstructure - see Figure 8.7	Chapter 6 Section 6.4.2
Chemistry of the precursor, activator, and curing temperature	Amount of N-(C-)A-S-H gels in the microstructure - see Figure 8.7	Chapter 6 Section 6.4.2

6. Thermodynamic and kinetic modelling are complementary for accurate simulations

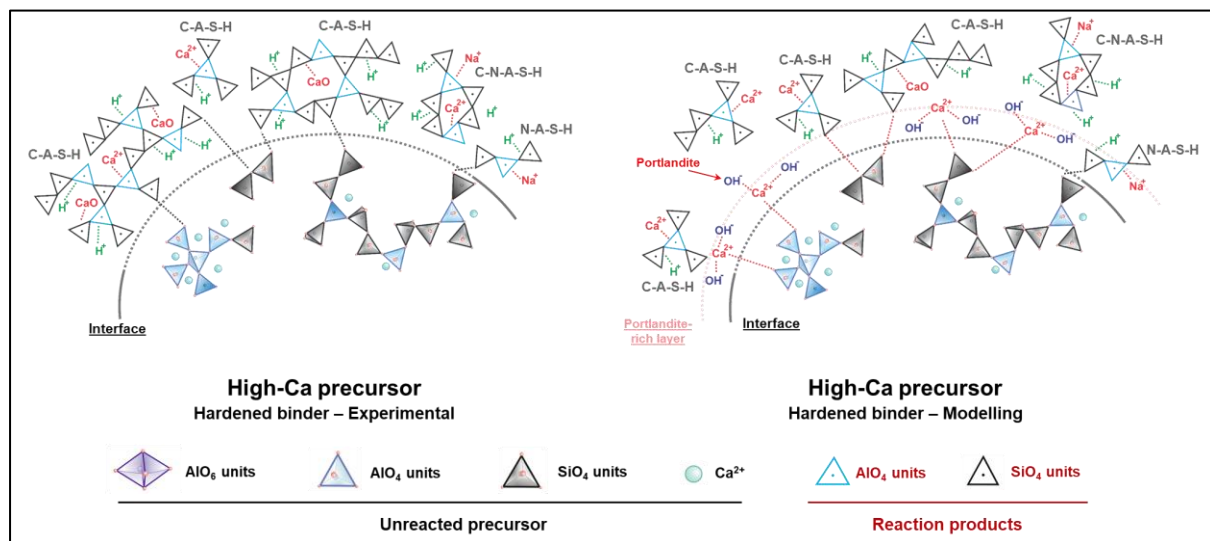


Figure 8.8: Schematic illustration of the differences between hardened binders obtained in experimental and simulated conditions.

The evolution of a binder until reaching a mature microstructure, composed of stable solid products and precursors with optimized degree of reaction, occurs through a sequence of processes. The features of the hardened binder are strongly influenced by the reaction kinetics of these different processes - dissolution, nucleation and growth of reaction products - and by the saturation indices of the reaction products. Chapter 4 demonstrated that the dissolution of precursors is not congruent for all of its components: in most cases, Ca displays faster detachment from the framework, followed by a release of Al and Si - and the congruency (or non-congruency) of the release of these two components is dependent on the curing temperature. Consequently, the contributions of each component to the overall reaction path are not expected to be proportional to their initial amount.

With respect to the digital microstructures simulated with GeoMicro3D, the results achieved in Chapter 7 demonstrated an overall good agreement with experimental findings. The quantitative determination of C-(N-A)-S-H-type gels presented a variance of approx. 10 wt% between the two scenarios, with numerical simulations underestimating the formation of the disordered gel. The reduced presence of the gels was combined with the overestimation of portlandite and other secondary Ca-bearing crystalline phases, following the schematic illustration shown in Figure 8.8. With respect to N-(C-)A-S-H species, the formation of a few zeolite phases was observed to overcome the nucleation of disordered gels in purely thermodynamic simulations performed with GEMs, as these crystalline products are more stable and display lower solubilities than amorphous arrangements.

With these observations, it is concluded that the generation of accurate microstructural models requires a combination of thermodynamic equilibrium constraints, initially, with kinetic considerations, with the latter being aided by experimental observations:

- i. The establishment of upper thermodynamic stability levels of zeolites and the limitation in the amount of considered phases, based on experimental findings, is required to promote the concurrent formation of these crystals with disordered N-(C-)A-S-H gels in the GEMs-based thermodynamic-only simulations. As discussed in Chapter 7, these constraints must be applied to the combined thermodynamic-kinetic modelling to enhance the accuracy of the GeoMicro3D simulation tool.
- ii. The excessive formation of portlandite, observed for the first time in the GEMs-based thermodynamic-only simulations, can also be corrected and lowered with the definition of upper thermodynamic stability limits based on experimental observations. However, the establishment of thermodynamic constraints in GeoMicro3D might hinder its precipitation mechanism as an activated complex, thus requiring additional kinetic constraints to consider portlandite as a temporary transitional component prior to the formation of more stable reaction products.

8.3 Outlooks and recommendations for future research

The utilization of chemistry-temperature correlations for the estimation of the microstructural characteristics of alkali-activated pastes, through both empirical correlations and numerical simulation, was proven to be accurate throughout the findings of this thesis. Nevertheless, the results obtained showed that additional approaches could be considered for the model development, targeting the development of a more relevant and robust microstructural simulation tool. In that context, the following aspects are suggested for future research work:

1. In-depth analysis and quantification of heterogeneous glass structures

The sub-microscopic heterogeneities of the precursors were shown to have great influence over their structures and, consequently, their reaction potential. However, the identification of these structures was only performed at a qualitatively level, which limited the implementation of their influence in the microstructure modelling performed with GeoMicro3D. The atomic arrangement of precursors can be affected by their processing method: for instance, the cooling rate of fly ashes and blast furnace slags, and the grinding methodology of the latter can create variations in their internal structures, which consequently influence their kinetics of reaction in alkali-activated binders. Therefore, the

combination of high precision analytical techniques - such as multidimensional SS NMR analysis with unconventional nuclei, and atom probe tomography - with molecular dynamics simulations could be utilised to provide additional structural characterization, and dissolution rates of precursors could be empirically determined based in initial glass structures.

2. Extend the range of the chemistry-based approach

Due to the chosen approach of investigation and to limitations with equipment, the precursors synthesized in this thesis were composed of only three oxides and had a relatively high CaO content. While this accurately replicated the composition and structure of fly ashes and slags, a few precursors do not fall in this range, e.g. Si-rich components - such as metakaolin and other calcined clays, rice husk ashes and other organic ashes - and other precursors bearing secondary components such as Mg, Fe, and Na, which are known to have major roles in commonly observed reaction products. Two routes could be implemented to extend the application range of the correlations proposed in this thesis:

- i. Experimental route: synthesis of additional glasses, evaluating the influence of other network modifying oxides in the kinetics of reaction and development of microstructures; additional curing regimes in temperatures beyond the 20 - 60 °C range;
- ii. Simulation route: utilization of force field models through molecular dynamics, to quantify the weakening effect of different network modifying oxides in Si-O-T networks, and the consequential influences in the reaction potential of the modified structures.

3. Utilise in-situ scans for monitoring early-stage reactions

The correlations made between pastes cured for 24 hours and dissolution experiments provided complementary observations of early-stage reactions, covering dissolution phenomena and initial phase precipitation. While the combination of SEM imaging with infrared characterization provided insights into the structural build-up of gels, the implementation of in-situ scanning techniques (such as XRD and pair distribution function - PDF) could provide detailed and fundamental information over the evolution of the atomic arrangement of the precipitated gels, providing important details over, for instance, the interactions of Ca with newly precipitated phases (either as a main component or charge balancing cation), or the ordering range and conversion of N-(C-)A-S-H-type gels into ordered structures resembling zeolite crystals.

4. Evaluate the mechanical properties of gels

Among the many potential applications of the simulated microstructures, the investigation of the mechanical properties of alkali-activated materials is perhaps the most important one. As demonstrated in this thesis, the utilization of synthetic precursors with simplified chemistry facilitated the formation of separate N-(C-)A-S-H and C-(N-A)S-H gels, and careful mix design is expected to promote the nucleation of specific gel compositions in

hardened binders. The use of accurate tools, such as nanoindentation, is therefore suggested to experimentally determine the mechanical properties of these reaction products, which would be crucial for the application of the microstructures obtained via GeoMicro3D in further modelling activities.

5. Thermodynamic and kinetic considerations of intermediate products

The formation of intermediate metastable complexes was observed to play a great influence in the reaction kinetics in all tested precursors. As demonstrated in Chapter 5, the precipitation of portlandite was usually the first indicator of the evolution of the reaction, which later was destabilized for the formation of other stable reaction products. However, while the numerical models identified the early nucleation of the component in early stages and positively demonstrated the replication of dissolution kinetics, the precipitated portlandite reduced the accuracy of the quantitative formation of other primary phases. For future works, the implementation of two new features in GeoMicro3D is suggested:

- i. In-depth study of the activity of intermediate complexes and their inclusion into the empirically defined dissolution rate equations, since these components have been shown to interact with the surrounding solution and consequently decelerate the kinetics of dissolution;
- ii. The implementation of phase transformations into GeoMicro3D, which would allow the initially precipitated portlandite to provide Ca ions for the formation of more stable reaction products, such as C-(N-A)-S-H-type gels and other Ca-bearing phases.

References

- [1] A. Khaertdinova, A. Maliashova, S. Gadelshina, Economic development of the construction industry as a basis for sustainable development of the country, *E3S Web Conf.* 274 (2021).
- [2] P.M. Hillebrandt, The construction industry and the economy, in: *Econ. Theory Constr. Ind.*, 3rd editio, MacMillan Press LTD, London, 2000: pp. 19-28.
- [3] S. Dlamini, The relationship of the construction sector to economic growth: analysis of South African and UK construction sectors, University of Reading, 2014.
- [4] B.A. Souza, C. Araújo, C. Oliveira, J. Carlos, O. De Santana, L. Antônio, V. Neto, Análise dos indicadores pib nacional e pib da indústria da construção civil (Analysis of national gdp indicators and gdp industry construction) Importância da indústria Importância do PIB para a economia nacional, *Rev. Desenvolv. Econômico Salvador* 17 (2015) 140-150.
- [5] L.S. Pheng, L.S. Hou, *The Economy and the Construction Industry*, 2019.
- [6] C.R. Gagg, Cement and concrete as an engineering material: An historic appraisal and case study analysis, *Eng. Fail. Anal.* (2014).
- [7] S.A. Miller, A. Horvath, P.J.M. Monteiro, Impacts of booming concrete production on water resources worldwide, *Nat. Sustain.* 1 (2018) 69-76.
- [8] J.M. Uratani, S. Griffiths, A forward looking perspective on the cement and concrete industry: Implications of growth and development in the Global South, *Energy Res. Soc. Sci.* 97 (2023) 102972.
- [9] Z. Huang, J. Wang, L. Bing, Y. Qiu, R. Guo, Global carbon uptake of cement carbonation accounts 1930-2021, *Earth Syst. Sci. Data* 15 (2023) 1-28.
- [10] F.A. Scrivener K., Habert G., De Wolf C., A sustainable future for the European cement and concrete industry. Technology assessment for full decarbonisation of the industry by 2050, ETH Zurich, 2019.
- [11] P. Friedlingstein, M.W. Jones, M. O'Sullivan, R.M. Andrew, D.C.E. Bakker, Global Carbon Budget 2021, raport Earth System Science Data, *Earth Syst. Sci. Data* 14 (2022) 1917-2005.
- [12] International Energy Agency, International Renewable Energy Agency, UN Climate Change High-Level Champions, The Breakthrough Agenda Report 2023. Accelerating Sector Transitions Through Stronger International Collaboration, (2023) 1-179.
- [13] X. Wang, P. Song, H. Yu, P. Taylor, S. Sadati, K. Freeseaman, Y. Ning, Extended life concrete bridge decks utilizing internal curing to reduce cracking - Materials characterization and engineering demonstration, *Constr. Build. Mater.* 275 (2021) 122163.
- [14] S.A. Bernal, J.L. Provis, D.G. Brice, A. Kilcullen, P. Duxson, J.S.J. Van Deventer, Accelerated carbonation testing of alkali-activated binders significantly underestimates service life: The role of pore solution chemistry, *Cem. Concr. Res.* 42 (2012) 1317-1326.
- [15] H. Saadatmanesh, Extending service life of concrete and masonry structures with fiber composites, *Constr. Build. Mater.* 11 (1997) 327-335.
- [16] Á.D. La Rosa, J.J. Ortega, G. Ruiz, J.L.G. Calvo, F.J.R. Sánchez, Á. Castillo, Cement and Concrete Research Autogenous self-healing induced by compressive fatigue in self-compacting steel-fiber reinforced concrete, *Cem. Concr. Res.* 173 (2023) 107278.
- [17] L. Peng, P. Shen, C.S. Poon, Y. Zhao, F. Wang, Development of carbon capture coating to improve the durability of concrete structures, *Cem. Concr. Res.* 168 (2023) 107154.
- [18] S. Jones, N. Martys, Y. Lu, D. Bentz, Simulation studies of methods to delay corrosion and

- increase service life for cracked concrete exposed to chlorides, *Cem. Concr. Compos.* 58 (2015) 59-69.
- [19] P.N. Venevere, An Artificial Concrete Aggregate Made From Coal Combustion Ashes, *Cem. Concr. Res.* 21 (1991) 262-268.
- [20] C. Pan, Y. Song, J. Wang, S. Zhan, C. Unluer, S. Ruan, Unlocking the role of recycled aggregates in the performance enhancement and CO₂ capture of reactive magnesia cement formulations, *Cem. Concr. Res.* 168 (2023) 107148.
- [21] A. Seco, J.M. del Castillo, C. Perlot, S. Marcelino, S. Espuelas, Recycled granulates manufacturing from spent refractory wastes and magnesium based binder, *Constr. Build. Mater.* 365 (2023) 130087.
- [22] Y. Liu, C. Yang, F. Wang, S. Hu, M. Zhu, C. Hu, L. Lu, Performance evaluation of regenerated clinker from completely recyclable mortar, *Constr. Build. Mater.* 309 (2021) 125184.
- [23] K.K. Sagoe-Crentsil, T. Brown, A.H. Taylor, Performance of concrete made with commercially produced coarse recycled concrete aggregate, *Cem. Concr. Res.* 31 (2001) 707-712.
- [24] D. Hou, D. Wu, X. Wang, S. Gao, R. Yu, M. Li, P. Wang, Y. Wang, Sustainable use of red mud in ultra-high performance concrete (UHPC): Design and performance evaluation, *Cem. Concr. Compos.* 115 (2021).
- [25] C. Shi, B. Qu, J.L. Provis, Recent progress in low-carbon binders, *Cem. Concr. Res.* 122 (2019) 227-250.
- [26] N. Ouffa, R. Trauchessec, M. Benzaazoua, A. Lecomte, T. Belem, A methodological approach applied to elaborate alkali-activated binders for mine paste backfills, *Cem. Concr. Compos.* 127 (2022).
- [27] S. Nasiru, L. Jiang, L. Yu, H. Chu, Y. Huang, C. Pei, Y. Gu, W. Jin, E. Eyrarn Klu, M.Z. Guo, Properties of cement mortar containing recycled glass and rice husk ash, *Constr. Build. Mater.* 299 (2021) 123900.
- [28] A. Maldonado-Alameda, J. Mañosa, T. López-Montero, R. Catalán-Parra, High-porosity alkali-activated binders based on glass and aluminium recycling industry waste, *Constr. Build. Mater.* 400 (2023).
- [29] L. Rossi, L.M. de Lima, Y. Sun, F. Dehn, J.L. Provis, G. Ye, G. De Schutter, Future perspectives for alkali-activated materials: from existing standards to structural applications, *RILEM Tech. Lett.* 7 (2022) 159-177.
- [30] A. Adesina, Performance and sustainability overview of alkali-activated self-compacting concrete, *Waste Dispos. Sustain. Energy* 2 (2020) 165-175.
- [31] V.D. Ho, A. Gholampour, D. Losic, T. Ozbakkaloglu, Enhancing the performance and environmental impact of alkali-activated binder-based composites containing graphene oxide and industrial by-products, *Constr. Build. Mater.* 284 (2021) 122811.
- [32] H. El-Hassan, S. Elkholy, Enhancing the performance of Alkali-Activated Slag-Fly ash blended concrete through hybrid steel fiber reinforcement, *Constr. Build. Mater.* 311 (2021) 125313.
- [33] T.A. Aiken, J. Kwasny, W. Sha, K.T. Tong, Mechanical and durability properties of alkali-activated fly ash concrete with increasing slag content, *Constr. Build. Mater.* 301 (2021) 124330.
- [34] J.L. Provis, F. Winnefeld, Outcomes of the round robin tests of RILEM TC 247-DTA on the durability of alkali-activated concrete, *MATEC Web Conf.* 199 (2018).
- [35] D. Bondar, Q. Ma, M. Soutsos, M. Basheer, J.L. Provis, S. Nanukuttan, Alkali activated slag concretes designed for a desired slump, strength and chloride diffusivity, *Constr. Build. Mater.* 190 (2018) 191-199.

- [36] J.L. Provis, S.L. Yong, P. Duxson, Nanostructure/microstructure of metakaolin geopolymers, *Geopolymers Struct. Process. Prop. Ind. Appl.* (2009) 72-88.
- [37] G. Cement, GBFS Focus 2030: Looking beyond Europe, (2022), Online. Available on www.globalcement.com/magazine/articles/1282-gbfs-focus-2030-looking-beyond-europe.
- [38] BP, BP Statistical Review of World Energy 2022,(71st edition), (2022) 1-60.
- [39] The Statistics Portal (Statista), Global cement production in 1990, 2000 and 2010, with forecasts for 2020 and 2030, Online. Available on [Www.Statista.Com/Statistics/373845/Global-Cement-Production-Forecast](http://www.Statista.Com/Statistics/373845/Global-Cement-Production-Forecast).
- [40] IEA - International Energy Association, Coal 2022 - Analysis and forecast to 2025, Coal (2022).
- [41] G.J.G. Gluth, K. Arbi, S.A. Bernal, D. Bondar, A. Castel, S. Chithiraputhiran, A. Dehghan, K. Dombrowski-Daube, A. Dubey, V. Ducman, K. Peterson, P. Pipilikaki, S.L.A. Valcke, G. Ye, Y. Zuo, J.L. Provis, RILEM TC 247-DTA round robin test: carbonation and chloride penetration testing of alkali-activated concretes, *Mater. Struct. Constr.* 53 (2020) 1-17.
- [42] F. Winnefeld, G.J.G. Gluth, S.A. Bernal, M.C. Bignozzi, L. Carabba, S. Chithiraputhiran, A. Dehghan, S. Dolenec, K. Dombrowski-Daube, A. Dubey, V. Ducman, Y. Jin, K. Peterson, D. Stephan, J.L. Provis, RILEM TC 247-DTA round robin test: sulfate resistance, alkali-silica reaction and freeze-thaw resistance of alkali-activated concretes, *Mater. Struct. Constr.* 53 (2020) 1-17.
- [43] R. Snellings, P. Suraneni, J. Skibsted, Future and emerging supplementary cementitious materials, *Cem. Concr. Res.* 171 (2023).
- [44] P. Suraneni, A. Hajibabaei, S. Ramanathan, Y. Wang, J. Weiss, New insights from reactivity testing of supplementary cementitious materials, *Cem. Concr. Compos.* 103 (2019) 331-338.
- [45] S. Ramanathan, M. Croly, P. Suraneni, Comparison of the effects that supplementary cementitious materials replacement levels have on cementitious paste properties, *Cem. Concr. Compos.* 112 (2020) 103678.
- [46] J.L. Provis, J.S.J. Van Deventer, Alkali Activated Materials: State-Of-The-Art Report, RILEM TC 224-AAM, Springer Science & Business Media, 2013.
- [47] T. Xie, P. Visintin, X. Zhao, R. Gravina, Mix design and mechanical properties of geopolymer and alkali activated concrete: Review of the state-of-the-art and the development of a new unified approach, *Constr. Build. Mater.* 256 (2020) 119380.
- [48] Z. Zhang, J.L. Provis, J. Zou, A. Reid, H. Wang, Toward an indexing approach to evaluate fly ashes for geopolymer manufacture, *Cem. Concr. Res.* 85 (2016) 163-173.
- [49] N. Li, C.J. Shi, Z.H. Zhang, D.J. Zhu, H.-J.J. Hwang, Y.H. Zhu, T.J. Sun, Z. Zhanga, D. Zhua, H.-J.J. Hwang, Y.H. Zhu, T.J. Sun, A mixture proportioning method for the development of performance-based alkali-activated slag-based concrete, *Cem. Concr. Compos.* 93 (2018) 163-174.
- [50] S.A. Bernal, E.D. Rodríguez, A.P. Kirchheim, J.L. Provis, Management and valorisation of wastes through use in producing alkali-activated cement materials, *J. Chem. Technol. Biotechnol.* 91 (2016) 2365-2388.
- [51] M. Mejdí, M. Saillio, T. Chaussadent, L. Divet, A. Tagnit-Hamou, Hydration mechanisms of sewage sludge ashes used as cement replacement, *Cem. Concr. Res.* 135 (2020) 106115.
- [52] H. Ilcan, O. Sahin, Z. Unsal, E. Ozcelikci, A. Kul, N. Cağatay Demiral, M. Ozkan Ekinci, M. Sahmaran, Effect of industrial waste-based precursors on the fresh, hardened and environmental performance of construction and demolition wastes-based geopolymers, *Constr. Build. Mater.* 394 (2023) 132265.
- [53] M. Giels, T. Hertel, K. Gijbels, W. Schroevers, Y. Pontikes, High performance mortars from vitrified bauxite residue; the quest for the optimal chemistry and processing conditions,

- Cem. Concr. Res. 155 (2022) 106739.
- [54] B. Chen, P. Perumal, M. Illikainen, G. Ye, A review on the utilization of municipal solid waste incineration (MSWI) bottom ash as a mineral resource for construction materials, *J. Build. Eng.* 71 (2023) 106386.
 - [55] R.J. Myers, S.A. Bernal, J.L. Provis, Phase diagrams for alkali-activated slag binders, *Cem. Concr. Res.* 95 (2017) 30-38.
 - [56] B. Lothenbach, M. Zajac, Application of thermodynamic modelling to hydrated cements, *Cem. Concr. Res.* 123 (2019) 105779.
 - [57] D. Damidot, B. Lothenbach, D. Herfort, F.P. Glasser, Thermodynamics and cement science, *Cem. Concr. Res.* 41 (2011) 679-695.
 - [58] R.J. Myers, S.A. Bernal, J.L. Provis, A thermodynamic model for C-(N-)A-S-H gel: CNASH-ss. Derivation and validation, *Cem. Concr. Res.* 66 (2014) 27-47.
 - [59] Y. Zuo, G. Ye, GeoMicro3D: A novel numerical model for simulating the reaction process and microstructure formation of alkali-activated slag, *Cem. Concr. Res.* 141 (2021) 106328.
 - [60] C. Ouellet-Plamondon, G. Habert, Life cycle assessment (LCA) of alkali-activated cements and concretes, Woodhead Publishing Limited, 2015.
 - [61] P. Duxson, J.L. Provis, G.C. Lukey, J.S.J. van Deventer, The role of inorganic polymer technology in the development of "green concrete," *Cem. Concr. Res.* (2007).
 - [62] N. Li, C. Shi, Z. Zhang, H. Wang, Y. Liu, A review on mixture design methods for geopolymer concrete, *Compos. Part B Eng.* 178 (2019) 107490.
 - [63] P. Duxson, A. Fernández-Jiménez, J.L. Provis, G.C. Lukey, A. Palomo, J.S.J. Van Deventer, Geopolymer technology: The current state of the art, *J. Mater. Sci.* 42 (2007) 2917-2933.
 - [64] A. Herrmann, A. Koenig, F. Dehn, Structural concrete based on alkali-activated binders: Terminology, reaction mechanisms, mix designs and performance, *Struct. Concr.* 19 (2018) 918-929.
 - [65] J.C.B. Moraes, M.M. Tashima, J.L. Akasaki, J.L.P. Melges, J. Monzó, M. V. Borrachero, L. Soriano, J. Payá, Effect of sugar cane straw ash (SCSA) as solid precursor and the alkaline activator composition on alkali-activated binders based on blast furnace slag (BFS), *Constr. Build. Mater.* 144 (2017) 214-224.
 - [66] I.I. Bashar, U.J. Alengaram, M.Z. Jumaat, A. Islam, H. Santhi, A. Sharmin, Engineering properties and fracture behaviour of high volume palm oil fuel ash based fibre reinforced geopolymer concrete, *Constr. Build. Mater.* 111 (2016) 286-297.
 - [67] S.A. Bernal, E.D. Rodríguez, R. Mejia De Gutiérrez, J.L. Provis, S. Delvasto, Activation of metakaolin/slag blends using alkaline solutions based on chemically modified silica fume and rice husk ash, *Waste and Biomass Valorization* 3 (2012) 99-108.
 - [68] Y.W. Liu, C.J. Shi, Z.H. Zhang, N. Li, An overview on the reuse of waste glasses in alkali-activated materials, 144 (2019) 297-309.
 - [69] A. Maldonado-Alameda, J. Giro-Paloma, A. Svobodova-Sedlackova, J. Formosa, J.M. Chimenos, Municipal solid waste incineration bottom ash as alkali-activated cement precursor depending on particle size, *J. Clean. Prod.* 242 (2020) 118443.
 - [70] H.T. Nguyen, N.N. Hoa, D.T. Vu, P.T. Kien, Properties of Geopolymer from Coal Bottom Ash and Water Glass Solution, (2016).
 - [71] M.C. Bignozzi, L. Barbieri, I. Lancellotti, New Geopolymers Based on Electric Arc Furnace Slag, *Adv. Sci. Technol.* 69 (2010) 117-122.
 - [72] I. Garcia Lodeiro, N. Cristelo, A. Palomo, A. Fernández-Jiménez, Use of industrial by-products as alkaline cement activators, *Constr. Build. Mater.* 253 (2020) 119000.

- [73] T.S. Naidu, C.M. Sheridan, L.D. van Dyk, Basic oxygen furnace slag: Review of current and potential uses, *Miner. Eng.* 149 (2020) 106234.
- [74] P. Ter Teo, S.K. Zakaria, S.Z. Salleh, M.A.A. Taib, N.M. Sharif, A.A. Seman, J.J. Mohamed, M. Yusoff, A.H. Yusoff, M. Mohamad, M.N. Masri, S. Mamat, Assessment of electric arc furnace (EAF) steel slag waste's recycling options into value added green products: A review, *Metals (Basel)*. 10 (2020) 1-21.
- [75] K. Tamanna, S.N. Raman, M. Jamil, R. Hamid, Coal bottom ash as supplementary material for sustainable construction: A comprehensive review, *Constr. Build. Mater.* 389 (2023) 131679.
- [76] L. Wang, N. Sun, H. Tang, W. Sun, A Review on Comprehensive Utilization of Red Mud, *Minerals* 9 (2019).
- [77] A. Adesina, Durability and microstructural characteristics of alkali activated materials made with waste glass as precursor: A review, *Clean. Mater.* 6 (2022).
- [78] J. Skibsted, M.D. Andersen, The effect of alkali ions on the incorporation of aluminum in the calcium silicate hydrate (C-S-H) phase resulting from portland cement hydration studied by ²⁹Si MAS NMR, *J. Am. Ceram. Soc.* 96 (2013) 651-656.
- [79] C.K. Yip, G.C. Lukey, J.S.J. Van Deventer, The coexistence of geopolymeric gel and calcium silicate hydrate at the early stage of alkaline activation, *Cem. Concr. Res.* 35 (2005) 1688-1697.
- [80] A. Font, L. Soriano, S.M. de Moraes Pinheiro, M.M. Tashima, J. Monzó, M.V. Borrachero, J. Payá, Design and properties of 100% waste-based ternary alkali-activated mortars: Blast furnace slag, olive-stone biomass ash and rice husk ash, *J. Clean. Prod.* 243 (2020).
- [81] I. Garcia-lodeiro, A. Palomo, Effect of calcium on the alkaline activation of aluminosilicate glass, *Ceram. Int.* 42 (2016) 7697-7707.
- [82] S.A. Bernal, J.L. Provis, B. Walkley, R. San Nicolas, J.D. Gehman, D.G. Brice, A.R. Kilcullen, P. Duxson, J.S.J. Van Deventer, Gel nanostructure in alkali-activated binders based on slag and fly ash, and effects of accelerated carbonation, *Cem. Concr. Res.* 53 (2013) 127-144.
- [83] J.L. Provis, S.A. Bernal, Geopolymers and Related Alkali-Activated Materials, *Annu. Rev. Mater. Res.* 44 (2014) 299-327.
- [84] I. Garcia-Lodeiro, A. Fernández-Jimenez, P. Pena, A. Palomo, Alkaline activation of synthetic aluminosilicate glass, *Ceram. Int.* 40 (2014) 5547-5558.
- [85] T. Bakharev, Geopolymeric materials prepared using Class F fly ash and elevated temperature curing, *Cem. Concr. Res.* 35 (2005) 1224-1232.
- [86] F. Winnefeld, A. Leemann, M. Lucuk, P. Svoboda, M. Neuroth, Assessment of phase formation in alkali activated low and high calcium fly ashes in building materials, *Constr. Build. Mater.* 24 (2010) 1086-1093.
- [87] A. Fernández-Jiménez, A. Palomo, Composition and microstructure of alkali activated fly ash binder: Effect of the activator, *Cem. Concr. Res.* 35 (2005) 1984-1992.
- [88] G. Le Saoût, M. Ben Haha, F. Winnefeld, B. Lothenbach, H. Degree, Hydration Degree of Alkali-Activated Slags : A ²⁹Si NMR Study, *J. Am. Ceram. Soc.* 94 (2021) 4541-4547.
- [89] T. Schade, F. Bellmann, B. Middendorf, Quantitative analysis of C-(K)-A-S-H-amount and hydrotalcite phase content in finely ground highly alkali-activated slag/silica fume blended cementitious material, *Cem. Concr. Res.* 153 (2022).
- [90] F. Puertas, A. Fernández-Jiménez, M.T. Blanco-Varela, Pore solution in alkali-activated slag cement pastes. Relation to the composition and structure of calcium silicate hydrate, *Cem. Concr. Res.* 34 (2004) 139-148.
- [91] M.D.A. Thomas, Optimizing the Use of Fly Ash in Concrete, *Portl. Cem. Assoc.* (2007) 24.

- [92] C. Heidrich, H. Feuerborn, A. Weir, Coal Combustion Products : a Global Perspective, (2013).
- [93] D. Hardjito, B. V Rangan, Development and Properties of Low-calcium Fly Ash Based Geopolymer Concrete, Curtin University of Technology, Faculty of Engineering, 2005.
- [94] C. Li, Y. Li, H. Sun, L. Li, The composition of fly ash glass phase and its dissolution properties applying to geopolymeric materials, *J. Am. Ceram. Soc.* 94 (2011) 1773-1778.
- [95] R.T. Chancey, P. Stutzman, M.C.G.G. Juenger, D.W. Fowler, Comprehensive phase characterization of crystalline and amorphous phases of a Class F fly ash, *Cem. Concr. Res.* 40 (2010) 146-156.
- [96] R.T. Hemmings, E.E. Berry, On the Glass in Coal Fly Ashes: Recent Advances, *MRS Proc.* 113 (1987).
- [97] G. Wei, B. Dong, G. Fang, Y. Wang, Understanding reactive amorphous phases of fly ash through the acidolysis, *Cem. Concr. Compos.* 140 (2023) 105102.
- [98] J. Ibáñez, O. Font, N. Moreno, J.J. Elvira, S. Alvarez, X. Querol, Quantitative Rietveld analysis of the crystalline and amorphous phases in coal fly ashes, *Fuel* (2013).
- [99] M. Criado, A. Fernández-Jiménez, A.G. de la Torre, M.A.G. Aranda, A. Palomo, An XRD study of the effect of the SiO₂/Na₂O ratio on the alkali activation of fly ash, *Cem. Concr. Res.* 37 (2007) 671-679.
- [100] R.S. Winburn, D.G. Grier, G.J. McCarthy, R.B. Peterson, Rietveld quantitative X-ray diffraction analysis of NIST fly ash standard reference materials, *Powder Diffr.* 15 (2000) 163-172.
- [101] World Steel Association, Steel facts, (2018).
- [102] R. Dones, T. Heck, Greenhouse Gas Emissions from Energy Systems, *Encycl. Energy* 3 (2004) 77-95.
- [103] I. Garcia-Lodeiro, A. Palomo, A. Fernández-Jiménez, Ch. 2: An overview of the chemistry of alkali-activated cement-based binders, in: *Handb. Alkali-Activated Cem. Mortars Concr.*, Woodhead Publishing Limited, 2015: pp. 19-47.
- [104] Y. Sun, L.M. de Lima, L. Rossi, D. Jiao, Z. Li, G. Ye, G. De Schutter, Interpretation of the early stiffening process in alkali-activated slag pastes, *Cem. Concr. Res.* 167 (2023) 107118.
- [105] F. Avet, R. Snellings, A. Alujas Diaz, M. Ben Haha, K. Scrivener, Development of a new rapid, relevant and reliable (R3) test method to evaluate the pozzolanic reactivity of calcined kaolinitic clays, *Cem. Concr. Res.* 85 (2016) 1-11.
- [106] S. Chithiraputhiran, N. Neithalath, Isothermal reaction kinetics and temperature dependence of alkali activation of slag, fly ash and their blends, *Constr. Build. Mater.* 45 (2013) 233-242.
- [107] B.S. Gebregziabiher, R. Thomas, S. Peethamparan, Very early-age reaction kinetics and microstructural development in alkali-activated slag, *Cem. Concr. Compos.* 55 (2015) 91-102.
- [108] Y. Zuo, M. Nedeljković, G. Ye, Coupled thermodynamic modelling and experimental study of sodium hydroxide activated slag, *Constr. Build. Mater.* 188 (2018) 262-279.
- [109] T. Williamson, M.C.G. Juenger, The role of activating solution concentration on alkali-silica reaction in alkali-activated fly ash concrete, *Cem. Concr. Res.* (2016).
- [110] G.S. Ryu, Y.B. Lee, K.T. Koh, Y.S. Chung, The mechanical properties of fly ash-based geopolymer concrete with alkaline activators, *Constr. Build. Mater.* 47 (2013) 409-418.
- [111] F. Puertas, B. González-Fonteboa, I. González-Taboada, M.M. Alonso, M. Torres-Carrasco, G. Rojo, F. Martínez-Abella, Alkali-activated slag concrete: Fresh and hardened behaviour, *Cem. Concr. Compos.* 85 (2018) 22-31.

- [112] A. Komkova, G. Habert, Environmental impact assessment of alkali-activated materials: Examining impacts of variability in constituent production processes and transportation, *Constr. Build. Mater.* 363 (2023) 129032.
- [113] P. Duxson, J.L. Provis, Designing precursors for geopolymer cements, *J. Am. Ceram. Soc.* 91 (2008) 3864-3869.
- [114] M. Palacios, S. Gismera, M.M. Alonso, J.B. d'Espinose de Lacaillerie, B. Lothenbach, A. Favier, C. Brumaud, F. Puertas, Early reactivity of sodium silicate-activated slag pastes and its impact on rheological properties, *Cem. Concr. Res.* 140 (2021) 106302.
- [115] F. Puertas, C. Varga, M.M. Alonso, Rheology of alkali-activated slag pastes. Effect of the nature and concentration of the activating solution, *Cem. Concr. Compos.* 53 (2014) 279-288.
- [116] M. Palacios, P.F.G. Banfill, F. Puertas, Rheology and setting of alkali-activated slag pastes and mortars: Effect if organic admixture, *ACI Mater. J.* 105 (2008) 140-148.
- [117] C. Qing-Hua, S.L. Sarkar, A study of rheological and mechanical properties of mixed alkali activated slag pastes, *Adv. Cem. Based Mater.* 1 (1994) 178-184.
- [118] E. Douglas, A. Bilodeau, V.M. Malhotra, Properties and durability of alkali-activated slag concrete, *ACI Mater. J.* 89 (1992) 509-516.
- [119] S. Aydın, B. Baradan, Effect of activator type and content on properties of alkali-activated slag mortars, *Compos. Part B Eng.* 57 (2014) 166-172.
- [120] B. Looney, Statistical Review of World Energy globally consistent data on world energy markets . and authoritative publications in the field of energy, *Rev. World Energy Data* 70 (2021) 8-20.
- [121] IEA - International Energy Association, Global Energy Review 2020, *Glob. Energy Rev.* 2020 (2020).
- [122] WorldSteel Association, Steel statistical yearbook 2020, (2020).
- [123] D.C.R. Center, Overview of the Steel and Iron Ore Market, (2020).
- [124] Accenture, Steel Demand Beyond 2030, *Steel Demand Beyond 2030 - Forecast Scenar.* (2017) 24-25.
- [125] A. Sarabèr, Co-combustion and its impact on fly ash quality; Pilot-scale experiments, *Fuel Process. Technol.* 104 (2012) 105-114.
- [126] M.F. Wu, W.H. Huang, Evaluation of Fly Ash from Co-Combustion of Paper Mill Wastes and Coal as Supplementary Cementitious Materials, *Materials (Basel).* 15 (2022).
- [127] F. Faleschini, M.A. Zanini, K. Brunelli, C. Pellegrino, Valorization of co-combustion fly ash in concrete production, *Mater. Des.* 85 (2015) 687-694.
- [128] P.O. Awoyera, O.E. Babalola, O.G. Aluko, The Structural Integrity of Recycled Aggregate Concrete Produced with Fillers and Pozzolans, in: *Struct. Integr. Recycl. Aggreg. Concr. Prod. With Fill. Pozzolans*, Woodhead Publishing Limited, 2021: pp. 145-170.
- [129] G.C. Wang, Ferrous metal production and ferrous slags, *Util. Slag Civ. Infrastruct. Constr.* (2016) 9-33.
- [130] H.R. Kokal, M.G. Ranade, Fluxes for Metallurgy, (1985) 661-675.
- [131] J.L. Provis, Alkali-activated materials, *Cem. Concr. Res.* 114 (2018) 40-48.
- [132] B. Sun, Y. Sun, G. Ye, G. De Schutter, A mix design methodology of slag and fly ash-based alkali-activated paste, *Cem. Concr. Compos.* 126 (2022) 104368.
- [133] R.S. Bie, X.F. Song, Q.Q. Liu, X.Y. Ji, P. Chen, Studies on effects of burning conditions and rice husk ash (RHA) blending amount on the mechanical behavior of cement, *Cem. Concr.*

- Compos. 55 (2015) 162-168.
- [134] W. Kroehong, T. Sinsiri, C. Jaturapitakkul, P. Chindaprasirt, Effect of palm oil fuel ash fineness on the microstructure of blended cement paste, *Constr. Build. Mater.* 25 (2011) 4095-4104.
 - [135] M. Amer Salih, N. Farzadnia, R. Demirboga, A.A.A. Ali, Effect of elevated temperatures on mechanical and microstructural properties of alkali-activated mortar made up of POFA and GGBS, *Constr. Build. Mater.* 328 (2022) 127041.
 - [136] G.F. Huseien, M. Khamsehchi, Z. Kubba, O. Benjeddou, M.J. Mahmoodi, Freeze-thaw cycle and abrasion resistance of alkali-activated FA and POFA-based mortars: Role of high volume GBFS incorporation, *Heliyon* 9 (2023) e17672.
 - [137] J.C.B. Moraes, J.P.B. Batista, M.J.B. Moraes, L.M. Gavioli, M.M. Tashima, J.L. Akasaki, A. Font, L. Soriano, M. V. Borrachero, J. Payá, Durability to chemical attacks and life cycle assessment of alkali-activated binders based on blast furnace slag and sugar cane straw ash, *J. Build. Eng.* 76 (2023).
 - [138] J. Castro-Gomes, N. Sedira, E. Grünhäuser Soares, Feasibility for alkali-activation of a Sewage Sludge Ash (SSA), 2022.
 - [139] I. Carević, A. Baričević, N. Štirmer, J. Šantek Bajto, Correlation between physical and chemical properties of wood biomass ash and cement composites performances, *Constr. Build. Mater.* 256 (2020).
 - [140] O.A. Abdulkareem, J.C. Matthews, A.M.M.A. Bakri, Strength and porosity characterizations of blended biomass wood ash-fly ash-based geopolymer mortar, *AIP Conf. Proc.* 2045 (2018).
 - [141] Z. Li, T. Ohnuki, K. Ikeda, Development of paper sludge ash-based geopolymer and application to treatment of hazardous water contaminated with radioisotopes, *Materials (Basel)*. 9 (2016).
 - [142] L. Mengasini, M. Mavroulidou, M.J. Gunn, Alkali-activated concrete mixes with ground granulated blast furnace slag and paper sludge ash in seawater environments, *Sustain. Chem. Pharm.* 20 (2021) 100380.
 - [143] A.K. Varshneya, J.C. Mauro, *Fundamentals of inorganic glass making*, Academic Press, Inc., 1994.
 - [144] W.D. Callister, *Materials Science and Engineering - An Introduction*, John Wiley & Sons, Inc., 2007.
 - [145] T. Oey, K.F. Frederiksen, N. Mascaraque, R. Youngman, M. Balonis, M.M. Smedskjaer, M. Bauchy, G. Sant, The role of the network-modifier's field-strength in the chemical durability of aluminoborate glasses, *J. Non. Cryst. Solids* 505 (2019) 279-285.
 - [146] J. Jiusti, E.D. Zanotto, S.A. Feller, H.J. Austin, H.M. Detar, I. Bishop, D. Manzani, Y. Nakatsuka, Y. Watanabe, H. Inoue, Effect of network formers and modifiers on the crystallization resistance of oxide glasses, *J. Non. Cryst. Solids* 550 (2020) 120359.
 - [147] K.C. Mills, L. Yuan, R.T. Jones, Estimating the physical properties of slags, *J. South. African Inst. Min. Metall.* 111 (2011) 649-658.
 - [148] A. Schöler, F. Winnefeld, M. Ben Haha, B. Lothenbach, The effect of glass composition on the reactivity of synthetic glasses, *J. Am. Ceram. Soc.* 100 (2017) 2553-2567.
 - [149] D.R. Neuville, L. Cormier, V. Montouillout, P. Florian, F. Millot, J.C. Rifflet, D. Massiot, Structure of Mg- and Mg/Ca aluminosilicate glasses: ²⁷Al NMR and Raman spectroscopy investigations, *Am. Mineral.* 93 (2008) 1721-1731.
 - [150] B. Mysen, Structure of Aluminosilicate Melts, *ISIJ Int.* 61 (2021) 2866-2881.
 - [151] B. Mysen, P. Richet, Silicate Glasses and Melt. Chapter 9: Silicate Structure of Aluminosilicate Glass and Melt, in: *Silic. Glas. Melts*, Elsevier, 2019: pp. 301-348.

- [152] B. Walkley, J.L. Provis, Solid-state nuclear magnetic resonance spectroscopy of cements, *Mater. Today Adv.* 1 (2019) 100007.
- [153] B.T. Poe, P.F. Mcmillan, B. Cote, SiO₂-Al₂O₃ Liquids: In-Situ Study by High-Temperature ²⁷Al NMR Spectroscopy and Molecular Dynamics Simulation, *J. Phys. Chem.* (1992) 8220-8224.
- [154] K. Shimoda, Y. Tobu, K. Kanehashi, T. Nemoto, K. Saito, Total understanding of the local structures of an amorphous slag: Perspective from multi-nuclear (²⁹Si, ²⁷Al, ¹⁷O, ²⁵Mg, and ⁴³Ca) solid-state NMR, (2007).
- [155] J. Liu, W. Kong, X. Yang, Q. Wang, Z. He, X. Hou, Polymeric Structure Evolution Behavior Analysis of Aluminosilicate-Based Smelting Slag, *Metals* (Basel). 12 (2022).
- [156] S. Kucharczyk, M. Zajac, C. Stabler, R.M. Thomsen, M. Ben Haha, J. Skibsted, J. Deja, Structure and reactivity of synthetic CaO-Al₂O₃-SiO₂ glasses, *Cem. Concr. Res.* 120 (2019) 77-91.
- [157] D.R. Neuville, L. Cormier, D. Massiot, Al coordination and speciation in calcium aluminosilicate glasses: Effects of composition determined by ²⁷Al MQ-MAS NMR and Raman spectroscopy, *Chem. Geol.* 229 (2006) 173-185.
- [158] S. Diamond, On the glass present in low-calcium and in high-calcium fly ashes, *Cem. Concr. Res.* 13 (1983) 489-464.
- [159] G.J. McCarthy, D.M. Johase, S.J. Steinwand, A. Thedchanamoorthy, X-ray diffraction analysis of fly ash, *Adv. X-Ray Anal.* 34 Thirty-Ninth Annu. Conf. Appl. X-Ray Anal. July 30 - August 3, 1990 34 (1990) 387-394.
- [160] S. Goto, H. Fujimori, A. Hidaka, K. Ioku, Effects of components on the rate of heat liberation of the hydration in the system of glass/gypsum/lime, *J. Eur. Ceram. Soc.* 26 (2006) 771-776.
- [161] B.B. Kenne Dikko, A. Elimbi, M. Cyr, J. Dika Manga, H. Tchakoute Kouamo, Effect of the rate of calcination of kaolin on the properties of metakaolin-based geopolymers, *J. Asian Ceram. Soc.* 3 (2015) 130-138.
- [162] M.A. Longhi, E.D. Rodríguez, S.A. Bernal, J.L. Provis, A.P. Kirchheim, Valorisation of a kaolin mining waste for the production of geopolymers, *J. Clean. Prod.* 115 (2016) 265-272.
- [163] R. Fernandez, F. Martirena, K.L. Scrivener, The origin of the pozzolanic activity of calcined clay minerals: A comparison between kaolinite, illite and montmorillonite, *Cem. Concr. Res.* 41 (2011) 113-122.
- [164] N. Saidi, B. Samet, S. Baklouti, Effect of Composition on Structure and Mechanical Properties of Metakaolin Based PSS-Geopolymer, *Int. J. Mater. Sci.* 3 (2013) 145.
- [165] O. Vogt, N. Ukrainczyk, C. Ballschmiede, E. Koenders, Reactivity and microstructure of metakaolin based geopolymers: Effect of fly Ash and liquid/solid contents, *Materials* (Basel). 12 (2019).
- [166] B. Kim, S. Lee, Review on characteristics of metakaolin-based geopolymer and fast setting, *J. Korean Ceram. Soc.* 57 (2020) 368-377.
- [167] A. Fernández-Jiménez, A. Palomo, Mid-infrared spectroscopic studies of alkali-activated fly ash structure, *Microporous Mesoporous Mater.* 86 (2005) 207-214.
- [168] D. Glosser, P. Suraneni, O.B. Isgor, W.J. Weiss, Using glass content to determine the reactivity of fly ash for thermodynamic calculations, *Cem. Concr. Compos.* 115 (2021) 103849.
- [169] Y. Jin, W. Feng, D. Zheng, Z. Dong, H. Cui, Structure refinement of fly ash in connection with its reactivity in geopolymerization, *Waste Manag.* 118 (2020) 350-359.
- [170] P.K. Mehta, Influence of Fly Ash Characteristics on the Strength of Portland-Fly Ash

- Mixtures, *Cem. Concr. Res.* 15 (1985) 669-674.
- [171] H. Uchikawa, S. Uchida, Effect of Characteristics of Glass Phase in Blending Components on Their Reactivity in Calcium Hydroxide Mixture, 8th Int. Conf. Chem. Cem. 4 (1986) 245-250.
 - [172] A. Hamdan, A. Hajimohammadi, A. Rawal, T. Kim, The intrinsic role of network modifiers (Ca versus Mg) in the reaction kinetics and microstructure of sodium silicate-activated CaO-MgO-Al₂O₃-SiO₂ glasses, *Cem. Concr. Res.* 164 (2023) 107058.
 - [173] K. Scrivener, R. Snellings, B. Lothenbach, A Practical Guide to Microstructural Analysis of Cementitious Materials, CRC Press - Taylor & Francis Group, 2016.
 - [174] W.K.W. Lee, J.S.J. Van Deventer, Structural reorganisation of class F fly ash in alkaline silicate solutions, *Colloids Surfaces A Physicochem. Eng. Asp.* 211 (2002) 49-66.
 - [175] Yibing Zuo, Experimental Study and Numerical Simulation of the Reaction Process and Microstructure Formation of Alkali-Activated Materials, Delft University of Technology, 2019.
 - [176] K.C. Newlands, M. Foss, T. Matschei, J. Skibsted, D.E. Macphee, Early stage dissolution characteristics of aluminosilicate glasses with blast furnace slag- and fly-ash-like compositions, *J. Am. Ceram. Soc.* 100 (2017) 1941-1955.
 - [177] Z. Hu, M. Wyrzykowski, P. Lura, Estimation of reaction kinetics of geopolymers at early ages, *Cem. Concr. Res.* 129 (2020) 105971.
 - [178] H. Ye, A. Radlińska, Quantitative analysis of phase assemblage and chemical shrinkage of Alkali-activated slag, *J. Adv. Concr. Technol.* 14 (2016) 245-260.
 - [179] Z. Zhang, H. Wang, J.L. Provis, F. Bullen, A. Reid, Y. Zhu, Quantitative kinetic and structural analysis of geopolymers. Part 1. the activation of metakaolin with sodium hydroxide, *Thermochim. Acta* 539 (2012) 23-33.
 - [180] L. Weng, K. Sagoe-Crentsil, Dissolution processes, hydrolysis and condensation reactions during geopolymer synthesis: Part I-Low Si/Al ratio systems, *J. Mater. Sci.* 42 (2007) 2997-3006.
 - [181] C.A. Rees, J.L. Provis, G.C. Lukey, J.S.J. van Deventer, The mechanism of geopolymer gel formation investigated through seeded nucleation, *Colloids Surfaces A Physicochem. Eng. Asp.* (2008).
 - [182] R. Zanini, G. Franceschin, E. Cattaruzza, A. Traviglia, A review of glass corrosion: the unique contribution of studying ancient glass to validate glass alteration models, *Mater. Degrad.* 7 (2023) 1-17.
 - [183] R. Dupuis, R. Pellenq, J. Champenois, A. Poulesquen, Dissociation Mechanisms of Dissolved Alkali Silicates in Sodium Hydroxide, *J. Phys. Chem.* 124 (2020) 8288-8294.
 - [184] R. Snellings, Solution-controlled dissolution of supplementary cementitious material glasses at pH 13: The effect of solution composition on glass dissolution rates, *J. Am. Ceram. Soc.* 96 (2013) 2467-2475.
 - [185] J.D. Vienna, J.J. Neeway, J. V. Ryan, S.N. Kerisit, Impacts of glass composition, pH, and temperature on glass forward dissolution rate, *Npj Mater. Degrad.* 2 (2018) 1-12.
 - [186] J.J. Neeway, P.C. Rieke, B.P. Parruzot, J. V. Ryan, R.M. Asmussen, The dissolution behavior of borosilicate glasses in far-from equilibrium conditions, *Geochim. Cosmochim. Acta* 226 (2018) 132-148.
 - [187] S. Gin, L. Neill, M. Fournier, P. Frugier, T. Ducasse, M. Tribet, A. Abdelouas, B. Parruzot, J. Neeway, N. Wall, S. Gin, L. Neill, M. Fournier, P. Frugier, T. Ducasse, The controversial role of inter-diffusion in glass alteration: Implications for Current Long-Term Modeling, *Chem. Geol.* 440 (2016) 115-123.
 - [188] G.V.P.B. Singh, C. Subrahmanyam, K.V.L. Subramaniam, Dissolution of the glassy phase in low-calcium fly ash during alkaline activation, *Adv. Cem. Res.* 30 (2018) 313-322.

- [189] R. Ramaswamy, J. Yliniemi, M. Illikainen, Dissolution-precipitation reactions of silicate mineral fibers at alkaline pH Cement and Concrete Research Dissolution-precipitation reactions of silicate mineral fibers at alkaline pH, *Cem. Concr. Res.* 160 (2022) 106922.
- [190] S. Shi, H. Li, Q. Zhou, H. Zhang, P.A.M. Basheer, Y. Bai, Alkali-activated fly ash cured with pulsed microwave and thermal oven: A comparison of reaction products, microstructure and compressive strength, *Cem. Concr. Res.* 166 (2023) 107104.
- [191] V.B. Jr, R. Novotný, J. Koplík, M. Kadlec, Cement and Concrete Research Philosophy of rational mixture proportioning of alkali-activated materials validated by the hydration kinetics of alkali-activated slag and its microstructure, 168 (2023).
- [192] S.K. Nath, S. Kumar, Role of alkali concentration on reaction kinetics of fly ash geopolymerization, *J. Non. Cryst. Solids* 505 (2019) 241-251.
- [193] D. Ravikumar, N. Neithalath, Reaction kinetics in sodium silicate powder and liquid activated slag binders evaluated using isothermal calorimetry, *Thermochim. Acta* 546 (2012) 32-43.
- [194] Z. Sun, A. Vollpracht, Isothermal calorimetry and in-situ XRD study of the NaOH activated fly ash, metakaolin and slag, *Cem. Concr. Res.* 103 (2018) 110-122.
- [195] I.G. Richardson, G.W. Groves, Microstructure and microanalysis of hardened cement pastes involving ground granulated blast-furnace slag, *J. Mater. Sci.* 27 (1992) 6204-6212.
- [196] H.F.W. Taylor, Nanostructure of CSH: Current status, *Adv. Cem. Based Mater.* (1993).
- [197] F. Puertas, M. Palacios, H. Manzano, J.S. Dolado, A. Rico, J. Rodríguez, A model for the C-A-S-H gel formed in alkali-activated slag cements, *J. Eur. Ceram. Soc.* 31 (2011) 2043-2056.
- [198] S. Grangeon, A. Fernandez-Martinez, A. Baronnet, N. Marty, A. Poulain, E. Elkaïm, C. Roosz, S. Gaboreau, P. Henocq, F. Claret, Quantitative X-ray pair distribution function analysis of nanocrystalline calcium silicate hydrates: A contribution to the understanding of cement chemistry, *J. Appl. Crystallogr.* 50 (2017) 14-21.
- [199] C.E. White, J.L. Provis, B. Bloomer, N.J. Henson, K. Page, In situ X-ray pair distribution function analysis of geopolymer gel nanostructure formation kinetics, *Phys. Chem. Chem. Phys.* 15 (2013) 8573-8582.
- [200] K. Gong, C.E. White, Impact of chemical variability of ground granulated blast-furnace slag on the phase formation in alkali-activated slag pastes, *Cem. Concr. Res.* 89 (2016) 310-319.
- [201] I.G. Richardson, A.R. Brough, R. Brydson, G.W. Groves, C.M. Dobson, Location of aluminium in substituted calcium silicate hydrate (C-S-H) gels as determined by Si-29 and Al-27 NMR and EELS, *J. Am. Ceram. Soc.* 76 (1993) 2285-2288.
- [202] R.R. Lloyd, J.L. Provis, J.S.J. Van Deventer, Microscopy and microanalysis of inorganic polymer cements. 2: The gel binder, *J. Mater. Sci.* 44 (2009) 620-631.
- [203] B. Lothenbach, T. Matschei, G. Möschner, F.P. Glasser, Thermodynamic modelling of the effect of temperature on the hydration and porosity of Portland cement, *Cem. Concr. Res.* 38 (2008) 1-18.
- [204] M. Ben Haha, G. Le Saout, F. Winnefeld, B. Lothenbach, Influence of activator type on hydration kinetics, hydrate assemblage and microstructural development of alkali activated blast-furnace slags, *Cem. Concr. Res.* (2011).
- [205] S.A. Bernal, J.L. Provis, V. Rose, R. Mejía De Gutierrez, Evolution of binder structure in sodium silicate-activated slag-metakaolin blends, *Cem. Concr. Compos.* 33 (2011) 46-54.
- [206] P. Rožek, M. Król, W. Mozgawa, Geopolymer-zeolite composites: A review, *J. Clean. Prod.* 230 (2019) 557-579.
- [207] B. Ma, B. Lothenbach, Synthesis, characterization, and thermodynamic study of selected Na-based zeolites, *Cem. Concr. Res.* 135 (2020) 106111.

- [208] A. Fernández-Jiménez, A. Palomo, Characterisation of fly ashes. Potential reactivity as alkaline cements, *Fuel* 82 (2003) 2259-2265.
- [209] B.S. Mohammed, S. Haruna, M. Mubarak bn Abdul Wahab, M.S. Liew, Optimization and characterization of cast in-situ alkali-activated pastes by response surface methodology, *Constr. Build. Mater.* 225 (2019) 776-787.
- [210] I. García-Lodeiro, A. Fernández-Jiménez, M.T. Blanco, A. Palomo, FTIR study of the sol-gel synthesis of cementitious gels: C-S-H and N-A-S-H, *J. Sol-Gel Sci. Technol.* 45 (2008) 63-72.
- [211] B. Walkley, R. San Nicolas, M.A. Sani, G.J. Rees, J. V. Hanna, J.S.J. van Deventer, J.L. Provis, Phase evolution of C-(N)-A-S-H/N-A-S-H gel blends investigated via alkali-activation of synthetic calcium aluminosilicate precursors, *Cem. Concr. Res.* 89 (2016) 120-135.
- [212] B. Walkley, R. San Nicolas, M.A. Sani, J.D. Gehman, J.S.J. Van Deventer, J.L. Provis, Phase evolution of Na₂O-Al₂O₃-SiO₂-H₂O gels in synthetic aluminosilicate binders, *Dalt. Trans.* 45 (2016) 5521-5535.
- [213] Z. Peng, K. Vance, A. Dakhane, R. Marzke, N. Neithalath, Microstructural and ²⁹Si MAS NMR spectroscopic evaluations of alkali cationic effects on fly ash activation, *Cem. Concr. Compos.* 57 (2014) 34-43.
- [214] C. Kuenzel, N. Ranjbar, Dissolution mechanism of fly ash to quantify the reactive aluminosilicates in geopolymerisation, *Resour. Conserv. Recycl.* 150 (2019) 104421.
- [215] V. Bílek, P. Hrubý, V. Iliushchenko, J. Koplík, J. Kříkala, M. Marko, J. Hajzler, L. Kalina, Experimental study of slag changes during the very early stages of its alkaline activation, *Materials (Basel)*. 15 (2022).
- [216] M. Nedeljković, Carbonation mechanism of alkali-activated fly ash and slag materials - In view of long-term performance predictions, Delft University of Technology, 2022.
- [217] D.A. Kulik, Improving the structural consistency of C-S-H solid solution thermodynamic models, *Cem. Concr. Res.* 41 (2011) 477-495.
- [218] R.J. Myers, B. Lothenbach, S.A. Bernal, J.L. Provis, Thermodynamic modelling of alkali-activated slag cements, *Appl. Geochemistry* 61 (2015) 233-247.
- [219] I. Garcia-Lodeiro, A. Palomo, A. Fernández-Jiménez, D.E. MacPhee, Compatibility studies between N-A-S-H and C-A-S-H gels. Study in the ternary diagram Na₂O-CaO-Al₂O₃-SiO₂-H₂O, *Cem. Concr. Res.* 41 (2011) 923-931.
- [220] B. Lothenbach, D.A. Kulik, T. Matschei, M. Balonis, L. Baquerizo, B. Dilnesa, G.D. Miron, R.J. Myers, Cemdata18: A chemical thermodynamic database for hydrated Portland cements and alkali-activated materials, *Cem. Concr. Res.* 115 (2019) 472-506.
- [221] T. Thoenen, W. Hummel, U. Berner, E. Curti, The PSI/Nagra Chemical Thermodynamic Database 12/07, Nuclear Energy and Safety Research Department Laboratory for Waste Management (LES), 2014.
- [222] L. Gomez-Zamorano, M. Balonis, B. Erdemli, N. Neithalath, G. Sant, C-(N)-S-H and N-A-S-H gels: Compositions and solubility data at 25 °C and 50 °C, *J. Am. Ceram. Soc.* 100 (2017) 2700-2711.
- [223] T. Williamson, J. Han, L. Katz, G. Sant, M. Juenger, Method for experimentally determining N-A-S-(H) solubility, *RILEM Tech. Lett.* 3 (2019) 104-113.
- [224] B. Walkley, X. Ke, O. Hussein, J.L. Provis, Thermodynamic properties of sodium aluminosilicate hydrate (N-A-S-H), *Dalt. Trans.* 50 (2021) 13968-13984.
- [225] Y. Chen, L. Miranda, D. Lima, Z. Li, B. Ma, B. Lothenbach, Synthesis, solubility and thermodynamic properties of N-A-S-H gels with various target Si / Al ratios, *Cem. Concr. Res.* 180 (2024) 107484.
- [226] Y. Chen, B. Ma, J. Chen, Z. Li, X. Liang, L.M. de Lima, C. Liu, S. Yin, Q. Yu, B. Lothenbach,

- G. Ye, Thermodynamic modeling of alkali-activated fly ash paste, *Cem. Concr. Res.* 186 (2024) 107699.
- [227] X. Ke, Y. Duan, Coupling machine learning with thermodynamic modelling to develop a composition-property model for alkali-activated materials, *Compos. Part B Eng.* 216 (2021).
- [228] I. Ismail, S.A. Bernal, J.L. Provis, R. San Nicolas, S. Hamdan, J.S.J. Van Deventer, Modification of phase evolution in alkali-activated blast furnace slag by the incorporation of fly ash, *Cem. Concr. Compos.* 45 (2014) 125-135.
- [229] F. Puertas, S. Martínez-Ramírez, S. Alonso, T. Vázquez, Alkali-activated fly ash/slag cements. Strength behaviour and hydration products, *Cem. Concr. Res.* 30 (2000) 1625-1632.
- [230] X. Ke, S.A. Bernal, J.L. Provis, B. Lothenbach, Thermodynamic modelling of phase evolution in alkali-activated slag cements exposed to carbon dioxide, *Cem. Concr. Res.* 136 (2020) 106158.
- [231] Y. Zuo, Effect of chloride salt on the phase evolution in alkali-activated slag cements through thermodynamic modelling, *Appl. Geochemistry* 136 (2022).
- [232] J. Mills, N. Wagner, Rheokinetic modeling of N-A-S-H gel formation related to alkali-activated aluminosilicate materials, *Rheol. Acta* 61 (2022) 601-612.
- [233] R. Caron, R.A. Patel, F. Dehn, Activation kinetic model and mechanisms for alkali-activated slag cements, *Constr. Build. Mater.* 323 (2022) 126577.
- [234] R. Caron, R.A. Patel, A. Bogner, F. Dehn, Multi-scale experimental investigation and analytical micro-mechanical modeling to determine Young's modulus of alkali-activated slag concrete, *Constr. Build. Mater.* 383 (2023).
- [235] J.L. Provis, J.S.J. Van Deventer, Geopolymerisation kinetics . 1 . In situ energy-dispersive X-ray diffractometry, 62 (2007) 2309-2317.
- [236] C.E. White, J.L. Provis, T. Proffen, van Deventer, Jannie S. J, Molecular Mechanisms Responsible for the Structural Changes Occurring During Geopolymerization: Multiscale Simulation, *AIChE J.* 00 (2011) 1-13.
- [237] J.W. Bullard, E. Enjolras, W.L. George, S.G. Satterfield, J.E. Terrill, A parallel reaction-transport model applied to cement hydration and microstructure development, *Model. Simul. Mater. Sci. Eng.* 18 (2010).
- [238] L. Valentini, Modeling Dissolution-Precipitation Kinetics of Alkali-Activated Metakaolin, *ACS Omega* 3 (2018) 18100-18108.
- [239] R. Zhang, Z. Wang, Y. Meng, S. Jiao, J. Jia, Y. Min, C. Liu, Quantitative insight into aluminum structures in CaO-Al₂O₃-SiO₂ system via Raman and 27Al MAS-NMR spectroscopies, *J. Non. Cryst. Solids* 573 (2021) 121116.
- [240] T.S. Kim, J.H. Park, Structure-viscosity relationship of low-silica calcium aluminosilicate melts, *ISIJ Int.* 54 (2014) 2031-2038.
- [241] F.S. Freitas, A.S. Gonçalves, A. De Moraes, J.E. Benedetti, A.F. Nogueira, Graphene-like MoS₂ as a low-cost counter electrode material for dye-sensitized solar cells, *This J. Is © NanoGe J. Energy Sustain.* (2012) 11002-11003.
- [242] Y. Gao, K. Duan, S. Xiang, W. Zeng, Basic Properties of fly Ash/Slag -Concrete Slurry Waste Geopolymer Activated by Sodium Carbonate and Different Silicon Sources, *Front. Mater.* 8 (2021) 1-13.
- [243] Y. Yan, S.Y. Yang, G.D. Miron, I.E. Collings, E. L'Hôpital, J. Skibsted, F. Winnefeld, K. Scrivener, B. Lothenbach, Effect of alkali hydroxide on calcium silicate hydrate (C-S-H), *Cem. Concr. Res.* 151 (2022).
- [244] M. Handke, W. Mozgawa, M. Nocuń, Specific features of the IR spectra of silicate glasses, *J. Mol. Struct.* 325 (1994) 129-136.

- [245] W.K.W. Lee, J.S.J. Van Deventer, Use of Infrared Spectroscopy to Study Geopolymerization of Heterogeneous Amorphous Aluminosilicates, *Langmuir* 19 (2003) 8726-8734.
- [246] A. Herrmann, S. Kuhn, M. Tiegel, C. Rüssel, J. Körner, D. Klöpfel, J. Hein, M.C. Kaluza, Structure and fluorescence properties of ternary aluminosilicate glasses doped with samarium and europium, *J. Mater. Chem. C* 2 (2014) 4328-4337.
- [247] E. Salje, C. Werneke, Contributions to Mineralogy and Petrology The Phase Equilibrium Between Sillimanite and Andalusite as Determined from Lattice Vibrations, *Contrib. to Mineral. Petrol.* 79 (1982) 56-67.
- [248] M. Criado, W. Aperador, I. Sobrados, Microstructural and mechanical properties of alkali activated Colombian raw materials, *Materials (Basel)*. 9 (2016).
- [249] Z. Chen, Z. Meng, L. Liu, H. Wang, Y. Sun, X. Wang, Structural and Viscous Insight into Impact of MoO₃ on Molten Slags, *Metall. Mater. Trans. B Process Metall. Mater. Process. Sci.* 52 (2021) 3730-3743.
- [250] W.R. Taylor, Application of infrared spectroscopy to studies of silicate glass structure: Examples from the melilite glasses and the systems Na₂O-SiO₂ and Na₂O-Al₂O₃-SiO₂, *Proc. Indian Acad. Sci. - Earth Planet. Sci.* 99 (1990) 99-117.
- [251] S. Blotvogel, V. Montouillout, A. Canizares, P. Simon, E. Chesneau, A. Danezan, T. Wattez, A. Ehrenberg, M. Poirier, C. Patapy, M. Cyr, Glass structure of industrial ground granulated blast furnace slags (GGBS) investigated by time-resolved Raman and NMR spectroscopies, *J. Mater. Sci.* 56 (2021) 17490-17504.
- [252] K. Kanehashi, Structural roles of calcium in alkaline and alkaline-earth aluminosilicate glasses by solid-state ⁴³Ca, ¹⁷O and ²⁷Al NMR, *Solid State Nucl. Magn. Reson.* 84 (2017) 158-163.
- [253] G.S. Henderson, D.R. Neuville, L. Cormier, An O K-edge XANES study of glasses and crystals in the CaO-Al₂O₃-SiO₂ (CAS) system, *Chem. Geol.* 259 (2009) 54-62.
- [254] R. Kaindl, D.M. Többsens, U. Haefeker, Quantum-mechanical calculations of the Raman spectra of Mg- and Fe-cordierite, *Am. Mineral.* 96 (2011) 1568-1574.
- [255] D.A. McKeown, F.L. Galeener, G.E. Brown Jr, Raman Studies of Al Coordination in Silica-rich Sodium Aluminosilicate Glasses and Some Related Minerals, *J. Non. Cryst. Solids* 68 (1984) 361-378.
- [256] T. Li, C. Zhao, C. Sun, S. Song, Q. Wang, Roles of MgO and Al₂O₃ in Viscous and Structural Behavior of Blast Furnace Primary Slag with C/S = 1.4, *Metall. Mater. Trans. B Process Metall. Mater. Process. Sci.* 51 (2020) 2724-2734.
- [257] A. Wang, J.J. Freeman, B.L. Jolliff, Understanding the Raman spectral features of phyllosilicates, *J. Raman Spectrosc.* 46 (2015) 829-845.
- [258] Q. Zheng, Y. Zhang, N. Xue, T. Liu, J. Huang, Vanadium occupation and its leachability differences in trioctahedral and dioctahedral mica, *RSC Adv.* 9 (2019) 27615-27624.
- [259] D.A. McKeown, M.I. Bell, E.S. Etz, Vibrational analysis of the dioctahedral mica: 2M1 muscovite, *Am. Mineral.* 84 (1999) 1041-1048.
- [260] K. Zhai, W. Xue, H. Wang, X. Wu, S. Zhai, Raman spectra of sillimanite, andalusite, and kyanite at various temperatures, *Phys. Chem. Miner.* 47 (2020) 1-11.
- [261] S. Murgier, H. Zanni, D. Gouvenot, Blast furnace slag cement: A ²⁹Si and ²⁷Al NMR study, *Comptes Rendus Chim.* 7 (2004) 389-394.
- [262] J.F. MacDowell, G.H. Beall, Immiscibility and Crystallization in Al₂O₃-SiO₂ Glasses, *J. Am. Ceram. Soc.* 52 (1969) 17-25.
- [263] C.R. Ward, D. French, Determination of glass content and estimation of glass composition in fly ash using quantitative X-ray diffractometry, *Fuel* 85 (2006) 2268-2277.

- [264] J. Malolepszy, W. Wons, The influence of the vitreous phase of fly ashes on sintering process, 11th Int. Conf. Exhib. Eur. Ceram. Soc. 2009 2 (2009) 902-907.
- [265] C. Claireaux, M.H. Chopinet, E. Burov, E. Gouillart, M. Roskosz, M.J. Toplis, Atomic mobility in calcium and sodium aluminosilicate melts at 1200 °C, *Geochim. Cosmochim. Acta* 192 (2016) 235-247.
- [266] Z. Liu, W. Ni, Y. Li, H. Ba, N. Li, Y. Ju, B. Zhao, G. Jia, W. Hu, The mechanism of hydration reaction of granulated blast furnace slag-steel slag-refining slag-desulfurization gypsum-based clinker-free cementitious materials, *J. Build. Eng.* 44 (2021) 103289.
- [267] X. Sun, J. Liu, Y. Zhao, J. Zhao, Z. Li, Y. Sun, J. Qiu, P. Zheng, Mechanical activation of steel slag to prepare supplementary cementitious materials: A comparative research based on the particle size distribution, hydration, toxicity assessment and carbon dioxide emission, *J. Build. Eng.* 60 (2022) 105200.
- [268] D. Kato, Raman spectrum and refractive index behavior of Al₂O₃ added high-silica-content glass, *J. Appl. Phys.* 47 (1976) 5344-5348.
- [269] P. McMillan, B. Piriou, The structures and vibrational spectra of crystals and glasses in the silica-alumina system, *J. Non. Cryst. Solids* 53 (1982) 279-298.
- [270] D.R. Neuville, L. Cormier, V. Montouillout, D. Massiot, Local Al site distribution in aluminosilicate glasses by ²⁷Al MQMAS NMR, *J. Non. Cryst. Solids* 353 (2007) 180-184.
- [271] S.K. Wilke, C.J. Benmore, J. Ilavsky, R.E. Youngman, A. Rezikyan, M.P. Carson, V. Menon, R. Weber, Phase separation in mullite-composition glass, *Sci. Rep.* 12 (2022) 1-7.
- [272] J.T. Klopogge, Infrared and Raman Spectroscopies of Clay Minerals. Chapter 6: Raman Spectroscopy of Clay Minerals, in: *Dev. Clay Sci.*, Elsevier, 2017: pp. 150-199.
- [273] H. Schneider, R.X. Fischer, J. Schreuer, Mullite: Crystal Structure and Related Properties, *J. Am. Ceram. Soc.* 98 (2015) 2948-2967.
- [274] M. Schmücker, H. Schneider, New evidence for tetrahedral triclusters in aluminosilicate glasses, *J. Non. Cryst. Solids* 311 (2002) 211-215.
- [275] L. Zhou, J. Xu, M. Allix, X. Kuang, Development of Melilite-Type Oxide Ion Conductors, *Chem. Rec.* 20 (2020) 1117-1128.
- [276] J.W.E. Drewitt, S. Jahn, V. Cristiglio, A. Bytchkov, M. Leydier, S. Brassamin, H.E. Fischer, L. Hennet, The structure of liquid calcium aluminates as investigated by neutron and high-energy x-ray diffraction in combination with molecular dynamics simulation methods, *J. Phys. Condens. Matter* 24 (2012).
- [277] L. Hennet, J.W.E. Drewitt, D.R. Neuville, V. Cristiglio, J. Kozaily, S. Brassamin, D. Zanghi, H.E. Fischer, Neutron diffraction of calcium aluminosilicate glasses and melts, *J. Non. Cryst. Solids* 451 (2016) 89-93.
- [278] B. Schwarz, S.G. Ebbinghaus, A. Eichhöfer, L. Simonelli, H. Krause, T. Bergfeldt, S. Indris, J. Janek, H. Ehrenberg, Structure, site symmetry and spin-orbit coupled magnetism of a Ca₁₂Al₁₄O₃₃ mayenite single crystal substituted with 0.26 at.% Ni, *Phys. B Condens. Matter* 666 (2023).
- [279] E. Stolper, Crystallization sequences of Ca-Al-rich inclusions from Allende: An experimental study, *Geochim. Cosmochim. Acta* 46 (1982) 2159-2180.
- [280] B.C.M. Butler, Al-rich pyroxene and melilite in a blast-furnace slag and a comparison with the Allende meteorite, *Mineral. Mag.* 41 (1977) 493-499.
- [281] B. Fegley Jr, Practical Chemical Thermodynamics for Geoscientists. Chapter 6: The Second Law of Thermodynamics and Entropy, Elsevier, 2013.
- [282] X. Pan, D. Zhang, Y. Wu, H. Yu, Synthesis and characterization of calcium aluminate compounds from gehlenite by high-temperature solid-state reaction, *Ceram. Int.* 44 (2018)

- 13544-13550.
- [283] V. Petkov, S.J.L. Billinge, S.D. Shastri, B. Himmel, Polyhedral units and network connectivity in calcium aluminosilicate glasses from high-energy x-ray diffraction, *Phys. Rev. Lett.* 85 (2000) 3436-3439.
 - [284] K. Shimoda, Y. Tobu, K. Kanehashi, T. Nemoto, K. Saito, First evidence of multiple Ca sites in amorphous slag structure: Multiple-quantum MAS NMR spectroscopy on calcium-43 at high magnetic field, *Solid State Nucl. Magn. Reson.* 30 (2006) 198-202.
 - [285] J.D. Vienna, J. V. Ryan, S. Gin, Y. Inagaki, Current understanding and remaining challenges in modeling long-term degradation of borosilicate nuclear waste glasses, *Int. J. Appl. Glas. Sci.* 4 (2013) 283-294.
 - [286] G. Libourel, A. Verney-Carron, A. Morlok, S. Gin, J. Sterpenich, A. Michelin, D. Neff, P. Dillmann, The use of natural and archeological analogues for understanding the long-term behavior of nuclear glasses, *Comptes Rendus - Geosci.* 343 (2011) 237-245.
 - [287] C.L. Thorpe, J.J. Neeway, C.I. Pearce, R.J. Hand, A.J. Fisher, S.A. Walling, N.C. Hyatt, A.A. Kruger, M. Schweiger, D.S. Kosson, C.L. Arendt, J. Marcial, C.L. Corkhill, Forty years of durability assessment of nuclear waste glass by standard methods, *Npj Mater. Degrad.* 5 (2021).
 - [288] S. Gin, J. Delaye, F. Angeli, S. Schuller, S. Gin, J. Delaye, F. Angeli, S. Schuller, Aqueous alteration of silicate glass : State of knowledge and perspectives, *Npj Mater. Degrad.* 5 (2021) 0-20.
 - [289] M. Fournier, S. Gin, P. Frugier, Resumption of nuclear glass alteration: State of the art, *J. Nucl. Mater.* 448 (2014) 348-363.
 - [290] M. Fournier, S. Gin, P. Frugier, S. Mercado-Depierre, Contribution of zeolite-seeded experiments to the understanding of resumption of glass alteration, *Npj Mater. Degrad.* 1 (2017) 1-12.
 - [291] K.C. Newlands, D.E. Macphee, The reactivity of aluminosilicate glasses in cements-effects of Ca content on dissolution characteristics and surface precipitation, *Adv. Appl. Ceram.* 116 (2017) 216-224.
 - [292] T. Chave, P. Frugier, S. Gin, A. Ayral, Glass-water interphase reactivity with calcium rich solutions, *Geochim. Cosmochim. Acta* 75 (2011) 4125-4139.
 - [293] A. Fernández-Jiménez, A. Palomo, I. Sobrados, J. Sanz, The role played by the reactive alumina content in the alkaline activation of fly ashes, *Microporous Mesoporous Mater.* 91 (2006) 111-119.
 - [294] G.S. Frankel, J.D. Vienna, J. Lian, J.R. Scully, S. Gin, J. V. Ryan, J. Wang, S.H. Kim, W. Windl, J. Du, A comparative review of the aqueous corrosion of glasses, crystalline ceramics, and metals, *Npj Mater. Degrad.* 2 (2018).
 - [295] M. Frías, J. Cabrera, Influence of MK on the reaction kinetics in MK/lime and MK-blended cement systems at 20°C, *Cem. Concr. Res.* 31 (2001) 519-527.
 - [296] P.T. Durdziński, R. Snellings, C.F. Dunant, M. Ben Haha, K.L. Scrivener, Fly ash as an assemblage of model Ca-Mg-Na-aluminosilicate glasses, *Cem. Concr. Res.* 78 (2015) 263-272.
 - [297] B.P. McGrail, W.L. Ebert, A.J. Bakel, D.K. Peeler, Measurement of kinetic rate law parameters on a Na-Ca-Al borosilicate glass for low-activity waste, *J. Nucl. Mater.* 249 (1997) 175-189.
 - [298] K. V Chudnenko, O. Avchenko, Minimization of Gibbs Free Energy in Geochemical Systems by Convex Programming, *Geochemistry Int.* 11 (2011) 1207-1219.
 - [299] D.A. Kulik, T. Wagner, S. V. Dmytrieva, G. Kosakowski, F.F. Hingerl, K. V. Chudnenko, U.R. Berner, GEM-Selektor geochemical modeling package: Revised algorithm and GEMS3K numerical kernel for coupled simulation codes, *Comput. Geosci.* 17 (2013) 1-24.

- [300] A.C. Lasaga, Fundamental approaches in describing mineral dissolution and precipitation rates, in: *Chem. Weather. Rates Silic. Miner.*, Volume 31, 2018: pp. 23-86.
- [301] A.E. Krauklis, A.I. Gagani, K. Vegere, I. Kalnina, M. Klavins, A.T. Echtermeyer, Dissolution Kinetics of R-Glass Fibres : Influence of Water Acidity , Temperature , and Stress Corrosion, (2019) 1-18.
- [302] B. Grambow, First-order dissolution rate law and the role of surface layers in glass performance assessment, *298 (2001) 112-124*.
- [303] B.R. Bickmore, J.C. Wheeler, B. Bates, K.L. Nagy, D.L. Eggett, Reaction pathways for quartz dissolution determined by statistical and graphical analysis of macroscopic experimental data, *Geochim. Cosmochim. Acta 72 (2008) 4521-4536*.
- [304] C. Panagiotopoulou, E. Kontori, T. Perraki, G. Kakali, Dissolution of aluminosilicate minerals and by-products in alkaline media, *J. Mater. Sci. 42 (2007) 2967-2973*.
- [305] S. Mercado-Depierre, F. Frizon, S. Gin, F. Angeli, Leaching of Nuclear Waste Glass in Cement Power Water: Effect of Calcium in Solution, Springer Science, 2013.
- [306] H. Maraghechi, F. Rajabipour, C.G. Pantano, W.D. Burgos, Effect of calcium on dissolution and precipitation reactions of amorphous silica at high alkalinity, *Cem. Concr. Res. 87 (2016) 1-13*.
- [307] S. Mercado-Depierre, F. Angeli, F. Frizon, S. Gin, Antagonist effects of calcium on borosilicate glass alteration, *J. Nucl. Mater. 441 (2013) 402-410*.
- [308] S. Gin, P. Jollivet, M. Fournier, C. Berthon, Z. Wang, A. Mitroshkov, Z. Zhu, J. V. Ryan, The fate of silicon during glass corrosion under alkaline conditions: A mechanistic and kinetic study with the International Simple Glass, *Geochim. Cosmochim. Acta 151 (2015) 68-85*.
- [309] X. Cheng, R.K. Brow, G. Chen, The dissolution behavior in alkaline solutions of a borosilicate glass with and without P2O5, *J. Am. Ceram. Soc. 100 (2017) 4519-4532*.
- [310] J.P. Icenhower, B.P. McGrail, W.J. Shaw, E.M. Pierce, P. Nachimuthu, D.K. Shuh, E.A. Rodriguez, J.L. Steele, Experimentally determined dissolution kinetics of Na-rich borosilicate glass at far from equilibrium conditions: Implications for Transition State Theory, *Geochim. Cosmochim. Acta 72 (2008) 2767-2788*.
- [311] G. Villain, M. Thiery, G. Platret, Measurement methods of carbonation profiles in concrete: Thermogravimetry, chemical analysis and gammadensimetry, *Cem. Concr. Res. 37 (2007) 1182-1192*.
- [312] M. Zajac, J. Skibsted, P. Durdzinski, F. Bullerjahn, J. Skocek, M. Ben Haha, Kinetics of enforced carbonation of cement paste, *Cem. Concr. Res. 131 (2020) 106013*.
- [313] Z. Sauman, Carbonization of porous concrete and its main binding components, *Cem. Concr. Res. 1 (1971) 645-662*.
- [314] S.R. Gislason, E.H. Oelkers, Mechanism, rates, and consequences of basaltic glass dissolution: II. An experimental study of the dissolution rates of basaltic glass as a function of pH and temperature, *Geochim. Cosmochim. Acta 67 (2003) 3817-3832*.
- [315] J.F. Stebbins, I. Farnan, Effects of high temperature on silicate liquid structure: A multinuclear NMR study, *Science (80-.). 255 (1992) 586-589*.
- [316] A.S. Brand, J.W. Bullard, Dissolution Kinetics of Cubic Tricalcium Aluminate Measured by Digital Holographic Microscopy, *Langmuir 33 (2017) 9645-9656*.
- [317] T. Oey, A. Kumar, I. Pignatelli, Y. Yu, N. Neithalath, J.W. Bullard, M. Bauchy, G. Sant, Topological controls on the dissolution kinetics of glassy aluminosilicates, *J. Am. Ceram. Soc. 100 (2017) 5521-5527*.
- [318] J.P. Hamilton, S.L. Brantley, C.G. Pantano, L.J. Criscenti, J.D. Kubicki, Dissolution of nepheline, jadeite and albite glasses: Toward better models for aluminosilicate dissolution,

- Geochim. Cosmochim. Acta 65 (2001) 3683-3702.
- [319] S.L. Brantley, L. Stillings, Feldspar dissolution at 25 °C and low pH, *Am. J. Sci.* 296 (1996) 101-127.
- [320] S.K. Sharma, H.S. Yoder, D.W. Matson, Raman study of some melilites in crystalline and glassy states, *Geochim. Cosmochim. Acta* 52 (1988) 1961-1967.
- [321] L. Cormier, *Encyclopedia of Materials: Technical Ceramics and Glasses. Glasses: Aluminosilicates*, in: Elsevier, 2021: pp. 496-518.
- [322] B.O. Mysen, Olivine/melt transition metal partitioning, melt composition, and melt structure-Influence of Al³⁺ for Si⁴⁺ substitution in the tetrahedral network of silicate melts, *Geochim. Cosmochim. Acta* 71 (2007) 5500-5513.
- [323] C.H. Rüschler, Thermic transformation of sillimanite single crystals to 3:2 mullite plus melt: Investigations by polarized IR-reflection micro spectroscopy, *J. Eur. Ceram. Soc.* 21 (2001) 2463-2469.
- [324] M. Zajac, J. Skibsted, J. Skocek, P. Durdzinski, F. Bullerjahn, M. Ben Haha, Phase assemblage and microstructure of cement paste subjected to enforced, wet carbonation, *Cem. Concr. Res.* 130 (2020) 105990.
- [325] J.J. Thomas, D. Rothstein, H.M. Jennings, B.J. Christensen, Effect of hydration temperature on the solubility behavior of Ca-, S-, Al-, and Si-bearing solid phases in Portland cement pastes, *Cem. Concr. Res.* 33 (2003) 2037-2047.
- [326] T. Williamson, T. Zhu, J. Han, G. Sant, O.B. Isgor, M.C.G. Juenger, L. Katz, Effect of temperature on N-A-S-(H) and zeolite composition, solubility, and structure, *Cem. Concr. Res.* 172 (2023).
- [327] P. Blanc, X. Bourbon, A. Lassin, E.C. Gaucher, Chemical model for cement-based materials: Temperature dependence of thermodynamic functions for nanocrystalline and crystalline C-S-H phases, *Cem. Concr. Res.* 40 (2010) 851-866.
- [328] J.P. Hamilton, C.G. Pantano, S.L. Brantley, Dissolution of albite glass and crystal, *Geochim. Cosmochim. Acta* 64 (2000) 2603-2615.
- [329] R. Hellmann, The albite-water system: Part II. The time-evolution of the stoichiometry of dissolution as a function of pH at 100, 200, and 300 °C, *Geochim. Cosmochim. Acta* 59 (1995) 1669-1697.
- [330] D. Wolff-Boenisch, S.R. Gislason, E.H. Oelkers, C. V. Putnis, The dissolution rates of natural glasses as a function of their composition at pH 4 and 10.6, and temperatures from 25 to 74 °C, *Geochim. Cosmochim. Acta* 68 (2004) 4843-4858.
- [331] Y. Inagaki, T. Kikunaga, K. Idemitsu, T. Arima, Initial dissolution rate of the international simple glass as a function of pH and temperature measured using microchannel flow-through test method, *Int. J. Appl. Glas. Sci.* 4 (2013) 317-327.
- [332] M. Heřmanská, M.J. Voigt, C. Marieni, J. Declercq, E.H. Oelkers, A comprehensive and internally consistent mineral dissolution rate database: Part I: Primary silicate minerals and glasses, *Chem. Geol.* 597 (2022).
- [333] E.H. Oelkers, J. Declercq, G.D. Saldi, S.R. Gislason, J. Schott, Olivine dissolution rates: A critical review, *Chem. Geol.* 500 (2018) 1-19.
- [334] J.L. Palandri, Y.K. Kharaka, A Compilation of Rate Parameters of Water-Mineral Interaction Kinetics For Application to Geochemical Modeling, U.S. Geol. Surv. - Open File Rep. 2004-1068 17 (2004) 1-10.
- [335] B. Parruzot, J. V. Ryan, J.L. George, R.K. Motkuri, J.F. Bonnett, L.M. Seymour, M.A. Derewinski, Multi-glass investigation of Stage III glass dissolution behavior from 22 to 90 °C triggered by the addition of zeolite phases, *J. Nucl. Mater.* 523 (2019) 490-501.

- [336] J.D. Rimstidt, S.L. Brantley, A.A. Olsen, Systematic review of forsterite dissolution rate data, *Geochim. Cosmochim. Acta* 99 (2012) 159-178.
- [337] Y. Chen, S.L. Brantley, Dissolution of forsteritic olivine at 65 °C and 2<pH<5, *Chem. Geol.* 165 (2000) 267-281.
- [338] P. Aagaard, H.C. Helgeson, Thermodynamic and kinetic constraints on reaction rates among minerals and aqueous solutions. I. Theoretical considerations., *Am. J. Sci.* 282 (1982) 237-285.
- [339] E.H. Oelkers, J. Schott, J.L. Devidal, The effect of aluminum, pH, and chemical affinity on the rates of aluminosilicate dissolution reactions, *Geochim. Cosmochim. Acta* 58 (1994) 2011-2024.
- [340] E.H. Oelkers, General kinetic description of multioxide silicate mineral and glass dissolution, *Geochim. Cosmochim. Acta* (2001).
- [341] J. Wang, Thermodynamic equilibrium and kinetic fundamentals of oxide dissolution in aqueous solution, *J. Mater. Res.* 35 (2020) 898-921.
- [342] E. Gambuzzi, A. Pedone, M.C. Menziani, F. Angeli, P. Florian, T. Charpentier, Calcium environment in silicate and aluminosilicate glasses probed by ⁴³Ca MQMAS NMR experiments and MD-GIPAW calculations, *Solid State Nucl. Magn. Reson.* 68 (2015) 31-36.
- [343] Z. Shi, C. Shi, S. Wan, Z. Ou, Effect of alkali dosage on alkali-silica reaction in sodium hydroxide activated slag mortars, *Constr. Build. Mater.* 143 (2017) 16-23.
- [344] W. Han, Y. Lv, S. Wang, J. Qiao, C. Zou, M. Su, H. Peng, Effects of Al/Na and Si/Na Molar Ratios on the Alkalinity of Metakaolin-Based Geopolymer Pore Solutions, *Materials (Basel)*. 16 (2023).
- [345] R.R. Lloyd, J.L. Provis, J.S.J. Van Deventer, Pore solution composition and alkali diffusion in inorganic polymer cement, *Cem. Concr. Res.* 40 (2010) 1386-1392.
- [346] R. Cao, S. Zhang, N. Banthia, Y. Zhang, Z. Zhang, Interpreting the early-age reaction process of alkali-activated slag by using combined embedded ultrasonic measurement, thermal analysis, XRD, FTIR and SEM, *Compos. Part B Eng.* 186 (2020) 107840.
- [347] J.N. Mills, N.J. Wagner, P. Mondal, Relating chemical composition, structure, and rheology in alkali-activated aluminosilicate gels, *J. Am. Ceram. Soc.* 104 (2021) 572-583.
- [348] X. Gao, Q.L. Yu, H.J.H. Brouwers, Reaction kinetics, gel character and strength of ambient temperature cured alkali activated slag-fly ash blends, *Constr. Build. Mater.* 80 (2015) 105-115.
- [349] R. Snellings, Surface chemistry of calcium aluminosilicate glasses, *J. Am. Ceram. Soc.* 98 (2015) 303-314.
- [350] R. Hellmann, Encyclopedia of Glass Science, Technology, History, and Culture. Mechanisms of Glass Corrosion by Aqueous Solutions, in: *Encycl. Glas. Sci. Technol. Hist. Cult.*, John Wiley & Sons, Inc., 2021: pp. 647-662.
- [351] S. Ribet, S. Gin, Role of neoformed phases on the mechanisms controlling the resumption of SON68 glass alteration in alkaline media, *J. Nucl. Mater.* 324 (2004) 152-164.
- [352] A. Kashani, J.L. Provis, G.G. Qiao, J.S.J. Van Deventer, The interrelationship between surface chemistry and rheology in alkali activated slag paste, *Constr. Build. Mater.* 65 (2014) 583-591.
- [353] Y. Sun, S. Zhang, A.V. V. Rahul, Y. Tao, F. Van Bockstaele, K. Dewettinck, G. Ye, G. De Schutter, Rheology of alkali-activated slag pastes: New insight from microstructural investigations by cryo-SEM, *Cem. Concr. Res.* 157 (2022) 106806.
- [354] Y. Rifaai, A. Yahia, A. Mostafa, S. Aggoun, E.H. Kadri, Rheology of fly ash-based geopolymer: Effect of NaOH concentration, *Constr. Build. Mater.* 223 (2019) 583-594.

- [355] M. Palacios, M.M. Alonso, C. Varga, F. Puertas, Influence of the alkaline solution and temperature on the rheology and reactivity of alkali-activated fly ash pastes, *Cem. Concr. Compos.* 95 (2019) 277-284.
- [356] B. Hehlen, D.R. Neuville, Raman response of network modifier cations in alumino-silicate glasses, *J. Phys. Chem. B* 119 (2015) 4093-4098.
- [357] E. Deir, B.S. Gebregziabher, S. Peethamparan, Influence of starting material on the early age hydration kinetics, microstructure and composition of binding gel in alkali activated binder systems, *Cem. Concr. Compos.* 48 (2014) 108-117.
- [358] D. Ravikumar, N. Neithalath, Effects of activator characteristics on the reaction product formation in slag binders activated using alkali silicate powder and NaOH, *Cem. Concr. Compos.* 34 (2012) 809-818.
- [359] T. Kim, M. Moradian, M.T. Ley, Dissolution and Leaching of Fly Ash in Nitric Acid Using Automated Scanning Electron Microscopy, *Adv. Civ. Eng. Mater.* 7 (2018) 20180016.
- [360] X. Gao, Q.L. Yu, H.J.H. Brouwers, Apply ^{29}Si , ^{27}Al MAS NMR and selective dissolution in identifying the reaction degree of alkali activated slag-fly ash composites, *Ceram. Int.* 43 (2017) 12408-12419.
- [361] W. Zhu, X. Chen, L.J. Struble, E.H. Yang, Characterization of calcium-containing phases in alkali-activated municipal solid waste incineration bottom ash binder through chemical extraction and deconvoluted Fourier transform infrared spectra, *J. Clean. Prod.* 192 (2018) 782-789.
- [362] S. Takashima, Systematic dissolution of calcium silicate in commercial Portland cement by organic acid dissolution, *Rev. 12th Gen. Meet. - Japan Cem. Eng. Assoc. Tokyo.* (1958) 12-13.
- [363] S. Puligilla, P. Mondal, Co-existence of aluminosilicate and calcium silicate gel characterized through selective dissolution and FTIR spectral subtraction, *Cem. Concr. Res.* 70 (2015) 39-49.
- [364] D. Sarbapalli, X. Chen, L. Struble, P. Mondal, Salicylic acid-methanol extraction of aluminosilicate hydrates, *J. Am. Ceram. Soc.* 105 (2022) 7003-7010.
- [365] W. Zhu, X. Chen, L.J. Struble, E.H. Yang, Quantitative characterization of aluminosilicate gels in alkali-activated incineration bottom ash through sequential chemical extractions and deconvoluted nuclear magnetic resonance spectra, *Cem. Concr. Compos.* 99 (2019) 175-180.
- [366] B.Z. Dilnesa, B. Lothenbach, G. Renaudin, A. Wichser, D. Kulik, Synthesis and characterization of hydrogarnet $\text{Ca}_3(\text{Al}_x\text{Fe}_{1-x})_2(\text{SiO}_4)_y(\text{OH})_{4(3-y)}$, *Cem. Concr. Res.* 59 (2014) 96-111.
- [367] N. Krautwurst, L. Nicoleau, M. Dietzsch, I. Lieberwirth, C. Labbez, A. Fernandez-Martinez, A.E.S. Van Driessche, B. Barton, S. Leukel, W. Tremel, Two-Step Nucleation Process of Calcium Silicate Hydrate, the Nanobrick of Cement, *Chem. Mater.* 30 (2018) 2895-2904.
- [368] S. Jiang, J.H. Ter Horst, Crystal nucleation rates from probability distributions of induction times, *Cryst. Growth Des.* 11 (2011) 256-261.
- [369] S. Garrault-Gauffinet, A. Nonat, Experimental investigation of calcium silicate hydrate (C-S-H) nucleation, *J. Cryst. Growth* 200 (1999) 565-574.
- [370] L. Nicoleau, A. Nonat, A new view on the kinetics of tricalcium silicate hydration, *Cem. Concr. Res.* 86 (2016) 1-11.
- [371] E.H. Oelkers, S. V. Golubev, C. Chairat, O.S. Pokrovsky, J. Schott, The surface chemistry of multi-oxide silicates, *Geochim. Cosmochim. Acta* 73 (2009) 4617-4634.
- [372] E.C. Ethridge, Mechanisms and kinetics of binary alkali silicate glass corrosion, University of Florida, 1977.

- [373] A.R. Brough, A. Atkinson, Sodium silicate-based, alkali-activated slag mortars - Part I. Strength, hydration and microstructure, *Cem. Concr. Res.* 32 (2002) 865-879.
- [374] R. Xiao, X. Jiang, M. Zhang, P. Polaczyk, B. Huang, Analytical investigation of phase assemblages of alkali-activated materials in CaO-SiO₂-Al₂O₃ systems: The management of reaction products and designing of precursors, *Mater. Des.* 194 (2020) 108975.
- [375] R.K. Chinnam, P.C.M. Fossati, W.E. Lee, Degradation of partially immersed glass: A new perspective, *J. Nucl. Mater.* 503 (2018) 56-65.
- [376] W.K.W. Lee, J.S.J. Van Deventer, The effect of ionic contaminants on the early-age properties of alkali-activated fly ash-based cements, *Cem. Concr. Res.* 32 (2002) 577-584.
- [377] Y. Zuo, M. Nedeljković, G. Ye, Pore solution composition of alkali-activated slag/fly ash pastes, *Cem. Concr. Res.* (2019).
- [378] J. Schott, O.S. Pokrovsky, E.H. Oelkers, The link between mineral dissolution/precipitation kinetics and solution chemistry, *Rev. Mineral. Geochemistry* 70 (2009) 207-258.
- [379] B. Lothenbach, Thermodynamic equilibrium calculations in cementitious systems, *Mater. Struct. Constr.* 43 (2010) 1413-1433.
- [380] E.M. Gartner, A Proposed Mechanism For The Growth of C-S-H During the Hydration of Tricalcium Silicate, *Cem. Concr. Res.* 27 (1997) 665-672.
- [381] T. Sowoidnich, D. Damidot, H.M. Ludwig, J. Germroth, R. Rosenberg, H. Cölfen, The nucleation of C-S-H via prenucleation clusters, *J. Chem. Phys.* 158 (2023).
- [382] Z. Zhang, F. Han, P. Yan, Modelling the dissolution and precipitation process of the early hydration of C3S, *Cem. Concr. Res.* 136 (2020) 106174.
- [383] M. Nedeljković, K. Arbi, Y. Zuo, G. Ye, Microstructural and Mineralogical Analysis of Alkali Activated Fly Ash- Slag Pastes, 3rd Int. RILEM Conf. Microstruct. Relat. Durab. Cem. (2016) 1-10.
- [384] M. Criado, A. Fernández-Jiménez, A. Palomo, I. Sobrados, J. Sanz, Effect of the SiO₂/Na₂O ratio on the alkali activation of fly ash. Part II: ²⁹Si MAS-NMR Survey, Microporous Mesoporous Mater. 109 (2008) 525-534.
- [385] S. Kwan, J. Larosa, M.W. Grutzeck, ²⁹Si and ²⁷Al MAS NMR Study of Strätlingite, *J. Am. Ceram. Soc.* 3 (1995) 1921-1926.
- [386] I. García Lodeiro, A. Fernández-Jimenez, A. Palomo, D.E. Macphee, Effect on fresh C-S-H gels of the simultaneous addition of alkali and aluminium, *Cem. Concr. Res.* 40 (2010) 27-32.
- [387] M.U. Okoronkwo, F.P. Glasser, Stability of strätlingite in the CASH system, *Mater. Struct. Constr.* 49 (2016) 4305-4318.
- [388] D.P. Prentice, B. Walkley, S.A. Bernal, M. Bankhead, M. Hayes, J.L. Provis, Thermodynamic modelling of BFS-PC cements under temperature conditions relevant to the geological disposal of nuclear wastes, *Cem. Concr. Res.* 119 (2019) 21-35.
- [389] D. Damidot, S. Stronach, A. Kindness, M. Atkins, F.P. Glasser, Thermodynamic investigation of the CaOAl₂O₃CaCO₃H₂O closed system at 25 °C and the influence of Na₂O, *Cem. Concr. Res.* 24 (1994) 563-572.
- [390] P. Juilland, E. Gallucci, R. Flatt, K. Scrivener, Dissolution theory applied to the induction period in alite hydration, *Cem. Concr. Res.* 40 (2010) 831-844.
- [391] P.M. Dove, N. Han, J.J. De Yoreo, Mechanisms of classical crystal growth theory explain quartz and silicate dissolution behavior, *Proc. Natl. Acad. Sci. U. S. A.* 102 (2005) 15357-15362.
- [392] M. Baggioli, Topological defects reveal the plasticity of glasses, *Nat. Commun.* 14 (2023) 1-3.
- [393] Messina, Ferone, F. Colangelo, Roviello, Cioffi, Alkali activated waste fly ash as sustainable

- composite: Influence of curing and pozzolanic admixtures on the early-age physico-mechanical properties and residual strength after exposure at elevated temperature, *Compos. Part B Eng.* 132 (2018) 161-169.
- [394] S.S. Hossain, P.K. Roy, C.J. Bae, Utilization of waste rice husk ash for sustainable geopolymer: A review, *Constr. Build. Mater.* 310 (2021).
- [395] J. Kalahe, T.S. Mahadevan, M. Ono, K. Miyatani, S. Urata, J. Du, Temperature dependence of interfacial reactions of sodium aluminosilicate glasses from reactive molecular dynamics simulations, *Appl. Surf. Sci.* 619 (2023) 156780.
- [396] L. Deng, K. Miyatani, M. Suehara, S. ichi Amma, M. Ono, S. Urata, J. Du, Ion-exchange mechanisms and interfacial reaction kinetics during aqueous corrosion of sodium silicate glasses, *Npj Mater. Degrad.* 5 (2021).
- [397] X. Aretxabaleta, J. López-Zorrilla, C. Labez, I. Etxebarria, H. Manzano, A potential C-S-H nucleation mechanism: atomistic simulations of the portlandite to C-S-H transformation, *Cem. Concr. Res.* 106965 (2022).
- [398] X. Ma, Z. Zhang, A. Wang, The transition of fly ash-based geopolymer gels into ordered structures and the effect on the compressive strength, *Constr. Build. Mater.* 104 (2016) 25-33.
- [399] M.I.M. Alzeer, H. Nguyen, T. Fabritius, H. Sreenivasan, V.-V. Telkki, A.M. Kantola, C. Cheeseman, M. Illikainen, P. Kinnunen, On the hydration of synthetic aluminosilicate glass as a sole cement precursor, *Cem. Concr. Res.* 159 (2022) 106859.
- [400] M. Askarian, Z. Tao, B. Samali, G. Adam, R. Shuaibu, Mix composition and characterisation of one-part geopolymers with different activators, *Constr. Build. Mater.* 225 (2019) 526-537.
- [401] A. D'Elia, D. Pinto, G. Eramo, L.C. Giannossa, G. Ventruti, R. Laviano, Effects of processing on the mineralogy and solubility of carbonate-rich clays for alkaline activation purpose: mechanical, thermal activation in red/ox atmosphere and their combination, *Appl. Clay Sci.* 152 (2018) 9-21.
- [402] G. Kabirdas B, S. Sharda M, Glass Delamination in sterile formulations and Drug Recalls: A Review, *Int. J. Pharm. Sci. Dev. Res.* 8 (2022) 006-115.
- [403] D. Ditter, A. Nieto, H.C. Mahler, H. Roehl, M. Wahl, J. Huwyler, A. Allmendinger, Evaluation of Glass Delamination Risk in Pharmaceutical 10 mL/10R Vials, *J. Pharm. Sci.* 107 (2018) 624-637.
- [404] C.. Cau Dit Coumes, S. Berger, P. Le Bescop, D. Damidot, Stabilization of ZnCl₂-containing Waste Using Calcium Sulfoaluminate Cement, *J. Hazard. Mater. Mater* (2011) 268-276.
- [405] J. Sheng, S. Luo, B. Tang, Temperature effects on the leaching behavior of a high-level waste glass form, *Nucl. Technol.* 123 (1998) 295-302.
- [406] M.R. Andalibi, A. Kumar, B. Srinivasan, P. Bowen, K. Scrivener, C. Ludwig, A. Testino, On the mesoscale mechanism of synthetic calcium-silicate-hydrate precipitation: A population balance modeling approach, *J. Mater. Chem. A* 6 (2018) 363-373.
- [407] D.L. Marchisio, On the use of bi-variate population balance equations for modelling barium titanate nanoparticle precipitation, *Chem. Eng. Sci.* 64 (2009) 697-708.
- [408] M. Ben Haha, B. Lothenbach, G. Le Saout, F. Winnefeld, Influence of slag chemistry on the hydration of alkali-activated blast-furnace slag - Part II: Effect of Al₂O₃, *Cem. Concr. Res.* 42 (2012) 74-83.
- [409] Z. Sun, A. Vollpracht, One year geopolymerisation of sodium silicate activated fly ash and metakaolin geopolymers, *Cem. Concr. Compos.* 95 (2019) 98-110.
- [410] A. Dehghani, F. Aslani, N. Ghaebi Panah, Effects of initial SiO₂/Al₂O₃ molar ratio and slag on fly ash-based ambient cured geopolymer properties, *Constr. Build. Mater.* 293 (2021) 123527.

- [411] R.P. Williams, R.D. Hart, A. Van Riessen, Quantification of the extent of reaction of metakaolin-based geopolymers using X-ray diffraction, scanning electron microscopy, and energy-dispersive spectroscopy, *J. Am. Ceram. Soc.* 94 (2011) 2663-2670.
- [412] F. Winnefeld, M. Ben Haha, G. Le Saout, M. Costoya, S.C. Ko, B. Lothenbach, Influence of slag composition on the hydration of alkali-activated slags, *J. Sustain. Cem. Mater.* 4 (2014) 85-100.
- [413] C. Panagiotopoulou, S. Tsivilis, G. Kakali, Application of the Taguchi approach for the composition optimization of alkali activated fly ash binders, *Constr. Build. Mater.* 91 (2015) 17-22.
- [414] E. Álvarez-Ayuso, X. Querol, F. Plana, A. Alastuey, N. Moreno, M. Izquierdo, O. Font, T. Moreno, S. Diez, E. Vázquez, M. Barra, Environmental, physical and structural characterisation of geopolymer matrixes synthesised from coal (co-)combustion fly ashes, *J. Hazard. Mater.* 154 (2008) 175-183.
- [415] K. Ferrand, M. Klinkenberg, S. Caes, J. Poonosamy, W. Van Renterghem, J. Barthel, K. Lemmens, D. Bosbach, F. Brandt, Dissolution kinetics of international simple glass and formation of secondary phases at very high surface area to solution ratio in young cement water, *Materials (Basel)*. 14 (2021) 1-22.
- [416] R.J. Myers, E. L'Hôpital, J.L. Provis, B. Lothenbach, Effect of temperature and aluminium on calcium (alumino)silicate hydrate chemistry under equilibrium conditions, *Cem. Concr. Res.* 68 (2015) 83-93.
- [417] S. Barzgar, M. Tarik, C. Ludwig, B. Lothenbach, The effect of equilibration time on Al uptake in C-S-H, *Cem. Concr. Res.* 144 (2021) 106438.
- [418] M. Criado, A. Fernández-Jiménez, A. Palomo, Alkali activation of fly ash: Effect of the SiO₂/Na₂O ratio. Part I: FTIR study, *Microporous Mesoporous Mater.* 106 (2007) 180-191.
- [419] S. Kumar, R. Kumar, S.P. Mehrotra, Influence of granulated blast furnace slag on the reaction, structure and properties of fly ash based geopolymer, *J. Mater. Sci.* 45 (2010) 607-615.
- [420] H. Peng, Y. Li, D. Luo, Y. Liu, C.S. Cai, Quantitative analysis of reaction degrees and factors influencing alkali-activated metakaolin-GGBFS blend, *Constr. Build. Mater.* 359 (2022) 129472.
- [421] S. Puligilla, X. Chen, P. Mondal, Does synthesized C-S-H seed promote nucleation in alkali activated fly ash-slag geopolymer binder?, *Mater. Struct. Constr.* 52 (2019) 1-13.
- [422] X. Zhao, C. Liu, L. Zuo, L. Wang, Q. Zhu, M. Wang, Investigation into the effect of calcium on the existence form of geopolymerized gel product of fly ash based geopolymers, *Cem. Concr. Compos.* 103 (2019) 279-292.
- [423] S.V.K. Vissa, C. Massion, Y. Lu, A. Bunger, M. Radonjic, Zeolite-Enhanced Portland Cement: Solution for Durable Wellbore-Sealing Materials, *Materials (Basel)*. 16 (2023).
- [424] M.M. Thakur, S. Enright, R.C. Hurley, Phase segmentation in X-ray CT images of concrete with implications for mesoscale modeling, *Constr. Build. Mater.* 403 (2023) 133033.
- [425] F. Georget, W. Wilson, K.L. Scrivener, edxia: Microstructure characterisation from quantified SEM-EDS hypermaps, *Cem. Concr. Res.* 141 (2021) 106327.
- [426] N. Doebelin, R. Kleeberg, Profex: A graphical user interface for the Rietveld refinement program BGMN, *J. Appl. Crystallogr.* 48 (2015) 1573-1580.
- [427] C. Shi, R.L. Day, A calorimetric study of early hydration of alkali-slag cements, *Cem. Concr. Res.* 25 (1995) 1333-1346.
- [428] G. Liang, W. Yao, A. She, New insights into the early-age reaction kinetics of metakaolin geopolymer by 1H low-field NMR and isothermal calorimetry, *Cem. Concr. Compos.* 137 (2023).

- [429] D. Ravikumar, S. Peethamparan, N. Neithalath, Structure and strength of NaOH activated concretes containing fly ash or GGBFS as the sole binder, *Cem. Concr. Compos.* 32 (2010) 399-410.
- [430] X. Yao, Z. Zhang, H. Zhu, Y. Chen, Geopolymerization process of alkali-metakaolinite characterized by isothermal calorimetry, *Thermochim. Acta* 493 (2009) 49-54.
- [431] M.D. S. Goto, K. Akazawa, Solubility of silica-alumina gels in different pH solutions - discussion on the hydration of slags and fly ashes in cement, *Cem. Concr. Res.* 22 (1992) 1216-1223.
- [432] H. Xu, J.L. Provis, J.S.J. van Deventer, V. Krivenko, Pavel, Characterization of Aged Slag Concretes, *ACI Mater. J.* 105 (2008) 131-139.
- [433] S.A. Bernal, R. Mejía De Gutiérrez, J.L. Provis, Engineering and durability properties of concretes based on alkali-activated granulated blast furnace slag/metakaolin blends, *Constr. Build. Mater.* 33 (2012) 99-108.
- [434] Y.J. Zhang, L. Kang, L.C. Liu, Handbook of Alkali-Activated Cements, Mortars and Concretes. Alkali-activated cements for photocatalytic degradation of organic dyes, Woodhead Publishing Limited, 2015.
- [435] M.I.M. Alzeer, H. Nguyen, C. Cheeseman, P. Kinnunen, Alkali-Activation of Synthetic Aluminosilicate Glass With Basaltic Composition, *Front. Chem.* 9 (2021) 1-10.
- [436] I.G. Richardson, S. Li, Composition and structure of an 18-year-old 5M KOH-activated ground granulated blast-furnace slag paste, *Constr. Build. Mater.* 168 (2018) 404-411.
- [437] M. Moranville-Regourd, S. Kamali-Bernard, Lea's Chemistry of Cement and Concrete. Cements made from blast furnace slag, Elsevier, 2019.
- [438] M. Regourd, H. Hornain, B. Mortureux, Microstructure of slag cements, *Rev. Des Mater. Constr.* (1976) 83-86.
- [439] L. Nguyen-Tuan, M.A. Etzold, C. Röbber, H.M. Ludwig, Growth and porosity of C-S-H phases using the sheet growth model, *Cem. Concr. Res.* 129 (2020) 105960.
- [440] M.A. Etzold, P.J. McDonald, A.F. Routh, Growth of sheets in 3D confinements - A model for the C-S-H meso structure, *Cem. Concr. Res.* 63 (2014) 137-142.
- [441] Y. Ma, J. Hu, G. Ye, The effect of activating solution on the mechanical strength, reaction rate, mineralogy, and microstructure of alkali-activated fly ash, *J. Mater. Sci.* 47 (2012) 4568-4578.
- [442] M.R. Rowles, B.H.O. Connor, Chemical and Structural Microanalysis of Aluminosilicate Geopolymers, 2361 (2009) 2354-2361.
- [443] S.M. Zabihi, H.R. Tavakoli, Mechanical and microstructural properties of GGBFS-RHA geopolymer concrete, *Emerg. Mater. Res.* 7 (2018) 233-241.
- [444] J.L. Provis, R.J. Myers, C.E. White, V. Rose, J.S.J. Van Deventer, X-ray microtomography shows pore structure and tortuosity in alkali-activated binders, *Cem. Concr. Res.* 42 (2012) 855-864.
- [445] Y. Ma, G. Ye, Quantification of the Degree of Reaction of Alkali Activated Fly Ash by Image Analysis, in: *Int. Congr. Durab. Concr.*, 2012.
- [446] Z. Li, B. Delsaute, T. Lu, A. Kostichenko, S. Staquet, G. Ye, A comparative study on the mechanical properties, autogenous shrinkage and cracking proneness of alkali-activated concrete and ordinary Portland cement concrete, *Constr. Build. Mater.* 292 (2021) 123418.
- [447] X. Gao, Q.L. Yu, H.J.H. Brouwers, Assessing the porosity and shrinkage of alkali activated slag-fly ash composites designed applying a packing model, *Constr. Build. Mater.* 119 (2016) 175-184.
- [448] S. Zhang, Z. Li, B. Ghiassi, S. Yin, G. Ye, Fracture properties and microstructure formation

- of hardened alkali-activated slag/fly ash pastes, *Cem. Concr. Res.* 144 (2021) 106447.
- [449] Y. Sun, Z. Liu, S. Ghorbani, G. Ye, G. De Schutter, Fresh and hardened properties of alkali-activated slag concrete: The effect of fly ash as a supplementary precursor, *J. Clean. Prod.* 370 (2022) 133362.
- [450] X. Ouyang, Y. Ma, Z. Liu, J. Liang, G. Ye, Effect of the sodium silicate modulus and slag content on fresh and hardened properties of alkali-activated fly ash/slag, *Minerals* 10 (2020).
- [451] Z. Shi, C. Shi, S. Wan, N. Li, Z. Zhang, Effect of alkali dosage and silicate modulus on carbonation of alkali-activated slag mortars, *Cem. Concr. Res.* 113 (2018) 55-64.
- [452] S.P. Zhdanov, N.N. Feoktistova, L.M. Vtjurina, Temperature dependence of nucleation of zeolites in alkaline aluminosilicate gels in hydrothermal crystallization conditions, *Stud. Surf. Sci.* 65 (1991) 287-296.
- [453] T.M. Davis, T.O. Drews, H. Ramanan, C. He, J. Dong, H. Schnablegger, M.A. Katsoulakis, E. Kokkoli, A. V. McCormick, R.L. Penn, M. Tsapatsis, Mechanistic principles of nanoparticle evolution to zeolite crystals, *Nat. Mater.* 5 (2006) 400-408.
- [454] D. Mierzwiński, M. Łach, M. Hebda, J. Walter, M. Szechyńska-Hebda, J. Miśka, Thermal phenomena of alkali-activated metakaolin studied with a negative temperature coefficient system, *J. Therm. Anal. Calorim.* 7 (2019) 4167-4175.
- [455] R. Maddalena, K. Li, P.A. Chater, S. Michalik, A. Hamilton, Direct synthesis of a solid calcium-silicate-hydrate (C-S-H), *Constr. Build. Mater.* 223 (2019) 554-565.
- [456] K.M.L. Alventosa, B. Wild, C.E. White, The effects of calcium hydroxide and activator chemistry on alkali-activated metakaolin pastes exposed to high temperatures, *Cem. Concr. Res.* 154 (2022).
- [457] A.A. Hoyos-Montilla, J.I. Tobón, F. Puertas, Role of calcium hydroxide in the alkaline activation of coal fly ash, *Cem. Concr. Compos.* 137 (2023).
- [458] I. García-Lodeiro, A. Fernández-Jiménez, A. Palomo, Variation in hybrid cements over time. Alkaline activation of fly ash-portland cement blends, *Cem. Concr. Res.* 52 (2013) 112-122.
- [459] L. Pegado, C. Labbez, S. V. Churakov, Mechanism of aluminium incorporation into C-S-H from ab initio calculations, *J. Mater. Chem. A* 2 (2014) 3477-3483.
- [460] R.J. Myers, E. L'Hôpital, J.L. Provis, B. Lothenbach, Composition-solubility-structure relationships in calcium (alkali) aluminosilicate hydrate (C-(N,K)-A-S-H), *Dalt. Trans.* 44 (2015) 13530-13544.
- [461] S. Zhang, Y. Zuo, Z. Li, G. Ye, Isothermal calorimetric study on heat evolution and apparent activation energy of alkali-activated slag/fly ash paste, *2nd Int. Conf. Sustain. Build. Mater.* (2019) 1-8.
- [462] M.M. Tashima, L. Reig, M.A. Santini, J.C. B Moraes, J.L. Akasaki, J. Payá, M. V. Borrachero, L. Soriano, Compressive Strength and Microstructure of Alkali-Activated Blast Furnace Slag/Sewage Sludge Ash (GGBS/SSA) Blends Cured at Room Temperature, *Waste and Biomass Valorization* 8 (2017) 1441-1451.
- [463] T. Yang, X. Yao, Z. Zhang, H. Wang, Mechanical property and structure of alkali-activated fly ash and slag blends, *J. Sustain. Cem. Mater.* 1 (2012) 167-178.
- [464] C.K. Yip, G.C. Lukey, J.L. Provis, J.S.J. van Deventer, Effect of calcium silicate sources on geopolymerisation, *Cem. Concr. Res.* 38 (2008) 554-564.
- [465] R. Si, S. Guo, Q. Dai, Influence of calcium content on the atomic structure and phase formation of alkali-activated cement binder, *J. Am. Ceram. Soc.* 102 (2019) 1479-1494.
- [466] B. Lu, C. Shi, J. Zhang, J. Wang, Effects of carbonated hardened cement paste powder on hydration and microstructure of Portland cement, *Constr. Build. Mater.* 186 (2018) 699-708.

- [467] X.C. P. Yu, J. Kirckpatrick, B. Poe, P. MacMillan, P. Yu, J. Kirckpatrick, B. Poe, P. McMillan, X. Cong, Structure of Calcium Silicate Hydrate (C-S-H): Near-, Mid-, and Far-Infrared Spectroscopy, *J. Am. Ceram. Soc.* (1999) 742-748.
- [468] S. Puligilla, P. Mondal, Role of slag in microstructural development and hardening of fly ash-slag geopolymer, *Cem. Concr. Res.* 43 (2013) 70-80.
- [469] R. Pouhet, M. Cyr, Studies of Natural and Accelerated Carbonation in Metakaolin-Based Geopolymer, 13th Int. Ceram. Congr. - Part F 92 (2014) 38-43.
- [470] J. Dang, X. Shen, A. Castel, J. Aldred, Monitoring apparent pH value in geopolymer concrete using glass electrode, *ISARC 2016 - 33rd Int. Symp. Autom. Robot. Constr.* (2016) 547-554.
- [471] J. Zhou, L. Chen, K. Zheng, G. Prateek, F. He, Z. Liu, Q. Yuan, Effect of elevated Al concentration on early-age hydration of Portland cement, *Cem. Concr. Compos.* 136 (2023) 104866.
- [472] J. Němeček, V. Šmilauer, L. Kopecký, Nanoindentation characteristics of alkali-activated aluminosilicate materials, *Cem. Concr. Compos.* 33 (2011) 163-170.
- [473] Z. Luo, W. Li, Y. Gan, K. Mendu, S.P. Shah, Maximum likelihood estimation for nanoindentation on sodium aluminosilicate hydrate gel of geopolymer under different silica modulus and curing conditions, *Compos. Part B Eng.* 198 (2020) 108185.
- [474] W. Cai, Z. Xu, Z. Zhang, J. Hu, H. Huang, Y. Ma, Z. Zhang, H. Wang, S. Yin, J. Wei, C. Shi, Q. Yu, Chloride binding behavior of synthesized reaction products in alkali-activated slag, *Compos. Part B Eng.* 238 (2022) 109919.
- [475] A. Runci, J. Provis, M. Serdar, Microstructure as a key parameter for understanding chloride ingress in alkali-activated mortars, *Cem. Concr. Compos.* 134 (2022) 104818.
- [476] G. Fang, M. Zhang, Multiscale micromechanical analysis of alkali-activated fly ash-slag paste, *Cem. Concr. Res.* 135 (2020) 106141.
- [477] B. Walkley, G.J. Rees, R. San Nicolas, J.S.J. Van Deventer, J. V. Hanna, J.L. Provis, New Structural Model of Hydrous Sodium Aluminosilicate Gels and the Role of Charge-Balancing Extra-Framework Al, *J. Phys. Chem. C* 122 (2018) 5673-5685.
- [478] A. Fernández-Jiménez, R. Vallepu, T. Terai, A. Palomo, K. Ikeda, Synthesis and thermal behavior of different aluminosilicate gels, *J. Non. Cryst. Solids* 352 (2006) 2061-2066.
- [479] J.L. Provis, Geopolymers and other alkali activated materials: Why, how, and what?, *Mater. Struct. Constr.* 47 (2014) 11-25.
- [480] T.C. Powers, Structure and Physical Properties of Hardened Portland Cement Paste Authorized Reprint from American Ceramic Society, *J. Am. Ceram. Soc.* 41 (1958) 7.
- [481] Y. Li, H. Pan, Q. Liu, X. Ming, Z. Li, Ab initio mechanism revealing for tricalcium silicate dissolution, *Nat. Commun.* 13 (2022) 1-10.
- [482] E.I. Nadelman, K.E. Kurtis, Application of Powers' model to modern portland and portland limestone cement pastes, *J. Am. Ceram. Soc.* 100 (2017) 4219-4231.
- [483] K. van Breugel, Numerical simulation of hydration and microstructural development in hardening cement-based materials (I) theory, *Cem. Concr. Res.* 25 (1995) 319-331.
- [484] J.J. Thomas, J.J. Biernacki, J.W. Bullard, S. Bishnoi, J.S. Dolado, G.W. Scherer, A. Luttge, Modeling and simulation of cement hydration kinetics and microstructure development, *Cem. Concr. Res.* 41 (2011) 1257-1278.
- [485] L.J. Parrot, D.C. Kiloh, Prediction of cement hydration, *Br. Ceram. Proc.* (1984) 41-53.
- [486] D. Fan, S. Yang, Mechanical properties of C-S-H globules and interfaces by molecular dynamics simulation, *Constr. Build. Mater.* 176 (2018) 573-582.
- [487] S. Chitsaz, A. Tarighat, Molecular dynamics simulation of N-A-S-H geopolymer macro

- molecule model for prediction of its modulus of elasticity, *Constr. Build. Mater.* 243 (2020) 118176.
- [488] H. Wu, J. Pan, J. Wang, Molecular dynamics simulation study on dynamic mechanical properties of C-S-H with diverse Ca/Si ratios, *Mater. Today Commun.* 31 (2022) 103755.
- [489] Y. Zhang, Q. Zhou, J.W. Ju, M. Bauchy, New insights into the mechanism governing the elasticity of calcium silicate hydrate gels exposed to high temperature: A molecular dynamics study, *Cem. Concr. Res.* 141 (2021) 106333.
- [490] S. Roosta, Y. Liu, Development of a Macro-Model for concrete masonry infilled frames, *Eng. Struct.* 257 (2022) 114075.
- [491] M. Königsberger, M. Hlobil, B. Delsaute, S. Staquet, C. Hellmich, B. Pichler, Hydrate failure in ITZ governs concrete strength: A micro-to-macro validated engineering mechanics model, *Cem. Concr. Res.* 103 (2018) 77-94.
- [492] R. Saravanakumar, K.S. Elango, V. Revathi, D. Balaji, Influence of Aggressive Environment in Macro and Microstructural Properties of Bottom Ash Geopolymer Concrete, *Sustain.* 16 (2024).
- [493] D. Tariku, A.B. Degefa, H.M. Son, S. Park, Exploring the applicability of thermodynamic modeling to predict the degree of reaction of supplementary cementitious materials in Portland cements, *Dev. Built Environ.* 16 (2023) 100256.
- [494] A.R.D. Costa, M. V. Coppe, W. V. Bielefeldt, S.A. Bernal, L. Black, A.P. Kirchheim, J.P. Gonçalves, Thermodynamic modelling of cements clinkering process as a tool for optimising the proportioning of raw meals containing alternative materials, *Sci. Rep.* 13 (2023) 1-19.
- [495] Z. Qian, E.J. Garboczi, G. Ye, E. Schlangen, Anm: a geometrical model for the composite structure of mortar and concrete using real-shape particles, *Mater. Struct. Constr.* 49 (2016) 149-158.
- [496] J.E. Oh, P.J.M. Monteiro, S.S. Jun, S. Choi, S.M. Clark, The evolution of strength and crystalline phases for alkali-activated ground blast furnace slag and fly ash-based geopolymers, *Cem. Concr. Res.* 40 (2010) 189-196.
- [497] H.R. Khalid, N.K. Lee, I. Choudhry, Z. Wang, H.K. Lee, Evolution of zeolite crystals in geopolymer-supported zeolites: effects of composition of starting materials, *Mater. Lett.* 239 (2019) 33-36.
- [498] J.L. Provis, G.C. Lukey, J.S.J. Van Deventer, Do geopolymers actually contain nanocrystalline zeolites? a reexamination of existing results, *Chem. Mater.* 17 (2005) 3075-3085.
- [499] A. Navrotsky, Z.R. Tian, Systematics in the enthalpies of formation of anhydrous aluminosilicate zeolites, glasses, and dense phases, *Chem. - A Eur. J.* 7 (2001) 769-774.
- [500] S. Barzgar, Y. Yan, M. Tarik, J. Skibsted, C. Ludwig, B. Lothenbach, A long-term study on structural changes in calcium aluminate silicate hydrates, *Mater. Struct. Constr.* 55 (2022) 1-22.
- [501] Y. Yan, B. Ma, G.D. Miron, D.A. Kulik, K. Scrivener, B. Lothenbach, Al uptake in calcium silicate hydrate and the effect of alkali hydroxide, *Cem. Concr. Res.* 162 (2022).
- [502] I. García-Lodeiro, A. Fernández-Jiménez, A. Palomo, D.E. MacPhee, Effect of calcium additions on N-A-S-H cementitious gels, *J. Am. Ceram. Soc.* 93 (2010) 1934-1940.
- [503] P.S. Deb, P. Nath, P.K. Sarker, The effects of ground granulated blast-furnace slag blending with fly ash and activator content on the workability and strength properties of geopolymer concrete cured at ambient temperature, *Mater. Des.* 62 (2014) 32-39.
- [504] M. Zhang, M. Zhao, G. Zhang, J.M. Sietins, S. Granados-Focil, M.S. Pepi, Y. Xu, M. Tao, Reaction kinetics of red mud-fly ash based geopolymers: Effects of curing temperature on chemical bonding, porosity, and mechanical strength, *Cem. Concr. Compos.* 93 (2018) 175-

- 185.
- [505] J.L. Poole, K.A. Riding, K.J. Folliard, M.C.G. Juenger, A.K. Schindler, Methods for calculating activation energy for portland cement, *ACI Mater. J.* 104 (2007) 86-94.
- [506] Q. Xu, J. Hu, J.M. Ruiz, K. Wang, Z. Ge, Isothermal calorimetry tests and modeling of cement hydration parameters, *Thermochim. Acta* 499 (2010) 91-99.
- [507] P. Teck, R. Snellings, J. Elsen, Method for quantifying the reaction degree of slag in alkali-activated cements using deep learning-based electron microscopy image analysis, (2022) 174-178.
- [508] N.K. Lee, H.K. Lee, Setting and mechanical properties of alkali-activated fly ash/slag concrete manufactured at room temperature, *Constr. Build. Mater.* 47 (2013) 1201-1209.
- [509] J.J. Thomas, A.J. Allen, H.M. Jennings, Density and water content of nanoscale solid C-S-H formed in alkali-activated slag (AAS) paste and implications for chemical shrinkage, *Cem. Concr. Res.* 42 (2012) 377-383.
- [510] N. Marjanović, M. Komljenović, Z. Baščarević, V. Nikolić, R. Petrović, Physical-mechanical and microstructural properties of alkali-activated fly ash-blast furnace slag blends, *Ceram. Int.* 41 (2015) 1421-1435.
- [511] M. Chi, Effects of dosage of alkali-activated solution and curing conditions on the properties and durability of alkali-activated slag concrete, *Constr. Build. Mater.* 35 (2012) 240-245.
- [512] O. Mikhailova, A. del Campo, P. Rovnanik, J.F. Fernández, M. Torres-Carrasco, In situ characterization of main reaction products in alkali-activated slag materials by Confocal Raman Microscopy, *Cem. Concr. Compos.* 99 (2019) 32-39.
- [513] W. Liu, T. Aldahri, C. Xu, C. Li, S. Rohani, Synthesis of sole gismondine-type zeolite from blast furnace slag during CO₂ mineralization process, *J. Environ. Chem. Eng.* (2020) 104652.
- [514] G.M. Kim, J.G. Jang, F. Naeem, H.K. Lee, Heavy Metal Leaching, CO₂ Uptake and Mechanical Characteristics of Carbonated Porous Concrete with Alkali-Activated Slag and Bottom Ash, *Int. J. Concr. Struct. Mater.* 9 (2015) 283-294.
- [515] A. Keulen, A. van Zomeren, J.J. Dijkstra, Leaching of monolithic and granular alkali activated slag-fly ash materials, as a function of the mixture design, *Waste Manag.* 78 (2018) 497-508.
- [516] R.J. Myers, S.A. Bernal, R. San Nicolas, J.L. Provis, Generalized structural description of calcium-sodium aluminosilicate hydrate gels: The cross-linked substituted tobermorite model, *Langmuir* 29 (2013) 5294-5306.
- [517] P. Suraneni, J. Weiss, Examining the pozzolanicity of supplementary cementitious materials using isothermal calorimetry and thermogravimetric analysis, *Cem. Concr. Compos.* 83 (2017) 273-278.
- [518] J. Aliques-Granero, M.T. Tognonvi, A. Tagnit-Hamou, Durability study of AAMs: Sulfate attack resistance, *Constr. Build. Mater.* 229 (2019) 117100.
- [519] M. Kamath, S. Prashant, M. Kumar, Micro-characterisation of alkali activated paste with fly ash-GGBS-metakaolin binder system with ambient setting characteristics, *Constr. Build. Mater.* 277 (2021) 122323.
- [520] S. Park, H.N. Yoon, J. Seo, H.K. Lee, J.G. Jang, Structural evolution of binder gel in alkali-activated cements exposed to electrically accelerated leaching conditions, *J. Hazard. Mater.* 387 (2020) 121825.
- [521] X. Huang, R.L. Zhuang, F. Muhammad, L. Yu, Y.C. Shiao, D. Li, Solidification/stabilization of chromite ore processing residue using alkali-activated composite cementitious materials, *Chemosphere* 168 (2017) 300.
- [522] T. Kim, Characteristics of alkali-activated slag cement-based ultra-lightweight concrete with

- high-volume cenosphere, *Constr. Build. Mater.* 302 (2021) 124165.
- [523] N. Hammad, A. El-Nemr, H. El-Deen Hasan, The performance of fiber GGBS based alkali-activated concrete, *J. Build. Eng.* 42 (2021) 102464.
- [524] J. Wang, T. Huang, L. Han, F. Xie, Z. Liu, D. Wang, Optimization of alkali-activated concrete based on the characteristics of binder systems, *Constr. Build. Mater.* 300 (2021) 123952.
- [525] Y. Wang, R. Chen, J. Hu, Z. Zhang, H. Huang, Y. Ma, J. Wei, Z. Zhang, S. Yin, H. Wang, Q. Yu, Surface characteristics and electrochemical behaviors of passive reinforcing steel in alkali-activated slag, *Corros. Sci.* 190 (2021) 109657.
- [526] A. Niş, N.A. Eren, A. Çevik, Effects of nanosilica and steel fibers on the impact resistance of slag based self-compacting alkali-activated concrete, *Ceram. Int.* 47 (2021) 23905-23918.
- [527] R. Cai, H. Ye, Clinkerless ultra-high strength concrete based on alkali-activated slag at high temperatures, *Cem. Concr. Res.* 145 (2021) 106465.
- [528] S. Marathe, I.R. Mithanthaya, R.Y. Shenoy, Durability and microstructure studies on Slag-Fly Ash-Glass powder based alkali activated pavement quality concrete mixes, *Constr. Build. Mater.* 287 (2021) 123047.
- [529] G. Fang, Q. Wang, M. Zhang, Micromechanical analysis of interfacial transition zone in alkali-activated fly ash-slag concrete, *Cem. Concr. Compos.* 119 (2021) 103990.
- [530] K. Kondepudi, K.V.L. Subramaniam, Formulation of alkali-activated fly ash-slag binders for 3D concrete printing, *Cem. Concr. Compos.* 119 (2021) 103983.
- [531] J. Huang, C. Zou, D. Sun, B. Yang, J. Yan, Effect of recycled fine aggregates on alkali-activated slag concrete properties, *Structures* 30 (2021) 89-99.
- [532] A. Alzaza, K. Ohenoja, M. Illikainen, One-part alkali-activated blast furnace slag for sustainable construction at subzero temperatures, *Constr. Build. Mater.* 276 (2021) 122026.
- [533] Z. Li, T. Lu, Y. Chen, B. Wu, G. Ye, Prediction of the autogenous shrinkage and microcracking of alkali-activated slag and fly ash concrete, *Cem. Concr. Compos.* 117 (2021) 103913.
- [534] S. Uppalapati, L. Vandewalle, Ö. Cizer, Monitoring the setting process of alkali-activated slag-fly ash cements with ultrasonic P-wave velocity, *Constr. Build. Mater.* 271 (2021) 121592.
- [535] G.F. Huseien, A.R.M. Sam, R. Alyousef, Texture, morphology and strength performance of self-compacting alkali-activated concrete: Role of fly ash as GBFS replacement, *Constr. Build. Mater.* 270 (2021) 121368.
- [536] B. Chen, Y. Zuo, S. Zhang, L.M. de Lima Junior, X. Liang, Y. Chen, M.B. van Zijl, G. Ye, Reactivity and leaching potential of municipal solid waste incineration (MSWI) bottom ash as supplementary cementitious material and precursor for alkali-activated materials (under review), *Constr. Build. Mater.* 409 (2023) 133890.
- [537] S. Deepika, G. Anand, A. Bahurudeen, M. Santhanam, Construction Products with Sugarcane Bagasse Ash Binder, *J. Mater. Civ. Eng.* 29 (2017) 1-10.
- [538] S.C. Paul, P.B.K. Mbewe, S.Y. Kong, B. Šavija, Agricultural solid waste as source of supplementary cementitious materials in developing countries, *Materials* (Basel). 12 (2019).
- [539] A. Pereira, J.L. Akasaki, J.L.P. Melges, M.M. Tashima, L. Soriano, M. V. Borrachero, J. Monzó, J. Payá, Mechanical and durability properties of alkali-activated mortar based on sugarcane bagasse ash and blast furnace slag, *Ceram. Int.* 41 (2015) 13012-13024.
- [540] V.N. Castaldelli, M.M. Tashima, J.L. Melges, J.L. Akasaki, J. Monzó, M. V. Borrachero, L. Soriano, J. Payá, Preliminary studies on the use of sugar cane bagasse ash (SCBA) in the manufacture of alkali activated binders, *Key Eng. Mater.* 600 (2014) 689-698.
- [541] A. Sales, S.A. Lima, Use of Brazilian sugarcane bagasse ash in concrete as sand replacement,

- Waste Manag. 30 (2010) 1114-1122.
- [542] A. Islam, U.J. Alengaram, M.Z. Jumaat, I.I. Bashar, The development of compressive strength of ground granulated blast furnace slag-palm oil fuel ash-fly ash based geopolymer mortar, *Mater. Des.* 56 (2014) 833-841.
- [543] M.O. Yusuf, M.A. Megat Johari, Z.A. Ahmad, M. Maslehuudin, Strength and microstructure of alkali-activated binary blended binder containing palm oil fuel ash and ground blast-furnace slag, *Constr. Build. Mater.* 52 (2014) 504-510.
- [544] M.M. Hossain, M.R. Karim, M.M.A. Elahi, M.N. Islam, M.F.M. Zain, Long-term durability properties of alkali-activated binders containing slag, fly ash, palm oil fuel ash and rice husk ash, *Constr. Build. Mater.* 251 (2020) 119094.
- [545] M.A. Salih, N. Farzadnia, A.A. Abang Ali, R. Demirboga, Development of high strength alkali activated binder using palm oil fuel ash and GGBS at ambient temperature, *Constr. Build. Mater.* 93 (2015) 289-300.
- [546] J.M. Mejía, R. Mejía de Gutiérrez, F. Puertas, Ceniza de cascarilla de arroz como fuente de sílice en sistemas cementicios de ceniza volante y escoria activados alcalinamente, *Mater. Constr.* 63 (2013) 361-375.
- [547] G.C. Cordeiro, R.D. Toledo Filho, L.M. Tavares, E.D.M.R. Fairbairn, S. Hempel, Influence of particle size and specific surface area on the pozzolanic activity of residual rice husk ash, *Cem. Concr. Compos.* 33 (2011) 529-534.
- [548] A. Nazari, A. Bagheri, S. Riahi, Properties of geopolymer with seeded fly ash and rice husk bark ash, *Mater. Sci. Eng. A* 528 (2011) 7395-7401.
- [549] C.L. Hwang, T.P. Huynh, Effect of alkali-activator and rice husk ash content on strength development of fly ash and residual rice husk ash-based geopolymers, *Constr. Build. Mater.* 101 (2015) 1-9.
- [550] W. Xu, T.Y. Lo, S.A. Memon, Microstructure and reactivity of rich husk ash, *Constr. Build. Mater.* 29 (2012) 541-547.
- [551] M.F.M. Zain, M.N. Islam, F. Mahmud, M. Jamil, Production of rice husk ash for use in concrete as a supplementary cementitious material, *Constr. Build. Mater.* 25 (2011) 798-805.
- [552] F. Baeza, J. Payá, O. Galao, J.M. Saval, P. Garcés, Blending of industrial waste from different sources as partial substitution of Portland cement in pastes and mortars, *Constr. Build. Mater.* 66 (2014) 645-653.
- [553] C.B. Cheah, W.K. Part, M. Ramli, The hybridizations of coal fly ash and wood ash for the fabrication of low alkalinity geopolymer load bearing block cured at ambient temperature, *Constr. Build. Mater.* 88 (2015) 41-55.
- [554] E.K. Serafimova, M. Mladenov, I. Mihailova, Y. Pelovski, Study on the characteristics of waste wood ash, *J. Univ. Chem. Technol. Metall.* 46 (2011) 31-34.
- [555] P. Thy, B.M. Jenkins, S. Grundvig, R. Shiraki, C.E. Leshner, Corrigendum to high temperature elemental losses and mineralogical changes in common biomass ashes [Fuel, vol. 85/5-6, pp. 793-795] (DOI:10.1016/j.fuel.2005.08.020), *Fuel* 88 (2009) 1151.
- [556] S. V. Vassilev, D. Baxter, L.K. Andersen, C.G. Vassileva, An overview of the composition and application of biomass ash.: Part 2. Potential utilisation, technological and ecological advantages and challenges, *Fuel* 105 (2013) 19-39.
- [557] J. Payá, J. Monzó, M.V. Borrachero, L. Soriano, New Trends in Eco-efficient and Recycled Concrete. Sewage sludge ash, in: *New Trends Eco-Efficient Recycl. Concr.*, Elsevier, 2018: pp. 121-152.
- [558] M. Záleská, Z. Pavlík, M. Pavlíková, L. Scheinherrová, J. Pokorný, A. Trník, P. Svora, J. Fořt, O. Jankovský, Z. Suchorab, R. Černý, Biomass ash-based mineral admixture prepared from municipal sewage sludge and its application in cement composites, *Clean Technol. Environ.*

- Policy 20 (2018) 159-171.
- [559] Z. Chen, J.S. Li, B.J. Zhan, U. Sharma, C.S. Poon, Compressive strength and microstructural properties of dry-mixed geopolymer pastes synthesized from GGBS and sewage sludge ash, *Constr. Build. Mater.* 182 (2018) 597-607.
- [560] M. Cyr, M. Coutand, P. Clastres, Technological and environmental behavior of sewage sludge ash (SSA) in cement-based materials, *Cem. Concr. Res.* 37 (2007) 1278-1289.
- [561] H. seok Jang, Y.T. Lim, J.H. Kang, S. young So, H. seok So, Influence of calcination and cooling conditions on pozzolanic reactivity of paper mill sludge, *Constr. Build. Mater.* 166 (2018) 257-270.
- [562] E. Mozaffari, J.M. Kinuthia, J. Bai, S. Wild, An investigation into the strength development of Wastepaper Sludge Ash blended with Ground Granulated Blastfurnace Slag, *Cem. Concr. Res.* 39 (2009) 942-949.
- [563] I. Vegas, J. Urreta, M. Frías, R. García, Freeze-thaw resistance of blended cements containing calcined paper sludge, *Constr. Build. Mater.* 23 (2009) 2862-2868.
- [564] C.R. Melo, E. Angioletto, H.G. Riella, M. Peterson, M.R. Rocha, A.R. Melo, L. Silva, S. Strugale, Production of metakaolin from industrial cellulose waste, *J. Therm. Anal. Calorim.* 109 (2012) 1341-1345.
- [565] P. Segui, J.E. Aubert, B. Husson, M. Measson, Characterization of wastepaper sludge ash for its valorization as a component of hydraulic binders, *Appl. Clay Sci.* 57 (2012) 79-85.
- [566] S. Yan, K. Sagoe-Crentsil, Properties of wastepaper sludge in geopolymer mortars for masonry applications, *J. Environ. Manage.* 112 (2012) 27-32.
- [567] W. Hu, Q. Nie, B. Huang, X. Shu, Q. He, Mechanical and microstructural characterization of geopolymers derived from red mud and fly ashes, *J. Clean. Prod.* 186 (2018) 799-806.
- [568] R.R. Bellum, C. Venkatesh, S.R.C. Madduru, Influence of red mud on performance enhancement of fly ash-based geopolymer concrete, *Innov. Infrastruct. Solut.* 6 (2021) 1-9.
- [569] J. Pascual, F.A. Corpas, J. López-Beceiro, M. Benítez-Guerrero, R. Artiaga, Thermal characterization of a Spanish red mud, *J. Therm. Anal. Calorim.* 96 (2009) 407-412.
- [570] A. Hasnaoui, E. Ghorbel, G. Wardeh, Performance of metakaolin/slag-based geopolymer concrete made with recycled fine and coarse aggregates, *J. Build. Eng.* 42 (2021) 102813.
- [571] R. Si, S. Guo, Q. Dai, J. Wang, Atomic-structure, microstructure and mechanical properties of glass powder modified metakaolin-based geopolymer, *Constr. Build. Mater.* 254 (2020) 119303.
- [572] A. Mobili, A. Belli, C. Giosuè, T. Bellezze, F. Tittarelli, Metakaolin and fly ash alkali-activated mortars compared with cementitious mortars at the same strength class, *Cem. Concr. Res.* 88 (2016) 198-210.
- [573] X. Liu, J. Jiang, H. Zhang, M. Li, Y. Wu, L. Guo, W. Wang, P. Duan, W. Zhang, Z. Zhang, Thermal stability and microstructure of metakaolin-based geopolymer blended with rice husk ash, *Appl. Clay Sci.* 196 (2020) 105769.
- [574] G.V.P. Bhagath Singh, K.V.L. Subramaniam, Quantitative XRD study of amorphous phase in alkali activated low calcium siliceous fly ash, *Constr. Build. Mater.* 124 (2016) 139-147.
- [575] B. Valentim, A. Guedes, D. Flores, C.R. Ward, J.C. Hower, Variations in fly ash composition with sampling location: Case study from a Portuguese power plant, *Coal Combust. Gasif. Prod.* 1 (2009) 14-24.
- [576] A. Schöler, B. Lothenbach, F. Winnefeld, M. Zajac, Hydration of quaternary Portland cement blends containing blast-furnace slag, siliceous fly ash and limestone powder, *Cem. Concr. Compos.* 55 (2015) 374-382.
- [577] G.V.P. Bhagath Singh, K.V.L. Subramaniam, Characterization of Indian fly ashes using

- different experimental techniques, *Indian Concr. J.* 92 (2018) 10-23.
- [578] P.T. Durdziński, M. Ben Haha, M. Zajac, K.L. Scrivener, Phase assemblage of composite cements, *Cem. Concr. Res.* 99 (2017) 172-182.
- [579] E.L. Shock, D.C. Sassani, M. Willis, D.A. Sverjensky, Inorganic species in geologic fluids: Correlations among standard molal thermodynamic properties of aqueous ions and hydroxide complexes, *Geochim. Cosmochim. Acta* 61 (1997) 907-950.
- [580] D.A. Sverjensky, E.L. Shock, H.C. Helgeson, Prediction of the thermodynamic properties of aqueous metal complexes to 1000°C and 5 kb, *Geochim. Cosmochim. Acta* 61 (1997) 1359-1412.
- [581] T. Matschei, B. Lothenbach, F.P. Glasser, Thermodynamic properties of Portland cement hydrates in the system CaO-Al₂O₃-SiO₂-CaSO₄-CaCO₃-H₂O, *Cem. Concr. Res.* (2007).
- [582] C.S. Walker, E. Agency, S. Anraku, S. Mitsui, E. Agency, Thermodynamic properties of SiO₂ (aq), HSiO₃⁻ and SiO₃²⁻, *Goldschmidt 2019*, Barcelona, Spain. Barcelona, Spain. (2019).
- [583] J.W. Johnson, E.H. Oelkers, H.C. Helgeson, SUPCRT92: A software package for calculating the standard molal thermodynamic properties of minerals, gases, aqueous species, and reactions from 1 to 5000 bar and 0 to 1000°C, *Comput. Geosci.* 18 (1992) 899-947.
- [584] R. Robie, B.S. Hemingway, Thermodynamic Properties of Minerals and Related Substances at 298.15K and 1 Bar, *U.S. Geol. Surv. Bull.* (1995) 1-461.
- [585] B. Lothenbach, L. Pelletier-Chaignat, F. Winnefeld, Stability in the system CaO-Al₂O₃-H₂O, *Cem. Concr. Res.* 42 (2012) 1621-1634.

Appendix A

Database of precursors utilised across scientific literature

Among the many challenges faced by alkali-activated binders, the variability in chemistry and mineralogy, and the non-homogeneous geographical availability of different precursors are considered the most relevant ones. This Appendix provides supporting data utilised in Chapter 2, in which the implementation of chemistry-based approaches to estimate characteristics of these binders is introduced.

A.1 Chemical compositions of traditional and alternative precursors

The diagram displayed in Figure 2.6 illustrates the large variations in the chemical composition of a range of precursors, comprising those which are scientifically mature and those which are pointed as future alternatives. Table A.1 details the chemical compositions of most of these precursors, as determined by XRF.

Table A.1: Detailed chemical compositions of precursors utilised for the compilation of the diagram shown in Figure 2.6.

Class of precursor	SiO ₂ (wt%)	Al ₂ O ₃ (wt%)	CaO (wt%)	Fe ₂ O ₃ (wt%)	MgO (wt%)	Ref.
Blast furnace slag (BFS)	21.00	17.00	56.10	0.62	0.00	[82]
	21.00	17.00	56.10	0.62	0.00	[508]
	30.80	10.90	51.80	0.64	4.57	[106]
	33.50	13.70	44.80	0.50	2.90	[509]
	34.57	10.88	44.56	0.61	4.19	[200]
	37.40	10.90	43.90	0.70	6.50	[200]
	30.04	12.74	43.83	1.16	4.79	[200]
	27.40	14.70	43.40	0.30	9.30	[200]
	32.50	13.00	43.20	0.55	4.70	[200]
	29.71	16.41	43.12	0.89	4.73	[200]
	27.60	13.51	42.96	0.54	9.31	[200]
	31.62	14.65	42.86	1.07	1.17	[178]
	37.40	7.10	42.80	0.55	6.40	[510]
	33.80	13.70	42.60	0.40	5.30	[509]
	34.48	11.48	42.43	0.00	7.08	[346]
	32.10	12.90	42.40	0.70	6.53	[194]
	32.25	13.29	42.33	0.60	5.21	[111]
	32.84	13.61	42.27	0.66	6.83	[511]
	32.59	13.94	42.22	0.78	4.96	[512]

	35.10	10.80	42.00	0.40	7.90	[108]
	40.00	4.10	42.00	2.00	6.20	[468]
	32.08	13.98	41.84	0.87	6.74	[513]
	34.10	9.90	41.80	0.48	7.70	[348]
	32.06	15.40	41.79	0.26	7.45	[80]
	33.22	13.49	41.57	0.40	7.04	[514]
	32.72	13.37	41.46	0.83	5.54	[204]
	34.95	13.11	41.37	0.69	7.12	[204]
	35.83	10.93	41.16	0.81	7.84	[515]
	32.91	11.85	40.96	0.46	9.23	[193]
	32.71	13.89	40.95	0.31	6.36	[516]
	34.58	13.69	40.67	0.44	7.05	[45]
	38.71	10.46	40.62	0.33	7.58	[72]
	31.80	13.30	40.50	0.50	9.30	[517]
	34.11	12.38	40.21	0.32	7.44	[517]
	30.53	10.55	40.15	1.29	7.43	[517]
	39.66	6.45	40.12	0.47	9.50	[517]
	36.00	12.50	40.00	0.50	7.74	[400]
	36.00	10.50	39.80	0.67	7.93	[518]
	36.00	10.50	39.80	0.67	7.93	[519]
	36.19	12.41	39.80	0.60	7.25	[520]
	41.01	9.26	39.73	0.66	12.19	[434]
	35.40	10.30	39.70	0.50	10.90	[209]
	35.40	10.30	39.70	0.50	10.90	[521]
	36.60	12.15	39.68	0.43	8.35	[522]
	35.15	13.07	39.60	0.28	8.47	[523]
	35.70	11.21	39.40	0.42	10.74	[524]
	41.20	7.10	39.40	1.00	7.40	[525]
	40.10	7.20	39.20	0.30	10.00	[526]
	35.50	14.80	38.70	0.27	6.70	[527]
	39.40	11.40	38.65	0.76	6.77	[528]
	37.50	7.27	38.48	0.73	10.86	[529]
	38.46	10.50	38.46	0.40	6.96	[530]
	31.63	17.98	38.10	0.42	7.55	[531]
	30.91	14.73	38.09	0.79	8.87	[532]
	33.04	14.48	37.40	0.44	9.63	[533]
	36.50	16.30	36.60	0.20	5.90	[534]
	37.40	12.00	36.50	0.58	8.00	[535]
	27.51	10.59	35.23	1.03	7.11	[536]
	40.28	10.53	34.54	0.39	8.63	[536]
	36.40	11.39	34.12	1.69	10.30	[536]
	37.04	8.95	33.92	0.40	14.32	[536]
	28.59	13.54	30.63	3.02	9.86	[536]
	35.00	14.30	30.40	0.30	16.10	[536]
	75.67	1.52	6.62	2.29	1.87	[537]

Sugar cane bagasse ash (SCBA)	65.30	6.90	4.00	3.70	1.10	[538]
	78.59	4.47	1.34	4.88	1.03	[539]
	31.41	7.57	16.06	6.02	1.07	[540]
	75.67	1.52	6.62	2.29	0.40	[541]
Palm oil fuel ash (POFA)	66.64	3.82	5.23	3.70	2.29	[538]
	63.41	5.55	4.34	4.19	3.74	[542]
	46.00	3.10	8.46	2.45	4.40	[543]
	53.50	2.51	5.31	2.71	5.51	[544]
Rice husk ash (RHA)	66.64	3.82	5.23	3.70	4.19	[545]
	93.40	0.05	0.31	0.06	0.35	[538]
	94.40	0.20	0.31	0.20	0.00	[546]
	94.10	0.20	0.00	0.20	0.00	[546]
	87.12	0.43	1.12	0.26	0.52	[544]
	82.60	0.40	0.80	0.50	0.70	[547]
	81.36	0.40	3.23	0.12	0.00	[548]
	95.60	0.00	0.70	0.24	0.00	[549]
	91.71	0.36	0.86	0.90	0.31	[550]
	79.84	0.14	0.55	1.16	0.19	[551]
	80.72	0.08	0.56	1.10	0.18	[551]
	86.49	0.01	0.50	0.91	0.13	[551]
Biomass wood ash (BWA)	82.37	0.44	1.24	0.16	0.68	[552]
	2.70	1.30	61.00	1.30	8.70	[553]
	0.00	0.00	52.20	0.00	1.32	[554]
	9.35	3.12	32.06	1.14	4.93	[555]
	3.68	1.06	67.85	0.63	4.31	[139]
	8.37	2.25	48.70	1.67	4.79	[139]
	9.28	2.28	51.90	1.47	3.75	[139]
	19.80	6.16	46.75	2.85	8.26	[139]
	39.95	10.50	16.25	4.23	4.30	[139]
	14.45	3.56	47.35	1.69	4.71	[139]
Sewadge sludge ash (SSA)	2.70	1.30	61.00	1.30	8.70	[140]
	12.33	0.12	67.80	1.09	11.43	[556]
	38.28	20.72	5.51	11.27	1.91	[462]
	20.80	14.90	31.30	7.40	2.60	[557]
Paper sludge ash (PSA)	30.10	11.90	25.90	7.10	2.20	[557]
	16.20	14.70	32.90	8.20	2.40	[557]
	15.50	14.00	32.10	8.30	2.60	[557]
	16.98	9.48	29.73	8.38	3.17	[552]
	30.80	7.90	19.70	3.50	4.10	[558]
	27.78	12.20	10.42	18.23	3.15	[559]
	34.20	12.60	20.60	4.70	1.90	[560]
	15.50	10.10	63.90	4.99	2.55	[561]
Paper sludge ash (PSA)	25.70	18.86	43.51	0.87	5.15	[562]
	21.60	14.40	36.50	0.50	2.40	[563]
	25.10	18.50	33.60	0.50	1.20	[564]

	13.90	8.30	47.10	0.50	1.60	[565]
	28.00	13.20	45.50	1.30	4.00	[565]
	16.70	16.50	22.50	0.90	0.00	[566]
Red mud	8.34	17.67	20.88	28.30	0.65	[76]
	25.50	26.40	1.30	23.20	0.10	[567]
	21.92	22.62	10.50	21.79	0.65	[568]
	19.21	22.91	5.36	33.77	0.39	[24]
	7.50	20.20	6.22	47.85	0.33	[569]
Metakaolin	61.24	32.58	0.13	1.17	0.15	[409]
	55.00	39.00	0.60	1.80	0.00	[570]
	56.61	39.16	0.05	1.87	0.09	[571]
	55.00	40.20	0.10	0.60	0.40	[572]
	54.50	43.00	0.20	1.00	0.80	[344]
	55.57	41.55	0.00	0.56	0.05	[179]
	53.33	43.35	0.02	1.69	0.22	[573]
	50.72	44.63	2.69	0.00	0.00	[205]
Municipal solid waste incineration bottom ash (MSWI)	61.39	14.22	24.38	-	-	[536]*
	62.56	14.31	23.13	-	-	[536]*
	44.34	8.11	47.55	-	-	[536]*
	55.65	12.48	31.87	-	-	[536]*
	17.60	10.83	71.57	-	-	[536]*
	71.35	9.74	18.92	-	-	[536]*
	68.90	9.42	21.68	-	-	[536]*
	70.50	10.55	18.94	-	-	[536]*
	34.15	22.07	43.78	-	-	[536]*
	56.60	16.72	26.69	-	-	[536]*
	55.03	17.31	27.66	-	-	[536]*
	54.91	17.22	27.87	-	-	[536]*
	25.74	16.21	58.06	-	-	[536]*
	65.61	8.79	25.61	-	-	[536]*
	41.80	18.63	39.57	-	-	[536]*
	52.02	16.43	31.55	-	-	[536]*
	66.50	15.28	18.23	-	-	[536]*
	58.86	18.14	23.00	-	-	[536]*
	55.80	13.07	31.13	-	-	[536]*
	39.59	20.52	39.89	-	-	[536]*
	37.52	26.95	35.52	-	-	[536]*
	41.15	24.88	33.97	-	-	[536]*
	34.93	22.05	43.02	-	-	[536]*

*Work was developed in the same research group - compositions comprise only SiO₂, Al₂O₃ and CaO, following the compiled data provided by the authors.

Besides chemistry, the mineralogy of fly ashes is also known to display large variations among different sources. Table A.2 details the amorphous content and the chemical composition of different fly ashes cited in literature, which were also utilised as data points in the diagram shown in Figure 2.6.

Table A.2: Detailed chemical compositions of fly ashes utilised for the compilation of the diagram shown in Figure 2.6 and in Table 2.2.

Type	CaO (wt%)	SiO ₂ (wt%)	Al ₂ O ₃ (wt%)	Fe ₂ O ₃ (wt%)	MgO (wt%)	Amorphous content	Ref.
F	4.85	52.72	21.67	9.55	1.89	73.00%	[409]
F	2.75	58.14	26.06	7.32	1.12	48.16%	[574]
F	8.52	49.08	19.20	10.42	1.98	60.60%	[575]
F	6.95	56.96	16.48	13.69	1.80	44.40%	[575]
F	8.09	45.91	23.50	8.09	1.98	64.70%	[575]
F	8.69	41.99	23.15	7.89	2.67	78.20%	[575]
F	3.19	56.77	26.03	5.07	1.34	68.80%	[576]
F	1.40	56.80	26.30	9.50	0.80	47.30%	[263]
F	1.50	57.00	25.00	9.90	0.70	45.00%	[263]
F	1.30	58.30	22.20	13.60	0.80	46.10%	[263]
F	4.20	44.50	30.70	14.40	1.60	80.00%	[263]
F	1.30	62.90	29.30	1.80	1.10	61.00%	[263]
F	1.00	67.00	24.80	1.00	0.60	79.10%	[263]
F	3.30	61.50	22.40	3.30	1.10	66.30%	[263]
F	3.80	57.50	28.20	3.80	1.20	66.00%	[263]
F	0.40	65.90	27.60	0.40	0.30	73.70%	[263]
F	2.70	52.32	37.18	3.73	0.43	72.60%	[94]
F	2.46	55.42	27.13	7.30	1.20	55.48%	[188]
F	1.65	56.57	29.01	5.47	0.63	38.87%	[188]
F	2.74	55.45	27.13	7.28	1.20	55.60%	[577]
F	1.65	56.57	29.01	5.47	0.63	38.90%	[577]
F	1.36	55.17	29.71	6.33	0.70	44.20%	[577]
F	3.80	48.81	31.40	7.85	0.70	36.00%	[577]
F	3.97	54.55	26.46	7.17	1.17	54.40%	[577]
F	1.63	56.23	29.42	5.86	0.80	46.30%	[577]
F	1.30	55.16	29.72	6.32	0.77	46.90%	[577]
F	1.11	56.06	29.90	5.76	0.67	40.00%	[577]
F	11.70	46.10	29.00	5.00	1.90	76.50%	[169]
F	11.00	52.80	22.80	6.60	1.50	72.10%	[169]
F	3.80	41.10	34.10	3.90	1.30	56.70%	[169]
F	2.50	40.40	39.10	3.10	1.10	66.10%	[169]
F	3.80	50.30	25.36	9.50	3.00	73.30%	[264]
F	5.70	46.85	25.70	9.40	2.54	82.30%	[264]
F	4.90	46.40	26.00	9.35	3.40	82.90%	[264]
F	4.71	51.81	26.92	6.07	2.56	71.80%	[264]
F	4.86	49.45	26.83	6.68	3.01	80.80%	[264]
F	4.63	48.43	28.72	6.35	2.60	82.80%	[264]
F	10.16	56.51	19.85	5.81	2.94	66.50%	[168]
F	13.30	49.82	23.84	4.41	3.27	62.10%	[168]
F	14.59	35.63	19.18	4.98	3.38	86.30%	[168]
F	14.14	52.42	19.59	4.78	3.17	76.60%	[168]
F	3.22	52.28	22.93	13.04	0.99	71.50%	[168]

F	1.31	59.62	23.97	6.56	1.16	62.50%	[168]
C	20.70	42.30	19.80	8.20	2.20	89.70%	[578]
C	26.50	33.60	18.20	6.40	6.40	85.90%	[578]
C	28.35	21.23	13.99	5.53	6.79	84.50%	[168]
C	26.55	28.08	14.40	4.45	3.67	78.00%	[168]
C	20.68	41.25	16.40	6.79	4.10	53.80%	[168]
C	20.92	39.62	16.58	6.15	4.27	56.40%	[168]
C	23.83	36.99	18.83	6.21	5.10	66.10%	[168]
C	21.54	38.21	19.37	6.20	5.19	81.00%	[168]
C	21.26	37.26	22.43	5.44	4.07	78.70%	[168]
C	27.76	32.79	16.34	5.79	6.87	56.20%	[168]
C	23.39	37.57	19.08	5.57	5.45	57.80%	[168]

A.2 Geographical distribution of primary sources of byproducts utilised as precursors

As fly ashes and slags, the two most utilised precursors in research and large-scale project, are not equally available in different regions of the planet, new alternatives of industrial byproducts have been investigated in the scientific literature. The utilization of these materials as precursors has been shown to have positive outcomes for alkali-activated binders, despite their low maturity level, raising them as future options for the building industry. In Figure 2.5, the 3 main producers of the primary resources for different byproducts as precursors have been listed, proving that the implementation of new raw materials can widen the availability of resources for the production of alkali-activated binders. Table A.3 details the amounts utilised for the obtainment of Figure 2.5.

Table A.3: Global leaders in the production of the primary resources utilised for the obtainment of precursors as byproducts - values in ton.

Precursor	Primary source	Country	Quantity	Ref.
Coal fly ash	Coal	China	4.15×10^9	IEA* - 2022
		India	8.63×10^8	
		Indonesia	6.93×10^8	
		United States	5.38×10^8	
		Australia	4.63×10^8	
Blast furnace slag	Pig iron	China	9.08×10^8	World Steel - 2021
		India	6.78×10^7	
		Japan	6.16×10^7	
		Russia	5.19×10^7	
		South Korea	4.54×10^7	
Palm oil fuel ash	Palm kernel	Indonesia	1.05×10^7	FAO** - 2021
		Malaysia	4.42×10^6	
		Thailand	6.72×10^5	
		Nigeria	3.55×10^5	
		Colombia	3.13×10^5	
Rice husk ash	Rice	China	2.08×10^8	FAO** - 2022
		India	1.96×10^8	
		Bangladesh	5.72×10^7	
		Indonesia	5.47×10^7	
		Vietnam	4.27×10^7	
Sugar cane bagasse ash	Sugar cane	Brazil	7.24×10^8	FAO** - 2022
		India	4.39×10^8	
		China	1.03×10^8	
		Thailand	9.21×10^7	
		Pakistan	8.80×10^7	

*IEA - International Energy Agency.

**FAO - Food and Agriculture Organization of the United Nations.

Appendix B

Structural characterization of synthetic glasses

The approach of this PhD thesis considered the synthesis of glasses with chemical compositions resembling coal fly ashes and blast furnace slags. The utilization of synthetic precursors allowed a simplification of the chemical composition of the investigated precursors, facilitating the comprehension of the influence of individual components in the characteristics of alkali-activated binders. A total of 6 synthesis batches were produced for glasses Si-FA and Ca-FA, and 4 for glasses BFS-1 and BFS-2. The synthesis method is described in Section 3.2.1, and their characterization methods are described in Section 3.2.2. This Appendix details the chemical composition of the each individual batch along with details of their structural characterization through ^{29}Si NMR and Raman spectroscopy.

B.1 Chemical compositions through XRF

The following tables detail the chemical compositions of each production batch for the four synthetic glasses.

Table B.1: Chemical composition of the six synthesis batches of glass Si-FA.

Batch number	Chemical composition			Atomic ratios	
	SiO_2 (wt%)	Al_2O_3 (wt%)	CaO (wt%)	Si/Al	Ca/Si
1	55.8	31.1	12.6	1.53	0.24
2	55.4	31.8	11.9	1.48	0.23
3	55.1	31.0	12.5	1.51	0.24
4	54.9	30.4	13.3	1.53	0.26
5	56.0	30.0	13.2	1.59	0.25
6	56.2	29.5	13.4	1.62	0.25
Average	55.6 ± 0.5	30.6 ± 0.8	12.8 ± 0.6	1.54 ± 0.05	0.25 ± 0.01
Target	55.7	31.3	13.0	1.50	0.25

Table B.2: Chemical composition of the six synthesis batches of glass Ca-FA.

Batch number	Chemical composition			Atomic ratios	
	SiO_2 (wt%)	Al_2O_3 (wt%)	CaO (wt%)	Si/Al	Ca/Si
1	48.9	28.0	22.6	1.48	0.49
2	49.1	28.0	22.0	1.49	0.48
3	48.8	28.9	21.3	1.43	0.47
4	48.1	27.4	23.2	1.49	0.41
5	49.2	26.7	23.4	1.56	0.41
6	49.5	25.2	24.3	1.67	0.53
Average	48.9 ± 0.5	27.4 ± 1.3	22.8 ± 1.1	1.52 ± 0.08	0.50 ± 0.02
Target	49.3	27.7	23.0	1.50	0.50

Table B.3: Chemical composition of the six synthesis batches of glass BFS-1.

Batch number	Chemical composition			Atomic ratios	
	SiO ₂ (wt%)	Al ₂ O ₃ (wt%)	CaO (wt%)	Si/Al	Ca/Si
1	39.8	21.8	37.6	1.55	1.01
2	38.9	24.5	35.8	1.35	0.98
3	37.6	23.3	38.5	1.37	1.09
4	38.8	20.4	40.2	1.61	1.11
Average	38.8 ± 0.9	22.5 ± 1.8	38.0 ± 1.8	1.47 ± 0.13	1.05 ± 0.06
Target	40.1	22.5	37.4	1.50	1.00

Table B.4: Chemical composition of the six synthesis batches of glass BFS-2.

Batch number	Chemical composition			Atomic ratios	
	SiO ₂ (wt%)	Al ₂ O ₃ (wt%)	CaO (wt%)	Si/Al	Ca/Si
1	33.9	22.5	44.0	1.28	1.35
2	36.8	19.5	43.0	1.59	1.25
3	33.8	20.2	45.0	1.42	1.42
4	34.9	16.9	49.2	1.76	1.45
Average	35.8 ± 1.4	19.8 ± 2.3	44.5 ± 2.0	1.52 ± 0.20	1.37 ± 0.09
Target	34.9	19.6	45.6	1.50	1.40

B.2 Structural characterization with ²⁹Si NMR and Raman

Figure 3.2, in Chapter 3, illustrates the similarities between the characterization of Si Qⁿ units obtained with both Raman and ²⁹Si NMR spectroscopy. The following Tables B.5 - B.8 detail the quantitative analysis of each SiO₄ units calculated with the techniques for the four glasses - the glasses synthesized in the batch 1 of each composition were utilised for this characterization.

Table B.5: Structural characterization of the SiO₄ units in glass Si-FA as obtained through the deconvolution of Raman and ²⁹Si NMR spectra - determination of individual quantities, and chemical shift of the centre of each individual curve.

Technique		Q ⁰	Q ¹	Q ²	Q ³	Q ⁴ (3 Al)	Q ⁴ (2 Al)	Q ⁴ (1 Al)	Q ⁴ (0 Al)	Q ⁴ (total)
Raman	Amount	0.5	1.19	9.76	12.29	-	-	-	-	76.72
	Chemical shift	876.8	905.2	946.6; 1016.2	1097.7	-	-	-	-	1169.0
²⁹ Si NMR	Amount	2.00	1.93	13.55	21.50	21.27	15.83	11.40	12.57	61.03
	Chemical shift	-62.4	-68.4	-72.2; -81.4	-89.3	-96.4	-102.4	-109.2	-116.4	-

Table B.6: Structural characterization of the SiO₄ units in glass Ca-FA as obtained through the deconvolution of Raman and ²⁹Si NMR spectra - determination of individual quantities, and chemical shift of the centre of each individual curve.

Technique		Q ⁰	Q ¹	Q ²	Q ³	Q ⁴ (3 Al)	Q ⁴ (2 Al)	Q ⁴ (1 Al)	Q ⁴ (0 Al)	Q ⁴ (total)
Raman	Amount	0.01	2.01	27.32	19.99	-	-	-	-	50.67
	Chemical shift	864.8	904.5	951.5; 1008.1	1066.4	-	-	-	-	1145.3
²⁹ Si NMR	Amount	0.17	2.34	17.50	23.08	17.43	13.11	12.36	14.02	56.91
	Chemical shift	-62.8	-69.8	-75.1; -79.9	-87.2	-95.5	-104.0	-111.4	-117.5	-

Table B.7: Structural characterization of the SiO₄ units in glass BFS-1 as obtained through the deconvolution of Raman and ²⁹Si NMR spectra - determination of individual quantities, and chemical shift of the centre of each individual curve.

Technique		Q ⁰	Q ¹	Q ²	Q ³	Q ⁴ (3 Al)	Q ⁴ (2 Al)	Q ⁴ (1 Al)	Q ⁴ (0 Al)	Q ⁴ (total)
Raman	Amount	4.57	11.09	38.71	19.83	-	-	-	-	25.81
	Chemical shift	886.2	929.0	975.4; 1023.1	1071.1	-	-	-	-	1176.4
²⁹ Si NMR	Amount	4.00	9.69	37.74	15.92	5.78	6.37	8.75	11.77	32.66
	Chemical shift	-63.7	-68.6	-73.5; -79.1	-86.8	-96.0	-102.5	-108.9	-117.0; -124.0	-

Table B.8: Structural characterization of the SiO₄ units in glass BFS-2 as obtained through the deconvolution of Raman and ²⁹Si NMR spectra - determination of individual quantities, and chemical shift of the centre of each individual curve.

Technique		Q ⁰	Q ¹	Q ²	Q ³	Q ⁴ (3 Al)	Q ⁴ (2 Al)	Q ⁴ (1 Al)	Q ⁴ (0 Al)	Q ⁴ (total)
Raman	Amount	8.93	14.67	38.78	11.76	-	-	-	-	25.86
	Chemical shift	875.6	922.2	966.6; 1018.1	1064.5	-	-	-	-	1166.6
²⁹ Si NMR	Amount	6.94	17.64	42.63	6.96	5.94	5.66	8.13	6.10	25.83
	Chemical shift	-63.5	-68.6	-73.1; -77.6	-84.8	-95.7	-104.4	-110.2	-116.7; -122.2	-

B.3 Structural characterization of precursors described in literature

Figures 3.8 and 3.9, in Chapter 3, illustrate the existence of structural correlations between Si Qⁿ units and the chemical composition of synthetic and commercial precursors. While the synthetic glasses utilized for these observations were already described in the previous sections, the structural details of the commercial precursors were obtained from literature. Table B.9 provides the quantitative analysis of Si Qⁿ units obtained by Fernández-Jimenez et al. [208], which were calculated through the deconvolution of ²⁹Si MAS NMR, and Table B.10 provides the chemical composition of the commercial fly ashes investigated in their study.

Table B.9: Structural details of SiO_4 units of commercial fly ashes described in [208], obtained through the deconvolution of ^{29}Si NMR spectra - determination of individual quantities, and chemical shift of the centre of each individual curve.

Fly Ash		Q^0	Q^1	Q^2	Q^3	Q^4 (3 Al)	Q^4 (2 Al)	Q^4 (1 Al)	Q^4 (0 Al)	Q^4 (total)
C	Amount	-	-	2.84	13.31	11.40	34.07	19.51	16.77	81.75
	Chemical shift	-	-	-80.1	-84.5; -90.8	-95.2	-99.8; -104.3;	-109.1	-114.5; -120.4	-
L	Amount	-	-	-	16.32	16.90	40.06	20.90	5.61	83.47
	Chemical shift	-	-	-	-84.0; -88.3	-94.0	-98.6; -103.4	-108.8	-115.0	-
PN	Amount	-	-	2.37	20.22	14.30	38.70	17.60	6.80	77.40
	Chemical shift	-	-	-78.6	-84.2; -89.6	-94.3	-98.6; -103.4	-108.0	-114.0	-
R	Amount	-	3.40	8.08	25.05	22.50	21.30	13.20	6.40	63.40
	Chemical shift	-	-70.5	-78.3	-85.0; -89.0	-95.2	-100.0; -103.7	-108.6	-114.4	-
T	Amount	-	-	-	19.33	13.50	29.40	18.40	19.42	80.72
	Chemical shift	-	-	-	-84.0; -88.9	-95.2	-99.0; -103.7	-108.6	-113.0; -118.7	-

Table B.10: Chemical composition of commercial fly ashes described in [208], obtained through XRF.

Fly Ash	Chemical composition				
	SiO_2 (wt%)	Al_2O_3 (wt%)	CaO (wt%)	Fe_2O_3 (wt%)	MgO (wt%)
C	53.08	24.80	2.44	8.01	1.94
L	51.51	27.47	4.39	7.23	1.86
PN	54.42	26.42	3.21	7.01	1.79
R	42.03	26.70	9.60	14.42	1.87
T	42.62	29.21	6.37	16.77	1.35

With respect to the work from Blotevogel et al. [251], an estimation of the amount of each $\text{Si } Q^n$ unit on different commercial slags was performed based on the available data. Those authors provided the total peak area of the different units obtained through deconvolution of Raman spectra analysis. In this thesis, the area of each unit was normalized to their sum, and the resulting values were corrected utilizing Raman scattering coefficients, following a similar approach as described in Section 3.3.2. Table B.11 provides the values available in literature and the final calculated quantities of each SiO_4 unit, and Table B.12 provides the chemical composition of each evaluated slag.

Table B.11: Structural details of SiO₄ units of commercial blast furnace slags described in [251], obtained through the deconvolution of Raman spectra, and the respective quantification of each unit calculated through the implementation of Raman scattering coefficients.

	Slag	Q ⁰ (850 cm ⁻¹)	Q ¹ (912 cm ⁻¹)	Q ² (970 cm ⁻¹)	Q ³ (1035 cm ⁻¹)
GGBS2	Peak area	69	60	32	18
	Normalized area (%)	38.54	33.52	17.88	10.06
	Corrected quantity* (%)	13.32	22.54	25.53	38.61
GGBS3	Peak area	70	62	26	22
	Normalized area (%)	38.89	34.44	14.44	12.22
	Corrected quantity* (%)	12.90	22.23	19.80	45.06
GGBS9	Peak area	73	59	38	22
	Normalized area (%)	38.02	30.73	19.79	11.46
	Corrected quantity* (%)	12.39	19.48	26.65	41.48
GGBS11	Peak area	66	57	29	17
	Normalized area (%)	39.05	33.73	17.16	10.06
	Corrected quantity* (%)	13.59	22.84	24.68	38.90
GGBS12	Peak area	66	62	30	20
	Normalized area (%)	37.08	34.83	16.85	11.24
	Corrected quantity* (%)	12.39	22.64	23.27	41.71
GGBS13	Peak area	53	74	36	23
	Normalized area (%)	28.49	39.78	19.35	12.37
	Corrected quantity* (%)	8.81	23.94	24.74	42.50
GGBS14	Peak area	71	55	28	18
	Normalized area (%)	41.28	31.98	16.28	10.47
	Corrected quantity* (%)	14.38	21.67	23.44	40.51

Table B.12: Chemical composition of commercial fly ashes described in [251], obtained through XRF.

Fly Ash	Chemical composition			
	SiO ₂ (wt%)	Al ₂ O ₃ (wt%)	CaO (wt%)	MgO (wt%)
GGBS2	36.6	12.0	42.0	7.0
GGBS3	37.6	9.61	40.9	6.4
GGBS9	37.4	11.0	39.5	6.6
GGBS11	36.3	11.8	43.2	6.3
GGBS12	36.8	11.7	42.0	6.6
GGBS13	39.2	11.2	33.9	10.4
GGBS14	34.6	13.7	38.9	8.4

Figure 3.12 provides an additional correlation of glass structure with chemical composition. The relationship between the X-ray diffractograms and the CaO content of different glasses, was successfully derived utilizing the glasses obtained in this thesis and data available in literature. Table B.13 provides the details of the chemistry of synthetic glasses obtained in the work of Goto et al. [160], and their respective maximum 2θ diffraction angle calculated through the linear correlation provided by those authors.

Table B.13: Chemical composition of synthetic glasses described in [160], and estimation of maximum 2θ diffraction angle.

Glass	Chemical composition			Max. diffraction angle (2θ)
	SiO ₂ (wt%)	Al ₂ O ₃ (wt%)	CaO (wt%)	
G1	53.0	14.0	33.0	28.4
G2	45.3	20.9	33.8	28.5
G3	43.6	25.6	30.8	28.2
G4	39.9	28.8	31.8	28.3
G5	36.8	31.0	32.0	28.4
G6	36.1	35.8	28.1	28.0
G7	44.2	13.6	42.2	29.3
G8	43.0	17.9	38.8	29.0
G9	35.8	23.6	40.4	29.1
G10	31.5	30.1	37.5	28.6
G11	43.3	7.4	49.3	30.0
G12	41.6	10.5	47.7	29.8
G13	36.0	15.3	48.5	29.9

Appendix C

Thermodynamic and kinetic properties of aqueous species and solid phases used for microstructure modelling

Thermodynamic modelling was implemented in different Chapters of this thesis for the calculation of effective saturation indices (ESI) and phase assemblage equilibrium in different stages of modelled pastes: in Chapter 3, the concentrations of Ca, Si and Al, as measured by ICP-OES, were utilised to verify the precipitation of reaction products during different periods of the dissolution experiments; in Chapter 7, the precipitation and stability of reaction products were determined to provide a simulation of equilibrium microstructures in both thermodynamic-only and combined thermodynamic-kinetic models. The complete set of thermodynamic data of aqueous species utilised for equilibrium calculations are detailed in Tables C.1. Tables C.2 and C.4 detail the solubility products and remaining thermodynamic data of the reaction products utilised in the thermodynamic equilibrium calculations. Finally, Table C.4 provides the kinetic and thermodynamic parameters of nucleation of the reaction products considered for the simulations performed with GeoMicro3D in Chapter 7.

Table C.1: Thermodynamic properties of aqueous species utilised for all modelling work performed in this thesis. The reference state is 298.15 K and 1 bar.

Phase	V^0 (cm ³ /mol)	$\Delta_G H^0$ (kJ/mol)	$\Delta_f H^0$ (kJ/mol)	S^0 (J/mol.K)	C_p^0 (J/mol.K)	Ref.
Al^{3+}	-45.2	-483.7	-530.6	-325.1	-128.7	[579]
AlO^+	0.3	-660.4	-713.6	-113.0	-125.1	[579]
AlO^{2-}	9.5	-827.5	-925.6	-30.2	-49.0	[579]
Ca^{2+}	-18.4	-552.8	-543.1	-56.5	-30.9	[579]
$CaOH^+$	5.8	-717.0	-571.6	28.0	6.0	[579]
Na^+	-1.2	-261.9	-240.3	58.5	38.1	[579]
$NaOH_{(aq)}$	3.5	-418.1	-471.1	44.8	-13.4	[579]
$HSiO_3^-$	4.5	-101.5	-114.5	20.9	-87.2	[580]
$SiO_{2(aq)}$	16.1	-833.4	-887.9	41.3	44.5	[581]
SiO_3^{2-}	4.3	-938.5	-1098.7	-96.2	-292.9	[582]
OH^-	-4.7	-157.3	-230.0	-10.7	-136.3	[579]
H^+	0	0	0	0	0	[579]
$H_2O_{(aq)}$	18.1	-237.2	-285.9	69.9	75.4	[583]

Table C.2: Solubility products of reaction products utilised for all modelling work performed in this thesis, divided by their categories as described in Chapters 6 and 7. The reference state is 298.15 K and 1 bar.

Category	Reaction product	Chemical composition	$\log k_{sp}$
C-(N-A)-S-H-type gels	5CA	$(CaO)_{1.25} \cdot (Al_2O_3)_{0.125} \cdot (SiO_2)_1 \cdot (H_2O)_{1.625}$	-10.75
	INFCNA	$(CaO)_1 \cdot (Al_2O_3)_{0.15625} \cdot (SiO_2)_{1.1875} \cdot (H_2O)_{1.65625}$	-8.90
	5CNA	$(CaO)_{1.25} \cdot (Na_2O)_{0.25} \cdot (Al_2O_3)_{0.125} \cdot (SiO_2)_1 \cdot (H_2O)_{1.25}$	-10.40
	INFCNA	$(CaO)_1 \cdot (Na_2O)_{0.34375} \cdot (Al_2O_3)_{0.15625} \cdot (SiO_2)_{1.1875} \cdot (H_2O)_{1.3}$	-10.00
	INFCN	$(CaO)_1 \cdot (Na_2O)_{0.3125} \cdot (SiO_2)_{1.25} \cdot (H_2O)_{1.1875}$	-10.70
	T2C	$(CaO)_{1.5} \cdot (SiO_2)_1 \cdot (H_2O)_{2.5}$	-11.60
	T5C	$(CaO)_{1.25} \cdot (SiO_2)_{1.25} \cdot (H_2O)_{2.5}$	-10.50
	TobH	$(CaO)_1 \cdot (SiO_2)_{1.5} \cdot (H_2O)_{2.5}$	-7.80
N-(C-)A-S-H-type gels	NASH-1	$(Na_2O)_{0.49} \cdot (Al_2O_3)_{0.46} \cdot (SiO_2)_1 \cdot (H_2O)_{0.48}$	-8.93
	NASH-2	$(Na_2O)_{0.3} \cdot (Al_2O_3)_{0.25} \cdot (SiO_2)_1 \cdot (H_2O)_{0.29}$	-6.94
	NASH-3	$(Na_2O)_{0.22} \cdot (Al_2O_3)_{0.18} \cdot (SiO_2)_1 \cdot (H_2O)_{0.26}$	-5.68
	N(C)ASH-1	$(Na_2O)_{0.25} \cdot (CaO)_{0.11} \cdot (Al_2O_3)_{0.25} \cdot (SiO_2)_1 \cdot (H_2O)_{0.39}$	-7.70
	N(C)ASH-2	$(Na_2O)_{0.23} \cdot (CaO)_{0.2} \cdot (Al_2O_3)_{0.23} \cdot (SiO_2)_1 \cdot (H_2O)_{0.4}$	-8.61
	N(C)ASH-3	$(Na_2O)_{0.23} \cdot (CaO)_{0.08} \cdot (Al_2O_3)_{0.16} \cdot (SiO_2)_1 \cdot (H_2O)_{0.39}$	-6.75
	N(C)ASH-4	$(Na_2O)_{0.24} \cdot (CaO)_{0.15} \cdot (Al_2O_3)_{0.18} \cdot (SiO_2)_1 \cdot (H_2O)_{0.37}$	-7.52
Crystalline secondary reaction products	Portlandite (CH)	$Ca(OH)_2$	-5.20
	Katoite (C3AH6)	$Ca_3Al_2(OH)_{12}$	-20.50
	Strätlingite (C ₂ ASH ₈)	$Ca_2Al_2SiO_2(OH)_{10} \cdot 3H_2O$	-19.70
	C ₄ AH ₁₃	$Ca_4Al_2(OH)_{14} \cdot 6H_2O$	-25.25
	Si-hydrogarnet (C ₃ AS _{0.84} H _{4.32})	$Ca_3Al_2(SiO_4)_{0.84}(OH)_{8.64}$	-26.70
Zeolites	Hydroxy-sodalite	$(Na_2O)_4 \cdot (Al_2O_3)_3 \cdot (SiO_2)_6 \cdot (H_2O)_3$	-67.32
	Chabazite	$(Na_2O)_1 \cdot (Al_2O_3)_1 \cdot (SiO_2)_4 \cdot (H_2O)_6$	-31.9
	Natrolite	$(Na_2O)_1 \cdot (Al_2O_3)_1 \cdot (SiO_2)_3 \cdot (H_2O)_2$	-26.6
	Gismondine	$(CaO)_1 \cdot (Al_2O_3)_1 \cdot (SiO_2)_2 \cdot (H_2O)_{4.5}$	-23.5

Table C.3: Remaining thermodynamic properties of reaction products utilised for all modelling work performed in this thesis, divided by their categories as described in Chapters 6 and 7. The reference state is 298.15 K and 1 bar.

Reaction product	V^0 (cm ³ /mol)	$\Delta_G H^0$ (kJ/mol)	$\Delta_f H^0$ (kJ/mol)	S^0 (J/mol.K)	C_p^0 (J/mol.K)	Ref.
5CA	57.3	-2292.8	-2491.3	163.1	177.2	[58]
INFCA	59.3	-2342.9	-2551.3	154.5	180.9	[58]
5CNA	64.5	-2381.8	-2568.6	195.0	176.2	[58]
INFCNA	69.3	-2474.3	-2666.7	198.4	179.7	[58]
INFCN	71.1	-2452.5	-2642.0	185.6	183.7	[58]
T2C	80.6	-2465.4	-2720.7	167.0	237.0	[217]
T5C	79.3	-2516.9	-2780.3	159.9	234.1	[217]
TobH	85.0	-2560.0	-2831.4	152.8	231.2	[217]
NASH-1	58.9	-2017.4	-2162.8	116.4	152.0	[225]
NASH-2	48.3	-1516.5	-1623.3	86.1	106.6	[225]
NASH-3	48.4	-1343.7	-1438.7	76.9	92.0	[225]
N(C)ASH-1	42.8	-1583.9	-1697.2	92.9	112.6	[226]
N(C)ASH-2	46.6	-1603.9	-1717.8	95.1	113.4	[226]
N(C)ASH-3	41.3	-1401.3	-1503.3	87.9	100.2	[226]
N(C)ASH-4	43.8	-1490.2	-1594.9	97.8	110.9	[226]
Portlandite (CH)	33.1	-897.0	-984.7	83.4	87.5	[584]
Katoite (C3AH6)	149.7	-5008.2	-5537.2	421.7	445.6	[585]
Strätlingite (C2ASH8)	216.1	-5705.1	-6360.0	5462	602.7	[581]
C4AH13	274.5	-7325.7	-8262.4	831.5	1142.0	[585]
Si-hydrogarnet (C3AS0.84H4.32)	142.5	-5365.2	-5847.4	375.2	413.7	[366]
Hydroxysodalite	424.7	-1322.1	-1412.0	943.0	895.0	[207]
Chabazite	250.0	-7117.5	-7808.3	548.0	578.0	[207]
Natrolite	169.4	-5305.1	-5707.0	360.0	359.0	[207]
Gismondine	157.6	-5076.0	-5527.4	491.0	435.0	[207]

Table C.4: Kinetic parameter A of solid reaction products utilised for combined thermodynamic-kinetic simulations through GeoMicro3D.

	C-(N-A)-S-H-type gels	Portlandite (CH)	Katoite (C3AH6)	Strätlingite (C2ASH8)	N-(C-)A-S-H-type gels	Hydroxysodalite
A (m ³ s ⁻¹)	4.24×10^7	4.71×10^9	27.6	0.101	4.24×10^7	9.62×10^3

Appendix D

Determination of forward dissolution rates

In Chapter 4, the forward dissolution rates - r_+ ($\text{mol} \cdot \text{m}^{-2} \cdot \text{s}^{-1}$) - of Ca, Si and Al in alkaline media were empirically defined for various scenarios. The methodology described in Section 4.3.4 utilised the experimental results obtained in the dissolution experiments in highly diluted conditions and data available in the literature. This Appendix provides the full dataset utilised for the discussions and conclusions made on Chapter 4.

D.1 Methodology

The preparation of the NaOH solutions, in different molarities, was described in Section 4.2.2. The temporal variation in the concentration of aqueous Ca, Si and Al was measured from 5 min to 24 hours at 20 °C (all four synthetic glasses) and at 60 °C (glasses Si-FA and Ca-FA). The dissolution rates were calculated using Equation 4.7, considering only the periods with quasi-linear change in element concentration versus time.

D.2 Experimental results

D.2.1 Results generated in this work

Tables D.1, D.2, D.3 and D.4 provide the complete dataset of concentrations measured during the dissolution experiments of the four synthetic glasses, performed at 20 °C. The tables also provides the individually determined forward dissolution rates, highlighting the range of values considered for calculations, along with the r^2 value of the linear trendlines of the steady dissolution period. Tables D.5 and D.6 provide details of the experiments performed at 60 °C, for glasses Si-FA and Ca-FA, respectively.

Table D.1: Temporal evolution in the concentrations (mmol/L) of Al, Si, and Ca, measured for dissolution experiments of glass Si-FA (20 °C), along with the respective forward dissolution rate and r^2 of the steady dissolution period - italic and bold numbers indicate the dataset range utilised for the determination of the forward dissolution period.

Time	NaOH (0.15 M)			NaOH (1.5 M)			NaOH (3 M)		
	Al	Si	Ca	Al	Si	Ca	Al	Si	Ca
5 min	0.025	0.013	0.062	0.027	0.039	0.067	0.037	0.053	0.215
10 min	0.027	0.036	0.077	0.018	0.031	0.060	0.037	0.046	0.147
15 min	0.013	0.012	0.027	0.015	0.026	0.042	0.028	0.043	0.147
30 min	0.012	0.017	0.040	0.016	0.030	0.055	0.044	0.050	0.140
45 min	0.014	0.014	0.035	0.017	0.030	0.040	0.048	0.057	0.165
1 h	0.013	0.020	0.035	0.016	0.035	0.052	0.041	0.053	0.090
2 h	0.013	0.015	0.030	0.022	0.039	0.050	0.030	0.039	0.105
4 h	0.014	0.017	0.030	0.026	0.039	0.032	0.035	0.043	0.105
6 h	0.022	0.025	0.037	0.036	0.050	0.037	0.044	0.057	0.115
24 h	0.031	0.039	0.030	0.085	0.096	0.080	0.100	0.093	0.107
r_+	-7.68	-7.57	-7.33	-7.14	-7.19	-7.23	-7.10	-7.22	-6.90
Slope	0.87	0.93	0.75	0.99	0.99	0.99	0.96	0.89	0.78

Table D.2: Temporal evolution in the concentrations (mmol/L) of Al, Si, and Ca, measured for dissolution experiments of glass Ca-FA (20 °C), along with the respective forward dissolution rate and r^2 of the steady dissolution period - italic and bold numbers indicate the dataset range utilised for the determination of the forward dissolution period.

Time	NaOH (0.15 M)			NaOH (1.5 M)			NaOH (3 M)		
	Al	Si	Ca	Al	Si	Ca	Al	Si	Ca
5 min	0.012	0.024	0.042	0.041	0.050	0.060	0.119	0.121	0.160
10 min	0.010	0.015	0.023	0.300	0.278	0.170	0.096	0.100	0.157
15 min	0.011	0.012	0.025	0.156	0.146	0.102	0.122	0.121	0.160
30 min	0.010	0.019	0.050	0.012	0.022	0.037	0.052	0.064	0.122
45 min	0.008	0.016	0.047	0.014	0.019	0.040	0.070	0.078	0.135
1 h	0.010	0.015	0.030	0.025	0.032	0.052	0.056	0.071	0.200
2 h	0.010	0.014	0.020	0.023	0.030	0.055	0.036	0.043	0.117
4 h	0.013	0.017	0.024	0.021	0.028	0.035	0.032	0.050	0.137
6 h	0.019	0.027	0.032	0.037	0.043	0.046	0.153	0.107	0.145
24 h	0.037	0.046	0.030	0.100	0.100	0.116	0.189	0.178	0.289
r_+	-7.53	-7.44	-7.11	-7.05	-7.07	-7.00	-6.77	-6.78	-6.72
Slope	0.98	0.94	0.95	0.98	0.97	0.99	0.77	0.85	0.99

Table D.3: Temporal evolution in the concentrations (mmol/L) of Al, Si, and Ca, measured for dissolution experiments of glass BFS-1 (20 °C), along with the respective forward dissolution rate and r^2 of the steady dissolution period - italic and bold numbers indicate the dataset range utilised for the determination of the forward dissolution period.

Time	NaOH (0.15 M)			NaOH (1.5 M)			NaOH (3 M)		
	Al	Si	Ca	Al	Si	Ca	Al	Si	Ca
5 min	0.021	0.030	0.052	0.489	0.445	0.462	0.111	0.107	0.192
10 min	0.009	0.015	0.035	0.096	0.085	0.110	0.044	0.053	0.145
15 min	0.019	0.026	0.045	0.044	0.046	0.075	0.100	0.089	0.157
30 min	0.015	0.020	0.037	0.082	0.061	0.075	0.048	0.050	0.100
45 min	<i>0.015</i>	<i>0.018</i>	0.025	0.070	0.061	0.077	0.052	<i>0.050</i>	0.110
1 h	<i>0.015</i>	<i>0.019</i>	0.037	<i>0.063</i>	<i>0.046</i>	<i>0.067</i>	<i>0.052</i>	<i>0.053</i>	0.102
2 h	<i>0.018</i>	<i>0.023</i>	<i>0.030</i>	<i>0.100</i>	<i>0.068</i>	<i>0.085</i>	<i>0.063</i>	<i>0.057</i>	<i>0.090</i>
4 h	<i>0.032</i>	<i>0.028</i>	<i>0.030</i>	<i>0.145</i>	<i>0.103</i>	<i>0.102</i>	<i>0.093</i>	<i>0.068</i>	<i>0.102</i>
6 h	<i>0.048</i>	<i>0.043</i>	<i>0.050</i>	<i>0.145</i>	<i>0.089</i>	<i>0.090</i>	<i>0.115</i>	<i>0.082</i>	<i>0.145</i>
24 h	<i>0.096</i>	<i>0.064</i>	0.052	<i>0.345</i>	<i>0.189</i>	<i>0.202</i>	<i>0.282</i>	<i>0.164</i>	<i>0.185</i>
r_+	-7.01	-7.26	-6.88	-6.47	-6.76	-6.79	-6.45	-6.77	-6.42
Slope	0.96	0.91	0.75	0.98	0.92	0.97	0.99	0.99	0.83

Table D.4: Temporal evolution in the concentrations (mmol/L) of Al, Si, and Ca, measured for dissolution experiments of glass BFS-2 (20 °C), along with the respective forward dissolution rate and r^2 of the steady dissolution period - italic and bold numbers indicate the dataset range utilised for the determination of the forward dissolution period.

Time	NaOH (0.15 M)			NaOH (1.5 M)			NaOH (3 M)		
	Al	Si	Ca	Al	Si	Ca	Al	Si	Ca
5 min	0.017	0.021	0.037	0.063	0.061	0.090	0.100	0.089	0.180
10 min	0.012	0.017	0.032	0.104	0.103	0.147	0.028	0.031	0.110
15 min	0.013	0.013	0.037	0.031	0.039	0.062	0.029	0.029	0.102
30 min	0.021	0.025	0.047	0.059	0.061	0.122	0.031	0.032	0.097
45 min	<i>0.016</i>	<i>0.018</i>	<i>0.037</i>	0.130	0.132	0.182	<i>0.037</i>	0.039	<i>0.105</i>
1 h	<i>0.017</i>	<i>0.020</i>	<i>0.040</i>	<i>0.096</i>	<i>0.096</i>	<i>0.130</i>	<i>0.036</i>	<i>0.035</i>	<i>0.107</i>
2 h	<i>0.032</i>	<i>0.032</i>	<i>0.047</i>	<i>0.156</i>	<i>0.142</i>	<i>0.177</i>	<i>0.052</i>	<i>0.053</i>	<i>0.150</i>
4 h	<i>0.048</i>	<i>0.046</i>	<i>0.060</i>	<i>0.156</i>	<i>0.132</i>	<i>0.207</i>	<i>0.070</i>	<i>0.057</i>	<i>0.142</i>
6 h	<i>0.059</i>	<i>0.057</i>	<i>0.072</i>	<i>0.208</i>	<i>0.203</i>	<i>0.230</i>	<i>0.133</i>	<i>0.114</i>	<i>0.192</i>
24 h	<i>0.115</i>	<i>0.100</i>	0.100	<i>0.300</i>	<i>0.249</i>	0.264	0.311	0.224	0.232
r_+	-6.93	-7.01	-6.73	-6.61	-6.73	-6.60	-6.29	-6.36	-6.32
Slope	0.93	0.91	0.99	0.87	0.76	0.91	0.93	0.86	0.85

Table D.5: Temporal evolution in the concentrations (mmol/L) of Al, Si, and Ca, measured for dissolution experiments of glass Si-FA (60 °C), along with the respective forward dissolution rate and r^2 of the steady dissolution period - italic and bold numbers indicate the dataset range utilised for the determination of the forward dissolution period.

Time	NaOH (0.15 M)			NaOH (1.5 M)			NaOH (3 M)		
	Al	Si	Ca	Al	Si	Ca	Al	Si	Ca
5 min	0.020	0.027	0.042	0.018	0.022	0.047	0.023	0.046	0.110
10 min	0.023	0.011	0.045	0.023	0.039	0.062	0.029	0.057	0.102
15 min	0.018	0.016	0.024	0.028	0.046	0.060	0.033	0.061	0.107
30 min	0.021	0.031	0.075	0.044	0.068	0.077	0.048	0.089	0.102
45 min	0.023	0.033	0.030	0.056	0.100	0.067	0.063	0.117	0.105
1 h	0.029	0.050	0.042	0.063	0.100	0.060	0.093	0.160	0.132
2 h	0.036	0.053	0.030	0.111	0.189	0.070	0.152	0.253	0.147
4 h	0.048	0.075	0.032	0.152	0.249	0.080	0.256	0.420	0.172
6 h	0.052	0.089	0.037	0.219	0.370	0.122	0.326	0.548	0.242
24 h	0.208	0.356	0.107	0.652	1.097	0.250	0.893	1.492	0.424
r_+	-6.70	-6.46	-7.08	-6.19	-5.97	-6.71	-6.04	-5.82	-6.46
Slope	0.99	0.99	0.93	0.99	0.99	0.98	0.98	0.99	0.96

Table D.6: Temporal evolution in the concentrations (mmol/L) of Al, Si, and Ca, measured for dissolution experiments of glass Ca-FA (60 °C), along with the respective forward dissolution rate and r^2 of the steady dissolution period - italic and bold numbers indicate the dataset range utilised for the determination of the forward dissolution period.

Time	NaOH (0.15 M)			NaOH (1.5 M)			NaOH (3 M)		
	Al	Si	Ca	Al	Si	Ca	Al	Si	Ca
5 min	0.021	0.028	0.035	0.017	0.020	0.040	0.067	0.125	0.157
10 min	0.025	0.034	0.047	0.036	0.053	0.057	0.056	0.100	0.142
15 min	0.022	0.033	0.030	0.027	0.036	0.045	0.063	0.117	0.150
30 min	0.022	0.030	0.035	0.031	0.046	0.050	0.193	0.324	0.259
45 min	0.027	0.039	0.045	0.037	0.064	0.055	0.074	0.132	0.152
1 h	0.063	0.093	0.072	0.056	0.082	0.075	0.089	0.150	0.167
2 h	0.041	0.061	0.050	0.104	0.157	0.092	0.174	0.292	0.232
4 h	0.056	0.093	0.067	0.193	0.310	0.150	0.237	0.392	0.267
6 h	0.078	0.128	0.050	0.241	0.392	0.185	0.341	0.563	0.334
24 h	0.241	0.409	0.147	0.634	1.043	0.349	1.049	1.730	0.462
r_+	-6.65	-6.65	-6.92	-6.20	-5.98	-6.50	-5.91	-5.70	-6.07
Slope	0.99	0.99	0.87	0.98	0.98	0.94	0.99	0.98	0.96

D.2.2 Results obtained from literature

Along with the data generated in this work, the empirical determination of the forward dissolution rates of Ca, Si and Al utilised results available in literature from different authors. Tables D.7 and D.8 detail the dataset and dissolution rates obtained from Yun during dissolution experiments of a commercial fly ash.

Table D.7: Temporal evolution in the concentration of Al, Si and Ca measured during the dissolution of a commercial fly ash, measured by Chen, at 20 °C.

Time	NaOH (1.5 M)			NaOH (3 M)			NaOH (5 M)		
	Al	Si	Ca	Al	Si	Ca	Al	Si	Ca
3 h	0.059	0.077	0.150	0.067	0.101	0.190	0.074	0.185	0.142
6 h	0.070	0.105	0.187	0.085	0.130	0.220	0.107	0.242	0.162
12 h	0.109	0.151	0.220	0.126	0.189	0.232	0.156	0.306	0.185
24 h	0.161	0.215	0.212	0.178	0.255	0.240	0.226	0.392	0.197
48 h	0.233	0.358	0.220	0.282	0.413	0.247	0.341	0.602	0.193
r_+	-7.24	-7.05	-7.26	-7.16	-6.99	-7.21	-7.07	-6.83	-7.01
Slope	0.94	0.90	0.76	0.92	0.91	0.90	0.94	0.91	0.98

Table D.8: Temporal evolution in the concentration of Al, Si and Ca measured during the dissolution of a commercial fly ash, measured by Chen, at 60 °C.

Time	NaOH (5 M) - 40 °C			NaOH (1.5 M) - 60 °C		
	Al	Si	Ca	Al	Si	Ca
6 h	0.219	0.634	0.232	0.871	2.304	0.252
12 h	0.397	1.072	0.207	1.342	3.632	0.185
24 h	0.589	1.592	0.202	2.001	5.590	0.157
48 h	0.934	2.460	0.202	2.698	7.406	0.097
r_+	-6.57	-6.15	-6.27	-6.11	-5.67	-6.23
Slope	0.97	0.97	-	0.99	0.99	-

Appendix E

Supplementary information utilised in Chapter 6

E.1 Isothermal calorimetry curves of alkali-activated synthetic glasses

In Section 6.3.1, the influence of the activator in the alkali-activating of synthetic precursors was discussed. Solutions of waterglass and NaOH with different molarities were prepared and individually discussed for all precursors in systems N8S0 and N8S12. Glasses Si-FA and BFS-2, the two extreme conditions with respect to their Ca content, were activated with additional solutions for further fundamental understanding of reaction kinetics - see Table 6.2 for more details on the activators. This Appendix provides the additional curves which were utilised for discussion but were not shown in Chapter 6 - Figure E.1 shows the curves obtained for glass Si-FA, and Figure E.2 shows the curves obtained for glass BFS-2.

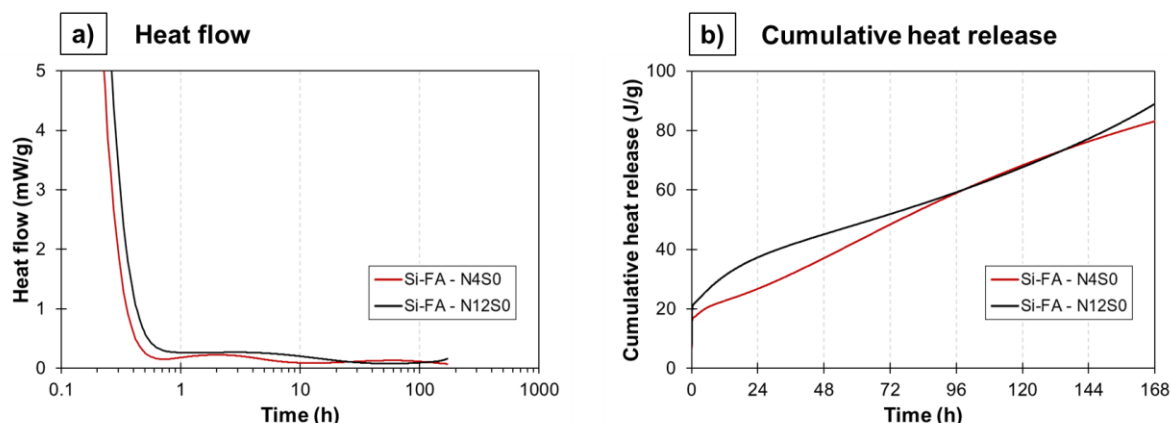


Figure E.1: Heat flow evolution and cumulative heat release of pastes made with glass Si-FA activated with 4 M and 12 M NaOH solutions - all samples were cured at 20 °C for 7 days; all values were normalized with the original weight of the precursor.

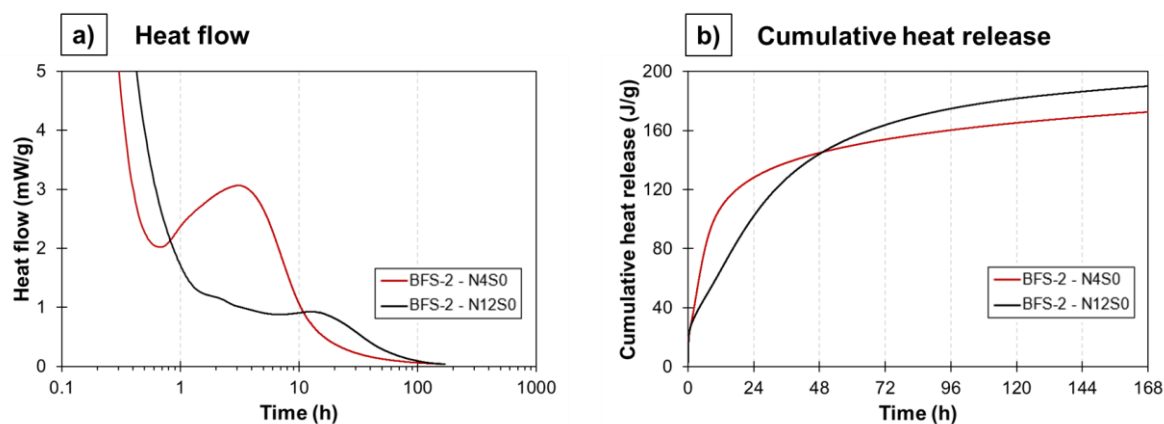


Figure E.2: Heat flow evolution and cumulative heat release of pastes made with glass BFS-2 activated with 4 M and 12 M NaOH solutions - all samples were cured at 20 °C for 7 days; all values were normalized with the original weight of the precursor.

E.2 SEM micrographs utilized for microanalysis with EDS

In Section 6.3.2, the influence of the activator in the gel composition throughout the cementitious matrix of hardened pastes was evaluated for the activation of glass Si-FA. The siliceous fly ash-type glass, cured for 7 days at 60 °C and for additional 21 days at 20 °C, was characterized by SEM for systems activated with NaOH (N8S0) and waterglass (N8S12). Backscattered images were collected for the two pastes, which were utilized for the EDS mapping and chemical microanalysis of the specimen. Figures E.3 and E.4 show the original images, and the area selected (highlighted in red) for the data analysis of pastes belonging to systems N8S0 and N8S12, respectively.

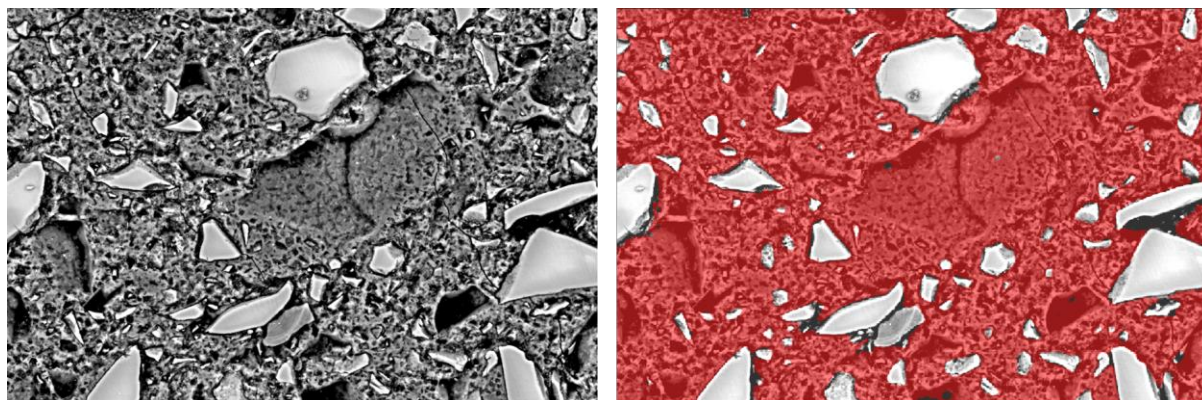


Figure E.3: BSE image of paste made with glass Si-FA, activated by NaOH (left), and the highlighted area in red of the cementitious matrix utilized for EDS mapping in Section 6.3.2 (right).

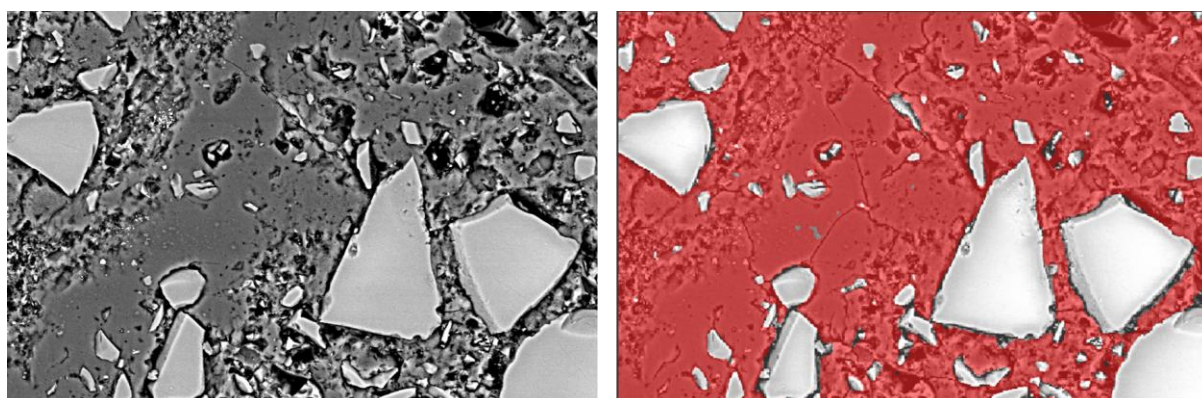


Figure E.4: BSE image of paste made with glass Si-FA, activated by waterglass (left), and the highlighted area in red of the cementitious matrix utilized for EDS mapping in Section 6.3.2 (right).

E.3 Detailed results from quantitative X-ray diffraction analysis

In Section 6.4.2, the estimation of the amount of different reaction products based on the chemical composition of a mixture was proposed through the calculation of *phase assemblage indices*. As explained in the methodology section of Chapter 6 (Section 6.2.5), the determination of these indices for alkali-activated pastes is performed through the quantitative analysis of three categories of reaction products by the combination of different experimental techniques: SAM selective dissolution treatment, estimation of the degree of reaction by SEM micrographs, and QXRD.

The schematic illustration in Figure E.5 describes the sequential process for the determination of the quantity of each reaction product. After the hardened pastes are subject to the SAM extraction method, it is assumed that amorphous and short-ordered C-(N-A)-S-H-type gels are eliminated, and the remainder material accounts for unreacted glass, crystalline Ca-Al bearing phases, disordered N-(C-)A-S-H-type gels and zeolites. The residual mass collected after the SAM treatment is subtracted by the amount of zeolite and other secondary phases - as determined by QXRD, and by the amount of unreacted glass - which is calculated by the reaction degree of each paste, and the resulting value represents the quantity of amorphous N-(C-)A-S-H gels in the hardened paste. Sequentially, the amount of amorphous C-(N-A)-S-H gels is determined by subtracting the amount of unreacted glass and amorphous N-(C-)A-S-H-type species from the total amount of amorphous material, determined by QXRD. Finally, the amorphous content of each category of gel is summed to their crystalline counterparts, and the final contents of N-(C-)A-S-H and C-(N-A)-S-H-type phases is determined. Table E.1 presents the detailed results of the QXRD analysis of each paste, while Table E.2 presents the estimation of the amorphous phases based on the method illustrated in Figure E.5.

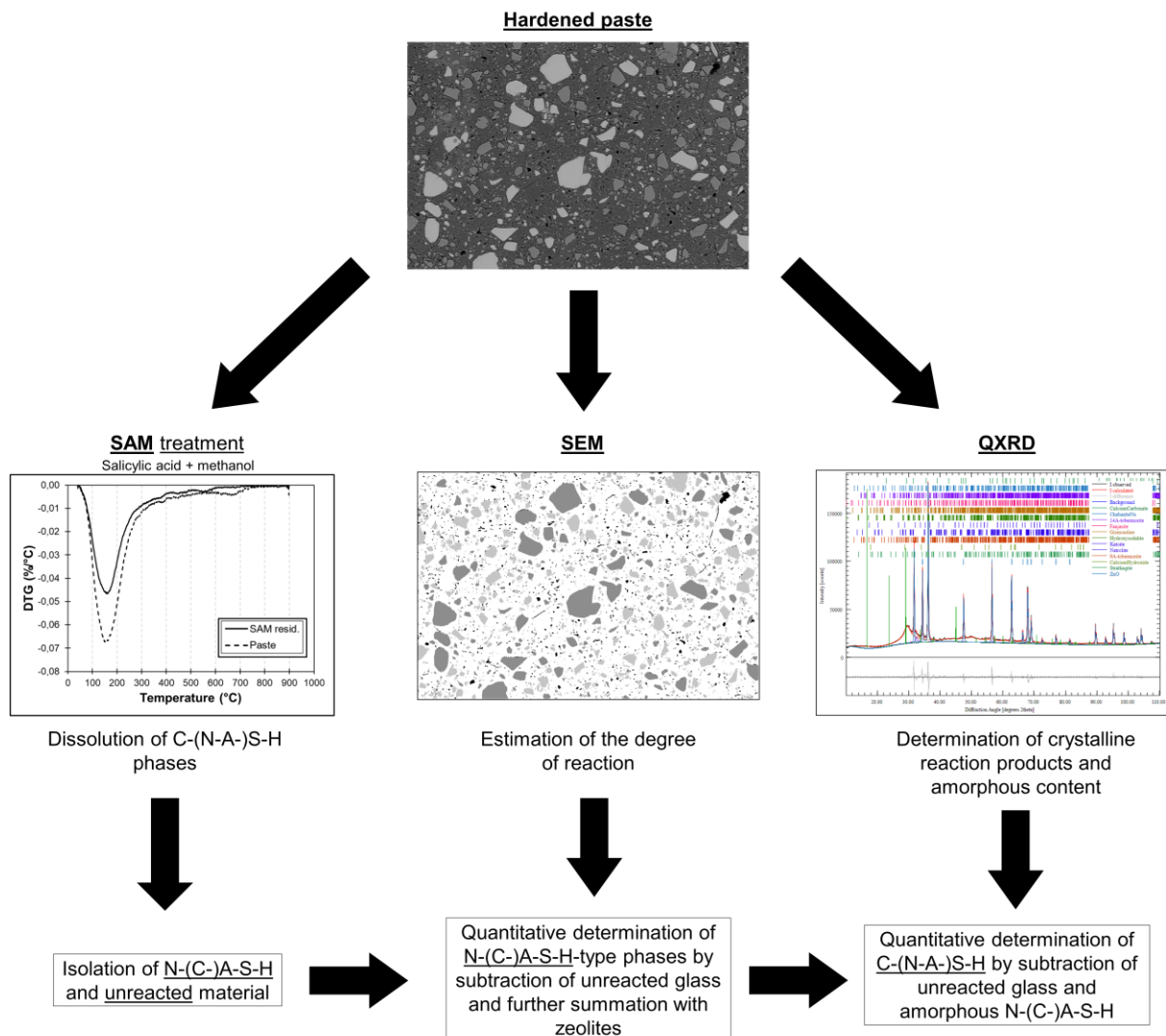


Figure E.5: Schematic illustration of the methodology implemented for the calculation of each category of reaction product for all pastes investigated in Chapter 6.

Table E.1: Detailed results of QXRD analysis performed for all pastes analyzed and discussed in Chapter 6.

Mix design		GOF*	Amorphous quantity (%)	C-(N-A-)S-H phases (%)	C3AH6/Strätlingite/ CaCO ₃ (%)	Zeolites (%)
Activator (Temperature)	Glass/Blend					
NaOH (20° C)	Si-FA	4.95	84.51	10.69	0.13	4.67
	Ca-FA	4.01	72.04	23.66	1.86	2.24
	BFS-1	2.85	61.80	33.88	3.81	0.51
	BFS-2	2.90	59.30	35.19	5.18	0.33
Waterglass (20° C)	Si-FA	5.27	85.72	8.76	0.10	5.42
	Ca-FA	5.50	78.73	11.06	0.45	6.08
	BFS-1	3.46	69.83	29.09	0.08	0.99
	BFS-2	2.83	53.20	44.80	0.07	1.59
NaOH (20° C)	B70	2.95	83.05	28.37	1.08	0.74
	B50	3.06	69.46	26.97	0.25	1.62
	B30	3.57	78.63	14.72	1.50	4.61
Waterglass (20° C)	B70	2.70	73.63	24.42	0.96	0.77
	B50	2.72	63.70	33.49	0.92	1.83
	B30	4.81	84.38	10.53	0.00	4.40
NaOH (60 and 20° C)	Si-FA	6.30	86.28	1.81	1.36	10.39
	Ca-FA	4.82	88.22	3.72	0.00	7.31
Waterglass (60 and 20° C)	Si-FA	5.44	90.31	1.58	1.41	6.23
	Ca-FA	6.01	85.49	2.82	1.13	9.05

*GOF is the goodness of fit of the Rietveld refinement, calculated as the ratio of the over .

Table E.2: Determination of the amount of amorphous N-(C-)A-S-H and C-(N-A-)S-H gels, based on the methodology described in this Appendix.

Mix design		Degree of reaction (%)	Weight loss - SAM (%)	Unreacted glass (%)	Amorphous N-(C-)A-S-H gels (%)	Amorphous C-(N-A-)S-H gels (%)
Activator (Temperature)	Glass/Blend					
NaOH (20° C)	Si-FA	37.55	19.11	42.19	34.03	8.29
	Ca-FA	34.03	33.25	44.57	22.18	7.73
	BFS-1	40.68	52.35	40.08	7.58	14.66
	BFS-2	43.41	47.61	38.23	14.16	7.24
Waterglass (20° C)	Si-FA	41.66	15.74	36.51	47.75	6.88
	Ca-FA	43.38	23.64	35.43	40.93	12.13
	BFS-1	44.46	54.28	34.76	10.96	25.11
	BFS-2	53.64	63.74	29.01	7.25	18.87
NaOH (20° C)	B70	41.49	43.52	42.34	14.14	12.31
	B50	38.70	40.83	41.42	17.75	11.93
	B30	40.98	42.49	37.91	19.60	25.83
Waterglass (20° C)	B70	49.30	47.21	30.69	22.10	21.80
	B50	46.09	35.29	33.74	30.97	0.88
	B30	49.07	24.31	34.91	40.79	13.48
NaOH (60 and 20° C)	Si-FA	48.74	19.72	34.63	45.65	16.55
	Ca-FA	43.74	34.61	38.01	27.38	30.60
Waterglass (60 and 20° C)	Si-FA	53.72	10.64	28.96	60.40	7.63
	Ca-FA	53.37	20.64	29.18	50.17	16.31

Summary

The continuous development of global infrastructure requires the use of reliable and cost-effective construction materials. Within this scope, alkali-activated materials (AAMs) excel as one of the most sustainable alternatives over traditional Portland cement (PC) based products, as they combine a similar-to-superior performance with the reduced consumption of carbon-intensive raw materials. Despite being the subject of extensive research for more than 70 years, the applicability of these binders in large-scale projects still faces practical issues towards their wide acceptance in industry. The non-homogeneous distribution of raw materials, the diverse list of potential activators and precursors, and their variations in mineralogy and chemical compositions, among others, are the main challenges in the path to their reliable performance evaluation. The short- and long-term behaviour of AAMs are intimately correlated with their mechanisms of reaction and, consequently, with the nature and the amount of reaction products present in their hardened microstructures. Therefore, the establishment of correlations between the characteristics of the raw materials and the microstructural evolution of the binders, through empirical observations and numerical modelling, can bring positive effects to the industry, providing accurate estimations and optimization of the short and long-term characteristics of structures made with AAMs.

This thesis aimed at understanding the various influencing factors in the reaction path of AAMs, from the early stages of dissolution to the obtainment of mature microstructures. First, glasses resembling commercial fly ashes and slags were produced. The synthetic precursors were obtained with simplified chemical composition, facilitating qualitative and quantitative studies of the effect of Ca, Al and Si in the mineralogy of each precursor, and consequently in the mechanisms of dissolution and precipitation of reaction products. The frameworks of the precursors were characterized by X-ray diffraction (XRD), Fourier transform infrared (FTIR) and Raman spectroscopy, and nuclear magnetic resonance (NMR), which identified CaO as the main network modifier (NWM) of the amorphous network. The shift from Al-modified cristobalite and mullite-type rich structures, in fly ash-type glasses, to gehlenite-type structures, in slag-type glasses, allowed the establishment of a direct relationship between the CaO content of each precursor and their degree of disorder.

Second, the dissolution kinetics of the synthetic precursors was investigated. The use of coarse glass particles, in highly diluted solutions (1:1000) of NaOH, allowed the measurement of the temporal evolution in the concentration of each element prior to the formation of the first reaction products. The release of Ca, Si and Al from the framework of the glasses was measured with inductively coupled plasma-optical electrical emission (ICP-OES) for five different scenarios, including three NaOH molarities at 20 °C and 60 °C. The combined influences of alkalinity and temperature were considered for the derivation of universal dissolution rate equations based on Arrhenius-type relationships. These equations provided an estimation of the leaching of aqueous species according to the composition of the precursors and to the characteristics of the experiment, and their accuracies were validated against experimental dissolution data available in literature by different authors.

Third, phase precipitation mechanisms and the phase assemblage of alkali-activated binders were investigated. Through additional dissolution experiments with fine precursors, results

obtained with ICP-OES identified the consumption of aqueous species for the formation of initial nuclei of solid products. The utilization of FTIR, differential thermogravimetry (DTG) and selective dissolution treatment aided the distinction of the type of disordered gels formed during the early stages of activation of different precursors. The precipitation of portlandite as an intermediate reaction product was verified to dominate the reactive systems in initial moments. In sequence, C-(N-A-)S-H-type gels were preferentially formed in all systems at 20 °C, while N-(C-)A-S-H-type gels were only favored at higher curing temperatures. Furthermore, the combination of in-situ isothermal calorimetry with SEM micrographs allowed the observation of different phase formation phenomena in the studied binders. Homogeneous-type precipitation mechanisms were mostly observed in waterglass-activated systems, and heterogeneous-type precipitation was the dominant phenomena in NaOH-media. The two mechanisms have been described before in literature, but the methodology implemented in this thesis allowed a unique observation of both.

In 28 days old systems, the combination of quantitative XRD (QXRD), selective dissolution treatments and SEM micrograph segmentation allowed the establishment of additional chemistry-temperature-based relationships. The reaction degree of precursors was empirically derived based on the binder composition. The proposed equation covered 16 different scenarios with individual and blended systems cured at 20 °C and 60 °C, and reached a coefficient of determination (r^2) of 0.84. The reaction products formed in hardened microstructures were divided in three categories, and their amounts were also proved to be estimated with high accuracy. Through the definition of *phase assemblage indices*, the estimation of C-(N-A-)S-H and N-(C-)A-S-H gels displayed r^2 values of 0.86 and 0.89, respectively, when comparing with experimental results. Secondary Ca-bearing crystalline phases displayed lower agreement with experiments, but their restricted formation contributed to a maximum of 9 % of all reaction products in all evaluated systems.

Fourth and finally, newly developed thermodynamic databases and the empirically defined dissolution rates in this work were included in GeoMicro3D. The numerical modelling tool was adapted to simulate the evolution of digital microstructures of systems containing a variety of precursors, working as an extension to the originally developed model. The simulations showed great agreement with experimental results in four different scenarios, including individual and blended precursors. The degree of reaction at 28 days displayed variations in the range of 1 - 3 % between modelled and experimental conditions of the four evaluated systems, and the amount of primary reaction products had variations of 2 - 11 % and 3 - 12 % for C-(N-A-)S-H and N-(C-)A-S-H gels, respectively. The precipitation of Ca-based secondary products - e.g. portlandite, strätlingite and katoite - was slightly overestimated, leaving room for the improvement of the tool in future researches through the definition of phase transformation reactions and kinetic parameters of nucleation.

This study successfully investigated the different stages of reaction of alkali-activated binders, mapping the influence of various parameters in each one of them. The chosen approach addressed one of the main challenges of these binders, proposing solutions to overcome the issues of the high variation in chemistry and mineralogy of precursors and activators under selected curing conditions. The obtained results provide accurate estimations of the microstructural characteristics of different alkali-activated binders, providing digital microstructures which can be used for different modelling purposes, including mechanical properties and service-life estimations. Finally, the contributions of this work are expected to aid the applicability and the acceptance of AAMs.

Samenvatting

De doorgaande ontwikkeling van wereldwijde infrastructuur vraagt om betrouwbare en kostenefficiënte bouwmaterialen. In dat licht gelden alkali-geactiveerde materialen (AAM's) als een van de duurzaamste alternatieven voor traditioneel portlandcement (PC): ze combineren vergelijkbare tot betere prestaties met een lager gebruik van CO₂-intensieve grondstoffen. Ondanks ruim zeventig jaar intensief onderzoek, blijft de praktische toepasbaarheid van deze bindmiddelen in grootschalige projecten problematisch, wat brede industriële acceptatie belemmert. De belangrijkste obstakels in betrouwbare bepaling van prestaties zijn de inhomogene verdeling van grondstoffen, de grote variatie in mogelijke activators/precursoren, en hun uiteenlopende mineralogische/chemische samenstellingen. Het korte- en langetermijngedrag van AAM's is nauw verbonden met hun reactiemechanismen, en daarmee met de aard en hoeveelheid van de reactieproducten in de verharde microstructuur. Door empirische observaties en numerieke modellering kan een verband worden gelegd tussen grondstofeigenschappen en de microstructurele ontwikkeling van het bindmiddel, wat de industrie in staat stelt om de korte en langetermijn eigenschappen van AAM-gebaseerde constructies nauwkeurig te voorspellen en te optimaliseren.

Dit proefschrift richtte zich op het begrijpen van de verschillende factoren die het reactiepad van AAM's beïnvloeden, vanaf de eerste stadia van oplossing tot de vorming van volgroeide microstructuren. Als eerste werden glazen geproduceerd die lijken op commerciële vliegglas en slakken. Deze synthetische precursoren hadden een vereenvoudigde chemische samenstelling, wat kwalitatieve en kwantitatieve analyse mogelijk maakte op de invloed van Ca, Al en Si op de mineralogie van elke precursor, en daarmee op de oplossings- en neerslagmechanismen van hun reactieproducten. De structuur van de precursoren werd gekarakteriseerd met röntgendiffractie (XRD), Fourier-transformatie infraroodspectroscopie (FTIR), Ramanspectroscopie en kernspinresonantie (NMR), waarbij CaO werd geïdentificeerd als de belangrijkste netwerkmodificator (NWM) van het amorfe netwerk. De overgang van Al-gemodificeerde structuren rijk aan cristobaliet en mulliet (in vliegglasachtige glazen) naar gehlenietachtige structuren (in slakachtige glazen) maakte het mogelijk een direct verband te leggen tussen het CaO-gehalte van elke precursor en de mate van wanorde in hun structuur.

Ten tweede werd de oplossingskinetiek van de synthetische precursoren onderzocht. Door gebruik te maken van grove glasdeeltjes in sterk verdunde oplossingen (1:1000) van NaOH kon de tijdsgebonden ontwikkeling van de concentratie van elk element worden gemeten, nog vóór de vorming van de eerste reactieproducten. Het vrijkomen van Ca, Si en Al uit het netwerk van de glazen werd gemeten met inductief gekoppeld plasma-optische emissiespectroscopie (ICP-OES), in vijf verschillende scenario's, waaronder drie NaOH-concentratie bij 20 °C en 60 °C. De gecombineerde invloed van pH en temperatuur werd meegenomen bij het opstellen van algemene oplossnelheidsvergelijkingen, gebaseerd op relaties van het Arrhenius-type. Deze vergelijkingen gaven een schatting van de uitloging van opgeloste stoffen op basis van de samenstelling van de precursoren en de experimentele omstandigheden. De nauwkeurigheid werd gevalideerd met experimentele gegevens uit de literatuur van verschillende auteurs.

Ten derde werden de mechanismen van de fase-neerslag en fase-samenstelling van alkali-geactiveerde bindmiddelen onderzocht. Aanvullende oplosproeven met fijne precursoren toonden, met behulp van ICP-OES, aan hoe opgeloste componenten werden verbruikt bij de vorming van eerste kiemen van vaste reactieproducten. Door gebruik te maken van FTIR, differentiële thermogravimetrie (DTG) en selectieve oplossingsbehandelingen kon worden bepaald welk type ongeordende gels ontstond tijdens de vroege activeringsstadia van verschillende precursoren. De neerslag van portlandiet als tussenproduct bleek dominant in de eerste fase van het reactiesysteem. Vervolgens werden C-(N-A-)S-H-achtige gels bij voorkeur gevormd in alle systemen bij 20 °C, terwijl N-(C-)A-S-H-achtige gels pas de voorkeur kregen bij hogere uithardingstemperaturen. Daarnaast maakte de combinatie van in-situ isotherme calorimetrie met SEM-beelden het mogelijk om verschillende fasevormingsmechanismen in de bindmiddelen waar te nemen. Homogene neerslag werd voornamelijk aangetroffen in met waterglas geactiveerde systemen, terwijl heterogene neerslag dominant was in systemen met NaOH. Beide mechanismen zijn eerder beschreven in de literatuur, maar de in dit proefschrift toegepaste methode maakte het mogelijk ze beide op unieke wijze waar te nemen.

In systemen van 28 dagen oud maakte de combinatie van kwantitatieve XRD (QXRD), selectieve oplossingsbehandelingen en SEM-beeldsegmentatie het mogelijk om aanvullende relaties op basis van chemie en temperatuur vast te stellen. De reactiegraad van precursoren werd empirisch afgeleid op basis van de bindmiddelsamenstelling. De voorgestelde vergelijking dekte 16 verschillende scenario's met zowel individuele als gemengde systemen die uithardden bij 20 °C en 60 °C, en behaalde een determinatiecoëfficiënt (r^2) van 0,84. De reactieproducten die zich vormden in de verharde microstructuren werden onderverdeeld in drie categorieën, en hun hoeveelheden bleken eveneens met hoge nauwkeurigheid te kunnen worden ingeschat. Via de definitie van fase-samenstellingsindices kon de hoeveelheid C-(N-A-)S-H- en N-(C-)A-S-H-gels worden ingeschat met r^2 -waarden van respectievelijk 0,86 en 0,89, ten opzichte van experimentele resultaten. Secundaire Ca-houdende kristallijne fasen hadden een lagere overeenkomst met de experimenten, maar hun beperkte vorming was in de geëvalueerde systemen maximaal 9 % van het totaal aan reactieproducten.

Ten vierde, en tot slot, werden de nieuw ontwikkelde thermodynamische databases en empirisch bepaalde oplosnelheden uit dit onderzoek opgenomen in GeoMicro3D. De numerieke modellerings-tool werd aangepast om de evolutie van digitale microstructuren te simuleren in systemen met uiteenlopende precursoren, als uitbreiding op het oorspronkelijk ontwikkelde model. De simulaties toonden een sterke overeenkomst met experimentele resultaten in vier verschillende scenario's, waaronder zowel individuele als gemengde precursoren. De reactiegraad na 28 dagen had variaties van 1-3 % tussen de gemodelleerde en experimentele omstandigheden in de vier geëvalueerde systemen. De hoeveelheid primaire reactieproducten week af met 2-11 % en 3-12 % voor respectievelijk C-(N-A-)S-H- en N-(C-)A-S-H-gels. De neerslag van Ca-gebaseerde secundaire producten - zoals portlandiet, strätlingiet en katoiet - werd licht overschat, wat ruimte laat voor verdere verbetering van het model in toekomstig onderzoek door het definiëren van faseformatie-reacties en kinetische parameters voor kiemvorming.

Dit onderzoek bracht de verschillende reactiestadia van alkali-geactiveerde bindmiddelen succesvol in kaart en toonde hoe diverse parameters elk van deze stadia beïnvloedden. De gekozen aanpak richtte zich op een van de grootste uitdagingen van deze bindmiddelen en

stelde oplossingen voor om de problemen van grote variatie in chemische samenstelling en mineralogie van precursoren en activators onder specifieke uithardingscondities te verminderen. De verkregen resultaten bieden nauwkeurige schattingen van de microstructurele eigenschappen van verschillende alkali-geactiveerde bindmiddelen, en leveren digitale microstructuren die gebruikt kunnen worden voor uiteenlopende modelleringsdoeleinden, waaronder de mechanische eigenschappen en levensduurinschattingen. Tot slot wordt verwacht dat de bevindingen uit dit werk bijdragen aan de toepasbaarheid en acceptatie van AAM's.

Acknowledgements

“I want a new mistake, lose is more than hesitate”; *“We could fly but we hold to the ground”*. These two contradictory sentences, belonging to songs that have followed me for so long (20 years for the first one!), had and still have a deep impact in the path that took me here. Starting a PhD was perhaps a not so thoroughly thought idea in the beginning. I honestly underestimated the dimension of this academic cycle, and I do advise people to think over if they really want to make this career move. It is a mix of adrenaline, anxiety, and a very tough mental battle against yourself, opening and exposing a significant amount of scars from the past that you may carry. And it is funny to think (I mean, it’s funny after some time...) that these challenges can be both a driver and a blocker towards the completion of a PhD research. Try your best to allow the former to win, and to have a positive balance in the end. The final results of this *new mistake* will allow you to detach from the *ground*, and to *fly* to new horizons. And as I complete a 6 years-cycle of hard, stressful, and rewarding work, there are plenty of people that I have to praise, who have contributed on this journey, and have helped me not to go completely crazy.

Initially, a special gratitude goes to the DuRSAAM European Training Network (Horizon2020 Marie Skłodowska-Curie agreement No. 813596) program for a few reasons: for providing the funding for this research; for allowing me to attend and experience high-level academic activities and to experience the evolution of the construction field; and for introducing me to a multi-disciplinary team filled with talented and ambitious young researchers, supported by a backbone of experienced and encouraging mentors.

I would like to express my sincere and huge gratitude to my two promoters, Prof. Guang Ye (formerly known as Dr. Ye) and Prof. John Provis. Both of you allowed me to develop my work and supported all the steps of this research, even when my ideas seemed a bit unconventional. Dr. Ye, the long sessions of productive discussions with you allowed me to develop a sense of critical thinking and helped me to build a complete story out of my work. Doing science is not merely running experiments and drawing conclusions: it is about finding relevant open research questions and prioritizing those that bring the highest impacts to society and to our field; it is about designing an efficient plan to provide answers to these questions, while leaving multiple contributions on the way. Moreover, you taught me to put the reader in focus, developing the sensibility of conveying one same message to different audiences. With your guidance, we made sure to translate a bunch of complex equations and plots into information that can be easily accessed by future researchers, allowing the continuity of what we started. And thank you for all the *baijiu* we had on the way! Jonh, you are the main reason why I am here today, being the main inspiration for my work as a MSc. student, and being the first person I contacted to get this PhD position. You made sure to be always available to calm my anxiety and to make me look at the bright side of things. Whenever I had struggles with unexpected results, and whenever I needed to deviate my line of thoughts and think from the point of view of different research fields, I was always secure by knowing I could count on you advices. During the most difficult periods of this cycle, your encouraging words made a big difference in my confidence and motivation, and showed me that it is ok not to answer all the questions I initially had: “A good PhD thesis is the one that leaves room to other 3 or 4 new PhD theses”, as you told me a couple of times. Cheers to you!

My gratitude goes also to the committee members of my PhD thesis defence: Prof. Barbara Lothenbach, Prof. Ruben Snellings, Prof. Stijn Matthys, Prof. Erik Schlangen, Dr. Oguzhan Copuroglu, and Prof. Henk Jonkers, whose words of motivation throughout these years and insightful comments made a great impact in the final quality of this work. Prof. Lothenbach and Prof. Snellings, you were a great inspiration for me since the beginning of this journey. Barbara, we have been meeting in conferences and exchanging emails since my first year. I remember how upset I was when, due to Covid, I was not able to attend your courses on thermodynamic modelling. And even so, you were always keen to promptly help me any time I had easy and more complex questions, and made sure to have your impact felt in the design of my research plan. Ruben, your work on dissolution kinetics, glass structures, and early-stage reactions were my favourite literature for the first half of this journey, acting as the spark that ignited my passion for reaction mechanisms of alkali-activated materials.

Stijn, it was great working with you as the coordinator of our dear DuRSAAM Project, giving me examples on how to lead such a large collaboration work with a challenging research topic. Be sure that this has inspired me to make use of academic and industrial networks towards the development of high quality research.

Erik and Oguzhan. From the easy lunch talks to more serious conversations. “*Hey Erik, you look so nice today!*”. Whenever you heard this sentence, you knew I was going to ask for something not necessarily easy. Thank you for always giving me support to conclude my research, and for always hearing our thoughts on how to make the Microlab a great and democratic place for all researchers. And thank you for allowing your dog on our hikes, so we could have remarkable scenes with him pulling you through his leash! Oguzhan, thank you for your always kind conversations. You are such an incredible person. It was easy for you to spot when I was not feeling comfortable, and for giving me encouraging words in the middle of the hurricane. From talking basketball to jamming and to attending rock concerts, it was a pleasure to have you around in these years, and to know I had a supporting person at only a door-knock distance. And Henk, thank you for the always friendly chats at late hours in the Microlab, and for always showing your enthusiasm with my work and motivating me!

The Microlab... oh the Microlab! An awesome place to be, and also an awesome place to get stressed. I could not get here without the support from a few magical people that form the backbone of our beloved Microlab. John: first of all, I am sorry for the thousands of ICP measurements I asked you to do. But I am truly, truly, grateful for your work and for your efforts towards my research. Thank you for teaching and giving me the responsibility to replicate the know-how of so many devices in the lab. We learned a few things together (how to fix the TGA, how to recalibrate the TAM Air, how to have many *ganbei* in the same night). You can read this thesis and realize how much impact you had in it, and how important were all the measurements you helped me with. And of course, we could share a few (or a lot) of beers together at Psor and other places to celebrate along the way! Thank you, once, twice, and a thousand times for everything, John! Arjan, your patience and guidance helped me to acquire amazing images and insights. From sample preparation teaching to image optimization, we were able to have clear observations of fundamental phenomena of dissolution and phase precipitation, and I know I would not have done the same job without your support. And the best is that we could listen to some nice music and some flight-comedy videos during our sessions! And Maiko... Your thank you comes in a bit! A huge thanks goes also to Ton, for the precise and careful cutting of my specimen, to Paul Vermeulen, for taking care of the furnaces and making them functional, and to Ruud Hendrikx, for all the support on the many XRD/XRF analysis.

I would also like to emphasize how much the team at the Microlab was and is important for me. First of all, the CMMB group was a great and safe field for discussions with so many bright researchers, and also for learning new cultures. Since the moment I joined, a group of fantastic people welcomed me and made me feel at home in Delft: Shizhe, Boyu, Zhiyuan, Zhenming, Xuhui, Yun Chen, Jiayi, Albina, Hua Dong. And then along the way, Yu Zeng, Farnaz, Irving, Guilherme, Qiu, Mayank, as the new members, always made sure that we were all supported in our work, with valuable discussions. Thank you for all the Chinese dinners, the summer barbeques, basketball playing and fruitful discussions. The Microlab also became a part of my family. Many discussions over life, many cups of coffee, many learnings and collaborations, many shared complaints, so many drinks at Psor or at some other conferences, and so many people I'm thankful for. Patrick and Marija, thank you for being there since the first days and for the always great discussions about research challenges and life. Technical discussions were always fruitful with you, and personal talks were even better! Mayank, Yun and Zhiyuan, you have no idea how important you were for me and how much you helped me to conclude my research. Thank you for all the discussions, ideas, combined stress and support on the final part of the thesis, especially on our Saturday sessions! Qiu, thank for being a great example of strength and how to fight for what we want, you know how much I admire you! Shizhe, thank you for the always encouraging words, and for the productive discussions over some fundamental phenomena of AAMs. Boyu, thank you for the great collaborations we had on the way! Shan, thank you for the SEM sessions, conversations about our life choices and for sharing the same fears of the future. Ameya, thank you for being my partner on drinking fancier beers at Psor, struggling with convincing John to run our ICP samples, and for the fun moments in the post-academic life. Yu Zhang, thank you for all your tremendous help with setting up my dissolution experiments and image analysis. Meme, thank you for being a great friend, always up for a nice chat about life and work, and for the amazing nights in Kyoto! Stefan and Bianca, thank you for being my first contact with life in here and for embracing me in the beginning of the journey, giving me a sensation of safety when things were all new for me. The team at the 6.25 office: Tiger, the runner and example for my goals; Ali, the best human being that has ever walked at the Microlab, listening to all my not-so-serious talks, sharing many laughs and binary code lessons on Saturdays, and supporting Brazil during the World Cup; Liu Chen for reminding to never stop working; Gabriele, even for a short moment, thank you for countless laughs, limitless jokes and spaghetti carbonara; Gabriel, thank you for being a great friend, for sharing the love for football, and for being open to discuss a vast amount of life-related topics; Irving, thank you for all the music talk and that took me away from research struggles. Jinbao, Wen, Rowin, Laura, thank you for showing me that the combination between hard work and *ganbeis* is the best we can have in academia; Branko, Mohammed, Max, Ze Chang, Zhi Wan, Burcu and all the others, thank you for the funny lunch discussions over sports and other unusual topics during all these years. Our administrative staff, Jacqueline, Sandra, Iris and Jaap: you did the work behind the scenes and reduced our concerns with non-research topics, listening to our demands and working hard to bring them to reality: a huge thank you to this team - Jaap, thank you for the bike tours and apple pies, and Jacqueline, thank you for the huisarts! And all the master students who passed by the Microlab: Dautse and Ivana (and Firas, a borrowed student), who allowed me to learn how to be a better leader and mentor. You have no clue how important you were in this journey.

Life also happened outside the University, and has also brought great moments and memories for me. Music is a true passion of mine and has always been a great portion of my life, and here in Delft it allowed me to connect with very special people. Matteo, I cherish the day I spotted you walking with your guitar case at campus, and all the great things that followed it. With you, Su, and Will, we had our Friday jamming gang that allowed us to

survive through the curfew, sharing many chords, Italian dinners, and fun. Thank you for giving a safe place for me, where I could steam off from all my stress at the University, and for reminding me that these are the moments that are actually worth in life. I could say that you have no idea of how important you were and are to me, but I actually phrased that many times after a couple of drinks. Thank you for everything, really! “I love my friends”.

The basketball gang. When I moved to Delft, pickup basketball courts at X were the first spaces I found to connect with people and don’t feel so lonely. Rafa and Ricardo, how lucky was I to find great friends as you two, to share the courts with you, to teach you to never miss *easy buckets*, to the point of convincing you to a Latvia trip me to watch a few matches, and to bond beyond the game and bringing Mirian and Sarah into my life with Barbara.

The Roland Holstlaan gang had also an amazing mark and contribution to my journey. It was late 2019-early 2020 when things started to become weird... And we were set to live in only one building for a few months. And that only increased the sense of friendship and support we had for each other. Tejas, Jackson, Kazuki and Sergio. You guys have no clue of how important it was to have you in this period of life. All the nice dinners and beers we shared, each time from a different cultural background. So many fun moments to cherish and remember. Tejas, I’m still waiting for the airplane tour and for your visit in Brazil. Thank you and your parents for your guided tours in Dubai, for the philosophical talks we will continue to have, and for all the foods you introduced me, even when you tried to kill us with your special chilly powders in our nachos. Jackson, thank you for being a great peer to discuss our vulnerabilities and to overcome them together, for showing us different foods, but a huge no thank you for using the kettle to warm your cold beer in front of us. Kazuki, thank you for teaching how to better use my pivot foot, block shots, and for the nicest tour I could have had in Tokyo! Marcelo and Luo, you were the first people I met outside of the universe of the PhD in my first weeks at Delft. Thank you for showing me the secrets of Delft and live in the Netherlands, with a nice unplanned trip to Texel as the peak, and fun for the fun dinners. I know that grown-up lives put a distance between us, but I keep good memories of my first years with you, and I’m always happy to meet you and cheer for your future!

Being a good Brazilian, we have to find other Brazilians out there to ease the coldness of living in the Netherlands. And I found incredible people in here, aka the Brazilian family that Delft gave me. Sérgio, thank you for all the concerts, music making and crazy stories that made me forget a bit about research. Since your first period here during the crazy Covid era, until now with our talks about how much we miss our culture and failed attempts to write our own songs, you have been an amazing and supportive friend! Iuri and Cristyna, the first Brazilians who I’ve met, and created a tight bond since the day you showed me how to get coffee at TU. Thank you for all the dinners, trips, advices for our life, taking care of Mixirica since his very first days, and for bringing Clarinha to this world! Alana, Rafa, Guilherme and Gustavo, thank you for making our group a mix of work talks and fun with the Brazilian touch. We all share very similar challenges and career paths, and together we built a foundation for all of us, taking care of each other and celebrating all the achievements we had all the way. Alaninha da concorrência, you taught me to be brave, to embrace professional challenges and to trust yourself to overcome them, despite trying to teach me that *croissant* is a funny word - by the way, you failed on this last one. Rafa, our favourite *Gringo* (don’t let others tell you the opposite!), who supported all of our struggles and showed us that there is (good!) life after PhD. Gustavo *topo que gira*, thank you for the questionable jokes and for joining me in my stupidity. Marvin, the new addition to our family who brought a bit of Dutch culture to our group! Far from Delft, thank you Wilson and Val for always making sure that we had a family while being abroad, even from a 5 hours

distance. Wilson, my brother for more than 15 years, and Val, who brought a bit of sense and control to our lives and dad-style jokes, we always knew that we could count on you, and we always enjoyed to the maximum all the times we met, even if it was for only a few days at a time. You even inspired us to get married! (sorry Lian, we love you but that's all the inspiration we are getting for now.) Natasha and Edu, you are technically not Brazilian but you connected us to our Latin roots since the day we met. Thank you for all the delicious dinners, cultural exchange between Brazil and Galicia, live concerts and discovery of new music, and for also not being big fans of complicated board games!

As a PhD should be, I chose two amazing paranymphs to stand next to me in the big day. Maiko and Guilherme. And how can I start to acknowledge you two for your impact in my life... Maiko, I remember that you took me under your wings in the first summer event I attended. We actually did not work together too much due to my research topic, but that did not prevent me from connecting to you through many different subjects. We always had fun and insightful talks about sports, making fun of the trophy-less Dutch team (sorry for that) or the fact that Brazil is not great anymore, music, and you always listened to all of our concerns and fears, acting behind the scenes to solve our issues as much as you could. Thank you, a huge thank you for opening the doors to your house, for sharing with me and listening to my moments of vulnerability, and for showing me that we are all humans, with our achievements, with our qualities, and with our problems, not afraid to continue to learn new things every day. You are a giant! Guilherme! The person whose life I *ruined* for indicating to a PhD position. I'll be a bit selfish now: how happy I am that you took the challenge, because you came to show me so many things: how to be a caring and patient person, how to bring energy to every single activity we do, how to be thankful for all things that happens to us, looking always to the positive side of situations even when I felt there was nothing to take from them. I don't know how many times you heard me complaining about everything, feeling down, and somehow you always found a way to make me smile again. You've been amazing these years, especially during the final sprint of the journey, and I could not say thank you enough times.

I also would like to acknowledge the importance that Paebbl had in my PhD cycle. The year of 2024 was a bit (actually it was a whole lot...) stressful, combining the end of the writing process with a new and exciting professional journey. For many times I felt like I was not able to deliver my best at my new place, because I was still stuck and thinking about the thesis. Fay and Ana, you made me feel calm, you understood my struggles, giving me sufficient space to conclude my personal goals, and helping me to handle this double-life for many months. Thank you for helping me on not going completely crazy. And Walter, thank you for the help with the samenvatting. I hope you have fun reading the whole thesis!

Finally, it is time to say how much my family meant and means to me. It is no surprise to anyone how much I am close to my family, and how much I miss them. Six years of video calls, many times saying 'Saudades, amo vocês', many words of comfort from the other side of the world. My dear parents, Luiz and Alba, I always said that you are the ones to be blamed for me not being next to you right now. You did such a fantastic job that you ended up raising a curious little guy, who just wanted to grow, learn new things, and explore new parts of the world. All the years of dedication, providing me education and values, took me far but always made me feel so close to your heart. I am proud to be here showing all the love, and all the values and principles that you gave me. My sisters, Carla and Natalia, who were my best friends since the day I was born - even during my teenage-hood when, man, I was a hard kid. Our bonds do not respect distance, and we are always connected and supportive to each other. Carla, you always impressed me with your resilience and your drive

to grow, without letting behind your care for your family and your friends around you. Naty, an example of strong mother and brave professional, who showed me that we have to stand up for our beliefs and adapt into different situations. You and Murilo constantly show me that a strong and solid family is the most important thing we can have, and that this can provide all the support each one needs to grow in life. And my beloved godchildren, Lucas and Laís, who every day teach me that we have to be humble, to be innocent, to slow down and enjoy all the phases and moments of our lives.

And for last, and definitely most importantly, I would like to say a few words about my wife Barbara. Or not. I don't know if I should. Baby, I don't think I can ever thank you enough, I don't know if I can express how much you mean to me in just a few words. You were with me when this experience was nothing but wild thought, you were with me during this hurricane. And the most impressive thing is that you still are with me despite the past six years (emphasizing the last two). You saw me falling, you saw me questioning myself, you witnessed all my struggles. I was moody, I was quiet, I was present but my mind was somewhere else. I lost weekends, I lost a whole summer, I lost energy, I lost motivation, I lost self-confidence. You always picked me up, hugged me, and showed me that I can do this. You smiled. You brought me back to reality. You made me forget about the struggles, even if that lasted only a few days, hours, minutes. And then you did it again. And again. You gave me all the support I could have, even more than what I could have asked for. You gave me ground. To be honest, more than half of this PhD thesis belongs to you. It is not that you actually wrote it, but I think every single word of this book has a bit of your mark on them. Even when we were 10 thousand km away from each other, you were always present. Two long years, Covid in the middle. The beginning of the journey, when I was still struggling to adapt myself to this environment. The many tears I dropped in the airports when you went back home, when I came back to Delft. Our first house. Our second house. The seven legs of Mixi and Mimosa that we have in our apartment, who wake us up every morning at 6AM asking for food. The care and passion behind every corner of our apartment. The one thousand meals you made. The five hundred failed meals I made. I could go on forever... And I will, I always will - even if you decide to do a PhD yourself, despite seeing so many stressed students next to you. Thank you. Just, thank you. I love you. Deeply.

To conclude this *long* session, here is one last paragraph that will work as a note for myself in the future. In *Wishlist*, Eddie Vedder sings a line that always made me think hard: "*I wish I was as fortunate, as fortunate as me*". As this cycle comes to an end, I think it is an appropriate moment to use it. Many things happened over the past 6 years: a few of them are described in here, a lot of them are not. In the end, all of this contributed to who I am now. At the end of a great challenge, we can reflect on that old *cliché* which says that what matters is the journey, not the destiny. And that is actually true. As hard as it can be sometimes, we should try our best to be happy with things the way they are - and continue our journey to be once again happy with the way things will be. A big challenge, as a PhD thesis is, often makes you feel like you have no reasons to celebrate before concluding the main goal. The truth is that we have to find joy in the small steps we take towards the final destination. I am thankful for the challenges I had, and how much they made me learn and grow. Don't get me wrong: this was no Disney special. I was not happy all the time, especially in the periods I struggled the most with my internal questions. But with time to reflect, I can easily say *I am as fortunate as I can be*, today. And all the names I cited here will have your contribution for me to be *as fortunate as I can be*, tomorrow. Thank you all.

Luiz Miranda de Lima

Delft. June, 2025.

CURRICULUM VITÆ



Personal information

Name	Luiz Cezar Miranda de Lima Junior
Nationality	Brazilian
Date of birth	October 1st, 1991. Guarapuava - PR, Brazil
Email	luizc.limajunior@gmail.com

Education and Work Experience

Feb 2009 - Dec 2013	BSc. in Materials Engineering State University of Ponta Grossa, Brazil
Feb 2014 - May 2016	MSc. in Materials Science and Engineering - Development and Characterization of Materials State University of Ponta Grossa, Brazil
Jan 2014 - Dec 2018	Product development engineer Smart - Building Systems, Brazil
Jan 2021 - Jun 2025	Portuguese language coordinator for the Netherlands Native Scientists
Jun 2019 - Jun 2025	Ph.D. candidate Faculty of Civil Engineering and Geosciences Delft University of Technology, Netherlands
Jan 2024 - Present	Researcher in alternative binders Paebbl BV, Netherlands

